IMPACT FACTOR
10.057

#1 NUCLEAR MEDICINE, MOLECULAR IMAGING AND MOLECULAR RADIOTHERAPY JOURNAL

Vol. 63 ▪ No. 4 ▪ April 2022

JNM
The Journal of Nuclear Medicine

FEATURED ARTICLE

[177]Lu-PSMA-617 and Idronoxil in Men with End-Stage Metastatic Castration-Resistant Prostate Cancer (LuPIN): Patient Outcomes and Predictors of Treatment Response in a Phase I/II Trial. Sarennya Pathmanandavel et al. See page 560.

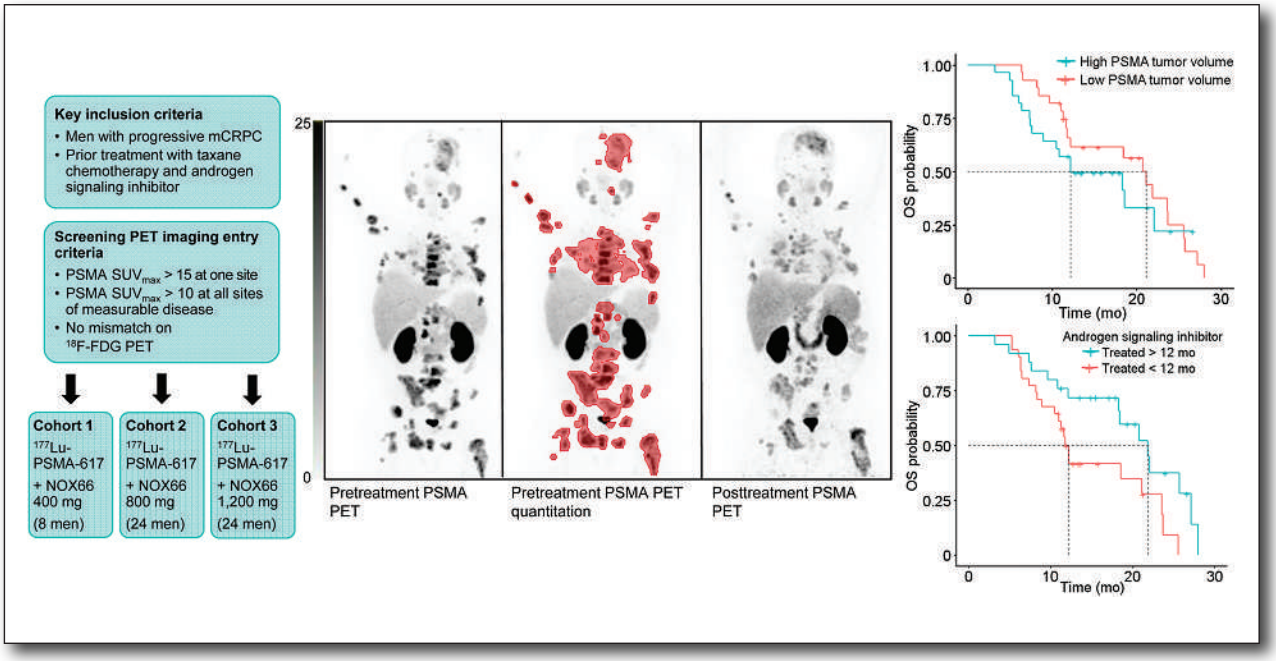

Blind image restoration: improving digital autoradiography for radiotracer and radiotherapy evaluation. Peng Lu et al. See page 591.

SNMMI Value Initiative
SOCIETY OF NUCLEAR MEDICINE & MOLECULAR IMAGING

THE UNIVERSITY OF TEXAS
MD Anderson Cancer Center
Making Cancer History®

OPEN RANK, CLINICAL FACULTY APPOINTMENT
DEPARTMENT OF NUCLEAR MEDICINE

The Department of Nuclear Medicine at MD Anderson is recruiting for an Open Rank, Clinical Faculty Appointment. The faculty member is expected to hold a Clinical Faculty Appointment (CFA) position at The University of Texas MD Anderson Cancer Center in the Department of Nuclear Medicine within the Division of Diagnostic Imaging. The faculty member is a clinician qualified to work in the field of Nuclear Medicine at either an Assistant, Associate or Professor level. The primary academic appointment will be in the Department of Nuclear Medicine.

Functional Responsibilities: The Sections of Positron Emission Tomography (PET) and Clinical Nuclear Medicine (CNM) are administrative units that provide comprehensive, diagnostic and therapeutic services within the Department of Nuclear Medicine. Faculty within these Sections provide (1) excellent, comprehensive and compassionate care for an oncologic patient population; (2) nuclear imaging and therapeutic procedures in a cost effective environment; (3) programs and projects conducted to advance fundamental or clinical understanding of oncology and nuclear medicine; (4) education for medical students, residents, fellows, graduate students and technologists; and (5) multidisciplinary and collaborative approaches to patient-centered imaging, transformative research, prevention and exceptional education.

The members of the Department are appointed upon the recommendation of the Chair of the Department of Nuclear Medicine with concurrence of the Division Head of Diagnostic Imaging, and approval by the President of the Institution. This position is supervised by the Section Chief(s) for day-to-day clinical operations. The primary evaluator on an Annual Faculty Performance Appraisal is the Department Chair, reflecting faculty member's education, research, patient care and administrative activities. These functional responsibilities require the mental ability to reason deductively; act decisively; communicate and execute the Institution's acceptable standards of conduct; interact with highly sophisticated technology; and understand complicated, comprehensive concepts and technologies.

Qualifications: Medical degree, board certification by the American Board of Nuclear Medicine, licensure by the Texas State Board of Medical Examiners and ACLS certification upon 90 days of employment.

Additional Preferred Qualifications:
- Board certification by the American Board of Radiology
- Record of high-quality, peer-reviewed publications
- ACLS certification preferred

Interested qualified candidates should submit their curriculum vitae and names and addresses of at least three references to:

Homer A. Macapinlac, M.D., Chair
Department of Nuclear Medicine
The University of Texas MD Anderson Cancer Center
1515 Holcombe Blvd, Unit 1485
Houston, TX 77030
Email: hmacapinlac@mdanderson.org
Req #: 00091341- 220131

MD Anderson Cancer Center is an equal opportunity employer and does not discriminate on the basis of race, color, religion, age, national origin, sex, sexual orientation, gender identity/expression, disability, veteran status, genetic information, or any other basis protected by federal, state, or local laws, unless such distinction is required by law. All positions at The University of Texas MD Anderson Cancer Center are security sensitive and subject to examination of criminal history record information. Smoke-free and drug-free environment.

THE UNIVERSITY OF TEXAS
MD Anderson Cancer Center
Making Cancer History®

OPEN RANK, CLINICAL FACULTY APPOINTMENT
DEPARTMENT OF NUCLEAR MEDICINE

The faculty member is expected to hold a Clinical Faculty Appointment (CFA) position at The University of Texas MD Anderson Cancer Center in the Department of Nuclear Medicine within the Division of Diagnostic Imaging. The faculty member is a clinician qualified to work in the field of Nuclear Medicine at either an Assistant, Associate or Professor level. The primary academic appointment will be in the Department of Nuclear Medicine.

Functional Responsibilities: The Sections of Positron Emission Tomography (PET) and Clinical Nuclear Medicine (CNM) are administrative units that provide comprehensive, diagnostic and therapeutic services within the Department of Nuclear Medicine. Faculty within these Sections provide (1) excellent, comprehensive and compassionate care for an oncologic patient population; (2) nuclear imaging and therapeutic procedures in a cost effective environment; (3) programs and projects conducted to advance fundamental or clinical understanding of oncology and nuclear medicine; (4) education for medical students, residents, fellows, graduate students and technologists; and (5) multidisciplinary and collaborative approaches to patient-centered imaging, transformative research, prevention and exceptional education.

The faculty will actively engage in clinical research and scholarly activity that promotes responsible conduct of research within the Department and Institution. The candidate is expected to assess and seek appropriate funding mechanisms to support clinical research focused on theranostics. Requires completion of grant applications and contracts, budget development and resource analysis.

The members of the Department are appointed upon the recommendation of the Chair of the Department of Nuclear Medicine with concurrence of the Division Head of Diagnostic Imaging, and approval by the President of the Institution. This position is supervised by the Section Chief(s) for day-to-day clinical operations. The primary evaluator on an Annual Faculty Performance Appraisal is the Department Chair, reflecting faculty member's education, research, patient care and administrative activities. These functional responsibilities require the mental ability to reason deductively; act decisively; communicate and execute the Institution's acceptable standards of conduct; interact with highly sophisticated technology; and understand complicated, comprehensive concepts and technologies.

Qualifications: Medical degree, board certification by the American Board of Nuclear Medicine, licensure by the Texas State Board of Medical Examiners and ACLS certification upon 90 days of employment.

Additional Preferred Qualifications:
- Board certification by the American Board of Radiology
- Record of high-quality, peer-reviewed publications
- ACLS certification preferred

Interested qualified candidates should submit their curriculum vitae and names and addresses of at least three references to:

Homer A. Macapinlac, M.D., Chair
Department of Nuclear Medicine
The University of Texas MD Anderson Cancer Center
1515 Holcombe Blvd, Unit 1485
Houston, TX 77030
Email: hmacapinlac@mdanderson.org
Req #: 00091342- 220131

MD Anderson Cancer Center is an equal opportunity employer and does not discriminate on the basis of race, color, religion, age, national origin, sex, sexual orientation, gender identity/expression, disability, veteran status, genetic information, or any other basis protected by federal, state, or local laws, unless such distinction is required by law. All positions at The University of Texas MD Anderson Cancer Center are security sensitive and subject to examination of criminal history record information. Smoke-free and drug-free environment.

FOR YOUR PATIENTS WITH ADVANCED PROSTATE CANCER

WHY IS PSMA A KEY PHENOTYPIC BIOMARKER IN ADVANCED PROSTATE CANCER?

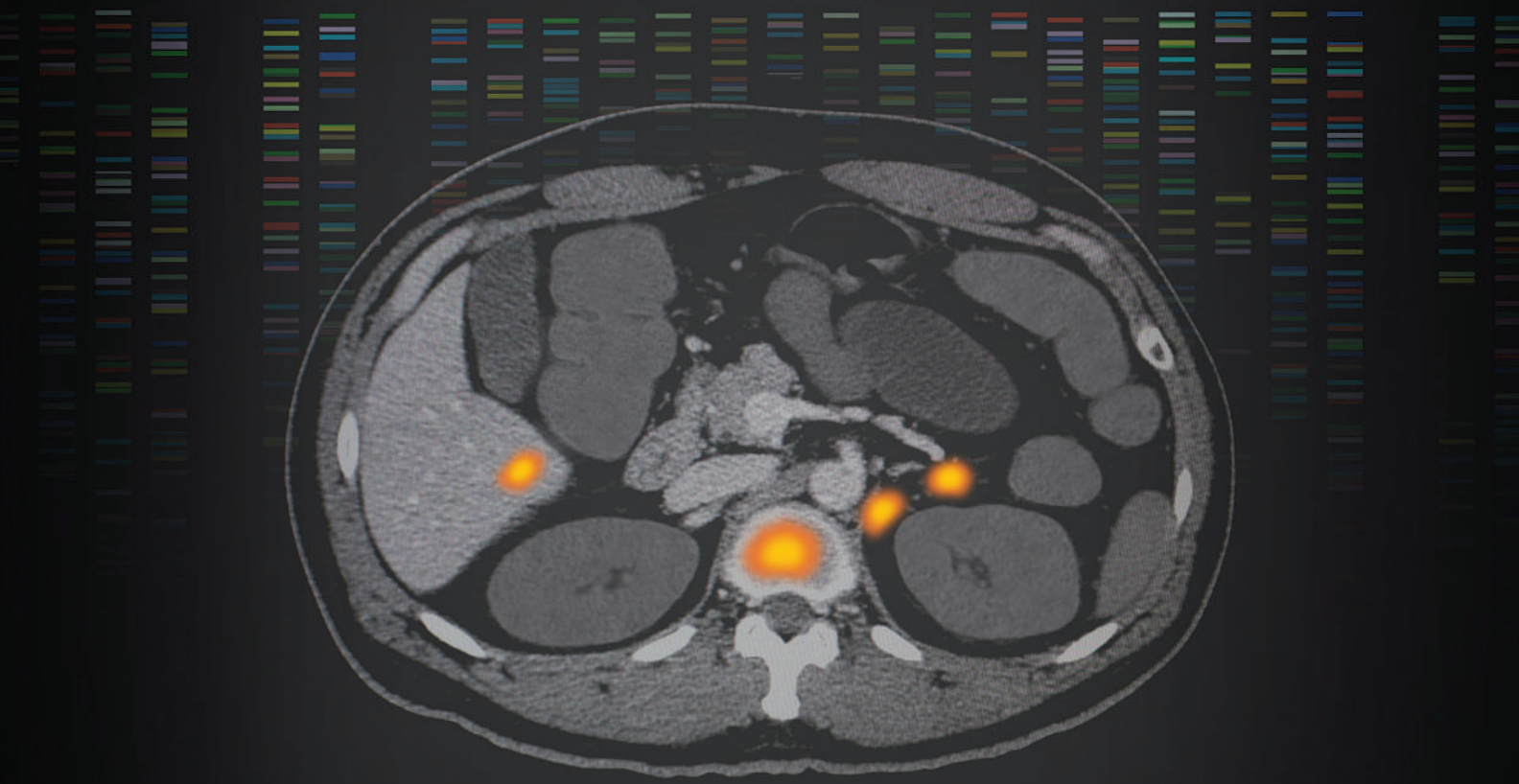

Prostate-specific membrane antigen (PSMA) is overexpressed in **>80%** of men with prostate cancer and can be detected by PSMA PET.[1-3]

PSMA is a diagnostic and potential therapeutic target, enabling a phenotypic precision medicine approach to treating advanced prostate cancer.[1,4-6]

Learn more at **www.PhenotypicPrecisionMedicine.com.**

Advanced Accelerator Applications
A Novartis Company

References

1. Hupe MC et al. *Front Oncol*. 2018;8:623. **2.** Hope TA et al. *J Nucl Med*. 2017;58(12):1956-1961. **3.** Pomykala KL et al. *J Nucl Med*. 2020;61(3):405-411. **4.** Hofman MS et al. *Lancet*. 2020;395(10231):1208-1216. **5.** Müller J et al. *Eur J Nucl Med Mol Imaging*. 2019;46(4):889-900. **6.** Kratochwil C et al. *J Nucl Med*. 2016;57:1170-1176.

© 2020 Advanced Accelerator Applications | All Rights Reserved

November 2020 | PSM-1237215

MIRION TECHNOLOGIES

BOOST EFFICIENCY FOR THYROID UPTAKE

Streamlined Workflow and Intuitive User Experience

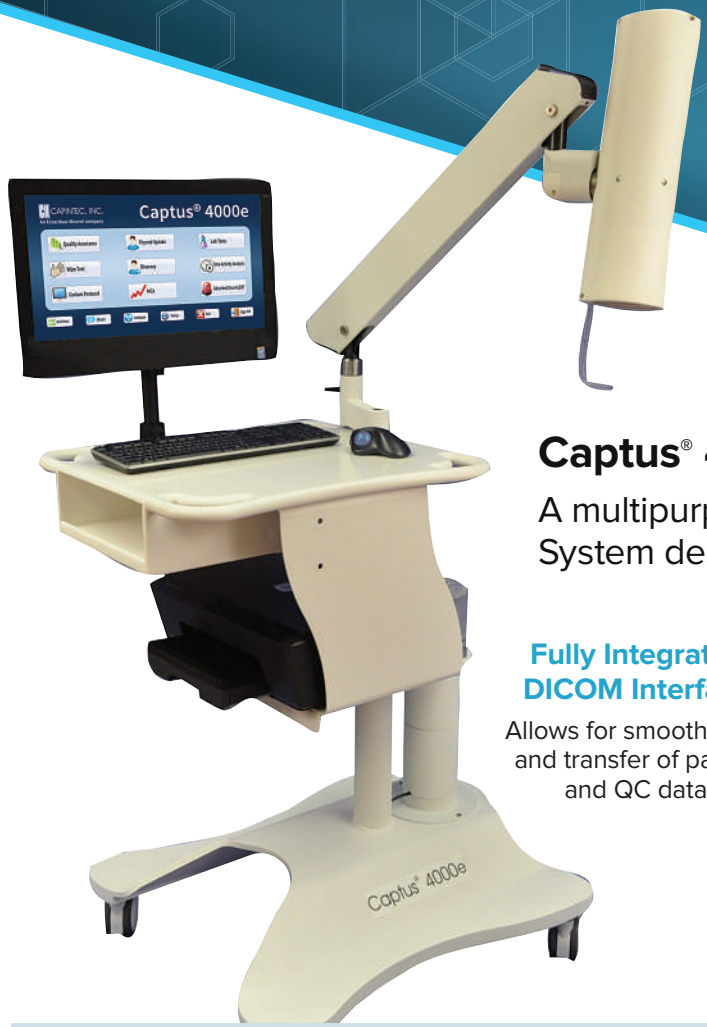

Captus® 4000e Thyroid Uptake System

A multipurpose Nuclear Medicine Measurement System designed with user-friendly benefits.

Fully Integrated DICOM Interface

Allows for smooth input and transfer of patient and QC data.

Comprehensive Software Modules

For thyroid uptake, wipe tests, automated QC, bioassay, and more.

Custom Protocol Program Included

Flexibility to design and implement protocol specified to your needs.

Rapid Patient Triage for Emergency Situations

Absorbed Dose ALERT Software
Designed for emergency incidents, ALERT measures internal contamination levels for the inhalation and ingestion of radioactive material, and notifies the user when contamination exceeds a preset level. **Upgrade Today!**

Visit capintec.com

Driving Innovation, Together: CAPINTEC, INC. Part of Mirion Technologies · BIODEX Part of Mirion Technologies

Visit capintec.com to learn how we can support your unique requirements.

Copyright © 2022 Mirion Technologies, Inc. or its affiliates. All rights reserved. Mirion, the Mirion logo, and other trade names of Mirion products listed herein are registered trademarks or trademarks of Mirion Technologies, Inc. or its affiliates in the United States and other countries. Third party trademarks mentioned are the property of their respective owners.

OPS-3624 - 3/22

JNM

Volume 63 • Number 4 • April 2022

JNM The Journal of NUCLEAR MEDICINE

The Official Publication of **SNMMI**

Publications Committee

Todd E. Peterson, PhD, FSNMMI
Chair

Carolyn Anderson, PhD, FSMMMI
Paige B. Bennett, MD
Joyita Dutta, PhD
Michael M. Graham, PhD, MD, FSNMMI
Hossein Jadvar, MD, PhD, FACNM, FSNMMI
Steven M. Larson, MD, FACNM
Heinrich R. Schelbert, MD, PhD, FSNMMI
Heiko Schöder, MD, MBA
David M. Schuster, MD
Jessica Williams, CNMT, RT(N), FSNMMI-TS
Harvey A. Ziessman, MD, FSNMMI

Ex officio

Johannes Czernin, MD
Kathy S. Thomas, MHA, CNMT, PET, FSNMMI-TS
Henry F. VanBrocklin, PhD, FSNMMI
Richard L. Wahl, MD, FACNM

Associate Director of Communications
Susan Alexander

Senior Copyeditor
Susan Nath

Senior Publications & Marketing Service Manager
Steven Klein

Editorial Production Manager
Paulette McGee

Editorial Project Manager
Mark Sumimoto

Director of Communications
Rebecca Maxey

CEO
Virginia Pappas

MISSION STATEMENT: *The Journal of Nuclear Medicine* advances the knowledge and practice of molecular imaging and therapy and nuclear medicine to improve patient care through publication of original basic science and clinical research.

JNM (ISSN 0161-5505 [print]; ISSN 2159-662X [online]) is published monthly by SNMMI, 1850 Samuel Morse Drive, Reston, VA 20190-5316. Periodicals postage is paid at Herndon, VA, and additional mailing offices. Postmaster, send address changes to *The Journal of Nuclear Medicine,* 1850 Samuel Morse Drive, Reston, VA 20190-5316. The costs of publication of all nonsolicited articles in *JNM* were defrayed in part by the payment of page charges. Therefore, and solely to indicate this fact, these articles are hereby designated "advertisements" in accordance with 18 USC section 1734.

DISCLOSURE OF COMMERCIAL INTEREST: Johannes Czernin, MD, editor-in-chief of *The Journal of Nuclear Medicine,* has indicated that he is a founder of Sofie Biosciences and holds equity in the company and in intellectual property invented by him, patented by the University of California, and licensed to Sofie Biosciences. He is also a founder and board member of Trethera Therapeutics and holds equity in the company and in intellectual property invented by him, patented by the University of California, and licensed to Triangle. He also serves on the medical advisory board of Actinium Pharmaceuticals and on the scientific advisory boards of POINT Biopharma, RayzeBio, and Jubilant Pharma and is a consultant for Amgen. No other potential conflicts of interest were reported. Manuscripts submitted to *JNM* with potential conflicts are handled by a guest editor.

EDITORIAL COMMUNICATIONS should be sent to: Editor-in-Chief, Johannes Czernin, MD, *JNM* Office, SNMMI, 1850 Samuel Morse Drive, Reston, VA 20190-5316. Phone: (703) 326-1185; Fax: (703) 708-9018. To submit a manuscript, go to https://submit-jnm.snmjournals.org.

BUSINESS COMMUNICATIONS concerning permission requests should be sent to the publisher, SNMMI, 1850 Samuel Morse Drive, Reston, VA 20190-5316; (703) 708-9000; home page address: jnm.snmjournals.org. Subscription requests and address changes should be sent to Membership Department, SNMMI at the address above. Notify the Society of change of address and telephone number at least 30 days before date of issue by sending both the old and new addresses. Claims for copies lost in the mail are allowed within 90 days of the date of issue. Claims are not allowed for issues lost as a result of insufficient notice of change of address. For information on advertising, contact Team SNMMI (Kevin Dunn, Rich Devanna, and Charlie Meitner; (201) 767-4170; fax: (201) 767-8065; TeamSNMMI@cunnasso.com). Advertisements are subject to editorial approval and are restricted to products or services pertinent to nuclear medicine. Closing date is the first of the month preceding the date of issue.

INDIVIDUAL SUBSCRIPTION RATES for the 2022 calendar year are $603 within the United States and Canada; $648 elsewhere. Make checks payable to the SNMMI. CPC IPM Sales Agreement No. 1415158. Sales of individual back copies from 1999 through the current issue are available for $60 at http://www.snmmi.org/subscribe (subscriptions@snmmi.org; fax: (703) 667-5134). Individual articles are available for sale online at http://jnm.snmjournals.org.

COPYRIGHT © 2022 by the Society of Nuclear Medicine and Molecular Imaging. All rights reserved. No part of this work may be reproduced or translated without permission from the copyright owner. Individuals with inquiries regarding permission requests, please visit http://jnm.snmjournals.org/site/misc/permission.xhtml. Because the copyright on articles published in *The Journal of Nuclear Medicine* is held by the Society, each author of accepted manuscripts must sign a statement transferring copyright (available for downloading at http://jnm.snmjournals.org/site/misc/ifora.xhtml). See Information for Authors for further explanation (available for downloading at http://www.snmjournals.org/site/misc/ifora.xhtml).

The ideas and opinions expressed in *JNM* do not necessarily reflect those of the SNMMI or the Editors of *JNM* unless so stated. Publication of an advertisement or other product mentioned in *JNM* should not be construed as an endorsement of the product or the manufacturer's claims. Readers are encouraged to contact the manufacturer with any questions about the features or limitations of the products mentioned. The SNMMI does not assume any responsibility for any injury or damage to persons or property arising from or related to any use of the material contained in this journal. The reader is advised to check the appropriate medical literature and the product information currently provided by the manufacturer of each drug to be administered to verify the dosage, the method and duration of administration, and contraindications.

EARLY-BIRD DEADLINE: APRIL 14

This year, the Annual Meeting will be offered as a hybrid event with in-person and remote registration options available—allowing you to customize your meeting attendance. Make your plans now to attend SNMMI's flagship meeting, in-person June 11-14 in Vancouver, BC, Canada, or virtually from your home or office.

Register Today

WWW.SNMMI.ORG/AM2022

SNMMI 2022 Annual Meeting

RADIATION SAFETY+ Review and Essentials

Let the SNMMI-TS Help You Prepare for the NMTCB's Radiation Safety Exam

Get the tools you need to successfully prepare for the exam with the **Radiation Safety + Review and Essentials** program. This 5 module/7.75 VOICE credit course provides a comprehensive review of all aspects of radiation safety including:

- Radiation physics and instrumentation
- Dosimetry
- Mathematics
- Security and control
- Shipping and receiving
- Disposal
- Emergency procedures
- Regulations
- Radiation protection and ALARA
- Radionuclide therapy best practices

2022 NMTCB Radiation Safety Exam Dates Announced!

Begin Your Preparation!

Order this popular program today!

You'll review content on CT. X-ray, fluoroscopy, and MRI, as well as optimizing radiation exposure, including appropriateness criteria, Image Wisely/Image Gently, and special populations. Plus, test what you've learned with a 150 question "Mock Exam," to ensure you're fully prepared for the exam.

Member: $99 | Non-Member: $249

Get started today!
www.snmmi.org/RadiationPlus

SNMMI Technologist Section
SOCIETY OF NUCLEAR MEDICINE & MOLECULAR IMAGING

Explore SNMMI's Online Career Center!

Explore the benefits of the SNMMI Career Center by logging in or creating a new account today.

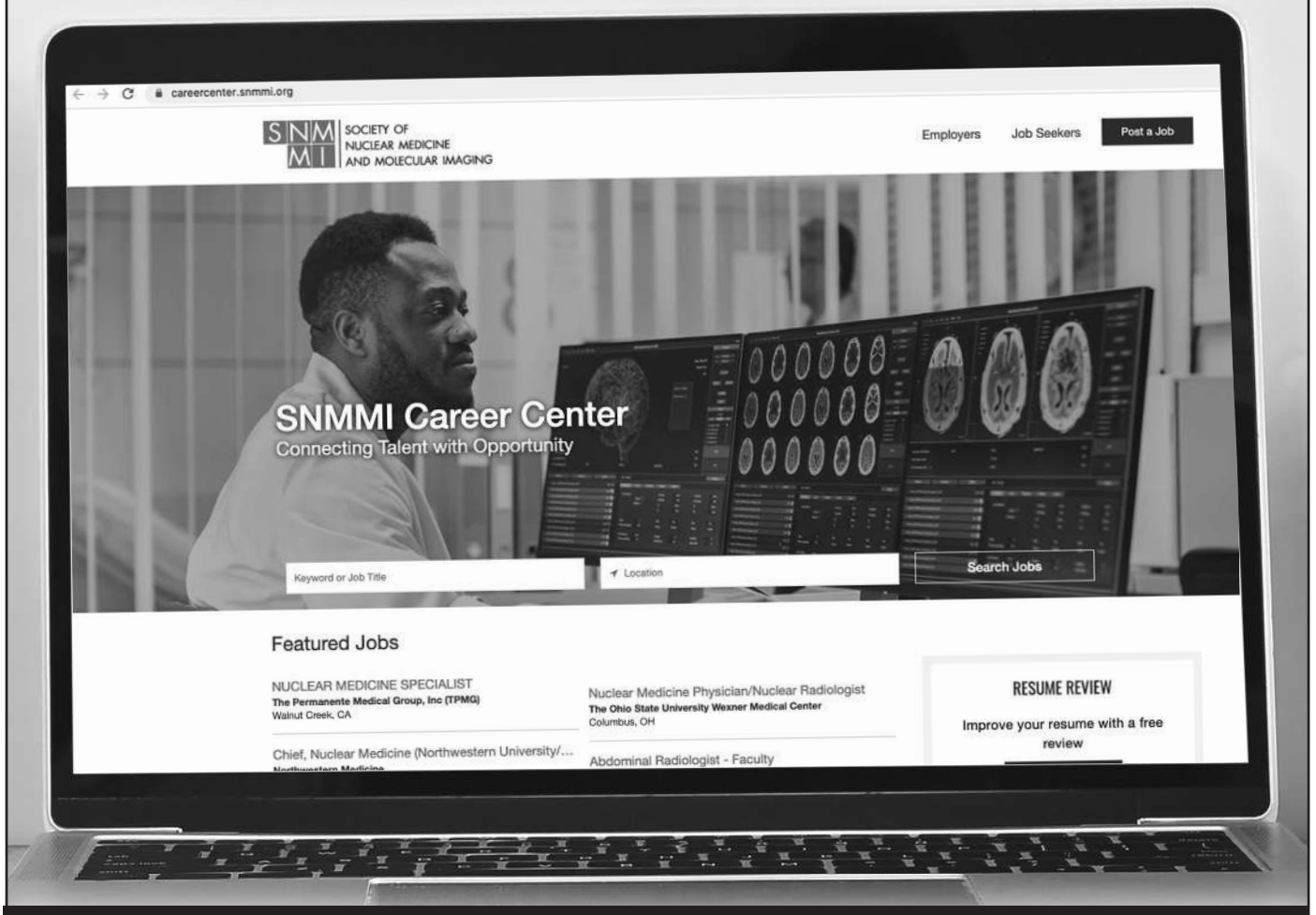

careercenter.snmmi.org

**Note: Single sign-on has been enabled for this platform and you can use your member login credentials to access the Career Center. If you are unsure of your password, to go to the SNMMI password reset link to create a new password.*

SNMMI Value Initiative

SOCIETY OF NUCLEAR MEDICINE & MOLECULAR IMAGING

JNM The Journal of NUCLEAR MEDICINE

EDITOR-IN-CHIEF
Johannes Czernin, MD
University of California at Los Angeles
Los Angeles, California

IMMEDIATE PAST EDITOR
Dominique Delbeke, MD, PhD
Vanderbilt University Medical Center
Nashville, Tennessee

NEWSLINE EDITOR
Harvey A. Ziessman, MD
Takoma Park, Maryland

ASSOCIATE EDITORS, CONTINUING EDUCATION
Heiko Schöder, MD
Memorial Sloan Kettering Cancer Center
New York, New York
H. William Strauss, MD
Memorial Sloan Kettering Cancer Center
New York, New York

ASSOCIATE EDITORS
Ramsey Derek Badawi, PhD
UC Davis Medical Center
Sacramento, California
Henryk Barthel, MD, PhD
Leipzig University
Leipzig, Germany
Frank M. Bengel, MD
Hannover Medical School
Hannover, Germany
Lisa Bodei, MD, PhD
Memorial Sloan Kettering Cancer Center
New York, New York
Irene Buvat, PhD
Université Paris Sud
Orsay, France
Jérémie Calais, MD
University of California at Los Angeles
Los Angeles, California
Marcelo F. Di Carli, MD
Brigham and Women's Hospital
Boston, Massachusetts
Alexander E. Drzezga
University Hospital of Cologne
Cologne, Germany
Jan Grimm, MD, PhD
Memorial Sloan Kettering Cancer Center
New York, New York
Ken Herrmann, MD, MBA
Universitätsklinikum Essen
Essen, Germany
Thomas A. Hope, MD
University of California, San Francisco
San Francisco, California
Lale Kostakoglu, MD, MPH
University of Virginia Health System
Charlottesville, Virginia
Jason S. Lewis, PhD
Memorial Sloan Kettering Cancer Center
New York, New York
David A. Mankoff, MD, PhD
University of Pennsylvania
Philadelphia, Pennsylvania
Wolfgang Weber, MD
Technical University of Munich
München, Germany

SERIES EDITOR, FOCUS ON MI
Carolyn J. Anderson, PhD
University of Missouri
Columbia, Missouri

SERIES EDITOR, HOT TOPICS
Heinrich R. Schelbert, MD, PhD
University of California at Los Angeles
Los Angeles, California

CONSULTING EDITORS
Nancy Knight, PhD
University of Maryland School of Medicine
Baltimore, Maryland
Barry A. Siegel, MD
Mallinckrodt Institute of Radiology
St. Louis, Missouri
Arnold M. Strashun, MD
SUNY Downstate Medical Center
Scarsdale, New York

ASSOCIATE EDITORS (INTERNATIONAL)
Gerald Antoch, MD
Dusseldorf, Germany
Richard P. Baum, MD, PhD
Bad Berka, Germany
Ambros J. Beer, MD
Ulm, Germany
Francois Benard, MD
Vancouver, Canada
Thomas Beyer, PhD
Vienna, Austria
Andreas K. Buck, MD
Würzburg, Germany
Ignasi Carrió, MD
Barcelona, Spain
June-Key Chung, MD
Seoul, Korea
Stefano Fanti, MD
Bologna, Italy
Markus Hacker, MD
Wien, Austria
Rodney J. Hicks, MD
Melbourne, Australia
Michael S. Hofman, MBBS
Melbourne, Australia
Ora Israel, MD
Haifa, Israel
Andreas Kjaer, MD, PhD, DMSc
Copenhagen, Denmark
Adriaan A. Lammertsma, PhD
Amsterdam, The Netherlands
Michael Lassman, PhD
Würzburg, Germany
Helmut R. Mäcke, PhD
Freiburg, Germany
Wim J.G. Oyen, MD, PhD
Milan, Italy
John O. Prior, MD, PhD
Lausanne, Switzerland
Osman Ratib, MD, PhD
Geneva, Switzerland
Mike Sathekge, MBChB, MMed, PhD
Pretoria, South Africa
Markus Schwaiger, MD
München, Germany
Andrew M. Scott, MD
Heidelberg, Australia
Nagara Tamaki, MD, PhD
Kyoto, Japan
Jia-He Tian, PhD
Beijing, China
Mei Tian, MD, PhD
Hangzhou, China

EDITORIAL CONSULTANTS
Martin S. Allen-Auerbach, MD
Los Angeles, California
Magnus Dahlbom, PhD
Los Angeles, California
Andrew Quon, MD
Los Angeles, California
Christiaan Schiepers, MD, PhD
Los Angeles, California
Daniel H. Silverman, MD, PhD
Los Angeles, California
Roger Slavik, PhD
Winterthur, Switzerland

EDITORIAL BOARD
Diane S. Abou, PhD
St. Louis, Missouri
Valentina Ambrosini, MD, PhD
Bologna, Italy
Norbert Avril, MD
Cleveland, Ohio
Shadfar Bahri
Los Angeles, California
Jacques Barbet, PhD
Saint-Herbalin, France
Bradley Jay Beattie, PhD
New York, New York
Matthias Richard Benz, MD
Los Angeles, California
Pradeep Bhambhvani, MD
Birmingham, Alabama
Angelika Bischof-Delaloye, MD
Lausanne, Switzerland
Christina Bluemel, MD
Würzburg, Germany
Ronald Boellaard, PhD
Groningen, The Netherlands
Nicolaas Bohnen, MD
Ann Arbor, Michigan
Wesley E. Bolch, PhD
Gainesville, Florida
Elias H. Botvinick, MD
San Francisco, California
Winfried Brenner, MD, PhD
Berlin, Germany
Richard C. Brunken, MD
Cleveland, Ohio
Ralph Buchert, PhD
Hamburg, Germany
Alfred Buck, MD
Menzingen, Switzerland
Denis B. Buxton, PhD
Bethesda, Maryland
Weibo Cai, PhD
Madison, Wisconsin
Federico Caobelli, MD
Basel, Switzerland
Giuseppe Carlucci, PhD
Los Angeles, California
Richard E. Carson, PhD
New Haven, Connecticut
Paolo Castellucci, MD
Bologna, Italy
Franscesco Ceci, MD, PhD
Turin, Italy
Juliano J. Cerci
Curitiba, Brazil
Delphine Chen, MD
Seattle, Washington
Xiaoyuan Chen, PhD
Singapore
Simon R. Cherry
Davis, California
Arturo Chiti, MD
Rozzano, Italy
Peter M. Clark, PhD
Los Angeles, California
Christian Cohade, MD
Montreal, Canada
Ekaterina (Kate) Dadachova, PhD
Saskatoon, Canada
Issa J. Dahabreh, MD
Boston, Massachusetts
Heike Elisabeth Daldrup-Link, MD, PhD
Stanford, California
Farrokh Dehdashti, MD
St. Louis, Missouri
Robert C. Delgado-Bolton, MD, PhD
Logroño, Spain
Thorsten Derlin, MD
Hannover, Germany
Elisabeth G.E. de Vries, PhD
Groningen, The Netherlands
David W. Dick, PhD
Iowa City, Iowa
Vasken Dilsizian, MD
Baltimore, Maryland
Sharmila Dorbala, MBBS
Lexington, Massachusetts
Jacob Dubroff, MD, PhD
Philadelphia, Pennsylvania
Janet F. Eary, MD
Bethesda, Maryland
W. Barry Edwards, PhD
Columbia, Missouri
Matthias Eiber, MD
Munich, Germany
David Eidelberg, MD
Manhasset, New York
Georges El Fakhri, PhD
Boston, Massachusetts
Peter J. Ell, MD
London, United Kingdom
Keigo Endo, MD
Nantan, Japan

EDITORIAL BOARD, continued
Einat Even-Sapir, MD, PhD
Tel Aviv, Israel
Frederic H. Fahey, DSc
Boston, Massachusetts
Melpomeni Fani, PhD, MSc
Basel, Switzerland
Wolfgang Peter Fendler, MD
Essen, Germany
James W. Fletcher, MD
Indianapolis, Indiana
Amy M. Fowler, MD, PhD
Madison, Wisconsin
Kirk A. Frey, MD, PhD
Ann Arbor, Michigan
Andrei Gafita
Los Angeles, California
Victor H. Gerbaudo, PhD, MSHCA
Boston, Massachusetts
Frederik L. Giesel, MD, PhD, MBA
Düsseldorf, Germany
Serge Goldman, MD, PhD
Brussels, Belgium
Stanley J. Goldsmith, MD
New York, New York
Martin Gotthardt, MD, PhD
Nijmegen, The Netherlands
Michael Graham, MD, PhD
Iowa City, Iowa
David Groheux, MD, PhD
Paris, France
Uwe A. Haberkorn, MD
Heidelberg, Germany
Mathieu Hatt, PhD, HDR
Brest, France
Wolf-Dieter Heiss, MD
Cologne, Germany
Karl Herholz, MD
Manchester, United Kingdom
Thomas F. Heston, MD
Las Vegas, Nevada
John M. Hoffman, MD
Salt Lake City, Utah
Carl K. Hoh, MD
San Diego, California
Jason P. Holland, DPhil
Zurich, Switzerland
Roland Hustinx, MD, PhD
Liege, Belgium
Andrei H. Iagaru, MD
Stanford, California
Masanori Ichise, MD
Chiba, Japan
Heather A. Jacene, MD
Boston, Massachusetts
Hossein Jadvar, MD, PhD, MPH, MBA
Los Angeles, California
Francois Jamar, MD, PhD
Brussels, Belgium
Jae Min Jeong, PhD
Seoul, Korea
John A. Katzenellenbogen, PhD
Urbana, Illinois
Kimberly A. Kelly, PhD
Charlottesville, Virginia
Laura M. Kenny, MD, PhD
London, United Kingdom
Fabian Kiessling, MD
Aachen, Germany
E. Edmund Kim, MD, MS
Orange, California
Francoise Kraeber-Bodéré, MD, PhD
Nantes, France
Clemens Kratochwil, MD
Heidelberg, Germany
Kenneth A. Krohn, PhD
Portland, Oregon
Brenda F. Kurland, PhD
Pittsburgh, Pennsylvania
Constantin Lapa, MD
Augsburg, Germany
Suzanne E. Lapi, PhD
Birmingham, Alabama
Steven M. Larson, MD
New York, New York
Dong Soo Lee, MD, PhD
Seoul, Korea
Jeffrey Leyton, PhD
Sherbrooke, Canada
Hannah M. Linden, MD
Seattle, Washington
Martin A. Lodge, PhD
Baltimore, Maryland
Egesta Lopci, MD, PhD
Milan, Italy
Katharina Lückerath, PhD
Los Angeles, California
Susanne Lütje, MD, PhD
Bonn, Germany
Umar Mahmood, MD, PhD
Boston, Massachusetts
H. Charles Manning, PhD
Nashville, Tennessee
Giuliano Mariani, MD
Pisa, Italy
Chester A. Mathis, PhD
Pittsburgh, Pennsylvania
Alan H. Maurer, MD
Philadelphia, Pennsylvania
Jonathan McConathy, MD, PhD
Birmingham, Alabama
Alexander J.B. McEwan, MD
Edmonton, Canada
Yusuf Menda, MD
Iowa City, Iowa
Philipp T. Meyer, MD, PhD
Freiburg, Germany
Matthias Miederer, MD
Mainz, Germany
Erik Mittra, MD, PhD
Portland, Oregon
Christine E. Mona, PhD
Los Angeles, California
Dae Hyuk Moon, MD
Seoul, Korea
Jennifer Murphy, PhD
Los Angeles, California
Helen Nadel, MD, FRCPC
Stanford, California
Matthias Nahrendorf, MD, PhD
Boston, Massachusetts
Yuji Nakamoto, MD, PhD
Kyoto, Japan
David A. Nathanson, PhD
Los Angeles, California
Sridhar Nimmagadda, PhD
Baltimore, Maryland
Egbert U. Nitzsche, MD
Aarau, Switzerland
Medhat M. Osman, MD, PhD
Saint Louis, Missouri
Christopher J. Palestro, MD
New Hyde Park, New York
Miguel Hernandez Pampaloni, MD, PhD
San Francisco, California
Neeta Pandit-Taskar, MD
New York, New York
Michael E. Phelps, PhD
Los Angeles, California
Gerold Porenta, MD, PhD
Vienna, Austria
Sophie Poty, PhD
Montpellier, France
Edwin (Chuck) Pratt, PhD, MS Eng
New York, New York
Daniel A. Pryma, MD
Philadelphia, Pennsylvania
Valery Radchenko, PhD
Vancouver, Canada
Caius G. Radu, MD
Los Angeles, California
Isabel Rauscher, MD
Munich, Germany
Nick S. Reed, MBBS
Glasgow, United Kingdom
Mark Rijpkema, PhD
Nijmegen, The Netherlands
Steven P. Rowe, MD, PhD
Baltimore, Maryland
Mehran Sadeghi, MD
West Haven, Connecticut
Orazio Schillaci, MD
Rome, Italy
Charles Ross Schmidtlein, PhD
New York, New York
David M. Schuster, MD
Atlanta, Georgia
Travis Shaffer, PhD
Stanford, California
Sai Kiran Sharma, PhD
New York, New York
Anthony F. Shields, MD, PhD
Detroit, Michigan
Barry L. Shulkin, MD, MBA
Memphis, Tennessee
Yu Shyr, PhD
Nashville, Tennessee
Albert J. Sinusas, MD
New Haven, Connecticut
Riemer H.J.A. Slart, MD, PhD
Groningen, The Netherlands
Piotr Slomka, PhD, FACC
Los Angeles, California
Ida Sonni, MD
Los Angeles, California
Michael G. Stabin, PhD
Richland, Washington
Lisa J. States, MD
Philadelphia, Pennsylvania
Sven-Erik Strand, PhD
Lund, Sweden
Rathan M. Subramaniam, MD, PhD, MPH
Dunedin, New Zealand
John Sunderland, PhD
Iowa City, Iowa
Suleman Surti, PhD
Philadelphia, Pennsylvania
Julie Sutcliffe, PhD
Sacramento, California
Laura H. Tang, MD, PhD
New York, New York
Ukihide Tateishi, MD, PhD
Tokyo, Japan
James T. Thackeray, PhD
Hannover, Germany
Mathew L. Thakur, PhD
Philadelphia, Pennsylvania
Alexander Thiel, MD
Montreal, Canada
Daniel L.J. Thorek, PhD
St. Louis, Missouri
David W. Townsend, PhD
Singapore
Timothy Turkington, PhD
Durham, North Carolina
Gary A. Ulaner, MD, PhD
Irvine, California
David Ulmert, MD, PhD
Los Angeles, California
Christopher H. van Dyck, MD
New Haven, Connecticut
Douglas Van Nostrand, MD
Washington, District of Columbia
Patrick Veit-Haibach, MD
Toronto, Canada
Nerissa Viola-Villegas, PhD
Detroit, Michigan
John R. Votaw, PhD
Atlanta, Georgia
Richard L. Wahl, MD
St. Louis, Missouri
Anne Marie Wallace, MD
La Jolla, California
Martin A. Walter, MD
Geneva, Switzerland
Rudolf A. Werner, MD
Wuerzburg, Germany
Andreas G. Wibmer, MD
New York, New York
Anna M. Wu, PhD
Duarte, California
Randy Yeh, MD
New York, New York
Hyewon (Helen) Youn, PhD
Seoul, Korea
Pat B. Zanzonico, PhD
New York, New York
Brian M. Zeglis, PhD
New York, New York
Robert Zeiser, MD
Freiburg, Germany
Hong Zhang, MD, PhD
Hangzhou, China
Hongming Zhuang, MD, PhD
Philadelphia, Pennsylvania
Sibylle I. Ziegler, PhD
Munich, Germany

ASSISTANT TO THE EDITOR
Joshua N. Wachtel
Los Angeles, California

alzheimer's association® | AAIC®22

ADVANCE DEMENTIA RESEARCH AND ACCELERATE YOUR CAREER.

Register for the premier dementia conference by May 13 and save.

Join us in San Diego and online for the Alzheimer's Association International Conference® (AAIC®), the largest and most influential international forum dedicated to advancing dementia science. Meet with colleagues from around the world to share discoveries that will lead to methods of prevention and treatment and improvements in diagnosis for Alzheimer's disease.

AAIC 2022: July 31-Aug. 4, San Diego, USA and Online

Educational Workshops and Preconferences: July 28-30

Exhibits: July 31-Aug. 3

Register at alz.org/AAIC-22.

Discussion with leaders: Thomas Hope talks with Josh Mailman, an internationally recognized advocate for neuroendocrine tumor patients as well as an advocate for nuclear medicine and molecular imaging. . . . . ***Page 497***

AI algorithm development best practices: Bradshaw and the SNMMI Artificial Intelligence Task Force outline good machine learning practices for algorithm development in nuclear medicine, including standards and recommendations, with specific points relevant to subspecialties. . . . . ***Page 500***

Virtual biopsy: Murray and colleagues look at the concept of virtual biopsies and the likelihood that traditional biopsies can be transformed from physical to virtual while still providing comparable or improved diagnostic and prognostic information. . . . . ***Page 511***

Kinetic analysis: Pantel and colleagues offer the second in a series of educational overviews, here focusing on applications of PET tracer kinetic analysis in oncology, current and future research and clinical implementations, and the future of kinetic modeling. . . . . ***Page 514***

^{18}F-FET PET/MRI in brain tumors: Brendle and colleagues report on the clinical results of multiparametric ^{18}F-FET PET/MRI in patients with brain tumors in a structured, retrospective evaluation of diagnostic performance and impact on clinical management. . . . . ***Page 522***

^{99m}Tc-DARPin imaging and HER2: Bragina and colleagues assess the safety, biodistribution, and dosimetry of this radiolabeled small-molecule, small-scaffold protein with picomolar affinity to human epidermal growth factor type 2 in patients with primary breast cancer. . . . . ***Page 528***

^{68}Ga-NOTA-WL12 PET in NSCLC: Zhou and colleagues conduct basic and first-in-humans studies of this agent's biodistribution, metabolism, dosimetry, safety, and potential for quantifying programmed death ligand-1 expression levels in non–small cell lung cancer. . . . . ***Page 536***

Cost-effectiveness of staging PET in FL: Lo and colleagues report on cost-effectiveness from the perspective of the Canadian health care system of staging PET/CT imaging in early-stage follicular lymphoma before curative-intent radiation treatment. . . . . ***Page 543***

WB-MATV and metabolic response in mCRC: Woff and colleagues validate the prognostic value of ^{18}F-FDG PET/CT–based biomarkers, such as baseline whole-body metabolically active tumor volume and early metabolic response, in patients with metastatic colorectal cancer. . . . . ***Page 549***

TACE + ^{131}I-metuximab in HCC: Chen and colleagues report on a multicenter clinical trial investigating the efficacy and safety of ^{131}I-labeled metuximab plus transcatheter arterial chemoembolization in treatment of unresectable hepatocellular carcinoma. . . . . ***Page 556***

^{177}Lu-PSMA-617 and NOX66 in mCRPC: Pathmanandavel and colleagues document safety and efficacy results of a phase I/II study combining ^{177}Lu-PSMA-617 and a radiosensitizer in patients with metastatic castration-resistant prostate cancer and identify potential clinical, blood-based, and imaging biomarkers. . . . . ***Page 560***

^{68}Ga-PSMA in recurrent PCa: Abghari-Gerst and colleagues detail a prospective investigation of the performance of ^{68}Ga-PSMA-11 PET/CT for detection of prostate adenocarcinoma in a large cohort of patients with elevated levels of prostate-specific antigen after initial therapy. . . . . ***Page 567***

^{89}Zr-PSMA-Df PET/CT in PCa: Dietlein and colleagues research whether this PSMA agent with a longer half-life allows more sensitive detection of weak PSMA-positive prostate cancer lesions. . . . . ***Page 573***

Preclinical and phantom ^{133}La imaging: Nelson and colleagues report on cyclotron production of clinically relevant ^{133}La activities, compare ^{133}La PET phantom imaging with common PET radionuclide imaging, and describe preclinical PET tumor imaging using ^{133}La-PSMA-I&T. . . . . ***Page 584***

Blind restoration digital autoradiogram: Lu and colleagues detail development of a penalized maximum-likelihood expectation–maximization algorithm for improved digital autoradiography resolution, intended to enhance radiotracer and radiotherapy evaluation. . . . . ***Page 591***

Perfusion-only PE screening protocol: Kumar and colleagues assess a pulmonary embolism perfusion-only screening protocol introduced during the COVID-19 pandemic surge. . . . . ***Page 598***

^{18}F-FDG PET and myocardial viability: Mhlanga and colleagues develop a practical protocol for intravenous glucose loading/insulin injection before ^{18}F-FDG administration for PET myocardial viability evaluation in patients with ischemic cardiomyopathy with and without type 2 diabetes. . . . . ***Page 602***

Kinetic analysis of pituitary V_{1B} tracer: Naganawa and colleagues characterize in humans the pharmacokinetic and binding profiles of ^{11}C-TASP699, a novel PET radiotracer with high affinity and selectivity for the vasopressin 1B receptor highly expressed in the pituitary. . . . . ***Page 609***

PET/MRI scanner trial qualification: Catana and a consortium of subject-matter experts propose a path for PET/MRI qualification for brain imaging studies using a patient as a phantom and address key PET/CT accreditation and qualification issues. . . . . ***Page 615***

Fast total-body PET K_i imaging: Wu and colleagues explore 2 new possible protocols for reducing scanning time for whole-body parametric ^{18}F-FDG PET imaging with the uEXPLORER. . . . . ***Page 622***

Antibody distribution and immunoPET: Sharma and colleagues report on the influence of crystallizable fragment modifications and IgG subclass on in vivo biodistribution of antibodies and potential associated effects on molecular imaging development of novel antibody-based theranostic agents. . . . . ***Page 629***

VISIT SNMMI'S
"Radiopharmaceutical Therapy Central"

YOUR SOURCE FOR THE LATEST RADIOPHARMACEUTICAL THERAPY NEWS, EDUCATION, AND RESOURCES FROM SNMMI.

www.snmmi.org/Therapy

SNMMI Value Initiative
SOCIETY OF NUCLEAR MEDICINE & MOLECULAR IMAGING

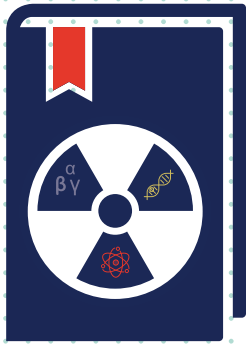

80 Hour Radionuclide Authorized User TRAINING COURSE

Debuting this April, the ASNC/SNMMI 80 Hour Authorized User Training Course features more than 40 expert lecturers from across nuclear medicine.

The course is designed to train authorized users and define the responsibilities inherent to the role while also meeting NRC-specified knowledge requirements for 80 hours of didactic training highlighted by real-world clinical scenarios.

This new course will be available as a standalone program in addition to special packages developed for training programs.

LEARN MORE: www.snmmi.org/80HourCourse

SNMMI Value Initiative
SOCIETY OF NUCLEAR MEDICINE & MOLECULAR IMAGING

American Society of Nuclear Cardiology

Medical Societies Seek Medicare Reform Collaboration

In a February 25 letter, SNMMI and almost 100 other major U.S. medical professional societies asked leaders of key Congressional committees to "immediately initiate formal proceedings (hearing, roundtables, expert panels, etc.) to discuss potential reforms to the Medicare physician payment system to ensure continued beneficiary access to care." The professional societies represent more than 1 million physician and nonphysician health care clinicians.

Although the letter's signatories noted with appreciation Congress's efforts over several years to mitigate scheduled cuts to the Medicare Physician Fee Schedule (MPFS), they cited systemic issues, including the negative impact of the MPFS budget neutrality requirements and the lack of an annual inflationary update, as factors that will "continue to generate significant instability for health care clinicians moving forward, threatening beneficiary access to essential health care services." Ongoing COVID-19 issues were noted as compounding these difficulties.

The group cited challenges associated with the Medicare Access and CHIP Reauthorization Act's (MACRA) Quality Payment Program (QPP) as "preventing most clinicians from meaningfully participating in the program." As an example, nonphysician clinicians have not been fully integrated into the Merit-Based Incentive Payment System (MIPS), because most are ineligible to report the cost and interoperability promotion measures that account for 55% of MIPS scoring. In addition, incentive payments "have also been historically low, far below the 9% Congress intended, rendering them an ineffective mechanism to offset the reductions required by budget neutrality." One focus of proposed collaboration would be improving MIPS and Alternative Payment Models (APMs), including extending current incentives for participating in Advanced APMs. "Under the current payment system, many health care clinicians continue to face steep annual reductions in their Medicare payments," the letter continued. "The inherent instability of the MPFS, coupled with the shortcomings of MACRA's QPP, has created an environment where many practices have seen their payments decrease year-over-year, despite increasing costs and growing inflation."

AMA Focuses on Permanent Medicare Pay System Fixes

On the same day, the American Medical Association (AMA), one of the professional groups signing the letter to Congress, highlighted the key points of a recent AMA Advocacy Insights webinar identifying 3 main efforts for the coming year. These efforts, also featured at the AMA Medical Student Advocacy Conference (March 3 and 4), include: reforming Medicare physician payment, reducing prior authorization burdens, and making expanded access to telehealth permanent.

These advocacy issues are intended to build on partial successes in delaying scheduled Medicare payment cuts in 2021. "Stopping the proposed Medicare payment cuts was a major victory, but this yearly cliffhanger must end—the broken record must stop playing," said Bobby Mukkamala, MD, chair of the AMA Board of Trustees. "We are calling on Congress to bring about a permanent solution to end the annual battles that threaten the solvency of physician practices."

Reforming Medicare physician payment. The AMA urged Congress to establish a reliable Medicare physician payment update that "at a minimum, should keep up with inflation and practice costs while encouraging innovation." In addition, AMA identified the need for development of ways to reduce the administrative and financial burdens of MIPS participation, while ensuring the program's clinical relevance.

Reducing prior authorization burdens. The AMA stated that this health plan utilization management mechanism "has morphed into an inefficient process that requires many practices to hire extra staff and causes delays that often lead to patients abandoning treatment," as well as contributing to physician burnout. According to a 2021 AMA survey, 93% of physicians reported care delays associated with prior authorization, and 34% of survey participants reported that prior authorization led to a serious adverse event, such as hospitalization, disability/permanent bodily damage, or death, for a patient in their care. Physicians were urged to contact Congressional representatives in support of proposed legislation that reduces the burden of prior authorization within Medicare Advantage and to support other efforts to reform prior authorization requirements.

Make expanded access to telehealth permanent. When the current Public Health Emergency expires, most Medicare beneficiaries will lose access to telehealth services, which have proven robust and effective. Under section 1834(m) of the Social Security Act, waived during the recent serial PHEs, Medicare patients must live in an eligible rural location and travel to an eligible "originating site"—a qualified health care facility—to access telehealth services covered by the Medicare program. These requirements were created decades ago, before most patients had in-home access to the devices that facilitate telehealth communication. The AMA supports legislation that would permanently fix the originating site and geographic restriction on telehealth coverage, thereby ensuring that patients can continue to access Medicare telehealth services regardless of where they are located. "Many patients and physicians want telehealth services as an option," Mukkamala said. "These changes to telehealth policy must remain even after the pandemic is over."

The AMA has prepared fact sheets and online action kits on each of the 3 focus issues for 2022 (https://www.ama-assn.org/system/files/2022-nac-action-kit.pdf).

NRC Vetoes T&E Changes; Approves ^{82}Rb and Emerging Tech Modernization

In a public meeting held on January 28, Nuclear Regulatory Commission (NRC) commissioners voted to disapprove staff recommendations to change training and experience (T&E) requirements for Authorized Users (AUs) of radiopharmaceuticals. The proposed changes had been the source of comment and protest from major professional societies and their members. In 2020, NRC staff formally recommended that the commission pursue regulatory changes to the T&E requirements, moving to board certification as the sole factor for determining and obtaining AU status and modifying NRC criteria to allow for additional medical specialty board diplomates (beyond nuclear medicine and radiation oncology) to qualify as AUs. In voting down this proposal, one commissioner noted that the proposed changes had suggested "that the current training and experience framework could be viewed as encroaching on the practice of medicine. I disagree. Ensuring that AUs meet training and experience requirements necessary for radiological safety does not insert NRC into the actual practice of medicine. The broad support among medical organizations for NRC's licensing role makes it clear that the medical community does not view the current framework as encroaching on the practice of medicine."

SNMMI was among the groups that opposed T&E changes and submitted comments in multiple formats to the NRC. In 2020, Vasken Dilsizian, MD, then SNMMI President, testified before the Commission during a public hearing. He noted that expansion of medical specialty training requirements was not within the purview of the NRC. Moreover, Nuclear Medicine, Radiation Oncology, and Diagnostic Radiology with 16-mo Nuclear Medicine/Nuclear Radiology (NM/NR) pathways are the only Accreditation Council for Graduate Medical Education (ACGME)–approved training programs with specific goals and objectives pertaining to administration of radioactive material, and such training must be completed under supervision of board-certified physicians trained in this area.

Feedback from stakeholders was considered by the commissioners in making their decision. Another commissioner stated in his final review: "Many stakeholders offer persuasive arguments that the current T&E framework is working effectively to ensure radiological safety and is not resulting in a shortage of authorized users to administer radiopharmaceuticals." In a February 4 statement, SNMMI praised the NRC for this decision.

Current pathways for obtaining AU status remain:

- Certification by a medical specialty board (e.g., the American Board of Nuclear Medicine) recognized by the NRC or an Agreement State;
- Completion of 200 hours of classroom training and 500 hours of supervised work experience in an ACGME-accredited program (Nuclear Medicine, Diagnostic Radiology with a 16-month NM/NR pathway, or Radiation Oncology); and
- Previous identification as an AU on an NRC or Agreement State license or permit.

^{82}Rb Generators and Emerging Medical Technologies

Along with voting on AU T&E requirements, the NRC approved initiation of rulemaking to modernize 10 *Code of Federal Regulations* (*CFR*) Part 35 to accommodate the increasing medical applications of radioisotopes and new advances in medical technologies. NRC staff recommended updating Part 35 to establish generally applicable performance-based requirements for emerging medical technologies that would focus on the essential safety-related elements necessary to ensure radiation safety for workers, patients, and the general public. The revised regulation would also include performance-based requirements for ^{82}Rb generators, gamma stereotactic radiosurgery units, and ^{90}Y-microspheres. Many stakeholders had expressed an interest in having a regulatory framework well-suited to the advancement and integration of innovative radiopharmaceuticals.

Part 35 does not currently address ^{82}Rb generators, and NRC has relied on enforcement discretion in this area. But, as explained by NRC staff in their proposed rulemaking plan: "Longstanding reliance on temporary enforcement guidance to exercise enforcement discretion is inconsistent with NRC Enforcement Policy and is not a substitute for resolving the underlying technical issues associated with calibration and dosage measurement for ^{82}Rb generators."

NRC will open comment periods and hold stakeholder response sessions to address proposed changes.

Nuclear Regulatory Commission
SNMMI

SNMMI Calls for Expanded Coverage/Reimbursement of Amyloid PET

On February 17, SNMMI released a second letter to the U.S. Centers for Medicare & Medicaid Services (CMS) in response to the January 11 proposed National Coverage Determination (NCD) decision memorandum that would cover U.S. Food and Drug Administration (FDA)–approved monoclonal antibodies that target β-amyloid for treatment of Alzheimer disease (AD) through coverage with evidence development (CED) (see *J Nucl Med.* 2022;63[3]:12N). In addition to indicating that FDA-approved drugs in this class would be covered only for people with Medicare who are enrolled in qualifying clinical trials, the NCD would have a number of potential negative effects for patients with or in the process of diagnosis for AD, according to the SNMMI letter.

After receiving initial comments from SNMMI experts, the society requested specific actions relative to coverage, including accompanying rationales:

(1) *CMS should cover an amyloid PET scan before a patient is considered eligible for a CMS-approved study.* Amyloid PET can identify ahead of time those patients who will not benefit from monoclonal antibodies and thereby simplify the enrollment process for patients and trial sponsors. It will also improve care for patients without β-amyloid, allowing treating professionals and caregivers to focus on treatment modalities that are appropriate for those patients. CMS should not limit coverage to trial participants but should provide coverage of amyloid PET to determine whether a patient should be enrolled in a trial.

(2) *CMS should not finalize a limit of 1 β-amyloid PET scan per lifetime.* No evidence currently suggests that a single amyloid PET scan per patient is appropriate or that an outdated scan can provide the diagnostic information needed to determine whether a patient is currently a candidate for therapy. Not only can β-amyloid status change over time, ongoing clinical trials for monoclonal antibody therapies for AD have used the results of posttreatment β-amyloid PET to inform decisions to discontinue monoclonal antibody therapy.

(3) *CMS should require posttreatment β-amyloid PET to be performed as needed to document the removal of β-amyloid from the brain.* CMS should allow as many PET scans as are needed to ensure that the trial design is optimal and reliable and provides physicians with the information needed to make informed decisions about initiating and continuing therapy. Notably, 1 or more scans must be covered during therapy to verify removal of amyloid.

(4) *CMS should retire the current PET CED in conjunction with finalizing the monoclonal antibody NCD.* Continuation of limitations on amyloid PET while other uses of PET for AD, such as tau PET, are covered at the discretion of the Medicare Administrative Contractors creates an illogical and confusing situation for physicians, patients, and clinical trial designers.

(5) *CMS should not limit sites of service for approved clinical trials to hospitals.* Limiting trials only to hospitals would greatly impede patient access because of geographic and payment considerations and would contribute to health care disparities.

In addition, SNMMI reiterated that appropriate reimbursement of amyloid PET agents is needed. Since 2008, CMS has packaged diagnostic radiopharmaceuticals (including the 3 amyloid agents) with the related PET scan in hospital outpatient settings. The packaging begins after the expiration of a passthrough period (about 3 years) during which drugs are paid separately. The result is a reimbursement rate of about 9% of the passthrough rate. Although CMS has the authority to fix this problem, it has resisted. SNMMI, the Medical Imaging & Technology Alliance, the Council on Radionuclides and Radiopharmaceuticals, and more than 70 supporting organizations are therefore pursuing legislative action through the Facilitating Nuclear Diagnostics (FIND) Act, a bipartisan and bicameral bill intended to unpackage these life-saving diagnostics.

In its summary, the latest SNMMI request recommended that CMS remove the coverage limitations on amyloid PET by retiring the NCD, by establishing that amyloid PET will be covered (before clinical trials) to identify patients who are candidates to receive monoclonal antibody therapy and as necessary after therapy initiation to inform treatment decisions, and by clarifying that there is no lifetime limit on the number of medically necessary amyloid PET scans that a patient can receive.

The January 11 CMS announcement of the proposed NCD and limited coverage of the drug included a 30-day period for public comment. After reviewing all comments received on the proposed determination, CMS is scheduled to announce its final decision by April 11.

SNMMI

ABNM: Nuclear Medicine In-Training Examination Goes Virtual

Leonie Gordon, MD, Associate Executive Director, American Board of Nuclear Medicine

In 2022, in keeping with the commitment to serve well our trainees and their valued residency programs, the American Board of Nuclear Medicine (ABNM) offered residents remote virtual in-training testing. In order to achieve this and update our virtual presence in testing, ABNM chose a vendor that offers a complete online solution for the management, delivery, and reporting of assessment programs. The vendor has led the industry with innovations in secure internet testing. ABNM migrated all its secure testing databases to the new vendor over several months, and this created a state-of-the-art online item-banking system. It runs on major browsers both for Windows and Mac and offers extensive configuration options.

The ABNM successfully delivered its in-training examination (ITE) as a remote computer-based exam during January 2022. Resident participation in the ITE fulfills Accreditation Council for Graduate Medical Education nuclear medicine training program requirements for summative assessment. The ITE also benchmarks individual resident scores for all residency levels. It offers residents an opportunity to evaluate their knowledge and to improve identified weaknesses prior to taking the ABNM certifying examination.

ABNM recognized that the logistics for programs and residents would be different for a virtual examination. New graphics were created (https://www.abnm.org/2022-ite-announcement). The board expected the examination to be proctored at local sites and held a proctor/virtual examination training webinar prior to administration of the examination. For those unable to attend the session or who wanted a refresh, the webinar was recorded and is available on YouTube (https://www.youtube.com/watch?v=kd3aa8JDnNg). As expected with any remotely delivered exam, a few candidates experienced connectivity and software issues. ABNM staff members were available to troubleshoot and help trainees with these issues. Test results are being validated through third-party psychometric analysis, and the data will be used for optimally accurate benchmarking.

Leonie Gordon, MD

Candidates expressed appreciation for the ability to take the exam at their local sites, which eliminated the need for exposure to groups of people during the COVID-19 pandemic. The length of time the examination was available online to programs and residents was also increased to overcome pandemic-related challenges. Although the ABNM prepared candidates well for the computer-based examination, concern was expressed about access to the exam and unfamiliarity with the exam screens. A help button was available during the exam on all computer screens to answer many questions, but some candidates did not avail themselves of this feature and did not realize that methods were available to zoom, adjust contrast, and scroll through images.

The ABNM hopes to have the ITE results available within 2 months and will include teaching key points for questions residents did not answer correctly. These will be included in the results correspondence, and the hope is that it will offer an opportunity to evaluate their knowledge and identify areas of deficiency relative to peers at the same level of training. In addition, ABNM has developed Certlink-in-Training, which provides residents the opportunity to participate in continuous online learning, as well as an opportunity for maximizing test preparation. Certlink questions have key points, critiques, and annotated references. ABNM hopes the ITE and participation in Certlink-in-Training will maximize opportunities for future testing preparation, including secure examinations. Certlink-related tutorials are available at: https://www.abnm.org/certlink-training-tutorial-video-series/.

ABNM will continue to offer the ITE virtually, with enrollment in September through October 2022 with the same device preparation. The ITE for U.S. and Canadian programs will be given in January 2023.

SNMMI Meetings Back in Full Swing

Virginia Pappas, CAE, SNMMI CEO

With 2 years of the COVID-19 pandemic behind us, SNMMI and its meeting attendees have mastered the art of the virtual meeting, as was clear at the 2022 Mid-Winter Meeting and American College of Nuclear Medicine (ACNM) Annual Meeting held February 25–27. Although virtual meetings will remain a part of SNMMI's education offerings in coming years, we are more than excited to be meeting again in person at the 2022 Therapeutics Conference and the 2022 Annual Meeting!

SNMMI Mid-Winter and ACNM Annual Meeting

When the Omicron variant derailed SNMMI's plans for an in-person meeting, the society seamlessly transitioned to a virtual meeting, which was attended by more than 600 nuclear medicine and molecular imaging professionals. Thirty-three sessions were organized into 3 simultaneous tracks: ACNM Annual Meeting, cardiovascular, and general nuclear medicine. The Science Pavilion hosted on a new easy-to-use platform, including 64 posters, many of which included recorded presentations of the abstracts. The exhibit hall featured 26 companies, including title sponsor Advanced Accelerator Applications. Several networking events were held during the meeting, including a virtual chocolate tasting hosted by the SNMMI Women in Nuclear Medicine, which led one participant to claim they "will never taste chocolate the same way again!"

SNMMI Therapeutics Conference

The SNMMI Therapeutics Conference was held March 10–12 in New Orleans. The meeting featured some of the leading nuclear medicine experts in areas such as MIBG therapy, therapeutic dosimetry, prostate cancer, and neuroendocrine cancer, to name just a few. The speakers also included a patient and a medical oncologist presenting their perspectives on radiopharmaceutical therapy. In addition, we were joined by 33 companies in the exhibit hall for the meeting. We would like to thank all of our exhibitors and sponsors, particularly our title sponsor, ITM.

SNMMI 2022 Annual Meeting—In Person at Last

SNMMI now switches its focus to the 2022 Annual Meeting, to be held June 11–14 in Vancouver, BC, Canada. In addition to the in-person event, a full virtual program will offer live-streaming of many sessions, on-demand access to all sessions, virtual poster and exhibit halls, and virtual networking events. In-person attendees will also have access to the live-streamed content, providing the ultimate flexibility.

The meeting kicks off on Saturday, June 11, with a lineup of 8 categorical seminars covering a variety of exciting topics in nuclear medicine and molecular imaging, including imaging biomarkers in neurodegenerative and neuropsychiatric disorders, radiopharmaceutical therapies, "what's now and what's next" in prostate cancer diagnosis and treatment, and more.

The official opening ceremony on Saturday afternoon will feature an overview of the meeting as well as an address from the French Society of Nuclear Medicine, representing this year's Highlight Country. An exhibitor reception will be held on Saturday night—a great chance to reconnect with colleagues in person. Sunday's program begins with the Henry N. Wagner Jr., MD, Lecture, delivered by oncologist and researcher E.G. Elisabeth de Vries, MD, PhD, professor of medical oncology at University Medical Centre Groningen (The Netherlands). She will discuss her groundbreaking research on increasing the sensitivity of tumor therapies using advanced imaging techniques.

Additional plenary sessions will include the SNMMI Business Meeting/Anger Lectureship, the SNMMI-TS Award Recognition and Plenary Session, and the always-popular Henry N. Wagner, Jr., MD, Highlights Symposium, which will summarize scientific highlights from the Annual Meeting in the fields of neuroscience, oncology, cardiology, and general nuclear medicine.

Ninety educational sessions will provide attendees with an in-depth view of the latest research and development and insights into practical clinical application, with 60 continuing education sessions available for physicians, pharmacists, and physicists and 30 technologist-organized continuing education sessions.

More than 1,450 abstracts were submitted from around the globe for this year's Annual Meeting, and the Scientific Poster Hall will showcase more than 1,000 posters. Forty-five scientific sessions will be offered. New this year are 12 "integrated" sessions combining lectures and related scientific oral presentations. Also new: SNMMI will host a large Meet the Author Session and Reception on Monday, June 13. On Tuesday afternoon, SNMMI will offer a series of poster oral presentations from award-nominated authors in the Scientific Poster Hall.

One of the best parts of in-person attendance is the opportunity to visit the Exhibit Hall. More than 140 companies will be on site in Vancouver, showcasing the latest advances in technology. Multiple industry satellite symposia will be offered on the Exhibit Hall floor throughout the meeting.

Special programming to be held during the Annual Meeting includes the Nuclear Medicine Review Course, Technologist Educators Forum, Physician Educators Symposium, and a new Grant Review Program. In addition, the meeting will feature a number of networking events, including the opening exhibitor reception, poster hall mixer, meet the author reception, and more.

SNMMI is committed to ensuring that appropriate and necessary health and safety protocols are in place for this event. We will follow all Centers for Disease Control and Prevention safety protocols and recommendations and will comply with all federal, state, and local regulations.

We look forward to seeing you in person at the 2022 Annual Meeting in Vancouver! To register, visit www.snmmi.org/am.

Radioisotope Supply Update

NRG, which operates the High Flux Reactor (Petten, The Netherlands), indicated in February plans to restart the reactor for a new cycle of radioisotope production on March 17 after a 2-mo outage. The Nuclear Medicine Europe Emergency Response Team (NMEu ERT; Brussels, Belgium) held an update call on February 14 on the unplanned outage that resulted in cancellation of the reactor's first operating cycle of 2022. The cause of the defect (a cooling system leak in a basement ceiling), detected during an inspection on 21 January before the scheduled cycle start, had been identified, and analysis of the underlying cause would be submitted to the Authority for Nuclear Safety and Radiation Protection (ANVS), along with a solution to restore functionality. After approval by ANVS, the solution would be implemented and the reactor cooling system restored. After a planned 1-mo maintenance period, NRG intended to restart the reactor for a full cycle. Additional updates were planned during the review and start-up period.

On the February 14 call, the ERT also provided updates from other reactors in Europe that continued to work to address radioisotope shortages caused by the Petten outage. The Maria research reactor (Świerk-Otwock, Poland) added additional operating days to increase supplies of ^{99}Mo. The BR2 reactor (Mol, Belgium) resumed operations on February 12 (3 days earlier than planned) and announced that it would extend its radioisotope production cycle. Curium Pharma (London, UK) harvested ^{99}Mo targets from short irradiations at BR2 and processed ^{99}Mo for customers. Belgium's National Institute of Radioelements (IRE) reactor in Fleurus also announced it would resume production on its high-enriched uranium line in February. The NMEu indicated that as a result of these measures, supplies of ^{99}Mo/^{99m}Tc and ^{177}Lu were expected to return to normal in February, and ^{131}I supplies should be back to normal in the first half of March.

In the United States, University of Missouri Research Reactor (MURR) staff announced on February 9 increased production of critical medial radioisotopes in an effort to help in alleviating disruptions in the global supply chain. J. David Robertson, executive director of MURR, anticipated that the reactor will maintain its increased production levels throughout the duration of the reactor shutdown in Europe. "MURR is fortunate to be in a position where we can increase our production when the global supply chain is impacted, because we operate 6 and a half days a week, 52 weeks per year," he said. "Our dedicated staff are committed to getting life-saving treatments delivered to the patients who need them."

Nuclear Medicine Europe
University of Missouri Research Reactor

SNMMI Launches New Quality Systems Personnel Training Program

SNMMI announced on January 31 the launch of a new program designed to educate, train, and develop individuals with pharmacy or chemistry backgrounds in the production and release of clinical radiopharmaceuticals. The Quality Systems Personnel Training Program (QSPTP), conceived and led by Sally Schwarz, MS, RPh, BCNP, FAPhA, will provide participants with the theoretical knowledge and practical experience needed to assume responsibility for production, quality control, and release of radiopharmaceuticals. Topics in the program include production and quality assurance, synthesis and clinical formulation of radiopharmaceuticals, regulatory requirements, and research applications. Experiential training at Current Good Manufacturing Practice–certified sites will also be incorporated into the program.

Specific needs to be addressed by the program include cross-training in the principles and practice of radiopharmaceutical science; manufacturing and quality assurance of radiopharmaceuticals—both in the academic and commercial settings; synthesis and pharmaceutical formulation of radiopharmaceuticals, especially from cyclotron-produced radionuclides; application of radiopharmaceuticals in biomedical research and clinical nuclear medicine; and compliance including all regulatory requirements associated with radiopharmaceutical manufacture and release.

"The manufacture and ongoing production of radiopharmaceuticals for clinical evaluation and use is dependent on skilled personnel who are cross-trained in several disciplines," said Alan Packard, PhD, SNMMI past president. "Currently, very few individuals have this type of training. To meet the growing need for qualified persons of this nature, SNMMI has developed a training program to cover the core competencies needed in this area of our field."

Individuals successfully completing the QSPTP will receive a certificate of training. In the future, SNMMI plans to collaborate with academic institutions to expand the program to include hands-on training in a production environment. "Having more professionals trained in the release of clinically important radiopharmaceuticals will benefit both academic and commercial entities," said Packard. "We hope that the QSPTP will provide a solid educational framework so that more individuals will become 'qualified persons' and will help to advance the field of radiopharmaceutical science." Detailed information on the program and its components is available at: www.snmmi.org/qsptp.

SNMMI

AI and Malpractice Liability

In an article published on February 1 ahead of print in the *Journal of the American College of Radiology*, Banja, from Emory University (Atlanta, Ga), and coauthors from Michigan State University (Grand Rapids) and the Penn State Milton S. Hershey Medical Center (Hershey) reported on ethical and legal implications associated with advances of artificial intelligence (AI) models and technologies in clinical practice, with a specific focus on exposure to liability for malpractice. The authors focused on 4 main considerations: (1) the importance of being able to explain AI models in patient care; (2) the

identification of strategies for diminishing clinician liability in poor patient outcomes that could be attributed to over- or under-reliance on AI; (3) the possibility of relieving liability burdens through legislation or regulation; and (4) conceptualizing AI models as "persons" with potential liability in legal proceedings.

Journal of the American College of Radiology

Thomas O'Dorisio, MD 1943–2022

Thomas M. O'Dorisio, MD, a pioneer in neuroendocrine cancer research and practice, died on February 2 in Ostrander, OH. He was a professor emeritus at the University of Iowa (Iowa City), having served as director of the Neuroendocrine Tumor Program and coleader of the Gastrointestinal Neuroendocrine group. In 1971, Dr. O'Dorisio graduated from the Creighton University School of Medicine (Omaha, NE) and went on to compete a residency in internal medicine and a fellowship in endocrinology at The Ohio State University (OSU; Columbus). He remained at OSU, serving as director of the Division of Endocrinology, held numerous leadership roles guiding components of the research mission, and received multiple teaching and education awards. In 1999, along with his wife, M. Sue O'Dorisio, MD, PhD, he was recruited to join the University of Iowa. His interest in nuclear medicine techniques in neuroendocrine cancer led to numerous collaborations with nuclear medicine and molecular imaging and therapy colleagues. He published more than 330 peer-reviewed articles, as well as texts and other scholarly works. Shortly before his final illness, he had begun work toward a master's degree in religious studies from Regis University (Denver, CO).

University of Iowa

^{153}Sm-DOTMP Agent Receives Rare Pediatric Disease Designation

QSAM Biosciences, Inc. (Austin, TX) announced on February 2 that the U.S. Food and Drug Administration (FDA) had granted its Rare Pediatric Disease (RPD) designation to CycloSam (^{153}Sm-DOTMP), a clinical-stage drug candidate for treatment of osteosarcoma. The agent has demonstrated preliminary safety and efficacy in animal studies. In 2020 it was successfully used under a single-patient Investigational New Drug approval to perform bone marrow ablation prior to allogenic marrow transplantation. In August 2021 the company received FDA Orphan Drug designation for use in osteosarcoma.

Douglas Baum, CEO of QSAM, said: "Combined with the orphan designation for osteosarcoma that we received last year from the FDA, the RPD Designation may allow QSAM to potentially bring CycloSam to market more rapidly through additional incentives and eligibilities that ultimately help these young patients for whom there is currently little hope. Patients with this disease are eligible to participate in our current Phase 1 clinical trial; however, we anticipate that we will initiate a separate clinical trial in the coming year specifically focused on primary bone cancers such as osteosarcoma and Ewing sarcoma. We are dedicated as a company to making a difference in the lives of children and their families battling these forms of bone cancer."

The RPD designation, covering diseases defined by the FDA as primarily affecting <200,000 Americans under the age of 18 each year, can provide substantial financial incentives by making companies eligible for a Priority Review Voucher (PRV) upon drug approval by the FDA. A PRV grants accelerated FDA review of a drug candidate for any indication, reducing the review period to 6 mo and potentially gaining early market access. PRVs may be used by the recipient company for any drug development program or can be sold or transferred to larger pharmaceutical companies.

QSAM Biosciences, Inc.
U.S. Food and Drug Administration

FROM THE LITERATURE

Each month the editor of Newsline selects articles on diagnostic, therapeutic, research, and practice issues from a range of international publications. Most selections come from outside the standard canon of nuclear medicine and radiology journals. These briefs are offered as a window on the broad arena of medical and scientific endeavor in which nuclear medicine now plays an essential role. The lines between diagnosis and therapy are sometimes blurred, as radiolabels are increasingly used as adjuncts to therapy and/or as active agents in therapeutic regimens, and these shifting lines are reflected in the briefs presented here. We have also added a small section on noteworthy reviews of the literature.

^{177}Lu-PSMA I&T Toxicities

Hartrampf et al. from University Hospital Würzburg (Germany), Johns Hopkins University School of Medicine (Baltimore, MD), and Okayama University (Japan) reported on January 27 in *Cancers (Basel)* (2022;14[3]:647) on a study evaluating the toxicity profiles of ^{177}Lu–prostate-specific membrane antigen (PSMA)–I&T in patients with metastatic, castrate-resistant prostate cancer. The study included 49 such patients treated with at least 3 cycles of ^{177}Lu-PSMA-I&T. Serum lab values were compared before and after radioligand therapy, and adverse events were documented. Under treatment, 11 (22%) patients were found to have nephrotoxicity of Common Terminology Criteria for Adverse Events (CTCAE) grades I or II by creatinine metrics and 33 (67%) as assessed by estimated glomerular filtration rate (eGFR). Only 13% showed reduced ^{99m}Tc-MAG3–derived tubular extraction rates. Over all renal functional metrics, absolute changes of only 2% were recorded. Recategorization based on renal parameters was infrequent. After 3 cycles of therapy, follow-up eGFR correlated negatively with age and eGFR change correlated with Gleason score at baseline. Leukocytopenia of CTCAE I and II was seen in 41% and 2% of patients, respectively. Thrombocytopenia of CTCAE I was seen in 14%, with absolute decreases of 15.2% and 16.6% for leukocyte and platelet counts, respectively. Thirty-six (73%) and 10 (20%) patients experienced CTCAE I and II anemia, respectively. The authors concluded that "after PSMA-targeted therapy using ^{177}Lu-PSMA I&T, no severe (CTCAE III/IV) toxicities occurred, thereby demonstrating that serious adverse renal or hematological events are unlikely to be a frequent phenomenon with this agent."

Cancers (Basel)

PET/MR and Lymphoma Imaging Biomarkers

In an article published on February 16 ahead of print in *Annals of Hematology*, Husby et al. from the Norwegian University of Science and Technology (Trondheim, Norway), St. Olavs Hospital/Trondheim University Hospital (Norway), University Hospital of North Norway (Tromsø), Aarhus University Hospital (Denmark), University Medical Center Groningen (The Netherlands), and the University Medical Centers Amsterdam (The Netherlands) reported on the diagnostic performance of ^{18}F-FDG PET/MR compared to that of ^{18}F-FDG PET/CT in a group of patients with Hodgkin lymphoma, diffuse large B-cell lymphoma, or high-grade B-cell lymphoma. A total of 61 patients were imaged with both modalities at baseline and again for response assessment after treatment. Images were interpreted by experienced physicians, and prognostic biomarkers (Deauville score, SUV_{max}, SUV_{peak}, and metabolic tumor volume [MTV]) were compared. Baseline PET/MR showed a sensitivity of 92.5% and specificity of 97.9% when compared with PET/CT as a reference standard for nodal sites. Corresponding PET/MR figures for extranodal sites were 80.4% and 99.5%. Concordance in expert reading was found in 57 patients, with disagreement attributed to misclassification of region rather than inaccuracy in lesion detection. For posttreatment response assessment, PET/MR showed a sensitivity of 100% and specificity of 99.9% for all sites combined compared to the PET/CT standard. Deauville scores 4 and 5 and criteria of response were found to be the same for the 2 modalities, with SUV_{max}, SUV_{peak}, and MTV values highly correlated. The authors concluded that "FDG PET/MR is a reliable alternative to PET/CT in this patient population, both in terms of lesion detection at baseline staging and response assessment, and for quantitative prognostic imaging biomarkers."

Annals of Hematology

Presurgical PET in Epilepsy

Steinbrenner et al. from the Charité-Universitätsmedizin Berlin (Germany), National Hospital for Neurology and Neurosurgery (London, UK), University College London Hospitals (UK), Smt. B. K. Shah (SBKS) Medical College (Vandodara, India), Evangelische Krankenhaus Königin Elisabeth Herzberge (Berlin, Germany), the Johns Hopkins School of Medicine (Baltimore, MD), and the Sree Chitra Tirunal Institute for Medical Sciences and Technology (Trivandrum, India) reported on February 15 ahead of print in *Epilepsia* on a multicenter retrospective study assessing the utility of ^{18}F-FDG PET as part of the management decision-making process in patients with drug-resistant focal epilepsy. The study included the records of 951 patients with epilepsy (temporal lobe [TLE], 479; extratemporal [ETLE], 219; and uncertain lobar origin, 253) who had undergone PET imaging as part of presurgical workups. PET indicated distinct hypometabolism in 62% and was concordant with ictal EEG in 74% of patients with TLE and 56% with ETLE. PET was determined to be useful in presurgical decision making in 396 (47%) patients, contributing to recommended resection in 78 (20%) and intracranial EEG in 187 cases (47%).

In a third of patients, PET led to the conclusion that surgery was not feasible. For patients with TLE, rates of freedom from seizures at 1 y after surgery did not differ between patients with negative MR and EEG–PET concordance (n = 30) and those with positive MR and concordant EEG (n = 46). Half of patients with ETLE with negative MR and EEG–PET concordance and three-fourths of those with positive MR and concordant EEG were seizure free at 1 y. The authors noted that this is by far the largest reported study of presurgical PET in patients with drug-resistant focal epilepsy and that their findings "confirm the significance of FDG PET in presurgical epilepsy diagnostics."

Epilepsia

^{177}Lu-PSMA-617 RLT After Failed ^{223}Ra-Dichloride

In an article in the January 22 issue of *Cancers (Basel)* (2022;14[3]:557), Baumgarten et al. from University Hospital Frankfurt (Germany) reported on the safety and efficacy of ^{177}Lu-prostate-specific membrane antigen (PSMA)–617 in patients with metastatic castrate-resistant prostate cancer and progressive bone involvement under treatment with ^{223}Ra-dichloride. The study included 28 such men (median age, 73 y; range, 63–89 y) with progressive disease who started ^{177}Lu-PSMA-617 within 8 wk after the last ^{223}Ra administration. Patients had received a median of 4 and a group total of 120 cycles of ^{223}Ra and then received a median of 4 cycles of ^{177}Lu-PSMA-617 with a mean treatment activity of 6.5 ± 1.2 GBq per cycle (mean cumulative activity of 30.7 ± 23.4 GBq). Serum responses (≥50% decline in prostate-specific antigen 12 wk after the first ^{177}Lu-PSMA-617) were observed in 18 (64.3%) patients. Imaging-based partial remission was seen in 11 (39.3%) patients. The median imaging-based progression-free survival was 10 mo and median overall survival (OS) was 18 mo. Patients with fewer bone lesions (2–20) had significantly longer OS (28 mo) than those with higher tumor burdens (14 mo). Six patients experienced grade ≥3 hematologic toxicities after their last treatment cycle, including anemia, leukopenia, and thrombocytopenia. The authors concluded that "in progressive bone-metastatic castrate-resistant prostate cancer patients, prompt initiation of ^{177}Lu-PSMA-617 after failing ^{223}Ra is effective with an acceptable toxicity profile."

Cancers (Basel)

Automated Image-Based Diagnosis in Parkinsonism

Papathoma et al. from the Karolinska Institutet (Stockholm, Sweden), Danderyd's Hospital (Stockholm, Sweden), the Academic Specialist Center (Stockholm, Sweden), and the Feinstein Institute for Medical Research (Manhasset, NY) reported in the February 17 issue of *Scientific Reports* (2002;12[1]: 2763) on a systematic assessment of the accuracy of a previously developed ^{18}F-FDG PET–based automated algorithm in the diagnosis of parkinsonian syndromes, including unpublished data from a prospective cohort. The study included first a series of 35 patients in which the automated image-based classification method showed excellent sensitivity and specificity for discriminating Parkinson disease from atypical parkinsonian syndromes. A systematic literature review and metaanalysis showed similar results (pooled sensitivity and specificity of 84% and 96%, respectively). The authors concluded that this ^{18}F-FDG PET automated analysis has excellent diagnostic potential early in the disease course and "may be a valuable tool in clinical routine as well as in research applications."

Scientific Reports

PET/CT and MALT Lymphoma Staging

In an article in the January 31 issue of *Cancers (Basel)* (2022;14[3]:750), Cohen et al. from the Tel Aviv Sourasky Medical Center and Tel Aviv University (Israel) reported on the role of ^{18}F-FDG PET/CT in staging and prediction of progression-free survival (PFS) in patients with newly diagnosed mucosa-associated lymphoid tissue (MALT) lymphoma. The retrospective study included 66 such patients. PET detected extranodal lesions in 38 (57.6%) patients and accompanying nodal disease in 13 (19.7%). The detection rate for extranodal lesions was higher in those located in tissues with low/homogeneous tracer uptake than in those with high/heterogeneous uptake (100% and 40.4%, respectively). Nodal lesions were found to have significantly lower SUV_{max}, metabolic tumor volume, and total lesion glycolysis than extranodal lesions in the same patients. The rates of detection and tracer avidity of extranodal lesions were higher in patients with advanced bulky disease and associated marrow/nodal involvement. Higher SUV_{max} in extranodal lesions predicted shorter PFS. Higher SUV_{max} and total lesion glycolysis trended toward shorter PFS in patients with localized disease. The authors concluded that "SUV_{max} of extranodal lesions may predict PFS" in patients with newly diagnosed MALT.

Cancers (Basel)

PSMA PET/CT and Prostate Cancer Outcomes

Bodar et al. from Amsterdam University Medical Center/VU University (The Netherlands) and the Prostate Cancer Network/The Netherlands Cancer Institute (Amsterdam) reported on February 15 ahead of print in *BJU International* on a study investigating associations between intraprostatic, intratumoral SUV_{max} on prostate-specific membrane antigen (PSMA) PET/CT in patients with prostate cancer before robot-assisted radical prostatectomy and pathology outcomes, including International Society of Urological Pathology score (pISUP) and lymph node status. The study drew data from 318 patients from 2 previous studies with biopsy-proven prostate cancer who were scheduled for robot-assisted radical prostatectomy. Patients underwent either ^{68}Ga-PSMA-11 (59%) or ^{18}F-DCFPyL (41%) PET/CT before surgery. Associations between the primary tumor SUV_{max} and pre- and postoperative variables were assessed.

Patients with pISUP ≤2 showed significantly lower SUV_{max} than patients with pISUP >2 for both tracers. Patients with tumor grades pN1 had significantly higher median SUV_{max} than those with pN0/pNx grades with both tracers. Additional analyses showed intraprostatic SUV_{max} to be an independent predictor of pN1 for both ^{68}Ga-PSMA-11 and ^{18}F-DCFPyL. The authors concluded that "intraprostatic, intratumoral PSMA intensity on PET/CT, as semiquantitatively expressed by SUV_{max}, may be a valuable innovative biomarker in patients with localized prostate cancer, as it is highly associated with known conventional prognostic factors, such as pISUP and lymph node status."

BJU International

First-Line ^{90}Y-Ibritumomab Tiuxetan in Follicular Lymphoma

In article published online on February 12 ahead of print in the *Annals of Hematology*, Rieger et al. from the Charité–Universitätsmedizin Berlin (Germany), the Universita degli Studi di Napoli Federico II (Italy), the National Cancer Institute (Bethesda, MD), Fondazione G. Pascale IRCCS (Naples, Italy), Lund University Hospital (Sweden), University Ulm (Germany), Johannes-Gutenberg University (Mainz, Germany), the Medical University Graz (Austria), the Technische Universität München (Germany), Max-Delbrück-Center for Molecular Medicine in the Helmholtz Association (Berlin, Germany), and the Vivantes Klinikum Am Urban (Berlin, Germany) reported on long-term follow-up of patients treated with ^{90}Y-ibritumomab tiuxetan as first-line therapy for follicular lymphoma. Previous studies have shown complete remission rates of 56% and a median progression-free survival (PFS) rate of 26 mo over a follow-up period of 30.6 mo with this radioimmunotherapeutic approach. The current study included 59 patients originally treated for grade 1–3A disease in stages II–IV. Patients with complete response and no evidence of minimal residual disease, partial response, or stable disease at 6 mo after treatment had been observed with no additional treatment. Patients with complete response but persistent minimal residual disease had received consolidation therapy with rituximab. After a median follow-up of 9.6 y, median overall PFS was 3.6 y, and 8-y PFS was 38.3%. The median overall survival (OS) was not reached during this follow-up, and 8-y OS was 69.2%. Shorter OS was associated with age (≥65 y) and disease progression within 24 mo of treatment. No increases in secondary malignancies or transformation into aggressive lymphoma were observed when compared to trials with similar follow-up periods. The authors concluded that ^{90}Y-ibritumomab tiuxetan as first-line treatment "demonstrates a favorable safety profile and long-term clinical activity in a substantial fraction of follicular lymphoma patients in need of therapy."

Annals of Hematology

Tracer-Specific Reference Tissue Selection and PET in AD

Li et al. from United Imaging Healthcare Group Co., Ltd. (Shanghai, China), University of Sydney (Australia), the Harvard Medical School (Boston, MA), University College Cork (Ireland), Zhengzhou University of Light Industry (China), and Xuanwu Hospital/Capital Medical University (Beijing, China) reported on February 15 ahead of print in *Human Brain Mapping* on a reference tissue–based quantification approach for improving change detection in brain glucose metabolism, amyloid, and tau deposition in PET imaging of Alzheimer disease (AD). Study data included large groups of PET images acquired with ^{18}F-FDG (794 scans), ^{18}F-florbetapir (906 scans), and ^{18}F-flortaucipir (903 scans) as well as T1-weighted MR images from the Alzheimer's Disease Neuroimaging Initiative database. The researchers calculated the statistical power of reference tissues in detecting longitudinal SUV ratio (SUVR) changes in cerebellum gray matter, centrum semiovale, and pons at both region-of-interest (ROI) and voxel levels, with results compared between cognitively normal and impaired individuals. The average ROI values for the pons were higher than those of the centrum semiovale and cerebellum gray matter in detecting glucose metabolism decreases, whereas the centrum semiovale reference tissue–based SUVRs provided higher values for detection of amyloid and tau deposition increases. The 3 reference tissue areas generated comparable images for the 3 tracers, although the pons-based map showed superior performance for ^{18}F-FDG. The authors concluded that "tracer-specific reference tissue improved the detection of ^{18}F-FDG, ^{18}F-florbetapir, and ^{18}F-flortaucipir PET SUVR changes, which helps the early diagnosis, monitoring of disease progression, and therapeutic response in AD."

Human Brain Mapping

^{18}F-Fluciclovine PET Amino Acid Imaging in Glioblastoma

In an article in the January 31 issue of *Frontiers in Oncology* (2022;12: 829050), Scarpelli et al. from Purdue University (West Lafayette, IN) and the Barrow Neurological Institute (Phoenix, AZ) reported on a study designed to characterize the biologic bases of enhanced fluciclovine uptake on PET in brain tumors by correlating multiple biologic factors with fluciclovine uptake across a range of human glioblastoma xenograft models. The investigation was performed in rats that underwent orthotopic implantation with 1 of 5 different human glioblastoma cell lines, followed by ^{18}F-fluciclovine PET (for tumor-to-normal uptake ratios) and MR imaging (for tumor volume and gadolinium enhancement assessment) of established tumors. Excised tumors underwent histologic analysis. Fluciclovine uptake ratios on PET were found to be most strongly correlated with tumor amino acid transporter ASCT2 levels and also significantly associated with tumor volume and tumor enhancement status on MR imaging. Both enhancing and nonenhancing tumors were visualized on PET, with a median tumor-to-normal uptake ratio across the 5 tumor lines of 2.4 (range, 1.1–8.9). The authors concluded that these data

suggest that "fluciclovine PET may be useful for assessing brain tumor amino acid metabolism" but noted that variables such as size of tumors and enhancement status could be confounding if not accounted for in fluciclovine-based metabolic measurements.

Frontiers in Oncology

Metabolism-Associated Gene Signatures for ^{18}F-FDG Avidity

Lee et al. from Samsung Medical Center/Sungkyunkwan University School of Medicine (Seoul, South Korea) and CHA University (Seongnam, South Korea) reported on January 31 in *Frontiers in Oncology* (2022;12:845900) on a study designed to elucidate metabolic genes and functions associated with ^{18}F-FDG uptake and to assess associated prognostic value in a sample group of patients with hepatocellular carcinoma. The study included 60 patients with Edmondson–Steiner grade II disease, who underwent ^{18}F-FDG PET/CT before initiation of treatment. RNA sequencing data were obtained from tumor and normal liver tissues, and associations between specific metabolism-associated genes and tumor tracer uptake were analyzed. The researchers applied a novel metabolic gene expression balance scoring system correlating glucose and lipid metabolism-associated gene expression. Nine genes related to glycolysis and the *HIF-1* signaling pathway were positively correlated with tumor tracer uptake, and 21 genes related to fatty acid metabolism and the *PPAR* signaling pathway were negatively associated with tumor tracer uptake. Seven potential biomarker genes were identified. Balance scoring according to dominance between glucose and lipid metabolism demonstrated good prognostic value in this patient group. The authors concluded that these data strongly support "the prognostic power of FDG PET/CT and indicate the potential usefulness of FDG PET/CT imaging biomarkers to select appropriate patients for metabolism-targeted therapy in hepatocellular carcinoma."

Frontiers in Oncology

PET/MR and SSTR2 Expression in Meningioma

In an article in the January 28 issue of *Frontiers in Oncology* (2022;11:820287), Roytman et al. from Weill Cornell Medicine/New York Presbyterian Hospital and Columbia University Medical Center (both in New York, NY) reported on a study using ^{68}Ga-DOTATATE PET/MR imaging to determine whether a relationship exists between tumor vascularity and somatostatin receptor-2 (SSTR2) expression in meningiomas. The prospective study included 36 patients with 60 meningiomas (World Health Organization [WHO]-1, 20; WHO-2, 27; and WHO-3, 13) who underwent ^{68}Ga-DOTATATE PET/MR with dynamic contrast-enhanced (DCE) perfusion. Tumor volumes were segmented and superimposed onto parametric DCE maps including multiple parameters, and PET tumor SUVs and SUV ratios to superior sagittal sinus were recorded. Results showed a strong and significant correlation between tumor vascularity and SSTR2 expression in WHO-2 and WHO-3 but not in WHO-1 meningiomas, which the authors concluded suggested "biological differences in the relationship between tumor vascularity and SSTR2 expression in higher-grade meningiomas." They called for additional work to expand on this finding.

Frontiers in Oncology

PET/CT + mpMR in Radiorecurrent Prostate Cancer

Rasing et al. from University Medical Center Utrecht and Amsterdam University Medical Center (both in The Netherlands) reported on February 3 in *Cancers (Basel)* (2022;14[3]:781) on the positive predictive value of combined multiparametric MR and prostate-specific membrane antigen (PSMA) PET/CT imaging in patients with locally recurrent prostate cancer after primary radiation therapy and on the added value of pathology verification with MR-targeted biopsies. The study included 41 patients with locally recurrent prostate cancer referred for 19-Gy single-dose MR-guided focal salvage high-dose-rate brachytherapy. All patients had undergone multiparametric MR and PSMA PET/CT before biopsy. Imaging results were used to identify lesions suspected for isolated tumor recurrence, and these were biopsied. Forty (97.6%) patients had positive biopsies for recurrent cancer. Five of these initially had negative biopsies of lesions identified on MR/PSMA PET, and recurrence was confirmed in 4 of the 5 after rebiopsy (1 patient refused a second biopsy). The positive predictive value for combined multiparametric MR and PSMA PET imaging was 97.6%. The authors concluded that biopsies can be withheld "when the results of the combined multiparametric MRI and PSMA PET/CT are conclusive, avoiding an unnecessary invasive and burdensome procedure."

Cancers (Basel)

MR and PET in Renal Cell Carcinoma Detection

In an article in the February 11 issue of *BMC Cancer* (2022;22[1]:163), Yin et al. from Wuxi No. 2 People's Hospital/Nanjing Medical University (China), the Affiliated Hospital of Jiangnan University (Wuxi, China), and Shanghai University of Medicine and Health Sciences (China) provided a systematic review and metaanalysis of the diagnostic performance of MR and PET imaging in detection of renal cell carcinoma. After a keyword search of the major scientific databases, a total of 44 articles were included for analysis. The resulting pooled sensitivities of MR, ^{18}F-FDG PET, and ^{18}F-FDG PET/CT were 80%, 83%, and 89%, respectively. The corresponding overall specificities were 90%, 86%, and 88%. The pooled sensitivity and specificity of 1.5-T MRI studies were 86% and 94%, respectively. For prospective PET studies, the pooled sensitivity, specificity and AUC were 90%, 93%, and 97%, respectively. For detection of primary renal cell carcinoma, PET as reported in the articles reviewed had a pooled sensitivity, specificity, and AUC of 77%, 80%, and 84%, respectively. For PET/CT, the corresponding percentages were 80%, 85%, and 89%.

The authors concluded that these results suggest that "MRI and PET/CT present better diagnostic value for the detection of renal cell carcinoma in comparison with PET" and that "MRI is superior in the diagnosis of primary renal cell carcinoma."

BMC Cancer

PET/CT and GEP NET Management

Magi et al. from Sant'Andrea University Hospital/ENETS Center of Excellence (Rome), Sapienza University of Rome, the University of Bologna, and the IRCCS Azienda Ospedaliero-Universitaria di Bologna (all in Italy) reported on February 11 ahead of print in *Endocrine* on a retrospective study evaluating the role of ^{18}F-FDG PET/CT in grade 1 gastroenteropancreatic neuroendocrine tumors (GEP NETs). The study included data from 55 patients (24 with pancreatic NETs, 31 with gastrointestinal NETS). At diagnosis, 28 (51%) had metastatic disease, and 50 (91%) patients had positive findings on ^{68}Ga-labeled somatostatin receptor PET/CT. All patients underwent ^{18}F-FDG PET/CT, and 27 (49%) had positive findings. ^{18}F-FDG PET/CT findings led to changes in therapeutic management in 29 (52.7%) patients. Progression-free survival (PFS) was longer in patients with negative ^{18}F-FDG PET/CT (median PFS not reached in the study period) than in those with positive findings (24 mo), particularly in the group with pancreatic NETs. The authors concluded that these data support "a more 'open' attitude toward the potential use of ^{18}F-FDG PET/CT in the diagnostic work-up of grade 1 GEP NETs, which may be used in selected cases to detect those at higher risk for an unfavorable disease course."

Endocrine

Reviews

Review articles provide an important way to stay up to date on the latest topics and approaches through valuable summaries of pertinent literature. The Newsline editor recommends several general reviews accessioned into the PubMed database in January and February. Parel et al. from the National Heart, Lung, and Blood Institute (Bethesda, MD) provided "Updates in the impact of chronic systemic inflammation on vascular inflammation by positron emission tomography (PET)" on February 16 in *Current Cardiology Reports*. In the same journal on February 16, Juarez et al. from University Medical Center Utrecht (The Netherlands), University of Turku/Turku University Hospital (Finland), University Medical Center Groningen (The Netherlands), King's College London/St. Thomas' Hospital (UK), and UMA-Health (Buenos Aires, Argentina) looked at the potential of "Artificial intelligence to improve risk prediction with nuclear cardiac studies." In an article on January 26 in *Nanomaterials* (Basel) (2022;12[3]:399), Murar et al. from the Barcelona Institute of Science and Technology (Spain) and the Eindhoven University of Technology (The Netherlands) reviewed "Advanced optical imaging-guided nanotheranostics towards personalized cancer drug delivery." Anan et al. from the Universiti Sains Malaysia (Pulau Pinang) and the Imam Abdulrahman Bin Faisal University (Dammam, Saudi Arabia) published "A review on advances in ^{18}F-FDG PET/CT radiomics standardisation and application in lung disease management" on February 5 ahead of print in *Insights into Imaging* (2002;13[2]:22). In an article published on January 21 online ahead of print in the *International Journal of Molecular Sciences* (2002;23[3]: 1158), Debnath et al. from the University of Texas Southwestern Medical Center (Dallas) summarized "PSMA-targeting imaging and theranostic agents—Current status and future perspective."

Leadership in Patient Advocacy

A Conversation Between Josh Mailman and Thomas Hope

Josh Mailman[1] and Thomas A. Hope[2]

[1]*NorCal CarciNET Community, Oakland, California; and* [2]*University of California, San Francisco, San Francisco, California*

Thomas Hope, an associate professor in the Department of Radiology and Biomedical Imaging at the University of California, San Francisco, spoke with Josh Mailman, an internationally recognized advocate for neuroendocrine tumor patients as well as an advocate for nuclear medicine and molecular imaging. Mr. Mailman is the inaugural chair of the SNMMI Patient Advocacy Advisory Board, a member of the Education and Research Foundation for Nuclear Medicine and Molecular Imaging Board, the treasurer and a board member of the Neuroendocrine Tumor Research Foundation, and the president of the NorCal CarciNET Community. In addition, he is a U.S. Food and Drug Administration (FDA) patient representative, a member of the National Cancer Institute's Gastrointestinal Steering Committee, a member of the American Society of Clinical Oncology Scientific Committee, and the sole patient representative on the Nuclear Regulatory Commission (NRC) Advisory Committee on the Medical Uses of Isotopes (ACMUI). Mr. Mailman has an MBA from the UCLA Anderson School of Management and has been a technology entrepreneur for more than 20 years.

Dr. Hope: *Could you start by talking for a couple of minutes about your diagnosis, what you remember about that time, and what nuclear medicine meant to you then?*

Mr. Mailman: What is nuclear medicine? As a newly diagnosed patient you have no idea. I think one of the more amazing aspects of my journey is that last year I became the patient's right advocate on the NRC ACMUI. Fifteen years ago, when I was diagnosed, I knew neither that the NRC had anything to do with nuclear medicine nor that there was an advisory committee I might be on.

As to my diagnosis: this was an incidental pick-up during an annual exam. I recommend that everyone continue annual checkups for this very reason. I'm the son of a doctor so am pretty religious about following up. At my annual exam in 2007, my checkup went well, my blood work was fine, but my general practitioner felt something a little weird under my rib cage and told me to get an ultrasound when I had some time. Two months later, I had a chest cold that brought me to urgent care, where the staff said, "It says here you need an ultrasound, so why don't you go while these other tests are being run?" I went for the ultrasound, and as I was coming back no one on the urgent care team would look me in the eye—my first indication that something was wrong. There was a finding on ultrasound, and I was scheduled for a CT, which showed a very large pancreatic mass. The biopsy showed a neuroendocrine tumor (NET). This led to my first nuclear medicine study, an OctreoScan (Mallinckrodt), which led to appointments with an oncologist and surgeon. Not many treatment options were available in 2007/2008 for a nonfunctioning pancreatic NET without a surgical possibility.

Josh Mailman, MBA

About 4 mo into my journey, I joined a support group for patients with NETs. The group was big on education and advised me to go to patient conferences and learn about this disease. The first patient conference that I attended was a two-day meeting in Toronto. The first day focused on surgery, somatostatin analogs, and more somatostatin analogs, and none of it applied to me. At the end of the day, I was pretty depressed, because I hadn't seen any possibilities of learning anything new.

On the morning of the next day, presenters from Europe discussed ^{68}Ga imaging and radioisotope therapy. All of a sudden, I was where I was supposed to be. I'm a tech guy. I cocreated eFax.com; I like more data and innovation. The first lecture I saw was from Richard P. Baum, from Germany, who presented data about how we can see more disease and see it more clearly and with greater accuracy than was standard at that time. I walked up to Dr. Baum after his presentation and said, "Where can I get one of these?" And he said, "In Germany in three weeks." And so, my journey in nuclear medicine began.

Dr. Hope: *Can you talk about the role of patient advocacy groups and how they benefit the community? Looking forward, how do you see their role changing or expanding to help improve patient care?*

Mr. Mailman: Patient advocacy groups are really important. First, I'll talk about patient support groups. As patients we all come to clinics, sit in the lobby, and none of us talk to each other about our disease. I went months without meeting anyone who looked like me or had anything that we could relate to, even though I was probably in waiting rooms with them all the time. No one goes around and says, "Hi, I have a neuroendocrine tumor; what's your name?"

A support group is a safe place to discuss your journey. I could meet people like me, hear about what other people were doing, and learn from that shared experience. I was fortunate to find a group that valued education and that reached out to our medical community to work with them. This relationship has been a major driver in northern California, making sure patients are comfortable with their treatment decisions/plans. As patients, we may get at most 30 min with our physicians, at a time when we're very stressed. The support group is a safe place to have a conversation about care, what you're doing, and what is new that's coming up.

COPYRIGHT © 2022 by the Society of Nuclear Medicine and Molecular Imaging.
DOI: 10.2967/jnumed.122.263989

The interesting part about these independent support communities is they can provide support in a way that doesn't feel rushed. One of the hardest things to convey when I talk to institutions that are interested in starting support groups is that, as a patient, I don't want to spend more time in your 4 walls. We feel different emotions when we walk through the doors at a hospital, and I'm going to spend as little time there as possible. Independent support communities don't have that weird feeling of "this is where I get treated."

Dr. Hope: *I would just add one thing, which is the importance that your group in particular and other support groups and patients in general have for people's careers, including my own. Travel grants provide opportunities to give lectures, participate in activities that help develop the community, and bring new investigators into the field.*

Mr. Mailman: That was one of the reasons we decided to become a nonprofit more than 10 years ago. We wanted to be able to give back to our community, to support not only patients but those who support us in our community. Our educational and travel grant program helps us support those interested in NETs, which, in turn, will help us as well. It's a symbiotic relationship. This is really about our community serving our community.

Dr. Hope: *You, like many people with serious disease, but particularly NETs, have gone to Europe to receive peptide-receptor radionuclide therapy through compassionate use and have benefited greatly. Can you talk about your thoughts on compassionate-use laws, their impact, and how you think about this as a patient?*

Mr. Mailman: This is a challenging topic. You and I work in the clinical trial environment of the National Cancer Institute, where we're trying to bring forward practice-changing clinical trials. I've benefited from what really are not clinical trials but compassionate use, the early use of therapies in patients. It allows therapies to get into patients earlier and may give us some signaling about benefits and results. That's great, but it's challenging when it becomes the only avenue by which a therapy can go forward.

It's a dichotomy I've benefited from, but it's useless unless it goes toward informing a registration trial. We're not benefiting the majority of patients—and that is what we need to be doing, going toward registered products. If we're going to use this avenue, it's really important that we push toward trials that produce data that can be used to inform registration. I'm encouraged by what's happened in the prostate-specific membrane antigen field. Yes, there was early compassionate use, but this moved to clinical trials (such as VISION or TheraP) much more quickly than we did with NETs.

Dr. Hope: *Can you comment on the United States, where access to compassionate use is much more limited? Is there anything you think about the way we approach the regulatory status here that might help move things forward?*

Mr. Mailman: This can be done individually. ^{90}Y-DOTATOC was used in Iowa for a while, but it's tough. It's a different environment, and the question is: How do we get movement toward phase 1 trials earlier? In the NET space, we didn't have an investor who was interested in taking trials further in the early years. The environment has changed; people are seeing market opportunities more quickly. I'm not even certain that, if we changed the regulations, our institutions would do this kind of work without some type of pharma backing, which would defeat the purpose of trying to do it.

Dr. Hope: *You've had several roles over the years. Which one do you think has had the greatest impact on patients?*

Mr. Mailman: That's an interesting question. I think the most impactful was my work with the ^{68}Ga Working Group. In 2011, I had a chance meeting with Henry VanBrocklin, from the University of California, San Francisco, while at dinner attending the first Theranostics World Congress in Germany. He was, at that time, the head of the SNMMI Patient Outreach Committee and invited me to join the Patient Advocacy Advisory Board and the ^{68}Ga Working Group. This was long before we had trials going on with ^{68}Ga, and, through the working group, we wrote the imaging manual for ^{68}Ga PET, which turned out to be the imaging manual that everyone in North America used. It was really important to bring the patient voice and urgency to our monthly meetings and to writing that imaging manual.

Through that committee, we persuaded the FDA to come to the Third Theranostics World Congress in Baltimore, MD, in 2015. We had 70 patients there on a Saturday listening to the FDA say that plenty of trials were going on. The patients responded that there were few and that new ones were needed now. The FDA basically said then and there that they would approve or expand Investigational New Drug approvals and encourage the filing of a New Drug Application for ^{68}Ga.

I have also worked to raise in excess of $20 million for NET research, and this has helped move progress forward. It has encouraged or kept researchers interested in the field. Those researchers will make significant discoveries and increase the number of people who provide patient care, ultimately impacting the patient experience.

So having dinner with Henry VanBrocklin in Germany, which led to my participation in the SNMMI ^{68}Ga Working Group, which moved us toward approval on a landmark imaging agent, has likely had the most impact on patient care.

> "It's just so important that we work with patients all the way through the journey."

Dr. Hope: *On the other side of that story, you've been involved with the FDA in different ways. Can you comment on the leadership of Lou Marzella, as the director of the Division of Imaging and Radiation Medicine in the Center for Drug Evaluation and Research at the FDA, and how he's adapted over time?*

Mr. Mailman: I first met Dr. Marzella in Baltimore. I think he was pleasantly surprised at the patient involvement—it was eye opening to hear patients come forward in that number and speak so eloquently. Over time we became friends in advancing patient care. We started emailing each other when issues came up or for clarification about the regulatory framework, for example in the early days of ^{68}Ga. We held ^{68}Ga sessions at all the annual meetings at which he spoke. The friendship became such that he started inviting me to give talks to the imaging directors' lunch at the FDA. It was a little intimidating to be a patient speaking to 10 imaging directors, giving my perspective on the challenges of getting these drugs to patients. Every interaction I have had with Lou and the imaging group at the FDA has been positive.

One of the last times I had lunch with them, I discussed the challenges associated with ^{68}Ga generators and how few generators were available. The FDA gets outage reports for every drug that is prescribed, but they don't have insight into radiopharmaceutical supplies. It was again patients who brought insight to the FDA about this access issue, and I think they've appreciated that.

Lou has been a champion of the patient, moving things forward and making sure that there's transparency in the process.

Dr. Hope: *How did your life before your diagnosis help you deal with cancer and be more effective in the role you have now?*

Mr. Mailman: My background is in business. I have a master's in finance and marketing from UCLA and worked in technology for more than 20 years. Developing new products in technology, you learn a great deal about patents and proprietary rights. The first set of meetings of the ^{68}Ga Working Group was all about patents and rights. We didn't really talk about drugs; we talked about patent expirations and marketing exclusivity to better understand how this imaging agent could come to market. That was right up my alley, because that's what we did in tech all the time.

My business background has helped the ways in which I run our support community. One of the things that I learned in graduate school and marketing is that there needs to be a drumbeat—something constant that people can count on. Consistency matters. We meet on specific days—the first Saturday of every other month for us in Walnut Creek.

Dr. Hope: *Switching topics here: What do you think is the next exciting thing for NET patients? What are you most excited about?*

Mr. Mailman: I'm going to answer a different question: What is the most exciting NET project I am working on? As you know, since you have been running with us at our annual charity run, we have shirts that remind us of the people we've lost over the last year. It is a constant reminder that we don't live forever. We don't do much for those who are facing end-of-life decisions. A NET patient may have spent years trying to find a NET specialist, but once beginning hospice care, he or she will see a generalist, who may not understand NETs at all. I have personally worked with several patients who have struggled with this transition. I am currently working to change this with guidance to help providers with patients as they enter hospice. It will cover the unique aspects of NETs that differ from other end-of-life scenarios. My hope is that it will be easier for those who are nearing death, because their care team will be able to better understand and comfort patients at the end of the journey. Over the years that part of this journey has been the most challenging, and we have to do better.

Dr. Hope: *That's a great point, particularly for nuclear medicine, where we usually come in for a portion of time and then go away. We do peptide-receptor radionuclide therapy, for example, and then we're out.*

Mr. Mailman: Several times a year I work with hospice patients' families. One example is when patients have hormone-producing symptoms but are taken off long-acting somatostatin analogs and can no longer get access to long- or short-acting somatostatin analogs. 2021 was a tipping point, with a patient who called me and asked if I could help him because he'd been in hospice for a month and his symptoms were getting worse. His hospice basically denied access to long- or short-acting octreotide. This went all the way up to the board of the hospice. The patient called me to say that he was about to exit hospice for 72 h, so that he could get a long-acting administration. In that 72 h, all the durable equipment that he'd come to use (beds, etc.) would have to be removed from his house. The whole process just got me angry. This was the impetus to ask the North American Neuroendocrine Tumor Society Guidelines Committee to write an end-of-life white paper. We have about 7 of us on the project at the moment

I'm also working with pharmaceutical companies in the background. Hospice gets $270 a day for nursing care, all meds, and all visits, so even if it's prescribed, most of them will not want to use it because it is too expensive, and I'm trying to solve that. This is the most important thing that I'm working on currently. It has nothing to do with what I normally do, but it's just so important that we work with patients all the way through their journeys.

Dr. Hope: *That is a perfect way to end. In this series we always talk about the next peptide, the next drug. What you bring to these discussions is patient centricity. You really highlighted why we do this, which is the patient. Sometimes we get lost in the science, the drugs, and the research. You did a perfect job of bringing us back to what matters: the patient.*

Mr. Mailman: It's the journey. We all talk about how we're going to make people live longer, but we're not going to make them live forever.

Nuclear Medicine and Artificial Intelligence: Best Practices for Algorithm Development

Tyler J. Bradshaw[1], Ronald Boellaard[2], Joyita Dutta[3], Abhinav K. Jha[4], Paul Jacobs[5], Quanzheng Li[6], Chi Liu[7], Arkadiusz Sitek[8], Babak Saboury[9], Peter J.H. Scott[10], Piotr J. Slomka[11], John J. Sunderland[12], Richard L. Wahl[13], Fereshteh Yousefirizi[14], Sven Zuehlsdorff[15], Arman Rahmim[16], and Irène Buvat[17]

[1]Department of Radiology, University of Wisconsin–Madison, Madison, Wisconsin; [2]Department of Radiology and Nuclear Medicine, Cancer Centre Amsterdam, Amsterdam University Medical Centres, Amsterdam, The Netherlands; [3]Department of Electrical and Computer Engineering, University of Massachusetts Lowell, Lowell, Massachusetts; [4]Department of Biomedical Engineering and Mallinckrodt Institute of Radiology, Washington University in St. Louis, St. Louis, Missouri; [5]MIM Software Inc., Cleveland, Ohio; [6]Department of Radiology, Massachusetts General Hospital and Harvard Medical School, Boston, Massachusetts; [7]Department of Radiology and Biomedical Imaging, Yale University, New Haven, Connecticut; [8]Sano Centre for Computational Medicine, Kraków, Poland; [9]Department of Radiology and Imaging Sciences, Clinical Center, National Institutes of Health, Bethesda, Maryland; [10]Department of Radiology, University of Michigan Medical School, Ann Arbor, Michigan; [11]Department of Imaging, Medicine, and Cardiology, Cedars-Sinai Medical Center, Los Angeles, California; [12]Departments of Radiology and Physics, University of Iowa, Iowa City, Iowa; [13]Mallinckrodt Institute of Radiology, Washington University in St. Louis, St. Louis, Missouri; [14]Department of Integrative Oncology, BC Cancer Research Institute, Vancouver, British Columbia, Canada; [15]Siemens Medical Solutions USA, Inc., Hoffman Estates, Illinois; [16]Departments of Radiology and Physics, University of British Columbia, Vancouver, British Columbia, Canada; and [17]Institut Curie, Université PSL, INSERM, Université Paris-Saclay, Orsay, France

The nuclear medicine field has seen a rapid expansion of academic and commercial interest in developing artificial intelligence (AI) algorithms. Users and developers can avoid some of the pitfalls of AI by recognizing and following best practices in AI algorithm development. In this article, recommendations on technical best practices for developing AI algorithms in nuclear medicine are provided, beginning with general recommendations and then continuing with descriptions of how one might practice these principles for specific topics within nuclear medicine. This report was produced by the AI Task Force of the Society of Nuclear Medicine and Molecular Imaging.

Key Words: computer/PACS; research methods; statistics, algorithm; artificial intelligence; best practices

J Nucl Med 2022; 63:500–510
DOI: 10.2967/jnumed.121.262567

Recent advances in artificial intelligence (AI) algorithms, together with the emergence of highly accessible AI software libraries, have led to an explosion of interest in AI within the nuclear medicine field (Fig. 1). AI, which is the development of computer systems able to perform tasks normally requiring human intelligence, is being explored in nearly every subspecialty in the chain of molecular imaging, from radiochemistry to physician report generation (Fig. 2).

The hype that propels the development of AI algorithms in nuclear medicine is counterbalanced by concerns about certain pitfalls of AI (*1*). The enthusiasm for AI is justified given its numerous potential benefits: AI might relieve physicians and staff from repetitive tasks, accelerate time-intensive processes, enhance image quantification, improve diagnostic reproducibility, and deliver clinically actionable information. AI promises to carry nuclear medicine beyond certain human limitations and biases. On the other hand, AI is susceptible to unique biases that are unlike the biases typically associated with human experts. There are also valid concerns about the reproducibility of claims made in many published AI studies (*2*) and the generalizability of trained algorithms (*3*). These serious issues must be addressed to ensure that algorithms earn the trust of care providers and care recipients (*4*).

This report was developed by the AI Task Force of the Society of Nuclear Medicine and Molecular Imaging and lays out good machine learning (ML) practices for algorithm development in nuclear medicine. Standards and recommendations for algorithm development, study design, and scientific reporting can help ensure safe technologies and reproducible gains. The report provides general recommendations for AI algorithm development, followed by recommendations that are specific to the individual subspecialities of nuclear medicine. The report focuses primarily on ML methods, as those are currently the predominant class of AI algorithms being explored in nuclear medicine, although many principles are applicable beyond ML. The target audience of the report is developers, including physicists and clinical scientists, who wish to develop AI algorithms in nuclear medicine, but the report can also benefit users (e.g., physicians) who wish to understand algorithm development. A forthcoming report from the AI Task Force focuses on appropriate methods of evaluating and validating AI algorithms in a clinical setting.

GENERAL RECOMMENDATIONS

The first part of this report describes the general pipeline of algorithm development (Fig. 3) and provides recommendations that are common to most ML applications in nuclear medicine.

Received May 12, 2021; revision accepted Nov. 1, 2021.
For correspondence or reprints, contact Tyler J. Bradshaw (tbradshaw@wisc.edu).
Published online Nov. 5, 2021.
COPYRIGHT © 2022 by the Society of Nuclear Medicine and Molecular Imaging.

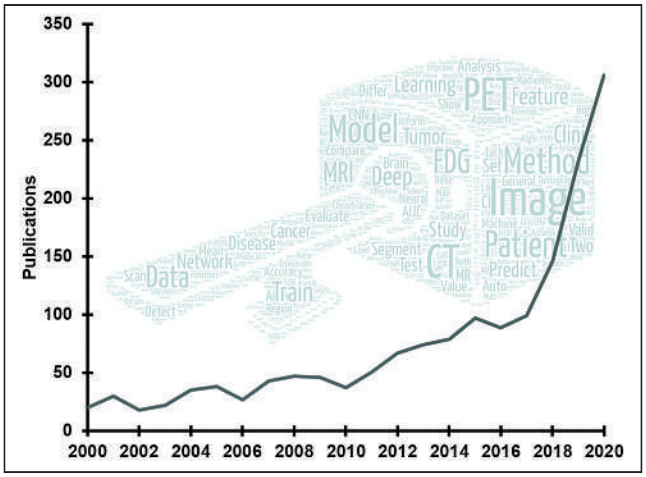

FIGURE 1. Trend in publications on AI within nuclear medicine according to Scopus (Elsevier). Word cloud contains most commonly used terms in recent abstracts.

The supplemental data (available at http://jnm.snmjournals.org) present a hypothetical tumor segmentation algorithm using a novel architecture (*5*) trained on a publicly available dataset (*6*,*7*) and follows it through all stages of development, from conception through reporting and dissemination, illustrating the recommendations provided here (Supplemental Fig. 1).

Study Design

The first step in AI algorithm development is to carefully define the task to be performed by the algorithm (Fig. 3). Investigators should collaborate with relevant stakeholders to understand whether and how the algorithm will be used in practice and then tailor the algorithm to the need. Early and regular feedback from users (e.g., clinicians) throughout the development process is necessary to properly align the algorithm's functionality with the clinical need. Once the algorithm's task is defined, studies should then be designed to train and evaluate the algorithm.

It is recommended that nuclear medicine AI studies be classified as either method development studies or evaluation studies, so that each class can be held to unique technical standards (Table 1). Method development studies are defined as studies that introduce a novel method or demonstrate the feasibility of a new application (i.e., proof of concept). Most recently published studies are method development studies. The evidence produced by these studies is insufficient to support a claim about how the trained algorithm is expected to perform clinically, often because of limited datasets and insufficient clinical evaluation techniques. Once an algorithm has shown technical promise in a method development study, the algorithm would then move on to a clinical evaluation phase in which a trained algorithm's biases and limitations in a clinical task are evaluated to provide evidence substantiating a clinical claim. Evaluation studies must be performed using datasets that are external to the development dataset and should use algorithms that are frozen—that is, are beyond the training stage (e.g., commercial software). Evaluation studies might include reader studies; phantom studies; and, potentially, multicenter masked randomized controlled trials. Both classes of studies play important roles in advancing the field, and well-conducted studies of both classes should have a pathway to publication (potentially even in the same publication, if appropriate). Yet both classes of studies require unique design considerations. By holding both types of study to higher technical standards, it is hoped that the field can better avoid common weaknesses found in AI publications, including poor reproducibility, overly optimistic performance estimation, lack of generalizability, and insufficient transparency. The technical standards for both study types are discussed throughout this report and are summarized in Tables 1 and 2. Requirements for clinical evaluation studies will be further described in a forthcoming companion report from the AI Task Force.

The pathway that a technology will take to reach clinical adoption should depend on the degree of risk it poses to patients. Risk categories for software have been proposed by the International Medical Device Regulators Forum and adopted by the U.S. Food and Drug Administration (*8*). Software in the highest risk category will require prospective studies to validate clinical claims. Prospective studies should use preregistered statistical analysis plans (*9*).

AI algorithms will require postdeployment monitoring to ensure safety and quality. A decline in performance might occur for a variety of reasons, such as new scanners or shifting patient demographics. Developers should plan to seek extensive user feedback and gather performance data after clinical deployment to detect and mitigate algorithm nonconformance and identify opportunities for improvement.

NOTEWORTHY

- AI studies are being published with increasing frequency in nearly all subspecialties of nuclear medicine.
- Common pitfalls to AI studies include poor reproducibility, overly optimistic performance statements, lack of generalizability, and insufficient transparency.
- Technical best practices in AI algorithm development can help ensure reproducible scientific gains and accelerated clinical translation.
- Some general recommendations include working closely with domain experts, collecting representative datasets, developing models using cross validation, following published reporting guidelines, making models and codes available, and being fully transparent about dataset characteristics and algorithm failure modes.
- Some specific recommendations for nuclear medicine subspecialties include evaluating image enhancement algorithms through reader studies, using multiple annotators to train and evaluate segmentation and diagnostic algorithms, making sure that algorithms performing clinical tasks are interpretable, and removing redundant features from radiomics analysis.

Data Collection

Collecting and labeling data are typically the most time-consuming aspects of algorithm development but also have the greatest dividends. An ML algorithm is ultimately a reflection of its training data, and its performance can be affected by the amount and quality of its training data. In nuclear medicine, collecting large datasets can be challenging because of the lower volumes of examinations compared with other modalities and applications.

A data collection strategy should be designed with a goal of avoiding the biases that might result from an insufficiently representative training dataset. Biases can be clinical (how well the

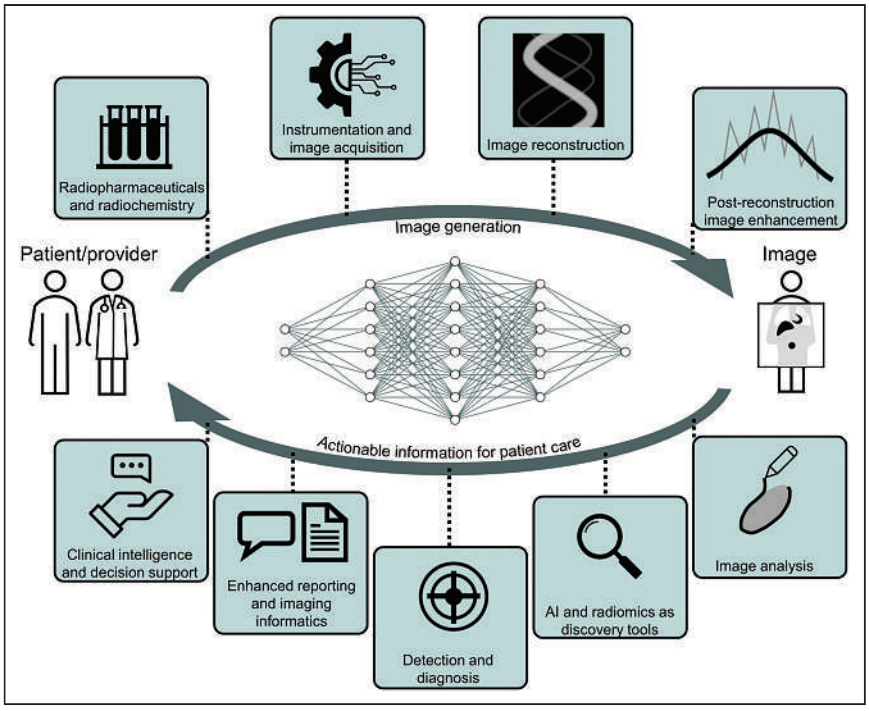

FIGURE 2. AI applications spanning the gamut of nuclear medicine subspecialties.

training data reflect the clinical condition or pathologic features), technical (scanner models, acquisition protocols, reconstruction settings), demographic (racial and socioeconomic demographics, age, sex, habitus), and selection-based (e.g., tertiary vs. community hospital). For each of these biases, a structural or distribution mismatch between the training and deployment domains can result in unintended model outputs. Datasets should ideally be curated to contain the features and abnormalities that the algorithm is expected to face once deployed. Domain experts (e.g., clinicians) should guide the collection of representative cases.

It is challenging to determine the number of cases needed for algorithm development. For algorithm training, having more data is better, as long as the data are of high quality (i.e., capturing the data distribution of the targeted population). No formal guidelines exist for estimating the size of the training set, although some practical approaches have been described (*10*), and trial and error are therefore often necessary (*11*). For evaluation studies, however, sample sizes can be guided by statistical power calculations (*12*).

Data augmentation can be particularly useful for deep learning applications in nuclear medicine. By synthetically modifying the input data, being careful not to break the association between the input data and their target labels, dataset sizes can be artificially increased (*13*). Also, using a different dataset to pretrain a model can enhance the model's capability to learn certain features and associations when labeled data are limited, although there is a risk of model overparameterization (*14*).

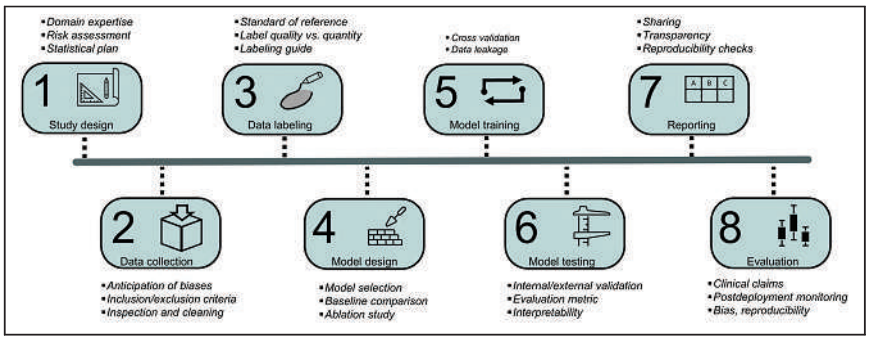

FIGURE 3. Pipeline for AI algorithm development together with key considerations of each stage of development.

Data Labeling

For supervised ML, labels should reflect the desired output of the algorithm in both form and quality. Labels might be generated by expert opinion, computer simulation, or other methods. The labels should be regarded by experts in the field to be sufficient standards of reference. Different labeling techniques are typically possible for a given task, often yielding different degrees of quality as illustrated in Figure 4 for diagnostic applications. When labels are based on expert opinion, it is recommended that a detailed and thorough guide to labeling be developed and discussed among labelers to reduce inter- and intraobserver variability.

Because of the high cost of expert labeling, tradeoffs are nearly always made between the number of cases that can be labeled and the quality of those labels. For some tasks, having more labelers per sample can produce greater performance gains than using a larger dataset but with fewer labelers (*15*,*16*).

Because of the scarcity of labeled nuclear medicine datasets, methods that minimize labeling efforts and maximize the use of unlabeled data should be considered. Labeling is often a bottleneck in algorithm development, yet troves of unlabeled data sit dormant in clinical databases. Developers should consider data-efficient approaches to algorithm development, including semisupervised learning algorithms (*17*), active learning, contrastive learning, pretraining with proxy tasks, and self-supervised learning (*18*).

Model Design

Investigators are often faced with numerous options when selecting or designing a model for a particular task. Options can include supervised or unsupervised learning and use of neural networks or decision trees, among others. Benchmark datasets and data science competitions are useful resources for exploring different options (*19*).

For development studies, investigators should compare different model types. To avoid unnecessary complexity, investigators using large models are encouraged to also evaluate simpler models as a baseline comparison (e.g., logistic regression (*20*)). For a fair comparison of models, hyperparameters for all models should be sufficiently tuned. The approach used for hyperparameter optimization, including how many models were trained and compared, should be reported in the publication. For method development studies that introduce a novel architecture, ablation analysis is recommended (*21*).

TABLE 1
Proposed Standards for Development Studies Vs. Evaluation Studies

Parameter	Development studies	Evaluation studies
Accessibility of code, models, and executables	Necessary for publication	Encouraged
Use of external datasets	Encouraged	Required
Subgroup analysis for biases	Encouraged (if applicable)	Required (if applicable)
Clinical claims	None	Required
Annotation quality	Fair to high	High
Ablation studies	Encouraged (if applicable)	Not necessary
Comparison of architectures	Encouraged (if applicable)	Not necessary
Novelty in technology or application	High (for publication)	Not necessary (for publication)
Data splitting	Cross validation	Holdout or external

When comparing AI models, small performance differences between candidate models have to be carefully interpreted. Random initialization of model weights can result in sizeable performance differences between training sessions even when identical architectures are trained with identical data. If feasible, repeated training with random initialization or with repeated holdout should be performed to provide confidence intervals of a model's performance, which can be used to more rigorously compare different models.

Model Training

A critical part of model training is the partitioning of labeled datasets into disjoint sets. Each set serves a different purpose: the training set for updating the model's weights, the validation set for hyperparameter tuning or model selection (if needed), and the testing set for estimating the model's performance on unseen data. Partitioning a dataset reduces the risk of obtaining overly optimistic performance estimates due to overfitting to its own dataset. For this same reason, careful attention should be paid to preventing information from being leaked from the test set to the model during training. This can happen when, for example, a model is repeatedly retrained after evaluating it on the test set (i.e., tuning to the test set). Investigators should use the validation set to monitor model convergence (i.e., loss curves) to prevent underfitting and overfitting.

Cross validation is recommended for method development studies, whereas holdout or external test sets should be used for evaluation studies. In cross validation, the training, validation, and test datasets are repeatedly sampled from the overall dataset and a different model is trained and evaluated with each sampling. There are several approaches to cross validation (*22*), some of which are illustrated in Figure 5. Generally, data partitioning should aim to preserve data and class distributions in each of the data splits. A drawback of cross validation is that it creates multiple models and may not be computationally feasible for large models. However, for limited datasets, cross validation produces a less biased estimate of a method's generalization performance than using 1-time partitions (i.e., holdout testing) (*23*). The latter should be used in development studies only when cross validation is technically infeasible or for large datasets.

Federated learning can be considered for multiinstitution studies in which pooling of data across institutions is challenging or prohibited because of privacy concerns. In federated learning, data cohorts reside within their respective institutional boundaries but models and weights are shared across institutions (*24*).

Model Testing and Interpretability

After model training and selection, the model's technical performance is determined. Model testing, especially when using the developmental dataset, does not typically result in evidence to substantiate broad clinical claims.

Models are tested using a test dataset, which should be an unseen holdout dataset or—for development studies—may consist of all the data through cross validation (Fig. 5). The test set should have data and class distributions similar to those of the target population. The target population must be explicitly defined (e.g., "Hodgkin lymphoma patients scanned in our department in 2020"). Additional test cohorts that are external to the developmental data are highly desirable, as they provide an estimate of the algorithm's sensitivity to covariate or dataset shift.

Model performance is quantified using evaluation metrics. Selection of evaluation metrics should be based on how well they reflect the failures and successes of the algorithm for the specific application. However, evaluation metrics are often unable to detect all the ways in which an algorithm fails, and summary statistics can hide meaningful errors (*25*). Investigators should seek to detect cases of failure and work to understand their causes. This work will often include visual inspection of the model output. It is recommended that challenging cases be included in the test set to probe the model's limitations. Investigators should also directly compare the AI model's performance with another acceptable standard, such as the standard of care. It is recommended that subgroup analysis be conducted to identify whether the algorithm is biased against any cohorts.

Investigators should attempt to make their algorithms interpretable to users, especially algorithms that perform clinical tasks (*4*). Interpretable algorithms attempt to explain their outputs by highlighting the properties of the input data that most impacted the model's prediction. Interpretability may help identify confounding factors that are unrelated to the task or pathology yet unintentionally guide the model's predictions (*3*). Popular approaches include tracking gradients through the network (e.g., gradient-weighted class activation mapping) or iteratively perturbing or occluding parts of the input data (e.g., Shapley additive explanations) (*26*).

Reporting and Dissemination

The quality of the reporting of AI studies is a key determinant of its subsequent impact on the field. Formal guidelines for reporting of AI studies are emerging (*27*,*28*), including some that have been proposed (*29–31*) and others that are forthcoming (*32–34*).

TABLE 2
Summary of Recommendations

Category	Topic	Recommendation
Study design	Task definition	Collaborate with domain experts, stakeholders
	Study types	Identify publications as development studies or evaluation studies
	Risk assessment	Assess the degree of risk that algorithm poses to patients and conduct study accordingly
	Statistical plan	Preregister statistical analysis plans for prospective studies
Data collection	Bias anticipation	Collect data belonging to classes or groups that are vulnerable to bias
	Training set size estimation	Estimate size on the basis of trial and error, or prior similar studies
	Evaluation of set size estimation*	Use statistical power analysis for guidance
	Data decisions	Use justified, objective, and documented inclusion and exclusion criteria
Data labeling	Reference standard	Use labels that are regarded as sufficient standards of reference by the field
	Label quality	Justify label quality by application, study type, and clinical claim (Fig. 4)
	Labeling guide*	Produce detailed guide for labelers in reader studies
	Quantity/quality tradeoff	Consider multiple labelers (quality) over greater numbers (quantity)
Model design	Model comparison*	Explore and compare different models for development studies
	Baseline comparison	Compare complex models with simpler models or standard of care
	Model selection	Report model selection and hyperparameter tuning techniques
	Model stability	Use repeated training with random initialization when feasible
	Ablation study*	Perform ablation studies for development studies focusing on novel architectures
Model training	Cross validation*	Use cross validation for development studies; preserve data distribution across splits
	Data leakage	Avoid information leaks from test set during model training
Model testing and interpretability	Test set	Use same data and class distribution as for target population; use high-quality labels
	Target population	Explicitly define target population
	External sets	Use external sets for evaluating model sensitivity to dataset shift
	Evaluation metric	Use multiple metrics when appropriate; visually inspect model outputs
	Model interpretability*	Use interpretability methods for clinical tasks
Reporting and dissemination	Reporting	Follow published reporting guidelines and checklists
	Sharing*	Make code and models from development studies accessible
	Transparency	Be forthcoming about failure modes and population characteristics in training and evaluation sets
	Reproducibility checks	Ensure that submitted materials to journals are sufficient for replication
Evaluation†		

*Not all recommendations are applicable to all types of studies.
†Addressed in separate report from AI Task Force.

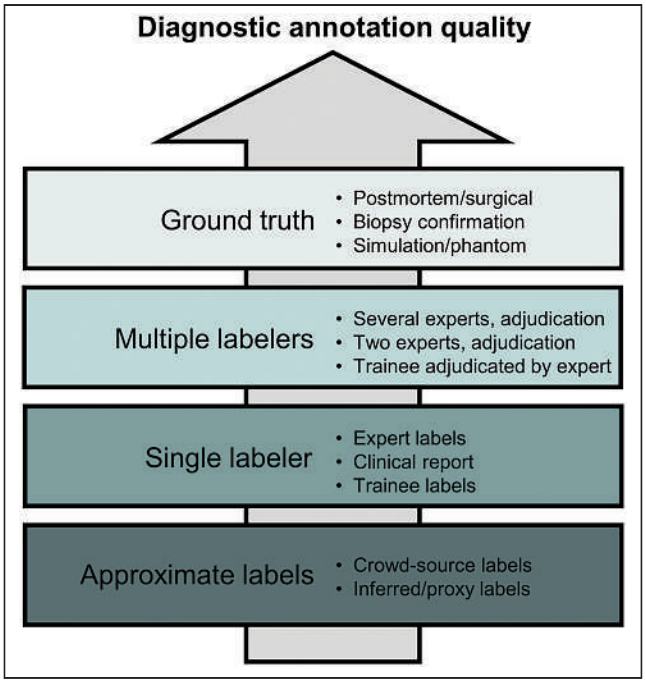

FIGURE 4. Annotation quality as function of different labeling techniques for diagnostic applications. This hierarchy does not imply how useful annotation method is (e.g., expert labels are often more useful than simulations because of limited realism of simulated data).

For development studies, journals should make publication contingent on the models and either the source codes (preferred) or executables being made accessible. Publications on development studies should contribute to the technical advancement of the field, which is often accomplished only through sharing. Many hosting resources are available for sharing, as listed in Table 3. Investigators should work with institutional review boards to ensure that datasets can be properly anonymized and openly shared. The paucity of large, high-quality multicenter datasets is a major hindrance to the clinical translation of AI tools in nuclear medicine, and open sharing of data would greatly benefit the nuclear medicine community. When data cannot be fully shared for privacy reasons, at least sample data should be made available so that the correct implementation of the model can be tested. Code should come with a modus operandi that does not leave any room for subjective settings, including a data dictionary defining variables and any preprocessing or parameter-tuning instructions.

In publishing evaluation studies, the scientific contribution is the reporting on the efficacy of a previously reported or commercial algorithm; therefore, referring to the description of the algorithm is deemed sufficient for publication.

Journal editors and reviewers are encouraged to systematically check that all provided materials are sufficient for replicating studies. This step could consist of reproducibility checklists (*35*) or dedicated data-expert reviewers, similar to statistics reviewers that are solicited for articles involving sophisticated statistical analyses. These demanding but desirable actions have been adopted in other fields and will serve to accelerate development and validation of AI algorithms.

Investigators should be forthcoming about limitations and failures of their algorithm (*36*). Failure modes should be carefully described, along with positive results. Developers should provide detailed descriptions of the characteristics and limitations of the training and evaluation datasets, such as any missing demographic groups.

Evaluation

Algorithm evaluation refers to the quantification of technical efficacy, clinical utility, biases, and postdeployment monitoring of a trained algorithm. After a successful development study, a trained algorithm should be subjected to a thorough evaluation study. Evaluation studies should involve clinical users of the algorithm and produce evidence to support specific claims about the algorithm. Clinical evaluation of a diagnostic algorithm requires reader studies, in which expert nuclear medicine physicians or radiologists assess how AI algorithms impact image interpretation or clinical decision making, often in comparison to a reference method. There are numerous additional considerations to algorithm evaluation, and a separate forthcoming report from the Society of Nuclear Medicine and Molecular Imaging AI Task Force focuses specifically on these evaluation studies and the claims that result from them.

SPECIFIC APPLICATIONS

The following subsections deal with the application of AI in the various subspecialties of nuclear medicine (Fig. 2). Each section describes how AI might be used in the different domains of nuclear medicine, together with best practices in algorithm development for each type of application and considering the different components of the development pipeline (Fig. 3).

Image Reconstruction

There is great anticipation about the benefits that AI might provide to image reconstruction, including faster reconstruction, improved signal-to-noise ratio, and fewer artifacts. AI might also contribute to different components of image reconstruction, such as direct parametric map estimation, accelerated scatter correction, and attenuation correction for PET/MRI, PET-only, and SPECT-only systems.

In general, 2 classes of approaches are being explored in nuclear medicine reconstruction: those that incorporate neural networks into current physics-based iterative reconstruction methods, and those that directly reconstruct images from projection data (*37*). Studies on the merits of end-to-end approaches versus penalty-based approaches are needed. Furthermore, for end-to-end algorithms, innovative solutions are needed to handle the large size of 3-dimensional time-of-flight sinograms, as the memory constraints of graphics processing units have limited methods to either single-slice and non–time-of-flight applications or have required sinogram rebinning (*38*). Solutions might include multi–graphics processing unit parallelization or dimensionality reduction strategies.

The large impact that AI-based reconstruction methods might have on patient care demands that algorithms be sufficiently validated. Investigators should use figures of merit to evaluate image quality, such as mean-squared error, structural similarity index, or peak signal-to-noise ratio, but should also recognize that these metrics might be misleading, as small, diagnostically important features could potentially be added or removed from images without significantly impacting summary statistics (*25*). Therefore, evaluation studies will require reader studies with clinically focused tasks (e.g., lesion detection). Models that use anatomic priors (e.g., CT) should be tested for robustness to functional–anatomic

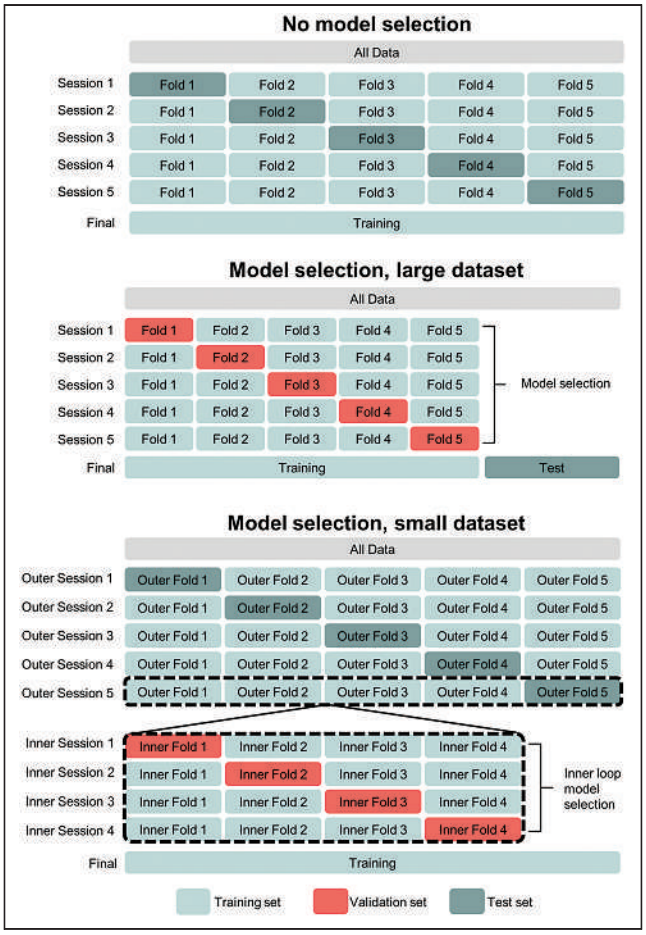

FIGURE 5. Different approaches to cross validation, depending on dataset size and whether model selection is needed. Figure illustrates 5-fold cross validation without model selection/hyperparameter tuning (top), 5-fold cross validation with holdout test set (middle), and nested cross validation (5-fold outer loop, 4-fold inner loop) (bottom).

misregistration. For development studies, computational model-observer–based studies might prove more economic in identifying promising methods (*39*).

Overall, comparative studies of different AI-based reconstruction approaches are needed, and evaluation studies should use task-oriented figures of merit and validation methods (i.e., reader studies).

Postreconstruction Image Enhancement

AI methods can enhance reconstructed nuclear medicine images with more favorable qualitative or quantitative properties, with many of the same benefits as AI-based reconstruction, including lower noise, artifact removal, and improved spatial resolution.

Denoising of low-count PET images has been the subject of numerous publications and even commercial software (*40*). Training data often consist of pairs of images reconstructed from fully sampled and subsampled list-mode data. Subsampling should span the entire length of the examination time so that motion and tracer distribution are consistent between the image pairs. Investigators should compare the performance of denoising networks with other denoising approaches, such as gaussian smoothing and more advanced methods such as nonlocal means. Contrast, feature quantification, and noise levels should be systematically evaluated.

Algorithms might be sensitive to outliers (e.g., implants) or artifacts (e.g., motion) and should always be evaluated on challenging, out-of-distribution cases. For applications that use coregistered CT or MR images as inputs, networks should be evaluated for robustness to misregistration (*41*).

Traditional figures of merit to evaluate denoising methods may be misleading (*42*). Metrics such as signal-to-noise ratio, mean squared error, and quantitative bias should be used to evaluate gains in image quality while also ensuring quantitative fidelity. However, these metrics may not reflect the presence or absence of clinically meaningful features. Also, AI can create synthetic-looking or overly smooth images. Thus, evaluation should consist of human observer or model observer studies.

In short, image enhancement algorithms should undergo sensitivity studies and reader evaluation studies, and performance should be compared with existing enhancement methods.

Image Analysis

AI is anticipated to automate several image analysis tasks in nuclear medicine, such as in oncologic imaging (e.g., lesion detection, segmentation, and quantification (*43*,*44*)), cardiac imaging (e.g., blood flow analyses), brain imaging (e.g., quantification of neurodegenerative diseases), and dosimetry, among others (*44*,*45*). Automation of these tasks has significant potential to save time, reduce interobserver variability, improve accuracy, and fully exploit the quantitative nature of molecular imaging (*46*,*47*).

AI-based segmentation algorithms should be task-specific. For instance, segmentation for radiotherapy target volume delineation requires datasets and labeling techniques different from those for segmentation for prediction of overall survival (though they are related). An algorithm might be sufficient for one metric but not another (*43*). Images from other modalities, such as CT and MRI, that provide complementary high-resolution information can also be considered as inputs to an algorithm if expected to be available clinically.

Segmentation algorithms are typically trained using expert-generated contours. To ensure appropriate and consistent labeling (Fig. 4), clear annotation instructions should be distributed to qualified labelers to guide them on viewing settings, on handling functional-anatomic misregistration, and other conditions that might affect segmentation. Expert contours will inevitably have interobserver variability, which should be measured and used as a point of comparison for automated methods. Various methods exist for creating consensus contours from multiple observers (e.g., simultaneous truth and performance-level estimation algorithm (*48*)). Investigators should also be aware of the various objective functions and evaluation metrics for segmentation and of the existing guidelines for validation and reporting of autosegmentation methods (*49*). Because of the sparsity of large, high-quality labeled datasets in nuclear medicine, phantom or realistic simulation data can also be used for model pretraining (*47*,*50*).

Overall, the development of AI segmentation algorithms should include meticulous, task-specific labeling practices, and published guidelines for validating and reporting of algorithms should be followed.

AI and Radiomics as a Discovery Tool

AI is expected to play a critical role in assisting physicians and scientists in discovering patterns within large biologic and imaging datasets that are associated with patient outcome. Modern ML methods have shown promise as useful tools to uncover hidden

TABLE 3
Resources for Hosting and Sharing Code, Models, and Data

Data type	Resources
Code	Git repository hosts (GitHub, GitLab, Bitbucket [Atlassian]), Matlab File Exchange (MathWorks), SourceForge
Models, containers, executables	Docker Hub (Docker Inc.), modelhub.ai, Model Zoo, Gradio, TensorFlow Hub, PyTorch Hub, Hugging Face
Data	The Cancer Imaging Archive, Kaggle Inc., paperswithcodes.com, LONI Image and Data Archive, Figshare (Figshare)

but meaningful relationships within datasets (*51*). AI is therefore a useful adjunct to radiomics.

First, ML can be used to identify deep radiomic features whose definitions depend completely on the data and on the task, unlike handcrafted radiomic features that are mathematically predefined whatever the data. Second, ML is an effective way to mine large numbers of radiomic features, possibly augmented by other omics or clinical data, to identify associations, reduce redundancy, produce tractable representations in low-dimension spaces, or design prediction models. Unsupervised ML might be used to combine correlated input features into a smaller, more tractable set of factors (*52*) or to select features relevant to a task. Redundancy in features can arise from technical causes (e.g., mathematic equivalence of radiomics features), from measurement of the same underlying biologic factor, or from a biologic causal relationship (some biologic factor influences multiple feature values). By distinguishing among these 3 situations, investigators can better approach dimensionality reduction (*53*). For example, mathematic equivalence of radiomics features can be detected by randomly perturbing the image and assessing which correlations persist through the perturbations (*54*).

The challenge of discovering predictive signatures in high-dimension datasets might necessitate a multistep approach. Investigators might first start with a selection of cases that represent both ends of the label's range of values, such as short and long survival, to maximize the chances of detecting features associated with outcome but at the cost of low specificity.

After initial discovery, whatever features or relationships have been identified must be rigorously evaluated and scrutinized. Investigators must explore the relationships across the entire dataset using cross validation, aim to understand the underlying cause, and then externally validate these findings, ruling out false-positives or spurious correlations. For example, they can repeat the whole AI-analysis pipeline on sham data (e.g., randomized labels) to determine the baseline false-positive rate for their set of methods and then compare it with the discovery rate found in the real dataset. Investigators should also test different models and architecture to see whether the discovered relationships hold, as it is unlikely that a real association will be identified by only 1 model.

In short, radiomics analysis should include the removal of redundant features, and a multistep approach of discovery (high sensitivity, low specificity) followed by rigorous validation might be considered.

Detection and Diagnosis

Computer-aided diagnosis and detection have long histories of successes and failures in radiology, but the recent advancements in AI have made widespread use of computer-aided diagnosis and computer-aided detection an approaching reality for nuclear medicine. Automation of diagnostic tasks in nuclear medicine can be challenging, as diagnostic tasks are subjective, have high stakes, and must be incredibly robust to rare cases (e.g., implants or amputations). However, the incentive to develop such tools is strong, with applications including assisted reads (*55*), tumor detection suggestions, neuro or cardiac diagnosis tools (*56*), training programs for residents, and many others.

Investigators should select an appropriate labeling technique according to the accuracy that is needed for their computer-aided diagnosis or computer-aided detection application (Fig. 4). Labels from specialists are superior to those from trainees or generalists, and labels resulting from multiple readers (adjudication or consensus) are superior to those from single readers. Labels extracted from clinical reports are considered inferior to those obtained from dedicated research readings (*57*). Intraobserver and interobserver variability in labels is often an indicator of label quality and should be quantified and reported.

Investigators are encouraged to integrate model interpretability (e.g., Shapley additive explanations) and uncertainty signaling (e.g., Bayesian approximation) into their algorithm. Because diagnostic algorithms will be used under the supervision of a physician, algorithm decisions should ideally be explainable so that clinicians have sufficient information to contest or provide feedback when algorithms fail. Developers also need to be transparent about their algorithm development and evaluation processes, including data sources and training set population characteristics, such as by using reporting checklists such as MI-CLAIM (*29*). The high visibility and public attention that AI-based diagnostic algorithms receive demands that developers make every effort to be fully transparent.

In short, for computer-aided detection and computer-aided diagnosis algorithms, label quality should be justified by the application (high quality for high-risk applications) and algorithms should be interpretable and fully transparent.

Enhanced Reporting and Imaging Informatics

ML has the potential to transform how the information within diagnostic images is translated into reports and clinical databases. AI can be used to prepopulate radiology reports, assist in real-time report generation, help standardize reporting, and perform structured synoptic reporting (*58*).

Algorithm development in medical imaging informatics has several unique considerations. A critical challenge is the large heterogeneity in diagnostic reporting standards and practices across institutions, individual physicians, and examination types. Heterogeneity in language can be more challenging for automation than is heterogeneity in medical images. Therefore, training data should be collected from diverse sources and annotators, and studies are

expected to require much larger sample sizes than for other applications. Tasks in this domain might be uniquely suitable to unsupervised or semisupervised approaches because of the large volume of unlabeled data available in clinical PACS systems. Various model types will likely be applied in this domain, but language models may need to be adapted to consider the unique nuclear medicine vocabulary that might not be represented in typical medical text corpora (e.g., the term *SUV*). Because of challenges in deidentification of radiology reports (*59*), federated learning should be considered to enable privacy-protected multiinstitutional studies. Reporting of model performance should be disaggregated according to data source, originating institution, and annotator.

Clinical Intelligence and Decision Support

Clinical intelligence and decision support are concerned with delivering actionable advice to clinicians after extracting, distilling, and consolidating clinical information across multiple data sources. These systems are expected to pull the most pertinent information generated by a nuclear medicine examination and combine it with other clinical data to best guide patient care. For example, ML can predict future myocardial infarction using PET features combined with other clinical variables (*60*). The development and validation of clinical decision support systems should be guided by physician needs and clinical experts, involving teams from nearly all sectors of health care.

An algorithm's ability to explain its decisions is key to safe, ethical, fair, and trustworthy use of AI for decision support, calling for the same recommendations as discussed in the section on detection and diagnosis. An AI model should ideally be able to provide an estimate of uncertainty together with its output, possibly by using Bayesian methods, and be willing to provide a no-decision answer when the model uncertainties are too large to make the output meaningful.

Instrumentation and Image Acquisition

Challenging problems in data acquisition and instrumentation could be well suited to ML-based solutions (*61*). For example, ML has been used to estimate 2- and 3-dimensional position of interaction for detectors (*62*). Other promising applications include timing pickoff for detector waveforms, intercrystal scatter estimation, patient motion detection, and the prediction of scanner failure from quality control tracking.

Precise data collection is critical to the success of AI applications within instrumentation. Simulations should be performed using appropriate models that incorporate geometric, physical, and statistical factors underlying image generation. Investigators should consider possible discrepancies between in silico and physical domains and are encouraged to conduct cross-validation studies when possible (*61*). Physical measurements, such as point source measurements, may require high-precision motion stages and lengthy acquisition studies to collect the full range of training data. Scanner quality control applications will likely require enterprise-level tracking to obtain sufficient data on failure patterns.

Algorithms that process events in real time and need to be implemented on front-end electronics will likely be memory- and operation-limited (*63*), favoring simpler model architectures. Ablation analysis can help identify more parsimonious models.

Radiopharmaceuticals and Radiochemistry

The potential for AI to challenge the current paradigms in synthesis (*64*) and administration (*65*) of radiopharmaceuticals is only beginning to be explored. Potential applications include predicting drug–target interactions (*66*), predicting and optimizing radiochemical reactions, and performing de novo design of drugs (*67*), as well as helping optimize radiopharmacy workflows. Proper integration of AI within the radiochemistry and radiopharmacy communities will require collaborations between key stakeholders, including industry, end users, and quality control personnel, as well as experts in information technology, cybersecurity, and regulatory aspects. It is strongly recommended that groups share manufacturing data freely, as this will accelerate innovation by providing large test sets for ML that cannot be sufficiently generated at individual labs (e.g., synthesis module and cyclotron log files).

DISCUSSION AND CONCLUSION

The recommendations listed in this article and summarized in Table 2 are intended to assist developers and users in understanding the requirements and challenges associated with the design and use of AI-based algorithms. They focus on specificities associated with nuclear medicine applications, whereas best practices for software development, data management, security, privacy, ethics, and regulatory considerations are largely covered elsewhere. It is also acknowledged that some standards of today are likely to be superseded by new standards as technologies continue to evolve. These recommendations should serve as a guide to developers and investigators at a time when AI is booming but should not be assumed to be comprehensive or unchanging.

These recommendations were drawn from various sources, including the authors' collective experiences in academia and industry, as well as other published position papers, and put into the context of nuclear medicine applications. They should be considered an add-on to other guidelines, including forthcoming guidelines from regulatory bodies (*68*) and relevant working groups (*69*).

AI is expected to influence and shape the future of nuclear medicine and many other fields. But the potential pitfalls of AI warrant a careful and methodic approach to AI algorithm development and adoption. Standards and guidelines can help nuclear medicine avoid the mismatch between the role that AI is expected to play and what it will actually deliver.

DISCLOSURE

Tyler Bradshaw receives research support from GE Healthcare. Ronald Boellaard is a scientific advisor (unpaid) for the EARL PET/CT accreditation program. Paul Jacobs is a full-time employee of MIM Software Inc. Sven Zuehlsdorff is a full-time employee of Siemens Medical Solutions USA, Inc. Piotr Slomka has a research grant from Siemens Medical Solutions, is a consultant for IBA, and receives royalties from Cedars-Sinai for nuclear cardiology software. No other potential conflict of interest relevant to this article was reported.

ACKNOWLEDGMENTS

The members of the AI Task Force acknowledge Bonnie Clarke for her excellent support of this project.

REFERENCES

1. Roberts M, Driggs D, Thorpe M, et al. Common pitfalls and recommendations for using machine learning to detect and prognosticate for COVID-19 using chest radiographs and CT scans. *Nat Mach Intell.* 2021;3:199–217.
2. Haibe-Kains B, Adam GA, Hosny A, et al. Transparency and reproducibility in artificial intelligence. *Nature.* 2020;586:E14–E16.
3. Zech JR, Badgeley MA, Liu M, Costa AB, Titano JJ, Oermann EK. Variable generalization performance of a deep learning model to detect pneumonia in chest radiographs: a cross-sectional study. *PLoS Med.* 2018;15:e1002683.
4. Buvat I, Orlhac F. The T.R.U.E. checklist for identifying impactful artificial intelligence-based findings in nuclear medicine: is it True? Is it Reproducible? Is it Useful? Is it Explainable? *J Nucl Med.* 2021;62:752–754.
5. Xue Y, Xu T, Zhang H, Long LR, Huang X. Segan: adversarial network with multi-scale L_1 loss for medical image segmentation. *Neuroinformatics.* 2018;16:383–392.
6. Vallières M, Kay-Rivest E, Perrin LJ, et al. Radiomics strategies for risk assessment of tumour failure in head-and-neck cancer. *Sci Rep.* 2017;7:10117.
7. Andrearczyk V, Oreiller V, Jreige M, et al. Overview of the HECKTOR challenge at MICCAI 2020: automatic head and neck tumor segmentation in PET/CT. In: *Lecture Notes in Computer Science*. Springer; 2020:1–21.
8. Center for Devices and Radiological Health. Software as a medical device (SAMD): clinical evaluation—guidance for industry and Food and Drug Administration staff. Food and Drug Administration website. https://www.fda.gov/media/100714/download. Published December 8, 2017. Accessed December 13, 2021.
9. Nosek BA, Ebersole CR, DeHaven AC, Mellor DT. The preregistration revolution. *Proc Natl Acad Sci USA.* 2018;115:2600–2606.
10. Dirand A-S, Frouin F, Buvat I. A downsampling strategy to assess the predictive value of radiomic features. *Sci Rep.* 2019;9:17869.
11. Riley RD, Ensor J, Snell KIE, et al. Calculating the sample size required for developing a clinical prediction model. *BMJ.* 2020;368:m441.
12. Smith SM, Nichols TE. Statistical challenges in "big data" human neuroimaging. *Neuron.* 2018;97:263–268.
13. Hwang D, Kim KY, Kang SK, et al. Improving the accuracy of simultaneously reconstructed activity and attenuation maps using deep learning. *J Nucl Med.* 2018;59:1624–1629.
14. Raghu M, Zhang C, Kleinberg J, Bengio S. Transfusion: understanding transfer learning for medical imaging. arXiv.org website. https://arxiv.org/abs/1902.07208. Published February 14, 2019. Revised October 29, 2019. Accessed December 13, 2021.
15. Gulshan V, Peng L, Coram M, et al. Development and validation of a deep learning algorithm for detection of diabetic retinopathy in retinal fundus photographs. *JAMA.* 2016;316:2402–2410.
16. Krause J, Gulshan V, Rahimy E, et al. Grader variability and the importance of reference standards for evaluating machine learning models for diabetic retinopathy. *Ophthalmology.* 2018;125:1264–1272.
17. Cheplygina V, de Bruijne M, Pluim JPW. Not-so-supervised: a survey of semi-supervised, multi-instance, and transfer learning in medical image analysis. *Med Image Anal.* 2019;54:280–296.
18. Zhu J, Li Y, Hu Y, Ma K, Zhou SK, Zheng Y. Rubik's Cube+: a self-supervised feature learning framework for 3D medical image analysis. *Med Image Anal.* 2020;64:101746.
19. Home page. Papers with Code website. https://paperswithcode.com/datasets. Accessed December 13, 2021.
20. Christodoulou E, Ma J, Collins GS, Steyerberg EW, Verbakel JY, Van Calster B. A systematic review shows no performance benefit of machine learning over logistic regression for clinical prediction models. *J Clin Epidemiol.* 2019;110:12–22.
21. Zhao K, Zhou L, Gao S, et al. Study of low-dose PET image recovery using supervised learning with CycleGAN. *PLoS One.* 2020;15:e0238455.
22. Raschka S. Model evaluation, model selection, and algorithm selection in machine learning. arXiv.org website. https://arxiv.org/abs/1811.12808. Published November 13, 2018. Revised November 11, 2020. Accessed December 13, 2021.
23. Arlot S, Celisse A. A survey of cross-validation procedures for model selection. *Stat Surv.* 2010;4:40–79.
24. Li T, Sahu AK, Talwalkar A, Smith V. Federated learning: challenges, methods, and future directions. *IEEE Signal Process Mag.* 2020;37:50–60.
25. Yang J, Sohn JH, Behr SC, Gullberg GT, Seo Y. CT-less direct correction of attenuation and scatter in the image space using deep learning for whole-body FDG PET: potential benefits and pitfalls. *Radiol Artif Intell.* 2020;3:e200137.
26. Huff DT, Weisman AJ, Jeraj R. Interpretation and visualization techniques for deep learning models in medical imaging. *Phys Med Biol.* 2021;66:04TR01.
27. Cruz Rivera S, Liu X, Chan A-W, Denniston AK, Calvert MJ; SPIRIT-AI and CONSORT-AI Working Group. Guidelines for clinical trial protocols for interventions involving artificial intelligence: the SPIRIT-AI extension. *Lancet Digit Health.* 2020;2:e549–e560.
28. Liu X, Cruz Rivera S, Moher D, Calvert MJ, Denniston AK, SPIRIT-AI and CONSORT-AI Working Group. Reporting guidelines for clinical trial reports for interventions involving artificial intelligence: the CONSORT-AI extension. *Nat Med.* 2020;26:1364–1374.
29. Norgeot B, Quer G, Beaulieu-Jones BK, et al. Minimum information about clinical artificial intelligence modeling: the MI-CLAIM checklist. *Nat Med.* 2020;26:1320–1324.
30. Sengupta PP, Shrestha S, Berthon B, et al. Proposed requirements for cardiovascular imaging-related machine learning evaluation (PRIME): a checklist. *JACC Cardiovasc Imaging.* 2020;13:2017–2035.
31. Hernandez-Boussard T, Bozkurt S, Ioannidis JPA, Shah NH. MINIMAR (MINimum Information for Medical AI Reporting): developing reporting standards for artificial intelligence in health care. *J Am Med Inform Assoc.* 2020;27:2011–2015.
32. Sounderajah V, Ashrafian H, Aggarwal R, et al. Developing specific reporting guidelines for diagnostic accuracy studies assessing AI interventions: the STARD-AI Steering Group. *Nat Med.* 2020;26:807–808.
33. Collins GS, Moons KGM. Reporting of artificial intelligence prediction models. *Lancet.* 2019;393:1577–1579.
34. DECIDE-AI Steering Group. DECIDE-AI: new reporting guidelines to bridge the development-to-implementation gap in clinical artificial intelligence. *Nat Med.* 2021;27:186–187.
35. Pineau J, Vincent-Lamarre P, Sinha K, et al. Improving reproducibility in machine learning research (a report from the NeurIPS 2019 Reproducibility Program). arXiv.org website. https://arxiv.org/abs/2003.12206. Published March 27, 2020. Revised December 30, 2020. Accessed December 13, 2021.
36. Reuzé S, Orlhac F, Chargari C, et al. Prediction of cervical cancer recurrence using textural features extracted from ^{18}F-FDG PET images acquired with different scanners. *Oncotarget.* 2017;8:43169–43179.
37. Reader AJ, Corda G, Mehranian AD, Costa-Luis C, Ellis S, Schnabel JA. Deep learning for PET image reconstruction. *IEEE Trans Radiat Plasma Med Sci.* 2021;5:1–25.
38. Whiteley W, Luk WK, Gregor J. DirectPET: full-size neural network PET reconstruction from sinogram data. *J Med Imaging (Bellingham).* 2020;7:032503.
39. Yu Z, Rahman MA, Schindler T, Laforest R, Jha AK. A physics and learning-based transmission-less attenuation compensation method for SPECT. In: *Proceedings of SPIE, Medical Imaging 2021: Physics of Medical Imaging*. SPIE; 2021:1159512.
40. Katsari K, Penna D, Arena V, et al. Artificial intelligence for reduced dose ^{18}F-FDG PET examinations: a real-world deployment through a standardized framework and business case assessment. *EJNMMI Phys.* 2021;8:25.
41. Lu W, Onofrey JA, Lu Y, et al. An investigation of quantitative accuracy for deep learning based denoising in oncological PET. *Phys Med Biol.* 2019;64:165019.
42. Yu Z, Rahman MA, Schindler T, et al. AI-based methods for nuclear-medicine imaging: need for objective task-specific evaluation [abstract]. *J Nucl Med.* 2020;61(suppl 1):575.
43. Weisman AJ, Kim J, Lee I, et al. Automated quantification of baseline imaging PET metrics on FDG PET/CT images of pediatric Hodgkin lymphoma patients. *EJNMMI Phys.* 2020;7:76.
44. Capobianco N, Meignan M, Cottereau A-S, et al. Deep-learning ^{18}F-FDG uptake classification enables total metabolic tumor volume estimation in diffuse large B-cell lymphoma. *J Nucl Med.* 2021;62:30–36.
45. Weisman AJ, Kieler MW, Perlman SB, et al. Convolutional neural networks for automated PET/CT detection of diseased lymph node burden in patients with lymphoma. *Radiol Artif Intell.* 2020;2:e200016.
46. Weisman AJ, Kieler MW, Perlman S, et al. Comparison of 11 automated PET segmentation methods in lymphoma. *Phys Med Biol.* 2020;65:235019.
47. Leung KH, Marashdeh W, Wray R, et al. A physics-guided modular deep-learning based automated framework for tumor segmentation in PET. *Phys Med Biol.* 2020;65:245032.
48. Warfield SK, Zou KH, Wells WM. Simultaneous truth and performance level estimation (STAPLE): an algorithm for the validation of image segmentation. *IEEE Trans Med Imaging.* 2004;23:903–921.
49. Hatt M, Lee JA, Schmidtlein CR, et al. Classification and evaluation strategies of auto-segmentation approaches for PET: report of AAPM task group no. 211. *Med Phys.* 2017;44:e1–e42.
50. Liu Z, Laforest R, Mhlanga J, et al. Observer study-based evaluation of a stochastic and physics-based method to generate oncological PET images. *Proceedings of SPIE, Medical Imaging 2021: Image Perception, Observer Performance, and Technology Assessment*. SPIE; 2021:1159905.
51. Pierson E, Cutler DM, Leskovec J, Mullainathan S, Obermeyer Z. An algorithmic approach to reducing unexplained pain disparities in underserved populations. *Nat Med.* 2021;27:136–140.
52. Peeters CFW, Übelhör C, Mes SW, et al. Stable prediction with radiomics data. arXiv.org website. https://arxiv.org/abs/1903.11696. Published March 27, 2019. Accessed December 13, 2021.

53. Pfaehler E, Mesotten L, Zhovannik I, et al. Plausibility and redundancy analysis to select FDG-PET textural features in non-small cell lung cancer. *Med Phys.* 2021; 48:1226–1238.
54. Welch ML, McIntosh C, Haibe-Kains B, et al. Vulnerabilities of radiomic signature development: the need for safeguards. *Radiother Oncol.* 2019;130:2–9.
55. Li Z, Kitajima K, Hirata K, et al. Preliminary study of AI-assisted diagnosis using FDG-PET/CT for axillary lymph node metastasis in patients with breast cancer. *EJNMMI Res.* 2021;11:10.
56. Betancur J, Hu L-H, Commandeur F, et al. Deep learning analysis of upright-supine high-efficiency SPECT myocardial perfusion imaging for prediction of obstructive coronary artery disease: a multicenter study. *J Nucl Med.* 2019;60:664–670.
57. Bluemke DA, Moy L, Bredella MA, et al. Assessing radiology research on artificial intelligence: a brief guide for authors, reviewers, and readers—from the Radiology editorial board. *Radiology.* 2020;294:487–489.
58. Panayides AS, Amini A, Filipovic ND, et al. AI in medical imaging informatics: current challenges and future directions. *IEEE J Biomed Health Inform.* 2020;24: 1837–1857.
59. Steinkamp JM, Pomeranz T, Adleberg J, Kahn CE, Cook TS. Evaluation of automated public de-identification tools on a corpus of radiology reports. *Radiol Artif Intell.* 2020;2:e190137.
60. Kwiecinski J, Tzolos E, Meah M, et al. Machine-learning with ^{18}F-sodium fluoride PET and quantitative plaque analysis on CT angiography for the future risk of myocardial infarction. *J Nucl Med.* April 23, 2021 [Epub ahead of print].
61. Arabi H, Zaidi H. Applications of artificial intelligence and deep learning in molecular imaging and radiotherapy. *Eur J Hybrid Imaging.* 2020;4:17–23.
62. Gong K, Berg E, Cherry SR, Qi J. Machine learning in PET: from photon detection to quantitative image reconstruction. *Proc IEEE.* 2020;108:51–68.
63. Müller F, Schug D, Hallen P, Grahe J, Schulz V. A novel DOI positioning algorithm for monolithic scintillator crystals in PET based on gradient tree boosting. *IEEE Trans Radiat Plasma Med Sci.* 2019;3:465–474.
64. de Almeida AF, Moreira R, Rodrigues T. Synthetic organic chemistry driven by artificial intelligence. *Nat Rev Chem.* 2019;3:589–604.
65. Nelson SD, Walsh CG, Olsen CA, et al. Demystifying artificial intelligence in pharmacy. *Am J Health Syst Pharm.* 2020;77:1556–1570.
66. Wen M, Zhang Z, Niu S, et al. Deep-learning-based drug-target interaction prediction. *J Proteome Res.* 2017;16:1401–1409.
67. Ståhl N, Falkman G, Karlsson A, Mathiason G, Boström J. Deep reinforcement learning for multiparameter optimization in de novo drug design. *J Chem Inf Model.* 2019;59:3166–3176.
68. Proposed regulatory framework for modifications to artificial intelligence/machine learning (AI/ML)-based software as a medical device (SaMD): discussion paper and request for feedback. U.S. Food and Drug Administration website. https://beta.regulations.gov/document/FDA-2019-N-1185-0001. Published April 2, 2019. Accessed December 13, 2021.
69. IEEE artificial intelligence medical device working group. IEEE Standards Association website. https://sagroups.ieee.org/aimdwg/. Accessed December 13, 2021.

Virtual Biopsy: Just an AI Software or a Medical Procedure?

Jacob M. Murray[1], Bodo Wiegand[2], Boris Hadaschik[3,4], Ken Herrmann[4–6], and Jens Kleesiek[1,4,5,7]

[1]Institute for AI in Medicine, University Hospital Essen, Essen, Germany; [2]Philips, Eindhoven, The Netherlands; [3]Department of Urology, University Hospital Essen, Essen, Germany; [4]German Cancer Consortium, University Hospital Essen, Essen, Germany; [5]West German Cancer Center Essen, Essen, Germany; [6]Department of Nuclear Medicine, University of Duisburg–Essen, Duisburg, Germany; and [7]Cancer Research Center Cologne Essen, Essen, Germany

The term *virtual biopsy* is gaining traction. Since 2015, the number of publications referencing the concept in the search engine PubMed has doubled, and in 2021 it reached its highest level yet. This raises the question of what the unique characteristics of a virtual biopsy are and how it might be distinguished from other advances in computer-assisted medicine. For optimists, it may be the next step toward a less invasive, more personalized era in medicine that harnesses recent advances in functional imaging and artificial intelligence (AI) to generate patient management decisions. For skeptics, the term may ring hollow, like yet another marketing phrase within the hype surrounding AI in the medical field. Ultimately, the juxtaposition of *virtual* and *biopsy* contains within it not merely the possibility of adding another tool to the physician's toolbox but the aspiration that the biopsy, a crucial procedure in the diagnosis of disease, may be transformed from physical to virtual while still providing diagnostic and prognostic information at least at the level of a traditional, physical biopsy, serving as reference standard. We assess the current state of this aspiration and conclude that although hurdles remain, the virtual biopsy is poised to replace the physical biopsy as a central step in the diagnosis and management of certain diseases.

Its origin from the Greek words *bios* for life and *opsis* for sight illustrates that a biopsy makes information that is relevant to biologic existence available for insight. This has traditionally occurred via the direct visual examination of invasively retrieved tissue specimens by a pathologist under a microscope. However, the term *virtual biopsy*—in analogy to the more commonly encountered liquid biopsy—suggests that what is relevant is not the type of specimen or direct visual appreciability but the usefulness and accuracy of the biologic insight that can be gleaned from the biopsy procedure. Interestingly, the term *virtual,* as describing something simulated, might be considered a misnomer here, since the radiologic images that serve as the inputs of a virtual biopsy reflect physical realities in the same way histology slides might. We stipulate that the validity of a virtual biopsy as a form of biopsy procedure, and as opposed to a piece of software, is determined by the quality and completeness of the medically relevant information it can deliver, even in excess of the imperfect physical biopsy reference standard. In particular, whereas the image resolution available in microscope-based analysis of physical biopsy samples will not be available in virtual biopsies, the volume of imaged tissue is larger, that is, the complete tumor manifestation of *primarius* and its *filiae* in a full-body PET exam. This may allow for a different, potentially more complete molecular phenotype characterization of disease—for example, addressing the topic of tumor heterogeneity. There is also hope that using advanced AI techniques, previously unavailable information can be extracted. For example, there are super-resolution approaches to enhancing resolution. But there are also efforts that attempt to see beyond—that is, to extract new information by identifying nonlinear relationships and to make it available to humans. This, although not yet a reality, could then allow for inference of genetic traits from phenotype. Furthermore, the validity of a virtual biopsy will depend on whether the provided information is accepted as a foundation of medical management by the various stakeholders, such as patients, physicians, insurance companies, and regulatory bodies. The acceptance of virtual biopsies by insurance companies and regulatory bodies will then also determine the status of virtual biopsies as procedures in the context of billability and health economics.

Currently, virtual biopsies are explored primarily within the research setting. Multiple areas of application in oncology are emerging. Morawitz et al. assessed the ability of 4 different imaging modalities in determining axillary lymph node status in women diagnosed with breast cancer. Comparing the imaging modalities with histopathology as a reference standard, they concluded that if both ^{18}F-FDG PET/MRI and sonography are positive, "one might consider dispensing with axillary histopathologic sampling" (*1*). Although the term *virtual biopsy* is not explicitly mentioned, the raised possibility of foregoing physical biopsy places the work within this context. For ovarian cancers, an entity with broadly intractable survival rates, Martin-Gonzalez et al. proposed a combination of quantitative imaging features and genomics markers to monitor therapy and improve patient management (*2*). For lung cancer, which remains the leading cause of cancer-related mortality, the introduction of targeted and immunotherapies has dramatically altered the treatment landscape and survival rates. Consequently, the identification of targetable mutations and expression levels has become a crucial step in patient management and constitutes a further reason, apart from determining the histologic cancer subtype, for performing a physical tissue biopsy. In this context, Wen et al. linked non–small cell lung cancer radiomics features and clinical markers to estimate expression levels of immunotherapy target proteins and to potentially inform patient management decisions without

Received Dec. 23, 2021; revision accepted Jan. 14, 2022.
For correspondence or reprints, contact Jens Kleesiek (jens.kleesiek@uk-essen.de).
Published online Feb. 10, 2022.
COPYRIGHT © 2022 by the Society of Nuclear Medicine and Molecular Imaging.
DOI: 10.2967/jnumed.121.263749

the need for physical biopsy (*3*). Taken together, this work highlights that virtual biopsies are being investigated for some of the most prevalent oncologic entities. Prostate cancer, too, belongs to this group.

The diagnostic algorithm for prostate cancer is changing to accommodate a more pronounced role of imaging in decisions surrounding physical biopsy. Prostate cancer is the most common solid cancer in men but presents with various forms of aggressiveness, and overdiagnosis of indolent disease causes more harm than benefit. As with other oncologic entities, a common aim of research that falls within the realm of virtual biopsy is to establish a robust link between radiologic imaging features and histopathology in terms of the presence or absence of clinically significant prostate cancer. In this context, Eklund et al. showed that the addition of MRI-targeted biopsy allows omission of a significant number of biopsies and reduces the detection of insignificant prostate cancer in performed biopsies in men undergoing prostate cancer screening (*4*). By combining multiparametric MRI with prostate-specific membrane antigen PET/CT imaging, the need for physical biopsy in patient management might disappear altogether. Emmett et al. investigated 291 patients for whom MRI, pelvic prostate-specific membrane antigen PET, and systematic or targeted transperineal biopsy were performed and concluded that on the basis of the high detection rate of clinically significant prostate cancer and the high negative predictive value, "further randomised studies will determine whether biopsy can safely be omitted in men with high clinical suspicion of [clinically significant prostate cancer] but negative combined imaging"(*5*). This conclusion is underscored further by a recent retrospective case series published by Meissner et al. including 25 patients who underwent radical prostatectomy without prior biopsy, based solely on MRI and prostate-specific membrane antigen PET results. All 25 patients showed clinically significant prostate cancer in the postsurgical histopathology examination (*6*). These results lay the scientific foundation for clinical trials examining virtual biopsies to change the diagnostic pathways in prostate cancer care. However, despite increased scientific exploration of topics that fall within the scope of virtual biopsies, few discoveries have so far bridged the divide between academia and industry.

Current Food and Drug Administration–cleared software tools are focused largely on providing decision support and decision automation within a diagnostic framework that continues to rely on physical biopsy.

On the one end of the diagnostic cascade, for instance, there are Food and Drug Administration–cleared solutions that aim to optimize the prostate MRI workflow through custom AI-augmented software before the extraction of a physical biopsy, such as Quantib (https://www.quantib.com/). On the other end of the cascade, there are Food and Drug Administration–approved AI tools to detect prostate cancer after the biopsy has been performed and the tissue sample is available for analysis, such as Paige (https://www.paige.ai/). In both cases, the software can be understood as a diagnostic tool or decision support system. They do not, however, directly replace the physical biopsy itself. Instead, they might indirectly influence management by providing evidence that a physical biopsy can safely be avoided. A medical procedure in the context of a virtual biopsy would refer to a software tool that provides a diagnosis of a histologic type without the need to perform an invasive biopsy. Whether this becomes possible depends on the density and extractability of the information that serves as input to these software tools. If imaging and clinical data were to contain a sufficient level of information that can effectively be used by machine learning techniques to accurately classify disease, then patient management without the need for a physical biopsy could become a reality. Because a virtual biopsy is not restricted to the actual target of a physical biopsy, patient management might even be improved in the future.

Defining and attaining the required level and reliability of information that is accessible through virtual biopsy to obtain stakeholder acceptance remain the central hurdle on the path toward virtual biopsies. As Penzkofer et al. pointed out, "a change in indication from a 'radiological diagnosis support tool' to 'clinical decision-making tool' would need to undergo rigorous testing against clinically valid endpoints, such as the presence of clinically significant lesions in positive and negative cases" (*7*). This implies that what is ultimately required are large-scale prospective randomized controlled trials providing evidence that virtual biopsies can serve as substitutes for real biopsies. In addition, assessments of health-economic effects (in terms of potential cost reductions) and of quality-of-life changes (in terms of avoidance of complications associated with a physical biopsy) that will result from switching to virtual biopsies are needed. Then, stakeholders, such as patients, individual physicians, and guideline-issuing professional societies, as well as regulatory bodies, might begin to adopt virtual biopsies as medical procedures with management-determining results.

The final component that will determine the future of virtual biopsies is acceptance by payers and the availability of a billing code for reimbursement. Health-care systems are nearing their breaking point, which has prompted regulators and budget holders to look critically at how medical devices and solutions benefit patients. Value-based health care becomes more and more important, whereby reimbursement is based on patient health outcomes instead of the volume of services provided by health-care professionals. Additionally, health technology assessment bodies are developing strategies to evaluate the new digital technologies entering the market. A case in point is the United Kingdom, where evidence of clinical effectiveness and economic value must be generated in accordance with the Evidence Standards Framework for Digital Health Technologies (*8*) outlined by the National Institute for Health and Care Excellence. Digital health-care technologies are becoming increasingly popular in other markets as well, and budget holders, payers, and providers are beginning to see their importance. As an example, the law on prescription and reimbursement of digital health technologies in Germany governs how statutory health insurances compensate digital health applications. Still, manufacturers must demonstrate to the Federal Institute for Drugs and Medical Devices that their solutions lead to positive health outcomes. The new law improves the legal status of digital health apps, which are considered low-risk medical devices. The future of high-risk health applications remains open. To establish virtual biopsies as medical procedures, in-depth consideration of their role within the low-risk to high-risk medical device spectrum will be necessary.

In conclusion, virtual biopsies are at the center of a flourishing and growing research effort. But the ascent of virtual biopsies is not limited to academia. Despite regulatory and reimbursement challenges that remain, virtual biopsies present the logical next step in patient care and thus resemble a very likely future development for the diagnosis and management of certain diseases.

DISCLOSURE

No potential conflict of interest relevant to this article was reported.

REFERENCES

1. Morawitz J, Bruckmann N-M, Dietzel F, et al. Determining the axillary nodal status with 4 current imaging modalities, including ^{18}F-FDG PET/MRI, in newly diagnosed breast cancer: a comparative study using histopathology as the reference standard. *J Nucl Med.* 2021;62:1677–1683.
2. Martin-Gonzalez P, Crispin-Ortuzar M, Rundo L, et al. Integrative radiogenomics for virtual biopsy and treatment monitoring in ovarian cancer. *Insights Imaging.* 2020;11:94.
3. Wen Q, Yang Z, Dai H, Feng A, Li Q. Radiomics study for predicting the expression of PD-L1 and tumor mutation burden in non-small cell lung cancer based on CT images and clinicopathological features. *Front Oncol.* 2021;11:620246.
4. Eklund M, Jäderling F, Discacciati A, et al. MRI-targeted or standard biopsy in prostate cancer screening. *N Engl J Med.* 2021;385:908–920.
5. Emmett L, Buteau J, Papa N, et al. The additive diagnostic value of prostate-specific membrane antigen positron emission tomography computed tomography to multiparametric magnetic resonance imaging triage in the diagnosis of prostate cancer (PRIMARY): a prospective multicentre study. *Eur Urol.* 2021;80:682–689.
6. Meissner VH, Rauscher I, Schwamborn K, et al. Radical prostatectomy without prior biopsy following multiparametric magnetic resonance imaging and prostate-specific membrane antigen positron emission tomography. *Eur Urol.* December 6, 2021 [Epub ahead of print].
7. Penzkofer T, Padhani AR, Turkbey B, et al. ESUR/ESUI position paper: developing artificial intelligence for precision diagnosis of prostate cancer using magnetic resonance imaging. *Eur Radiol.* 2021;31:9567–9578.
8. Unsworth H, Dillon B, Collinson L, et al. The NICE evidence standards framework for digital health and care technologies: developing and maintaining an innovative evidence framework with global impact. *Digit Health.* 2021;7:20552076211018617.

Principles of Tracer Kinetic Analysis in Oncology, Part II: Examples and Future Directions

Austin R. Pantel[1], Varsha Viswanath[1], Mark Muzi[2], Robert K. Doot[1], and David A. Mankoff[1]

[1]*Department of Radiology, University of Pennsylvania, Philadelphia, Pennsylvania; and* [2]*Department of Radiology, University of Washington, Seattle, Washington*

Learning Objectives: On successful completion of this activity, participants should be able to (1) describe examples of the application of PET tracer kinetic analysis to oncology; (2) list applications research and possible clinical applications in oncology where kinetic analysis is helpful; and (3) discuss future applications of kinetic modeling to cancer research and possible clinical cancer imaging practice.

Financial Disclosure: This work was supported by KL2 TR001879, R01 CA211337, R01 CA113941, R33 CA225310, Komen SAC130060, R50 CA211270, and K01 DA040023. Dr. Pantel is a consultant or advisor for Progenics and Blue Earth Diagnostics and is a meeting participant or lecturer for Blue Earth Diagnostics. Dr. Mankoff is on the scientific advisory boards of GE Healthcare, Philips Healthcare, Reflexion, and ImaginAb and is the owner of Trevarx; his wife is the chief executive officer of Trevarx. The authors of this article have indicated no other relevant relationships that could be perceived as a real or apparent conflict of interest.

CME Credit: SNMMI is accredited by the Accreditation Council for Continuing Medical Education (ACCME) to sponsor continuing education for physicians. SNMMI designates each *JNM* continuing education article for a maximum of 2.0 AMA PRA Category 1 Credits. Physicians should claim only credit commensurate with the extent of their participation in the activity. For CE credit, SAM, and other credit types, participants can access this activity through the SNMMI website (http://www.snmmilearningcenter.org) through April 2025.

Kinetic analysis of dynamic PET imaging enables the estimation of biologic processes relevant to disease. Through mathematic analysis of the interactions of a radiotracer with tissue, information can be gleaned from PET imaging beyond static uptake measures. Part I of this 2-part continuing education paper reviewed the underlying principles and methodology of kinetic modeling. In this second part, the benefits of kinetic modeling for oncologic imaging are illustrated through representative case examples that demonstrate the principles and benefits of kinetic analysis in oncology. Examples of the model types discussed in part I are reviewed here: a 1-tissue-compartment model (^{15}O-water), an irreversible 2-tissue-compartment model (^{18}F-FDG), and a reversible 2-tissue-compartment model (3′-deoxy-3′-^{18}F-fluorothymidine). Kinetic approaches are contrasted with static uptake measures typically used in the clinic. Overall, this 2-part review provides the reader with background in kinetic analysis to understand related research and improve the interpretation of clinical nuclear medicine studies with a focus on oncologic imaging.

Key Words: kinetic analysis; dynamic imaging; PET/CT

J Nucl Med 2022; 63:514–521
DOI: 10.2967/jnumed.121.263519

In part I of this review (*1*), we illustrated the complex interactions in tissue that a PET radiotracer undergoes after injection, reflecting factors that mediate tracer delivery, retention, and release based on the cancer biology targeted by the tracer and its pharmacologic properties. By continuously imaging time course data of radiotracer uptake, retention, and washout and applying mathematic models to the time-varying 3-dimensional (4-dimensional) image dataset, PET and kinetic analysis can quantify tumor biology relevant to diagnosis and treatment guidance. In part I of this 2-part review, the underlying principles and methodology of kinetic modeling were discussed, including dynamic imaging protocols, model formulation based on tracer biology, kinetic parameter estimation, mathematic testing of a model, and graphical or simplified approaches. In this part II, we provide representative real-world examples of the principles outlined in part I.

Beyond an exercise in mathematics, the quantitation of a biologic process as measured by kinetic analysis can provide insight into the underlying biology. The true benefit of kinetic analysis lies in its application. Here, in part 2 of this review, representative examples of PET studies are discussed that exemplify cases whereby the interpretation of radiotracer uptake benefitted from kinetic analysis. A 1-tissue-compartment model (^{15}O-water), an irreversible 2-tissue-compartment model (^{18}F-FDG), and a reversible 2-tissue-compartment model (3′-deoxy-3′-^{18}F-fluorothymidine [^{18}F-FLT]) are reviewed in detail. Kinetic measures are contrasted with static approaches to illuminate the benefits of full kinetic analysis. The limitations of widely adopted static measures are also highlighted to guide the interpretation of routine static images as are typically obtained in the nuclear medicine clinic.

ILLUSTRATIVE EXAMPLES

These representative examples are chosen to illustrate the application of the principles and methodology reviewed in part I of this continuing education review (*1*).

1-Tissue-Compartment Model

^{15}O-Water to Measure Blood Flow. Measures of tissue perfusion provide clinically important information in several contexts, most notably cardiology and neurology. Perfusion measures also provide insight into tumor biology and have been used for largely investigational biomarker applications in oncology. Although other tracers (e.g., ^{82}RbCl) and other modalities (e.g., dynamic contrast-enhanced MRI and arterial spin labeling MRI) have been studied (*2–4*), ^{15}O-water is a freely diffusible, inert radiotracer that, even though less clinically practical largely because of an approximately 2-min half-life, serves as a reference standard for perfusion imaging (*5*). The traced substance, water, diffuses freely from the capillaries into and out of a cell without trapping. Accordingly, a 1-tissue-compartment

Received Apr. 1, 2021; revision accepted Feb. 17, 2022.
For correspondence or reprints, contact Austin Pantel (austin.pantel@pennmedicine.upenn.edu).
COPYRIGHT © 2022 by the Society of Nuclear Medicine and Molecular Imaging.

model characterizes this biology (Fig. 3 from part I (*1*)). The differential equation for a 1-tissue-compartment model is written below and can be solved for the variables of interest, blood flow and volume of distribution (*6*):

$$\frac{dC_t(t)}{dt} = F \cdot C_a(t) - \left(\frac{F}{V_T} + \boldsymbol{\lambda}\right)(C_t(t)),$$

where $C_t(t)$ is the tissue concentration of tracer, $C_a(t)$ is the arterial activity, F is blood flow ($=K_1$), and V_T is volume of distribution ($=K_1/k_2$). This model can also directly account for physical decay of this short-lived isotope by including the ^{15}O decay constant, $\boldsymbol{\lambda}$, in the right side of the equation (boldface letter). We do note that if decay-corrected data are used, the decay constant can be omitted from the equation, and identical results will be achieved if appropriate weighting factors to account for frame length and delay are used. From PET images, both the arterial activity (e.g., an image-derived input function) and the tissue concentration of tracer can be measured so that blood flow and distribution volume may be solved, providing estimates of biologically relevant parameters. High blood-pool activity combined with rapid washout makes it challenging to use static uptake measures to estimate blood flow with this radiotracer. As such, the use of kinetic analysis is vital to image interpretation.

Blood flow imaging with ^{15}O-water has been explored as a biomarker in the context of cancer blood flow, including in applications to breast cancer (*7–11*). In these studies, kinetic analysis of ^{18}F-FDG PET studies accompanied ^{15}O-water studies to study the ability of 2 radiotracers, each measuring different aspects of biology, to predict tumor behavior, including response to therapy. These studies are discussed further below.

^{18}F-Fluciclovine to Detect Biochemical Recurrence of Prostate Cancer. Similar to ^{15}O-water, ^{18}F-fluciclovine kinetics can be modeled with 1 tissue compartment and reversible transport. As a synthetic amino acid, ^{18}F-fluciclovine enters the cell through bidirectional amino acid transporters but is neither metabolized nor incorporated into macromolecules (*12*) so uptake of this radiotracer tracks amino acid transport. Consequently, like ^{15}O-water, the radiotracer washes out over time. As expected on the basis of this biology, a 1-tissue-compartment model fits the data well. Distribution volume was well estimated using both a 1-tissue-compartment model and a Logan plot, consistent with a reversible transport model for this radiotracer. A 2-tissue-compartment model that separated the extracellular and intracellular space into 2 tissue compartments was also tested but did not yield meaningful improvements in the quality of fit as judged by the Akaike information criterion (*13*). Reversible kinetics inform the clinical imaging protocol of ^{18}F-fluciclovine in men with prostate cancer. Imaging begins at the pelvis 3–5 min after radiotracer injection and moves cranially so that peak lesional activity is captured in anatomic regions (the pelvis) most likely to harbor metastases. Since ^{18}F-fluciclovine washes out, sensitivity for disease can decrease for imaging times late after injection. Early imaging to identify metastases with high target-to-background contrast differs from other clinical protocols, including ^{18}F-FDG and ^{68}Ga-DOTATATE, which are usually imaged at 60 min after injection to leverage trapping of the radiotracer (*14–16*). Likewise, the recently approved prostate-specific membrane antigen agents—^{18}F-DCFPyL and ^{68}Ga-PSMA-11—are both imaged at 1 h, reflecting (nearly) irreversible kinetics (*17–19*). In the clinic, detection of sites of disease in men with biochemical recurrence of prostate cancer with ^{18}F-fluciclovine is largely qualitative, comparing uptake in suspected lesions with blood pool and marrow uptake. Given rapid radiotracer kinetics over the imaging interval, semiquantitative analysis—for example, SUV_{max}—for prostate cancer is of limited utility, although such data may be given for reference (*20*). However, for other indications, such as imaging of gliomas, kinetic estimates or quantitative static uptake measures from later imaging may prove useful (*21*).

Kinetic Analysis of ^{18}F-FDG (2-Tissue-Compartment Irreversible Model), in Combination with ^{15}O-Water, to Predict Outcome in Locally Advanced Breast Cancer

As detailed as the representative example in our companion paper discussing the principles and methodology of kinetic analysis, the biology of ^{18}F-FDG requires modeling with a 2-tissue-compartment irreversible model in most tissues. From this model, kinetic parameters that estimate biologic processes of energy metabolism can be estimated, including ^{18}F-FDG blood-to-tissue delivery (K_1) and ^{18}F-FDG flux (K_i). Multiplying the K_i (units of mL/min/cm^3) by the measured plasma glucose concentration (μmol/mL) of a subject yields the metabolic rate of ^{18}F-FDG (MR_{FDG}), an approximation of glucose flux as estimated by ^{18}F-FDG PET (plasma glucose concentration multiplied by K_i), with resultant units in the form of μmol/min/cm^3. Of note, a proportionality factor, the ^{18}F-FDG lumped constant, is necessary to convert the MR_{FDG} to the metabolic rate of glucose (*22*), underscoring the known differences between glucose and ^{18}F-FDG metabolism.

Kinetic analysis of ^{18}F-FDG and ^{15}O-water dynamic PET have been well explored as biomarkers for response in breast cancer, with kinetic analysis of both tracers demonstrating value (*7,10,23*). In these studies that leveraged dynamic imaging and kinetic analysis of sequential ^{15}O-water and ^{18}F-FDG dynamic PET, it was noted that, unlike normal breast tissue, the relationship between tumor glucose metabolism estimated by dynamic ^{18}F-FDG PET and blood flow estimated by ^{15}O-water was highly variable (*10,23*). Studies showed the utility of parameters quantifying the delivery of ^{18}F-FDG (measured by the blood-to-tissue transport constant, K_1) and its flux through the glucose metabolism rate-limiting step and hexokinase (measured by the flux constant, K_i). In a study of women with newly diagnosed locally advanced breast cancer (LABC), patients with high MR_{FDG} relative to blood flow had a poor response to neoadjuvant chemotherapy. In this study, among many clinical, pathologic, and PET kinetic parameters, only the ratio of MR_{FDG} to blood flow, as assessed by ^{15}O-water, demonstrated a significant difference for patients with versus without a macroscopic pathologic complete response to neoadjuvant chemotherapy (i.e., no macroscopic tumor seen on gross analysis of surgically resected tissue), a clinical endpoint with prognostic implications. A low ratio predicted response to chemotherapy. Alternatively, a high MR_{FDG}-to-flow ratio, indicative of elevated glycolysis relative to flow such as would be seen with tumor hypoxia, portended a poor response to neoadjuvant therapy, corroborating independent observations supporting resistance of hypoxic tumors to chemotherapy (*7*). A representative example of this observation is shown in Figure 1A. In another study of untreated breast cancer patients, there was no correlation between estimates of blood flow from dynamic images of ^{15}O-water versus an ^{15}O-water SUV image from 4–6 min. This supports the concept that flow information cannot be captured in a late static SUV image, and kinetic analysis is required for this tracer with rapid washout (*8*). In addition to predicting treatment response, combined dynamic ^{15}O-water and ^{18}F-FDG PET revealed differences in the relationship between perfusion and glucose metabolism for different subtypes of breast cancer, providing insight into observed differences in patterns of treatment response in the clinic (*24*). These studies illustrate the clinical and biologic insights that can be gleaned from more detailed PET image acquisition and analysis.

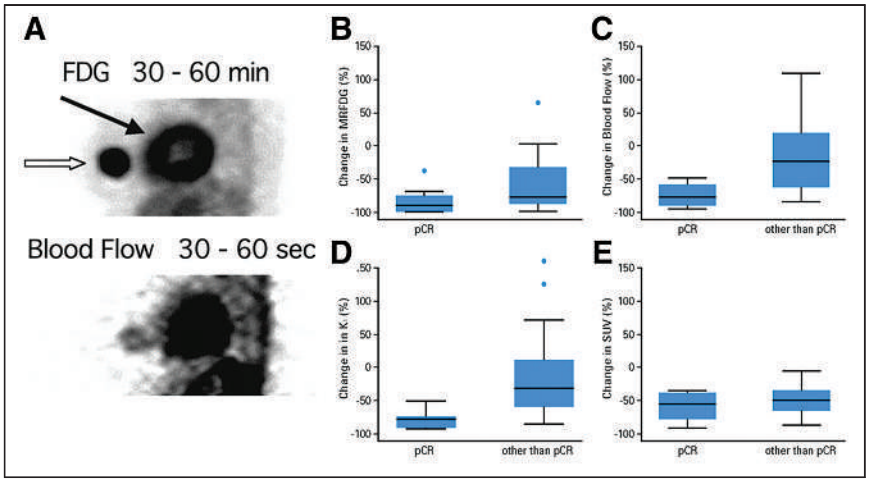

FIGURE 1. (A) Thick sagittal PET images of ^{18}F-FDG (top) and ^{15}O-water (bottom) demonstrate ^{18}F-FDG uptake throughout breast cancer (open arrow), with relatively decreased blood flow centrally; solid arrow denotes heart. This regional metabolism–blood flow mismatch centrally suggests region of hypoxia. After chemotherapy, residual viable tumor was seen in center of tumor, suggesting chemotherapy resistance. (Reprinted from (*7*), noting that analysis in this publication used ROIs that did not account for tumoral heterogeneity.) (B–D) Changes in kinetic parameters (MR_{FDG} [B]; blood flow estimated by ^{15}O-water [C]; ^{18}F-FDG K_i [D]) from baseline to mid therapy in study of patients with LABC demonstrate associations with tumor response. (E) Changes in SUV, however, were not significant. pCR = pathologic complete response. (Reprinted from (*11*).)

Sequential dynamic imaging and kinetic analysis can also provide insights into therapeutic response. In a follow-up analysis of the aforementioned study with LABC patients (*7*), dynamic ^{18}F-FDG and ^{15}O-water PET studies were performed at both baseline and after 2 mo of chemotherapy. A decrease in blood flow between scans was seen in responders but not in nonresponders who had an average increase (−32% and +48%, respectively) (*9*). Patents whose tumor blood flow failed to decline with treatment had poorer disease-free and overall survival. Increased angiogenesis, possibly related to hypoxia, was hypothesized to explain these findings (*9*). Additional analysis of these patients demonstrated normalization of the metabolism–to–blood flow ratio after therapy, suggesting successful treatment of hypoxia (*10*). In analysis with an additional 18 patients, patients with persistent or elevated blood flow estimated by ^{15}O-water and ^{18}F-FDG K_1 between baseline and the midpoint of neoadjuvant chemotherapy had higher rates of recurrence and mortality risks (*11*). Multivariate analysis controlling for known prognostic factors demonstrated that changes in blood flow and ^{18}F-FDG K_1 retained predictive ability for disease-free survival and overall survival; change in SUV was not predictive. Additionally, changes in kinetic parameters from baseline to mid therapy were significantly associated with tumor pathologic response, whereas change in SUV was not (Fig. 1B) (*11*). These results exemplify the added value of kinetic analysis.

Expanding the aforementioned ^{18}F-FDG analysis, a second analysis of data from 75 LABC patients with dynamic imaging showed that the serial dynamic ^{18}F-FDG alone, even without the water data, added key measures predictive of response. The study-observed changes in ^{18}F-FDG K_1 and K_i predicted both disease-free survival and overall survival; changes in SUV predicted only overall survival (*25*). Only a change in K_1 remained a significant predictor of overall survival when known prognostic factors were included in the model; a change in SUV was not significant (*25*). This study indicated that estimates of glucose delivery to tissue (^{18}F-FDG K_1) have value as a predictive marker of response and again underscored the benefits of kinetic measures over static measures.

Additional Applications of Blood Flow and ^{18}F-FDG Kinetic Analysis. The ability of both ^{18}F-FDG K_1 and blood flow, as estimated by ^{15}O-water, motivated studying ^{18}F-FDG K_1 as a proxy for flow, recognizing the difficulties and inherent challenges in regularly using ^{15}O-water given its 2-min half-life. ^{18}F-FDG K_1, as discussed in part I, represents the delivery of radiotracer to tissue, inclusive of blood flow and transport across membranes. As such, this rate constant is not synonymous with blood flow. By the Fick principle, K_1 can be approximated by blood flow multiplied by the first-pass extraction fraction of the tracer. For ^{15}O-water, the extraction fraction is assumed to equal 1 so that ^{15}O-water K_1 equals blood flow (*26*). For tracers with lower first-pass extraction (e.g., ^{18}F-FDG), the extraction fraction is less than 1, and K_1 consequently does not equal blood flow. Nevertheless, there is a moderately strong correlation between blood flow as measured by ^{15}O-water and ^{18}F-FDG K_1 (*10*). In a follow-on related approach, tumor blood flow has been estimated from the first pass of ^{18}F-FDG using a 1-tissue-compartment model with data obtained during the first 2 min after injection (*27,28*). By analyzing such a short period after injection, the metabolic extraction fraction from ^{18}F-FDG phosphorylation can be separated from the first-pass extraction fraction of ^{18}F-FDG, which in turn can better estimate blood flow. In a study that included various tumor types, a correlation coefficient of 0.86 was found between measures of blood flow by the first pass of ^{18}F-FDG and blood flow as estimated by ^{15}O-water (*28*). Humbert et al. applied these methods and reported that blood flow changes were capable of stratifying patient groups with different overall survival percentages in women whose triple-negative breast cancer did not have a complete pathologic response (*29*). This approach could be implemented as a short flow-phase ^{18}F-FDG PET scan early after injection, which could be practical in the clinic, akin to a 3-phase bone scan.

PET kinetic analysis can help inform the interpretation of dynamic contrast studies from other modalities. For example, blood flow estimated by ^{15}O-water and ^{18}F-FDG delivery (K_1) have been correlated with dynamic contrast-enhanced MRI, a measure of tumor perfusion, noting that breast MRI plays a role in current diagnostic algorithms for breast cancer (*30*). Peak signal enhancement ratio, a measure of contrast washout in the tumor, correlated with blood flow and K_1 (with each $r > 0.7$), suggesting a relationship between MRI contrast enhancement and blood flow. MR_{FDG} did not correlate with peak signal enhancement ratio, underscoring the different facets of biology queried with each modality (*31*). The association between these measures was also studied in LABC patients undergoing neoadjuvant chemotherapy. Changes in response to chemotherapy in ^{18}F-FDG K_1 correlated with changes in dynamic contrast-enhanced MRI signal enhancement ratio. Greater decreases in K_1, K_i, signal enhancement ratio, and peak enhancement were seen in patients with a pathologic complete response than in those without, suggesting utility in both modalities in predicting response (*32*). This finding also supports the use of a combination of MRI and ^{18}F-FDG PET to predict and measure the response of LABC to neoadjuvant chemotherapy (*33*). In addition, blood flow by ^{15}O-water has been shown to directly correlate with uptake of ^{99m}Tc-sestamibi, a blood flow tracer used for both cardiac and breast cancer imaging,

and inversely with ^{99m}Tc-sestamibi washout (*34*). These findings suggest that, in tumors, both ^{99m}Tc-sestamibi uptake and washout are influenced by blood flow, which should be considered in the interpretation of static breast ^{99m}Tc-sestamibi images, such as those obtained for molecular breast imaging (*35*).

Static Versus Kinetic Measures of ^{18}F-FDG Uptake

Static uptake measures, such as SUV, may serve as a proxy for kinetic measures and may have clinical relevance but do not directly estimate a specific biologic process. Rather, these static uptake measures represent the aggregate of many processes. In particular, static uptake measures cannot account for nonspecific radiotracer uptake, of particular importance when measuring response in tumors with low baseline uptake. For example, in a study of quantifying response to chemotherapy in LABC, a static SUV was compared with the MR_{FDG} (*36*). The percentage change in SUV versus that in MR_{FDG} from baseline to after therapy was analyzed for patients in the lowest tertile of baseline SUV uptake (SUV_{mean}, 2.5; range, 1.6–3.0) compared with all others (SUV_{mean}, 6.2; range, 3.1–12.3). The slope of the correlation for patients in the lowest tertile was significantly lower than for the other patients (0.4 vs. 0.85), indicating a falsely blunted assessment of response using SUV compared with MR_{FDG}, particularly for subjects with low baseline uptake (Fig. 2). When the MR_{FDG} was extrapolated to −100%, indicating complete inhibition of ^{18}F-FDG metabolism, the percentage change in SUV in the lowest tertile was 65%, compared with 86% in the other patients. The inability to distinguish nonmetabolized and trapped ^{18}F-FDG in the static measure blunts the maximum detectable response and again underscores the limitations of using a static uptake measure as a proxy for a complex biologic process (*36*). These insights derived from kinetic modeling were corroborated in another clinical study in LABC patients with tumors larger than 3 cm monitored with ^{18}F-FDG throughout therapy. If the pretherapy tumor-to-background ratio was less than 5, changes in ^{18}F-FDG uptake from baseline were not predictive of tumor response; however, changes in patients with a tumor-to-background ratio of more than 5 were predictive (*37*). For these reasons, caution should be exercised when interpreting changes, or lack therefore, in ^{18}F-FDG uptake in lesions with low baseline uptake in the clinic. These limitations in static measures may hamper the potential of these measures to serves as biomarkers, such as was exemplified in the study by Dunnwald et al. described above, in which kinetic measures were predictive of response in LABC but static measures were not for all response metrics (*25*).

The inherent limitations of static imaging, particularly the inability of static measures to account for nonspecific ^{18}F-FDG uptake, are considered in imaging response criteria. For example, target lesions in PERCIST must have uptake greater than a threshold defined by background liver uptake, in large part to ensure the ability to detect a decrease in percentage radiotracer uptake with effective treatment (*38*). This understanding of the principles of kinetic analysis benefits the interpretation of even routine static images.

Kinetic analysis can avoid the pitfalls of measuring a dynamic process at a single time point with a static image and can even suggest that correction approaches could enhance static analyses. In a study of untreated breast cancers undergoing both dynamic and static ^{18}F-FDG PET in a single session, ^{18}F-FDG SUV_{max} changed linearly after 27 min, with both positive and negative slopes observed (range, from −0.02 to 0.15 SUV units/min). The rate of change of SUV also had a linear relationship with instantaneous SUV, and an empiric linear model to correct SUV for a variable uptake time was developed (*39*). Although this model demonstrated feasibility, such corrections are not used in routine clinical practice, and consensus recommendations suggest a consistent interval between injection and scanning (*40*).

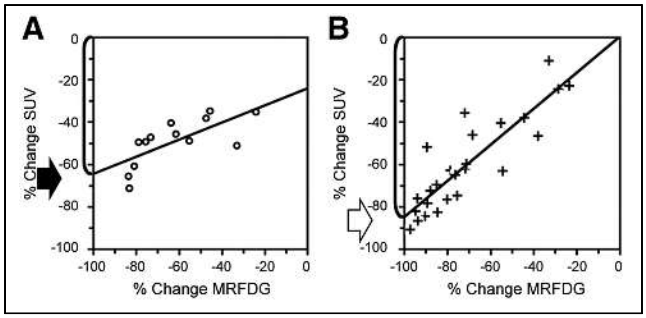

FIGURE 2. In study quantifying response to chemotherapy in breast cancer, percentage change in SUV is compared with percentage change in MR_{FDG}. For patient in lowest tertile of baseline SUV uptake (A), only 65% of maximum detectable percentage change (solid arrow) in SUV (change in SUV when change in MR_{FDG} = −100%) is able to be theoretically achieved. This is compared with 86% of maximum detectable percentage change in SUV in patients with greater baseline uptake (open arrow) (B), underscoring impact of nonspecific uptake on static ^{18}F-FDG uptake measures. (Adapted from (*36*).)

The consequences of using static uptake measures on clinical trial design has been explored in virtual clinical trials. To explore the effect of variable uptake time, simulated ^{18}F-FDG time–activity curves in women with LABC and static SUV measures were obtained at various time points in 4 distinct scenarios. These scenarios ranged from strict adherence to standardized uptake of 60–65 min to a combination of early and delayed scans with uptake times ranging from 45 to 115 min. Given that the ground truth of lesion uptake was known for any time point, the sensitivity and specificity of detecting a response to chemotherapy in breast cancer was studied. A sensitivity and specificity of 96% and 99%, respectively, was achieved in the scenario with highest compliance; this fell to 73% and 91%, respectively, for the least compliant group (*41*). Use of the correction algorithm above (*39*) improved both metrics. Simulated power analysis demonstrated that this variability increased sample sizes for simulated single-arm phase II trials (*41*). An additional study explored the effect of kinetic versus static measures on power or sample sizes for a virtual clinical trial. Sensitivity to detecting a response between a baseline and follow-up ^{18}F-FDG PET scan was estimated for static uptake measures (SUV) and stratified by baseline uptake. As expected, larger sample sizes were required when static measures were used than when kinetic measures were used, and sample sizes were greatest for lesions with low baseline uptake. Sample size also decreased with better calibration of the PET scanners, underscoring the need for standardization in clinical trials, particularly in multisite clinical trials (*42*). In recognition of the variability of radiologic measures and the impact on biomarker development, the Radiological Society in North America established the Quantitative Imaging Biomarkers Alliance in 2007. A recent profile published by this alliance discusses many of these issues and provides claims on the precision of SUV measurements (*43*). The European Advanced Translational Research Infrastructure in Medicine serves as the European equivalent (*44*).

Proliferation Imaging: ^{18}F-FLT (2-Tissue-Compartment Reversible Model)

We discuss the analysis of images for ^{18}F-FLT as a tracer with similar, but not identical, kinetics to ^{18}F-FDG as a further illustration of the application of kinetic modeling to oncologic imaging.

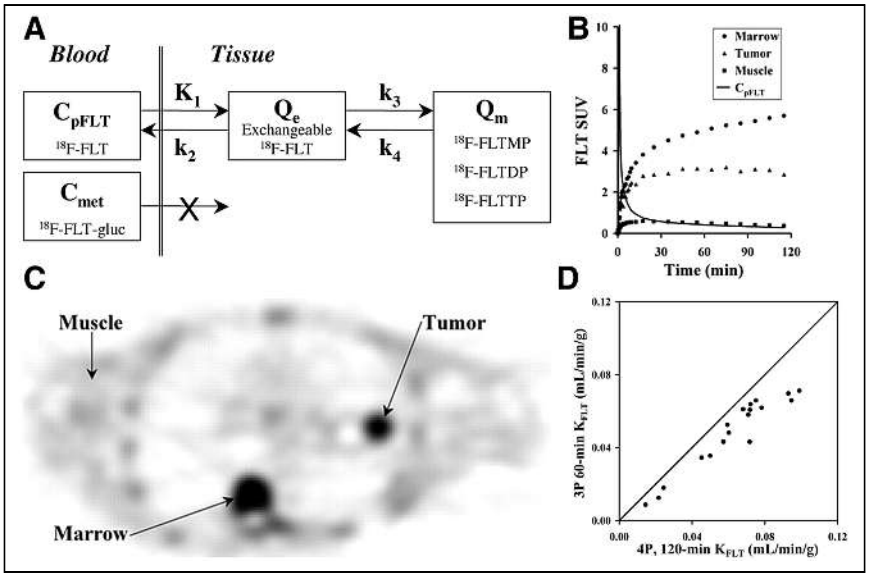

FIGURE 3. (A) Compartmental model of ^{18}F-FLT with 2 reversible tissue compartments. (B) Representative time–activity curves for tumor, muscle, and marrow. (C) ^{18}F-FLT-PET image demonstrating left lung cancer and normal marrow uptake. (D) Correlation of K_{FLT} from 3-parameter model using 60 min of data compared with 4-parameter model with 120 min of data shows underestimate of K_{FLT} with 3-parameter model using more data, as expected from preliminary mathematic studies. (Adapted from (*54*).) C_{met} = concentration of metabolites in arterial plasma; C_{pFLT} = concentration of ^{18}F-FLT in arterial plasma; FLT-gluc = ^{18}F-FLT-glucuronide; FLTDP = ^{18}F-FLT-diphosphate; FLTMP = ^{18}F-FLT-monophosphate; FLTTP = ^{18}F-FLT-triphosphate; Q_e = exchangeable tissue compartment; Q_m = compartment of trapped ^{18}F-FLT phosphorylated nucleotides.

Radiolabeled thymidine and its analogs have been studied as markers of cellular proliferation, with increased rates of proliferation characteristic of malignancy (*45,46*). Through the exogenous salvage pathway, extracellular thymidine is incorporated into DNA, with the phosphorylation of thymidine by thymidine kinase I representing the initial and rate-limiting step. Because thymidine is incorporated into DNA, but not RNA, thymidine uptake reflects DNA synthesis and, thus, cellular proliferation (*45,47*).

Initial studies of ^{11}C-thymidine demonstrated the ability to estimate cellular proliferation through kinetic analysis of this radiolabeled native analog. A 5-tissue-compartment model accounting for blood metabolites was able to estimate the flux constant accurately, though all model microparameters could not be estimated independently (*48,49*). The short half-life of ^{11}C, combined with a complex analysis, precluded widespread use of this radiotracer, necessitating a different analog for clinical translation.

The complexity of acquiring and analyzing ^{11}C-thymidine PET images motivated the development of less heavily metabolized thymidine analogs as proliferation tracers (*45*). A fluorinated analog of thymidine, ^{18}F-FLT, has advanced into clinical trials, benefitting from a longer half-life and fewer metabolites than for ^{11}C-thymidine. Similar to ^{11}C-thymidine, though, ^{18}F-FLT traces the exogenous (salvage) thymidine pathway and can, as such, provide information on cellular proliferation similar to that from thymidine. However, unlike thymidine, ^{18}F-FLT is not incorporated into DNA. Flux through the thymidine salvage pathway is ideated by retention of the ^{18}F-FLT phosphorylated by thymidine kinase I, as the downstream product—^{18}F-FLT-monophosphate or a related compound—is predominately trapped in the cell. Thus, like ^{18}F-FDG, ^{18}F-FLT is another largely trapped tracer that can be modeled with 2 tissue compartments (Fig. 3) (*50*).

However, several nuances for ^{18}F-FLT necessitate considerations in the model that are not present for ^{18}F-FDG. Metabolism of ^{18}F-FLT by the liver produces ^{18}F-FLT-glucuronide, which is restricted to the vascular space and contaminates the input function. This requires a metabolite-corrected input function in humans. Also, the washout rate from the trapped compartment (indicated by k_4), related to dephosphorylation or transport of phosphorylated ^{18}F-FLT (*51*), is more variable than it is for ^{18}F-FDG (*50,52*). These factors were examined in a series of studies in both humans and animals (*50,52,53*). Simulation studies over a range of expected parameter values from clinical studies with 120 min of data demonstrated a 2-tissue-compartment reversible model with 4 rate constants, and a metabolite-corrected arterial input function accurately estimated ^{18}F-FLT flux ($K_{FLT} = (K_1k_3)/(k_2 + k_3)$) and K_1 ($r = 0.99$ and 0.94, respectively). In contrast, k_3, representing the rate-limiting phosphorylation by thymidine kinase I, was not well estimated ($r = 0.73$), corroborating sensitivity and identifiability analysis (*50*). Using only the initial 60 min of data and eliminating k_4, as suggested in earlier analyses (*53*), demonstrated −28% bias in K_{FLT}. Such an underestimate may lead to incorrect conclusions in response studies, underscoring the importance of appropriate model selection and testing (*50*).

Validation studies in patients with lung cancer corroborated results from the mathematic simulation study. Compared with a 4-parameter model using 120 min of data, a 3-parameter model with 60 min of data underestimated K_{FLT}, underscoring the need to account for dephosphorylation in this tissue type (Fig. 3). An SUV of 30–60 min demonstrated a poor correlation with K_{FLT} with 120 min of data ($r = 0.62$). Tissue correlation studies demonstrated a high correlation of K_{FLT} (ρ of 0.92 and 0.88 with 4 parameters and 120 or 90 min of data, respectively), with Ki-67, an in vitro assay of proliferation, validating the model as a marker of cellular proliferation. The correlation between Ki-67 and average SUV was lower, with a ρ of 0.65 (*54*). The inability to accurately estimate the microparameter k_3 precludes direct correlation with Ki-67, also noting that Ki-67 is a protein marker of proliferation but not directly involved in the thymidine pathway, mitigating the utility for direct correlation (*55*). These detailed kinetic studies suggest that human translational studies with ^{18}F-FLT should include detailed kinetic analysis before obtaining only simpler static measures (*47*).

After the above studies, a mouse study with subcutaneously implanted tumors supported the use of a 2-tissue-compartment model with reversible phosphorylation. These investigators concluded that scans at least 90 min in duration that include k_4 are necessary if absolute quantification of K_{FLT} is needed. Correlation of dynamic PET measures with Ki-67 revealed a high correlation with K_{FLT}, and K_{FLT} was estimated with better precision than k_3. The correlation with SUV and Ki-67 was weaker (*52*). We do note that the macroparameter K_{FLT} [$K_{FLT} = (K_1k_3)/(k_2 + k_3)$] includes the microparameters K_1 and k_3 and is thus influenced by the transfer rate constant (K_1, which is dependent on blood flow) and rate-limiting phosphorylation by thymidine kinase I (k_3).

To facilitate translation into the clinic, there have been efforts to simplify the imaging protocol of ^{18}F-FLT. A blood input function derived from 8 venous samples and a single sample at 60 min for

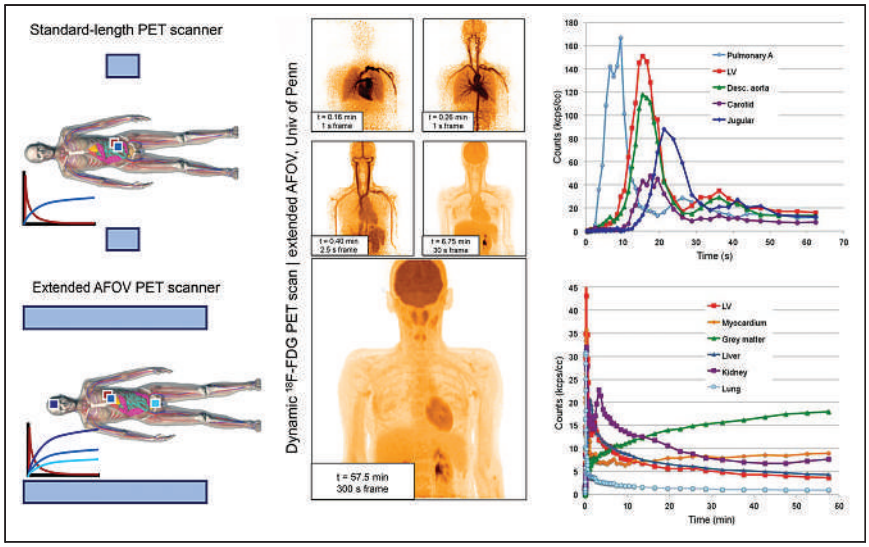

FIGURE 4. (Left) Schematic illustrating benefit of extended AFOV total-body (TB) PET scanners (blue rectangles represent AFOV of each scanner). Extended AFOV TB PET scanners enable simultaneous kinetic analysis of all major body organs. Images (middle) and time–activity curves (right) from dynamic ^{18}F-FDG dataset of healthy human subject imaged on the extended AFOV scanner at the University of Pennsylvania demonstrate ability to capture relatively noise-free time–activity curves. (Adapted from (*62*).) Univ of Penn = University of Pennsylvania.

metabolite analysis has been validated. An image-derived input function from the aorta also correlated with venous blood sampling (*56*). Additional work with a population-based input function combined with limited blood samples (as few as 3) have been used to estimate K_i, which showed a good correlation with estimates using full arterial sampling, as well as a good correlation with Ki-67 (*57*). An image-derived input function has also been validated in patients with high-grade glioma patients, further suggesting clinically feasible protocols (*58*). As detailed, kinetic measures have been shown to better correlate with Ki-67. Nonetheless, obtaining kinetic parameter estimates requires dynamic scanning and, in this case, metabolite correction. Moreover, in a reproducibility study in non–small cell lung cancer, kinetic measures (Patlak analysis and 2-tissue-compartment analysis with $k_4 = 0$) with 60 min of dynamic data were less reproducible than static measures (*59*). Ultimately, the need for practical reproducible clinical protocols must be balanced with the ability of static uptake measures to capture relevant biology to improve clinical care.

Future Direction: Whole-Body Scanners

Although dramatic improvements in PET technology have revolutionized PET imaging, kinetic analysis applications, particularly in oncology, remain hampered by the limited axial field of view (AFOV) of modern PET scanners (<30 cm). To realize the full potential of PET imaging, long-AFOV PET scanners have been developed. The increased axial coverage of these instruments enables data collection from the entire burden of disease across the patient while simultaneously imaging a large blood vessel from which the image-derived input function can be measured without significant partial-volume effects. The 2-m total-body (TB) PET scanner at the University of California Davis (*60,61*) images the entire body in a single field of view; the TB PET scanner at the University of Pennsylvania can capture all major organs of the body in a single bed position (Fig. 4) and has recently been expanded from an AFOV of 1.12 m to one of 1.36 m (*62–64*). Additionally, the marked sensitivity gains of these instruments also enable relatively noise-free time–activity curves, as shown in Figure 4, in which early frames are 1 s in duration, particularly for the image-derived input function, for which short time bins may be used early in imaging (*63*). With advanced reconstruction methods on a TB PET scanner, a 100-ms temporal resolution was achieved (*65*). These sensitivity gains can be leveraged to image radiotracers at lower doses while maintaining accuracy of kinetic parameter estimation (*66*), of particular importance for new radiotracers with production challenges or an elevated organ dose. Imaging at lower doses may also be leveraged for dual-tracer imaging of 2 fluorinated radiotracers in a single imaging session (*67*), where the first radiotracer is injected at a markedly lower dose, minimizing residual activity during the second tracer acquisition, followed by a higher dose of a second tracer (*68*). Lastly, the inclusion of all major organs in the long AFOV enables whole-body kinetics to study the dynamic interactions between organs (*69*). With increased count statistics, these approaches may include a fit of the blood input curve and not just its use as a driving input function.

CONCLUSION

In this second part of this 2-part continuing education review, the benefits of kinetic analysis of PET data were explored through representative case examples. Representative 1-tissue-compartment and reversible or irreversible 2-tissue-compartment models were reviewed to demonstrate the application of the principles and methodology discussed in part I. As demonstrated here, a kinetic model must be designed to estimate biologically relevant processes in an accurate and reproducible manner. Kinetic measures can avoid many of the pitfalls of using static measures to characterize a dynamic process as illustrated by the selected examples discussed in part II of this review. Although dynamic imaging for kinetic analysis is often impractical for the clinic, and many of the examples focus on research applications and questions, the concepts of tracer kinetics and kinetic analysis apply to the interpretation of static images for clinical oncologic PET imaging, including ^{18}F-FDG, and should be considered in clinical image interpretation.

REFERENCES

1. Pantel AR, Viswanath V, Muzi M, Doot R, Mankoff DA. Principles of tracer kinetic analysis in oncology, part I: principles and overview of methodology. *J Nucl Med.* 2021;63:342–352.
2. Telischak NA, Detre JA, Zaharchuk G. Arterial spin labeling MRI: clinical applications in the brain. *J Magn Reson Imaging.* 2015;41:1165–1180.
3. Gordon Y, Partovi S, Müller-Eschner M, et al. Dynamic contrast-enhanced magnetic resonance imaging: fundamentals and application to the evaluation of the peripheral perfusion. *Cardiovasc Diagn Ther.* 2014;4:147–164.
4. Germino M, Ropchan J, Mulnix T, et al. Quantification of myocardial blood flow with ^{82}Rb: validation with ^{15}O-water using time-of-flight and point-spread-function modeling. *EJNMMI Res.* 2016;6:68.
5. Aboagye EO, Gilbert FJ, Fleming IN, et al. Recommendations for measurement of tumour vascularity with positron emission tomography in early phase clinical trials. *Eur Radiol.* 2012;22:1465–1478.
6. Wilson CB, Lammertsma AA, McKenzie CG, Sikora K, Jones T. Measurements of blood flow and exchanging water space in breast tumors using positron emission tomography: a rapid and noninvasive dynamic method. *Cancer Res.* 1992; 52:1592–1597.

7. Mankoff DA, Dunnwald LK, Gralow JR, et al. Blood flow and metabolism in locally advanced breast cancer: relationship to response to therapy. *J Nucl Med.* 2002;43:500–509.
8. Zasadny KR, Tatsumi M, Wahl RL. FDG metabolism and uptake versus blood flow in women with untreated primary breast cancers. *Eur J Nucl Med Mol Imaging.* 2003;30:274–280.
9. Mankoff DA, Dunnwald LK, Gralow JR, et al. Changes in blood flow and metabolism in locally advanced breast cancer treated with neoadjuvant chemotherapy. *J Nucl Med.* 2003;44:1806–1814.
10. Tseng J, Dunnwald LK, Schubert EK, et al. ^{18}F-FDG kinetics in locally advanced breast cancer: correlation with tumor blood flow and changes in response to neoadjuvant chemotherapy. *J Nucl Med.* 2004;45:1829–1837.
11. Dunnwald LK, Gralow JR, Ellis GK, et al. Tumor metabolism and blood flow changes by positron emission tomography: relation to survival in patients treated with neoadjuvant chemotherapy for locally advanced breast cancer. *J Clin Oncol.* 2008;26:4449–4457.
12. Schuster DM, Nanni C, Fanti S. Evaluation of prostate cancer with radiolabeled amino acid analogs. *J Nucl Med.* 2016;57(suppl 3):61S–66S.
13. Sörensen J, Owenius R, Lax M, Johansson S. Regional distribution and kinetics of [^{18}F]fluciclovine (anti-[^{18}F]FACBC), a tracer of amino acid transport, in subjects with primary prostate cancer. *Eur J Nucl Med Mol Imaging.* 2013;40:394–402.
14. Boellaard R, Delgado-Bolton R, Oyen WJ, et al. FDG PET/CT: EANM procedure guidelines for tumour imaging: version 2.0. *Eur J Nucl Med Mol Imaging.* 2015;42:328–354.
15. Velikyan I, Sundin A, Sörensen J, et al. Quantitative and qualitative intrapatient comparison of ^{68}Ga-DOTATOC and ^{68}Ga-DOTATATE: net uptake rate for accurate quantification. *J Nucl Med.* 2014;55:204–210.
16. Virgolini I, Ambrosini V, Bomanji JB, et al. Procedure guidelines for PET/CT tumour imaging with ^{68}Ga-DOTA-conjugated peptides: ^{68}Ga-DOTA-TOC, ^{68}Ga-DOTA-NOC, ^{68}Ga-DOTA-TATE. *Eur J Nucl Med Mol Imaging.* 2010;37:2004–2010.
17. Jansen BHE, Yaqub M, Voortman J, et al. Simplified methods for quantification of ^{18}F-DCFPyL uptake in patients with prostate cancer. *J Nucl Med.* 2019;60:1730–1735.
18. Fendler WP, Eiber M, Beheshti M, et al. ^{68}Ga-PSMA PET/CT: joint EANM and SNMMI procedure guideline for prostate cancer imaging—version 1.0. *Eur J Nucl Med Mol Imaging.* 2017;44:1014–1024.
19. Ringheim A, Campos Neto GC, Anazodo U, et al. Kinetic modeling of ^{68}Ga-PSMA-11 and validation of simplified methods for quantification in primary prostate cancer patients. *EJNMMI Res.* 2020;10:12.
20. Nanni C, Zanoni L, Bach-Gansmo T, et al. [^{18}F]fluciclovine PET/CT: joint EANM and SNMMI procedure guideline for prostate cancer imaging—version 1.0. *Eur J Nucl Med Mol Imaging.* 2020;47:579–591.
21. Parent EE, Benayoun M, Ibeanu I, et al. [^{18}F]fluciclovine PET discrimination between high- and low-grade gliomas. *EJNMMI Res.* 2018;8:67.
22. Spence AM, Muzi M, Graham MM, et al. Glucose metabolism in human malignant gliomas measured quantitatively with PET, 1-[C-11]glucose and FDG: analysis of the FDG lumped constant. *J Nucl Med.* 1998;39:440–448.
23. Zasadny KR, Wahl RL. Standardized uptake values of normal tissues at PET with 2-[fluorine-18]-fluoro-2-deoxy-D-glucose: variations with body weight and a method for correction. *Radiology.* 1993;189:847–850.
24. Specht JM, Kurland BF, Montgomery SK, et al. Tumor metabolism and blood flow as assessed by positron emission tomography varies by tumor subtype in locally advanced breast cancer. *Clin Cancer Res.* 2010;16:2803–2810.
25. Dunnwald LK, Doot RK, Specht JM, et al. PET tumor metabolism in locally advanced breast cancer patients undergoing neoadjuvant chemotherapy: value of static versus kinetic measures of fluorodeoxyglucose uptake. *Clin Cancer Res.* 2011;17:2400–2409.
26. Carson RE. Tracer kinetic modeling in PET. In: Bailey DL, Townsend DW, Valk PE, Maisey MN, eds. *Positron Emission Tomography*. Springer; 2005:127–159.
27. Mullani NA, Gould KL. First-pass measurements of regional blood flow with external detectors. *J Nucl Med.* 1983;24:577–581.
28. Mullani NA, Herbst RS, O'Neil RG, Gould KL, Barron BJ, Abbruzzese JL. Tumor blood flow measured by PET dynamic imaging of first-pass ^{18}F-FDG uptake: a comparison with ^{15}O-labeled water-measured blood flow. *J Nucl Med.* 2008;49:517–523.
29. Humbert O, Riedinger JM, Vrigneaud JM, et al. ^{18}F-FDG PET-derived tumor blood flow changes after 1 cycle of neoadjuvant chemotherapy predicts outcome in triple-negative breast cancer. *J Nucl Med.* 2016;57:1707–1712.
30. Mann RM, Cho N, Moy L. Breast MRI: State of the art. *Radiology.* 2019;292:520–536.
31. Eby PR, Partridge SC, White SW, et al. Metabolic and vascular features of dynamic contrast-enhanced breast magnetic resonance imaging and ^{15}O-water positron emission tomography blood flow in breast cancer. *Acad Radiol.* 2008;15:1246–1254.
32. Partridge SC, Vanantwerp RK, Doot RK, et al. Association between serial dynamic contrast-enhanced MRI and dynamic ^{18}F-FDG PET measures in patients undergoing neoadjuvant chemotherapy for locally advanced breast cancer. *J Magn Reson Imaging.* 2010;32:1124–1131.
33. Semple SI, Staff RT, Heys SD, et al. Baseline MRI delivery characteristics predict change in invasive ductal breast carcinoma PET metabolism as a result of primary chemotherapy administration. *Ann Oncol.* 2006;17:1393–1398.
34. Mankoff DA, Dunnwald LK, Gralow JR, et al. [Tc-99m]-sestamibi uptake and washout in locally advanced breast cancer are correlated with tumor blood flow. *Nucl Med Biol.* 2002;29:719–727.
35. Dibble EH, Hunt KN, Ehman EC, O'Connor MK. Molecular breast imaging in clinical practice. *AJR.* 2020;215:277–284.
36. Doot RK, Dunnwald LK, Schubert EK, et al. Dynamic and static approaches to quantifying ^{18}F-FDG uptake for measuring cancer response to therapy, including the effect of granulocyte CSF. *J Nucl Med.* 2007;48:920–925.
37. McDermott GM, Welch A, Staff RT, et al. Monitoring primary breast cancer throughout chemotherapy using FDG-PET. *Breast Cancer Res Treat.* 2007;102:75–84.
38. Wahl RL, Jacene H, Kasamon Y, Lodge MA. From RECIST to PERCIST: evolving considerations for PET response criteria in solid tumors. *J Nucl Med.* 2009;50(suppl 1):122S–150S.
39. Beaulieu S, Kinahan P, Tseng J, et al. SUV varies with time after injection in ^{18}F-FDG PET of breast cancer: characterization and method to adjust for time differences. *J Nucl Med.* 2003;44:1044–1050.
40. Shankar LK, Hoffman JM, Bacharach S, et al. Consensus recommendations for the use of ^{18}F-FDG PET as an indicator of therapeutic response in patients in National Cancer Institute trials. *J Nucl Med.* 2006;47:1059–1066.
41. Kurland BF, Muzi M, Peterson LM, et al. Multicenter clinical trials using ^{18}F-FDG PET to measure early response to oncologic therapy: effects of injection-to-acquisition time variability on required sample size. *J Nucl Med.* 2016;57:226–230.
42. Doot RK, Kurland BF, Kinahan PE, Mankoff DA. Design considerations for using PET as a response measure in single site and multicenter clinical trials. *Acad Radiol.* 2012;19:184–190.
43. Kinahan PE, Perlman ES, Sunderland JJ, et al. The QIBA profile for FDG PET/CT as an imaging biomarker measuring response to cancer therapy. *Radiology.* 2020;294:647–657.
44. van Dongen GA, Ussi AE, de Man FH, Migliaccio G. EATRIS, a European initiative to boost translational biomedical research. *Am J Nucl Med Mol Imaging.* 2013;3:166–174.
45. Bading JR, Shields AF. Imaging of cell proliferation: status and prospects. *J Nucl Med.* 2008;49(suppl 2):64S–80S.
46. Mankoff DA, Eary JF, Link JM, et al. Tumor-specific positron emission tomography imaging in patients: [^{18}F] fluorodeoxyglucose and beyond. *Clin Cancer Res.* 2007;13:3460–3469.
47. Mankoff DA, Eary JF. Proliferation imaging to measure early cancer response to targeted therapy. *Clin Cancer Res.* 2008;14:7159–7160.
48. Mankoff DA, Shields AF, Graham MM, Link JM, Eary JF, Krohn KA. Kinetic analysis of 2-[carbon-11]thymidine PET imaging studies: compartmental model and mathematical analysis. *J Nucl Med.* 1998;39:1043–1055.
49. Mankoff DA, Shields AF, Link JM, et al. Kinetic analysis of 2-[^{11}C]thymidine PET imaging studies: validation studies. *J Nucl Med.* 1999;40:614–624.
50. Muzi M, Mankoff DA, Grierson JR, Wells JM, Vesselle H, Krohn KA. Kinetic modeling of 3′-deoxy-3′-fluorothymidine in somatic tumors: mathematical studies. *J Nucl Med.* 2005;46:371–380.
51. Plotnik DA, McLaughlin LJ, Chan J, Redmayne-Titley JN, Schwartz JL. The role of nucleoside/nucleotide transport and metabolism in the uptake and retention of 3′-fluoro-3′-deoxythymidine in human B-lymphoblast cells. *Nucl Med Biol.* 2011;38:979–986.
52. Kim SJ, Lee JS, Im KC, et al. Kinetic modeling of 3′-deoxy-3′-^{18}F-fluorothymidine for quantitative cell proliferation imaging in subcutaneous tumor models in mice. *J Nucl Med.* 2008;49:2057–2066.
53. Visvikis D, Francis D, Mulligan R, et al. Comparison of methodologies for the in vivo assessment of ^{18}FLT utilisation in colorectal cancer. *Eur J Nucl Med Mol Imaging.* 2004;31:169–178.
54. Muzi M, Vesselle H, Grierson JR, et al. Kinetic analysis of 3′-deoxy-3′-fluorothymidine PET studies: validation studies in patients with lung cancer. *J Nucl Med.* 2005;46:274–282.
55. Scholzen T, Gerdes J. The Ki-67 protein: from the known and the unknown. *J Cell Physiol.* 2000;182:311–322.

56. Shields AF, Briston DA, Chandupatla S, et al. A simplified analysis of [^{18}F]3′-deoxy-3′-fluorothymidine metabolism and retention. *Eur J Nucl Med Mol Imaging.* 2005;32:1269–1275.
57. Contractor KB, Kenny LM, Coombes CR, Turkheimer FE, Aboagye EO, Rosso L. Evaluation of limited blood sampling population input approaches for kinetic quantification of [^{18}F]fluorothymidine PET data. *EJNMMI Res.* 2012;2:11.
58. Backes H, Ullrich R, Neumaier B, Kracht L, Wienhard K, Jacobs AH. Noninvasive quantification of ^{18}F-FLT human brain PET for the assessment of tumour proliferation in patients with high-grade glioma. *Eur J Nucl Med Mol Imaging.* 2009;36:1960–1967.
59. Shields AF, Lawhorn-Crews JM, Briston DA, et al. Analysis and reproducibility of 3′-deoxy-3′-[^{18}F]fluorothymidine positron emission tomography imaging in patients with non-small cell lung cancer. *Clin Cancer Res.* 2008;14:4463–4468.
60. Badawi RD, Shi H, Hu P, et al. First human imaging studies with the EXPLORER total-body PET scanner. *J Nucl Med.* 2019;60:299–303.
61. Spencer BA, Berg E, Schmall JP, et al. Performance evaluation of the uEXPLORER total-body PET/CT scanner based on NEMA NU 2-2018 with additional tests to characterize PET scanners with a long axial field of view. *J Nucl Med.* 2021;62:861–870.
62. Karp JS, Viswanath V, Geagan MJ, et al. PennPET Explorer: design and preliminary performance of a whole-body imager. *J Nucl Med.* 2020;61:136–143.
63. Pantel AR, Viswanath V, Daube-Witherspoon ME, et al. PennPET Explorer: human imaging on a whole-body imager. *J Nucl Med.* 2020;61:144–151.
64. Pantel AR, Viswanath V, Karp JS. Update on the PennPET Explorer: a whole-body imager with scalable axial field-of-view. *PET Clin.* 2021;16:15–23.
65. Zhang X, Cherry SR, Xie Z, Shi H, Badawi RD, Qi J. Subsecond total-body imaging using ultrasensitive positron emission tomography. *Proc Natl Acad Sci USA.* 2020;117:2265–2267.
66. Viswanath V, Pantel AR, Daube-Witherspoon ME, et al. Quantifying bias and precision of kinetic parameter estimation on the PennPET Explorer, a long axial field-of-view scanner. *IEEE Trans Radiat Plasma Med Sci.* 2020;4:735–749.
67. Kadrmas DJ, Rust TC, Hoffman JM. Single-scan dual-tracer FLT+FDG PET tumor characterization. *Phys Med Biol.* 2013;58:429–449.
68. Mankoff DA, Pantel AR, Viswanath V, Karp JS. Advances in PET diagnostics for guiding targeted cancer therapy and studying in vivo cancer biology. *Curr Pathobiol Rep.* 2019;7:97–108.
69. Surti S, Pantel AR, Karp JS. Total body PET: why, how, what for? *IEEE Trans Radiat Plasma Med Sci.* 2020;4:283–292.

Impact of ^{18}F-FET PET/MRI on Clinical Management of Brain Tumor Patients

Cornelia Brendle[1], Caroline Maier[2,3], Benjamin Bender[1], Jens Schittenhelm[4], Frank Paulsen[5], Mirjam Renovanz[6], Constantin Roder[7], Salvador Castaneda-Vega[8,9], Ghazaleh Tabatabai[6], Ulrike Ernemann[1], and Christian la Fougère[8,10,11]

[1]*Diagnostic and Interventional Neuroradiology, Department of Radiology, University Hospital Tuebingen, Tuebingen, Germany;* [2]*Diagnostic and Interventional Radiology, Department of Radiology, University Hospital Tuebingen, Tuebingen, Germany;* [3]*Department of Radiology, Cantonal Hospital Muensterlingen, Muensterlingen, Switzerland;* [4]*Department of Neuropathology, University Hospital Tübingen, Tuebingen, Germany;* [5]*Department of Radiation Oncology, University Hospital Tuebingen, Tuebingen, Germany;* [6]*Department of Neurology and Neurooncology, University Hospital Tuebingen, Hertie Institute for Clinical Brain Research, Tübingen, Germany;* [7]*Department of Neurosurgery, University Hospital Tübingen, Tuebingen, Germany;* [8]*Nuclear Medicine and Clinical Molecular Imaging, Department of Radiology, University Hospital Tuebingen, Tuebingen, Germany;* [9]*Werner Siemens Imaging Center, Department of Preclinical Imaging and Radiopharmacy, Eberhard Karls University Tuebingen, and University Medical Center, Tuebingen, Germany;* [10]*Cluster of Excellence iFIT (EXC 2180) "Image Guided and Functionally Instructed Tumor Therapies," University of Tuebingen, Tuebingen, Germany; and* [11]*German Cancer Consortium, Partner Site Tuebingen, Tuebingen, Germany*

Multiparametric PET/MRI with the amino-acid analog *O*-(2-^{18}F-fluoroethyl)-L-tyrosine (^{18}F-FET) enables the simultaneous assessment of molecular, morphologic, and functional brain tumor characteristics. Although it is considered the most accurate noninvasive approach in brain tumors, its relevance for patient management is still under debate. Here, we report the diagnostic performance of ^{18}F-FET PET/MRI and its impact on clinical management in a retrospective patient cohort. **Methods:** We retrospectively analyzed brain tumor patients who underwent ^{18}F-FET PET/MRI between 2017 and 2018. ^{18}F-FET PET/MRI examinations were indicated clinically because of equivocal standard imaging results or the clinical course. Histologic confirmation or clinical and standard imaging follow-up served as the reference standard. We evaluated ^{18}F-FET PET/MRI accuracy in identifying malignancy in untreated suspected lesions (category, new diagnosis) and true progression during adjuvant treatment (category, detection of progression) in a clinical setting. Using multiple regression, we also estimated the contribution of single modalities to produce an optimal PET/MRI outcome. We assessed the recommended and applied therapies before and after ^{18}F-FET PET/MRI and noted whether the treatment changed on the basis of the ^{18}F-FET PET/MRI outcome. **Results:** We included 189 patients in the study. ^{18}F-FET PET/MRI allowed the identification of malignancy at new diagnosis with an accuracy of 85% and identified true progression with an accuracy of 93%. Contrast enhancement, ^{18}F-FET PET uptake, and tracer kinetics were the major contributors to an optimal PET/MRI outcome. In the previously equivocal patients, ^{18}F-FET PET/MRI changed the clinical management in 33% of the untreated lesions and 53% of the cases of tumor progression. **Conclusion:** Our results suggest that ^{18}F-FET PET/MRI helps clarify equivocal conditions and profoundly supports the clinical management of brain tumor patients. The optimal modality setting for ^{18}F-FET PET/MRI and the clinical value of a simultaneous examination need further exploration. At a new diagnosis, multiparametric ^{18}F-FET PET/MRI might help prevent unnecessary invasive procedures by ruling out malignancy; however, adding static ^{18}F-FET PET to an already existing MRI examination seems to be of equal value. At detection of progression, multiparametric ^{18}F-FET PET/MRI may increase therapy effectiveness by distinguishing between tumor progression and therapy-related imaging alterations.

Key Words: multiparametric ^{18}F-FET PET/MRI; brain tumor; accuracy; clinical impact; human

J Nucl Med 2022; 63:522–527
DOI: 10.2967/jnumed.121.262051

PET with radiolabeled amino-acid analogs such as *O*-(2-^{18}F-fluoroethyl)-L-tyrosine (^{18}F-FET) is an advanced noninvasive imaging method for various disease-related indications of brain tumors (*1–5*). Combining it with MRI using a hybrid scanner may further improve its diagnostic validity (*6,7*). However, excellent diagnostic performance does not necessarily correlate with better patient outcomes. To determine a diagnostic procedure's actual clinical utility, one must additionally assess its impact on clinical management, patient-relevant outcomes, and cost-effectiveness (*8,9*).

There is limited evidence of the impact of PET on clinical decisions (*10*). Single studies have reported clinical management changes in a significant proportion of patients (*11–14*). Ideally, scientific studies should compare the clinical consequence of a new procedure with an established diagnostic test in a randomized, controlled design (*9,10*). This comparison can be challenging for several reasons. First, the patient outcome depends mainly on applied therapies. Extensive sample sizes will be needed to filter out a diagnostic procedure's small and multifold impact on a patient cohort with various therapeutic approaches (*15–17*). Also, an artificial patient selection may not reflect the disease's actual prevalence and distribution of clinical manifestations (*15*). Amino acid PET/MRI in brain tumors currently serves as add-on diagnostics in patients with equivocal findings on clinical routine MRI. A direct comparison of both modalities would not be helpful. Therefore, several authors recommend performing studies in a routine clinical setup (*15,16*).

Summarized, defining the impact of an imaging procedure such as PET/MRI is challenging but essential to establish an

Received Feb. 2, 2021; revision accepted Jul. 15, 2021.
For correspondence or reprints, contact Cornelia Brendle (cornelia.brendle@med.uni-tuebingen.de).
Published online Aug. 5, 2021.
COPYRIGHT © 2022 by the Society of Nuclear Medicine and Molecular Imaging

efficient application in clinical routine. We aimed to investigate the clinical consequences of multiparametric ^{18}F-FET PET/MRI in brain tumors by performing a structured evaluation of its diagnostic performance and impact on clinical management under real-world conditions.

MATERIALS AND METHODS

Patients and Data Collection

The institutional review board approved this retrospective study, and all subjects gave written informed consent. We retrospectively reviewed all ^{18}F-FET PET/MRI brain tumor examinations and disease outcomes in our institution in 2017 and 2018. Our institution treats over 600 newly diagnosed brain tumor patients per year. ^{18}F-FET PET/MRI serves as a second-line diagnostic procedure performed only on recommendation by a multidisciplinary tumor board in a minority of cases at both initial diagnosis and during the disease course. Thus, ^{18}F-FET PET/MRI is performed predominately in patients presenting with uncertain MRI features or an equivocal clinical course after or during treatment. We evaluated all clinical data from the patient reports of each medical specialty and the multidisciplinary neurooncologic tumor board. We recorded the patient age and sex, tumor pathology, periods between examinations, and follow-up duration. We also documented the medical history, including treatment recommendations immediately before the ^{18}F-FET PET/MRI examination, and the subsequent disease course, including pathologic examinations, subsequent therapies, clinical status, and imaging follow-up. In single cases, we could not retrieve retrospectively precise information about the treatment recommendations before ^{18}F-FET PET/MRI. The clinical specialists of the tumor board reviewed these cases for the study and determined the appropriate treatment recommendation.

^{18}F-FET PET/MRI Examinations and Data Analysis

All ^{18}F-FET PET/MRI examinations were performed on a hybrid 3-T PET/MRI scanner (Biograph mMR; Siemens Healthineers) for the clinical indication. An ultrashort-echo-time MRI sequence provided by the vendor was used for PET attenuation correction. The diagnostic MRI comprised sequences according to the standardized brain tumor protocol, dynamic susceptibility contrast perfusion MRI, and ^{1}H-MR spectroscopy (MRS) (*18–20*). Multislice dynamic susceptibility contrast perfusion MRI was assessed during the first pass of a 0.1 mmol/kg bolus of gadobutrol (Gadovist [Bayer Healthcare]; injection rate of 3 mL/s), 3 min after a 0.25 mmol/kg prebolus of gadobutrol. MRS was performed as a 2-dimensional multivoxel chemical-shift imaging technique based on a point-resolved MRS sequence with an echo time of 135 ms over a central slice of the tumor, including contrast-enhancing parts if present. We used syngo.via (Siemens Healthcare) to semiautomatically calculate the cerebral blood volume from the perfusion raw data (including software-based leakage correction) and to assess the MRS data. For the ^{18}F-FET PET, a 40-min dynamic emission recording in 3-dimensional mode consisting of 16 frames was started on injection of approximately 185 MBq of ^{18}F-FET. Dynamic and static PET data were reconstructed according to our clinical protocol using a 3-dimensional ordered-subset expectation-maximization algorithm and corrections for attenuation, scatter, random events, and dead time. ^{18}F-FET PET image analysis was performed as described previously and included the evaluation of both dynamic data (0–40 min after injection) and static images (summation of PET images between 20 and 40 min after injection) (*21*). ^{18}F-FET tracer kinetics and maximum tumor-to-background ratio (TBR_{max}) were assessed using a dedicated software package (Hermes Medical Solutions) following the current joint practice guidelines (*22*). To minimize MRI-related attenuation correction artifacts (especially for the kinetic analysis), we used a threshold-based segmentation with high thresholds, defining only the most metabolic active areas (*23*). The final interpretation of the multiparametric imaging results was produced by a board-certified neuroradiologist and nuclear medicine specialist in a clinical-routine consensus session masked to the future clinical course. Consensus reading routinely includes several measures: the presence of MRI contrast enhancement, visual hyperperfusion in dynamic susceptibility contrast perfusion MRI, a visually increased choline–to–*N*-acetyl-aspartate ratio in MRS, TBR_{max} in static ^{18}F-FET PET images, and the presence of a washout curve in the kinetic PET analysis. For evaluating the accuracy of single modalities, we focused on the presence of the results mentioned above from the original PET/MRI reports.

Our patient cohort was divided into 2 main categories following the indication of ^{18}F-FET PET/MRI: newly diagnosed tumors and progressive disease during or after postoperative therapy. To evaluate ^{18}F-FET PET/MRI prediction metrics, we used histologic confirmation or the disease course based on follow-up examinations as ground truth. At the new diagnosis, we rated whether malignancy (World Health Organization grades III and IV) was present. At detection of progression, we defined 2 dichotomic outputs: true progression or remission. In cases with follow-up as the reference standard, malignancy or true progression was defined by the continuing imaging expansion of a tumor beginning within 3 mo after ^{18}F-FET PET/MRI—the standard period until the first imaging follow-up—or by patient death within 6 mo. The absence of malignancy or progression was defined as clinically stable disease or regression without therapy for at least 6 mo. We judged other follow-up constellations as not assessable, for example, remission under continued or new therapy. Here, therapeutic effect on a vital tumor cannot be differentiated from the natural course of therapy-related changes. To estimate the impact of PET/MRI on clinical management, we tabulated the treatment changes after the disclosure of the imaging results (Table 1). We assessed whether ^{18}F-FET PET/MRI was causative for a treatment change. For example, we rated ^{18}F-FET PET/MRI as decisive if MRI could not determine true progression based on the Response Assessment for Neuro-Oncology criteria (*24,25*) but not if a treatment change was recommended before the examination but was realized only afterward.

Statistical Analysis

We tabulated a confusion matrix using the respective ^{18}F-FET PET/MRI single-modality outcomes and the reference standard and calculated commonly used performance metrics. Missing measurements (e.g., due to technical failure) were counted as false outcomes since they did not help solve the diagnostic question. For calculating the diagnostic performance of static ^{18}F-FET PET, we used the established TBR_{max} cutoff of 2.5 at new diagnosis (*22*). At detection of progression, we performed receiver-operating-characteristics analysis for the optimal TBR_{max} cutoff, as there is no general recommendation covering a heterogeneous patient cohort. We calculated the contribution of single modalities for best predicting the reference outcome by multiple-logistic-regression analysis. We noted the percentage of cases with treatment changes based on ^{18}F-FET PET/MRI results. JMP, version 15.1 (SAS), and statpages.org served as tools for the statistical calculations. In addition, we used SankeyMATIC (https://sankeymatic.com/) for building the Sankey diagrams.

RESULTS

Patients

A total of 172 brain tumor patients (median age, 53 y; range, 4–86 y, 71 females) received 201 ^{18}F-FET PET/MRI examinations in 2017 and 2018. Seventeen patients underwent 2, 6 patients 3, and 149 patients 1 examination. Finally, we included 189 ^{18}F-FET PET/MRI examinations for evaluating the impact on clinical management and 158 for assessing the diagnostic performance (Fig. 1 provides a flow chart; Supplemental Table 1, the specific tumor pathologies; and Supplemental Table 2, the imaging characteristics

TABLE 1
Categories of Clinical Management Changes Based on ^{18}F-FET PET/MRI

Management change	Criteria
Active treatment to monitoring	Waiving of invasive diagnostics for tumor characterization
	Waiving of surgery or adjuvant therapy during disease course
Monitoring to active treatment	Subsequent invasive diagnostics
	Treatment start
Therapy stratification	Shift from adjuvant therapy to surgery or reversely, or change of adjuvant treatment
	Begin of or waiving additional adjuvant treatment
	Waiving planned change and continuing present treatment
Treatment adaptation	Change of location or extent of biopsy or resection
	Adjustment of irradiation volume or chemotherapy dose

of the lesions) (supplemental materials are available at http://jnm.snmjournals.org). Histologic confirmation served as the reference standard in 32% of the cases (51/158; median interval to the PET/MRI, 17 d; range, 0–113 d), and clinical and imaging follow-up served as the reference standard in 68% (107/158; median duration, 14 mo; range, 0–45 mo). Overall, ^{18}F-FET PET/MRI reached an accuracy of 91% (95% CI, 85%–95%) and changed the clinical management in 47% of the cases (88/189; 95% CI, 40%–54%).

^{18}F-FET PET/MRI at a New Diagnosis

The new-diagnosis category included 58 ^{18}F-FET PET/MRI examinations. The indications leading to ^{18}F-FET PET/MRI consisted of grading of inhomogeneous masses with predominantly low-grade features (24%, 14/58), grading in tumor locations at risk for surgery complications (14%, 8/58), identification of hot spots for biopsies (16%, 9/58), or differentiation of glioma from other entities (47%, 27/58). The accuracy of ^{18}F-FET PET/MRI for identifying malignancy reached 85%, and the clinical management changed in 33% of the cases (19/58; 95% CI, 22%–46%) (Table 2; Fig. 2).

^{18}F-FET PET/MRI at Detection of Progression

In total, 131 ^{18}F-FET PET/MRI examinations were performed during the disease course. The mean disease duration was $2^1/_4$ y, and 79% (104/131) of the patients had undergone surgery. The number of previously received treatments was tabulated as follows: 1 standard adjuvant therapy, either combined radiochemotherapy, radiation, or chemotherapy (27%, 36/131); 1 advanced immunotherapy or experimental treatment (2%, 3/131); 2 or more standard adjuvant therapies (15%, 19/131); standard and advanced therapy (21%, 28/131); or no adjuvant therapy within the last year (34%, 45/131). The medical history leading to ^{18}F-FET PET/MRI was categorized as follows: baseline status before a new therapy (9%, 12/131), first progression under the current therapy through MRI (53%, 70/131) or with clinical symptoms (2%, 3/151), slight ongoing imaging progression (13%, 17/131), alternating imaging progression and regression (4%, 5/131), and ongoing imaging progression initially rated as therapy-associated change (18%, 24/131). ^{18}F-FET PET/MRI reached an accuracy of 93% in identifying true progression and changed the clinical management in 53% (69/131, 95% CI 44%–61%) of the cases (Table 2; Fig. 3).

The largest subgroup in this category constituted 62 IDH-wild-type high-grade gliomas (anaplastic astrocytomas, World Health Organization grade III, and glioblastomas, World Health Organization grade IV). Here, the prevalence of true progression was 90%, which was detected with an accuracy of 96% (95% CI, 87%–100%) through ^{18}F-FET PET/MRI. Subsequently, the clinical management changed in 47% of these patients (29/62; 95% CI, 35%–59%).

Contribution of Single Modalities to an Optimal Disease Prediction

MRS was the modality with the most artifacts (26%, 49/189), often because of unfavorable lesion localization for the acquisition or because of measurement missing the hotspot in large lesions (Supplemental Table 3 lists the artifacts of all modalities). At a new diagnosis, static ^{18}F-FET PET and contrast enhancement yielded the highest accuracies as single modalities (83% and 79%). They also contributed most to an optimal disease prediction ($P = 0.002$ and $P = 0.001$). At detection of progression, contrast enhancement and static ^{18}F-FET PET yielded the highest accuracies (80% and 79%). ^{18}F-FET kinetics and static ^{18}F-FET PET contributed most to an optimal disease prediction ($P = 0.006$ and $P = 0.009$; Supplemental Table 4; Table 3). Multiparametric ^{18}F-FET PET/MRI using standardized criteria yielded an accuracy of 87% at new diagnosis and 89% at detection of progression.

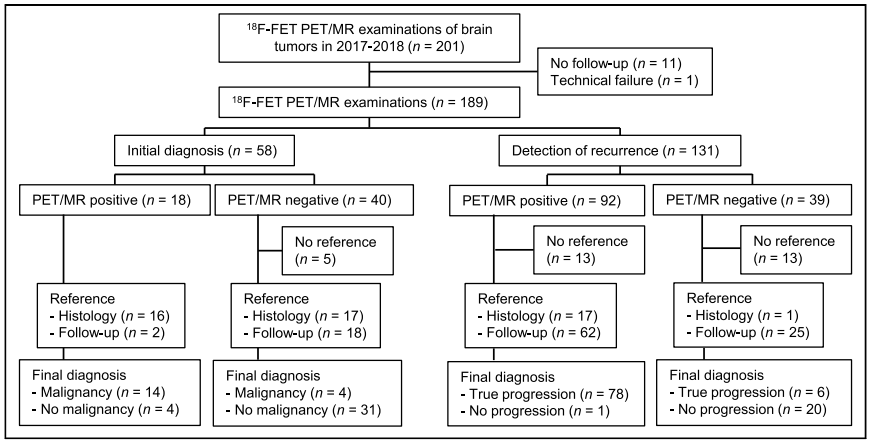

FIGURE 1. Flowchart of inclusion process for patients.

TABLE 2
Diagnostic Performance of ^{18}F-FET PET/MRI in Clinical Setting

Parameter	New diagnosis	Detection of progression
Total case number	53	105
Disease prevalence	34%	80%
True-positive/true-negatives	14/31	78/20
False-positives/false-negatives	4/4	1/6
Sensitivity	78% (52%–94%)	93% (85%–97%)
Positive predictive value	78% (57%–90%)	99% (92%–100%)
Specificity	89% (73%–97%)	95% (76%–100%)
Negative predictive value	89% (76%–95%)	77% (61%–88%)
Accuracy	85% (72%–93%)	93% (87%–97%)

Data in parentheses are 95% CIs.

DISCUSSION

The accuracy of ^{18}F-FET PET/MRI to identify malignancy at new diagnosis was 85%. The slightly lower sensitivity (78%) and slightly higher specificity (89%) than in a prior ^{18}F-FET PET metaanalysis might be due to a more conservative interpretation of imaging findings in our study (*1*). The high specificity and negative predictive value of ^{18}F-FET PET/MRI at new diagnosis might help rule out malignancy in untreated lesions. In accordance, 20% of the examined patients were able to avoid further invasive diagnostic procedures. Therefore, ^{18}F-FET PET/MRI at new diagnosis may particularly benefit the significant proportion of patients with nonmalignant brain tumors, for whom a watch-and-wait strategy is sufficient. MRI contrast enhancement and static ^{18}F-FET PET contributed most to the ^{18}F-FET PET/MRI outcome at new diagnosis. Surprisingly, the diagnostic performance of static ^{18}F-FET PET was almost as high as that of ^{18}F-FET PET/MRI. Also, the proportion of clinical management changes in 33% of the patients by ^{18}F-FET PET/MRI was in the range of prior reports for ^{11}C-methionine PET alone, with clinical management changes in 30%–63% of the patients (*11,14*). Therefore, adding static amino acid PET to an existing MRI examination might be a cost-effective alternative to the multiparametric examination. Still, different studies revealed the additional value of dynamic ^{18}F-FET PET for initial glioma staging, and this topic needs further evaluation (*26–28*).

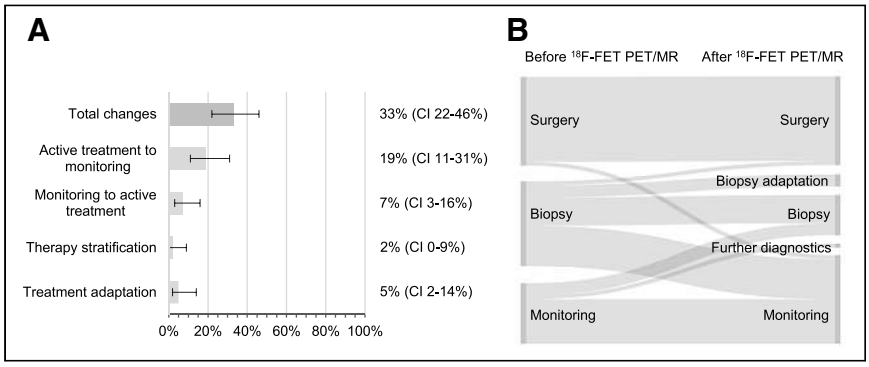

FIGURE 2. (A) Frequency (percentage with 95% CIs) of clinical management changes based on ^{18}F-FET PET/MRI outcome at new tumor diagnosis. Categories are as explained in Table 1. (B) Sankey diagram showing therapies recommended before and applied after ^{18}F-FET PET/MRI at new diagnosis.

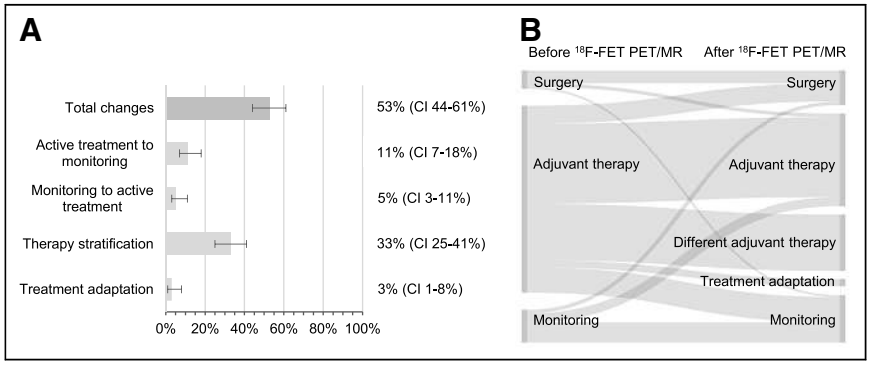

FIGURE 3. (A) Frequency (percentage with 95% CIs) of clinical management changes based on ^{18}F-FET PET/MRI outcome at detection of brain tumor progression. Categories are as explained in Table 1. (B) Sankey diagram showing therapies recommended before and applied after ^{18}F-FET PET/MRI at detection of progression.

At detection of progression, ^{18}F-FET PET/MRI reached an accuracy of 93%. The prevalence of true progression, at 80%, was high per se in our cohort. Nevertheless, ^{18}F-FET PET/MRI still improved the diagnostic validity. The positive predictive value reached nearly 100%, and the sensitivity (93%) and specificity (95%) were in the range of prior reports with amino acid PET/MRI (*29,30*). Dynamic ^{18}F-FET PET was the crucial component of the multiparametric examination at detection of progression. Nevertheless, the diagnostic performance of multiparametric ^{18}F-FET PET/MRI surpassed that of every single modality, and consensus reading with an individual interpretation of the results further improved the diagnostic security. ^{18}F-FET PET/MRI may save time by identifying

TABLE 3
Contribution of Single Modalities in Multiparametric ^{18}F-FET PET/MRI to Predict Outcome

Parameter	*P*	
	New diagnosis	Detection of progression
MRI contrast enhancement	0.001*	0.735
DSC MRI	0.480	0.411
MRS	0.229	0.814
Static ^{18}F-FET PET	0.002*	0.009*
^{18}F-FET tracer kinetics	0.939	0.006*

*Significant in multiple logistic regression.
DSC MRI = dynamic susceptibility contrast perfusion MRI.

true progression in lesions with first-time imaging progression during adjuvant therapy, whereas the Response Assessment for Neuro-Oncology criteria require confirmation by follow-up MRI. This condition applied to more than half our patients at detection of progression. The prompt diagnosis accelerates effective therapy decisions, benefiting patients with a severely reduced life expectancy. Additionally, ^{18}F-FET PET/MRI can clarify the nature of equivocal disease courses under therapy, another common condition in our cohort. ^{18}F-FET PET/MRI changed the clinical management in 53% of the cases at detection of progression, primarily resulting in an altered therapy stratification. This proportion was slightly higher than in a previous study with ^{11}C-methionine PET (*11*). On the basis of our results, the particular benefit of multiparametric ^{18}F-FET PET/MRI may be the confirmation of true progression since false-positive outcomes are scarce.

The full potential of advanced MRI techniques as components of ^{18}F-FET PET/MRI might not have unfolded in this study, as specialized studies reported higher accuracies (*31,32*). Dynamic susceptibility contrast perfusion MRI and MRS were hindered by acquisition failures and a lack of standardized quantification and might be of minor importance than amino acid PET according to our results. Future multicenter studies might explore the most efficient modality combination of ^{18}F-FET PET/MRI in glioma and whether the clinical impact is higher than with a separate acquisition of the modalities (*11,33*). Furthermore, we did not investigate the patient outcome and cost-effectiveness directly in our study. However, it seems reasonable that waiving unnecessary invasive procedures and fast-tracking clinical management decisions are beneficial (*11,34*). Adding ^{18}F-FET PET to MRI, such as in a hybrid scanner, has been reported to be reasonable in terms of cost-effectiveness in selected patients (*35–37*). Further studies considering these aspects might evaluate finally whether ^{18}F-FET PET/MRI as a hybrid modality qualifies for evidence-based use in clinical routine.

Our study has several limitations. The results when performing ^{18}F-FET PET/MRI examinations on clinical demand may differ from a randomized controlled trial. Our patient cohort was heterogeneous, and we did not evaluate specific histologic entities separately. The used attenuation correction for PET may have a minor impact on TBR_{max} and tracer kinetics, especially in patients with borderline findings. However, the impact can be minimized by a careful assessment of the multimodal datasets (*23*). Partially missing recommendations and clinical applications for standardized acquisition, image postprocessing, assessment, or quantification might lead to over- or underestimating the diagnostic performance of single modalities (*38*). A stepwise assessment of the single parameter's incremental value might better identify the most efficient composition of multiparametric ^{18}F-FET PET/MRI. Therefore, the exact data of this study are not generally transferable. However, it provides an exemplary insight into the actual impact of ^{18}F-FET PET/MRI on clinical management of brain tumor patients outside clinical trials.

CONCLUSION

^{18}F-FET PET/MRI has high accuracy in clarifying equivocal conditions in brain tumor patients, particularly at detection of progression. The clinical value of a simultaneous examination and the optimal modality combination need further exploration. At a new diagnosis, ^{18}F-FET PET/MRI appears to help rule out malignancy, with separate static ^{18}F-FET PET having a comparable accuracy. During the disease course, ^{18}F-FET PET/MRI facilitates clinical management by distinguishing between true tumor progression and therapy-related alterations.

DISCLOSURE

The work was funded by the Deutsche Forschungsgemeinschaft (DFG, German Research Foundation) under Germany's Excellence Strategy (EXC 2180-390900677). Ghazaleh Tabatabai has served on advisory boards for AbbVie, Bayer, and BMS; received consulting fees from AbbVie and Bayer; received speaker fees from Medac and Novocure; received travel grants from Novocure, Medac, and BMS; and received research grants from Roche Diagnostics and Medac, all not related to this work. Christian la Fougère has served on advisory boards for AAA, Bayer, ImaginAB, and SIRTEX; received consulting fees from Astellas and IPSEN; and received research grants from GE Healthcare, Siemens Healthineers, and Oncovision, all not related to this work. No other potential conflict of interest relevant to this article was reported.

KEY POINTS

QUESTION: Does ^{18}F-FET PET/MRI improve the clinical management of brain tumor patients with equivocal findings?

PERTINENT FINDINGS: We retrospectively evaluated the diagnostic performance of ^{18}F-FET PET/MRI and its impact on clinical management at new diagnosis of brain tumors and detection of progression. ^{18}F-FET PET/MRI identified malignancy or true progression with an accuracy of 91% and changed the clinical management in 47% of the cases.

IMPLICATIONS FOR PATIENT CARE: ^{18}F-FET PET/MRI as add-on diagnostics for equivocal findings in brain tumors might improve patients' outcome by increasing the diagnostic certainty and leading to prompt changes in clinical management at different disease stages.

REFERENCES

1. Treglia G, Muoio B, Trevisi G, et al. Diagnostic performance and prognostic value of PET/CT with different tracers for brain tumors: a systematic review of published meta-analyses. *Int J Mol Sci.* 2019;20:4669.

2. Vettermann F, Suchorska B, Unterrainer M, et al. Non-invasive prediction of IDH-wildtype genotype in gliomas using dynamic ^{18}F-FET PET. *Eur J Nucl Med Mol Imaging.* 2019;46:2581–2589.
3. Bauer EK, Stoffels G, Blau T, et al. Prediction of survival in patients with IDH-wildtype astrocytic gliomas using dynamic *O*-(2-[^{18}F]-fluoroethyl)-L-tyrosine PET. *Eur J Nucl Med Mol Imaging.* 2020;47:1486–1495.
4. Maurer GD, Brucker DP, Stoffels G, et al. ^{18}F-FET PET imaging in differentiating glioma progression from treatment-related changes: a single-center experience. *J Nucl Med.* 2020;61:505–511.
5. Albert NL, Weller M, Suchorska B, et al. Response Assessment in Neuro-Oncology Working Group and European Association for Neuro-Oncology recommendations for the clinical use of PET imaging in gliomas. *Neuro Oncol.* 2016;18:1199–1208.
6. Fink JR, Muzi M, Peck M, Krohn KA. Multimodality brain tumor imaging: MR imaging, PET, and PET/MR imaging. *J Nucl Med.* 2015;56:1554–1561.
7. Ferda J, Ferdova E, Hes O, Mracek J, Kreuzberg B, Baxa J. PET/MRI: multiparametric imaging of brain tumors. *Eur J Radiol.* 2017;94:A14–A25.
8. Fryback DG, Thornbury JR. The efficacy of diagnostic imaging. *Med Decis Making.* 1991;11:88–94.
9. Merlin T, Lehman S, Hiller JE, Ryan P. The "linked evidence approach" to assess medical tests: a critical analysis. *Int J Technol Assess Health Care.* 2013;29:343–350.
10. Siepe B, Hoilund-Carlsen PF, Gerke O, Weber WA, Motschall E, Vach W. The move from accuracy studies to randomized trials in PET: current status and future directions. *J Nucl Med.* 2014;55:1228–1234.
11. Yamane T, Sakamoto S, Senda M. Clinical impact of ^{11}C-methionine PET on expected management of patients with brain neoplasm. *Eur J Nucl Med Mol Imaging.* 2010;37:685–690.
12. Pfannenberg C, Gueckel B, Wang L, et al. Practice-based evidence for the clinical benefit of PET/CT: results of the first oncologic PET/CT registry in Germany. *Eur J Nucl Med Mol Imaging.* 2019;46:54–64.
13. Humbert O, Bourg V, Mondot L, et al. ^{18}F-DOPA PET/CT in brain tumors: impact on multidisciplinary brain tumor board decisions. *Eur J Nucl Med Mol Imaging.* 2019;46:558–568.
14. Pirotte B, Acerbi F, Lubansu A, Goldman S, Brotchi J, Levivier M. PET imaging in the surgical management of pediatric brain tumors. *Childs Nerv Syst.* 2007;23:739–751.
15. Valk PE. Randomized controlled trials are not appropriate for imaging technology evaluation. *J Nucl Med.* 2000;41:1125–1126.
16. Hillman BJ, Frank RA, Abraham BC. The Medical Imaging & Technology Alliance conference on research endpoints appropriate for Medicare coverage of new PET radiopharmaceuticals. *J Nucl Med.* 2013;54:1675–1679.
17. Vach W, Hoilund-Carlsen PF, Gerke O, Weber WA. Generating evidence for clinical benefit of PET/CT in diagnosing cancer patients. *J Nucl Med.* 2011;52(suppl 2):77S–85S.
18. Ellingson BM, Bendszus M, Boxerman J, et al. Consensus recommendations for a standardized brain tumor imaging protocol in clinical trials. *Neuro Oncol.* 2015;17:1188–1198.
19. Welker K, Boxerman J, Kalnin A, et al. ASFNR recommendations for clinical performance of MR dynamic susceptibility contrast perfusion imaging of the brain. *AJNR.* 2015;36:E41–E51.
20. Oz G, Alger JR, Barker PB, et al. Clinical proton MR spectroscopy in central nervous system disorders. *Radiology.* 2014;270:658–679.
21. Jansen NL, Graute V, Armbruster L, et al. MRI-suspected low-grade glioma: is there a need to perform dynamic FET PET? *Eur J Nucl Med Mol Imaging.* 2012;39:1021–1029.
22. Law I, Albert NL, Arbizu J, et al. Joint EANM/EANO/RANO practice guidelines/SNMMI procedure standards for imaging of gliomas using PET with radiolabelled amino acids and [^{18}F]FDG: version 1.0. *Eur J Nucl Med Mol Imaging.* 2019;46:540–557.
23. Rausch I, Zitterl A, Berroteran-Infante N, et al. Dynamic [^{18}F]FET-PET/MRI using standard MRI-based attenuation correction methods. *Eur Radiol.* 2019;29:4276–4285.
24. Wen PY, Macdonald DR, Reardon DA, et al. Updated response assessment criteria for high-grade gliomas: Response Assessment in Neuro-Oncology Working Group. *J Clin Oncol.* 2010;28:1963–1972.
25. Okada H, Weller M, Huang R, et al. Immunotherapy response assessment in neuro-oncology: a report of the RANO working group. *Lancet Oncol.* 2015;16:e534–e542.
26. Albert NL, Winkelmann I, Suchorska B, et al. Early static ^{18}F-FET-PET scans have a higher accuracy for glioma grading than the standard 20-40 min scans. *Eur J Nucl Med Mol Imaging.* 2016;43:1105–1114.
27. Suchorska B, Giese A, Biczok A, et al. Identification of time-to-peak on dynamic ^{18}F-FET-PET as a prognostic marker specifically in IDH1/2 mutant diffuse astrocytoma. *Neuro Oncol.* 2018;20:279–288.
28. Lohmann P, Herzog H, Rota Kops E, et al. Dual-time-point O-(2-[^{18}F]fluoroethyl)-L-tyrosine PET for grading of cerebral gliomas. *Eur Radiol.* 2015;25:3017–3024.
29. Deuschl C, Kirchner J, Poeppel TD, et al. ^{11}C-MET PET/MRI for detection of recurrent glioma. *Eur J Nucl Med Mol Imaging.* 2018;45:593–601.
30. Pyka T, Hiob D, Preibisch C, et al. Diagnosis of glioma recurrence using multiparametric dynamic ^{18}F-fluoroethyl-tyrosine PET-MRI. *Eur J Radiol.* 2018;103:32–37.
31. Delgado AF, Delgado AF. Discrimination between glioma grades II and III using dynamic susceptibility perfusion MRI: a meta-analysis. *AJNR.* 2017;38:1348–1355.
32. van Dijken BRJ, van Laar PJ, Holtman GA, van der Hoorn A. Diagnostic accuracy of magnetic resonance imaging techniques for treatment response evaluation in patients with high-grade glioma, a systematic review and meta-analysis. *Eur Radiol.* 2017;27:4129–4144.
33. Marner L, Nysom K, Sehested A, et al. Early postoperative ^{18}F-FET PET/MRI for pediatric brain and spinal cord tumors. *J Nucl Med.* 2019;60:1053–1058.
34. Merlin T. The use of the 'linked evidence approach' to guide policy on the reimbursement of personalized medicines. *Per Med.* 2014;11:435–448.
35. Miles KA, Voo SA, Groves AM. Additional clinical value for PET/MRI in oncology: moving beyond simple diagnosis. *J Nucl Med.* 2018;59:1028–1032.
36. Mayerhoefer ME, Prosch H, Beer L, et al. PET/MRI versus PET/CT in oncology: a prospective single-center study of 330 examinations focusing on implications for patient management and cost considerations. *Eur J Nucl Med Mol Imaging.* 2020;47:51–60.
37. Heinzel A, Muller D, Langen KJ, et al. The use of *O*-(2-^{18}F-fluoroethyl)-L-tyrosine PET for treatment management of bevacizumab and irinotecan in patients with recurrent high-grade glioma: a cost-effectiveness analysis. *J Nucl Med.* 2013;54:1217–1222.
38. Ladefoged CN, Law I, Anazodo U, et al. A multi-centre evaluation of eleven clinically feasible brain PET/MRI attenuation correction techniques using a large cohort of patients. *Neuroimage.* 2017;147:346–359.

Phase I Trial of ^{99m}Tc-(HE)$_3$-G3, a DARPin-Based Probe for Imaging of HER2 Expression in Breast Cancer

Olga Bragina[1,2], Vladimir Chernov[1,2], Alexey Schulga[2,3], Elena Konovalova[3], Eugeniy Garbukov[4], Anzhelika Vorobyeva[2,5], Anna Orlova[2,6], Liubov Tashireva[7], Jens Sörensen[8], Roman Zelchan[1,2], Anna Medvedeva[1], Sergey Deyev*[2,3], and Vladimir Tolmachev*[2,5]

[1]*Department of Nuclear Medicine, Cancer Research Institute, Tomsk National Research Medical Center, Russian Academy of Sciences, Tomsk, Russia;* [2]*Research Centrum for Oncotheranostics, Research School of Chemistry and Applied Biomedical Sciences, Tomsk Polytechnic University, Tomsk, Russia;* [3]*Shemyakin-Ovchinnikov Institute of Bioorganic Chemistry of the Russian Academy of Sciences, Moscow, Russia;* [4]*Department of General Oncology, Cancer Research Institute, Tomsk National Research Medical Center Russian Academy of Sciences, Tomsk, Russia;* [5]*Department of Immunology, Genetics and Pathology, Uppsala University, Uppsala, Sweden;* [6]*Department of Medicinal Chemistry, Uppsala University, Uppsala, Sweden;* [7]*Department of General and Molecular Pathology, Tomsk National Research Medical Center, Tomsk, Russia; and* [8]*Radiology and Nuclear Medicine, Department of Surgical Sciences, Uppsala University, Uppsala, Sweden*

Radionuclide molecular imaging of human epidermal growth factor receptor type 2 (HER2) expression may enable a noninvasive discrimination between HER2-positive and HER2-negative breast cancers for stratification of patients for HER2-targeted treatments. DARPin (designed ankyrin repeat proteins) G3 is a small (molecular weight, 14 kDa) scaffold protein with picomolar affinity to HER2. The aim of this first-in-humans study was to evaluate the safety, biodistribution, and dosimetry of ^{99m}Tc-(HE)$_3$-G3. **Methods:** Three cohorts of patients with primary breast cancer (each including at least 4 patients with HER2-negative and 5 patients with HER2-positive tumors) were injected with 1,000, 2,000, or 3,000 μg of ^{99m}Tc-(HE)$_3$-G3 (287 ± 170 MBq). Whole-body planar imaging followed by SPECT was performed at 2, 4, 6, and 24 h after injection. Vital signs and possible side effects were monitored during imaging and up to 7 d after injection. **Results:** All injections were well tolerated. No side effects were observed. The results of blood and urine analyses did not differ before and after studies. ^{99m}Tc-(HE)$_3$-G3 cleared rapidly from the blood. The highest uptake was detected in the kidneys and liver followed by the lungs, breasts, and small intestinal content. The hepatic uptake after injection of 2,000 or 3,000 μg was significantly ($P < 0.05$) lower than the uptake after injection of 1,000 μg. Effective doses did not differ significantly between cohorts (average, 0.011 ± 0.004 mSv/MBq). Tumor–to–contralateral site ratios for HER-positive tumors were significantly ($P < 0.05$) higher than for HER2-negative at 2 and 4 h after injection. **Conclusion:** Imaging of HER2 expression using ^{99m}Tc-(HE)$_3$-G3 is safe and well tolerated and provides a low absorbed dose burden on patients. This imaging enables discernment of HER2-positive and HER2-negative breast cancer. Phase I study data justify further clinical development of ^{99m}Tc-(HE)$_3$-G3.

Key Words: HER2; DARPin G3; ^{99m}Tc; SPECT; phase I

J Nucl Med 2022; 63:528–535
DOI: 10.2967/jnumed.121.262542

Breast cancer with high levels of human epidermal growth factor receptor type 2 (HER2) expression (3+ immunohistochemistry status) or *HER2* gene amplification (6 or more copies found using in situ hybridization measurements) is clinically defined as HER2-positive (*1*). HER2-positive tumors (15%–20% of total cases) respond to HER2-targeting therapeutics, such as the antibodies trastuzumab and pertuzumab, the tyrosine kinase inhibitor lapatinib, or trastuzumab-based antibody–drug conjugates. Information concerning HER2 expression levels is required for every invasive primary or recurrent breast cancer (*2*) as it is critical for making a decision to use HER2-targeting therapies. To determine HER2 expression in breast cancer, the American Society of Clinical Oncology and College of American Pathologists has recommended biopsy sampling, followed by testing using immunohistochemistry and in situ hybridization in the case of equivocal results from immunohistochemistry tests (*2*).

Although biopsy-based methodology is instrumental in clinical decision making, it is associated with several issues, such as HER2 expression heterogeneity, changing of HER2 expression levels with time, and poor accessibility of some metastases for sampling (*3,4*). Since radionuclide molecular imaging provides global information about HER2 expression and is noninvasive, and therefore might be used repeatedly, there is an appreciable interest to develop radiolabeled probes for HER2 visualization (*5–7*).

A common approach to imaging HER2 is through the use of therapeutic monoclonal antibodies labeled with long-lived positron emitters, for example, ^{89}Zr or ^{64}Cu, for PET imaging (*8*). However, the clearance of antibodies from the blood is slow, which is associated with a high background even 4–7 d after injection. Furthermore, harnessing the high sensitivity of PET is essential in this case. This approach is viable in Western Europe and North America, where PET infrastructure is routinely available. However, access to PET is limited in most of the world's populations living in Africa, Latin America, and Asia. For these regions, a ^{99m}Tc-labeled imaging probe would be desirable because SPECT cameras are much more common there.

The use of ^{99m}Tc-labeled engineered scaffold proteins for SPECT imaging is a feasible approach for HER2 imaging because these types of imaging probes provide a high contrast only several hours after injection, according to preclinical studies (*9*). Designed

Received May 5, 2021; revision accepted Jul. 22, 2021.
For correspondence or reprints, contact Vladimir Tolmachev (vladimir.tolmachev@igp.uu.se).
*Contributed equally to this work.
Published online Aug. 12, 2021.
COPYRIGHT © 2022 by the Society of Nuclear Medicine and Molecular Imaging.

ankyrin repeat proteins (DARPins) are one such promising class of engineered scaffold proteins, having small molecular weights (14–18 kDa), high affinity and specificity to selected targets, high chemical and thermal stability, and potentially low production costs (*10*). DARPin G3 binds to HER2 with an affinity of 90 pM and exquisite selectivity (*11*). Goldstein et al. demonstrated that ^{111}In-labeled G3 provides specific high-contrast imaging of HER2 in human xenografts in mice 4 h after injection (*12*). For site-specific labeling of G3 with ^{99m}Tc, we evaluated the use of $^{99m}Tc(CO)_3^+$ in combination with histidine-containing tags at different positions in the DARPin (*13*). For clinical translation, we selected DARPin $(HE)_3$-G3 with the HEHEHE-tag placed at the N terminus. This variant demonstrated significantly ($P < 0.05$) higher tumor-to-liver, tumor-to-muscle, and tumor-to-bone uptake ratios compared with the other tested variants. These higher uptake ratios indicated that the imaging contrast would be higher in the main metastatic sites of breast cancer.

The aim in this first-in-humans study was to evaluate the safety and distribution of ^{99m}Tc-$(HE)_3$-G3 in patients with primary HER2-positive and HER2-negative breast cancer.

The primary objectives of this study (ClinicalTrials.gov identifier: NCT04277338) were to obtain initial information concerning the safety and tolerability of ^{99m}Tc-$(HE)_3$-G3 after a single intravenous injection; to assess the distribution of ^{99m}Tc-$(HE)_3$-G3 in normal tissues and in tumors over time; and to evaluate the dosimetry of ^{99m}Tc-$(HE)_3$-G3.

The secondary objective was to compare the tumor imaging data with HER2 expression data obtained by immunohistochemistry and fluorescent in situ hybridization (FISH) analysis of biopsy samples.

Because clinical data for other scaffold proteins (*14,15*) had demonstrated that the mass of injected protein has a strong influence on its biodistribution and targeting properties, 3 levels of the injected protein mass (1,000, 2,000, and 3,000 μg) were tested.

MATERIALS AND METHODS

Patients

This was a prospective, open-label, nonrandomized phase I diagnostic study in patients with untreated primary breast cancer. Both the initial protocol and the further extension of patient cohorts were approved by the Scientific Council of the Cancer Research Institute and Board of Medical Ethics, Tomsk National Research Medical Center of the Russian Academy of Sciences, and all subjects provided written informed consent. Female patients (age, 18–80 y) with HER2 status previously determined using biopsy material from the primary tumor according to the guidelines of the American Society of Clinical Oncology (*2*) were eligible.

According to protocol, patients were divided into 3 cohorts (injected with 1,000, 2,000, or 3,000 μg of ^{99m}Tc-$(HE)_3$-G3), each including at least 5 patients with HER2-positive and at least 4 patients with HER2-negative tumors. Enrollment into the cohort with higher injected dose was initiated following accomplished safety evaluation for the preceding cohort with lower injected dose. In each cohort, consecutive patients were enrolled until required numbers for each category (HER2-positive and HER2-negative) were obtained.

The inclusion criteria were diagnosis of primary breast cancer with possible lymph node metastases; at least 1 lesion > 1.0 cm in greatest diameter; hematologic, liver, and renal function test results within the normal limits; a negative pregnancy test for patients of childbearing potential; and capability to undergo the diagnostic investigations planned in the study.

The exclusion criteria were other concurrent malignancies; autoimmune disease or history of autoimmune disease; and active infection or history of severe infection. One patient had a previous nephrectomy because of a car accident injury. Although such situations were not listed in the exclusion criteria, the patient was excluded from the study because this might influence the renal elimination rate and result in a nonrepresentative biodistribution pattern.

Twenty-eight patients were enrolled in the trial (Table 1; Fig. 1).

Mammograms (Giotto Image); biopsy samples; breast, regional lymph nodes, and liver ultrasound images (GE LOGIQ E9); bone scans (Siemens E.Cam 180) using ^{99m}Tc-pyrophosphate; and chest CT scans (Siemens Somatom Emotions 16 ECO) were obtained for all patients according to the local standard of care.

The level of HER2 expression in biopsy samples was determined by immunohistochemistry using the Herceptest (DAKO). In tumors with a score of 2+ or in cases of questionable results, HER2 amplification was assessed by FISH using a KBI-10701 probe (Kreatech). To confirm imaging results, FISH analysis was performed after imaging for all patients. The tumors were classified as HER2-positive (HercepTest score 3+ or HercepTest score 2+ and FISH-positive) and HER2-negative (HercepTest score 0 or 1+, or score 2+ but FISH-negative).

Imaging Protocol

$(HE)_3$-G3 was labeled with ^{99m}Tc using the protocol reported earlier (*13*). The yield was 83% ± 9% and the radiochemical purity was more than 98%.

^{99m}Tc-$(HE)_3$-G3 was injected as an intravenous bolus. The injected protein dose was 1,000 μg of $(HE)_3$-G3 for patients 1–9, 2,000 μg of $(HE)_3$-G3 for patients 10–18, and 3,000 μg of $(HE)_3$-G3 for patients 19–29. The average injected activity was 287 ± 170 MBq. A Siemens E.Cam 180 scanner equipped with a high-resolution low-energy collimator was used for imaging. Anterior and posterior whole-body planar imaging (at a scan speed of 12 cm/min, 1,024 × 256 pixel matrix) and SPECT scanning (32 projections, 30 s each, 128 × 128 pixel matrix) were performed at 2, 4, 6, and 24 h. The SPECT data were reconstructed by iterative reconstruction with a gaussian filter and the application of scatter correction using the E.Soft computer system for scintigraphic data processing. Patient 27 was imaged using a Siemens Symbia Intevo Bold scanner equipped with a high-resolution low-energy collimator. Whole-body imaging (at 2, 4, 6, and 24 h) and SPECT scanning (at 4, 6, and 24 h) were performed in the same mode as above. After 2 h, 2 SPECT/CT bed scans were obtained (60 projections, 20 s each, 256 × 256 pixel matrix, 130 kV, effective 36 mAs).

Vital signs and possible side effects were monitored during the investigation (0–24 h after injection) and 3–7 d after the injection. Blood and urine analyses were performed 1 and 3 d after the injection.

Evaluation of Distribution and Dosimetry

Regions of interest (ROI) were drawn over organs of interest and the body contour on the anterior and posterior whole-body images, and a geometric mean of counts at 2, 4, 6, and 24 h was calculated for each ROI. For quantification, a known activity of ^{99m}Tc in a water-filled phantom in combination with Chang's correction was used. A ROI was placed over the heart to assess the activity in the blood. Data were fitted to single exponential functions, and residence times were calculated as areas under fitted curves using Prism 8 (GraphPad Software, LLC). Absorbed doses were calculated by OLINDA/EXM 1.1 using an adult female phantom.

To calculate tumor–to–contralateral breast and tumor-to-liver ratios, a 3.5-cm^3 volume of interest was drawn on tomograms centered on the highest tumor uptake, and counts were recorded. Thereafter, this volume of interest was copied to the contralateral breast to obtain reference counts. The tumor–to–contralateral breast ratio for each primary tumor was calculated and matched with the biopsy-based data concerning HER2 expression in the same tumor.

Statistics

Values are reported as mean ± SD. Differences between uptake in organs at different time points were analyzed using 1-way ANOVA.

TABLE 1
Patient Characteristics

Patient	Age (y)	HER2 status in primary tumor before imaging (IHC/FISH)	*HER2* gene amplification (determined after imaging)	Primary tumor status (ER/PgR)	Clinical stage before imaging
1,000 μg; mean tumor size, 28 ± 11 mm					
1	68	1+ (IHC)	FISH-	ER+/PgR-	IIA (T2N0M0)
2	62	1+ (IHC)	FISH-	ER+/PgR+	I (T1N0M0)
3	66	1+ (IHC)	FISH-	ER+/PgR+	IIA (T2N0M0)
4	48	0 (IHC)	FISH-	ER-/PgR-	IIA (T2N0M0)
5	50	3+ (IHC)	FISH+	ER+/PgR+	IIA (T2N0M0)
6	70	3+ (IHC)	FISH-	ER+/PgR+	IIA (T2N0M0)
7	30	3+ (IHC)	FISH+	ER+/PgR+	IIB (T2N1M0)
8	59	2+ (IHC)/FISH+		ER-/PgR-	IIA (T2N0M0)
9	45	(IHC)3+	FISH-	ER+/PgR-	IIB (T2N1M0)
2,000 μg; mean tumor size, 25 ± 6 mm					
10	50	1+ (IHC)	FISH-	ER+/PgR+	IIA (T2N0M0)
11	57	1+ (IHC)	FISH-	ER+/PgR+	I (T1N0M0)
12	43	1+ (IHC)	FISH-	ER+/PgR+	IIA (T2N0M0)
13	51	1+ (IHC)	FISH-	ER-/PgR-	IIA (T2N0M0)
14	65	3+ (IHC)	FISH+	ER+/PgR+	IIA (T2N0M0)
15	35	3+ (IHC)	FISH+	ER+/PgR+	I (T1N0M0)
16	50	1+ (IHC)*	FISH+	ER+/PgR+	IIA (T2N0M0)
17	68	2+ (IHC)/FISH+		ER+/PgR-	IIA (T2N0M0)
18	68	3+ (IHC)	FISH+	ER+/PgR+	IIA (T2N0M0)
3,000 μg; mean tumor size 22 ± 7 mm					
19	37	1+ (IHC)	FISH-	ER-/PgR-	IIA (T2N0M0)
20	45	1+ (IHC)	FISH-	ER+/PgR+	IIA (T2N0M0)
21	56	1+ (IHC)	FISH-	ER+/PgR+	IIA (T2N0M0)
22	45	1+ (IHC)	FISH-	ER+/PgR+	IIA (T2N0M0)
23	36	1+ (IHC)	FISH-	ER+/PgR+	IIA (T2N0M0)
24	48	3+ (IHC)	FISH+	ER+/PgR+	IIB (T2N1M0)
25	58	3+ (IHC)	FISH+	ER+/PgR+	IIA (T2N0M0)
26	47	1+ (IHC)*	FISH+	ER+/PgR+	IIA (T2N0M0)
27	61	3+ (IHC)	FISH+	ER+/PgR-	IV (T4N3M1)
28	49	3+ (IHC)	FISH+	ER+/PgR+	I (T1N0M0)

*Postimaging FISH evaluation demonstrated *HER2* gene amplification.
IHC = immunohistochemistry; ER = estrogen receptor; PgR = progesterone receptor; + = positive; - = negative.

The nonparametric Mann–Whitney *U* test was used to determine whether the differences between tumor–to–contralateral breast ratios for HER2-positive and HER2-negative tumors were significant. A 2-sided *P* value of less than 0.05 was considered significant.

RESULTS

Safety and Tolerability

The intravenous bolus administration of ^{99m}Tc-(HE)$_3$-G3 was well tolerated by all 29 patients, independent of the injected protein mass. Changes in vital signs or adverse reactions were not registered during imaging or the follow-up period. No relevant changes in blood or urine samples were found after their analyses.

Evaluation of Distribution and Dosimetry

The kinetics of ^{99m}Tc-(HE)$_3$-G3 elimination from blood is shown in Figure 2. The elimination half-lives were comparable for all injected protein doses. These elimination half-lives were 3.5 h (95% CI 2.3–6.0 h), 3.8 h (95% CI 3.4–4.3 h), and 3.4 h (95% CI 2.6–4.6 h) for 1,000 μg, 2,000 μg, and 3,000 μg, respectively.

The kidneys and liver were the organs with the highest uptake of activity (Table 2; Fig. 3). Noticeable activity was also observed in the

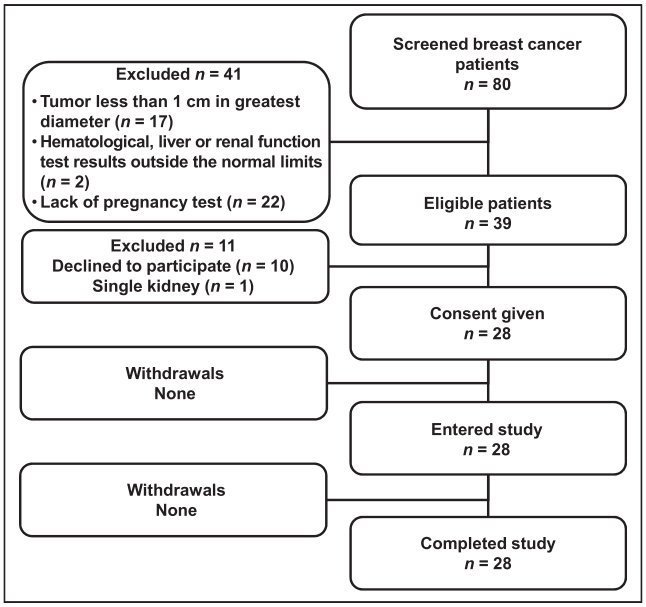

FIGURE 1. Standards for Reporting of Diagnostic Accuracy Studies (STARD) flow diagram.

lungs, small intestines, and lacrimal and salivary glands. Injections with 2,000 and 3,000 μg resulted in a significant ($P < 0.05$) reduction in hepatic uptake compared with 1,000-μg injections. The difference between hepatic uptake after injection with 2,000 and 3,000 μg was not significant, although there was a strong tendency toward reduced uptake with an increase in injected mass (R^2 in the range between 0.86 and 0.95) (Supplemental Fig. 1; supplemental materials are available at http://jnm.snmjournals.org). The decay-corrected uptake in the liver and kidneys did not differ significantly between 2 and 24 h. There was a significant gradual decrease in uptake in the small intestines and lungs between the first and last time points.

The evaluation of the absorbed doses is shown in Table 3. The highest absorbed dose was in the kidneys, followed by the adrenals, urinary bladder wall, liver, gallbladder wall, and ovaries. The absorbed dose to the liver was significantly ($P < 0.05$) higher after injection with 1,000 μg than after injection with 2,000 and 3,000 μg. The effective doses were 0.011 ± 0.001, 0.012 ± 0.006, and 0.012 ± 0.003 mSv/MBq for 1,000, 2,000 and 3,000 μg, respectively. An

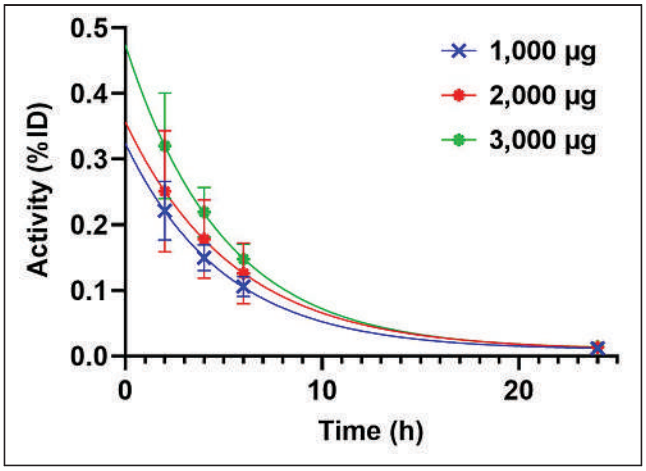

FIGURE 2. Kinetics of elimination of ^{99m}Tc-(HE)$_3$-G3 from blood. Data were calculated on the basis of count rates in ROIs placed over hearts.

TABLE 2
Uptake of ^{99m}Tc in Tumor-Free Areas of Organs with Highest Uptake on SPECT Images After Injection of ^{99m}Tc-(HE)$_3$-G3 (Decay Corrected)

Organ	2 h			4 h			6 h			24 h		
	1,000 μg	2,000 μg	3,000 μg	1,000 μg	2,000 μg	3,000 μg	1,000 μg	2,000 μg	3,000 μg	1,000 μg	2,000 μg	3,000 μg
Breast	2.1 ± 0.6	2.4 ± 0.6	2.4 ± 0.6	2.1 ± 0.4	2.0 ± 0.5	2.1 ± 0.5	2.3 ± 1.1	1.8 ± 0.5	1.9 ± 0.3	1.7 ± 0.2	1.7 ± 0.5	1.6 ± 0.4
Small intestines	2.5 ± 0.6	2.4 ± 0.5	2.9 ± 0.6	2.1 ± 0.4	2.2 ± 0.4	2.5 ± 0.6	2.1 ± 0.8	1.9 ± 0.5	2.0 ± 0.4	1.7 ± 0.4	1.7 ± 0.5	1.8 ± 0.6
Kidney	24 ± 5	28 ± 6	29 ± 11	22 ± 5	28 ± 6	29 ± 11	24 ± 5	28 ± 6	29 ± 11	21 ± 5	21 ± 5	26 ± 12
Liver	11 ± 2	6 ± 2*	5 ± 2*	12 ± 4	6 ± 2*	5 ± 2*	10 ± 3	6 ± 2*	4 ± 1*	9 ± 3	5 ± 2*	4 ± 2*
Lungs	2.4 ± 0.6	2.4 ± 0.7	2.7 ± 0.9	2.2 ± 0.5	2.2 ± 0.7	2.2 ± 0.6	1.9 ± 0.6	2.0 ± 0.6	2.0 ± 0.4	1.9 ± 0.5	1.8 ± 0.6	1.6 ± 0.4

*Significant difference in uptake compared with injection of 1,000 μg ^{99m}Tc-(HE)$_3$-G3.

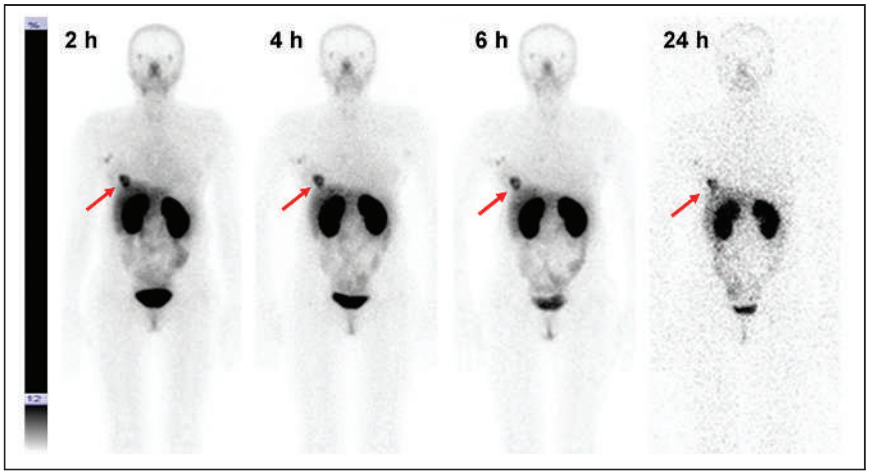

FIGURE 3. Anterior planar images at 2, 4, 6, and 24 h after injection of 3,000 μg of ^{99m}Tc-(HE)$_3$-G3 (patient 24). Upper setting of scale window is 12% of maximum counts. Arrows point at lesions.

effective dose of 3.2–3.4 mSv would result from the typical injected activity of 250 MBq used in this study.

Discrimination Between Tumors with High and Low HER2 Expression

Imaging using ^{99m}Tc-(HE)$_3$-G3 enabled the visualization of all known tumors (including HER2-negative tumors) already 2 h after injection (Figs. 3 and 4). HER2-positive tumors remained visible at all time points, but HER2-negative tumors could not be visualized 24 h after injection. Involved lymph nodes were also visualized in 9 patients. The involvement of lymph nodes was confirmed by histologic analysis after core biopsies ($n = 2$) or cytologic analysis after fine-needle biopsies ($n = 7$).

TABLE 3
Absorbed Doses after Injection of 1,000, 2,000, and 3,000 μg of ^{99m}Tc-(HE)$_3$-G3

Site	Absorbed dose, mGy/MBq		
	1,000 μg	2,000 μg	3,000 μg
Adrenals	0.031 ± 0.007	0.031 ± 0.007	0.032 ± 0.002
Brain	0.0010 ± 0.0004	0.0011 ± 0.0002	0.0012 ± 0.0001
Breasts	0.008 ± 0.002	0.007 ± 0.001	0.008 ± 0.001
Gallbladder wall	0.017 ± 0.003	0.015 ± 0.004	0.014 ± 0.002
LLI wall	0.005 ± 0.001	0.006 ± 0.003	0.006 ± 0.001
Small intestine	0.0076 ± 0.0010	0.009 ± 0.004	0.009 ± 0.002
Stomach wall	0.0060 ± 0.0008	0.006 ± 0.001	0.007 ± 0.002
ULI wall	0.007 ± 0.001	0.008 ± 0.003	0.009 ± 0.002
Heart wall	0.004 ± 0.001	0.004 ± 0.001	0.0042 ± 0.0007
Kidneys	0.10 ± 0.02	0.10 ± 0.03	0.13 ± 0.05
Liver	0.016 ± 0.003	0.011 ± 0.003*	0.0100 ± 0.0008*
Lungs	0.005 ± 0.001	0.005 ± 0.001	0.006 ± 0.001
Muscle	0.0024 ± 0.0005	0.003 ± 0.001	0.0028 ± 0.0007
Ovaries	0.014 ± 0.005	0.014 ± 0.008	0.013 ± 0.003
Pancreas	0.012 ± 0.001	0.013 ± 0.003	0.016 ± 0.004
Red marrow	0.0033 ± 0.0007	0.004 ± 0.001	0.004 ± 0.001
Osteogenic cells	0.006 ± 0.002	0.006 ± 0.002	0.007 ± 0.001
Skin	0.0014 ± 0.0004	0.0015 ± 0.0003	0.0017 ± 0.0003
Spleen	0.010 ± 0.001	0.010 ± 0.003	0.012 ± 0.004
Thymus	0.006 ± 0.001	0.007 ± 0.003	0.0068 ± 0.0002
Thyroid	0.017 ± 0.003	0.018 ± 0.005	0.022 ± 0.003
Urinary bladder wall	0.013 ± 0.007	0.014 ± 0.009	0.019 ± 0.007
Uterus	0.008 ± 0.002	0.055 ± 0.01	0.009 ± 0.003
Total body	0.004 ± 0.001	0.004 ± 0.001	0.004 ± 0.001
Effective dose equivalent (mSv/MBq)	0.017 ± 0.002	0.020 ± 0.012	0.019 ± 0.005
Effective dose (mSv/MBq)	0.011 ± 0.001	0.012 ± 0.006	0.012 ± 0.003

*Significant ($P < 0.05$) difference with absorbed dose after the injection of 1,000 μg ^{99m}Tc-(HE)$_3$-G3.
LLI = lower large intestine; ULI = upper large intestine.

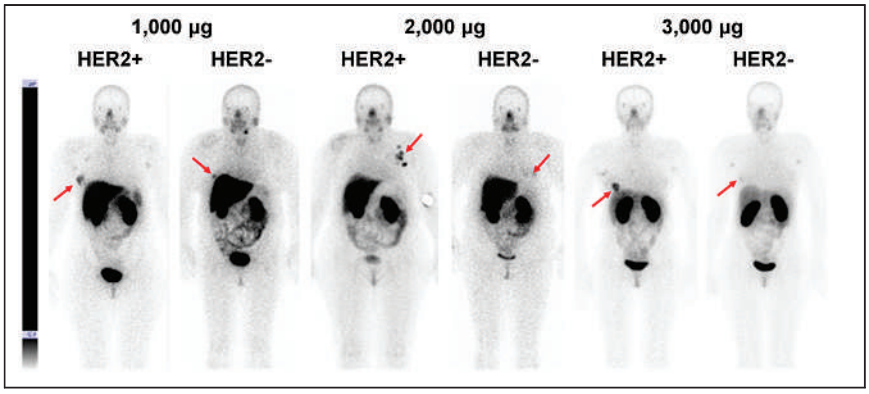

FIGURE 4. Representative anterior planar images of patients with HER2-positive and HER2-negative tumors 4 h after injections of 1,000, 2,000, or 3,000 µg of ^{99m}Tc-$(HE)_3$-G3. Upper setting of scale window is same for all images, 12% of maximum count rate. Arrows point at lesions.

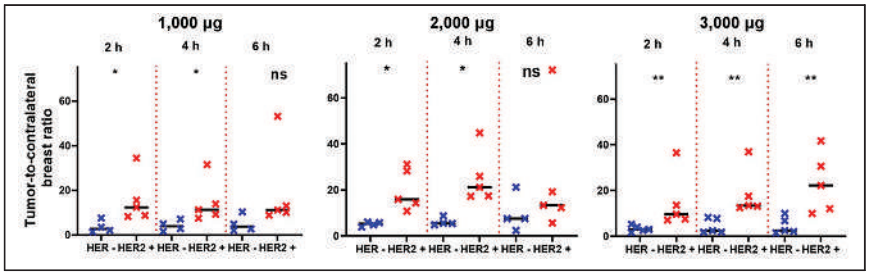

FIGURE 5. Primary tumor–to–contralateral site ratios after injections of 1,000, 2,000, and 3,000 µg of ^{99m}Tc-$(HE)_3$-G3. *Marks significant ($P < 0.05$) difference. **Marks highly significant ($P < 0.01$) difference. ns = not significant.

Tumor–to–contralateral site ratios were significantly higher ($P < 0.05$, Mann–Whitney test) for HER2-positive than for HER2-negative tumors at 2 and 4 h after injection with 1,000 and 2,000 µg, but the difference was not significant 6 h after injection (Fig. 5). Tumor–to–contralateral ratios after injection with 3,000 µg were significantly ($P < 0.05$, Mann–Whitney test) higher for HER2-positive tumors at 2, 4, and 6 h after injection (Fig. 5).

Patient 26 was enrolled in this study as a patient with a HER2-negative tumor based on a 1+ immunohistochemistry score from her core biopsy sample (Fig. 6A). However, the tumor–to–contralateral breast ratio was unusually high (12.5 at 2 h, 3,000-µg dose) for a patient with a HER2-negative lesion (Fig. 6B). On our request, her surgery samples were evaluated, and 35% of the tumor was found to display elevated HER2 expression from immunohistochemistry (Fig. 6C) while the rest of the tumor was HER2-negative (Fig. 6D). On the basis of this finding, trastuzumab treatment was added to her adjuvant therapy. Similarly, a high tumor–to–contralateral site ratio (14.4 at 2 h, 2,000-µg dose) for patient 16 prompted the reevaluation of her biopsy samples using a FISH analysis, which actually suggested a HER2-positive tumor. Further postimaging FISH analysis demonstrated agreement between IHC and FISH data for all other patients except from patient 6, who had HER2 overexpression without gene amplification.

Patient 27 was enrolled in the study with a large HER2-positive inflammatory breast cancer with axillary node involvement, as well as suspected metastatic sites in the liver. ^{99m}Tc-$(HE)_3$-G3 imaging demonstrated multiple sites of abnormal accumulation of activity. Presence of metastases in the sites of abnormal accumulation in, for example, the liver (Fig. 7A, tumor–to–reference zone ratio 2.97) and iliac bone (Fig. 7C, tumor–to–reference zone ratio 9.5), was confirmed by diagnostic CT images (Figs. 7B and 7D).

DISCUSSION

Numerous preclinical studies have demonstrated that small scaffold proteins are promising types of probes for molecular imaging (*16*). Still, only a limited number of such probes have been tested in clinical trials: Affibody molecules (*17*), ADAPTs (*15*), and adnectins (*18*). At the same time, scaffold proteins represents a large variety of molecular forms with different structures, charges and lipophilicity of solvent-exposed amino acids (*19*). These features can substantially modify off-target interactions, impact the biodistribution of these probes, and influence their imaging contrast. Such considerations necessitate the clinical evaluation of different scaffolds to select the most promising ones.

This study demonstrated that the injection of DARPins (up to 3 mg) is well tolerated and not associated with any adverse effects. A combination of rapid systemic clearance and the favorable dosimetry properties of ^{99m}Tc ensured a moderate effective dose. In the current study, typical equivalent doses were 3.2–3.4 mSv. However, because the optimal imaging time is between 4 and 6 h, the injected activity could still be reduced at least twice and accordingly further reduce the dose burden to patients. This aspect

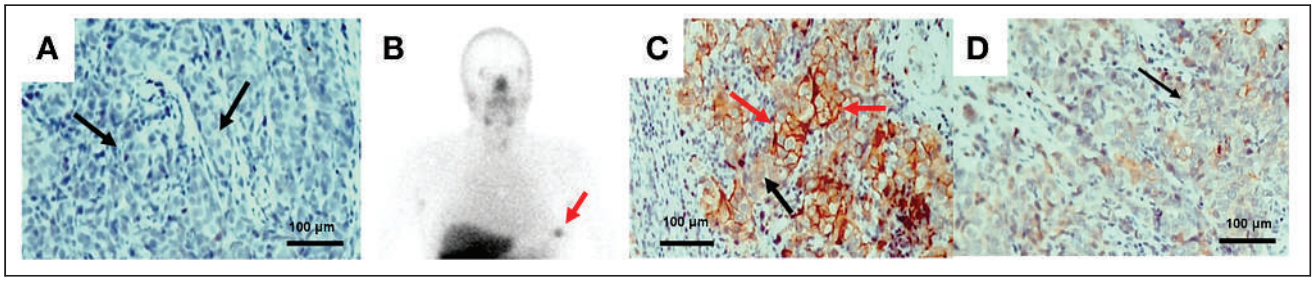

FIGURE 6. Patient 26. (A) Immunohistochemistry analysis shows very low HER2 expression in biopsy material. (B) Anterior planar image at 4 h after injection; upper setting of scale window is 12% of maximum counts, showing tumor–to–contralateral site ratio typical for HER2-positive tumors. Immunohistochemistry analysis of surgery material shows areas with high (B) and low (C) HER2 expression. Magnification 400×. Black arrows show cells with low and red arrows show cells with high HER2 expression. Arrows point at tumor.

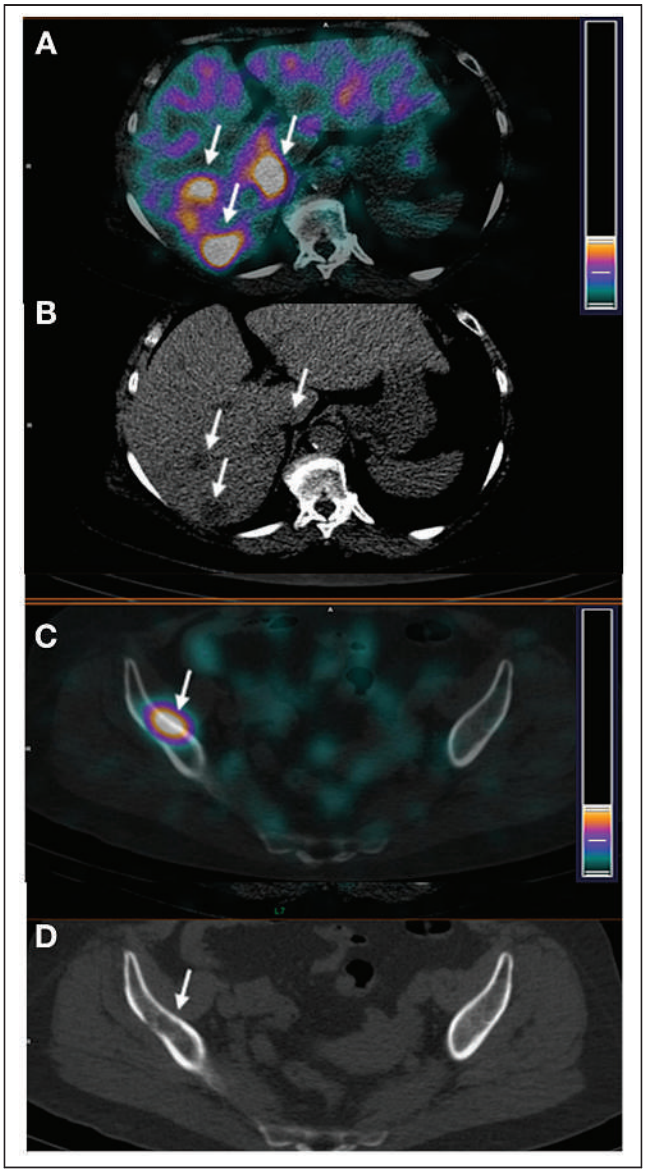

FIGURE 7. Patient 27. SPECT/CT (A) and CT (B) images of hepatic lesions. SPECT/CT (C) and CT (D) images of iliac bone lesions. Arrows point at lesions.

offers advantages compared with immuno-PET, where the radiation burden is higher by an order of magnitude.

The important features of ^{99m}Tc-(HE)$_3$-G3 are rapid localization in tumors and quick clearance from the blood (Fig. 3). Both of these features might be explained by the small size of this targeting probe and they enabled the clear visualization of tumors as early as 2 h after injection (Fig. 3). It should also be noted that cells in clinically defined HER2-negative tumors (immunohistochemistry score of 2+ and FISH-negative) might still express hundreds of thousands of HER2 receptors per cell (*20*). Accordingly, HER2-negative tumors were also visualized (Fig. 4). However, tumor–to–contralateral breast ratios were significantly ($P < 0.05$, Mann–Whitney test) higher for HER2-positive lesions at 2 and 4 h in 1,000-μg and 2,000-μg cohorts, and at 2, 4, and 6 h in the 3,000-μg cohort (Fig. 5). Such a simple approach is feasible even in developing countries as it does not require regular exact calibration of SPECT cameras. Unexpectedly, HER2 imaging using ^{99m}Tc-(HE)$_3$-G3 has already proved its worth in this study. High tumor–to–contralateral breast ratios triggered the reevaluation of HER2 status for patients 16 and 26, who were enrolled in this trial as having HER2-negative tumors. In both cases, a HER2-positive status has been confirmed, indicating that radionuclide molecular imaging can overcome the limitations of biopsy-based methods caused by heterogeneous target expression and associated sampling errors.

The aspect of injected mass was found essential in earlier studies with Affibody molecules (*14,17*) and ADAPT6 (*15*). When a low protein mass is injected (100 μg for Affibody molecules or 250 μg for ADAPT6 in the case of HER2 imaging), the binding to HER2 expressed on hepatocytes results in a high liver uptake and sequestration of the probe from circulation. This prevents delivery of the radionuclide to tumors and increases the background during the imaging of liver metastases, which are common in breast cancer. The current study demonstrated that optimization of the injected mass is essential for DARPin-based HER2 imaging probes as well. An increase of the injected mass from 1,000 to 3,000 μg decreased hepatic uptake by more than half (Table 2; Supplemental Fig. 1). This decrease of hepatic uptake created a precondition for the clear visualization of HER2-positive liver metastases in patient 27 (Fig. 7). The example of patient 27 indicates that ^{99m}Tc-(HE)$_3$-G3 has the capability to enable visualization of metastases in multiple locations, including the bone and liver. Ultimately, the tracer should be used for detection of HER2 expression in metastatic breast cancer. Such findings during the phase I trial motivate its further development.

CONCLUSION

Injections of ^{99m}Tc-(HE)$_3$-G3 are safe and result in low absorbed and effective doses. Preliminary data suggest that SPECT/CT using ^{99m}Tc-(HE)$_3$-G3 could distinguish HER2-positive from HER2-negative primary breast cancer. An injected protein mass between 2,000 and 3,000 μg is desirable to suppress hepatic uptake. Further clinical development of ^{99m}Tc-(HE)$_3$-G3 for imaging of HER2 expression in cancers is warranted.

DISCLOSURE

This research was financially supported by the Ministry of Science and Higher Education of the Russian Federation (grant 075-15-2019-1925). No other potential conflict of interest relevant to this article was reported.

KEY POINTS

QUESTION: Is the use of ^{99m}Tc-(HE)$_3$-G3 for HER2 imaging tolerable, safe, and informative?

PERTINENT FINDINGS: ^{99m}Tc-(HE)$_3$-G3 is safe, is associated with low dose burdens, and enables the differentiation of HER2-positive and HER2-negative primary breast cancer lesions at 2–4 h after injection.

IMPLICATION FOR PATIENT CARE: Results from this study suggest that further clinical development of ^{99m}Tc-(HE)$_3$-G3 might provide a probe for the SPECT imaging of HER2 expression.

REFERENCES

1. Loibl S, Gianni L. HER2-positive breast cancer. *Lancet.* 2017;389:2415–2429.
2. Wolff AC, Hammond MEH, Allison KH, et al. Human epidermal growth factor receptor 2 testing in breast cancer: American Society of Clinical Oncology/College of American Pathologists clinical practice guideline focused update. *J Clin Oncol.* 2018;36:2105–2122.
3. Van Poznak C, Somerfield MR, Bast RC, et al. Use of biomarkers to guide decisions on systemic therapy for women with metastatic breast cancer: American Society of Clinical Oncology clinical practice guideline. *J Clin Oncol.* 2015;33: 2695–2704.
4. Niikura N, Tomotaki A, Miyata H, et al. Changes in tumor expression of HER2 and hormone receptors status after neoadjuvant chemotherapy in 21,755 patients from the Japanese breast cancer registry. *Ann Oncol.* 2016;27:480–487.
5. Gebhart G, Lamberts LE, Wimana Z, et al. Molecular imaging as a tool to investigate heterogeneity of advanced HER2-positive breast cancer and to predict patient outcome under trastuzumab emtansine (T-DM1): the ZEPHIR trial. *Ann Oncol.* 2016;27:619–624.
6. Mankoff DA, Edmonds CE, Farwell MD, Pryma DA. Development of companion diagnostics. *Semin Nucl Med.* 2016;46:47–56.
7. Tolmachev V, Orlova A, Sörensen J. The emerging role of radionuclide molecular imaging of HER2 expression in breast cancer. *Semin Cancer Biol.* 2021 Jan 16: S1044-579X(20)30210-8.
8. Henry KE, Ulaner GA, Lewis JS. Human epidermal growth factor receptor 2-targeted PET/single- photon emission computed tomography imaging of breast cancer: noninvasive measurement of a biomarker integral to tumor treatment and prognosis. *PET Clin.* 2017;12:269–288.
9. Garousi J, Orlova A, Frejd FY, Tolmachev V. Imaging using radiolabelled targeted proteins: radioimmunodetection and beyond. *EJNMMI Radiopharm Chem.* 2020;5:16.
10. Plückthun A. Designed ankyrin repeat proteins (DARPins): binding proteins for research, diagnostics, and therapy. *Annu Rev Pharmacol Toxicol.* 2015;55: 489–511.
11. Zahnd C, Wyler E, Schwenk JM, et al. A designed ankyrin repeat protein evolved to picomolar affinity to Her2. *J Mol Biol.* 2007;369:1015–1028.
12. Goldstein R, Sosabowski J, Livanos M, et al. Development of the designed ankyrin repeat protein (DARPin) G3 for HER2 molecular imaging. *Eur J Nucl Med Mol Imaging.* 2015;42:288–301.
13. Vorobyeva A, Schulga A, Konovalova E, et al. Optimal composition and position of histidine-containing tags improves biodistribution of ^{99m}Tc-labeled DARPin G3. *Sci Rep.* 2019;9:9405.
14. Sandström M, Lindskog K, Velikyan I, et al. Biodistribution and radiation dosimetry of the anti-HER2 Affibody molecule ^{68}Ga-ABY-025 in breast cancer patients. *J Nucl Med.* 2016;57:867–871.
15. Bragina O, von Witting E, Garousi J, et al. Phase I study of ^{99m}Tc-ADAPT6, a scaffold protein-based probe for visualization of HER2 expression in breast cancer. *J Nucl Med.* 2021;62:493–499.
16. Krasniqi A, D'Huyvetter M, Devoogdt N, et al. Same-day imaging using small proteins: clinical experience and translational prospects in oncology. *J Nucl Med.* 2018;59:885–891.
17. Sörensen J, Velikyan I, Sandberg D, et al. Measuring HER2-receptor expression in metastatic breast cancer using [^{68}Ga]ABY-025 Affibody PET/CT. *Theranostics.* 2016;6:262–271.
18. Huisman MC, Niemeijer AN, Windhorst AD, et al. Quantification of PD-L1 expression with ^{18}F-BMS-986192 PET/CT in patients with advanced-stage non-small cell lung cancer. *J Nucl Med.* 2020;61:1455–1460.
19. Gebauer M, Skerra A. Engineered protein scaffolds as next-generation therapeutics. *Annu Rev Pharmacol Toxicol.* 2020;60:391–415.
20. Ross JS, Fletcher JA, Bloom KJ, et al. Targeted therapy in breast cancer: the HER-2/neu gene and protein. *Mol Cell Proteomics.* 2004;3:379–398.

First-in-Humans Evaluation of a PD-L1–Binding Peptide PET Radiotracer in Non–Small Cell Lung Cancer Patients

Xin Zhou*[1], Jinquan Jiang*[1], Xue Yang*[2], Teli Liu[1], Jin Ding[1], Sridhar Nimmagadda[3], Martin G. Pomper[3], Hua Zhu[1], Jun Zhao[2], Zhi Yang[1], and Nan Li[1]

[1]*Key Laboratory of Carcinogenesis and Translational Research (Ministry of Education/Beijing), Department of Nuclear Medicine, NMPA Key Laboratory for Research and Evaluation of Radiopharmaceuticals (National Medical Products Administration), Peking University Cancer Hospital & Institute, Beijing, China;* [2]*Key Laboratory of Carcinogenesis and Translational Research (Ministry of Education/Beijing), Department I of Thoracic Oncology, Peking University Cancer Hospital & Institute, Beijing, China; and* [3]*The Russell H. Morgan Department of Radiology and Radiological Science, Johns Hopkins University School of Medicine, Baltimore, Maryland*

^{68}Ga-NOTA-WL12 is a peptide-based PET imaging agent. We conducted a first-in-human study of ^{68}Ga-NOTA-WL12 for PET to study the in vivo biodistribution, metabolism, radiation dosimetry, safety, and potential for quantifying programmed death ligand-1 (PD-L1) expression levels in patients with advanced non–small cell lung cancer (NSCLC). **Methods:** In vitro assessment of the PD-L1 expression and cellular uptake of ^{68}Ga-NOTA-WL12 was performed, followed by in vivo evaluation of ^{68}Ga-NOTA-WL12 uptake in mouse models with tumors. Nine patients with NSCLC with lesions expressing PD-L1 were enrolled and monitored for adverse events during the study. ^{68}Ga-NOTA-WL12 and paired ^{18}F-FDG PET/CT imaging were performed. Uptake (SUV, SUL [SUV_{lean}], and kBq/mL) values of tumors and normal organs were obtained. Radiopharmaceutical biodistribution, radiation dosimetry, and the relationship of tumor uptake to PD-L1 expression were evaluated. Follow-up ^{18}F-FDG PET/CT was performed in patients who had undergone treatment with a combination of pembrolizumab with chemotherapy. **Results:** ^{68}Ga-NOTA-WL12 exhibited PD-L1–specific uptake in vitro and in PD-L1–positive tumors in vivo. ^{68}Ga-NOTA-WL12 PET imaging proved safe with acceptable radiation dosimetry. Physiologic tracer uptake was mainly visible in the liver, spleen, small intestine, and kidney. Tumors were clearly visible, particularly in the lungs, with a tumor-to-lung ratio of 4.45 ± 1.89 at 1 h. One hour was a suitable time point for image acquisition because no significant differences were noted in tumor-to-background ratios between 1 and 2 h. A strong, positive correlation was found between tumor uptake (SUV_{peak}) and PD-L1 immunohistochemistry results ($r = 0.9349$; $P = 0.002$). ^{68}Ga-NOTA-WL12 and ^{18}F-FDG PET studies suggest that PD-L1 PET before therapy may indicate the therapeutic efficacy of pembrolizumab plus chemotherapy combination treatment. **Conclusion:** Our first-in-human findings demonstrate the safety and feasibility of ^{68}Ga-NOTA-WL12 for noninvasive, in vivo detection of tumor PD-L1 expression levels, indicating potential benefits for clinical PD-L1 therapy.

Key Words: PD-(L)1; PET/CT; immune checkpoint inhibitor; non–small cell lung cancer; pembrolizumab

J Nucl Med 2022; 63:536–542
DOI: 10.2967/jnumed.121.262045

Treatment of non–small cell lung cancer (NSCLC) has advanced considerably over the past 40 y. In addition to the advent of molecularly targeted therapies, inhibition of immune checkpoints using anti–programmed cell death (ligand)-1 (PD-[L]1) monoclonal antibodies has revolutionized the management of patients with advanced NSCLC (*1–6*).

Therapeutics targeting the PD-(L)1 axis are now a first-line option for advanced NSCLC without genetic aberrations (*7*). Numerous clinical studies have shown that PD-L1 expression identified NSCLC patients who are most likely to respond to immunotherapy, such as pembrolizumab (*7,8*). U.S. Food and Drug Administration–approved PD-L1 assessment using immunohistochemistry and its interpretation is often based on a single biopsy or several small biopsies, which poorly represent the heterogeneity of PD-L1 expression within and between patients (*9,10*). Additionally, tumor biopsy is not always practical when the lesion site is inaccessible. These limitations indicate a need for tools to detect PD-L1 levels in the whole body to improve our understanding of the response of NSCLC to therapies targeting the PD-(L)1 axis.

PET enables quantitative, real-time, noninvasive assessment of target expression levels and dynamics in the whole body (*11,12*). Recently, several studies have investigated molecular imaging of PD-L1 expression. Biologics, such as radiolabeled antibodies and adnectin-derived small protein radiotracers, have shown promise in early phase clinical trials (*13–18*). High-affinity, low-molecular-weight radiotracers labeled with ^{64}Cu, ^{68}Ga, and ^{18}F have been developed and shown to detect graded levels of PD-L1 expression in vivo in preclinical models of several cancer types, including NSCLC (*13–15,19,20*). One of those agents, WL12, is a high-affinity PD-L1–binding small peptide labeled with ^{68}Ga. ^{68}Ga-WL12 proved a suitable scaffold for imaging PD-L1 expression in preclinical studies with PET (*19*). The tractable pharmacokinetics and high-contrast PD-L1–specific images exhibited by ^{68}Ga-WL12 within 60 min of injection indicate the potential for further evaluation and clinical translation. Here, we report the first-in-humans evaluation of a peptide-based PET imaging agent derived from WL12, ^{68}Ga-NOTA-WL12 (Supplemental Fig. 1A; supplemental materials are available at http://jnm.snmjournals.org), as well as its safety, radiation dosimetry, and imaging characteristics, to compare PET imaging with immunohistochemistry and therapy evaluation in patients with advanced NSCLC.

Received Jan. 31, 2021; revision accepted Jun. 29, 2021.
For correspondence or reprints, contact Nan Li (rainbow6283@sina.com), Zhi Yang (pekyz@163.com), Hua Zhu (zhuhuananjing@163.com), and Jun Zhao (ohjerry@163.com).
*Contributed equally to this work.
Published online Jul. 29, 2021.
COPYRIGHT © 2022 by the Society of Nuclear Medicine and Molecular Imaging.

MATERIALS AND METHODS

General

This was a prospective, phase I, open-label, nonrandomized, diagnostic imaging study in advanced NSCLC patients ($n = 9$) between March 2020 and September 2020 (trial registration ID NCT04304066). The Medical Ethics Committee of Peking University Cancer Hospital (2019 KT62) approved this study. Oral and written informed consent was obtained from all the participants.

NOTA-WL12 was custom synthesized and provided by Chinapeptides. Briefly, to radiolabel NOTA-WL12, $^{68}GaCl_3$ (925–1,110 MBq) was mixed with 195 μL of 1 *M* (pH 8.5) sodium acetate buffer and reacted with NOTA-WL12 (30 μg) at 60°C for 15 min. The final product was purified using a Sep-Pak (Waters) and obtained in >99% radiochemical purity by high-performance liquid chromatography. Details regarding the production, quality control, and murine radiotoxicity of ^{68}Ga-NOTA-WL12 can be found in the supplemental materials (Supplemental Table 1).

Patient inclusion criteria were being clinically diagnosed with NSCLC, with lesions expressing positive PD-L1; and having an Eastern Cooperative Oncology Group performance score of 0–2. Exclusion criteria were severe liver or kidney dysfunction and chemoradiotherapy or targeted therapy before PET/CT scans. PD-L1 expression in available lesions was evaluated by immunohistochemistry using antibody clone 22C3 (Dako Denmark A/S; catalog M3653). Dako PD-L1 immunohistochemistry 22C3 pharmDx is an approved screening criterion for pembrolizumab application in NSCLC (*21,22*). Positive PD-L1 expression was defined as a tumor proportion score (TPS) ≥ 1%, whereas high PD-L1 expression was defined as a TPS ≥ 50%.

Flow Cytometric Analysis and Small-Animal PET

The Chinese hamster ovary (CHO) cell line was obtained from American Type Culture Collection. A CHO cell line with constitutive PD-L1 expression (CHO-hPD-L1) was generated in our laboratory and described previously (*23*). Details of the cell culture, flow cytometry analysis for PD-L1 expression, and in vitro assays are provided in the supplemental materials.

For PET imaging, nonobese diabetic (NOD)/severe combined immunodeficient (SCID) mice bearing CHO-hPD-L1 or CHO tumors were intravenously injected with approximately 7.4 MBq (~0.17 μg) of ^{68}Ga-NOTA-WL12 in 200 μL of saline, and PET images were acquired at 30, 60, and 120 min. To establish in vivo specificity, animals were coinjected with 50 μg of unlabeled WL12. Image analysis and PD-L1 immunohistochemistry of the CHO-hPD-L1 and CHO tumors are described in the supplemental materials.

PET/CT

Patients were injected intravenously with ^{68}Ga-NOTA-WL12 (1.9–3.7 MBq/kg). To determine the optimal peptide dose required to obtain high-contrast images, an escalated nonradiolabeled WL12 mass dose was coadministered with the imaging agent. The first 2 patients received 0 μg, the next 3 received 5 ug, then 60 ug, and the final group of 3 received 120 μg. Because patients coadministered with 120 μg of WL12 showed lower uptake in the liver, the last 4 patients were coinjected with 120 μg of WL12. The first patient underwent a dynamic scan at 6 time points in 1 h. The remaining 8 patients underwent PET/CT at 1 h after injection, and 6 of those were also scanned at 2 h after injection (2 patients were unable to tolerate the full 2-h examination). Imaging was performed using a Biograph mCT Flow 64 scanner (Siemens) (120 kV; 146 mAs; slice: 3 mm; matrix: 200 × 200; iterations:2; subsets: 11; filter: 5 mm gaussian), continuously moving the patient bed at a speed of 1.5 mm/s to cover the entire body, from the top of the skull to the middle of the femur. Images were reconstructed with ordered-subset expectation maximization. CT reconstruction used a standard method with a 512 × 512 matrix and a layer thickness of 3–5 mm. CT data were used to correct the PET images for attenuation. Vital signs, laboratory studies, and electrocardiograms were obtained before injection, during the screening period, and 2 d after PET/CT. All patients underwent paired ^{18}F-FDG PET/CT scans (1 h after injection) within a week after ^{68}Ga-NOTA-WL12 PET/CT using the same imaging system. Three patients repeated the ^{18}F-FDG PET/CT examination within 3 wk after combination therapy including pembrolizumab and chemotherapy.

Radiation Dosimetry

Data from 4 patients with 120 μg of coinjected WL12 were used for ^{68}Ga-NOTA-WL12 dosimetry analysis, and the heart contents, lungs, liver, spleen, pancreas, kidneys, uterus, urinary bladder contents, and body remainder were selected as source organs. The volumes of the source organs manually drawn on CT images were calculated, and their mean counts/mL (kBq/mL) were determined from PET images at 1 and 2 h time points. Dosimetry was estimated using OLINDA/EXM software (version 2.0; Hermes Medical Solutions AB). Detailed procedures are provided in the supplemental materials.

Image Analysis

Images were analyzed by 2 experienced nuclear medicine physicians. The uptake parameters of major organs, tissues, and lesions were obtained to determine the organ biodistribution. SUV_{lean} (SUL) was obtained by standardizing SUV to the body mass, which is less dependent on body habitus (*24*). No significant difference was observed in the coefficients of variation between SUL_{mean} and SUV_{mean} (Supplemental Fig; 2A; Supplemental Table 2). Accordingly, we used SUL_{mean} and percentage of injected activity to describe radiopharmaceutical uptake in normal organs. To compare the uptake differences between the liver, spleen, small intestine (SI), and kidney among patients coadministered with different doses of WL12, multisite measurement was applied, and the uptake was calculated as an average of the number of patients corresponding to different dose administrations separately (Supplemental Fig. 3). To analyze normal organ uptake at different time points, 6 patients with 1- and 2-h imaging were involved. The maximum, peak, and mean values of SUV and SUL in biopsied lesions were obtained and used to correlate with PD-L1 TPS. Tumor uptake of ^{68}Ga-NOTA-WL12 higher than that of blood pool (BP) was considered positive. Evaluation of the therapeutic response was based on PERCIST (*24*) (for ^{18}F-FDG PET/CT evaluations) and RECIST 1.1 (*25*) (for CT evaluations) standards.

Statistics

Differences and correlations among parameters were tested using the Wilcoxon signed-rank test, Mann–Whitney *U* test, and Spearman correlation using IBM SPSS Statistics (version 24; IBM Corp.) software. *P* values < 0.05 were considered statistically significant.

RESULTS

Safety Assessment

^{68}Ga-NOTA-WL12 was produced with >99% purity with a specific activity of 18.5–296 GBq/μmol (Supplemental Fig. 1B). The safety parameters were measured. Murine radiotoxicity indicated that 167–200 MBq of ^{68}Ga-NOTA-WL12 were safe for humans (Supplemental Fig. 4). Details can be found in the Supplemental Materials.

In Vitro Cellular Studies and Small-Animal PET Imaging

Flow cytometry showed that the mean fluorescence intensity values of CHO-hPD-L1 were higher than those of CHO, as was cellular uptake extent (Supplemental Fig. 5).

NOD/SCID mice bearing CHO-hPD-L1 tumors showed intense uptake of ^{68}Ga-NOTA-WL12 in the tumors by 120 min (tumor–to–blood-pool uptake [T/BP]: 4.5 ± 0.2; tumor-to-muscle uptake [T/M]: 19.1 ± 1.2) (Fig. 1), whereas negative control CHO tumors showed minimal uptake (Supplemental Fig. 6A). Additionally, tumor uptake decreased with the coinjection of NOTA-WL12, indicating in vivo specificity (Fig. 2). Immunohistochemistry analysis showed high PD-L1 expression in CHO-hPD-L1 tumors (Supplemental Fig. 6B).

Patient Characteristics

Nine patients (8 men and 1 woman; median age, 68 y; age range, 47–80 y) with histopathologically proven NSCLC (5 adenocarcinoma, 4 squamous cell carcinoma) were included. Clinical stage, therapeutic regimen, PD-L1 expression and other characteristics are summarized in Table 1. The mean administered radioactivity of ^{68}Ga-NOTA-WL12 was 195 ± 30 MBq (range, 167–270 MBq).

Safety

Nine ^{68}Ga-NOTA-WL12 PET/CT examinations were performed, with no adverse or clinically detectable pharmacologic effects. No significant changes were observed in vital signs, results of laboratory studies, or electrocardiograms.

Biodistribution

Uptake of ^{68}Ga-NOTA-WL12 was mainly observed in the SI and liver, followed by moderate-to-low uptake in the kidneys, tumor, and spleen, and low uptake in the lungs and bone marrow (Fig. 3). This uptake pattern was similar to that observed in preclinical studies (*19,20,26,27*). With an increasing precursor dose coadministered with ^{68}Ga-NOTA-WL12, we observed decreased and increased uptake in the liver and SI, respectively, as well as a gradual decrease in the spleen uptake. Radioactivity uptake in the kidneys and BP at 1 h remained similar irrespective of the mass of WL12 used (Fig. 3; Supplemental Figs. 7A and 7B). Uptake observed in the liver, SI, and kidneys indicates that clearance of ^{68}Ga-NOTA-WL12 was primarily through the hepatobiliary system and secondarily through renal excretion. Except for the significant increase in uptake in the SI and the significant decrease in uptake in the liver from 1 to 2 h, other normal organs showed a downward trend with no significant differences (Supplemental Figs. 7C and 7D).

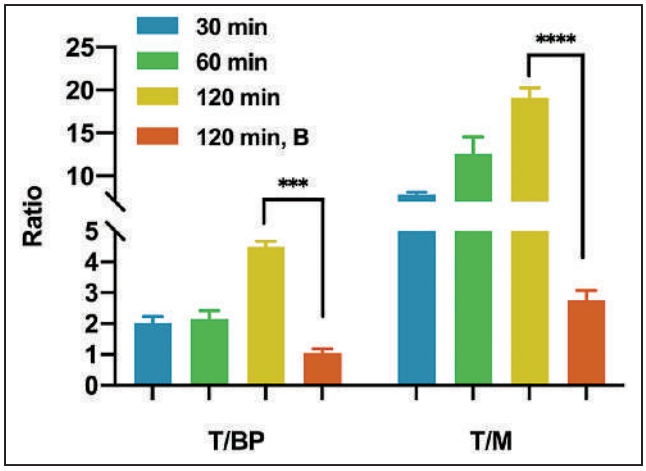

FIGURE 2. Ratios of T/BP and T/M in mice receiving ^{68}Ga-NOTA-WL12 with and without blocking dose at different time points.

Radiation Dosimetry

Table 2 summarizes the individual organ doses and effective doses of patients administered ^{68}Ga-NOTA-WL12 with120 μg of WL12 (n = 4) (administered dose: 224 ± 37 [range, 192–270 MBq]). The SI (3.47E–01 mGy/MBq) received the highest dose, indicating that WL12 is metabolized by hepatobiliary clearance, a characteristic observed with lipophilic agents. The intestinal absorbed dose remained well below the threshold for the human intestinal acute dose (6 Gy) (*28*). Radiation dosimetry was acceptable at 1.85E–02 ± 4.07E–03 mSv/MBq (4.1 mSv per patient), which is lower than the radiation dose of conventional ^{18}F-FDG PET/CT (7.0–14 mSv) (*29*).

Tumor Uptake and Correlation with Immunohistochemistry

Rapid clearance of radioactivity was observed from the BP, resulting in high T/BP (and muscle) ratios. Thus, the T/BP and T/M ratios were 1.48 ± 0.42 and 1.56 ± 0.49 and 5.31 ± 1.99 and 4.87 ± 1.28 at 1 and 2 h, respectively. High contrast was also observed in the lungs with tumor-to-lung ratios of 4.45 ± 1.89 and 5.18 ± 2.27 at 1 and 2 h, respectively. No significant differences were noted in the tumor-to-background ratios (BP, lungs, and M) at 1 and 2 h (Supplemental Fig. 2B), indicating that 1 h after radiotracer administration is a suitable time point for image acquisition.

In patients with high PD-L1 expression, tumor uptake of ^{68}Ga-NOTA-WL12 (TPS: 80%; SUV_{max}: 4.87) was higher than that in patients with low PD-L1 expression (TPS: 8%; SUV_{max}: 1.84) (Fig. 4). All calculated PET parameters of ^{68}Ga-NOTA-WL12, except for the ratios of tumor uptake to BP, correlated with the corresponding PD-L1 TPS on immunohistochemistry (Supplemental Table 3) (SUV_{peak} [r = 0.9349, r_s = 0.8741; P = 0.002] [Fig. 5A]). In contrast to ^{68}Ga-NOTA-WL12, uptake of ^{18}F-FDG in the lesions did not correlate with PD-L1 expression, with a tenuous relationship to SUV_{peak} (r = 0.5529, r_s = 0.3057; P = 0.1226) (Fig. 5B).

We also noted the intra- and intertumoral heterogeneity of ^{68}Ga-NOTA-WL12 uptake in some patients, reflecting the heterogeneity

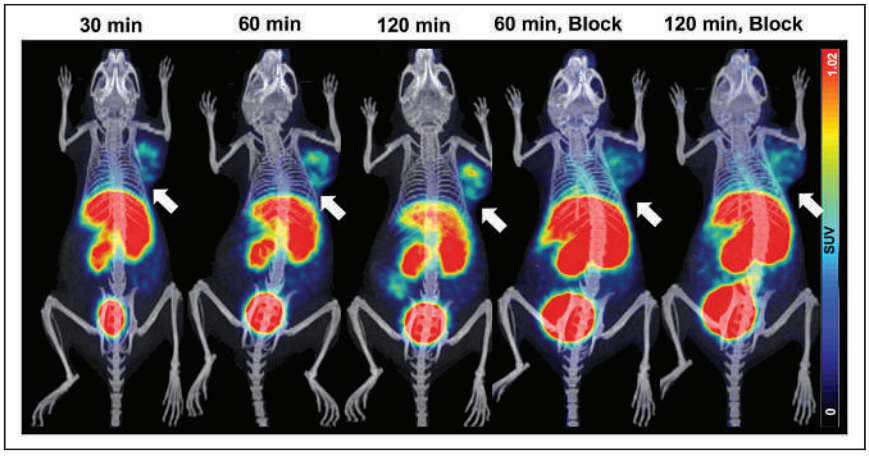

FIGURE 1. PET/CT images of NOD/SCID mice with CHO-hPD-L1 tumors at different time points after ^{68}Ga-NOTA-WL12 injection and of mice receiving 50 μg amount of blocking dose.

TABLE 1
Patient Characteristics

Addition of WI12 (MG)	Patient	Sex	Age (y)	ECOG score	Tumor type	PD-L1 expression*	Clinical stage	Tumor size (cm)	Therapy regimen
0	1	M	47	1	LUSC	8%	cT4N2M1a IVa	7.2 × 6.1	Nab-paclitaxel + carboplatin + pembrolizumab
0	2	M	72	0	LUSC	35%	cT2N3M0 IIIb	4 × 3.4	Paclitaxel + cisplatin
5	3	M	68	0	LUSC	8%	cT4N1M1a IVa	5.8 × 4.7	Nab-paclitaxel + carboplatin + pembrolizumab
60	4	M	68	1	LUAC	25%	cT4N1M0 IIIa	5.1 × 4.0	Nab-paclitaxel + carboplatin
120	5	M	80	2	LUAC	40%	cT4N3M1c IVb	5.7 × 3.9	toripalimab
	6	M	58	0	LUAC	30%	cT2aN2M1c IVb	3.1 × 2.3	Pemetrexed + carboplatin + pembrolizumab
	7	M	63	1	LUSC	25%	cT2bN2M1b IVa	4.2 × 4.1	pembrolizumab
	8	M	53	1	LUAC	35%	cT2bN2M1b IVa	3.1 × 1.9	Pemetrexed + carboplatin + sintilimab
	9	F	80	2	LUAC	80%	cT3N3M1c IVb	5.9 × 5.3	Pembrolizumab

ECOG = Eastern Cooperative Oncology Group; LUSC = lung squamous cell carcinoma; LUAC = lung adenocarcinoma.

of PD-L1 expression reported with other PD-L1 imaging agents (Fig. 6) (*13,16*). The uptake of ^{18}F-FDG was intense in the tumors regardless of PD-L1 expression levels, with no significant heterogeneity among or within lesions.

Relationship of ^{68}Ga-NOTA-WL12 Uptake to Therapy

Three patients underwent ^{18}F-FDG PET/CT after combination (pembrolizumab plus chemotherapy) treatment. In patients 1 and 6, with PD-L1 TPS values of 8% and 30%, respectively, ^{68}Ga-NOTA-WL12 uptake in tumors before treatment showed an SUV_{max} of 2.21 and 3.05 (Figs. 7A and 7B; Supplemental Table 4), respectively. These 2 patients were rated as partial metabolic responses (PMR, PERCIST (*24*)) and stable disease (RECIST 1.1 (*25*)).

Patient 3, with a PD-L1 TPS value of 8%, showed negative ^{68}Ga-NOTA-WL12 uptake before therapy (SUV_{max} of tumor: 1.84; SUV_{max} of BP: 1.78). This patient showed increased uptake of ^{18}F-FDG in the primary tumor and a new brain metastasis on the posttherapy scan, and he was further rated as progressive disease (PD, PERCIST and RECIST) (Fig. 7C; Supplemental Table 4). Thus, patients with PMR/stable disease exhibited positive uptake of ^{68}Ga-NOTA-WL12 before therapy.

DISCUSSION

We describe the first-in-humans evaluation of ^{68}Ga-NOTA-WL12, a peptide-based PD-L1 imaging agent, in patients with NSCLC. We demonstrated that ^{68}Ga-NOTA-WL12 is safe and effective for PET imaging of PD-L1 expression.

Inhibition of the PD-(L)1 axis has proved a remarkable success in treating patients with NSCLC (*1–4*). PD-L1 expression, determined by needle biopsy, is currently the only validated biomarker used as a companion diagnostic test for NSCLC patient selection for pembrolizumab therapy (*22*). Several studies have demonstrated variations in PD-L1 expression within patients and within tumors, due to heterogeneity of target expression (*30*). PD-L1 heterogeneity may still confound a single positive biopsy result, leading to inappropriate administration of therapy, contributing to the moderate correlation between PD-L1 status and survival rates (*30*). However, nuances in PD-L1 heterogeneity and its relevance to response are emerging. Patients with PD-L1 TPS values ≥ 50% can now be treated with pembrolizumab as a first-line option, indicating that increased PD-L1 expression is related to improved clinical outcomes (*31*). Patients with PD-L1 expression > 75% and > 90%

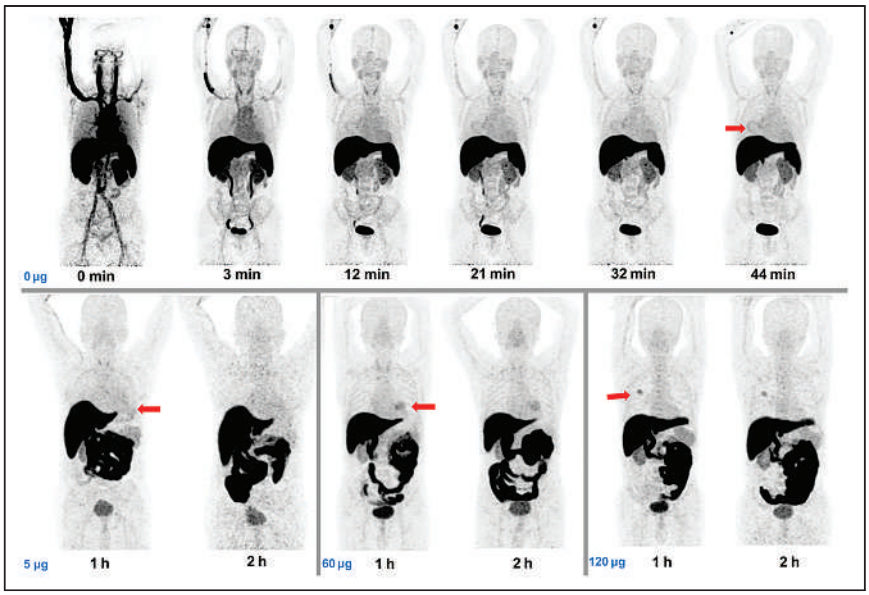

FIGURE 3. Maximum-intensity-projection imaging for biodistribution and organ uptake of ^{68}Ga-NOTA-WL12 at different time points after injection administered without and with increasing precursor doses (5 μg, 60 μg, 120 μg). Primary lesions are indicated by red arrows.

TABLE 2
Organ Observed Doses and Whole-Body Effective Doses

Organ/tissue	Absorbed dose (mGy/MBq)
Adrenals	2.60e–02
Brain	8.80e–04
Esophagus	7.43e–03
Eyes	8.88e–04
Gallbladder wall	3.21e–02
Left colon	1.52e–02
SI	3.47e–01
Stomach wall	8.41e–03
Right colon	1.26e–02
Rectum	6.83e–03
Heart wall	1.45e–02
Kidneys	3.42e–02
Liver	1.92e–01
Lungs	1.55e–02
Pancreas	2.13e–02
Prostate	4.39e–03
Salivary glands	1.09e–03
Red marrow	6.10e–03
Osteogenic cells	4.05e–03
Spleen	2.89e–02
Testes	1.16e–03
Thymus	3.85e–03
Thyroid	2.15e–03
Urinary bladder wall	1.16e–02
Total body	1.04e–02
Effective dose (mSv/MBq)	1.85e–02

have benefitted more than those with 50%–75%, suggesting that analysis and correlation of outcome data using PD-L1 expression on a continuous 0%–100% scale rather than using predefined cutoffs (≥50%) would be more accurate. These studies indicate that

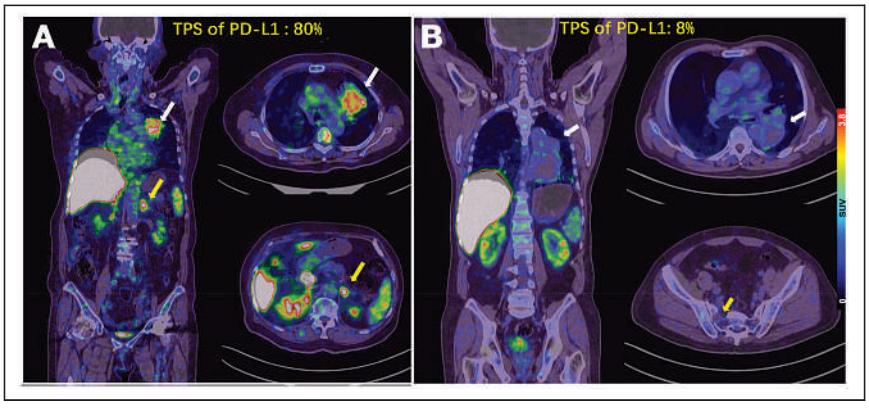

FIGURE 4. (A) Patient 9, an 80-y-old woman with advanced NSCLC and a PD-L1 TPS of 80%. SUV_{max} of primary tumor was 4.87 (white arrow) and that of left adrenal metastasis was 5.47 (yellow arrow) on ^{68}Ga-NOTA-WL12 PET. (B) Patient 3, a 68-y-old man with a PD-L1 TPS of 8%. SUV_{max} of primary tumor in left lung (white arrow) and right sacral metastasis (yellow arrow) were 1.84 and 0.8, respectively, on ^{68}Ga-NOTA-WL12 PET.

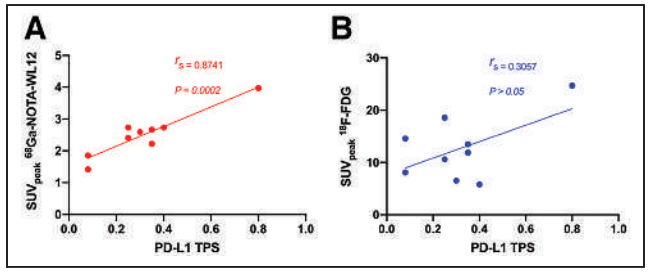

FIGURE 5. Relationship between PD-L1 expression detected by immunohistochemistry and tumor uptake (SUV_{peak}) of ^{68}Ga-NOTA-WL12 (r_s = 0.8741, $P < 0.0005$) (A) and ^{18}F-FDG (r_s = 0.3057, $P > 0.05$) (B).

PD-L1 heterogeneity is an underappreciated aspect in assessing and guiding immune checkpoint therapies. Furthermore, these issues are compounded in advanced-stage NSCLC patients because a biopsy of every lesion is not feasible. Noninvasive quantification of PD-L1 levels could provide complementary information to address those challenges, as shown herein and by other groups (*13,16*).

Many radiolabeled probes targeting PD-L1 have been validated in preclinical models, such as antibodies, antibody fragments, small proteins, and peptides (*13–17*). Correspondingly, the preclinical experiments in this study confirmed that the uptake of ^{68}Ga-NOTA-WL12 was highly correlated to PD-L1 expression. The accumulation of ^{89}Zr-atezolizumab, a PD-L1 antibody, in patients with breast, lung, and bladder cancers showed a higher predictive value than immunohistochemistry or genomic sequencing for therapeutic response (*16*). Additionally, the accumulation of ^{89}Zr-atezolizumab and another PD-L1 PET imaging agent, ^{18}F-BMS-986192, was found to be heterogeneous between and within patients (*13,16*). Several studies revealed that the addition of nonradiolabeled peptide precursor reduced liver uptake through competitive metabolism; however, the excretion of ^{68}Ga-NOTA-WL12 to the SI was elevated with the increase in the peptide dose. That finding differed from other saturation antibody studies (*32*), suggesting that the mass of ^{68}Ga-NOTA-WL12 in circulation was relatively stable, and the addition of peptide would not likely affect tumor uptake. Therefore, patients with different mass doses of peptide precursor were enrolled. The correlation between uptake and therapeutic outcome, together with the inter- and intratumor heterogeneity observed with ^{68}Ga-NOTA-WL12 uptake, indicated the potential to predict the effectiveness of immune therapy.

Radiolabeled antibodies such as ^{89}Zr-atezolizumab and ^{89}Zr-nivolumab, because of their long physical half-lives and circulation times, may encounter difficulties in delineating the changes in PD-L1 expression (*13,16*). Additionally, PET measures of radiolabeled antibodies do not accurately measure target expression; they are a combination of tracer exposure and target expression (*16*). Small-molecule radiotracers such as ^{68}Ga-NOTA-WL12 provide a direct measure of the PD-L1 status within hours of radiotracer administration, likely because of better tissue penetration. Determining the characteristics of WL12 peptide binding to PD-L1 also presents opportunities to quantify the pharmacologic activity

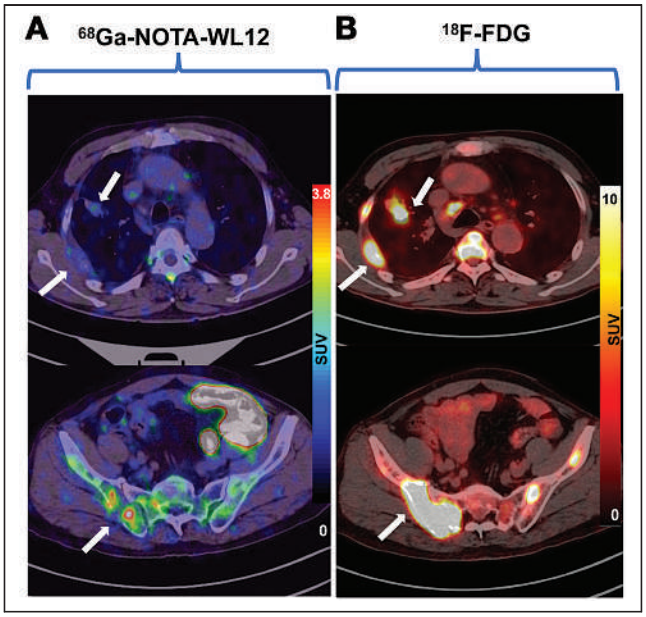

FIGURE 6. For patient 8, a 68-y-old man with lung adenocarcinoma, images showed inhomogeneous intra- and intertumoral uptake on ^{68}Ga-NOTA-WL12 PET/CT (A) and high homogeneous uptake in tumors (white arrow) on ^{18}F-FDG PET/CT (B).

of PD-L1 antibodies within the tumor bed in a manner agnostic to the antibody type, as recently shown in preclinical models (*20*).

Therapeutic evaluation based on ^{18}F-FDG PET/CT for lung cancer is widely recognized by physicians (*24,33*). Three patients in this study who received immunotherapy underwent ^{18}F-FDG PET/CT for therapeutic evaluation. Patients with positive uptake of ^{68}Ga-NOTA-WL12 were rated as having a PMR, and patients with a negative uptake of ^{68}Ga-NOTA-WL12 were rated as having PD. Although 2 of the 3 patients shared the same PD-L1 expression level (TPS: 8%), the outcomes (PMR and PD) were quite different. These results suggest that higher ^{68}Ga-NOTA-WL12 uptake in lesions may indicate a better prognosis than lower ^{68}Ga-NOTA-WL12 uptake, regardless of the level of PD-L1 expression determined by immunohistochemistry. Those observations in a small number of patients merit further validation in larger patient cohorts.

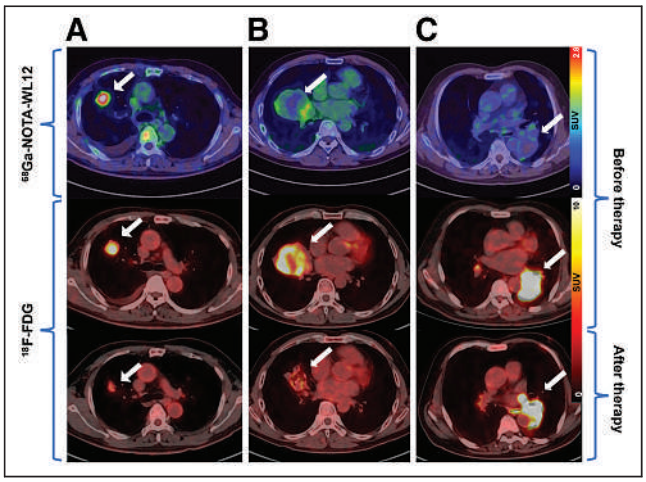

FIGURE 7. (A) Patient 6, a 58-y-old man with adenocarcinoma and a PD-L1 TPS of 30%. SUV_{max} of ^{68}Ga-NOTA-WL12 was 3.05 and that of ^{18}F-FDG decreased from 8.03 to 3.10. (B) Patient 1, a 47-y-old man with squamous cell carcinoma and a TPS of 8%. SUV_{max} of ^{68}Ga-NOTA-WL12 was 2.21 and that of ^{18}F-FDG decreased from 9.13 to 3.54. (C) Patient 3, a 68-y-old man with squamous cell carcinoma and a TPS of 8%. SUV_{max} of ^{68}Ga-NOTA-WL12 was1.84 and that of ^{18}F-FDG increased from 16.55 to 21.38. All lesions were indicated by white arrows.

A potential limitation of our study is the small number of patients involved. Nonetheless, our study is similar to other first-in-humans phase 1 studies of radiopharmaceuticals and has sufficient power to assess safety, suitable imaging time points, radiation dosimetry, and preliminary correlation of ^{68}Ga-NOTA-WL12 uptake with immunohistochemistry. Another limitation of the study is that immunohistochemistry was performed only on index lesions, limiting our ability to quantify intralesional variation within a given patient.

CONCLUSION

This first-in-humans study of ^{68}Ga-NOTA-WL12, a low-molecular-weight peptide-derived imaging agent, demonstrates the feasibility and potential of quantifying PD-L1 levels in NSCLC with PET within a clinically viable time frame. ^{68}Ga-NOTA-WL12 proved safe, with favorable biodistribution and radiation dose estimates similar to those of other radiopharmaceuticals. ^{68}Ga-NOTA-WL12 uptake measures correlated with PD-L1 levels detected by immunohistochemistry, suggesting its suitability as a complementary diagnostic to immunohistochemistry to quantify PD-L1 levels for patient selection and therapeutic monitoring in anti-PD-L1 therapy.

DISCLOSURE

Financial support for this study was provided by the National Science and Technology Major Project (no. 2020ZX09201023), National Natural Science Foundation of China (81671733, 81871386, and 81871387), and Beijing Excellent Talents Funding (2017000021223ZK33). Sridhar Nimmagadda and Martin G. Pomper are supported by NIH 1R01CA236616 and NIH P41EB024495; they are coinventors on a pending U.S. patent covering WL12 and, as such, are entitled to a portion of any licensing fees and royalties generated by this technology. This arrangement has been reviewed and approved by Johns Hopkins University in accordance with its conflict-of-interest policies. Sridhar Nimmagadda and Martin G. Pomper are consultants for Precision Molecular Inc., which has licensed the patent covering WL12 from Johns Hopkins University, and own equity in D&D Pharmatech, the parent company of Precision Molecular, Inc. No other potential conflict of interest relevant to this article was reported.

KEY POINTS

QUESTION: Can the peptide-based radiotracer ^{68}Ga-NOTA-WL12 detect and represent the expression levels of PD-L1 in patients with NSCLC?

PERTINENT FINDINGS: We demonstrated the feasibility and potential of ^{68}Ga-NOTA-WL12 to quantify PD-L1 levels in preclinical models and in patients with NSCLC, with a strong relationship between tumor uptake and PD-L1 immunohistochemistry.

IMPLICATIONS FOR PATIENT CARE: ^{68}Ga-NOTA-WL12 can be used to image PD-L1 in vivo, indicating its potential as a complementary diagnostic to immunohistochemistry to quantify PD-L1 levels for patient selection and therapeutic monitoring in anti-PD-L1 therapy.

REFERENCES

1. Rittmeyer A, Barlesi F, Waterkamp D, et al. Atezolizumab versus docetaxel in patients with previously treated non-small-cell lung cancer (OAK): a phase 3, open-label, multicentre randomised controlled trial. *Lancet.* 2017;389:255–265.
2. Brahmer J, Reckamp KL, Baas P, et al. Nivolumab versus docetaxel in advanced squamous-cell non-small-cell lung cancer. *N Engl J Med.* 2015;373:123–135.
3. Borghaei H, Paz-Ares L, Horn L, et al. Nivolumab versus docetaxel in advanced nonsquamous non-small-cell lung cancer. *N Engl J Med.* 2015;373:1627–1639.
4. Gandhi L, Rodríguez-Abreu D, Gadgeel S, et al. Pembrolizumab plus chemotherapy in metastatic non-small-cell lung cancer. *N Engl J Med.* 2018;378:2078–2092.
5. Antonia SJ, Borghaei H, Ramalingam SS, et al. Four-year survival with nivolumab in patients with previously treated advanced non-small-cell lung cancer: a pooled analysis. *Lancet Oncol.* 2019;20:1395–1408.
6. Remon J, Passiglia F, Ahn MJ, et al. Immune checkpoint inhibitors in thoracic malignancies: review of the existing evidence by an IASLC expert panel and recommendations. *J Thorac Oncol.* 2020;15:914–947.
7. Rosner S, Reuss JE, Forde PM. PD-1 blockade in early-stage lung cancer. *Annu Rev Med.* 2019;70:425–435.
8. Mok TSK, Wu Y-L, Kudaba I, et al. Pembrolizumab versus chemotherapy for previously untreated, PD-L1-expressing, locally advanced or metastatic non-small-cell lung cancer (KEYNOTE-042): a randomised, open-label, controlled, phase 3 trial. *Lancet.* 2019;393:1819–1830.
9. Kluger HM, Zito CR, Turcu G, et al. PD-L1 studies across tumor types, its differential expression and predictive value in patients treated with immune checkpoint inhibitors. *Clin Cancer Res.* 2017;23:4270–4279.
10. McLaughlin J, Han G, Schalper KA, et al. Quantitative assessment of the heterogeneity of PD-L1 expression in non-small-cell lung cancer. *JAMA Oncol.* 2016;2:46–54.
11. Willmann JK, van Bruggen N, Dinkelborg LM, Gambhir SS. Molecular imaging in drug development. *Nat Rev Drug Discov.* 2008;7:591–607.
12. Kobayashi H, Longmire MR, Ogawa M, Choyke PL, Kawamoto S. Multiplexed imaging in cancer diagnosis: applications and future advances. *Lancet Oncol.* 2010;11:589–595.
13. Niemeijer AN, Leung D, Huisman MC, et al. Whole body PD-1 and PD-L1 positron emission tomography in patients with non-small-cell lung cancer. *Nat Commun.* 2018;9:4664.
14. Xing Y, Chand G, Liu C, et al. Early phase I study of a ^{99m}Tc-labeled anti-programmed death ligand-1 (PD-L1) single-domain antibody in SPECT/CT assessment of PD-L1 expression in non-small cell lung cancer. *J Nucl Med.* 2019;60:1213–1220.
15. Donnelly DJ, Smith RA, Morin P, et al. Synthesis and biologic evaluation of a novel ^{18}F-labeled adnectin as a PET radioligand for imaging PD-L1 expression. *J Nucl Med.* 2018;59:529–535.
16. Bensch F, van der Veen EL, Lub-de Hooge MN, et al. ^{89}Zr-atezolizumab imaging as a non-invasive approach to assess clinical response to PD-L1 blockade in cancer. *Nat Med.* 2018;24:1852–1858.
17. Heskamp S, Hobo W, Molkenboer-Kuenen JD, et al. Noninvasive imaging of tumor PD-L1 expression using radiolabeled anti-PD-L1 antibodies. *Cancer Res.* 2015;75:2928–2936.
18. Huisman MC, Niemeijer AN, Windhorst AD, et al. Quantification of PD-L1 expression with ^{18}F-BMS-986192 PET/CT in patients with advanced-stage non-small cell lung cancer. *J Nucl Med.* 2020;61:1455–1460.
19. De Silva RA, Kumar D, Lisok A, et al. Peptide-based ^{68}Ga-PET radiotracer for imaging PD-L1 expression in cancer. *Mol Pharm.* 2018;15:3946–3952.
20. Kumar D, Lisok A, Dahmane E, et al. Peptide-based PET quantifies target engagement of PD-L1 therapeutics. *J Clin Invest.* 2019;129:616–630.
21. U.S. Food and Drug Administration. Dako PD-L1 IHC 22C3 pharmDx. September 2015. FDA website. https://www.accessdata.fda.gov/cdrh_docs/pdf15/P150013c.pdf. Accessed January 19, 2022.
22. Herbst RS, Baas P, Kim D-W, et al. Pembrolizumab versus docetaxel for previously treated, PD-L1-positive, advanced non-small-cell lung cancer (KEYNOTE-010): a randomised controlled trial. *Lancet.* 2016;387:1540–1550.
23. Chatterjee S, Lesniak WG, Gabrielson M, et al. A humanized antibody for imaging immune checkpoint ligand PD-L1 expression in tumors. *Oncotarget.* 2016;7:10215–10227.
24. Wahl RL, Jacene H, Kasamon Y, Lodge MA. From RECIST to PERCIST: evolving considerations for PET response criteria in solid tumors. *J Nucl Med.* 2009;50(suppl 1):122S–150S.
25. Eisenhauer EA, Therasse P, Bogaerts J, et al. New response evaluation criteria in solid tumours: revised RECIST guideline (version 1.1). *Eur J Cancer.* 2009;45:228–247.
26. Lesniak WG, Mease RC, Chatterjee S, et al. Development of [^{18}F]FPy-WL12 as a PD-L1 specific PET imaging peptide. *Mol Imaging.* 2019;18:1536012119852189.
27. Chatterjee S, Lesniak WG, Miller MS, et al. Rapid PD-L1 detection in tumors with PET using a highly specific peptide. *Biochem Biophys Res Commun.* 2017;483:258–263.
28. Stewart FA, Akleyev AV, Hauer-Jensen M, et al. ICRP publication 118: ICRP statement on tissue reactions and early and late effects. *Ann ICRP.* 2012;41:1–322.
29. Delbeke D, Coleman RE, Guiberteau MJ, et al. Procedure guideline for tumor imaging with ^{18}F-FDG PET/CT 1.0. *J Nucl Med.* 2006;47:885–895.
30. Hofman P. PD-L1 immunohistochemistry for non-small cell lung carcinoma: which strategy should be adopted? *Expert Rev Mol Diagn.* 2017;17:1097–1108.
31. Aguilar EJ, Ricciuti B, Gainor JF, et al. Outcomes to first-line pembrolizumab in patients with non-small-cell lung cancer and very high PD-L1 expression. *Ann Oncol.* 2019;30:1653–1659.
32. Sörensen J, Velikyan I, Sandberg D, et al. Measuring HER2-receptor expression in metastatic breast cancer using [^{68}Ga]ABY-025 affibody PET/CT. *Theranostics.* 2016;6:262–271.
33. Beer L, Hochmair M, Haug AR, et al. Comparison of RECIST, iRECIST, and PERCIST for the evaluation of response to PD-1/PD-L1 blockade therapy in patients with non-small cell lung cancer. *Clin Nucl Med.* 2019;44:535–543.

PET-Based Staging Is Cost-Effective in Early-Stage Follicular Lymphoma

Andrea C. Lo[1], Lyndon P. James[2,3], Anca Prica[4], Adam Raymakers[5], Stuart Peacock[5], Melody Qu[6], Alex V. Louie[7], Kerry J. Savage[8], Laurie H. Sehn[8], David Hodgson[9], Joanna C. Yang[10], Hans T.T. Eich[11], Andrew Wirth[12], and M.G. Myriam Hunink[3,13]

[1]Department of Radiation Oncology, BC Cancer, University of British Columbia, Vancouver, British Columbia, Canada; [2]PhD Program in Health Policy, Harvard University, Cambridge, Massachusetts; [3]Center for Health Decision Science, Harvard T.H. Chan School of Public Health, Boston, Massachusetts; [4]Department of Medical Oncology and Hematology, Princess Margaret Cancer Centre, Toronto, Ontario, Canada; [5]Cancer Control Research, BC Cancer, Vancouver, British Columbia, Canada; [6]Department of Radiation Oncology, London Health Sciences Centre, Western University, London, Ontario, Canada; [7]Department of Radiation Oncology, Sunnybrook Health Sciences Centre, University of Toronto, Toronto, Ontario, Canada; [8]Centre for Lymphoid Cancer, Department of Medical Oncology, BC Cancer, Vancouver, British Columbia, Canada, [9]Radiation Medicine Program, Princess Margaret Cancer Centre, Toronto, Ontario, Canada; [10]Department of Radiation Oncology, University of California, San Francisco, San Francisco, California; [11]Department of Radiation Oncology, University Hospital Muenster, Muenster, Germany; [12]Department of Radiation Oncology, Peter MacCallum Cancer Centre, Melbourne, Australia; and [13]Clinical Epidemiology and Radiology, Erasmus University, Rotterdam, Netherlands

The objective was to assess the cost-effectiveness of staging PET/CT in early-stage follicular lymphoma (FL) from the Canadian health-care system perspective. **Methods:** The study population was FL patients staged as early-stage using conventional CT imaging and planned for curative-intent radiation therapy (RT). A decision analytic model simulated the management after adding staging PET/CT versus using staging CT alone. In the no-PET/CT strategy, all patients proceeded to curative-intent RT as planned. In the PET/CT strategy, PET/CT information could result in an increased RT volume, switching to a noncurative approach, or no change in RT treatment as planned. The subsequent disease course was described using a state-transition cohort model over a 30-y time horizon. Diagnostic characteristics, probabilities, utilities, and costs were derived from the literature. Baseline analysis was performed using quality-adjusted life years (QALYs), costs (2019 Canadian dollars), and the incremental cost-effectiveness ratio. Deterministic sensitivity analyses were conducted, evaluating net monetary benefit at a willingness-to-pay threshold of $100,000/QALY. Probabilistic sensitivity analysis using 10,000 simulations was performed. Costs and QALYs were discounted at a rate of 1.5%. **Results:** In the reference case scenario, staging PET/CT was the dominant strategy, resulting in an average lifetime cost saving of $3,165 and a gain of 0.32 QALYs. In deterministic sensitivity analyses, the PET/CT strategy remained the preferred strategy for all scenarios supported by available data. In probabilistic sensitivity analysis, the PET/CT strategy was strongly dominant in 77% of simulations (i.e., reduced cost and increased QALYs) and was cost-effective in 89% of simulations (i.e., either saved costs or had an incremental cost-effectiveness ratio below $100,000/QALY). **Conclusion:** Our analysis showed that the use of PET/CT to stage early-stage FL patients reduces cost and improves QALYs. Patients with early-stage FL should undergo PET/CT before curative-intent RT.

Key Words: PET/CT; follicular lymphoma; radiation therapy; cost-effectiveness analysis; staging

Received Mar. 25, 2021; revision accepted Jul. 15, 2021.

For correspondence or reprints, contact Andrea C. Lo (andrea.lo@bccancer.bc.ca).

Published online Aug. 19, 2021.

COPYRIGHT © 2022 by the Society of Nuclear Medicine and Molecular Imaging.

J Nucl Med 2022; 63:543–548
DOI: 10.2967/jnumed.121.262324

For patients with early-stage follicular lymphoma (FL), definitive radiation therapy (RT) is a potentially curative treatment, with a 10-y event-free survival of 40%–50% (*1–3*). On the other hand, advanced-stage disease is considered incurable but is still associated with a long median overall survival of 15–20 y (*4*), given its indolent nature and response to various treatments.

Since its introduction, CT scanning has been an integral part of lymphoma staging, allowing anatomic visualization of nodal and extranodal disease. In the current era, ^{18}F-FDG PET combined with CT in a single procedure is considered state-of-the-art imaging in lymphoma (*3,5,6*). A recent retrospective cohort study of early-stage FL patients staged with PET/CT suggested a modest improvement in intermediate-term outcomes when compared with conventionally staged early-stage FL cohorts (*7,8*), and guidelines have been revised to recommend both staging CT and staging PET/CT to confirm localized disease or in the case of suspected transformation (*4,9*). Nevertheless, not all centers have shifted to routinely using PET/CT in the staging of FL patients (*3,5,6,10*). Furthermore, neither the prior studies nor the recent guidelines considered the potential downstream impact of PET/CT staging on patient outcomes or the cost-effectiveness of adding functional imaging to CT alone.

A complete assessment of the impact of staging PET/CT requires the altered outcomes of the patients who are upstaged to be accounted for. Furthermore, evaluation of quality-adjusted life expectancy and cost-effectiveness facilitates comparison of staging PET/CT with other medical interventions for which these outcomes have been described. Thus, we sought to determine the impact of staging PET/CT on quality-adjusted life years (QALYs) and cost to the Canadian health-care system in patients with early-stage FL planned for curative-intent RT.

MATERIALS AND METHODS

The population examined was patients with low-grade (grades 1–3A) FL staged as early-stage (stage I or II) using conventional CT imaging and planned for curative-intent RT; the age of the base-case patient was 60 y. A decision analytic model was developed to simulate the management of patients after adding staging PET/CT to the staging approach, versus using staging CT alone (Fig. 1). In the no-PET/CT strategy, all patients proceeded to curative-intent RT as planned. In the PET/CT strategy, PET/CT information could result in an increased RT volume, a switch to a noncurative approach, or no change in treatment.

Patients' subsequent disease course was described using a state-transition cohort model over a 30-y lifetime horizon. A simplified version of the model is displayed in Figure 2. Patients upstaged to the advanced stage on PET/CT were managed with rituximab monotherapy, watchful waiting, palliative RT (4 Gy in 2 fractions), or bendamustine-rituximab. Patients staged as early stage received curative-intent RT (24 Gy in 2 fractions). On relapse or progression, patients were treated with either bendamustine-rituximab plus rituximab maintenance if they had not previously received it or with salvage chemotherapy if they had. After bendamustine-rituximab, patients could receive up to 3 further lines of chemotherapy, after which they transitioned into a palliative state and eventually death. Patients were assumed to still have indolent disease on relapse or progression rather than transformation to high-grade disease.

Direct medical costs from the perspective of the Canadian health-care system were estimated from published literature and adjusted to 2019 Canadian dollars. Incremental cost-effectiveness ratios were calculated, and a willingness-to-pay threshold of $100,000 per QALY was adopted (*11*). QALYs and costs were discounted at an annual rate of 1.5% (*12*).

Various sensitivity analyses were performed to address model uncertainties and to establish the thresholds whereby each treatment strategy would be preferred. The baseline values and probability distributions are listed in Supplemental Tables 1 and 2 (supplemental materials are available at http://jnm.snmjournals.org). Deterministic 1-way sensitivity analysis was performed to evaluate each variable's influence on the net monetary benefit at a willingness to pay of $100,000/QALY. Probabilistic sensitivity analysis was performed using 10,000 simulations, each using a parameter set drawn from the distributions described in Supplemental Tables 1 and 2. TreeAge Pro 2019 (TreeAge Software) was used to construct the model and perform the analyses.

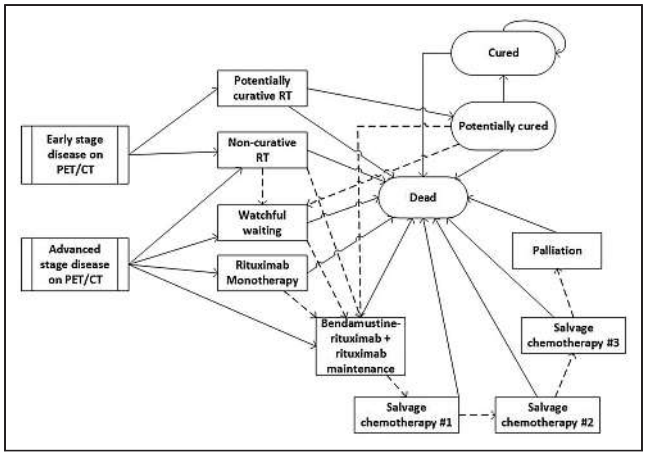

FIGURE 2. Simplified state-transition cohort model (dotted arrows represent transition to next state after relapse or progression; solid arrows represent transition to next state without relapse or progression.

Transition Probabilities

The probabilities used in the model are shown in Supplemental Table 1 (*3,13–22*). The diagnostic probabilities of PET/CT were derived from a study by Wirth et al. assessing the impact of PET/CT on early-stage FL (*13*). Based on the data of Wirth et al. (as described in the supplemental materials), a uniform distribution ranging between 62% (8/13) and 92% (12/13) was used in sensitivity analysis to conservatively estimate the uncertainty of the probability of a new PET/CT finding of advanced-stage disease. Similarly, a uniform distribution ranging between 0% (0/6) and 100% (6/6) was selected for the probability of early-stage disease truly outside the planned RT field for those in whom this was diagnosed on PET/CT.

Probabilities reflecting disease course were derived from randomized controlled trials if available and cohort studies if no relevant randomized controlled trials had been published. Further details are found in the supplemental materials (*14,15,19,20,23,24*). The probability of death from other causes was the age-related mortality per 6-mo cycle according to Statistics Canada life tables (*22*).

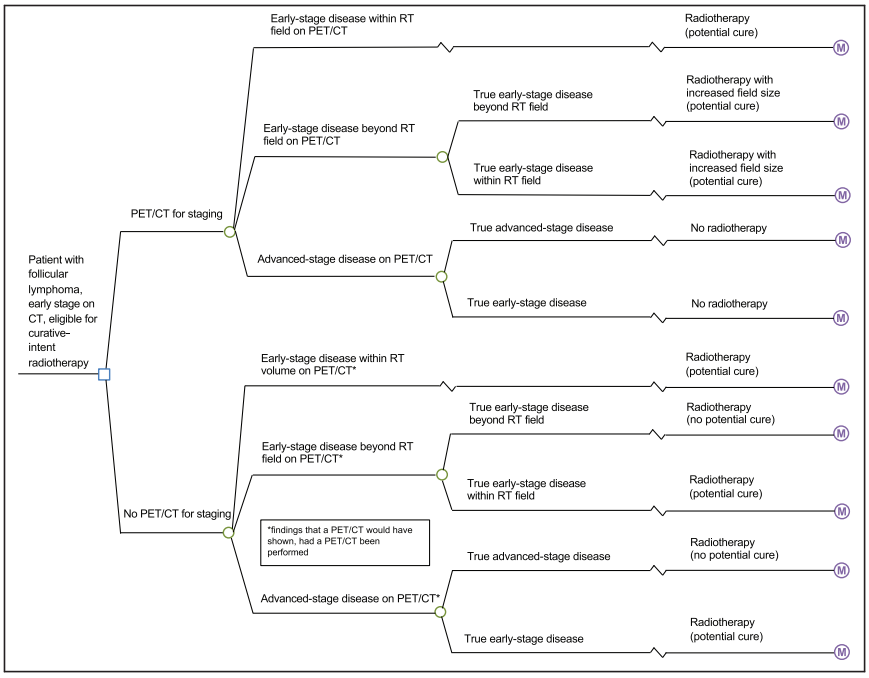

FIGURE 1. Decision tree depicting management after staging PET/CT vs. no staging PET/CT. M = state-transition cohort model.

Utilities and Costs

A utility value representing health-related quality of life was assigned to each health state on the basis of published values (Supplemental Table 1 (*25–29*)).

Costs were considered from the perspective of the Canadian health-care system and were adjusted to 2019 Canadian dollars with the Consumer Price Index (http://www.bankofcanada.ca). On the basis of Wirth et al. (*13*), we accounted for the additional cost of a biopsy in approximately 16% of patients who had new findings on PET/CT. The costs

of PET/CT and core biopsy were based on the 2019 Ontario Schedule of Benefits for Physician Services. The cost of a 12-fraction course (*27*) of intensity-modulated RT was derived from a Canadian costing model (*30*). Further medical costs and their derivations are detailed in Supplemental Table 2 (*19,23,30–39*).

RESULTS

Cost-Utility Analysis

In the base-case scenario, PET/CT was the dominant strategy. The no-PET/CT strategy resulted in 14.09 QALYs and a cost of $98,657. The PET/CT strategy resulted in 14.40 QALYs at a cost of $95,491, representing a gain of 0.32 QALYs and an average lifetime cost saving of $3,165.

Sensitivity Analyses

One-way sensitivity analyses were conducted for each variable, evaluating net monetary benefit at a willingness-to-pay threshold of $100,000/QALY; a range of 0%–100% was used for testing probabilities, 0–1 for utilities, and 0–$500,000 for costs. As shown in Supplemental Figure 1, the no-PET/CT strategy became the preferred strategy only in scenarios that were not supported by available data, including when the probability of progression after rituximab monotherapy in advanced-stage disease was more than 8.3% per 6 mo, when the probability of progression after watchful waiting in advanced-stage disease was less than 4% per 6 mo, and when the utility of first remission was less than 0.66. The no-PET/CT strategy also became preferred when the proportion of advanced-stage patients requiring bendamustine-rituximab was more than 48.0%, receiving watchful waiting was more than 89.3%, and receiving palliative-intent RT was more than 75.4%. The model was robust to a very wide range of costs in 1-way sensitivity analyses. The no-PET/CT strategy was preferred only when costs were unrealistically high: more than $36,040 for PET/CT, more than $340,653 for bendamustine-rituximab after rituximab monotherapy, and more than $60,815 for a follow-up appointment. The model was not sensitive to the costs of RT, biopsy, salvage chemotherapy, rituximab maintenance, biopsy, medical oncology consultation, palliation, or bendamustine-rituximab after RT or watchful waiting.

The net monetary benefit of the PET/CT strategy increased with increasing probability that PET/CT would detect advanced-stage disease or would detect early-stage disease outside the planned RT field. PET/CT also remained the optimal strategy across the range of relevant values for both parameters in 1-way sensitivity analyses. In 2-way sensitivity analysis, the PET/CT strategy remained preferred unless advanced-stage disease was less than 1% and early-stage disease outside the planned RT field was less than 5% (Supplemental Fig. 3).

One-way sensitivity analyses were also performed on the probability that new findings on the PET/CT would be correct. When advanced-stage disease is detected on PET/CT, the probability of a true positive only needs to be greater than 20.3% for the PET/CT strategy to be preferred. PET/CT remained the optimal strategy across the full range of probabilities of a true-positive result when PET/CT detects early-stage disease beyond the planned RT volume.

Probabilistic Sensitivity Analyses

A probabilistic sensitivity analysis using 10,000 simulations was performed with the distributions described in Supplemental Tables 1 and 2. In 89.1% of simulations, the PET/CT strategy was cost-effective (i.e., either cost-saving and QALY-improving or with an incremental cost-effectiveness ratio below $100,000/QALY) (Supplemental Fig. 2). In 77.1% of simulations, the PET/CT strategy was strongly dominant (i.e., reduced costs and increased QALYs).

DISCUSSION

Our analysis shows that adding PET/CT to the staging of early-stage FL patients reduces cost and improves QALYs. The existing literature on PET/CT in low-grade FL has focused on its diagnostic accuracy and impact on clinical management (*13,40–43*). Although such analyses are important, they do not demonstrate the effect of PET/CT on clinical outcomes. Moreover, whereas outcomes of PET/CT-staged early-stage FL have been reported (*7,8*), the comparison with outcomes for conventionally staged early-stage FL does not reflect the true effect of staging PET/CT, given the exclusion of some patients after upstaging on PET/CT. Our decision analysis allows a more comprehensive evaluation of highly relevant endpoints, QALYs and cost-effectiveness. To our knowledge, this is the first cost-effectiveness analysis assessing the impact of PET/CT on early-stage FL.

Although several studies have demonstrated that PET/CT changed Ann Arbor staging in a significant proportion of patients with FL (*40,41,44*), most additional lesions detected by PET/CT have not been accompanied by subsequent biopsy and confirmation of lymphoma. A systematic review showed that only 3 of the 349 patients included across 7 studies had histologic confirmation. Although the false-negative rate for PET/CT in early-stage FL is low (*41,42, 45,46*), the false-positive rate is uncertain and limited by a lack of systematic biopsies of relevant sites; thus, the implications of upstaging solely on the basis of PET/CT are unclear (*10,47*). There were 2 parameters in our model that were related to the false-positive–versus–true-positive rate of PET/CT, which were both tested in 1-way sensitivity analyses: the first parameter is the probability that a new PET/CT finding of advanced-stage disease is a true-positive, and the second parameter is the probability that a new PET/CT finding of early-stage disease outside the planned RT field is a true-positive. When advanced-stage disease is detected on PET/CT, the PET/CT strategy is advantageous as long as the probability of a true positive is more than 20%; in other words, only if there is a high proportion (>80%) of "false-positives" (i.e., patients whose PET/CT show advanced-stage disease but truly have early-stage disease) leading to inappropriate treatment will the PET/CT strategy be detrimental. In the context of a new PET/CT finding of early-stage disease outside the planned RT field, the model is not sensitive to the true positivity rate; this lack of sensitivity is because inadvertently enlarging the RT field does not lead to a significant reduction in QALYs, given the low toxicity of RT (*27*). The uncertainty of PET/CT diagnostic accuracy was incorporated conservatively into the probabilistic sensitivity analysis using wide uniform distributions. Our model remained robust in deterministic and probabilistic sensitivity analyses, suggesting that the PET/CT strategy is likely to increase QALYs and reduce cost regardless of the exact value of the true-positive rate.

The upstaging of FL by PET/CT has been investigated in a few studies, but to our knowledge, Wirth et al. is the only group that also reported the proportion of patients whose RT field was enlarged due to PET/CT findings (*13*). Thus, the study of Wirth et al. had the most complete data from which we derived our PET/CT-related transitional probabilities. However, given such scarce data on the probability of RT field enlargement, and the wide variation in the probability of upstaging across studies (*13,48–51*), we tested these parameters in sensitivity analyses. As expected, the

benefit of PET/CT decreased with decreasing proportion of new findings identified; however, the no-PET/CT strategy became preferred only if the probability that PET/CT would detect advanced-stage disease was less than 0.09% and the probability that PET/CT would detect early-stage disease outside the planned RT was less than 4%, a scenario that is extremely unlikely.

Of the patients upstaged to advanced-stage disease, a small proportion would have indications for chemoimmunotherapy and would receive bendamustine-rituximab, according to our model, whereas the other patients would be treated with rituximab monotherapy or watchful waiting. A large randomized, controlled trial by Ardeshna et al. investigating upfront rituximab monotherapy versus watchful waiting for asymptomatic stage II–IVA FL demonstrated significant improvements in progression-free survival and the time to initiation of the next treatment, with no overall survival benefit at a median follow-up of 4 y (*18*). Furthermore, a cost-effectiveness analysis comparing the 2 approaches showed that rituximab monotherapy increased life expectancy and QALYs over watchful waiting while being cost-saving (*23*), and the U.K. NICE guidelines recommend that rituximab monotherapy be offered to patients with asymptomatic advanced-stage FL (*52*). Despite the benefits of rituximab monotherapy, it is not universally used in asymptomatic advanced-stage FL; its use over watchful waiting and palliative-intent RT depends on factors such as physician practice and patient preference. Although the net monetary benefit of the PET/CT strategy decreases with increasing probability of watchful waiting or palliative-intent RT, the PET/CT strategy was preferred as long as the probability of watchful waiting was less than 89% and that of palliative-intent RT was less than 75%. Because our baseline probability of watchful waiting of 17.7% and palliative-intent RT of 5.6% were derived from a cohort predating randomized evidence on the benefit of rituximab monotherapy (*14,19*), it is unlikely that the probability of watchful waiting would approach 89% and that of palliative-intent RT would approach 75% in a given population. However, our model does suggest that the benefit of staging PET/CT over CT alone is smaller in a clinical practice where asymptomatic FL patients routinely undergo watchful waiting or palliative-intent RT; this is because a large driver of the benefit of staging PET/CT is the diversion of advanced-stage patients to rituximab monotherapy, rather than RT (with no potential cure) followed by observation.

Although our study population was defined as conventionally staged early-stage FL patients planned for curative-intent RT alone, it is worthwhile to consider the cost-effectiveness of staging PET/CT if alternative practices were used for early-stage FL, such as RT plus adjuvant systemic therapy, systemic therapy alone, or watchful waiting. The main advantage of PET/CT is revealing disease that is not detected by CT alone, resulting in enlargement of the RT field, or a switch to systemic therapy or watchful waiting if the patient has advanced-stage disease; in a practice where all early-stage FL is treated with RT plus adjuvant systemic therapy, PET/CT would likely still be cost-effective, as the aforementioned benefits would still apply. In our current model, the main disadvantage of the "no PET/CT for staging" strategy is that some patients are treated inappropriately with curative-intent RT when in fact there is no curative potential; this disadvantage is likely exacerbated when an additional inappropriate treatment (i.e., rituximab, cyclophosphamide, vincristine sulfate, and prednisone) is added, thereby increasing the net benefit of the staging PET/CT strategy. In a practice where early-stage FL patients are treated with systemic therapy or watchful waiting, the upstaging from PET/CT would likely result in more patients treated with systemic therapy than watchful waiting; given the superior progression-free survival and cost-effectiveness associated with rituximab induction over watchful waiting (*18,23*), we suspect that staging PET/CT would remain cost-effective in this setting. On the other hand, in a practice where all early-stage FL patients are treated with systemic therapy or all are treated with watchful waiting, staging PET/CT would not change management and would therefore be unlikely to be cost-effective.

Several limitations to our model need to be considered. Autologous and allogeneic hematopoietic cell transplantation (HCT) were not included as salvage therapy. HCT is controversial (*53,54*) and uncommonly used in FL, especially in a low-burden population such as this one (*55,56*); thus, HCT would be unlikely to have a large impact on results. If HCT were to be included, it would lead to more conservative estimates, as HCT should preferentially increase expenditures in the no-PET/CT strategy. More people in this strategy would require salvage therapy because fewer of them receive potentially curative RT and fewer receive rituximab monotherapy. Furthermore, the fact that salvage therapy options are rapidly evolving, with varying practice patterns across centers, could affect costs; however, the model was extremely robust to costs for salvage therapy. As in many prior cost-effectiveness analyses in FL (*55,57–61*), we did not account for the possibility of transformation to high-grade disease, which occurs at a cumulative incidence of approximately 1%–2% per year (*3,62,63*). As this transformation risk applies to patients in both strategies, it is unlikely that incorporating it would significantly change the impact of staging PET/CT.

CONCLUSION

Our study indicates that the addition of PET/CT for staging of early-stage FL patients planned for curative-intent RT reduces lifetime costs and improves patient QALYs. Patients with early-stage FL should therefore undergo PET/CT before curative-intent RT. Although the costs of drugs and imaging studies are typically higher in the United States than in Canada, our model was not sensitive to any such cost unless it far exceeded its true cost in either country. Therefore, whereas our analysis focuses on Canada, the results are relevant to international health-care settings such as the United States, where clinical pathways are similar.

DISCLOSURE

Stuart Peacock is the Academic Representative Member of the Board of Directors for the Canadian Agency for Drugs and Technologies in Health. Alex Louie has received honoraria from AstraZenca, RefleXion, and Varian Medical Systems. Kerry Savage has received institutional research funding from Roche. Laurie Sehn has a consultancy and has received honoraria from Incyte, Gilead, Kite, Janssen, Celgene, Acerta, Genentech, Inc., AstraZeneca, Apobiologix, AbbVie, Amgen, Karyopharm, Lundbeck, Merck, MorphoSys, F. Hoffmann-La Roche Ltd., Seattle Genetics, Teva, Servier, Takeda, Chugai, TG Therapeutics, and Verastem Oncology and has received research funding from Genentech, Inc., F. Hoffmann-LaRoche Ltd., and Teva. David Hodgson is the medical director of the Pediatric Oncology Group of Ontario. M.G. Myriam Hunink receives (or received) royalties from Cambridge University Press for a textbook on medical decision making, reimbursement of expenses from the European Society of Radiology (ESR) for work on the ESR guidelines for imaging referrals, reimbursement of expenses from the European Institute for Biomedical Imaging Research for

membership on the Scientific Advisory Board, and research funding from the American Diabetes Association, The Netherlands Organization for Health Research and Development, the German Innovation Fund, Netherlands Educational Grant ("Studie Voorschot Middelen"), and the Gordon and Betty Moore Foundation. No other potential conflict of interest relevant to this article was reported.

KEY POINTS

QUESTION: Is the addition of staging PET/CT cost-effective in early-stage FL?

PERTINENT FINDINGS: A decision analytic and state-transition cohort model simulated patients' management and disease course after adding staging PET/CT versus using conventional CT staging alone. Staging PET/CT was found to be the dominant strategy, resulting in both a lifetime cost saving and a gain in QALY.

IMPLICATIONS FOR PATIENT CARE: Patients with early-stage FL should undergo PET/CT before curative-intent RT.

REFERENCES

1. Mac Manus MP, Hoppe RT. Is radiotherapy curative for stage I and II low-grade follicular lymphoma? Results of a long-term follow-up study of patients treated at Stanford University. *J Clin Oncol.* 1996;14:1282–1290.
2. Wilder RB, Jones D, Tucker SL, et al. Long-term results with radiotherapy for stage I-II follicular lymphomas. *Int J Radiat Oncol Biol Phys.* 2001;51:1219–1227.
3. Lo AC, Campbell BA, Pickles T, et al. Long-term outcomes for patients with limited-stage follicular lymphoma: update of a population-based study. *Blood.* 2020;136:1006–1010.
4. Dreyling M, Ghielmini M, Rule S, et al. Newly diagnosed and relapsed follicular lymphoma: ESMO clinical practice guidelines for diagnosis, treatment and follow-up. *Ann Oncol.* 2016;27(suppl 5):v83–v90.
5. König L, Herfarth K, Hörner-Rieber J, Dietrich S, Wiegel T, Jürgen D, et al. Oncological outcome and recurrence pattern analysis after involved-field irradiation in combination with rituximab for early-stage nodal and extranodal follicular lymphoma. *Strahlenther Onkol.* 2020;196:705–714.
6. Pei S-N, Wang M-C, Ma M-C, Kuo C-Y, Liao C-K, Qiu H, et al. A comprehensive retrospective cohort study of the journey of B-cell lymphoma in Taiwan. *Sci Rep.* 2021;11:10069.
7. Brady JL, Binkley MS, Hajj C, et al. Definitive radiotherapy for localized follicular lymphoma staged by ^{18}F-FDG PET-CT: a collaborative study by ILROG. *Blood.* 2019;133:237–245.
8. Ng SP, Khor R, Bressel M, et al. Outcome of patients with early-stage follicular lymphoma staged with ^{18}F-fluorodeoxyglucose (FDG) positron emission tomography (PET) and treated with radiotherapy alone. *Eur J Nucl Med Mol Imaging.* 2019;46:80–86.
9. Cheson BD, Fisher RI, Barrington SF, et al. Recommendations for initial evaluation, staging, and response assessment of Hodgkin and non-Hodgkin lymphoma: the Lugano classification. *J Clin Oncol.* 2014;32:3059–3068.
10. Adams HJA, Nievelstein RAJ, Kwee TC. Systematic review on the additional value of ^{18}F-fluoro-2-deoxy-D-glucose positron emission tomography in staging follicular lymphoma. *J Comput Assist Tomogr.* 2017;41:98–103.
11. Neumann PJ, Cohen JT, Weinstein MC. Updating cost-effectiveness: the curious resilience of the $50,000-per-QALY threshold. *N Engl J Med.* 2014;371:796–797.
12. *Guidelines for the Economic Evaluation of Health Technologies: Canada.* 4th ed. Canadian Agency for Drugs and Technologies in Health; 2017:1–76.
13. Wirth A, Foo M, Seymour JF, MacManus MP, Hicks RJ. Impact of [^{18}F] fluorodeoxyglucose positron emission tomography on staging and management of early-stage follicular non-Hodgkin lymphoma. *Int J Radiat Oncol Biol Phys.* 2008;71:213–219.
14. Friedberg JW, Taylor MD, Cerhan JR, et al. Follicular lymphoma in the United States: first report of the National LymphoCare Study. *J Clin Oncol.* 2009;27:1202–1208.
15. Binkley MS, Brady JL, Hajj C, Chelius M, Chau K, MD AB, et al. Salvage treatment and survival for relapsed follicular lymphoma following primary radiation therapy: a collaborative study on behalf of ILROG. *Int J Radiat Oncol Biol.* 2019;104:522–529.
16. Barzenje DA. Radiotherapy compared to other strategies in the treatment of stage I/II follicular lymphoma: a study of 404 patients with a median follow-pp of 15 years. *PLoS One.* 2015;10:e0131158.
17. Ardeshna KM, Smith P, Norton A, et al. Long-term effect of a watch and wait policy versus immediate systemic treatment for asymptomatic advanced-stage non-Hodgkin lymphoma: a randomised controlled trial. *Lancet.* 2003;362:516–522.
18. Ardeshna KM, Qian W, Smith P, et al. Rituximab versus a watch-and-wait approach in patients with advanced-stage, asymptomatic, non-bulky follicular lymphoma: an open-label randomised phase 3 trial. *Lancet Oncol.* 2014;15:424–435.
19. Rummel MJ, Niederle N, Maschmeyer G, et al. Bendamustine plus rituximab versus CHOP plus rituximab as first-line treatment for patients with indolent and mantle-cell lymphomas: an open-label, multicentre, randomised, phase 3 non-inferiority trial. *Lancet.* 2013;381:1203–1210.
20. van Oers MHJ, Van Glabbeke M, Giurgea L, et al. Rituximab maintenance treatment of relapsed/resistant follicular non-Hodgkin's lymphoma: long-term outcome of the EORTC 20981 phase III randomized intergroup study. *J Clin Oncol.* 2010;28:2853–2858.
21. Salles G, Seymour JF, Offner F, et al. Rituximab maintenance for 2 years in patients with high tumour burden follicular lymphoma responding to rituximab plus chemotherapy (PRIMA): a phase 3, randomised controlled trial. *Lancet.* 2011;377:42–51.
22. Data tables in PDF and TXT format. Statistics Canada website. https://www150.statcan.gc.ca/n1/pub/84-537-x/4064441-eng.htm. Modified July 31, 2006. Accessed January 6, 2022.
23. Prica A, Chan K, Cheung M. Frontline rituximab monotherapy induction versus a watch and wait approach for asymptomatic advanced-stage follicular lymphoma: a cost-effectiveness analysis. *Cancer.* 2015;121:2637–2645.
24. Barzenje DA, Cvancarova Småstuen M, Liestøl K, et al. Radiotherapy compared to other strategies in the treatment of stage I/II follicular lymphoma: a study of 404 patients with a median follow-up of 15 years. *PLoS ONE.* 2015;10:e0131158.
25. Wang H, Smith A, Yu G, et al. UK utility elicitation in patients with follicular lymphoma [abstract]. *Value Health.* 2017;20:PA449.
26. Wild D, Walker M, Pettengell R, Lewis G. PCN62 utility elicitation of patients with follicular lymphoma [abstract]. *Value Health.* 2006;9:A294.
27. Hoskin PJ, Kirkwood AA, Popova B, et al. 4 Gy versus 24 Gy radiotherapy for patients with indolent lymphoma (FORT): a randomised phase 3 non-inferiority trial. *Lancet Oncol.* 2014;15:457–463.
28. Wang H-I, Roman E, Crouch S, Aas E, Burton C, Patmore R, et al. A generic model for follicular lymphoma: predicting cost, life expectancy, and quality-adjusted-life-year using UK population–based observational data. *Value Health.* 2018;21:1176–1185.
29. Fagnoni P, Milpied N, Limat S, Deconinck E. Cost effectiveness of high-dose chemotherapy with autologous stem cell support as initial treatment of aggressive non-Hodgkin's lymphoma. *Pharmacoeconomics.* 2009;27:55–68.
30. Yong JHE, McGowan T, Redmond-Misner R, et al. Estimating the costs of intensity-modulated and 3-dimensional conformal radiotherapy in Ontario. *Curr Oncol.* 2016;23:e228–e238.
31. Adams SJ, Rakheja R, Bryce R, Babyn PS. Incidence and economic impact of incidental findings on ^{18}F-FDG PET/CT imaging. *Can Assoc Radiol J.* 2018;69:63–70.
32. Schedule of benefits: physician services under the Health Insurance Act. Ontario Ministry of Health and Long-Term Care website. https://www.health.gov.on.ca/en/pro/programs/ohip/sob/physserv/sob_master.pdf. Published July 2, 2021. Accessed January 6, 2022.
33. Mittmann N. Economic analysis of alemtuzumab (MabCampath®) in fludarabine-refractory chronic lymphocytic leukemia. *Open Pharmacoecon Health Econ J.* 2012;4:18–25.
34. RiTUXimab. Cancer Care Ontario website. https://www.cancercareontario.ca/en/drugformulary/drugs/riTUXimab. Published 2020. Accessed January 6, 2022.
35. Schedule of benefits for laboratory services. Ontario Ministry of Health and Long-Term Care website. http://www.health.gov.on.ca/en/pro/programs/ohip/sob/lab/lab_mn2020.pdf. Published July 1, 2020. Accessed January 6, 2022.
36. Lathia N, Mittmann N, DeAngelis C, et al. Evaluation of direct medical costs of hospitalization for febrile neutropenia. *Cancer.* 2010;116:742–748.
37. Treanda for non-Hodgkin lymphoma. Canadian Agency for Drugs and Technologies in Health website. https://cadth.ca/treanda-indolent-non-hodgkin-lymphoma. Updated December 14, 2012. Accessed January 6, 2022.
38. Herold M, Sacchi S, Hieke K. The cost of treating relapsed indolent non-Hodgkin's lymphoma in an international setting: retrospective analysis of resource use. *Haematologica.* 2002;87:719–729.
39. Dumont S, Jacobs P, Fassbender K, Anderson D, Turcotte V, Harel F. Costs associated with resource utilization during the palliative phase of care: a Canadian perspective. *Palliat Med.* 2009;23:708–717.

40. Metser U, Dudebout J, Baetz T, Hodgson DC, Langer DL, MacCrostie P, et al. [^{18F}]-FDG PET/CT in the staging and management of indolent lymphoma: a prospective multicenter PET registry study. *Cancer.* 2017;123:2860–2866.
41. Fueger BJ, Yeom K, Czernin J, Sayre JW, Phelps ME, Allen-Auerbach MS. Comparison of CT, PET, and PET/CT for staging of patients with indolent non-Hodgkin's lymphoma. *Mol Imaging Biol.* 2009;11:269–274.
42. Tsukamoto N, Kojima M, Hasegawa M, et al. The usefulness of ^{18}F-fluorodeoxyglucose positron emission tomography (^{18}F-FDG-PET) and a comparison of ^{18}F-FDG-PET with ^{67}gallium scintigraphy in the evaluation of lymphoma. *Cancer.* 2007;110:652–659.
43. Ng SP, Khor R, Bressel M, et al. Outcome of patients with early-stage follicular lymphoma staged with ^{18}F-fluorodeoxyglucose (FDG) positron emission tomography (PET) and treated with radiotherapy alone. *Eur J Nucl Med Mol Imaging.* 2019;46:80–86.
44. Adams HJA, Nievelstein RAJ, Kwee TC. Systematic review on the additional value of ^{18}F-fluoro-2-deoxy-D-glucose positron emission tomography in staging follicular lymphoma. *J Comput Assist Tomogr.* 2017;41:98–103.
45. Elstrom R, Guan L, Baker G, et al. Utility of FDG-PET scanning in lymphoma by WHO classification. *Blood.* 2003;101:3875–3876.
46. Wöhrer S, Jaeger U, Kletter K, et al. ^{18}F-fluoro-deoxy-glucose positron emission tomography (^{18}F-FDG-PET) visualizes follicular lymphoma irrespective of grading. *Ann Oncol.* 2006;17:780–784.
47. McNamara C, Davies J, Dyer M, et al. Guidelines on the investigation and management of follicular lymphoma. *Br J Haematol.* 2012;156:446–467.
48. Le Dortz L, De Guibert S, Bayat S, et al. Diagnostic and prognostic impact of ^{18}F-FDG PET/CT in follicular lymphoma. *Eur J Nucl Med Mol Imaging.* 2010;37:2307–2314.
49. Luminari S, Biasoli I, Arcaini L, et al. The use of FDG-PET in the initial staging of 142 patients with follicular lymphoma: a retrospective study from the FOLL05 randomized trial of the Fondazione Italiana Linfomi. *Ann Oncol.* 2013;24:2108–2112.
50. Janikova A, Bolcak K, Pavlik T, Mayer J, Král Z. Value of [^{18}F]fluorodeoxyglucose positron emission tomography in the management of follicular lymphoma: the end of a dilemma? *Clin Lymphoma & Myeloma.* 2011;8:287–293.
51. Ngeow JYY, Quek RHH, Ng DCE, et al. High SUV uptake on FDG-PET/CT predicts for an aggressive B-cell lymphoma in a prospective study of primary FDG-PET/CT staging in lymphoma. *Ann Oncol.* 2009;20:1543–1547.
52. Non-Hodgkin's lymphoma: diagnosis and management. National Institute for Health and Care Excellence website. https://www.nice.org.uk/guidance/ng52. Published July 20, 2016. Accessed January 6, 2022.
53. Freedman A. Follicular lymphoma: 2018 update on diagnosis and management. *Am J Hematol.* 2018;93:296–305.
54. Montoto S, Corradini P, Dreyling M, et al. Indications for hematopoietic stem cell transplantation in patients with follicular lymphoma: a consensus project of the EBMT-Lymphoma Working Party. *Haematologica.* 2013;98:1014–1021.
55. Hayslip JW, Simpson KN. Cost-effectiveness of extended adjuvant rituximab for US patients aged 65-70 years with follicular lymphoma in second remission. *Clin Lymphoma Myeloma.* 2008;8:166–170.
56. van Agthoven M, Kramer MHH, Sonneveld P, et al. Cost analysis of common treatment options for indolent follicular non-Hodgkin's lymphoma. *Haematologica.* 2005;90:1422–1432.
57. Kasteng F, Erlanson M, Hagberg H, Kimby E, Relander T, Lundkvist J. Cost-effectiveness of maintenance rituximab treatment after second line therapy in patients with follicular lymphoma in Sweden. *Acta Oncol.* 2008;47:1029–1036.
58. Ray JA, Carr E, Lewis G, Marcus R. An evaluation of the cost-effectiveness of rituximab in combination with chemotherapy for the first-line treatment of follicular non-Hodgkin's lymphoma in the UK. *Value Health.* 2010;13:346–357.
59. Deconinck E, Miadi-Fargier H, Le Pen C, Brice P. Cost effectiveness of rituximab maintenance therapy in follicular lymphoma. *Pharmacoeconomics.* 2010;28:35–46.
60. Soini EJ, Martikainen JA, Vihervaara V, Mustonen K, Nousiainen T. Economic evaluation of sequential treatments for follicular non-Hodgkin lymphoma. *Clin Ther.* 2012;34:915–925.e2.
61. Chen Q, Ayer T, Nastoupil LJ, Rose AC, Flowers CR. Comparing the cost-effectiveness of rituximab maintenance and radioimmunotherapy consolidation versus observation following first-line therapy in patients with follicular lymphoma. *Value Health.* 2015;18:189–197.
62. Montoto S, Davies AJ, Matthews J, et al. Risk and clinical implications of transformation of follicular lymphoma to diffuse large B-cell lymphoma. *J Clin Oncol.* 2007;25:2426–2433.
63. Federico M, Caballero Barrigón MD, Marcheselli L, et al. Rituximab and the risk of transformation of follicular lymphoma: a retrospective pooled analysis. *Lancet Haematol.* 2018;5:e359–e367.

Combined Metabolically Active Tumor Volume and Early Metabolic Response Improve Outcome Prediction in Metastatic Colorectal Cancer

Erwin Woff[1], Lisa Salvatore[2], Federica Marmorino[3], Dario Genovesi[4], Gabriela Critchi[1], Thomas Guiot[1], Lieveke Ameye[5], Francesco Sclafani[6], Alain Hendlisz*[6], and Patrick Flamen*[1]

[1]Nuclear Medicine Department, Institut Jules Bordet–Université Libre de Bruxelles (ULB), Brussels, Belgium; [2]Medical Oncology Department, Comprehensive Cancer Center, Fondazione Policlinico Universitario Agostino Gemelli IRCCS, Rome, Italy; [3]Department of Translational Research and New Technologies in Medicine and Surgery, Unit of Medical Oncology 2, Azienda Ospedaliera Universitaria Pisana, Pisa, Italy; [4]Nuclear Medicine Department, Fondazione Toscana "Gabriele Monasterio," Pisa, Italy; [5]Data Centre, Institut Jules Bordet–Université Libre de Bruxelles (ULB), Brussels, Belgium; and [6]Medical Oncology Department, Institut Jules Bordet–Université Libre de Bruxelles (ULB), Brussels, Belgium

Stratification of metastatic colorectal cancer (mCRC) patients is mostly based on clinical and biologic characteristics. This study aimed to validate the prognostic value of ^{18}F-FDG PET/CT–based biomarkers such as baseline whole-body metabolically active tumor volume (WB-MATV) and early metabolic response (mR) in mCRC. **Methods:** The development cohort included chemorefractory mCRC patients enrolled in 2 prospective Belgian multicenter trials evaluating last-line treatments (multikinase inhibitors). The validation cohort included mCRC patients from an Italian center treated with chemotherapy and bevacizumab as first-line. Baseline WB-MATV was defined as the sum of metabolically active volumes of all target lesions identified on the baseline ^{18}F-FDG PET/CT. Early mR assessment was performed following usual response criteria (response threshold of 30% [PERCIST–30%], response threshold of 15% [PERCIST–15%], European Organization for Research and Treatment of Cancer) and the so-called CONSIST method, which defines response as a decrease of $SUL_{max} \geq 15\%$ for all target lesions. Baseline WB-MATV and early mR assessment were investigated along with usual clinical factors and correlated with overall survival (OS) and progression-free survival (PFS). **Results:** Clinical factors, baseline WB-MATV, and early mR were evaluable in 192 of 239 and 94 of 125 patients of the development and validation cohorts, respectively. Except for PERCIST–30%, all response methods were equivalent in terms of outcome prediction, and CONSIST was found to be the most accurate. Baseline WB-MATV and early mR using the CONSIST method were independent prognostic parameters after adjustment for clinical factors in the development and validation sets for both OS (hazard ratio [HR] WB-MATV: 1.87 [95% CI, 1.17–2.97], $P = 0.005$, and HR early mR: 1.79 [95% CI, 1.08–2.95], $P = 0.02$ for the validation set) and PFS (HR WB-MATV: 1.94 [95% CI, 1.27–2.97], $P = 0.002$, and HR early mR: 1.69 [95% CI, 1.04–2.73], $P = 0.03$ for the validation set). **Conclusion:** Baseline WB-MATV and early mR are strong independent prognostic biomarkers for OS and PFS in mCRC, regardless of treatment received. Therefore, combining these biomarkers improves risk stratification for OS and PFS in mCRC.

Key Words: ^{18}F-FDG PET/CT-based biomarkers; metabolically active tumor volume; early metabolic response; metastatic colorectal cancer

Received Feb. 26, 2021; revision accepted Jun. 29, 2021.
For correspondence or reprints, contact Erwin Woff (erwin.woff@bordet.be).
*Contributed equally to this work.
Published online Jul. 29, 2021.
COPYRIGHT © 2022 by the Society of Nuclear Medicine and Molecular Imaging.

J Nucl Med 2022; 63:549–555
DOI: 10.2967/jnumed.120.245357

Despite significant improvements over the last 15 y, patients with metastatic colorectal cancer (mCRC) still hold a poor prognosis, with a 5-y survival rate less than 15% (*1*). Nevertheless, survival differs significantly among patients, creating the need for prognostic biomarkers to improve patient stratification and personalized care.

Baseline whole-body metabolically active tumor volume (WB-MATV), an ^{18}F-FDG PET–based quantitative parameter, has recently been reported by our group to be a strong independent prognostic imaging biomarker in chemorefractory mCRC, with a higher prognostic value than the usual clinical prognostic factors (*2*). However, these findings still required validation in mCRC patients undergoing first-line treatment.

Early metabolic response (mR) assessment using ^{18}F-FDG PET/CT is a valuable tool for the rapid identification of patients with treatment-resistant tumors, faster than with conventional, morphology-based imaging (CT/MRI). It has also been shown to be a strong predictor of outcome in many tumor types (*3,4*). The high negative predictive value of early mR assessment (performed as early as after 1 treatment cycle) is a key strength of metabolic imaging, essential to avoid pursuing ineffective and potentially toxic treatments, thereby allowing a rapid and cost-effective way to reallocate societal resources toward more promising therapies (*3,5*). To our knowledge, no prospective validation study has been reported so far on the predictive value of early mR assessment and its independence from baseline WB-MATV and clinical prognostic factors in mCRC.

Different mR assessment criteria have been explored in many cancer types including mCRC, but until now, no consensus has been reached on which criteria are best to use and whether these different response criteria are equivalent in terms of outcome prediction (*6,7*).

The aims of this study were first, to validate the prognostic value of baseline WB-MATV and early mR assessment in chemonaïve mCRC patients; second, to assess whether early mR yields additional predictive value when combined with clinical factors and baseline WB-MATV; and last, to evaluate the relative predictive values of the usual mR criteria.

MATERIALS AND METHODS

Study Population

This study included mCRC patients from 3 prospective datasets. The development set was composed of 2 Belgian multicenter single-arm phase II trials: SoMore and RegARd-C, which have already been described in a previous report (*2*). These trials were conducted in chemorefractory mCRC patients ($n = 239$) treated with capecitabine/sorafenib (SoMore) or regorafenib (RegARd-C). The external validation set consisted of an Italian monocentric single-arm study. This study investigated the correlation between early mR and survival outcomes (overall survival [OS] and progression-free survival [PFS]) in chemonaïve mCRC patients ($n = 125$) treated with standard first-line chemotherapy combined with targeted agents (*8*).

Patient eligibility criteria and study design for the first 2 datasets were previously reported (*9,10*) but can be described shortly as follows: histologically proven colon or rectum adenocarcinoma; tumor refractory to all standard chemotherapy agents; age greater than 18 y; Eastern Cooperative Oncology Group (ECOG) performance status (PS) of 1 or less; life expectancy greater than 12 wk; a baseline (before treatment start) and an early ^{18}F-FDG PET/CT (after 2–3 wk of therapy) with at least 1 measurable target lesion on the baseline examination; a minimum washout period of 4 wk before inclusion in the trial; and provision of signed informed consent. Eligibility criteria for the external validation set were the same except that all patients were chemonaïve.

Ethics approvals for these 3 trials were obtained from the relevant local ethical committee of each center. All procedures performed in this study involving human participants were in accordance with the ethical standards of the institutional or national research committee and the 1964 Helsinki declaration and its later amendments or comparable ethical standards.

^{18}F-FDG PET/CT Imaging

Eight Belgian EANM Research Ltd. (EARL)–accredited and 1 Italian PET/CT centers were involved in this study, with each following strict procedural guidelines for standardization of patient preparation, scan acquisition, and image processing to ensure the most accurate and reproducible quantitative PET measurements (*11,12*). In brief, patients fasted 6 h before the radiotracer injection (target serum glucose $\leq$ 150 mg/dL). A static whole-body (skull to mid-thigh) PET scan was started 60 min (range, 55–75 min) after injection of ^{18}F-FDG (3–4 MBq/kg), with an acquisition time of 90 s per bed position. A low-dose CT was obtained before the PET scan. All PET data were normalized and corrected for scatter and random events, attenuation, and decay.

Quality assessment for patient preparation, imaging protocols, and anonymization for central review of PET/CT images were ensured by an independent dedicated academic PET/CT imaging core lab (ORI-LaB). Items checked in the quality control analysis were already described in a previous report, and this quality control was applied to all ^{18}F-FDG PET/CT scans of the current study (*2*). Any violation with respect to uptake time, administered dose, complete image dataset, good quality of images (high statistics suitable for diagnostic interpretation), PET/CT scans of the same patient performed on the same scanner for baseline and early time points, and time between baseline PET/CT and treatment start for all ^{18}F-FDG PET/CT scans of this study led to the exclusion from the central review analysis. None of the nuclear medicine physicians involved in this study had access to the medical records and treatment outcomes. Those were centralized and stored in the data center. All PET measurements were computed on a dedicated workstation (Advantage Workstation; GE Healthcare) using the commercial PETVCAR software, version 4.6 (GE Healthcare).

Target lesions identified for each patient were defined as follows: unequivocal tumor origin, transverse diameter greater than 15 mm on a registered CT image, and an ^{18}F-FDG SUV normalized to lean body mass (SUL) higher than 1.5 $\times$ the mean liver SUL + 2 $\times$ SD, or in the presence of liver metastasis, 2.0 $\times$ mean aorta SUL + 2 $\times$ SD, following PERCIST methodology (*13*). In the case there was no target lesion identified on the baseline PET/CT, the patient was excluded from the baseline WB-MATV and from the response analysis.

The image analysis procedure for the different PET metrics used in this study was as follows: the MATV of a lesion was defined as the volume of tumor tissue demonstrating metabolic activity at or higher than the calculated PERCIST threshold described above. Baseline WB-MATV was calculated as the sum of the MATV values of all target lesions, without a predefined limitation on their number. To minimize overestimation of WB-MATV, volume of interest for each lesion was manually placed so as to exclude both surrounding physiologic uptake and adjacent lesions' uptake.

Different response criteria were used for the evaluation of the early mR: PERCIST with the usual threshold of 30% (PERCIST–30%), PERCIST with an adapted response threshold of 15% (PERCIST–15%), EORTC–15% (European Organization for Research and Treatment of Cancer, response threshold of 15%), and CONSIST–15% (response threshold of 15%) (*5,13,14*).

For all these response criteria, the early mR assessment was dichotomized into mR and metabolic nonresponder (mNR). With CONSIST methodology, a patient was classified as nonresponder when there was at least 1 target lesion not reaching an SUL_{max} decrease of $>$ 15% (*5,15*). With PERCIST and EORTC methodologies, patients who had a complete or partial mR were classified as mR, and patients who had a stable or progressive metabolic disease were classified as mNR. More details on criteria used in this study for the different mR assessment methodologies can be found in Supplemental Table 1 (supplemental materials are available at http://jnm.snmjournals.org).

All PET measurements were normalized to lean body mass except for EORTC measurements, which were normalized to body surface area as required in the guidelines (*14*).

Statistical Analysis

The baseline clinical characteristics and survival data were collected prospectively. For univariable analyses, survival outcomes were measured from the date of treatment start to death from any cause for OS, and to the point of tumor progression or recurrence (based on radiologic assessment according to RECIST 1.1 with either contrast-enhanced CT or MRI, which was done at baseline and every 2 cycles [8 wk]) or death from any cause for PFS. For univariable and multivariable analyses of the early mR assessment, survival outcomes were measured from the date of the early mR assessment to death from any cause for OS and to the point of progression or recurrence (according to RECIST 1.1 evaluation, which was done every 2 cycles) or death from any cause for PFS. All patients alive or not progressing at last follow-up were censored.

As the optimal cutoff value for baseline WB-MATV was determined and validated in a recent report to be 100 cm^3 in chemorefractory mCRC patients, the same cutoff was applied in the external validation set (*2*).

The prognostic values of the clinical and PET parameters (baseline WB-MATV and early mR) were assessed using Kaplan–Meier estimation for survival probabilities (OS and PFS), the log-rank test for comparisons of groups, and the Cox proportional hazards regression model for regression analysis to estimate the hazard ratios (HRs) with 95% CIs. In the multivariable Cox model, the following variables were considered for association with OS and PFS: age, sex, body mass index, ECOG PS, KRAS mutational status, primary tumor location (right- versus left-sided colon and rectum), baseline WB-MATV, and early mR following the response criteria as described above. BRAF mutational status was included only in the statistical analyses of the validation set because of the small number of BRAF-mutant patients remaining in last-line of treatment.

The predictive accuracy for OS and PFS of the different early mR methods was assessed by the Harrell's c-index. P values of $<$ 0.05

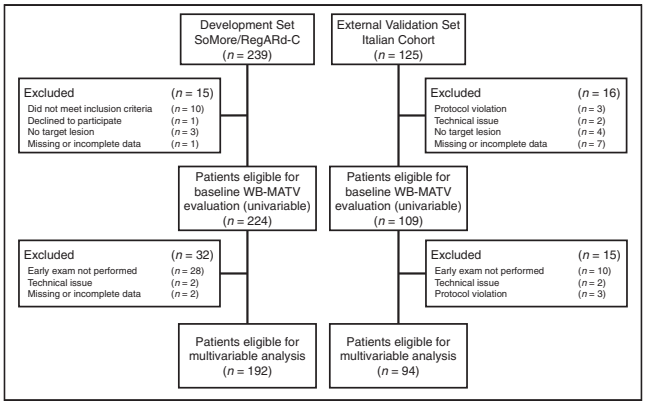

FIGURE 1. Study flow diagram of development and external validation sets.

were considered statistically significant, and all tests were 2-sided. Statistical analyses were performed using SAS, version 9.4 (SAS Institute), IBM SPSS Statistics 25 (IBM Corp.), and GraphPad Prism, version 7.04 (GraphPad Software Inc.).

RESULTS

Patients

Of 239 mCRC patients included in the Belgian cohort and 125 in the Italian cohort, 224 (94%) and 109 (87%), respectively, were considered suitable for baseline WB-MATV analysis, whereas 192 (80%) and 94 (75%) patients, respectively, were retained for early mR analysis. The reasons for ineligibility are shown in the study flow diagram in Figure 1. Patient and disease characteristics are summarized in Supplemental Table 2.

The median durations of follow-up were, respectively, 24.0 mo and 25.1 mo for the development and the validation sets. At the end of the studies of the development and external validation sets, 217 of 224 (97%) and 87 of 109 (80%) patients had died, respectively, and all patients had a progression event. Median OS and PFS for all patients eligible for analysis were 6.9 mo (95% CI, 6.2–8.1 mo) and 3.3 mo (95% CI, 2.2–3.7 mo), respectively, for the development set and 25.2 mo (range, 20.9–27.2 mo) and 9.7 mo (95% CI, 8.4–11.5 mo), respectively, for the validation set.

Baseline Clinical Factors and Patient Outcomes

Among the clinical factors, the following were found to be statistically significant for OS in the development set—ECOG PS (HR, 1.59 [1.21–2.09], $P = 0.001$) and body mass index (HR, 0.57 [0.43–0.76], $P < 0.001$)—and for OS in the validation set—BRAF mutational status (HR, 3.43 [1.11–10.54], $P = 0.03$) and ECOG PS (HR, 1.97 [1.06–3.69], $P = 0.03$).

Baseline WB-MATV

The median values for baseline WB-MATV in the development and validation sets were 164 cm^3 (5th–95th percentiles, 6–1,755 cm^3), and 134 cm^3 (5th–95th percentiles, 6–1,426 cm^3), respectively.

The median values of the number of weeks that have passed between the baseline PET to the start of treatment in the development and validation sets were 1 (range, 0–4) and 1 (range, 0–6), respectively.

Baseline WB-MATV and Patient Outcomes

In the development set, patients with a high baseline WB-MATV (≥100 cm^3) had a significantly worse outcome compared with patients with a low baseline WB-MATV (<100 cm^3) in terms of both median OS (4.5 mo [95% CI, 3.4–5.5] vs. 11.2 mo [95% CI, 9.4–13.9]; HR, 2.70, $P < 0.001$) and median PFS (1.9 mo [95% CI, 3.5–5.7] vs. 4.3 mo [95% CI, 9.4–13.9]; HR, 1.98, $P < 0.001$).

These results were confirmed in the validation set: patients with a high baseline WB-MATV had a significantly worse outcome compared with patients with a low baseline WB-MATV in terms of both median OS (20.9 mo [95% CI, 17.2–24.6] vs. 35.7 mo [95% CI, 22.2–49.1]; HR, 1.93, $P = 0.003$) and median PFS (9.1 mo [95% CI, 7.4–10.7] vs. 12.4 mo [95% CI, 9.0–15.9]; HR, 1.86, $P = 0.002$) (Figs. 2A and 2B and Table 1).

Early mR Following Different Response Criteria and Patient Outcomes

All mR methods applied at an early time point (PERCIST–15%, EORTC, and CONSIST), except for PERCIST–30%, have shown to be highly predictive of OS and PFS in both the development and the validation sets (Figs. 3A and 3B and Table 1).

In terms of diagnostic performance, the early mR assessment according to the CONSIST criteria was found to be the most predictive method for both OS and PFS in the development and validation sets (Supplemental Table 3). The median values of the number of target lesions per patient evaluated with the CONSIST method in the development and validation sets were 4 (range, 1–35) and 3 (range, 1–21), respectively.

As early mR with PERCIST–30% was not found to be predictive of PFS in the development set and of OS and PFS in the validation set, this method was included only in the multivariable analyses of OS in the development set.

PET images with examples of patients showing low and high WB- MATV associated with response and nonresponse are illustrated in Figure 4. An example of a patient subject to differences in response assessment following PERCIST and EORTC methodologies is shown in Supplemental Figure 1.

Independent Predictors of OS and PFS Among PET and Clinical Parameters

After adjustment for clinical parameters, the multivariable analyses identified baseline WB-MATV as a significant independent predictor of OS (HR, 2.56 and 1.87, $P < 0.001$ and $P = 0.005$, for the development and validation sets, respectively) and PFS (HR, 2.0 and 1.94, $P < 0.001$ and $P = 0.002$) (Table 2).

After adjustment for clinical parameters and baseline WB-MATV, early mR according to CONSIST was identified as a significant independent predictor of OS (HR, 1.55 and 1.79, $P = 0.005$ and $P = 0.02$) and PFS (HR, 1.64 and 1.69, $P < 0.001$ and $P = 0.03$) (Table 2).

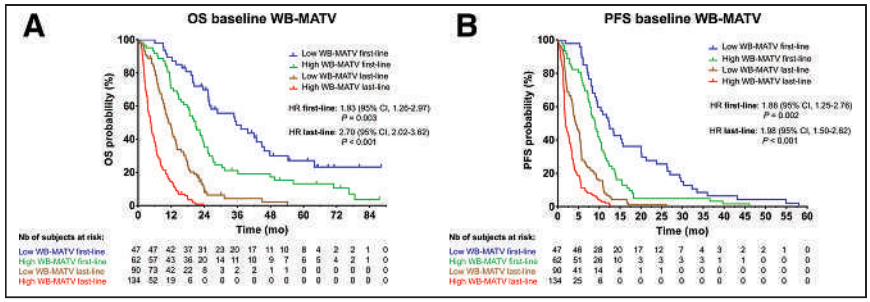

FIGURE 2. Kaplan–Meier estimates of OS (A) and PFS (B) according to baseline WB-MATV in development set (last-line) and validation set (first-line).

TABLE 1
Univariable Analyses of Baseline WB-MATV and Early mR According to Different Methods for OS and PFS in Development and Validation Sets

	Development set				Validation set			
	OS		PFS		OS		PFS	
Variable	HR (95% CI)	*P*	HR (95% CI)	*P*	HR (95% CI)	*P*	HR (95% CI)	*P*
Baseline WB-MATV	2.70 (2.02–3.62)	<0.001	1.98 (1.50–2.62)	<0.001	1.93 (1.26–2.97)	0.003	1.86 (1.25–2.76)	0.002
Early mR according to								
PERCIST–30%	1.39 (1.03–1.86)	0.03	1.31 (0.98–1.75)	0.06	1.54 (0.97–2.45)	0.07	1.33 (0.87–2.03)	0.19
PERCIST–15%	1.49 (1.07–2.06)	0.02	1.97 (1.40–2.78)	<0.001	1.71 (1.0–2.92)	0.05	1.76 (1.05–2.95)	0.03
EORTC	1.47 (1.02–2.10)	0.04	1.62 (1.12–2.34)	0.01	1.73 (0.96–3.12)	0.07	1.56 (0.91–2.68)	0.11
CONSIST	1.60 (1.18–2.16)	0.002	1.86 (1.37–2.52)	<0.001	2.37 (1.42–4.0)	0.001	2.16 (1.33–3.51)	0.002

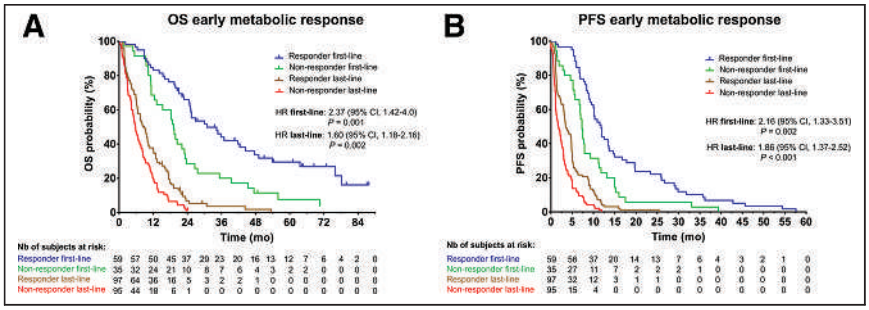

FIGURE 3. Kaplan–Meier estimates of OS (A) and PFS (B) according to early mR using CONSIST method in development set (last-line) and validation set (first-line).

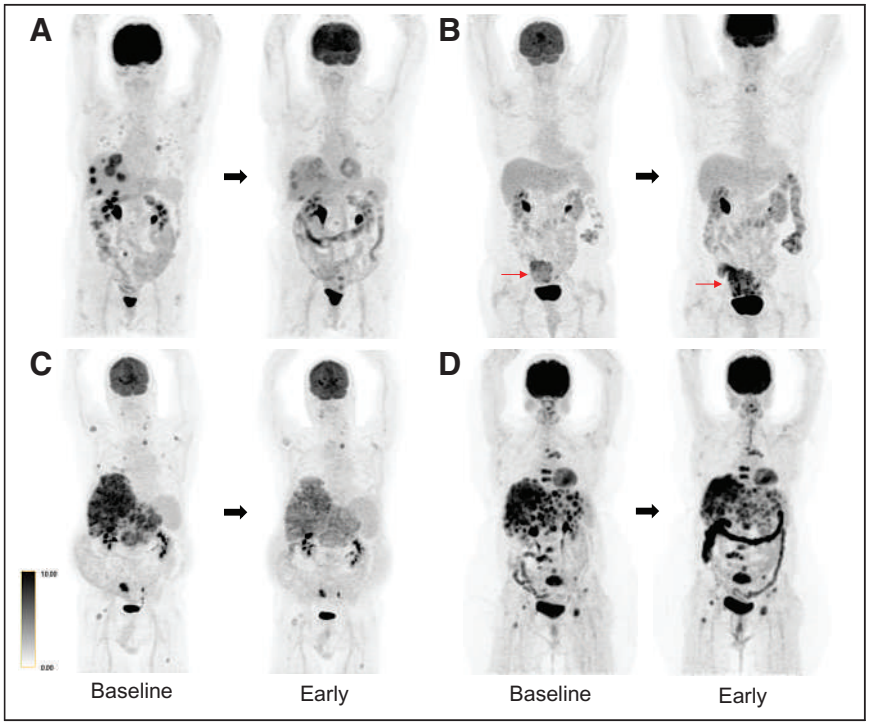

FIGURE 4. Examples of PET maximum-intensity-projection images of patients at baseline and early time points with a low baseline WB-MATV (85 cm^3) who respond (A), with a low baseline WB-MATV (30 cm^3) who did not respond (resistant lesion shown by red arrows) (B), with a high baseline WB-MATV (2,336 cm^3) who respond (C), and with a high baseline WB-MATV (1,065 cm^3) who did not respond (multiple resistant lesions) (D).

Combining Baseline WB-MATV and Early mR Assessment

The combination of baseline WB-MATV and early mR according to CONSIST classified the patients into 4 categories. Survival graphs of these 4 risk groups in the development and validation sets for both OS and PFS are shown in Figure 5.

DISCUSSION

This study is the first, to our knowledge, to prospectively validate baseline WB-MATV and early mR assessment as strong ^{18}F-FDG PET/CT–based biomarkers in both chemonaïve (treated with standard first-line chemotherapy combined with targeted agents) and chemorefractory (treated with targeted agents) mCRC patients. This study showed that baseline WB-MATV and early mR performed after 1 treatment cycle (i.e., at 2 wk) were able to identify a subset of high-risk patients. These high-risk patients (high WB-MATV and mNRs) had a risk of experiencing disease progression or dying 3 times higher than low-risk patients (low WB-MATV and mRs). The predictive value of early mR was demonstrated to be independent of baseline WB-MATV and clinical factors in the 2 clinical settings. Moreover, combining WB-MATV and early mR allowed a better risk stratification in identifying distinct patient risk groups in first- or last-line of treatment.

Our study confirmed the added prognostic value of baseline WB-MATV beyond the usual clinical prognostic parameters for both OS and PFS in chemonaïve patients. To the best of our knowledge, this is the first report that investigated baseline WB-MATV as a prognostic biomarker in a first-line setting. Our results have shown that baseline WB-MATV is predictive of survival regardless of treatment administered and, therefore, can be considered as a pure prognostic biomarker (*16*).

TABLE 2
Multivariable Analyses of Clinical (Age, Sex, ECOG PS, KRAS, BMI) and PET-Based Variables (Baseline WB-MATV and Early mR According to Different Methods) for OS and PFS in Development and Validation Sets

	Development set				Validation set			
	OS		PFS		OS		PFS	
Variable	HR (95% CI)	*P*	HR (95% CI)	*P*	HR (95% CI)	*P*	HR (95% CI)	*P*
Baseline WB-MATV (adjusted for clinical factors)	2.56 (1.90–3.44)	<0.001	2.00 (1.51–2.66)	<0.001	1.87 (1.17–2.97)	0.005	1.94 (1.27–2.97)	0.002
ECOG PS	1.47 (1.12–1.94)	0.006			2.01 (1.08–3.74)	0.03		
BMI	1.62 (1.22–2.16)	0.001						
Early mR (adjusted for clinical factors)								
PERCIST–30%	1.48 (1.09–2.02)	0.01	—	—	—	—	—	—
PERCIST–15%	1.60 (1.17–2.18)	0.003	1.84 (1.35–2.51)	<0.001	1.50 (0.90–2.50)	0.12	1.68 (1.02–2.79)	0.04
EORTC	1.52 (1.08–2.13)	0.02	1.52 (1.09–2.11)	0.01	1.43 (0.83–2.47)	0.20	1.49 (0.88–2.50)	0.14
CONSIST	1.70 (1.26–2.29)	<0.001	1.71 (1.27–2.28)	<0.001	1.99 (1.22–3.26)	0.006	1.98 (1.24–3.15)	0.004
ECOG PS	1.50 (1.11–2.01)	0.008						
BMI	1.89 (1.38–2.58)	<0.001						
Early mR (adjusted for clinical factors and baseline WB-MATV)								
PERCIST–30%	1.36 (1.00–1.85)	0.05	—	—	—	—	—	—
PERCIST–15%	1.56 (1.14–2.12)	0.005	1.91 (1.39–2.61)	<0.001	1.41 (0.84–2.38)	0.19	1.49 (0.89–2.48)	0.13
EORTC	1.45 (1.03–2.03)	0.03	1.54 (1.10–2.15)	0.01	1.37 (0.79–2.37)	0.26	1.33 (0.79–2.24)	0.29
CONSIST	1.55 (1.15–2.11)	0.005	1.64 (1.23–2.20)	<0.001	1.79 (1.08–2.95)	0.02	1.69 (1.04–2.73)	0.03
ECOG PS	1.38 (1.02–1.86)	0.035						
BMI	1.71 (1.25–2.34)	0.001						
Baseline WB-MATV	2.22 (1.61–3.06)	<0.001	1.69 (1.24–2.30)	0.001	1.82 (1.12–2.97)	0.016	1.79 (1.14–2.80)	0.01

BMI = body mass index.

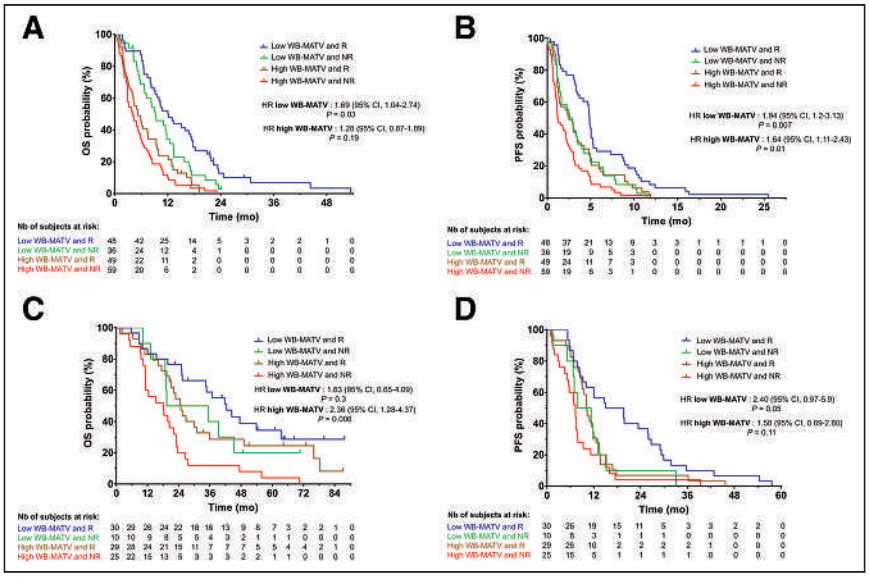

FIGURE 5. Kaplan–Meier estimates of OS and PFS according to baseline WB-MATV combined with early mR using CONSIST method in development set (A and B) and validation set (C and D) classifying patients into 4 risk groups.

In addition to the validation of WB-MATV as a baseline stratification factor in mCRC in a first-line setting, another important contribution of this study is that it highlighted the predictive value of early mR assessment for OS and PFS in both first- and last-line treatment settings. The predictive values of early mR in the first-line were almost the same as those obtained in the last-line setting and in line with those reported in small case series, which were conducted without clinical validation (*5,6,17,18*). Conversely, a few studies investigating mCRC patients reported a lack of correlation between early mR and outcomes, but those had several methodologic limitations (*19,20*). In particular the study of Byström et al. lacked basic conditions of imaging standardization and quality control. The results of our prospective validation study strongly contradict the conclusion made in the study of Byström et al. that "routine monitoring of mCRC patients by PET scans is not recommended due to its too

limited clinical value and notably in first-line treatment setting" (*19*).

Several mR methods applying different criteria were also investigated in the current study. Our findings indicate that the clinical impact of using a mR method or another is minimal in terms of outcome prediction, except for PERCIST.

PERCIST–30% applied in the context of early mR assessment was not predictive of outcomes in both first- and last-line treatment settings, except for OS in last-line. Conversely, PERCIST–15% was found to be a strong predictor of outcomes in both first- and last-line treatment settings. These results suggest that the PERCIST method with the response threshold set at 30% for a response assessment usually performed after 3–4 cycles of therapy has to be adapted in an early response setting with a threshold set at 15%.

Interestingly, the CONSIST method, based on the hypothesis that treatment-resistant emergent clones are reflected by lesions that do not significantly decrease their metabolism under treatment, was shown to have the highest predictive value for OS and PFS. This method, when a response threshold of 15% was applied, was previously reported by our group to have a high negative predictive value (95%) (*5*). As this response threshold (15%) was also applied in this study to the adapted PERCIST–15% and EORTC and those did not demonstrate a predictive value of outcomes as high as the CONSIST method, the criteria used in this methodology could explain its higher predictive value.

Another major finding of this study in addition to the validation of baseline WB-MATV and early mR as strong predictive biomarkers independently of treatment lines is that the added predictive value of early mR when combined with WB-MATV strongly depends on the baseline tumor load and the treatment line.

In low baseline WB-MATV patients in the last-line of treatment, where OS is the most important endpoint, the combination of the 2 biomarkers has enabled the identification of 2 risk groups of patients with significantly distinct median OS: responders versus nonresponders. A trend, due to the limited number of patients included in the low WB-MATV and nonresponders group ($n = 10$), was also found in low baseline WB-MATV patients in the first-line of treatment for PFS, as in this setting PFS is the relevant endpoint when a treatment change may be considered. In both settings, for the group of responder patients with low baseline WB-MATV, the prognostic information provided could reinforce the oncologist's therapeutic decisions. In the group of nonresponder patients with low baseline WB-MATV, the rapid identification of a limited number of nonresponding lesions (oligo-resistance) could lead to treatment adaptation by adding locoregional ablative treatments centered on the PET-resistant lesions. If metabolic treatment resistance is observed in most lesions, rapid shift to an alternative treatment regimen or referral to an appropriate clinical trial could be considered. In patients showing clinical or biologic signs of intolerance, the absence of a mR can be an additional argument for deciding an early treatment adaptation before radiologic progression is documented. Our findings, therefore, support the clinical use of early mR to discriminate the level of risk of low baseline WB-MATV mCRC patients across all treatment lines.

For high baseline WB-MATV patients in both treatment lines, the fact that they are responders or nonresponders does not significantly affect their outcomes. This result suggests that performing an early mR in these high-tumor-load patients is probably not useful. Several factors may explain these results. First, the low mR threshold (minimum 15% SUL_{max} decrease) used by the CONSIST method maximizes the negative predictive value to avoid eliminating a potentially efficient treatment. This low threshold also minimizes the positive predictive value, impairing any distinction on the depth of response. Second, for high baseline WB-MATV patients, the lack of randomized control group precludes knowing whether responders have a survival benefit over untreated patients. Therefore, we can only state that performing an early mR may not be useful in these high-tumor-load patients but we should in no way extrapolate from this finding that treatments are not effective.

A potential limitation of this study is that the population of the development set was already used in a previous study assessing the prognostic value of baseline WB-MATV (population split in 2 sets for internal validation) (*2*).

In terms of perspectives, PET-driven treatment escalation strategies for high-risk patients, identified at an early time point, might be effective to prolong survival. Further studies would be needed to assess the impact of these adaptive treatment strategies on survival outcomes.

CONCLUSION

This study validates baseline WB-MATV and early mR as strong independent prognostic biomarkers for OS and PFS in first- and last-line mCRC treatment settings—stronger than the relevant usual clinical parameters. Combining these 2 biomarkers significantly increased the overall prognostic accuracy and allowed a better risk stratification in identifying distinct risk groups of patients with significant different median OS and PFS in first- and last-line treatment settings. Therefore, the use of these 2 biomarkers could be proposed as stratification factors in clinical trials. Their use could also be recommended in clinical oncology for risk stratification in mCRC patients.

DISCLOSURE

Francesco Sclafani was a consultant for and on the advisory board of Bayer; he received research funding from AstraZeneca, Bayer, BMS, and Roche and travel grants from Bayer and Lilly. Alain Hendlisz was a consultant for and on the advisory board of Amgen, Bayer, Eli Lilly, Merck, Pierre Fabre, Servier, and Sirtex; he received research funding from Amgen, AstraZeneca, Ipsen, Leo Pharma, Merck, Roche, Sanofi, and Teva Pharma and travel grants from Merck, Roche, and Sirtex. No other potential conflict of interest relevant to this article was reported.

KEY POINTS

QUESTION: Does early mR yield additional prognostic value compared with baseline clinical parameters and WB-MATV in mCRC patients under first- or last-line of treatment?

PERTINENT FINDINGS: This study, including 3 prospective trials (2 development and 1 external validation datasets), validates baseline WB-MATV and early mR as independent prognostic biomarkers for OS/PFS in mCRC, independently of patients' treatment line. The added prognostic value of early mR assessment was found mostly in those patients with low baseline WB-MATV.

IMPLICATIONS FOR PATIENT CARE: Combining these 2 PET biomarkers should be implemented in future clinical trials and in clinical routine for monitoring mCRC patients under first- or last-line of treatment.

REFERENCES

1. Siegel RL, Miller KD, Jemal A. Cancer statistics, 2019. *CA Cancer J Clin.* 2019; 69:7–34.

2. Woff E, Hendlisz A, Ameye L, et al. Validation of metabolically active tumor volume and total lesion glycolysis as ^{18}F-FDG PET/CT–derived prognostic biomarkers in chemorefractory metastatic colorectal cancer. *J Nucl Med.* 2019;60:178–184.
3. Hendlisz A, Golfinopoulos V, Garcia C, et al. Serial FDG–PET/CT for early outcome prediction in patients with metastatic colorectal cancer undergoing chemotherapy. *Ann Oncol.* 2012;23:1687–1693.
4. Gebhart G, Gámez C, Holmes E, et al. ^{18}F-FDG PET/CT for early prediction of response to neoadjuvant Lapatinib, Trastuzumab, and their combination in HER2-positive breast cancer: results from Neo-ALTTO. *J Nucl Med.* 2013;54:1862–1868.
5. Woff E, Hendlisz A, Garcia C, et al. Monitoring metabolic response using FDG PET-CT during targeted therapy for metastatic colorectal cancer. *Eur J Nucl Med Mol Imaging.* 2016;43:1792–1801.
6. Skougaard K, Nielsen D, Jensen BV, Hendel HW. Comparison of EORTC criteria and PERCIST for PET/CT response evaluation of patients with metastatic colorectal cancer treated with Irinotecan and Cetuximab. *J Nucl Med.* 2013;54:1026–1031.
7. Kim JH. Comparison of the EORTC criteria and PERCIST in solid tumors: a pooled analysis and review. *Oncotarget.* 2016;7:58105–58110.
8. Cremolini C, Schirripa M, Antoniotti C, et al. First-line chemotherapy for mCRC—a review and evidence-based algorithm. *Nat Rev Clin Oncol.* 2015;12:607–619.
9. Deleporte A, Hendlisz A, Garcia C, et al. SoMore trial: early metabolic response assessment of a sorafenib (SOR) and capecitabine (CAP) combination in chemorefractory metastatic colorectal cancer (mCRC). *J Clin Oncol.* 2014;32:524.
10. Hendlisz A, Deleporte A, Vandeputte C, et al. Regorafenib assessment in refractory advanced colorectal cancer: RegARd-C study protocol. *BMJ Open.* 2015;5:e007189.
11. Boellaard R, Delgado-Bolton R, Oyen WJG, et al. FDG PET/CT: EANM procedure guidelines for tumour imaging: version 2.0. *Eur J Nucl Med Mol Imaging.* 2015;42:328–354.
12. Aide N, Lasnon C, Veit-Haibach P, Sera T, Sattler B, Boellaard R. EANM/EARL harmonization strategies in PET quantification: from daily practice to multicentre oncological studies. *Eur J Nucl Med Mol Imaging.* 2017;44:17–31.
13. Wahl RL, Jacene H, Kasamon Y, Lodge MA. From RECIST to PERCIST: evolving considerations for PET response criteria in solid tumors. *J Nucl Med.* 2009;50:122S–150S.
14. Young H, Baum R, Cremerius U, et al. Measurement of clinical and subclinical tumour response using [18F]-Fluorodeoxyglucose and positron emission tomography: review and 1999 EORTC recommendations. *Eur J Cancer.* 1999;35(13):1773–1782.
15. Hendlisz A, Deleporte A, Delaunoit T, et al. The prognostic significance of metabolic response heterogeneity in metastatic colorectal cancer. *PLOS ONE.* 2015;10:e0138341.
16. Ballman KV. Biomarker: predictive or prognostic? *J Clin Oncol.* 2015;33:3968–3971.
17. Lim Y, Bang J-I, Han S-W, et al. Total lesion glycolysis (TLG) as an imaging biomarker in metastatic colorectal cancer patients treated with regorafenib. *Eur J Nucl Med Mol Imaging.* 2017;44:757–764.
18. de Geus-Oei L-F, Vriens D, van Laarhoven HWM, van der Graaf WTA, Oyen WJG. Monitoring and predicting response to therapy with ^{18}F-FDG PET in colorectal cancer: a systematic review. *J Nucl Med.* 2009;50:43S–54S.
19. Byström P, Berglund A, Garske U, et al. Early prediction of response to first-line chemotherapy by sequential [^{18}F]-2-fluoro-2-deoxy-D-glucose positron emission tomography in patients with advanced colorectal cancer. *Ann Oncol.* 2009;20:1057–1061.
20. Choi M, Kollepara SLS, Heilbrun LK, Smith D, Shields AF, Philip PA. PET scans as a predictive marker of survival in advanced colorectal cancer. *Clin Colorectal Cancer.* 2015;14:35–40.

Hepatic Artery Injection of ^{131}I-Metuximab Combined with Transcatheter Arterial Chemoembolization for Unresectable Hepatocellular Carcinoma: A Prospective Nonrandomized, Multicenter Clinical Trial

Hui Chen*[1], Gang Nan*[2], Ding Wei[2], Ren-You Zhai[3], Ming Huang[4], Wu-Wei Yang[5], Bao-Cai Xing[1], Xu Zhu[1], Hai-Feng Xu[1], Xiao-Dong Wang[1], Xiao-Yong Zhang[6], Bao-Rang Zhu[5], Peng Liu[1], Guang Cao[1], Song Gao[1], Chun-Yi Hao[1], Ren-Jie Yang[1], Jian-Hai Guo[1], Xin Zhang[1], Kun Gao[3], Kun Wang[1], Jian-Feng Wang[3], Zi-Yu Li[1], Lin-Zhong Zhu[1], Rong Ding[4], Jing Li[5], Ling Zhao[4], Yu-Jun Shao[6], Hai-Chun Liu[6], Jie-Lai Xia[7], Ling Wang[7], Ling-Min Kong[2], Zhi-Nan Chen[2], and Huijie Bian[2]

[1]Key Laboratory of Carcinogenesis and Translational Research, Peking University Cancer Hospital, Beijing, China; [2]National Translational Science Center for Molecular Medicine and Department of Cell Biology, State Key Laboratory of Cancer Biology, Fourth Military Medical University, Xi'an, China; [3]Beijing Chao-Yang Hospital, Capital Medical University, Beijing, China; [4]Yunnan Cancer Hospital, Third Affiliated Hospital of Kunming Medical University, Kunming, China; [5]Fifth Medical Center, Chinese PLA General Hospital, Beijing, China; [6]China Nuclear Industry Beijing 401 Hospital, Beijing, China; and [7]College of Military Preventive Medicine, Fourth Military Medical University, Xi'an, China

This prospective nonrandomized, multicenter clinical trial was performed to investigate the efficacy and safety of ^{131}I-labeled metuximab in adjuvant treatment of unresectable hepatocellular carcinoma. **Methods:** Patients were assigned to treatment with transcatheter arterial chemoembolization (TACE) combined with ^{131}I-metuximab or TACE alone. The primary outcome was overall tumor recurrence. The secondary outcomes were safety and overall survival. **Results:** The median time to tumor recurrence was 6 mo in the TACE + ^{131}I-metuximab group (n = 160) and 3 mo in the TACE group (n = 160) (hazard ratio, 0.55; 95% CI, 0.43–0.70; $P < 0.001$). The median overall survival was 28 mo in the TACE + ^{131}I-metuximab group and 19 mo in the TACE group (hazard ratio, 0.62; 95% CI, 0.47–0.82; P = 0.001). **Conclusion:** TACE + ^{131}I-metuximab showed a greater antirecurrence benefit, significantly improved the 5-y survival of patients with advanced hepatocellular carcinoma, and was well tolerated by patients.

Key Words: ^{131}I-labeled metuximab; transcatheter arterial chemoembolization; hepatocellular carcinoma

J Nucl Med 2022; 63:556–559
DOI: 10.2967/jnumed.121.262136

Hepatocellular carcinoma (HCC) is the sixth most common malignancy and the third leading cause of cancer-related death worldwide (*1*). Systematic treatment for advanced HCC remains of great concern (*2*). Although transcatheter arterial chemoembolization (TACE) is frequently used for the treatment of HCC, it fails to lead to a complete response in most patients, especially in the middle or late stage when the tumor is larger than 5 cm. ^{131}I-metuximab is a radioimmunoconjugate generated by labeling metuximab directed against CD147, which is associated with hepatocarcinogenesis and tumor metastasis (*3*,*4*). Previous studies have shown the beneficial treatment effects of ^{131}I-metuximab combined with TACE in patients with HCC, and no severe toxicities were reported in these studies (*5*,*6*). In this study, we conducted a prospective clinical trial to evaluate the therapeutic efficacy of ^{131}I-metuximab combined with TACE in patients with unresectable HCC.

MATERIALS AND METHODS

Patient Population and Study Design

Between November 2, 2011, and December 31, 2015, a prospective, nonrandomized concurrent controlled, multicenter, open-label clinical trial was performed on patients with unresectable HCC at 4 medical centers in China. Patients diagnosed with unresectable HCC according to the guidelines of the American Association for the Study of Liver Diseases were assigned to the TACE + ^{131}I-metuximab or TACE group (*7*). To minimize bias, we matched patients between the 2 groups based on age, sex, Barcelona Clinic Liver Cancer stage, Child–Pugh class, and Eastern Cooperative Oncology Group score. The Medicine Ethics Committee of Peking University Cancer Hospital approved this study, and all subjects gave written informed consent. The study was registered at http://www.chictr.org.cn/ (ChiCTR-ONRC-11001664).

Inclusion and Exclusion Criteria

The eligibility criteria included men and women aged 18–80 y, with confirmed HCC according to the criteria of the American Association for the Study of Liver Diseases, Barcelona Clinic Liver Cancer stage B or C, Eastern Cooperative Oncology Group performance status of no more than 2, Child–Pugh liver function class A or B, platelet count of at least 70×10^9 per liter, white blood cell count of at least 3×10^9 per liter, no organ dysfunction, and a life expectancy of at least 3 mo. Patients who were allergic to biologic products, pregnant, or

Received Feb. 22, 2021; revision accepted Jul. 15, 2021.
For correspondence or reprints, contact Huijie Bian (hjbian@fmmu.edu.cn) or Zhi-Nan Chen (znchen@fmmu.edu.cn).
*Contributed equally to this work.
Published online Sep. 2, 2021.
COPYRIGHT © 2022 by the Society of Nuclear Medicine and Molecular Imaging.

lactating or had thyroid hypofunction, brain metastases, or a positive initial skin test for metuximab were excluded. The selection criteria and algorithm used to determine patient grouping were completely and strictly consistent across different centers.

Drugs and Treatments

The patients in both groups underwent standard TACE treatment according to the Clinical Guidelines for the Diagnosis and Treatment of Primary Liver Cancer, China, 2011. For TACE administration, a catheter was placed into the proper hepatic artery through the femoral artery using the Seldinger technique. For hepatic lesions with a rich blood supply, hepatic arterial chemoembolization was conducted first (pharmorubicin [40 mg] and ultra-fluid lipiodol [3–20 mL] were administered according to the tumor size). After embolization, 750 mg of diluted 5-fluorouracil was perfused via a 2.4-F microcatheter. In the TACE + ^{131}I-metuximab group, patients were transferred to the nuclear medicine ward after TACE, and a 27.75 MBq/kg dose of ^{131}I-metuximab was administered into the proper hepatic artery (*8*).

Sample Size

According to our previous research, the assumptions were a 1-y recurrence rate of 50% in the TACE + ^{131}I-metuximab group and 69.5% in the TACE group. We needed 141 patients in each group (power of 90%, 2-sided significance level of 5%, 1:1 allocation) to detect a 19.5% difference in recurrence rate between groups. We also estimated and added 10% to account for patients who might have been lost to follow-up. On the basis of these calculations, we estimated that we needed to enroll at least 155 patients.

Outcomes and Evaluation

The primary outcome was overall tumor recurrence, which was measured from the date of the first TACE after allocation until the first documented tumor recurrence event and based on the assessment criteria of the modified Response Evaluation Criteria in Solid Tumors. The secondary outcomes were safety and overall survival. Safety was assessed according to the National Cancer Institute's Common Terminology Criteria for adverse effects (version 4.0).

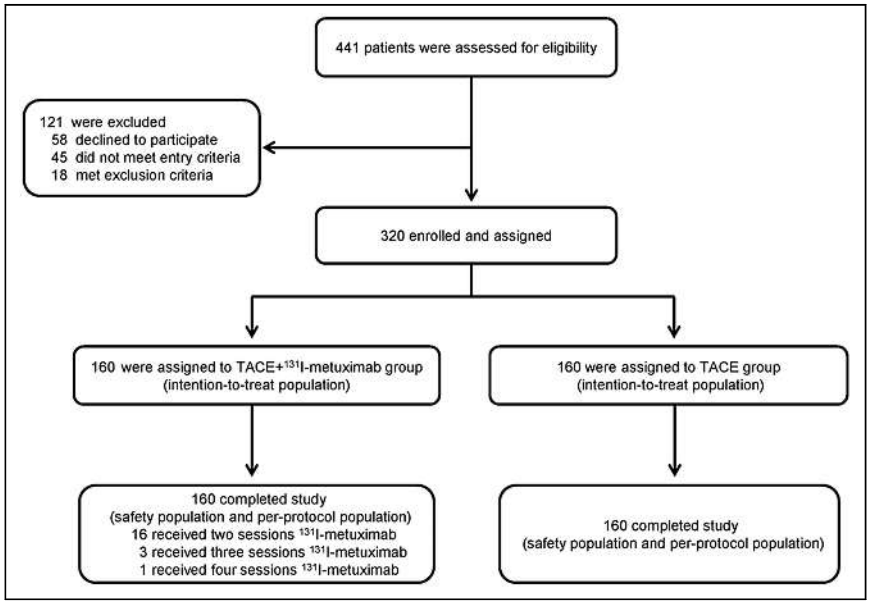

FIGURE 1. Trial profile: enrollment and outcomes.

Statistical Analysis

Overall recurrence and overall survival were analyzed using the Kaplan–Meier method and a log-rank test with a 2-sided overall α-level of 0.05. *P* values were 2-sided, and less than 0.05 was considered statistically significant. Statistical analyses were performed using SPSS software (version 16.0; IBM Corp.).

RESULTS

We evaluated 441 Chinese patients with a confirmed diagnosis of HCC. On the basis of the inclusion and exclusion criteria, 320 patients were enrolled in our study, with 160 (50%) patients assigned to the TACE + ^{131}I-metuximab group and 160 (50%) patients assigned to the TACE group (Fig. 1). Baseline patient characteristics are shown in Supplemental Tables 1 and 2 (supplemental materials are available at http://jnm.snmjournals.org).

The study was completed on March 30, 2020. The median follow-up period was 17 mo (interquartile range, 8–30 mo). At that time, 121 (76%) patients in the TACE + ^{131}I-metuximab group and 151 (94%) patients in the TACE group had developed tumor recurrence. In the TACE + ^{131}I-metuximab group, 100 (63%) patients had new intrahepatic recurrence, 102 (64%) patients had intrahepatic residual recurrence, and 52 (33%) patients had extrahepatic metastasis, compared with 128 (80%), 130 (81%), and 98 (61%) patients, respectively, in the TACE group—a significant difference between the 2 groups (Supplemental Table 3). The median time to overall tumor recurrence was significantly longer in the TACE + ^{131}I-metuximab group than in the TACE group (6 vs. 3 mo; hazard ratio, 0.55; 95% CI, 0.43–0.70; $P < 0.001$). The log-rank test revealed a significant difference in the recurrence rates between the 2 groups ($P < 0.001$) (Fig. 2A). The significant antirecurrence benefits represented a relative reduction of 23% in tumor recurrence at 12 mo (Supplemental Table 4). An exploratory multivariate analysis using the Cox proportional-hazards model identified 7 baseline characteristics that were prognostic indicators of overall tumor recurrence. After adjusting for these prognostic factors, the effect of ^{131}I-metuximab on overall recurrence remained significant (hazard ratio, 0.46; 95% CI, 0.35–0.61; $P < 0.001$). A prespecified subgroup analysis showed an antirecurrence benefit for TACE + ^{131}I-metuximab over TACE alone in most of the subgroups analyzed (Fig. 3A).

At the time of the final analysis, 93 (58%) patients in the TACE + ^{131}I-metuximab group and 113 (71%) patients in the TACE group had died. The median overall survival was significantly longer in the TACE + ^{131}I-metuximab group than in the TACE group (28 vs. 19 mo; hazard ratio, 0.62; 95% CI, 0.47–0.82; $P = 0.001$). The log-rank test revealed a significant difference in survival rate between the 2 groups ($P = 0.001$) (Fig. 2B). The survival rates are shown in Supplemental Table 4. An exploratory multivariate analysis using the Cox proportional-hazards model identified 7 baseline characteristics that were prognostic indicators of overall survival. After adjusting for these prognostic factors, the effect of TACE + ^{131}I-metuximab on overall survival was significantly different from that of TACE alone (hazard ratio, 0.55; 95%

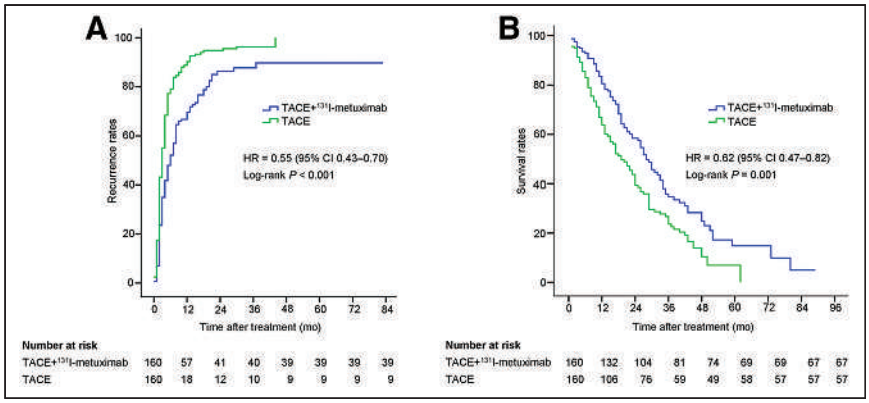

FIGURE 2. Overall recurrence (A) and overall survival (B) data analyzed using Kaplan–Meier method and log-rank test. HR = hazard ratio.

CI, 0.41–0.74; $P < 0.001$). A prespecified subgroup analysis showed a survival benefit for TACE + ^{131}I-metuximab over TACE alone in Barcelona Clinic Liver Cancer stage C, Child–Pugh class A, Eastern Cooperative Oncology Group score 0, extrahepatic spread (no), macroscopic vascular invasion (no), size range of tumor, number of tumors (single), and previous therapy (no) subgroups (Fig. 3B).

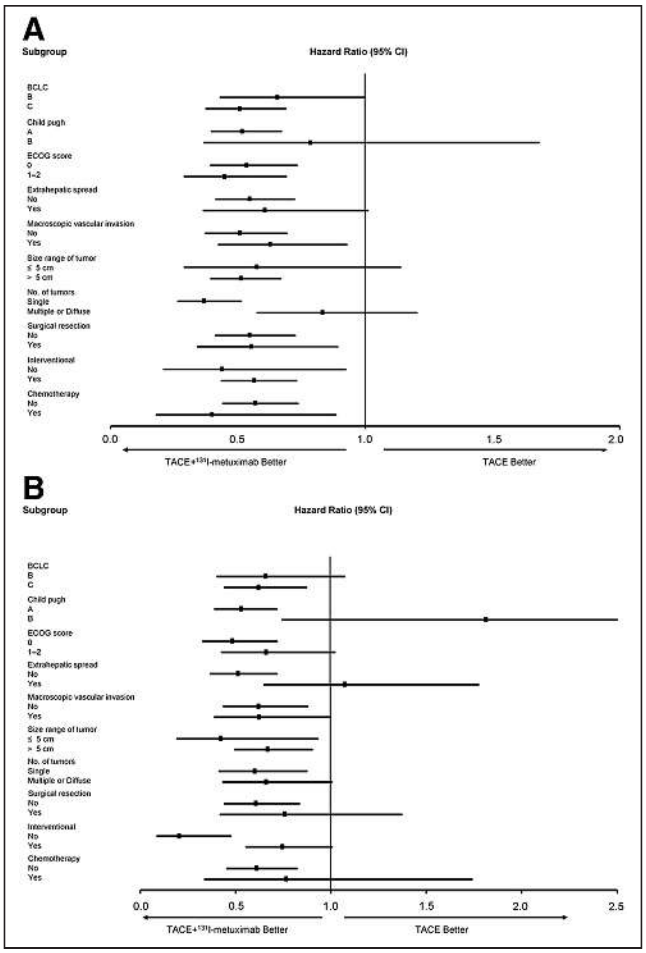

FIGURE 3. Analysis of overall recurrence (A) and overall survival (B) in selected subgroups according to baseline prognostic factors, performed using Cox regression models. BCLC =Barcelona Clinic Liver Cancer; ECOG = Eastern Cooperative Oncology Group.

The reported adverse effects for patients receiving TACE + ^{131}I-metuximab were predominantly grade 1 or 2 in constitutional symptoms and gastrointestinal events such as fever, pain, vomiting, and fatigue (Supplemental Table 5). Grade 3 laboratory abnormalities included a decrease in white blood cell count (5% in the TACE + ^{131}I-metuximab group vs. 0.6% in the TACE group, $P = 0.04$). No serious adverse effects and treatment-related deaths were observed. Taken together, the descriptive data suggested that ^{131}I-metuximab as a radioimmunotherapeutic agent did not pose a hazard to hepatic function in the TACE + ^{131}I-metuximab group.

At the time of analysis, 206 (64%) patients in the 2 groups had died. A total of 93 (58%) patients in the TACE + ^{131}I-metuximab group died, and 113 (71%) patients in the TACE group died. The causes of death are shown in Supplemental Table 6. The χ^2 test showed a significant difference between the 2 groups ($P = 0.018$).

DISCUSSION

TACE is still an important therapy for unresectable HCC, but the median recurrence time is reported to be 3 mo (*9*). Our study indicated that ^{131}I-metuximab combined with TACE delayed tumor recurrence by 3 mo in patients with unresectable HCC and preserved liver function compared with TACE alone. The results also demonstrated that the TACE group had a higher risk of recurrence and extrahepatic metastasis, and, especially, early recurrence, relative to the TACE + ^{131}I-metuximab group, suggesting that TACE alone could manage the existing intrahepatic tumor and that ^{131}I-metuximab could inhibit tumor recurrence and metastasis.

In this study, tumor parenchyma was embolized with lipiodol instead of particles, whereas the main tumor-supplying artery was preserved. Therefore, the formation of tortuous blood circulation in the tumor was relatively less, as was conducive with subsequent interventional therapy. For ethical reasons, we did not use ^{131}I-metuximab alone for comparison. Because of the radioactivity of the drug, we could not perform a double-blind study for the safety of patients and doctors. This study had several limitations, including mixed populations of previously treated and untreated individuals and a lack of double blinding and randomization, which may result in a subjective bias. In addition, when recurrence was detected, the fact that patients were treated with various treatments may affect the overall survival results. Nevertheless, caution should be exercised when analyzing the results of a nonrandomized concurrent control trial; well-designed prospective, randomized, controlled trials remain necessary.

CONCLUSION

The combination of TACE and ^{131}I-metuximab represents a logical, new, and encouraging approach to neoadjuvant therapy for advanced HCC. ^{131}I-metuximab is associated with a significant reduction in the risk of recurrence and death and is well tolerated in patients with unresectable HCC. The combination of TACE and ^{131}I-metuximab using the present regimen may postpone relapse in a selected group of patients with unresectable HCC and is an effective palliative treatment option.

DISCLOSURE

This work was supported by grants from the National Science and Technology Major Project (2012ZX10002-015), the State Key Laboratory of Cancer Biology (CBSKL2019ZZ16), and the Natural Science Foundation of Shaanxi Province (2020SF-252). No other potential conflict of interest relevant to this article was reported.

KEY POINTS

QUESTION: Can ^{131}I-metuximab combined with TACE be used as an effective palliative therapy in patients with unresectable HCC?

PERTINENT FINDINGS: ^{131}I-metuximab combined with TACE showed a greater antirecurrence benefit than TACE alone, significantly improved the 5-y survival of patients with advanced HCC over TACE alone, and was well tolerated.

IMPLICATIONS FOR PATIENT CARE: The combination of TACE and ^{131}I-metuximab using the present regimen postpones relapse in a selected group of patients with unresectable HCC and is an effective palliative treatment option.

REFERENCES

1. Bray F, Ferlay J, Soerjomataram I, Siegel RL, Torre LA, Jemal A. Global cancer statistics 2018: GLOBOCAN estimates of incidence and mortality worldwide for 36 cancers in 185 countries. *CA Cancer J Clin.* 2018;68:394–424.
2. Forner A, Reig M, Bruix J. Hepatocellular carcinoma. *Lancet.* 2018;391: 1301–1314.
3. Lu M, Wu J, Hao ZW, et al. Basolateral CD147 induces hepatocyte polarity loss by E-cadherin ubiquitination and degradation in hepatocellular carcinoma progress. *Hepatology.* 2018;68:317–332.
4. Zhao P, Zhang W, Wang SJ, et al. HAb18G/CD147 promotes cell motility by regulating annexin II-activated RhoA and Rac1 signaling pathways in hepatocellular carcinoma cells. *Hepatology.* 2011;54:2012–2024.
5. He Q, Lu WS, Liu Y, Guan YS, Kuang AR. ^{131}I-labeled metuximab combined with chemoembolization for unresectable hepatocellular carcinoma. *World J Gastroenterol.* 2013;19:9104–9110.
6. Wu L, Yang YF, Ge NJ, et al. Hepatic artery injection of ^{131}I-labelled metuximab combined with chemoembolization for intermediate hepatocellular carcinoma: a prospective nonrandomized study. *Eur J Nucl Med Mol Imaging.* 2012;39:1306–1315.
7. Bruix J, Sherman M; American Association for the Study of Liver Diseases. Management of hepatocellular carcinoma: an update. *Hepatology.* 2011;53:1020–1022.
8. Chen ZN, Mi L, Xu J, et al. Targeting radioimmunotherapy of hepatocellular carcinoma with iodine (^{131}I) metuximab injection: clinical phase I/II trials. *Int J Radiat Oncol Biol Phys.* 2006;65:435–444.
9. Park JW, Koh YH, Kim HB, et al. Phase II study of concurrent transarterial chemoembolization and sorafenib in patients with unresectable hepatocellular carcinoma. *J Hepatol.* 2012;56:1336–1342.

^{177}Lu-PSMA-617 and Idronoxil in Men with End-Stage Metastatic Castration-Resistant Prostate Cancer (LuPIN): Patient Outcomes and Predictors of Treatment Response in a Phase I/II Trial

Sarennya Pathmanandavel[1–3], Megan Crumbaker[2–4], Andrew O. Yam[2–4], Andrew Nguyen[1], Christopher Rofe[2], Elizabeth Hovey[5,6], Craig Gedye[7,8], Edmond M. Kwan[9,10], Christine Hauser[11,12], Arun A. Azad[11], Peter Eu[11], Andrew J. Martin[13], Anthony M. Joshua[2–4,6], and Louise Emmett[1,3,4,6]

[1]Department of Theranostics and Nuclear Medicine, St. Vincent's Hospital, Sydney, New South Wales, Australia; [2]Kinghorn Cancer Centre, St. Vincent's Hospital, Sydney, New South Wales, Australia; [3]Garvan Institute of Medical Research, Sydney, New South Wales, Australia; [4]St. Vincent's Clinical School, University of New South Wales, Sydney, New South Wales, Australia; [5]Nelune Comprehensive Cancer Centre, Prince of Wales Hospital, Sydney, New South Wales, Australia; [6]Faculty of Medicine, University of New South Wales, Sydney, New South Wales, Australia; [7]Department of Medical Oncology, Calvary Mater Hospital, Newcastle, New South Wales, Australia; [8]Hunter Medical Research Institute, New Lambton Heights, Newcastle, New South Wales, Australia; [9]Department of Medicine, School of Clinical Sciences, Monash University, Melbourne, Victoria, Australia; [10]Department of Medical Oncology, Monash Health, Melbourne, Victoria, Australia; [11]Peter MacCallum Cancer Centre, Melbourne, Victoria, Australia; [12]Sir Peter MacCallum Department of Oncology, University of Melbourne, Melbourne, Victoria, Australia; and [13]NHMRC Clinical Trials Centre, University of Sydney, Sydney, New South Wales, Australia

^{177}Lu-PSMA-617 is an effective therapy for metastatic castration-resistant prostate cancer (mCRPC). However, treatment resistance occurs frequently, and combination therapies may improve outcomes. We report the final safety and efficacy results of a phase I/II study combining ^{177}Lu-PSMA-617 with idronoxil (NOX66), a radiosensitizer, and examine potential clinical, blood-based, and imaging biomarkers. **Methods:** Fifty-six men with progressive mCRPC previously treated with taxane chemotherapy and novel androgen signaling inhibitor (ASI) were enrolled. Patients received up to 6 doses of ^{177}Lu-PSMA-617 (7.5 GBq) on day 1 in combination with a NOX66 suppository on days 1–10 of each 6-wk cycle. Cohort 1 ($n = 8$) received 400 mg of NOX66, cohort 2 ($n = 24$) received 800 mg, and cohort 3 ($n = 24$) received 1,200 mg. ^{68}Ga-PSMA and ^{18}F-FDG PET/CT were performed at study entry, and semiquantitative imaging analysis was undertaken. Blood samples were collected for analysis of blood-based biomarkers, including androgen receptor splice variant 7 expression. The primary outcomes were safety and tolerability; secondary outcomes included efficacy, pain scores, and xerostomia. Regression analyses were performed to explore the prognostic value of baseline clinical, blood-based, and imaging parameters. **Results:** Fifty-six of the 100 men screened were enrolled (56%), with a screening failure rate of 26% (26/100) for PET imaging criteria. All men had received prior treatment with ASI and docetaxel, and 95% (53/56) had received cabazitaxel. Ninety-six percent (54/56) of patients received at least 2 cycles of combination NOX66 and ^{177}Lu-PSMA-617, and 46% (26/56) completed 6 cycles. Common adverse events were anemia, fatigue, and xerostomia. Anal irritation attributable to NOX66 occurred in 38%. Forty-eight of 56 had a reduction in prostate-specific antigen (PSA) level (86%; 95% CI, 74%–94%); 34 of 56 (61%; 95% CI, 47%–74%) had a PSA reduction of at least 50%. Median PSA progression-free survival was 7.5 mo (95% CI, 5.9–9 mo), and median overall survival was 19.7 mo (95% CI, 9.5–30 mo). A higher PSMA SUV_{mean} correlated with treatment response, whereas a higher PSMA tumor volume and prior treatment with ASI for less than 12 mo were associated with worse overall survival. **Conclusion:** NOX66 with ^{177}Lu-PSMA-617 is a safe and feasible strategy in men being treated with third-line therapy and beyond for mCRPC. PSMA SUV_{mean}, PSMA-avid tumor volume, and duration of treatment with ASI were independently associated with outcome.

Key Words: metastatic prostate cancer; theranostics; lutetium-PSMA

J Nucl Med 2022; 63:560–566
DOI: 10.2967/jnumed.121.262552

Metastatic castration-resistant prostate cancer (mCRPC) is a lethal disease, and treatment options remain limited. ^{177}Lu-prostate-specific membrane antigen-617 (^{177}Lu-PSMA-617) is a radioligand therapy that targets prostate-specific membrane antigen (PSMA), a receptor highly expressed on prostate cancer cells (*1*). ^{177}Lu-PSMA-617 has shown promising results in prospective single-center studies, the phase II TheraP trial, and the phase III VISION trial (*2–5*). However, secondary treatment resistance hinders longer-term outcomes for many men (*2*,*3*,*6*).

Combination therapies may overcome resistance mechanisms and improve clinical outcomes. Idronoxil (NOX66) is a derivative of the flavonoid genistein that binds to external NADH oxidase 2, a tumor-specific enzyme that induces apoptosis and inhibits topoisomerase II. It has shown potential as a radiation sensitizer in prostate cancer (*7–9*). We hypothesized that combining NOX66 with ^{177}Lu-PSMA-617 may improve treatment responses, with a minimal increase in toxicity.

Received May 10, 2021; revision accepted Jun. 29, 2021.
For correspondence or reprints, contact Louise Emmett (louise.emmett@svha.org.au).
Published online Jul. 29, 2021.
COPYRIGHT © 2022 by the Society of Nuclear Medicine and Molecular Imaging.

Improving treatment response with targeted radionuclide therapy involves not only optimizing treatment responses through effective combinations but also improving patient selection. Quantitative parameters on ^{68}Ga-HBEDD-PSMA-11 and ^{18}F-FDG PET/CT have shown potential as predictive and prognostic biomarkers for ^{177}Lu-PSMA-617 therapy (*6*,*10*–*13*). The duration of prior treatments and other markers of treatment resistance, such as androgen receptor splice variant 7, may also have prognostic utility (*11*,*14*,*15*). We report the results of a trial of combination NOX66 and ^{177}Lu-PSMA-617. Additionally, we evaluate the predictive and prognostic potential of blood-based markers, clinical factors, and molecular imaging.

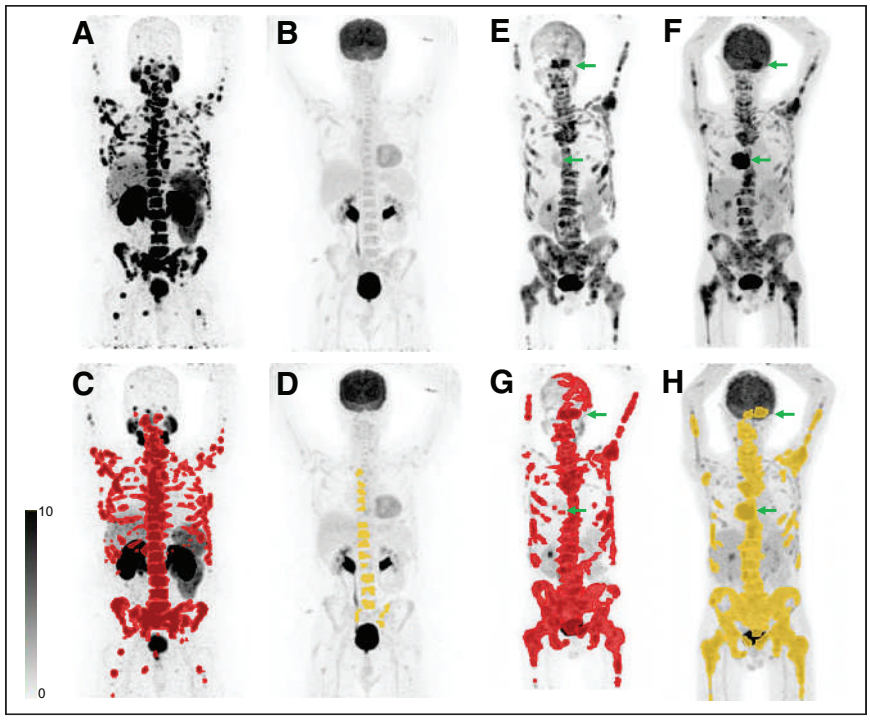

FIGURE 1. (A–D) Patient who was eligible on the basis of imaging with PSMA-avid disease (A) and no sites of discordant ^{18}F-FDG (B). Quantitative PSMA tumor volume (C) and ^{18}F-FDG tumor volume (D) are also shown. (E–H) Patient who was ineligible on the basis of imaging showing 2 sites (arrows) with higher ^{18}F-FDG avidity (F) than PSMA avidity (E). Quantitative PSMA tumor volume (G) and ^{18}F-FDG tumor volume (H) are also shown.

MATERIALS AND METHODS

Study Design

This was a prospective single-center phase I/II dose escalation/expansion trial of combination ^{177}Lu-PSMA-617 and NOX66. The St. Vincent's Hospital institutional review board approved the study protocol (HREC/17/SVH/19 and ACTRN12618001073291), and all patients provided written informed consent.

Screening

Men with mCRPC experiencing progression on conventional imaging (CT and bone scanning) or a rising level of prostate-specific antigen (PSA) based on Prostate Cancer Working group 3 criteria (*16*), and previously treated with at least 1 line of taxane chemotherapy (docetaxel or cabazitaxel) and at least 1 androgen signaling inhibitor (ASI) (abiraterone or enzalutamide), were screened. All patients had adequate organ function (baseline hemoglobin $\geq$ 100 g/L, platelet count $\geq$ 100 $\times$ 10^9/L, and estimated glomerular filtration rate $\geq$ 40 mL/min), an estimated life expectancy of more than 12 wk, and a World Health Organization Eastern Cooperative Oncology Group performance status of no more than 2.

Men underwent screening with ^{18}F-FDG and PSMA PET/CT, bone scanning, and CT and were eligible if they had an SUV_{max} of more than 15 on PSMA PET at 1 or more sites, an SUV_{max} of more than 10 at all measurable sites, and no ^{18}F-FDG avidity without corresponding PSMA uptake (Fig. 1).

Study Treatment

All men received up to 6 cycles of ^{177}Lu-PSMA-617 at 6-wk intervals in combination with 1 of 3 doses of NOX66 (400, 800, and 1,200 mg). NOX66 was administered via suppository on days 1–10 after each ^{177}Lu-PSMA-617 injection. All cohorts were administered 7.5 GBq of ^{177}Lu-PSMA-617 on day 1 via a slow intravenous injection. In addition, participants in cohort 1 (n = 8) received 400 mg of NOX66. After interim safety data reviews, the dose of NOX66 was escalated to 800 mg for cohort 2 (n = 24) and 1,200 mg for cohort 3 (n = 24).

The PSMA-617 precursor (AAA, Novartis) was radiolabeled to no-carrier-added ^{177}Lu-chloride according to the manufacturer's instructions by a qualified radiopharmacist or radiochemist. Quality control tests for radionuclidic and radiochemical purity were performed using high-pressure liquid chromatography and thin-layer chromatography. NOX66 (Noxopharm Ltd.) was commercially produced.

Imaging Procedures and Analysis

^{68}Ga-HBEDD-CC PSMA-11 was produced on-site in compliance with good laboratory practices using a Trasis automated radiopharmacy cassette. ^{18}F-FDG was produced off-site commercially. Radiopharmacy quality control testing used a high-pressure liquid chromatography method. Patients were injected with a 2.0 MBq/kg dose of PSMA and a 3.5 MBq/kg dose of ^{18}F-FDG, with identical imaging parameters (dose, time after injection, and imaging protocols) for each patient. All PET/CT imaging was undertaken using a Phillips Ingenuity TOF-PET/64-slice CT scanner. An unenhanced low-dose CT scan was performed 60 min after tracer injection. Immediately after CT, a whole-body PET scan was acquired for 2 min per bed position.

PET/CT scans were analyzed semiquantitatively using MIM software and a standardized semiautomated workflow to delineate regions of interest with a minimum SUV_{max} cutoff of 3 for PSMA and blood pool intensity, plus 1.5 SDs for ^{18}F-FDG (*17*). Quantitation derived total metabolic tumor volume, SUV_{max}, SUV_{mean}, and total lesional activity for both ^{18}F-FDG and PSMA (MIM Software).

Study Endpoints

Safety and tolerability were assessed using the National Cancer Institute Common Terminology Criteria for Adverse Events (version 5.0) every 2 wk during each 6-wk cycle until 6 wk after the final study treatment. To assess efficacy, we measured the PSA decline from baseline (absolute and $\geq$50% [PSA50]) at any time point, PSA progression-free survival (PFS), and overall survival (OS). Time-to-event endpoints (PSA PFS and OS) were defined as the interval from the date of enrollment to the event date, or the date last known to be event-free (at which point the observation was censored). Patient-reported outcomes were measured on day 1 of each cycle and during follow-up using the University of Michigan xerostomia-related quality-of-life scale (XeQoLS) (*18*) and the short form of the brief pain

inventory (*19*). Pain palliation was defined as a reduction by at least 30% in the worst pain intensity score over the last 24 h observed at 2 consecutive evaluations (*20*).

Clinical, Blood-Based, and Molecular Analysis

Clinical information regarding initial diagnosis, Gleason score, previous lines of therapy, and prior treatment responses was collected. Blood was prospectively collected for biomarker measurement, including hemoglobin, platelets, alkaline phosphatase, albumin, and PSA. Whole-blood samples were collected at baseline, before cycle 3, and before cycle 6 for analysis of potential molecular biomarkers, including androgen receptor splice variant 7. Androgen receptor splice variant 7 analysis was performed using the method described by To et al. (*21*).

Statistical Analyses

The study sample size was calculated to characterize the toxicity profile of the combination, based on the expectation that an adverse event with a true 5% incidence would be detected with 70% probability in a sample of 24 and detected with over 90% probability in a sample of 56. All patients who received at least 1 cycle of study treatment were included in the safety and efficacy analyses. *P* values below 5% were considered significant but interpreted cautiously. A 2-sided exact binomial 95% CI was calculated for PSA response rates. The Kaplan–Meier method was used to characterize time-to-event endpoints (PSA PFS, and OS) and to estimate medians (presented with 95% CIs). The 3 NOX66 dose levels were compared in terms of adverse events, PSA50, and OS.

Cox proportional-hazards regression, and logistic regression, were used to identify prognostic factors for time-to-event (PSA PFS, and OS) and binary endpoints (PSA50), respectively. The covariates investigated included baseline clinical, blood-based, and imaging parameters, including tumor volume and intensity scores (SUV_{max} and SUV_{mean}). In the absence of compelling evidence of a dose–response effect on PSA50, the cohorts were grouped, and prognostic analyses were performed on the grouped cohort.

We used the relaxed LASSO (least absolute shrinkage and selection operator) regression method to identify covariates for inclusion in a multivariable model (*22*). These were fitted in a standard multivariable Cox regression model to obtain conventional hazard ratios (HRs), 95% CIs, and *P* values.

All patients with a worst pain score of at least 4 were included in the analysis, and changes in score between baseline, precycle 3, and end of treatment were compared. Scores from the XeQoLS questionnaire were compared between baseline, precycle 3, and end of treatment. A 2-tailed paired *t* test was used to assess for a change in scores. Analyses were performed using R (version 4.0.5) and SPSS (version 25).

RESULTS

Baseline Patient Characteristics

One hundred men were screened, of whom 56 (56%) were enrolled between November 2017 and February 2020. Twenty-six percent were ineligible on the basis of the PET imaging criteria (13% because of low-PSMA-intensity disease and 13% because of sites with ^{18}F-FDG/PSMA mismatch). Remaining screening fails (18%) were from clinical deterioration (6%), concurrent illness (3%), low hemoglobin (7%), or personal reasons (2%). Baseline characteristics are summarized in Table 1. All patients had prior treatment with at least 1 ASI and taxane chemotherapy, with 95% (53/56) having 2 lines of taxane chemotherapy; 66% (37/56) had at least 20 PSMA-avid metastases, 88% (49/56) had metastases in bone, 55% (31/56) had metastases in lymph nodes, and 19% (11/56) had visceral metastases.

TABLE 1
Patient Characteristics (n = 56)

Characteristic	Data
Age (y)	69 (64–74)
Eastern Cooperative Oncology Group status	
0 or 1	49 (88)
2	7 (12)
PSA at C1 (μg/L)	115 (46–476)
Hemoglobin (reference range [RR], 130–180 g/L)	122 (110–131)
Alkaline phosphatase (RR, 30–100 U/L)	113 (86–231)
Albumin (RR, 36–52 g/L)	38 (34–41)
De novo metastatic disease	29 (52)
Gleason score	
≤7	9 (16)
8–10	35 (63)
Unknown/not available	12 (21)
Prior systemic treatments	
Luteinizing hormone–releasing hormone agonist or antagonist	56 (100)
Chemotherapy	56 (100)
Docetaxel	56 (100)
Cabazitaxel	53 (91)
Other chemotherapy	5 (9)
ASI	56 (100)
Enzalutamide only	27 (48)
Abiraterone only	13 (23)
Abiraterone + enzalutamide	16 (29)
Clinical trial medication	4 (7)
PSMA PET	
SUV_{mean}	8 (7–10)
SUV_{max}	39 (29–61)
Volume (L)	0.64 (0.19–1.21)
^{18}F-FDG PET	
SUV_{mean}	4 (3–5)
SUV_{max}	8 (5–10)
Volume (L)	0.07 (0.02–0.31)
Disease volume	
<20 metastases	19 (33)
≥ 0 metastases	37 (66)
Sites of disease on PSMA PET	
Bone	49 (88)
Lymph node	31 (55)
Viscera	12 (21)

Qualitative data are absolute counts and percentage; continuous data are median and interquartile range.

Because of the small numbers in each NOX66 dose cohort, with ^{177}Lu-PSMA-617 as the key treatment, we combined the 3 patient cohorts for reporting of outcomes and for exploratory analysis of

TABLE 2
Summary of Common and Therapeutically Relevant Adverse Events (n = 56)

Adverse event	Grade 1	Grade 2	Grade 3	All grades
Anemia	31 (55)	16 (29)	4 (7)	51 (91)
Xerostomia	30 (54)	3 (5)	0 (0)	33 (59)
Fatigue	27 (48)	8 (14)	0 (0)	35 (63)
Anal inflammation	18 (32)	3 (5)	0 (0)	21 (38)
Nausea	15 (27)	0 (0)	0 (0)	15 (27)
Thrombocytopenia	12 (21)	3 (5)	0 (0)	15 (27)
Constipation	11 (20)	1 (2)	0 (0)	12 (21)
Neutropenia	5 (9)	0 (0)	0 (0)	5 (9)
Pneumonitis*	0 (0)	1 (3)	0 (0)	1 (3)

*Attributed to radiation therapy prior to enrollment.
Data are number followed by percentage.

biomarkers of response and survival. Analysis of the 3 dose escalation cohorts of NOX66 did not reveal any statistical differences in adverse events, PSA response rate, PSA PFS, or OS.

Safety and Tolerability

Adverse events were predominantly grade 1 (149/188; 79%). The most common toxicities were anemia (50/56; 89%), fatigue (36/56; 64%), and xerostomia (33/56; 59%) (Table 2). Anal inflammation due to the NOX66 suppository occurred in 38% (21/56), with 27% (15/56) requiring topical treatment for anal inflammation. The rate of grade 1 anal inflammation was higher in cohort 3 (46%) than in cohort 1 or 2 (25% and 21%, respectively). Two men in cohort 2 and 1 man in cohort 3 required dose reduction or omission of NOX66. Four cases of grade 3 anemia were reported. There were no other significant differences in toxicities across the 3 cohorts and no grade 4–5 adverse events or treatment-related deaths.

Treatment Duration

Participants received a median of 5 (interquartile range, 3–6) cycles of ^{177}Lu-PSMA-617 and NOX66; 96% (54/56) received at least 2 cycles, and 46% (26/56) completed all 6 cycles. Of the 30 participants who ceased treatment before completing 6 cycles, 2 participants ceased because of exceptional responses, and the other patients ceased because of progressive disease (46%, n = 26), withdrawal of consent (2%, n = 1), or inability to continue the study because of COVID-19 travel restrictions (2%, n = 1). One participant ceased NOX66 because of grade 2 anal inflammation but continued ^{177}Lu-PSMA-617. No participants ceased LuPSMA-617 because of toxicity.

Treatment Response

At a median follow-up of 21.8 mo, PSA50 occurred in 61% (34/56; 95% CI, 47%–74%), whereas any decline in PSA occurred in 86% (48/56; 95% CI, 74%–94%). The waterfall plot of best PSA responses at any time point is shown in Figure 2. At the time of this analysis, 91% (51/56) of participants have had PSA progression and 66% (37/56) have died. The median PSA PFS was 7.5 mo (95% CI, 5.9–9.0 mo) (Fig. 3A), and the median OS was 19.7 mo (95% CI, 9.5–30.0 mo) (Fig. 3B).

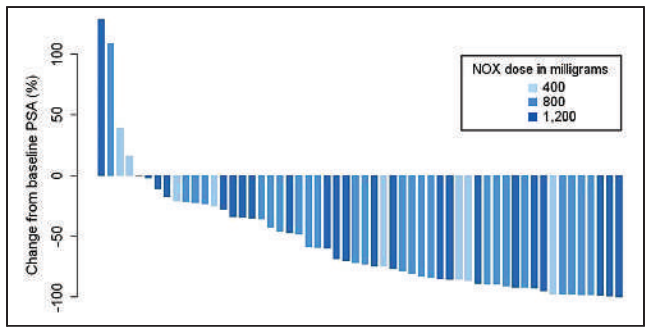

FIGURE 2. Waterfall plot of best PSA responses as indicated by maximum percentage change from baseline at any time point. NOX = NOX66.

Quality of Life

The baseline brief pain inventory assessment (short form) was completed by 95% (53/56) of the men. The mean worst pain score at baseline was 4.21 (range, 0–10; SD, 2.99). Fifty-six percent (29/52) of the men recorded a worst pain score of at least 4, and of these, 41% (12/29) experienced pain palliation at any time point.

The baseline XeQoLS assessment was completed by 48 (86%) of 56 men at baseline, with serial results at cycle 3 (48/56) and cycle 6 (26/48). There was no significant difference in XeQoLS scores between baseline and cycle 3, but a statistically significant difference was found between baseline and cycle 6 (P = 0.04). There were no differences in XeQoLS scores among the 3 dose levels.

Potential Prognostic Factors

We performed exploratory univariable analysis to identify potential markers of PSA50 and OS.

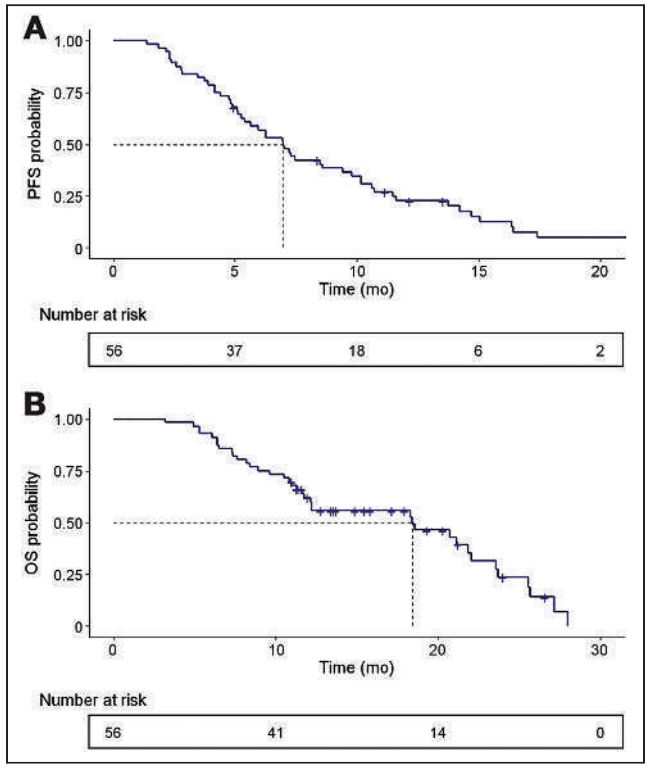

FIGURE 3. Kaplan–Meier curves for PSA progression-free survival (A) and OS (B).

Quantitative PET Imaging Markers. Comparative screening imaging characteristics are detailed in Table 1. A higher tumor volume on PSMA PET was associated with a lower likelihood of achieving PSA50 (odds ratio [OR], 0.41 [95% CI, 0.19–0.87]; $P = 0.02$) and shorter OS (HR, 2.18 [95% CI, 1.36–3.51]; $P = 0.001$). PSMA SUV_{mean} was associated with an increased likelihood of achieving PSA50 (OR, 1.57 [95% CI, 1.12–2.19]; $P = 0.008$). A higher ^{18}F-FDG–avid tumor volume at baseline was associated with a worse OS (HR, 3.02 [95% CI, 1.04–8.79]; $P = 0.04$). The presence of visceral metastases was also associated with a worse OS (HR, 2.35 [95% CI, 1.06–5.20]; $P = 0.04$).

Impact of Prior Treatments on Outcome. The most common treatment immediately before enrollment in the trial was cabazitaxel (70%, 39/56). Receiving either chemotherapy or ASI immediately before the trial did not predict treatment response or survival. Similarly, the duration of chemotherapy did not predict a response to therapy. However, an ASI treatment duration of more than 12 mo was significantly associated with improved OS (HR, 0.45 [95% CI, 0.22–0.91]; $P = 0.03$).

Blood-Based Markers. A higher baseline level of hemoglobin was associated with higher odds of PSA50 (OR, 1.05 [95% CI, 1.01–1.10]; $P = 0.03$) and improved OS (HR, 0.96 [95% CI, 0.93–0.99]; $P = 0.004$). Other known prognostic markers, including baseline alkaline phosphatase, PSA, and use of opioid analgesia, did not correlate with outcome.

Thirty-five patients had androgen receptor splice variant 7 (ARV7) assessed before cycle 1; of these, 9 (26%) were ARV7-positive. Two patients remained positive at cycle 3, and 2 patients became positive while on treatment. A total of 11 patients had ARV7 detected at any time point. The presence of ARV7 at any time point was not significantly associated with treatment response or survival.

Multivariable Analysis of Potential Prognostic Factors. A higher PSMA mean intensity score (SUV_{mean}) (OR, 1.61 [95% CI, 1.12–3.32]; $P = 0.01$) and a lower PSMA tumor volume (OR, 0.42 [95% CI, 0.18–0.94]; $P = 0.04$) remained predictive of PSA50, whereas PSMA tumor volume (HR, 2.19 [95% CI, 1.38–3.46]; $P = 0.001$) predicted a worse OS (Fig. 4). The only clinical parameter predictive of survival was treatment with ASI for more than 12 mo (HR, 0.42 [95% CI, 0.20–0.87]; $P = 0.02$). Baseline ^{18}F-FDG tumor volume, presence of visceral disease, and hemoglobin did not remain independently predictive of outcome (Tables 3 and 4).

DISCUSSION

PSMA-targeted radionuclide therapy is emerging as a new treatment paradigm in men with mCRPC. The randomized TheraP trial demonstrated a significantly improved treatment response (PSA50), PFS, and quality-of-life parameters for ^{177}Lu-PSMA-617, compared with cabazitaxel chemotherapy, in mCRPC. However, whereas results from TheraP are encouraging, PFS remains short, with a median of 5.1 mo (95% CI, 3.4–5.7) (*4*). We postulate that deepening and prolonging responses to ^{177}Lu-PSMA-617 therapy for men with mCRPC may be possible by targeting intracellular resistance mechanisms to maximize treatment effect. This article reports the results of a dose escalation trial of ^{177}Lu-PSMA-617 with a radiation sensitizer (NOX66) and evaluates potential predictive markers of response to PSMA-targeted therapy.

Treatment response rates to the ^{177}Lu-PSMA-617 and NOX66 combination were high with a 61% PSA50, even though most men in this trial had high-volume disease, baseline anemia, high baseline opiate requirements, and 95% had undergone 2 lines of taxane therapy. Despite these high-risk features, the treatment response rate is in line with previous prospective single-center trials and the TheraP study (range, 36%–66%) (*2–4*). Further, PFS and OS were longer than those reported in previous studies with ^{177}Lu-PSMA-617 and longer than those reported using alternative treatments after taxane chemotherapy (*3*,*23*). These results are encouraging for men with ASI and taxane-refractory mCRPC, but a randomized trial—possibly with less stringent imaging enrollment criteria—will be required to determine whether these results are due to the novel treatment combination or to patient selection.

NOX66 was included in the trial as a potential tumor-specific radiation sensitizer that binds to external NADH oxidase 2, a tumor-specific enzyme inducing apoptosis and inhibiting topoisomerase II and demonstrating radiation sensitization in preclinical models (*7*). We did not find an association between an increasing dose of NOX66 and PSA50 or OS. However, the role of NOX66 in the study was as a radiation sensitizer, rather than having a direct effect on therapy, and it may be that either the lower dose of NOX66 was sufficient to induce radiation sensitivity or the impact of NOX66 was limited. The safety of combination therapy with ^{177}Lu-PSMA-617 and NOX66 has been previously reported for the first 2 cohorts of the LuPIN trial and was confirmed in this study (*24*).

Predictors of treatment response are important to further improve PSMA-targeted therapy. Men were screened for this study with molecular imaging, with a requirement for an SUV_{max} of at least 15 on PSMA PET and no sites of ^{18}F-FDG/PSMA PET mismatch. An SUV_{max} of at least 15 has been previously reported to stratify men into responders and nonresponders for ^{177}Lu-PSMA-617 therapy (*2*). Hence it is not surprising that PSMA SUV_{max} was not predictive of a treatment response in this study. However, PSMA SUV_{mean} was an independent predictor of treatment response in this

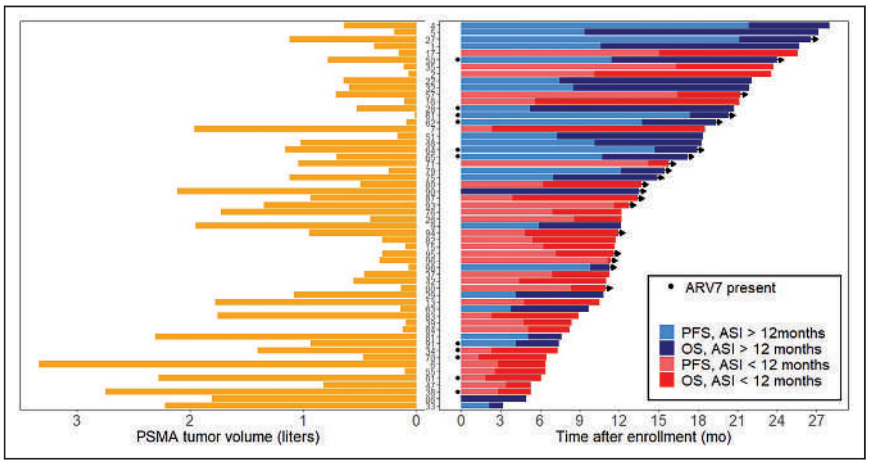

FIGURE 4 Graphical representation of important markers of OS. (Right) Swimmer plot showing individual-patient PFS and OS. (Left) Graph showing corresponding baseline tumor volume for each patient.

TABLE 3
Final Multivariable Model for Association of Baseline Markers with PSA50

Variable	LASSO OR	Multivariable logistic regression			Backward elimination model		
		OR	95% CI	*P*	OR	95% CI	*P*
PSMA TV	0.73	0.47	0.20–1.09	0.08	0.42	0.18–0.94	0.04
PSMA SUV_{mean}	1.20	1.61	1.10–2.34	0.01	1.61	1.12–2.32	
Hemoglobin	1.02	1.04	0.99–1.10	0.12	NA	NA	NA

TV = tumor volume; NA = not applicable.

TABLE 4
Final Multivariable Model for Association of Baseline Markers with OS

Variable	LASSO OR	Multivariable Cox regression			Backward elimination model		
		HR	95% CI	*P*	HR	95% CI	*P*
PSMA TV	1.67	2.05	1.19–3.53	0.009	2.19	1.381–3.463	0.001
ASI > 12 mo	0.70	0.56	0.24–1.31	0.56	0.42	0.202–0.869	0.02
^{18}F-FDG tumor volume (L)	NA	0.99	0.25–3.98	0.99	NA	NA	NA
Hemoglobin	0.99	0.98	0.95–1.02	0.30	NA	NA	NA
Presence of visceral disease	1.499	2.01	0.89–4.53	0.09	NA	NA	NA

TV = tumor volume; NA = not applicable.

study and previously (*10*). A relationship between a higher SUV_{mean} and improved clinical outcomes is biologically plausible. Intra- and interlesional heterogeneity of PSMA is common in mCRPC, and high heterogeneity of expression is likely to impact treatment response (*25*). SUV_{mean} is likely a better indicator of lesional heterogeneity than is SUV_{max}. Further, dosimetry studies have shown that SUV_{mean} correlates with the mean absorbed radiation dose and treatment response (*13*). Although SUV_{mean} requires quantitative analysis, its repeated association with treatment response suggests that it may have a future role as a predictive biomarker for PSMA-targeted radionuclide therapy.

PSMA tumor volume at baseline was the strongest independent predictor of treatment response and was also prognostic for OS. ^{18}F-FDG tumor volume was also prognostic, but not independently of other variables. Essentially, men with higher tumor volumes responded poorly to treatment. This finding agrees with retrospective analyses of men undergoing ^{177}Lu-PSMA-617 therapy (*12*,*26*) and raises questions about the timing of PSMA-targeted therapy in men with mCRPC, suggesting that earlier referral for treatment after prior treatment failure may both improve treatment responses and prolong survival.

The duration of response to prior therapies may help predict the treatment response to PSMA-targeted agents and OS. We found that men with a shorter duration of response to ASI (<12 mo) had a worse OS, though the depth of the treatment response was not affected. By contrast, the duration of the response to chemotherapy, or whether the patient received chemotherapy or ASI immediately before the trial, was not predictive of either survival or response.

This study enrolled a population of heavily pretreated men with mCRPC; therefore, the identified prognostic markers may not be generalizable to other stages of prostate cancer. Larger studies are needed to validate the prognostic markers identified in this study.

CONCLUSION

^{177}Lu-PSMA-617 in combination with NOX66 is a safe treatment for heavily pretreated men with mCRPC, with encouraging results that warrant further evaluation. PSMA SUV_{mean} and tumor volume merit further investigation as imaging markers of treatment response and survival.

DISCLOSURE

This investigator-initiated study was sponsored by St. Vincent's Hospital Sydney and supported by a Cancer Institute NSW prostate translational research grant. Noxopharm Limited provided funding for drug and PET scans, and AAA/Novartis provided PSMA-617 ligand. Edmond Kwan receives honoraria from Janssen, Ipsen, and Astellas Pharma; has a research review, consulting, or advisory role with Astellas Pharma, Janssen and Ipsen; and receives research funding from Astellas Pharma and AstraZeneca. Anthony Joshua has an advisory role with Noxopharm Limited and receives institutional funding from Novartis. Louise Emmett has an advisory role with Noxopharm Limited and receives trial support from Novartis and Astellas. No other potential conflict of interest relevant to this article was reported.

ACKNOWLEDGMENTS

We thank the patients, as well as the clinical trials teams at the Department of Theranostics and Nuclear Medicine and the Kinghorn Cancer Centre, St. Vincent's Hospital, for their support.

KEY POINTS

QUESTION: Is combination therapy with ^{177}Lu-PSMA-617 and NOX66 feasible and safe?

PERTINENT FINDINGS: This phase I/II dose escalation and expansion study found that the combination is feasible and potentially efficacious. Evaluation of clinical, blood-based, and quantitative imaging markers identified PSMA SUV_{mean}, tumor volume, and duration of prior treatment with ASI as potential prognostic markers.

IMPLICATIONS FOR PATIENT CARE: Further randomized studies combining ^{177}Lu-PSMA-617 and NOX66 are needed. Quantitative imaging markers correlate with treatment response and survival and should be explored further.

REFERENCES

1. Kaittanis C, Andreou C, Hieronymus H, et al. Prostate-specific membrane antigen cleavage of vitamin B9 stimulates oncogenic signaling through metabotropic glutamate receptors. *J Exp Med.* 2018;215:159–175.
2. Emmett L, Crumbaker M, Ho B, et al. Results of a prospective phase 2 pilot trial of ^{177}Lu-PSMA-617 therapy for metastatic castration-resistant prostate cancer including imaging predictors of treatment response and patterns of progression. *Clin Genitourin Cancer.* 2019;17:15–22.
3. Hofman MS, Violet J, Hicks RJ, et al. [^{177}Lu]-PSMA-617 radionuclide treatment in patients with metastatic castration-resistant prostate cancer (LuPSMA trial): a single-centre, single-arm, phase 2 study. *Lancet Oncol.* 2018;19:825–833.
4. Hofman MS, Emmett L, Sandhu S, et al. [^{177}Lu]Lu-PSMA-617 versus cabazitaxel in patients with metastatic castration-resistant prostate cancer (TheraP): a randomised, open-label, phase 2 trial. *Lancet.* 2021;397:797–804.
5. Sartor AO, Morris MJ, Messman R, et al. VISION: an international, prospective, open-label, multicenter, randomized phase III study of ^{177}Lu-PSMA-617 in the treatment of patients with progressive PSMA-positive metastatic castration-resistant prostate cancer (mCRPC). *J Clin Oncol.* 2020;38:TPS259.
6. Rahbar K, Ahmadzadehfar H, Kratochwil C, et al. German multicenter study investigating ^{177}Lu-PSMA-617 radioligand therapy in advanced prostate cancer patients. *J Nucl Med.* 2017;58:85–90.
7. Hillman GG, Wang Y, Kucuk O, et al. Genistein potentiates inhibition of tumor growth by radiation in a prostate cancer orthotopic model. *Mol Cancer Ther.* 2004;3:1271–1279.
8. Mahoney S, Arfuso F, Rogers P, et al. Cytotoxic effects of the novel isoflavone, phenoxodiol, on prostate cancer cell lines. *J Biosci.* 2012;37:73–84.
9. Raffoul JJ, Wang Y, Kucuk O, et al. Genistein inhibits radiation-induced activation of NF-kappaB in prostate cancer cells promoting apoptosis and G2/M cell cycle arrest. *BMC Cancer.* 2006;6:107.
10. Ferdinandus J, Violet J, Sandhu S, et al. Prognostic biomarkers in men with metastatic castration-resistant prostate cancer receiving [^{177}Lu]-PSMA-617. *Eur J Nucl Med Mol Imaging.* 2020;47:2322–2327.
11. Kessel K, Seifert R, Weckesser M, et al. Molecular analysis of circulating tumor cells of metastatic castration-resistant prostate cancer patients receiving ^{177}Lu-PSMA-617 radioligand therapy. *Theranostics.* 2020;10:7645–7655.
12. Seifert R, Kessel K, Schlack K, et al. PSMA PET total tumor volume predicts outcome of patients with advanced prostate cancer receiving [^{177}Lu]Lu-PSMA-617 radioligand therapy in a bicentric analysis. *Eur J Nucl Med Mol Imaging.* 2021;48:1200–1210.
13. Violet J, Jackson P, Ferdinandus J, et al. Dosimetry of ^{177}Lu-PSMA-617 in metastatic castration-resistant prostate cancer: correlations between pretherapeutic imaging and whole-body tumor dosimetry with treatment outcomes. *J Nucl Med.* 2019;60:517–523.
14. Antonarakis ES, Lu C, Wang H, et al. AR-V7 and resistance to enzalutamide and abiraterone in prostate cancer. *N Engl J Med.* 2014;371:1028–1038.
15. Kwan EM, Fettke H, Docanto MM, et al. Prognostic utility of a whole-blood androgen receptor-based gene signature in metastatic castration-resistant prostate cancer. *Eur Urol Focus.* 2021;7:63–70.
16. Scher HI, Morris MJ, Stadler WM, et al. Trial design and objectives for castration-resistant prostate cancer: updated recommendations from the Prostate Cancer Clinical Trials Working Group 3. *J Clin Oncol.* 2016;34:1402–1418.
17. Niman R, Buteau JP, Kruzer A, et al. Evaluation of a semi-automated whole body PET segmentation method applied to diffuse large B cell lymphoma [abstract]. *J Nucl Med.* 2018;59(suppl 1):592.
18. Henson BS, Inglehart MR, Eisbruch A, et al. Preserved salivary output and xerostomia-related quality of life in head and neck cancer patients receiving parotid-sparing radiotherapy. *Oral Oncol.* 2001;37:84–93.
19. Cleeland CS. *The Brief Pain Inventory User Guide.* M.D. Anderson Cancer Center; 2009.
20. de Bono JS, Logothetis CJ, Molina A, et al. Abiraterone and increased survival in metastatic prostate cancer. *N Engl J Med.* 2011;364:1995–2005.
21. To SQ, Kwan EM, Fettke HC, et al. Expression of androgen receptor splice variant 7 or 9 in whole blood does not predict response to androgen-axis-targeting agents in metastatic castration-resistant prostate cancer. *Eur Urol.* 2018;73:818–821.
22. Meinshausen N. Relaxed Lasso. *Comput Stat Data Anal.* 2007;52:374–393.
23. Buonerba C, Federico P, Bosso D, et al. Carboplatin plus etoposide in heavily pretreated castration-resistant prostate cancer patients. *Future Oncol.* 2014;10:1353–1360.
24. Crumbaker M, Pathmanandavel S, Yam AO, et al. Phase I/II trial of the combination of ^{177}lutetium prostate specific membrane antigen 617 and idronoxil (NOX66) in men with end-stage metastatic castration-resistant prostate cancer (LuPIN). *Eur Urol Oncol*. August 2, 2020 [Epub ahead of print].
25. Paschalis A, Sheehan B, Riisnaes R, et al. Prostate-specific membrane antigen heterogeneity and DNA repair defects in prostate cancer. *Eur Urol.* 2019;76:469–478.
26. Seifert R, Herrmann K, Kleesiek J, et al. Semiautomatically quantified tumor volume using ^{68}Ga-PSMA-11 PET as a biomarker for survival in patients with advanced prostate cancer. *J Nucl Med.* 2020;61:1786–1792.

A Comprehensive Assessment of ^{68}Ga-PSMA-11 PET in Biochemically Recurrent Prostate Cancer: Results from a Prospective Multicenter Study on 2,005 Patients

Monica Abghari-Gerst[1], Wesley R. Armstrong[2], Kathleen Nguyen[2], Jeremie Calais[2], Johannes Czernin[2], David Lin[3], Namasvi Jariwala[3], Melissa Rodnick[1], Thomas A. Hope[3], Jason Hearn[4], Jeffrey S. Montgomery[5], Ajjai Alva[6], Zachery R. Reichert[6], Daniel E. Spratt[4], Timothy D. Johnson[7], Peter J.H. Scott[1], and Morand Piert[1]

[1]Radiology Department, University of Michigan, Ann Arbor, Michigan; [2]Ahmanson Translational Theranostics Division, Department of Molecular and Medical Pharmacology, UCLA, Los Angeles, California; [3]Department of Radiology and Biomedical Imaging, University of California San Francisco, San Francisco, California; [4]Department of Radiation Oncology, University of Michigan, Ann Arbor, Michigan; [5]Urology Department, University of Michigan, Ann Arbor, Michigan; [6]Internal Medicine Department, University of Michigan, Ann Arbor, Michigan; and [7]Department of Biostatistics, University of Michigan, Ann Arbor, Michigan

We prospectively investigated the performance of the prostate-specific membrane antigen (PSMA) ligand ^{68}Ga-PSMA-11 for detecting prostate adenocarcinoma in patients with elevated levels of prostate-specific antigen (PSA) after initial therapy. **Methods:** ^{68}Ga-PSMA-11 hybrid PET was performed on 2,005 patients at the time of biochemically recurrent prostate cancer after radical prostatectomy (RP) (50.8%), definitive radiation therapy (RT) (19.7%), or RP with postoperative RT (PORT) (29.6%). The presence of prostate cancer was assessed qualitatively (detection rate = positivity rate) and quantitatively on a per-patient and per-region basis, creating a disease burden estimate from the presence or absence of local (prostate/prostate bed), nodal (N1: pelvis), and distant metastatic (M1: distant soft tissue and bone) disease. The primary study endpoint was the positive predictive value (PPV) of ^{68}Ga-PSMA-11 PET/CT confirmed by histopathology. **Results:** After RP, the scan detection rate increased significantly with rising PSA level (44.8% at PSA $< 0.25\%$–96.2% at PSA > 10 ng/mL; $P < 0.001$). The detection rate significantly increased with rising PSA level in each individual region, overall disease burden, prior androgen deprivation, clinical T-stage, and Gleason grading from the RP specimen ($P < 0.001$). After RT, the detection rate for in-gland prostate recurrence was 64.0%, compared with 20.6% prostate bed recurrence after RP and 13.3% after PORT. PSMA-positive pelvic nodal disease was detected in 42.7% after RP, 40.8% after PORT, and 38.8% after RT. In patients with histopathologic validation, the PPV per patient was 0.82 (146/179). The SUV_{max} of histologically proven true-positive lesions was significantly higher than that of false-positive lesions (median, 11.0 [interquartile range, 6.3–22.2] vs. 5.1 [interquartile range, 2.2–7.4]; $P < 0.001$). **Conclusion:** We confirmed a high PPV for ^{68}Ga-PSMA-11 PET in biochemical recurrence and the PSA level as the main predictor of scan positivity.

Key Words: prostate cancer; prostate-specific membrane antigen; PSMA; disease pattern; hybrid PET

J Nucl Med 2022; 63:567–572
DOI: 10.2967/jnumed.121.262412

Received Apr. 8, 2021; revision accepted Jun. 28, 2021.
For correspondence, contact Morand Piert (mpiert@med.umich.edu).
Guest Editor: Barry Siegel, Mallinckrodt Institute of Radiology
Published online Jul. 29, 2021.
COPYRIGHT © 2022 by the Society of Nuclear Medicine and Molecular Imaging.

Biochemical recurrence (BCR) is an independent risk factor in survival outcomes (*1*) after radical prostatectomy (RP) and radiation therapy (RT) for localized prostate cancer. BCR after definitive therapy is common, especially in higher-risk disease, and may affect more than 50% of patients over the long term (*2*,*3*).

With broadened use of newer prostate-specific membrane antigen (PSMA)–based radioligands to identify the location of prostate cancer using PET, the treatment of BCR is rapidly changing to more personalized and targeted approaches (*4*). Although a large body of retrospective evidence is available suggesting that ^{68}Ga-PSMA-11 has high accuracy (*5*,*6*), prospective studies that include gold-standard histologic verification are rare (*7*). The difficulty in obtaining pathologic confirmation of PSMA PET–positive (suggestive) lesions is related to the high positivity rate at a relatively low disease burden and the challenges in sampling small and difficult-to-reach lesions.

To better comprehensively assess the performance characteristics of ^{68}Ga-PSMA-11 PET, 3 institutions—the University of Michigan, UCLA, and the University of California San Francisco—combined their prospective trial datasets of patient populations with BCR disease to determine the accuracy of ^{68}Ga-PSMA-11 based on histopathology and to identify predictors of PET positivity and patterns of recurrence.

MATERIALS AND METHODS

Patients

The Food and Drug Administration granted the use of ^{68}Ga-PSMA-11 under 3 investigational-new-drug applications. Imaging was performed within registered prospective clinical studies assessing the diagnostic performance of ^{68}Ga-PSMA-11 PET in BCR of prostate cancer at the University of Michigan (ClinicalTrials.gov NCT03396874), UCLA (NCT02940262), and the University of California San Francisco (NCT03803475). The respective Institutional Review Boards of each institution approved these study protocols. From February 2018 to December 2020, 2,005 patients were enrolled with histologically proven prostate cancer and BCR after RP with or without postoperative RT (PORT) (prostate-specific antigen [PSA] level > 0.2 ng/mL, >6 wk after surgery) or definitive RT (PSA nadir + ≥ 2 ng/mL). Patients with another active malignancy within the last 2 y (excluding skin basal cell or cutaneous superficial squamous cell

carcinoma that has not metastasized and superficial bladder cancer) were not eligible. Patients who received any interval treatment other than androgen deprivation therapy (ADT) were excluded. Prior conventional imaging was not required for study participation. All subjects provided written informed consent.

^{68}Ga-PSMA-11 PET

The investigational radiotracer ^{68}Ga-PSMA-11 was manufactured as described in the literature either from generator-produced ^{68}Ga-$GaCl_3$ (*8*,*9*) or from cyclotron production of ^{68}Ga via a liquid target and a GE Healthcare FASTlab synthesis module (*10*). Imaging was performed on dedicated hybrid PET/CT ($n = 1886$) or PET/MRI ($n = 119$) scanners according to a standardized imaging protocol (*8*). On average, 61 min (median, 60 min; interquartile range [IQR], 57–65 min) after intravenous administration of 203.5 MBq (5.5 mCi) (IQR, 185–229 MBq [5.0–6.2 mCi]) of ^{68}Ga-PSMA-11, a static emission scan was performed from the thighs to the vertex. A time-of-flight acquisition was performed in 936 of 2,005 (47%) scans. Images were reconstructed using iterative ordered-subset expectation maximization according to vendor recommendations. UCLA performed a diagnostic 2.5-mm collimation CT scan (200–240 mAs, 120 kV) with intravenous contrast medium on either a Siemens Biograph 64 TruePoint or a Siemens Biograph mCT scanner. At the University of Michigan, CT scans (3-mm collimation) were either low-dose (100 mAs, 120 kV on a Biograph 6 TruePoint) or dose-modulated (Biograph mCT) without intravenous contrast medium. The University of California San Francisco investigators performed PET/CT (GE Healthcare Discovery, Biograph mCT, or Philips Vereos scanners) or PET/MRI at 2.5-mm collimation, dependent on scanner availability and contraindications. Diagnostic CT was performed with a standard protocol (80–100 mA, 120 kV) before the PET scan, with intravenous contrast medium for most scans (*7*). All imaging devices received American College of Radiology accreditation.

Image Data

^{68}Ga-PSMA-11 scans were analyzed locally at each institution according to recent guidelines (*8*) by experienced nuclear medicine physicians with access to clinical information, histopathology results, and prior imaging studies when available. Any focal ^{68}Ga-PSMA-11 uptake above location-specific background levels was considered PSMA-positive.

The presence of prostate cancer was quantitatively assessed on a per-region (prostate/prostate bed, pelvis, soft tissue, bone) and per-patient basis. Each involved region was added to estimate the total disease burden (0 = no disease, 1–4 = sum of positive regions). Figure 1 indicates the sampled specific disease locations among these 4 regions.

Lesion Validation and Quantification

Lesion validation was based on histopathologic analysis only. For lesions with histopathologic verification, the SUV_{max} was obtained. When the lesion could be identified with a clear margin on anatomic imaging (either CT or MRI), the maximum lesion diameter was also recorded.

Statistical Analysis

The positive predictive value (PPV) of ^{68}Ga-PSMA-11 PET/CT confirmed by histopathology was the primary study endpoint. Receiver-operating-characteristic analysis was used to determine the optimal SUV_{max} threshold to separate benign from malignant foci. For contingency table analyses, χ^2 tests were used to assess hypotheses. For continuous data, the Wilcoxon rank-sum test was applied. Logistic regression was used to study the association between clinically relevant disease parameters, scan characteristics, and scan positivity rates.

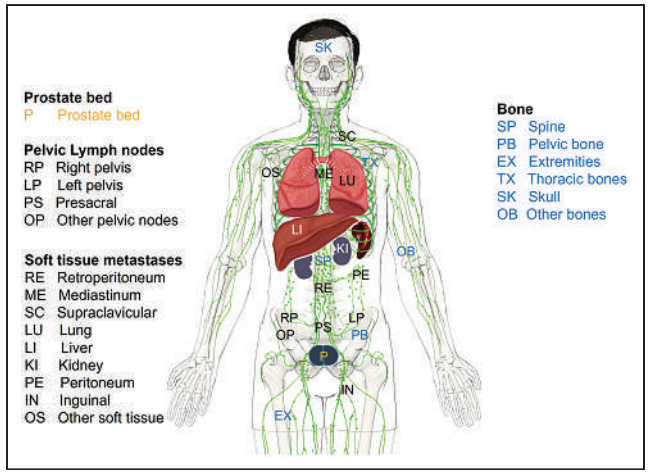

FIGURE 1. Schematic of identified PSMA-positive lesion locations.

RESULTS

Patient Characteristics

Table 1 displays the characteristics of 2,005 enrolled subjects with BCR of prostate cancer after RP (51.2%), PORT (29.4%), or definitive RT (19.4%). Age, initial PSA level, PSA nadir, clinical T-stage, and T-stage from the RP specimen were similar among groups. As shown in Supplemental Table 1 (supplemental materials are available at http://jnm.snmjournals.org), Gleason grade groups derived from 1,586 RP specimens did not significantly differ between RP- and PORT-treated patients ($P = 0.1$). However, the Gleason grade groups at biopsy were significantly higher in the 389 patients receiving RT than in the 481 RP patients ($P < 0.001$).

Most patients treated by RP and PORT had no treatment between the initial therapy and the scan (83.0%), whereas 50.2% of RT-treated patients had received ADT. The interval between the initial therapy and the scan was significantly shorter for patients with persistent PSA after RP or PORT (18.1 mo; IQR, 4.5–72.4 mo) than for patients who achieved undetectable PSA levels after RP or PORT (75.0 mo; IQR, 41.0–125.5 mo) ($P < 0.001$).

Detection Rate

Given the differences in PSA entry criteria after definitive RT, scan detection rates for RT below a PSA level of 2.0 ng/mL were not available. The scan positivity rate was 78.0% for the entire population but was not evenly distributed among treatment groups ($n = 712$ [67.1%] for RP; $n = 590$ [83.1%] for PORT; $n = 422$ [95.9%] for RT).

Table 2 displays the detection rate for all 3 therapy groups categorized by PSA ranges. A significant increase in the detection rate with rising PSA level was seen for RP-treated ($P < 0.001$) and PORT-treated ($P < 0.001$) patients. In a subcohort of 777 patients treated by RP with lower PSA levels (<1.0 ng/mL) at the time of the scan, the detection rate was significantly higher in PORT-treated ($n = 208$; 71.6%) than in RP-treated ($n = 569$; 52.7%) patients ($P < 0.001$). In the same subcohort, the detection rate was also higher in patients with interval ADT (71.2%) than in those without (54.4%, $P < 0.02$). The detection rate was positively correlated with the Gleason grade groups obtained from the RP specimen ($n = 1,586$ [999 RP and 587 PORT]; $P < 0.001$) and with clinical T-stage ($n = 670$ [242 RP, 160 PORT, and 242 RT];

TABLE 1
Patient Characteristics

Characteristic	RP ($n = 1,018$ [51.2%])	PORT ($n = 593$ [29.4%])	RT ($n = 394$ [19.4%])
Site (*n*)			
University of Michigan	372 (36.5%)	264 (44.5%)	192 (48.7%)
University of California San Francisco	109 (10.7%)	82 (13.8%)	81 (20.6%)
UCLA	537 (52.8%)	247 (41.7%)	121 (30.7%)
Age (y)			
Median	68 (IQR, 63–73)	70 (IQR, 65–74)	72 (IQR, 67–77)
No. missing	0	0	0
PSA at scan (ng/mL)			
Median	0.78 (IQR, 0.4–2.3)	1.58 (IQR, 0.7–3.3)	5.7 (IQR, 3.4–10.9)
No. missing	0	0	0
PSA nadir (ng/mL)			
Median	0.2 (IQR, <0.1–0.3)	<0.1 (IQR, <0.1–0.7)	0.3 (IQR, 0.1–0.8)
No. missing	458	212	46
Initial PSA at diagnosis (ng/mL)			
Median	7 (IQR, 5.1–11.3)	6.4 (IQR, 4.7–10.2)	7.6 (IQR, 5.4–7.6)
No. missing	651	336	209
T-stage (RP)			
Median	8 (IQR, 6–10)	7 (IQR, 6–10)	NA
No. missing	230	433	
Clinical T-stage			
Median	3 (IQR, 3–4)	3 (IQR, 3–4)	3 (IQR, 3–6)
No. missing	19	433	126
Gleason grade group (RP)			
Median	3 (IQR, 2–5)	3 (IQR, 2–5)	NA
No. missing	19	5	
Gleason grade group at biopsy			
Median	3 (IQR, 2–4)	3 (IQR, 2–4)	3 (IQR, 2–4)
No. missing	727	403	5
PSMA injected dose (MBq)			
Median	200 (IQR, 185–229)	204 (IQR, 185–229)	215 (IQR, 185–233)
No. missing	4	3	1
Treatment-to-scan interval (mo)			
Median	40.2 (IQR, 8.4–104.0)	82.3 (IQR, 48.4–130.6)	75.4 (IQR, 40.3–122.5)
No. missing	23	15	24

NA = not applicable.
T-stage nomenclature: T1 = 1, T1a = 2, T1b = 3, T1c = 4, T2 = 5, T2a = 6, T2b = 7, T2c = 8, T3 = 9, T3a = 10, T3b = 11, T4 = 12.

$P < 0.01$) but not with Gleason grade groups at the initial prostate biopsy ($n = 870$ [291 RP, 190 PORT, and 289 RT]; $P = 0.86$).

Given the high detection rate for patient treated by RT (roughly 95% at any PSA range), no significant relationship was found between PSA and detection rate (Table 2). When the entire patient population was considered ($n = 2,005$), the regional detection rates for local failure (prostate or prostate bed) (Supplemental Table 2; $P < 0.001$), pelvic nodal disease (Supplemental Table 3; $P < 0.001$), distant metastatic disease in soft tissue (Supplemental Table 4; $P < 0.001$), and bone (Supplemental Table 5; $P < 0.001$) increased significantly with PSA level.

Lesion Validation per Histopathology

Supplemental Table 6 summarizes the patient characteristics of positive scans with ($n = 179$) or without ($n = 1,360$) histopathologic analyses of PSMA-positive lesions. Risk parameters (PSA, PSA nadir, clinical T-stage, Gleason grade groups, locoregional and distant metastatic disease extent) and scan parameters were similar among groups. The average lesion-based PPV was 0.82 for the entire histopathologically assessed population (Table 3). Tissue samples were obtained by either needle biopsy (75%) or surgical resection (25%). Given varying accessibility and risk of specific lesion locations, the number of samples obtained decreased from

TABLE 2
^{68}Ga-PSMA-11 Per-Patient Detection Rate Stratified by PSA Level and Prior Therapy

PSA range (ng/mL)	Total			RP			PORT			RT		
	No. Neg.	No. Pos.	% Pos.	No. Neg.	No. Pos.	% Pos.	No. Neg.	No. Pos.	% Pos.	No. Neg.	No. Pos.	% Pos.
<0.25	64	52	44.8	61	44	41.9	3	8	72.7			
0.25–<0.5	160	163	50.5	138	120	46.5	22	43	66.2			
0.5–<1.0	104	234	69.2	70	136	66.0	34	98	74.2			
1.0–<2.0	66	235	78.1	40	128	76.2	26	107	80.5			
2.0–<5.0	46	414	90.0	18	120	87.0	19	131	87.3	9	163	94.8
5.0–<10.0	18	238	93.0	10	74	88.1	3	55	94.8	5	109	95.6
≥10	8	203	96.2	3	56	94.9	1	43	97.7	4	104	96.3
Total	466	1539	76.8	340	678	66.6	108	485	81.8	18	376	95.4

Neg. = negative; Pos. = positive.

prostate gland/prostate bed (43%) to soft tissues (26%), pelvic lymph nodes (24%), and bone (7%). The region-specific PPV increased from 0.72 in pelvic lymph nodes to 0.83 in prostate/prostate bed and bone and to 0.88 in soft-tissue lesions. Most false-positive (FP) lesions ($n = 33$) were noted in the prostate region, including 10 foci (after RT) in the prostate gland and 4 lesions in the prostate bed, as well as 1 in a seminal vesicle. Other common locations were pelvic lymph nodes ($n = 9$) and soft-tissue lesions ($n = 8$), including extrapelvic lymph nodes or masses, inguinal lymph nodes, and 1 benign neoplasm (Supplemental Table 7).

On a per-patient basis, the available SUV_{max} was significantly higher for the 141 true-positive (TP) lesions (median, 11.0; IQR, 6.3–22.2) than for the 30 FP lesions (median, 5.1; IQR, 2.2–7.4) ($P < 0.001$), whereas the maximum size of lesions was similar between groups (TP, 1.3 [IQR, 0.8–2.13]; FP, 1.05 [IQR, 0.75–2.13]). Receiver-operating-characteristic analysis as a function of lesion SUV_{max} resulted in an area under the receiver-operating-characteristic curve of 0.77. At the optimal SUV_{max} threshold (7.5) for differentiating malignant from benign findings, the sensitivity was 69% and the specificity was 80%.

Disease Burden and Pattern

As shown in Supplemental Table 8, involvement of a single region was the most common outcome except for patients with a PSA level of at least 10 ng/mL. Nonetheless, the rate of multiregion involvement increased steadily with rising PSA level in the entire patient population, as we saw for each individual treatment group (RP, PORT, and RT) ($P < 0.001$).

Figure 2 displays the rate of observed disease at encountered locations indicating differences among treatment groups. The supplemental videos highlight the rising disease burden at each region and location per PSA level. After RT, the most likely positive single region was the prostate (252/394, 64.0%), whereas nodal metastatic disease was the predominant location for RP (435/1,018, 42.7%) and PORT (301/593, 50.8%). Among pelvic lymph nodes, predominant locations were central pelvic nodes (internal/external/common iliac, including obturator), followed by presacral and all other pelvic nodal stations. The probability of bilateral disease involvement increased with PSA level in all 3 treatment groups (RP and RT, $P < 0.001$; PORT, $P < 0.05$). When considering only patients with PSA levels of at least 2 ng/mL, the rate of locoregional disease (prostate/bed or pelvic lymph nodes) was similar among groups (Supplemental Table 9).

As shown in Supplemental Table 10, distant metastatic disease increased with rising PSA level, though it was unequally distributed among treatment groups and disease locations (soft tissue vs. bone). Soft-tissue metastases (Supplemental Table 4), including the frequently encountered retroperitoneal lymph node metastases, were found more often after PORT (188/593, 31.7%) than after RP (154/1,018, 15.1%) at any PSA level. Similar results were noted for osseous metastases (PORT, 162/593 [27.3%], vs. RP, 162/1,018 [15.9%]) (Supplemental Table 5). When osseous lesions was detected, the most common locations were pelvic, thoracic, and spinal.

TABLE 3
^{68}Ga-PSMA-11 Accuracy Confirmed by Histopathology per Region

Site	All groups combined				RP				PORT				RT			
	n	TP	FP	PPV	*n*	TP	FP	PPV	*n*	TP	FP	PPV	*n*	TP	FP	PPV
Prostate and prostate bed	77	64	13	0.83	10	8	2	0.80	7	6	1	0.86	60	50	10	0.83
Pelvic lymph nodes	47	34	13	0.72	25	16	9	0.64	19	16	3	0.84	3	2	1	0.67
Soft tissue	43	38	5	0.88	7	5	2	0.71	26	25	1	0.96	10	8	2	0.80
Bone	12	10	2	0.83	2	2	0	1.00	4	3	1	0.75	6	5	1	0.83
Total	179	146	33	0.82	44	31	13	0.80	56	50	6	0.89	79	65	14	0.82

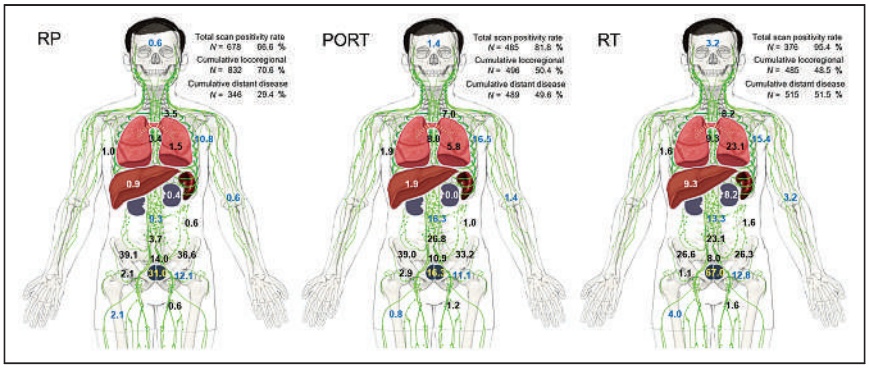

FIGURE 2. Cumulative total scan positivity rate (relative to entire population in treatment groups RP [n = 1,018], RP and PORT [n = 593], or definitive RT [n = 394]). Percentage of individual PSMA-positive disease locations as listed in Figure 1 and cumulative locoregional and distant disease positivity rates are from PSMA scans rated positive (RP, n = 678; PORT, n = 485; RT, n = 376).

DISCUSSION

As reviewed recently in a large, retrospective cohort (*11*) and prior metaanalyses (*6*,*12*), a substantial body of evidence exists to support the use of ^{68}Ga-PSMA-11 in BCR of prostate cancer. However, this evidence is derived mostly from retrospective studies, and prospective data are rare (*7*).

We present the largest prospectively obtained population of patients with BCR of prostate cancer undergoing ^{68}Ga-PSMA-11 PET after initial therapy with curative intent. It comprises the highest number of histologically confirmed PSMA-positive lesions and the largest prospective dataset assessing scan detection rates, particularly at the most relevant PSA range below 1.0 ng/mL after RP and cases of biochemical failure after primary RT.

The primary endpoint of the study was the PPV and not the sensitivity and specificity of the test. This approach was required because histopathologic verification is typically obtained only from PSMA-positive lesions. By limiting the analysis of diagnostic efficacy to histopathologically proven PSMA-positive lesions, we avoided uncertainties related to less stringent clinical endpoints, often referred to as composite endpoints.

The results indicated a high PPV similar to other prospectively obtained data obtained with ^{68}Ga-PSMA-11 (*7*) and ^{18}F-DCFPyL (*13*), although slightly lower than retrospective single-center data, as recently reviewed (*14*). The discrepancy may be related to differences in patient populations with unknown proportions of sampling errors. Furthermore, tissue sampling is often obtained from equivocal findings. Histopathologic sampling was overrepresented after RT compared with RP or PORT. In contrast to Fendler et al. (*15*), the probability of FP results was similar in all treatment groups and thus not elevated in the setting of prostate lesions after RT. In our cohort, FP assessments were more likely with a lower SUV_{max} whereas the average lesion size of FP and TP lesions was comparable, indicating that simple sampling errors (due to smaller lesion size) could not explain a higher FP rate of low-uptake lesions. However, the individual reader threshold to define positive lesions may have influenced the probability of a TP outcome. Although we cannot exclude this possibility, interreader agreement with ^{68}Ga-PSMA-11 is generally high (*16*). Although the selected SUV_{max} threshold of 7.5 differentiated malignant from benign findings with moderate sensitivity and specificity, the large overlap between the SUV_{max} of TP and FP lesions limits the ability of this threshold to reliably predict prostate cancer.

A large body of evidence exists to support a strong relationship between lesion detection rates and PSA levels in BCR of prostate cancer (*7*). Our data show a scan positivity rate of 44.8% at a PSA level of below 0.25 ng/mL and 50.5% for a PSA level of between 0.25 and 0.5 ng/mL for patients after RP. These data are in line with the literature obtained from retrospective analyses (*11*,*12*,*17*). The correlation of PSMA-scan positivity and PSA level has relevant clinical implications. First, it is well established that the success of salvage RT (SRT) after RP is related to the pre-SRT PSA level (*18*). Patients with a high pre-SRT PSA level (>2 ng/mL) have very high rates of recurrence after SRT. In contrast, in patients with PSA levels close to 0.2 ng/mL, more than 75% treated with SRT have long-term durable tumor control (*19*). Additionally, the finding that the pattern of spread after RP with a rising PSA level demonstrates increased nodal, distant, and multiregion disease further helps explain the findings from Radiation Therapy Oncology Group trial 9601. This trial showed a large overall survival benefit from the addition of hormone therapy at PSA levels of more than 1.5 ng/mL after RP but no improvement in metastases or survival for patients treated with early SRT (*20*). This finding may be due to the benefit of ADT in patients with metastatic disease, and men with a presalvage PSA level of more than 1.5 ng/mL have a high probability of already harboring regional and distant metastatic disease.

Prior conventional imaging (CT of abdomen or pelvis and bone scans) was not required for participation in this study, mainly because conventional imaging is often noncontributory in biochemically recurrent prostate cancer and therefore is increasingly omitted as part of the standard of care (*16*,*21*). However, since available prior conventional imaging was allowed to contribute to scan interpretations, such information may have been a potential source of bias.

In our patient population, we noted substantial differences in the pattern of PSMA-positive disease across PSA ranges and treatment groups, as highlighted in the supplemental videos. However, these differences may be based wholly on a pronounced selection bias. We emphasize that the risk of recurrent prostate cancer and the location and extent of metastatic disease are dependent on many factors not assessed in this trial. Confounding factors include differences in risk at the time of diagnosis, heterogeneity and interval advances in therapeutic techniques within treatment groups, and variations in disease management after initial therapy. Furthermore, the observed rate of recurrent and metastatic disease per region in each treatment group does not provide information about the overall rate of recurrent prostate cancer, as scans were performed exclusively on patients expected to present with recurrent disease. Nonetheless, the study offers insight about the relationship of initial risk factors (Gleason score, initial PSA, PSA nadir, age), interval treatment (ADT), and PSA outcome at the time of the scan with ^{68}Ga-PSMA-11 scan findings.

CONCLUSION

Our prospective multicenter trial confirmed that ^{68}Ga-PSMA-11 PET is an accurate and effective modality to identify BCR of prostate cancer. Our data indicate a specific recurrent disease pattern

for initial therapy approaches and PSA ranges. Half of all scans performed at PSA levels below 0.5 ng/mL had positive results, opening the door for PSMA-targeted focal therapy approaches at an early time point of disease recurrence. Although knowledge of the disease location is of great importance for SRT planning, it remains to be seen whether PSMA image–guided (focal) therapy of BCR of prostate cancer can improve outcomes.

DISCLOSURE

Jeremie Calais reports prior consulting activities for Advanced Accelerator Applications, Blue Earth Diagnostics, Curium Pharma, GE Healthcare, EXINI, IBA RadioPharma, Janssen Pharmaceuticals, Lantheus, POINT Biopharma, Progenics, Radiomedix, and Telix Pharmaceuticals outside the submitted work. Daniel Spratt received personal fees from Janssen, AstraZeneca, Blue Earth, and Boston Scientific and funding from Janssen. Morand Piert reports prior consulting activities for Bayer and received grant funding from Endocyte/Novartis, Blue Earth Diagnostics, Progenics, the Michigan Prostate SPORE (NIH/NCI 5P50CA186786), and the Department of Radiology of the University of Michigan. Peter Scott received funding from the Department of Radiology of the University of Michigan and grants from Endocyte/Novartis and GE Healthcare. Thomas Hope received grant funding from the National Cancer Institute (R01CA212148 and R01CA235741), the Prostate Cancer Foundation (2017 Young Investigator Award and 2019 VAlor Challenge Award 18CHAL03), Advanced Accelerator Applications, and Philips and served as a consultant for Ipsen, Blue Earth Diagnostics, and Curium. Zachery Reichert received personal fees from AstraZeneca and Dendreon and grant funding from AstraZeneca, the Prostate Cancer Foundation (2018 Young Investigator Award), and the Michigan Prostate SPORE (NIH/NCI 5P50CA186786). No other potential conflict of interest relevant to this article was reported.

ACKNOWLEDGMENTS

We thank Ali Afshar-Oromieh, MD, PhD, Klaus Kopka, PhD, and colleagues at the University Hospital of Heidelberg and the German Cancer Research Center (DKFZ) Heidelberg for valuable assistance in qualifying the University of Michigan for clinical production of ^{68}Ga-PSMA-11.

KEY POINTS

QUESTION: What is the diagnostic efficacy of ^{68}Ga-PSMA-11 in BCR of prostate cancer?

PERTINENT FINDINGS: Compared with histopathology, ^{68}Ga-PSMA-11 PET provides a high PPV to identify biochemically recurrent prostate cancer locoregionally and in distant metastases. The scan detection rate increases with PSA level and is PSA-dependent within individual regions. Higher detection rates are noted with increasing overall disease burden, prior ADT, higher clinical T-stage, and Gleason grade group ratings after RP.

IMPLICATIONS FOR PATIENT CARE: ^{68}Ga-PSMA-11 PET provides a high diagnostic value in BCR of prostate cancer.

REFERENCES

1. Van den Broeck T, van den Bergh RCN, Arfi N, et al. Prognostic value of biochemical recurrence following treatment with curative intent for prostate cancer: a systematic review. *Eur Urol.* 2019;75:967–987.
2. Shipley WU, Seiferheld W, Lukka HR, et al. Radiation with or without antiandrogen therapy in recurrent prostate cancer. *N Engl J Med.* 2017;376:417–428.
3. Sanda MG, Cadeddu JA, Kirkby E, et al. Clinically localized prostate cancer: AUA/ASTRO/SUO guideline. Part I: risk stratification, Shared decision making, and care options. *J Urol.* 2018;199:683–690.
4. Calais J, Fendler WP, Eiber M, et al. Impact of ^{68}Ga-PSMA-11 PET/CT on the management of prostate cancer patients with biochemical recurrence. *J Nucl Med.* 2018;59:434–441.
5. Afshar-Oromieh A, Holland-Letz T, Giesel FL, et al. Diagnostic performance of ^{68}Ga-PSMA-11 (HBED-CC) PET/CT in patients with recurrent prostate cancer: evaluation in 1007 patients. *Eur J Nucl Med Mol Imaging.* 2017;44:1258–1268.
6. Perera M, Papa N, Christidis D, et al. Sensitivity, specificity, and predictors of positive ^{68}Ga–prostate-specific membrane antigen positron emission tomography in advanced prostate cancer: a systematic review and meta-analysis. *Eur Urol.* 2016;70:926–937.
7. Fendler WP, Calais J, Eiber M, et al. Assessment of ^{68}Ga-PSMA-11 PET accuracy in localizing recurrent prostate cancer: a prospective single-arm clinical trial. *JAMA Oncol.* 2019;5:856–863.
8. Fendler WP, Eiber M, Beheshti M, et al. ^{68}Ga-PSMA PET/CT: joint EANM and SNMMI procedure guideline for prostate cancer imaging: version 1.0. *Eur J Nucl Med Mol Imaging.* 2017;44:1014–1024.
9. Jackson IM, Lee SJ, Sowa AR, et al. Use of 55 PET radiotracers under approval of a Radioactive Drug Research Committee (RDRC). *EJNMMI Radiopharm Chem.* 2020;5:24–40.
10. Rodnick ME, Sollert C, Stark D, et al. Cyclotron-based production of ^{68}Ga, [^{68}Ga]$GaCl_3$, and [^{68}Ga]Ga-PSMA-11 from a liquid target. *EJNMMI Radiopharm Chem.* 2020;5:25.
11. Afshar-Oromieh A, da Cunha ML, Wagner J, et al. Performance of [^{68}Ga]Ga-PSMA-11 PET/CT in patients with recurrent prostate cancer after prostatectomy: a multi-centre evaluation of 2533 patients. *Eur J Nucl Med Mol Imaging.* 2021;48:2925–2934.
12. Tan N, Bavadian N, Calais J, et al. Imaging of prostate specific membrane antigen targeted radiotracers for the detection of prostate cancer biochemical recurrence after definitive therapy: a systematic review and meta-analysis. *J Urol.* 2019;202:231–240.
13. Morris MJ, Rowe SP, Gorin MA, et al. Diagnostic performance of ^{18}F-DCFPyL-PET/CT in men with biochemically recurrent prostate cancer: results from the CONDOR phase III, multicenter study. *Clin Cancer Res.* 2021;27:3674–3682.
14. Hope TA, Goodman JZ, Allen IE, Calais J, Fendler WP, Carroll PR. Metaanalysis of ^{68}Ga-PSMA-11 PET accuracy for the detection of prostate cancer validated by histopathology. *J Nucl Med.* 2019;60:786–793.
15. Fendler WP, Calais J, Eiber M, et al. False positive PSMA PET for tumor remnants in the irradiated prostate and other interpretation pitfalls in a prospective multicenter trial. *Eur J Nucl Med Mol Imaging.* 2021;48:501–508.
16. Hofman MS, Lawrentschuk N, Francis RJ, et al. Prostate-specific membrane antigen PET-CT in patients with high-risk prostate cancer before curative-intent surgery or radiotherapy (proPSMA): a prospective, randomised, multicentre study. *Lancet.* 2020;395:1208–1216.
17. Ceci F, Castellucci P, Graziani T, et al. ^{68}Ga-PSMA-11 PET/CT in recurrent prostate cancer: efficacy in different clinical stages of PSA failure after radical therapy. *Eur J Nucl Med Mol Imaging.* 2019;46:31–39.
18. Tendulkar RD, Agrawal S, Gao T, et al. Contemporary update of a multi-institutional predictive nomogram for salvage radiotherapy after radical prostatectomy. *J Clin Oncol.* 2016;34:3648–3654.
19. Abugharib A, Jackson WC, Tumati V, et al. Very early salvage radiotherapy improves distant metastasis-free survival. *J Urol.* 2017;197:662–668.
20. Dess RT, Sun Y, Jackson WC, et al. Association of presalvage radiotherapy PSA levels after prostatectomy with outcomes of long-term antiandrogen therapy in men with prostate cancer. *JAMA Oncol.* 2020;6:735–743.
21. Rowe SP, Macura KJ, Mena E, et al. PSMA-based [^{18}F]DCFPyL PET/CT is superior to conventional imaging for lesion detection in patients with metastatic prostate cancer. *Mol Imaging Biol.* 2016;18:411–419.

An ^{89}Zr-Labeled PSMA Tracer for PET/CT Imaging of Prostate Cancer Patients

Felix Dietlein[1,2], Carsten Kobe[1], Sergio Muñoz Vázquez[1], Thomas Fischer[1], Heike Endepols[1,3], Melanie Hohberg[1], Manuel Reifegerst[1], Bernd Neumaier[3,4], Klaus Schomäcker*[1], Alexander E. Drzezga*[1,5], and Markus Dietlein*[1]

[1]Department of Nuclear Medicine, University Hospital of Cologne, Cologne, Germany; [2]Department of Medical Oncology, Dana-Farber Cancer Institute, Harvard Medical School, Boston, Massachusetts; [3]Institute of Radiochemistry and Experimental Molecular Imaging, University Hospital of Cologne, Cologne, Germany; [4]Institute of Neuroscience and Medicine, INM-5 (Radiochemistry), Forschungszentrum Jülich GmbH, Jülich, Germany; and [5]Institute of Neuroscience and Medicine, INM-2, Forschungszentrum Jülich GmbH, Jülich, Germany

The short half-life of existing prostate-specific membrane antigen (PSMA) tracers limits their time for internalization into tumor cells after injection, which is an essential prerequisite for robust detection of tumor lesions with low PSMA expression on PET/CT scans. Because of its longer half-life, the ^{89}Zr-labeled ligand ^{89}Zr-PSMA-DFO allows acquisition of PET scans up to 6 d after injection, thereby overcoming the above limitation. We investigated whether ^{89}Zr-PSMA-DFO allowed more sensitive detection of weak PSMA-positive prostate cancer lesions. **Methods:** We selected 14 prostate cancer patients with biochemical recurrence who exhibited no PSMA-positive lesions on a PET scan acquired with existing PSMA tracers (^{68}Ga-PSMA-11, ^{18}F-JK-PSMA-7). Within 5 wk after the negative scan result, we obtained a second PSMA PET scan using ^{89}Zr-PSMA-DFO (117 ± 16 MBq, PET acquisition within 6 d of injection). **Results:** ^{89}Zr-PSMA-DFO detected 15 PSMA-positive lesions in 8 of 14 patients, who had a PET-negative reading of their initial PET scans with existing tracers. In these 8 patients, the new scans revealed localized recurrence of disease (3/8), metastases in lymph nodes (3/8), or lesions at distant sites (2/8). On the basis of these results, patients received lesion-targeted radiotherapies (5/8), androgen deprivation therapies (2/8), or no therapy (1/8). The plausibility of 14 of 15 lesions was supported by histology, clinical follow-up after radiotherapy, or subsequent imaging. Furthermore, comparison of the 15 ^{89}Zr-PSMA-DFO–positive lesions with their correlates on the original PET scan revealed that established tracers exhibited mild accumulation in 7 of 15 lesions; however, contrast-to-noise ratios were too low for robust detection of these lesions (contrast-to-noise ratios, 2.4 ± 3.7 for established tracers vs. 10.2 ± 8.5 for ^{89}Zr-PSMA-DFO, $P = 0.0014$). The SUV_{max} of the 15 ^{89}Zr-PSMA-DFO–positive lesions (11.5 ± 5.8) was significantly higher than the SUV_{max} on the original PET scans (4.7 ± 2.8, $P = 0.0001$). Kidneys were the most exposed organ, with doses of 3.3 ± 0.7 mGy/MBq. The effective dose was 0.15 ± 0.04 mSv/MBq. **Conclusion:** In patients with weak PSMA expression, a longer period of time might be needed for ligand internalization than that offered by existing PSMA tracers to make lesions visible on PET/CT scans. Hence, ^{89}Zr-PSMA-DFO might be of significant benefit to patients in whom the search for weak PSMA-positive lesions is challenging. Radiation exposure should be weighed against the potential benefit of metastasis-directed therapy or salvage radiotherapy, which we initiated in 36% (5/14) of our patients based on their ^{89}Zr-PSMA-DFO PET scans.

Key Words: prostate cancer; PET; PSMA tracer; ^{89}Zr-PSMA-DFO; ^{68}Ga-PSMA-11; ^{18}F-JK-PSMA-7

J Nucl Med 2022; 63:573–583
DOI: 10.2967/jnumed.121.262290

In a substantial number of prostate cancer patients, prostate-specific antigen (PSA) serum levels rise after surgery or radiotherapy (biochemical recurrence [BCR]). Early localization of recurrent tumor lesions is critical for selecting the accurate salvage therapy to improve the survival of these patients. Prostate-specific membrane antigen (PSMA) PET/CT imaging is widely used for localizing prostate cancer after BCR, and an extensive series of clinical studies has established the increased detection rate of PSMA tracers relative to alternative PET tracers or imaging techniques (*1,2*). Nevertheless, PSMA PET scans fail to localize tumor lesions in approximately 20% of the patients with BCR (*3*). In a series of prostatectomies, PSMA staining intensity was reported as absent or weak for 23% and 19% of patients with malignant tissue and Gleason scores of 3 + 4 or 4 + 3, respectively (*4*). Furthermore, negative PSMA PET scan results are significantly associated with weak PSMA levels based on immunohistochemistry (*5*). This might explain why PSMA PET scans reveal negative results in a substantial number of prostate cancer patients, even at high PSA levels. Patients with detectable but weak PSMA expression in the recurrent tumor lesions pose a challenge for existing PSMA ligands.

One limitation of existing PSMA tracers is the short half-life of their radioactive labels (^{18}F: 1.8 h, ^{68}Ga: 1.1 h), which means that PET images must be acquired within 3 h of injection. Experimental data suggest, however, that internalization of PSMA ligands gradually increases over 24 h (*6*). Ligand internalization is an important prerequisite for tracer accumulation in recurrent tumor lesions. Moreover, mildly increased tumor-to-background ratios could be observed with existing tracers when PET/CT scans were acquired later (3 h vs. 1 h) after tracer injection (*7,8*). Hence, if PET/CT images could be acquired much later, such as days after injection, even prostate cancer lesions with weak PSMA expression might become detectable on PSMA PET scans.

Given that existing PSMA tracers cannot overcome this limitation due to their short half-lives, we explored the value of a new

Received Mar. 11, 2021; revision accepted Jun. 29, 2021.
For correspondence or reprints, contact Markus Dietlein (markus.dietlein@uk-koeln.de).
*Contributed equally to this work.
Published online Jul. 29, 2021.
COPYRIGHT © 2022 by the Society of Nuclear Medicine and Molecular Imaging.

^{89}Zr-labeled PSMA tracer (^{89}Zr-PSMA-DFO) in prostate patients with BCR. Unlike existing PSMA tracers, the long half-life of the ^{89}Zr label (77 h) allows image acquisition several days after tracer injection. Furthermore, our ex vivo data on LNCaP tumor xenograft–bearing mice revealed that ^{89}Zr-PSMA-DFO exhibited an increased tumor-to-background ratio compared with the widely used PSMA tracers ^{68}Ga-PSMA-11 and ^{18}F-JK-PSMA-7 due to a prolonged period for ligand internalization (*6*). Moreover, many existing PSMA tracers are excreted through the kidney, and ^{89}Zr-PSMA-DFO might improve the detection of tumor lesions in lymph nodes near the ureter after renal clearance. Here, we present the first-in-humans application of ^{89}Zr-PSMA-DFO for PET imaging in 14 prostate cancer patients after BCR. Using ^{89}Zr-PSMA-DFO, we aimed to identify tumor lesions for metastasis-directed therapy (MTD) or salvage radiotherapy (S-RT) in these 14 patients, who had negative PET scan results using existing PSMA tracers (^{68}Ga-PSMA-11, ^{18}F-JK-PSMA-7). We also compared ^{89}Zr-PSMA-DFO–positive lesions with their correlates in the initial, negative PET scan results and examined the clinical plausibility of the ^{89}Zr-PSMA-DFO–positive lesions.

MATERIALS AND METHODS

Patient Characteristics

Patients with biochemically relapsed prostate cancer underwent PET/CT imaging with the widely used tracers ^{68}Ga-PSMA-11 or ^{18}F-JK-PSMA-7 as part of clinical routine diagnostics. The first PET scan was read as entirely PSMA-negative (13/14) or exhibited PSMA-positive findings exclusively in or near the urinary tract, which were interpreted as residual activity in the urine (1/14). When the irradiation of an empiric field within the prostate fossa was no longer an option, since either S-RT had already been performed after prostatectomy (11/14), or S-RT after prostatectomy had been refused by the patient before imaging (2/14), or radiotherapy had already been performed as the first-line therapy (1/14), we offered a second PET scan with ^{89}Zr-PSMA-DFO. Between December 2019 and July 2020, 14 patients were interested in a second PET scan because these patients were in good condition and expressed a clear preference for a MTD over an androgen deprivation therapy (ADT). The 14 patients were selected from an overall group of 633 patients, who underwent PSMA PET/CT within the 8 mo of recruitment.

In these 14 patients (average age, 62.1 ± 8.6 y), we performed a second PET scan using ^{89}Zr-PSMA-DFO within 5 wk of the first scan. Most patients (11/14) had undergone 2 therapy lines for prostate cancer (i.e., prostatectomy followed by S-RT with an empiric field). Two patients had undergone only initial prostatectomy, and 1 patient had received radiotherapy alone. Tables 1 and 2 provide more details on patient characteristics. Because the option of MDT or S-RT depends on the exact localization of the tumor and no other PSMA tracers or imaging options with comparable sensitivity are available, we determined that the benefit of the PET imaging outweighed the radiation exposure of an additional PET/CT scan using the ^{89}Zr-labeled ligand. The Institutional Review Board approved this study and the use of the data for a retrospective analysis. All subjects signed a written informed consent form to PET imaging and the use of their data for a retrospective analysis. All procedures were performed in compliance with the regulations of the responsible local authorities (District Administration of Cologne, Germany).

Tracer Preparation

^{89}Zr-PSMA-DFO was produced following applicable good manufacturing practice (*6*). The precursor for the ^{89}Zr-based PSMA-vector EuK-2NaI-AMCHA-N-sucDf-Fe (E = glutamic acid, u = urea, K = lysine, 2Nal = 2-naphthyl-alanine, AMCHA = traxamic acid) (ABX) was formed by the pharmacophore EuK coupled to a naphthylic linker and the chelator agent N-sucDf-Fe. The N-sucDf-Fe moiety functionalized the molecule for labeling with ^{89}Zr. It proved to be a suitable chelator for ^{89}Zr. Labeling of the precursor Fe-N-PSMA-Df with ^{89}Zr required a multistep procedure due to the presence of Fe(III), which was removed by transchelation to ethylenediaminetetraacetic acid (EDTA) (100:1) at 35°C for 30 min, forming [Fe(III)EDTA]. The purification of the Fe(III)-free compound from byproducts such as EDTA and [Fe(III)EDTA] was performed using a Sep-Pak C_{18} plus light cartridge (130 mg of sorbent per cartridge, 55- to 105-μm particle size) (Waters Corp.) and PD MidiTrap G-10 column (>700 Mr, 5.3-mL bed package of Sephadex G-10) (GE Healthcare). After elution of PSMA-Df, the radiolabeling procedure was performed by adjusting the pH of a solution of ^{89}Zr in 1 M oxalic acid to 6.8–7.2 with 1 M sodium carbonate, 0.5 M *N*-(2-hydroxyethyl)piperazine-*N*′-(2-ethanesulfonic acid) (HEPES) (pH 6.8), and 0.25 M sodium acetate (5 mg/1 mL gentisic acid, 50 μL). Unbound ^{89}Zr was then efficiently removed by solid-phase extraction using a Sep-Pak C_{18} plus light cartridge.

Specification of ^{89}Zr-PSMA-DFO and quality control included assessment of radiochemical purity (≥97%), pH-value (5.0–8.0), endotoxin content (≤11.7 IE/mL), testing for sterility, and chemical purity (HEPES ≤ 40 μg/mL, ethanol ≤ 10%). During this study, none of the 7 syntheses failed to reach these specifications.

Imaging and Reading

All PET/CT images were acquired from midthigh to the tip of the skull on a Biograph mCT 128 Flow PET/CT scanner (Siemens Healthineers) and reconstructed using an ultra-high-definition (UHD) algorithm. For existing PSMA tracers, PET scans were acquired 1 h (^{68}Ga-PSMA-11, 153 ± 30 MBq, 4 patients) or 2 h (^{18}F-JK-PSMA-7, 286 ± 26 MBq, 10 patients) after injection. For ^{89}Zr-PSMA-DFO (117 ± 16 MBq), we acquired PET/CT scans 2 and 3 d after tracer injection (10 patients). For logistical reasons, we slightly deviated from this protocol for 4 patients (images acquired on days 1 and 2, or on days 1 and 3, or on days 2 and 6, or on days 1, 2, and 6, respectively). Acquisition times were adapted to the PSMA ligand with a flow motion bed speed of 1.5 mm/s for ^{68}Ga-PSMA-11 and ^{18}F-JK-PSMA-7, of 0.9 mm/s for the first ^{89}Zr-PSMA-DFO PET scan, and of 0.6 mm/s for the subsequent ^{89}Zr-PSMA-DFO PET scans. CT scans (slice thickness of 5.0 mm, pitch 1.2) were acquired using a low-dose technique with kV and mA modulation adapted to the patient's size.

Because we applied lower activities of ^{89}Zr-PSMA-DFO than of ^{68}Ga-PSMA-11 or ^{18}F-JK-PSMA-7, we measured the signal-to-noise ratio (SNR) and the contrast-to-noise ratio (CNR) to describe the image quality obtained with ^{89}Zr-PSMA-DFO on the Biograph mCT 128 Flow PET/CT scanner (*9*). The SNR was calculated as the ratio of SUV_{mean} to SD in a volume of interest (VOI) with 3-cm diameter in the liver. The CNR was calculated as the ratio of the difference of the SUV_{mean} in the lesion and the SUV_{mean} in the background to SD in the background. The SUV_{mean} in a lesion was obtained by delineating a VOI at 41% of the SUV_{max} of the same lesion. The SUV_{mean} of the background and its SD were measured in a 3-cm VOI in the local background around the lesion.

For cross-calibration of the ^{89}Zr label, we filled an ^{89}Zr-phantom with 6.283 L of a specific activity of ^{89}Zr (43.287 MBq/L). The activity of ^{89}Zr, measured by the PET/CT scanner, was 35.597 MBq/L, resulting in a dose cross-calibration factor of 1.216. To avoid overestimating the SUV in ^{89}Zr-PSMA-DFO–positive tumor lesions with the UHD algorithm (*10*), we did not multiply ^{89}Zr-PSMA-DFO SUVs by the cross-calibration factor for ^{89}Zr. The cross-calibration factors for ^{68}Ga and ^{18}F were 1.01 and 1.02, respectively.

PET/CT scans were interpreted according to published criteria for standardization of PSMA PET/CT interpretation (*11,12*) by a team of 2 specialists in nuclear medicine and 1 radiologist. Any disagreement

was resolved in consensus. The same team interpreted PET/CT scans acquired with ^{89}Zr-PSMA-DFO and existing PSMA tracers (^{68}Ga-PSMA-11, ^{18}F-JK-PSMA-7). Statistical analyses were performed with Microsoft Excel, comparing the SUVs in the areas with a suspicious PSMA accumulation, the SNRs, and the CNRs.

Dosimetric Measurement

Estimation of the kidney dose was determined on the basis of 3 patients who underwent PET/CT scans with an interval between 2 scans of at least 2 d. The following assumptions were made for the estimation: between time 0 (injection) and the first measuring point the time–activity curve has a constant progression. All measuring points were integrated numerically using trapezoidal approximation. From the last measuring point to infinity, a monoexponential function was fitted and integrated. As the effective half-life could not be accurately determined from 2 measurement points in 2 of the 3 patients, the physical half-life of ^{89}Zr was used instead.

RESULTS

PSMA-Positive Lesions with ^{89}Zr-PSMA-DFO PET

We acquired ^{89}Zr-PSMA-DFO PET/CT scans of 14 patients with BCR, who had been examined with ^{68}Ga-PSMA-11 ($n = 4$) or ^{18}F-JK-PSMA-7 ($n = 10$) less than 5 wk previously without any PSMA-positive tumor lesions being revealed (Tables 1 and 2). In 8 of 14 patients (57%), ^{89}Zr-PSMA-DFO identified at least 1 PSMA-positive lesion (15 additional lesions in total). We detected these lesions in the prostate or prostate fossa of 3 patients, in lymph nodes of 3 patients, and at distant lesions for 2 patients (bone marrow, lung). In addition, we interpreted PSMA-positive lesions according to PSMA-RADS version 1.0 and the miTNM classification (Tables 1 and 2). To avoid false-positive interpretations because of low SNRs, we applied the following additional criteria: we interpreted a lesion as PSMA-positive, if it could be detected on 2 independent scans (14/15 lesions); and we interpreted a PSMA-positive lesion as a PSMA-positive lymph node or as a suspicious lung lesion, if we detected a radiologic correlate on the parallel low-dose CT scan.

To examine which aspects might have contributed to the detection of these 15 additional lesions, we compared lesions identified by ^{89}Zr-PSMA-DFO with the corresponding areas on the initial PET scans (^{68}Ga-PSMA-11, ^{18}F-JK-PSMA-7), using the mediastinal blood pool as a reference. This comparison revealed that 7 of 15 lesions also exhibited a mild tracer accumulation on the PET scans acquired with ^{68}Ga-PSMA-11 or ^{18}F-JK-PSMA-7 (average ratio of the tumor area to the mediastinal blood pool for both tracers: 3.1 ± 2.4; ^{68}Ga-PSMA-11: 2.6 ± 1.8; ^{18}F-JK-PSMA-7: 3.5 ± 2.9), but that this signal was not strong enough to allow robust detection of those lesions.

In contrast, PET/CT scans acquired with ^{89}Zr-PSMA-DFO exhibited a significantly higher ratio of the 15 lesions to the mediastinal blood pool (14.2 ± 7.7, $P < 0.0001$, paired t test), and this difference remained significant when comparing the signal of ^{89}Zr-PSMA-DFO with that of ^{68}Ga-PSMA-11 ($P = 0.0072$, 7 lesions, Figs. 1 and 2) and ^{18}F-JK-PSMA-7 ($P = 0.026$, 8 lesions, Fig. 3) separately (Tables 3 and 4). When we used the SUV_{max} as an alternative measure, these differences were similarly significant ($P = 0.0002$), and the corresponding numbers were 4.7 ± 2.0 (^{68}Ga-PSMA-11), 4.7 ± 3.5 (^{18}F-JK-PSMA-7), and 11.1 ± 5.8 (^{89}Zr-PSMA-DFO).

Furthermore, like many existing PSMA tracers, ^{68}Ga-PSMA-11 and ^{18}F-JK-PSMA-7 are excreted through the kidney, which interferes with the detection of lesions near the ureter due to residual activity in the urine. The ^{89}Zr-PSMA-DFO PET scans were uncompromised by residual activity in the urinary tract, because they were acquired after the tracer was fully cleared from the bloodstream. This might have facilitated the detection of tumor lesions near the ureter (Supplemental Fig. 1).

Image Quality

SNRs of ^{89}Zr-PSMA-DFO were 2.1 ± 0.5 and 2.1 ± 0.4 in the first and second PET scans, respectively. These ratios were significantly lower than those of established tracers (SNR of ^{68}Ga-PSMA-11: 3.7 ± 0.9, $P = 0.0034$; SNR of ^{18}F-JK-PSMA-7: 7.7 ± 1.3, $P < 0.0001$, paired t test) (Table 5). However, ^{89}Zr-PSMA-DFO PET/CT exhibited significantly higher CNRs in PSMA-positive lesions (10.2 ± 8.5 and 11.0 ± 10.1 in scans 1 and 2) than ^{68}Ga-PSMA-11 (4.5 ± 4.6, $P = 0.0016$), ^{18}F-JK-PSMA-7 (0.7 ± 1.0, $P = 0.036$), or ^{68}Ga- and ^{18}F-PSMA tracers in combination (2.4 ± 3.7, $P = 0.0014$, paired t test) (Table 6, Supplemental Table 1). This suggests that the detection of weak PSMA-avid lesions was facilitated by significantly higher CNR of ^{89}Zr-PSMA-DFO.

Timing Between Tracer Injection and ^{89}Zr-PSMA-DFO PET Scans

Finally, we investigated whether the time between injection and image acquisition had a substantial impact on the sensitivity of ^{89}Zr-PSMA-DFO. For all tumor patients, we acquired PET/CT scans with ^{89}Zr-PSMA-DFO on 2 or more days after tracer injection (2 whole-body scans for 13 patients, 3 whole-body scans for 1 patient). Most lesions (14/15) were visible on all consecutive scans. Only 1 lesion became visible on day 6 only (SUV_{max} 8.1) and could not be detected previously (day 1: SUV_{max} 3.2; day 2: SUV_{max} 2.5). The SNR did not differ significantly between first (2.1 ± 0.5) and second (2.1 ± 0.4) ^{89}Zr-PSMA-DFO PET scans ($P = 0.79$, paired t test). CNRs of the 15 PSMA-positive lesions did not differ significantly between scans 1 and 2 either (10.2 ± 8.5 vs. 11.0 ± 10.1, $P = 0.69$, paired t test). Similar results were obtained when using the SUV_{max} instead (11.5 ± 5.8 vs. 9.9 ± 5.1, $P = 0.27$) (Tables 3 and 6), suggesting that the exact time of acquisition has no more than a minor impact on detection of PSMA lesions, as long as PET/CT images are acquired at least 2 d after tracer injection when ligand internalization has reached a steady state.

Verification and Therapeutic Consequences

We verified ^{89}Zr-PSMA-DFO–positive lesions in 5 of 8 patients by histology (1 patient) and clinical follow-up (4 patients, drop-in PSA levels after metastasis-directed radiotherapy). On the basis of the results of the ^{89}Zr-PSMA-DFO PET/CT scan, these 5 patients received MDT or S-RT (3 patients: prostate fossa, 1 patient: PSMA-positive lymph-nodes, 1 patient: solitary bone marrow metastasis). Another 2 patients with ^{89}Zr-PSMA-DFO–positive PET scan results received ADT because they were not eligible for MDT. One patient with a PSMA-positive coin lesion in the lung exhibited stable disease in a follow-up CT after 7 mo and PSA levels remained stable for 11 mo, so that the urologists pursued watchful waiting for this patient. Further data on clinical follow-up are presented in Tables 1 and 2.

Dosimetric Measurement

The ^{89}Zr-PSMA-DFO PET scans exhibited the highest tracer activity in the kidneys, the organ with the highest radiation exposure. We calculated the kidney dose to be 3.3 ± 0.73 mGy/MBq. The overall effective dose (*13*) was 0.15 ± 0.04 mSv/MBq.

TABLE 1
Clinical Data from Patients 1–7 with PET-1 Scan Results Interpreted as PSMA-Negative

Patient	Indication	Gleason score, TNM	PSA value, dt PSA, and iPSA	PSMA tracer used in PET-1	No. of lesions interpreted as PSMA-positive with ^{89}Zr-PSMA-DFO in PET-2	Therapeutic consequence	Verification
1	BCR after RT	NA, NA	3.2, >12 mo, 4.21	^{18}F-JK-PSMA-7	Prostate lobe right PSMA-RADS 4 Prostate lobe left PSMA-RADS 4 miT2mN0M0	Biopsy, S-RT at a PSA level of 4.2	Histologically confirmed on both sides. Decrease in PSA level to 1.5 after S-RT
2	BCR after RPE and S-RT	4 + 3, pT2 cN0	0.88, >12 mo, 4.53	^{68}Ga-PSMA-11	Coin lesion in the lung, dignity unclear PSMA-RADS 3C miT0N0M1c	Watchful waiting with low-dose CT of the lung	Stable in the CT of the lung after 7 mo, PSA stable after 11 mo, suggestive of vascular malformation
3	BCR after RPE and S-RT	3 + 4, pT3a pN0	7.2, 4 mo, 12	^{18}F-JK-PSMA-7	3 l.n. retroperitoneal PSMA-RADS 3A l.n. supraclav. left PSMA-RADS 3A miT0N1bM0	ADT after rapid increase of PSA to 14.6	Increase in PSA level before ADT
4	BCR after RT and S-RPE	4 + 5, Tx pN1	0.46, 3 mo, NA	^{18}F-JK-PSMA-7	None PSMA-RADS 0 miT0N0M0	Watchful waiting with PSMA PET/CT	PSMA-negative, bone metastases detected after 9 mo
5	BCR after RPE. ADT until 12 mo before	5 + 5, pT4 pN0	0.31, NA, 444	^{18}F-JK-PSMA-7	None PSMA-RADS 0 miT0N0M0	Start with ADT at a PSA level of 1.74. S-RT of the prostate fossa	Decrease in PSA level to 0.03 after S-RT and ADT
6	BCR after RPE and S-RT	4 + 4, pT2a pN0	0.72, 7 mo, 13.15	^{68}Ga-PSMA-11	l.n. iliac right PSMA-RADS 3A Os ilium left PSMA-RADS 3B miT0N1aM1b	RT of the solitary bone metastasis at a PSA level of >1, RT of the l.n. iliac right 9 mo later	Decrease in PSA level to 0.71 after RT; ^{18}F-JK-PSMA PET/CT after 9 mo: progress of the l.n. iliac right
7	BCR after RPE and S-RT	3 + 4, pT3b pN0	0.62, 3 mo, 7.1	^{18}F-JK-PSMA-7	None PSMA-RADS 0 miT0N0M0	Watchful waiting with PSMA PET/CT	PET/CT after 6 mo also PSMA-negative at a PSA level of 1.3

TABLE 2
Clinical Data from Patients 8–14 with PET-1 Scan Results Interpreted as PSMA-Negative

Patient	Indication	Gleason score, TNM	PSA value, dt PSA, and iPSA	PSMA tracer used in PET-1	No. of lesions interpreted as PSMA-positive with ^{89}Zr-PSMA-DFO in PET-2	Therapeutic consequence	Verification
8	BCR after RPE and S-RT	3 + 4, pT2 pN1	4.4, 5 mo, 24	^{68}Ga-PSMA-11	2 l.n. retroperitoneal PSMA-RADS 3A l.n. supraclav. left PSMA-RADS 3A miT0N1bM0	All 3 PSMA-positive l.n. treated with S-RT; start of temporary ADT	Decrease in PSA level to 0.17 ng/mL
9	BCR after RPE and S-RT	4 + 3, pT3 pN0	1.1, >12 mo, 14	^{18}F-JK-PSMA-7	None PSMA-RADS 0 miT0N0M0	Watchful waiting	MRI also without finding
10	BCR after RPE. S-RT refused before PET	4 + 4, pT3a pN0	0.54, 10 mo, 7.7	^{18}F-JK-PSMA-7	Prostate fossa right PSMA-RADS 4 miT2uN0M0	S-RT	Decrease in PSA level to 0.3 after S-RT
11	BCR after RPE and S-RT. ADT until 2 y before	4 + 5, pT3b pN0 R1	0.81, NA, 184	^{18}F-JK-PSMA-7	None PSMA-RADS 0 miT0N0M0	Start with ADT at a PSA level of 1.71	MRI also without finding
12	BCR after RPE and S-RT	3 + 4, NA	1.78, 4 mo, 6.2	^{18}F-JK-PSMA-7	None PSMA-RADS 0 miT0N0M0	Start with ADT for 1 y	MRI also without finding
13	BCR after RPE and S-RT	4 + 3, pT3b pN0	2.01, 1 mo, 8.5	^{68}Ga-PSMA-11	l.n. iliac right PSMA-RADS 3A miT0N1aM0	Start with ADT at a PSA level of 3.8	MRI with enlarged l.n. iliac right
14	BCR after RPE. S-RT not recommended before PET	3 + 4, pT2c pN0	0.7, 7 mo, NA	^{18}F-JK-PSMA-7	Prostate fossa left PSMA-RADS 4 miT2uN0M0	S-RT	Decrease in PSA level to 0.09 after S-RT (6 wk after the end of S-RT)

Eight of the 14 patients showed PSMA-positive lesions with ^{89}Zr-PSMA-DFO. In 6 patients, the PSMA-negative interpretation from PET-1 was confirmed by the ^{89}Zr-PSMA-DFO PET-2. The location of each PSMA-positive lesion detected with ^{89}Zr-PSMA-DFO is described for each patient.

dtPSA = doubling time of PSA; iPSA = initial PSA; l.n. = lymph node; NA = not available; RPE = radical prostatectomy; RT = radiotherapy.

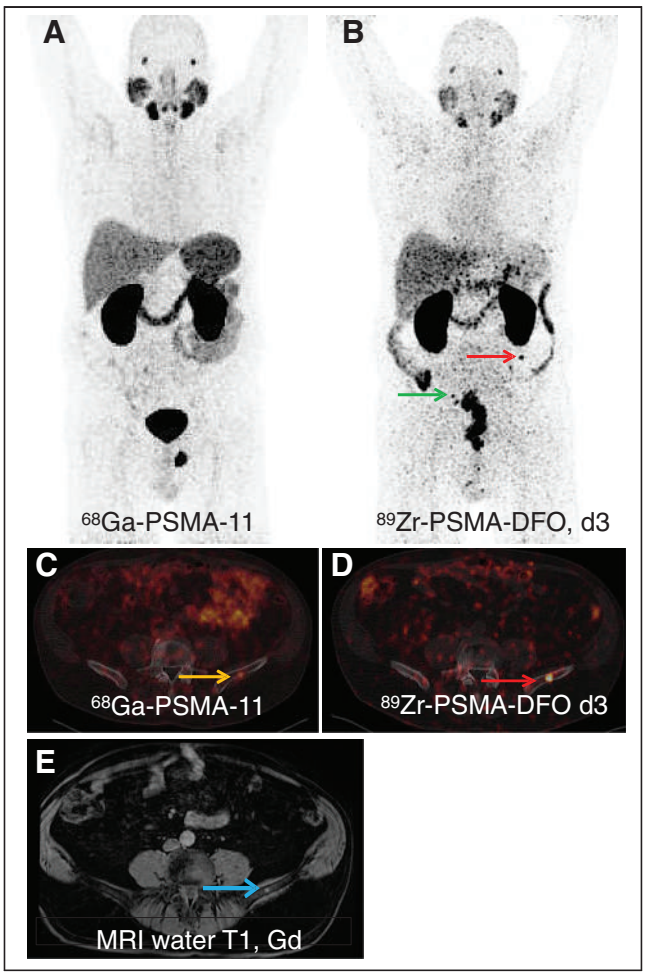

FIGURE 1. ^{68}Ga-PSMA-11 PET with maximum-intensity-projection (MIP) (A) and PET/low-dose CT fusion images (C), and ^{89}Zr-PSMA-DFO PET 3 d after injection with MIP (B) and PET/low-dose CT fusion images (D) of patient 6 with BCR after prostatectomy and S-RT. Images are highly suggestive of a PSMA-positive osteomedullary metastasis in os ilium left, clearly visible with ^{89}Zr-PSMA-DFO (red arrows in B and D). PSMA overexpression in os ilium left with ^{68}Ga-PSMA-11 was faint (yellow arrow in C). Small lesion is retrospectively visible in the MRI scan (blue arrow in E) without any correlate in low-dose CT. After PSA level further increased above 1 ng/mL, bone metastasis was irradiated and PSA levels dropped to 0.7 ng/mL. Nine months later, ^{18}F-JK-PSMA-7 PET/CT revealed further progression of tumor in right iliac lymph node with weak ^{89}Zr-PSMA-DFO expression (green arrow in B), and the lymph node was locally irradiated. d = day; Gd = gadolinium; p.i. = after injection.

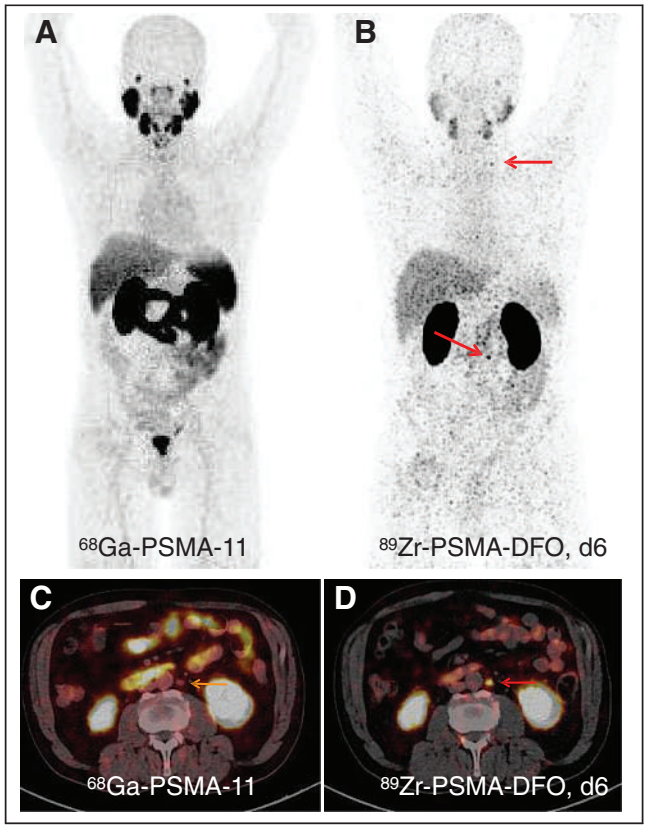

FIGURE 2. ^{68}Ga-PSMA-11 PET with maximum-intensity-projection (MIP) (A) and PET/low-dose CT fusion images (C), and ^{89}Zr-PSMA-DFO PET 6 d after injection with MIP (B) and PET/low-dose CT fusion images (D) of patient 8 with BCR after prostatectomy and S-RT. Images are highly suggestive of PSMA-positive lymph node metastases supraclavicular left and retroperitoneal left, visible with ^{89}Zr-PSMA-DFO (red arrows in B and D). Lymph nodes were PSMA-negative with ^{68}Ga-PSMA-11 (yellow arrow in C). Patient underwent S-RT and temporary ADT. PSA level dropped to 0.17 ng/mL. d = day; p.i. = after injection.

Adverse Events

All patients tolerated the tracer injection and the PET/CT examination well. We asked each patient whether they had experienced any adverse side effects when the PET results were communicated with the patient in person and again when the therapeutic consequences were discussed on the phone. None of the patients reported nausea, diarrhea, dizziness, or any other adverse events or side effects during these conversations.

DISCUSSION

Our study revealed that ^{89}Zr-PSMA-DFO has the ability to localize lesions with weak PSMA expression in patients with BCR when the preceding ^{68}Ga-PSMA-11 or ^{18}F-JK-PSMA-7 PET scans have been read as PSMA-negative. In our small group, localization was successful in more than half of the prostate cancer patients (8/14). This observation is in marked contrast to the results obtained with other PSMA tracers we have examined recently. For example, when comparing ^{68}Ga-PSMA-11 with ^{18}F-DCFPyL, we obtained an ^{18}F-DCFPyL–positive PET scan after a prior ^{68}Ga-PSMA-11–negative scan in only 1 of 25 patients (*3,14*). Similarly, ^{18}F-JK-PSMA-7 (1/10 patients) and ^{18}F-PSMA-1007 (0/7 patients) rarely revealed a positive scan result after a previous negative PET scan result (*15,16*). Hence, our study demonstrates that ^{89}Zr-PSMA-DFO has the ability to identify tumor lesions with detectable but low PSMA expression.

In this study, ^{89}Zr-PSMA-DFO PET was offered with the goal of initiating MDT and delaying the start of ADT with the risk of later castration resistance. MDT is described as a promising therapeutic approach in men with hormone-sensitive oligometastatic prostate cancer with up to 3 metastases in international guidelines, but its efficacy depends on the exact and sensitive localization of all tumor lesions (*17,18*). In a phase 2 randomized study, MDT of the PSMA-positive lesions improved the progression-free survival and decreased the risk of new lesions in the PSMA PET at 6 mo (*19*). On the basis of the ^{89}Zr-PSMA-DFO PET scans, an MDT or S-RT could be initiated in 5 of 14 patients. However, this clinical

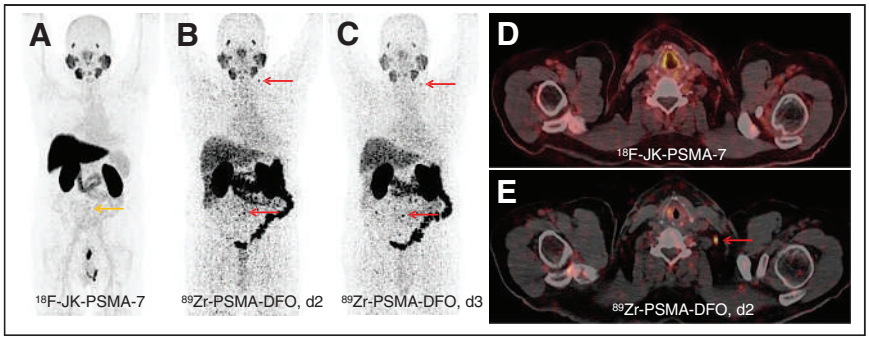

FIGURE 3. ^{18}F-JK-PSMA-7 PET with maximum-intensity-projection (MIP) (A) and PET/low-dose CT fusion images (D), and ^{89}Zr-PSMA-DFO PET 2 and 3 d after injection with MIP (B and C) and PET/low-dose CT fusion images (E) of patient 3 with BCR after prostatectomy and S-RT. Images are highly suggestive of PSMA-positive lymph node metastases supraclavicular left and retroperitoneal, visible with ^{89}Zr-PSMA-DFO (red arrows in B, C, and E). Lymph node supraclavicular left was PSMA-negative with ^{18}F-JK-PSMA-7, and lymph node retroperitoneal was faintly PSMA-positive with ^{18}F-JK-PSMA-7 (yellow arrow in A). Because of rapid increase in PSA level, patient underwent ADT. D = day; p.i. = after injection.

benefit required an ^{89}Zr-PSMA-DFO PET/CT scan, resulting in a radiation exposure of 3.3 ± 0.73 mGy/MBq for the kidneys and an overall effective dose of 0.15 ± 0.04 mSv/MBq. Our dosimetry estimates suggest that the effective dose of ^{89}Zr-PSMA-DFO is lower than that of an ^{89}Zr-labeled antibody in metastatic castration-resistant prostate cancer patients (0.44 mSv/MBq), but the renal dose of ^{89}Zr-PSMA-DFO is higher than that of an ^{89}Zr-labeled antibody (0.73 mSv/MBq) (*20*). Dosimetry estimates in larger patient cohorts will be required to establish ^{89}Zr-PSMA-DFO in routine clinical diagnostics.

Multiple orthogonal observations suggest that the prolonged acquisition time after tracer injection led to increased accumulation of ^{89}Zr-PSMA-DFO in prostate cancer lesions. First, comparison of matched PET scans revealed that ^{68}Ga-PSMA-11 and ^{18}F-JK-PSMA-7 also accumulated in the lesions identified by ^{89}Zr-PSMA-DFO, suggesting that the 3 ligands consistently bound to the surface of these tumor cells. However, prolonged time was required for sufficient ligand internalization, so that these lesions could be identified only on ^{89}Zr-PSMA-DFO PET/CT scans. Second, experimental studies suggest that internalization of PSMA ligands increases over time, thereby gradually enhancing the signal-to-background ratio (*6*). Third, recent clinical studies have indicated that the performance of existing tracers can be marginally improved by acquiring PET images with ^{68}Ga-PSMA-11 or ^{18}F-JK-PSMA-7 at later time points (*7,8*). Fourth, many tracers are excreted through the kidney, and acquisition at later time points facilitates detection of lesions near the ureter due to low residual activity in the urine. As such, ^{89}Zr-PSMA-DFO might be particularly suitable for detecting tumor lesions with low PSMA expression.

Our study further suggests that images with ^{89}Zr-PSMA-DFO can be acquired anytime 48–72 h after tracer injection. The exact acquisition time point within this period has only a marginal impact on tracer sensitivity (half-life of ^{89}Zr-PSMA-DFO is 77 h).

TABLE 3
SUV_{max} Values from 8 Patients with PET-2 Scan Results Interpreted as PSMA-Positive with ^{89}Zr-PSMA-DFO

	Lesions interpreted as PSMA-positive with ^{89}Zr-PSMA-DFO in PET-2						
Patient	PET finding	SUV_{max}, day 1	SUV_{max}, day 2	SUV_{max}, day 3	SUV_{max}, day 6	Corresponding area with ^{18}F-JK-PSMA-7 in PET-1, SUV_{max} (2 h)	Corresponding area with ^{68}Ga-PSMA-11 in PET-1, SUV_{max} (1 h)
1	Prostate lobe right		13.3	13.1		5.4	
	Prostate lobe left		9.5	7.1		4.6	
2	Lung left (dignity unclear)		5.7		6.7		4.1
3	l.n. retroperitoneal		3.1	6.1		1.4	
	l.n. retroperitoneal		17.0	11.0		2.4	
	l.n. retroperitoneal		14.2	8.9		1.7	
	l.n. supraclav. left		12.1	6.9		2.2	
6	l.n. iliac right		7.8	13.2			4.3
	Os ilium left		14.3	15.8			8.2
8	l.n. retroperitoneal	11.5	9.6		15.6		3.1
	l.n. retroperitoneal	12.2	8.3		7.2		6.0
	l.n. supraclav. left	3.2	2.5		8.1		2.0
10	Prostate fossa right		14.7	22.8	11.1	10.9	
13	l.n. iliac right		7.6	4.5			5.5
14	Prostate fossa left		25.5	12.8		8.7	

When one or several PSMA-positive areas were detected by ^{89}Zr-PSMA-DFO PET, the SUV_{max} within the corresponding area of the ^{18}F-JK-PSMA-7 or the ^{68}Ga-PSMA-11 PET scan was measured. The SUV_{max} of ^{89}Zr-PSMA-DFO PET-2 (first measurement) was significantly higher than the SUV_{max} of the PET-1 scan with ^{68}Ga-PSMA-11 or ^{18}F-JK-PSMA-7 in the corresponding areas ($P = 0.0001$, paired t test).

l.n. = lymph node.

TABLE 4
SUV Ratios from 8 Patients Whose PET-2 scans Were Interpreted as PSMA-Positive with ^{89}Zr-PSMA-DFO

	Lesions interpreted as PSMA-positive with 89Zr-PSMA-DFO in PET-2						
Patient	PET finding	Ratio SUV_{max}: MBP_{mean}, day 1	Ratio SUV_{max}: MBP_{mean}, day 2	Ratio SUV_{max}: MBP_{mean}, day 3	Ratio SUV_{max}: MBP_{mean}, day 6	Corresponding area with ^{18}F-JK-PSMA-7 in PET-1, ratio SUV_{max}:MBP_{mean} (2 h)	Corresponding area with ^{68}Ga-PSMA-11 in PET-1, ratio SUV_{max}:MBP_{mean} (1 h)
1	Prostate lobe right		13.5	10.1		4.6	
	Prostate lobe left		9.7	5.5		4.0	
2	Lung left (dignity unclear)		7.6		13.3		3.3
3	l.n. retroperitoneal		4.8	11.3		0.8	
	l.n. retroperitoneal		26.2	20.4		1.3	
	l.n. retroperitoneal		21.9	16.5		0.9	
	l.n. supraclav. left		18.6	12.7		1.2	
6	l.n. iliac right		10.5	19.9			0.9
	Os ilium left		19.4	23.9			1.7
8	l.n. retroperitoneal	8.5	9.9		21.7		1.8
	l.n. retroperitoneal	9.1	8.6		10.0		3.5
	l.n. supraclav. left	2.4	2.5		11.3		1.2
10	Prostate fossa right		11.9	17.8	NA	6.7	
13	l.n. iliac right		19.6	11.5			6.1
14	Prostate fossa left		28.1	12.0		8.4	

When one or several PSMA-positive areas were detected by ^{89}Zr-PSMA-DFO PET, the SUV_{max} within the corresponding area of the ^{18}F-JK-PSMA-7 or the ^{68}Ga-PSMA-11 PET was measured. The SUV_{max} within the suspicious area was divided by the SUV_{mean} in the mediastinal blood pool. The ratio SUV_{max} (lesion): SUV_{mean} (MBP) was a measure of the contrast between the suspicious area and the background. The ratio of the ^{89}Zr-PSMA-DFO PET-2 (first measurement) was significantly higher than the ratio of the PET-1 scan with ^{68}Ga-PSMA-11 or ^{18}F-JK-PSMA-7 in the corresponding areas ($P < 0.0001$, paired t test). In patient 10, the PET scan on day 6 was confined to the pelvis and the ratio between lesion and the MBP was not calculated

l.n. = lymph node; MBP = mediastinal blood pool; NA = not available.

TABLE 5
Image Quality Obtained with ^{89}Zr-PSMA-DFO, ^{18}F-JK-PSMA-7, and ^{68}Ga-PSMA-11 on the Biograph mCT 128 Flow PET/CT scanner

		^{89}Zr-PSMA-DFO PET/CT					
Patient	Parameter (liver)	Day 1	Day 2	Day 3	Day 6	^{18}F-JK-PSMA-7 PET/CT (2 h)	^{68}Ga-PSMA-11 PET/CT (1 h)
1	$SUV_{mean} \pm SD$		2.3 ± 1.2	2.1 ± 1.0		13.1 ± 2.4	
	SNR		1.9	2.0		5.5	
2	$SUV_{mean} \pm SD$		2.7 ± 1.3		2.1 ± 1.4		6.0 ± 1.4
	SNR		2.1		1.5		4.5
3	$SUV_{mean} \pm SD$		2.4 ± 1.8	2.1 ± 1.2		16.3 ± 2.0	
	SNR		1.4	1.8		8.1	
4	$SUV_{mean} \pm SD$	2.9 ± 1.0		1.9 ± 0.8		8.5 ± 1.1	
	SNR	2.8		2.4		8.1	
5	$SUV_{mean} \pm SD$		2.6 ± 1.2	2.6 ± 1.2		13.4 ± 1.8	
	SNR		2.3	2.2		7.6	
6	$SUV_{mean} \pm SD$		2.2 ± 1.4	2.0 ± 0.9			5.0 ± 1.7
	SNR		1.6	2.2			3.0
7	$SUV_{mean} \pm SD$	2.5 ± 1.1	2.3 ± 1.0			10.6 ± 1.7	
	SNR	2.3	2.3			6.4	
8	$SUV_{mean} \pm SD$	3.0 ± 1.1	2.7 ± 0.9		2.3 ± 1.4		4.5 ± 1.0
	SNR	2.6	3.0		1.6		4.5
9	$SUV_{mean} \pm SD$		2.5 ± 1.2	2.5 ± 1.2		10.7 ± 1.4	
	SNR		2.1	2.1		7.8	
10	$SUV_{mean} \pm SD$		2.7 ± 1.3	1.9 ± 0.9		11.9 ± 2.4	
	SNR		2.2	2.2		5.0	
11	$SUV_{mean} \pm SD$		2.8 ± 1.2	2.3 ± 0.9		14.7 ± 1.7	
	SNR		2.4	2.6		8.5	
12	$SUV_{mean} \pm SD$		2.7 ± 1.3	2.5 ± 1.0		14.1 ± 2.2	
	SNR		2.1	2.5		6.4	
13	$SUV_{mean} \pm SD$		1.5 ± 1.3	1.5 ± 0.9			3.5 ± 1.3
	SNR		1.1	1.7			2.8
14	$SUV_{mean} \pm SD$		2.9 ± 1.0	2.4 ± 1.3		14.6 ± 2.9	
	SNR		2.9	1.9		5.1	

The SNR was calculated as the ratio of SUV_{mean} to SD in a VOI with 3 cm diameter in the liver. Image quality was significantly higher with ^{18}F-JK-PSMA-7 ($P < 0.0001$, paired t test) and ^{68}Ga-PSMA-11 ($P = 0.0034$) than with ^{89}Zr-PSMA-DFO.

TABLE 6
CNR of 15 Lesions in 8 Patients with ^{89}Zr-PSMA-DFO PET Scan Results (PET-2) Interpreted as PSMA-Positive

	CNR in the lesions interpreted as PSMA-positive with ^{89}Zr-PSMA-DFO in PET-2						
Patient	PET finding	CNR, day 1	CNR, day 2	CNR, day 3	CNR, day 6	Corresponding area with ^{18}F-JK-PSMA-7 in PET-1, CNR (2 h)	Corresponding area with ^{68}Ga-PSMA-11 in PET-1, CNR (1 h)
1	Prostate lobe right		3.8	3.0		0.9	
	Prostate lobe left		3.5	1.1		0.6	
2	Lung left (dignity unclear)		20.3		23.7		12.1
3	l.n. retroperitoneal		1.1	3.1		0.1	
	l.n. retroperitoneal		8.3	6.6		1.1	
	l.n. retroperitoneal		8.6	4.7		−0.2	
	l.n. supraclav. left		18.8	11.9		2.9	
6	l.n. iliac right		11.5	20.6			3.0
	Os ilium left		17.7	37.9			9.4
8	l.n. retroperitoneal	4.6	4.9		12.2		0.03
	l.n. retroperitoneal	3.9	6.5		5.5		1.7
	l.n. supraclav. left	3.0	3.1		13.0		0.7
10	Prostate fossa right		3.5	13.2	8.4	−0.2	
13	l.n. iliac right		12.9	8.0			4.3
14	Prostate fossa left		30.8	16.7		−0.3	

When one or several PSMA-positive areas were detected by ^{89}Zr-PSMA-DFO PET, the SUV_{mean} within the corresponding area of the ^{18}F-JK-PSMA-7 or the ^{68}Ga-PSMA-11 PET was measured. The CNR was calculated as the ratio of the difference of the SUV_{mean} in the lesion and the SUV_{mean} in the background to SD in the background. The SUV_{mean} of the background and its SD were measured in a 3-cm VOI in the local background around the lesion. The CNR of ^{89}Zr-PSMA-DFO PET-2 (first measurement) was significantly higher than the CNR of the PET-1 scan with ^{68}Ga-PSMA-11 ($P = 0.0016$, paired t test) or ^{18}F-JK-PSMA-7 ($P = 0.036$).

l.n. = lymph node.

However, our logistics for tracer injection and PET scans on different days were designed for a few patients with a rare constellation of inclusion criteria. Very late time points (up to 6 d after tracer injection) might occasionally identify additional lesions but should be combined with earlier image acquisition time points, because PET/CT scans after 6 d exhibit a decrease in the SNR. In the future, the technology of a digital PET/CT will allow lower activities to be applied than those used here with ^{89}Zr-PSMA-DFO (*21*).

Hence, our data provide a solid rationale to further evaluate the performance of ^{89}Zr-PSMA-DFO in prospective clinical trials and overcome potential limitations of our first-in-humans study. Since our study was not designed as a prospective clinical trial, readers were not masked regarding the PSMA PET tracers. Furthermore, the sensitivity of ^{89}Zr-PSMA-DFO cannot be compared in an unbiased manner, because ^{89}Zr-PSMA-DFO PET scans were obtained only in patients with a negative, prior PET scan using ^{68}Ga-PSMA-11 or ^{18}F-JK-PSMA-7. It might have increased the sensitivity of the ^{89}Zr-PSMA-DFO PET that readers could revisit their initial interpretation of the ^{68}Ga-PSMA-11 PET or the ^{18}F-JK-PSMA-7 PET scans based on the ^{89}Zr-PSMA-DFO PET scan in ambiguous cases.

CONCLUSION

^{89}Zr-PSMA-DFO allows more time for ligand internalization and renal clearance before image acquisition, whereas existing PSMA tracers require image acquisition within a few hours of injection. Our findings suggest that ^{89}Zr-PSMA-DFO might be used in men with BCR after a PET/CT scan with established PSMA tracers was read as negative. In particular, acquiring ^{89}Zr-PSMA-DFO PET/CT scans 2 or 3 d after tracer injection might be beneficial in patients with detectable but low PSMA expression in the recurrent tumor lesions, in which the search for PSMA-positive lesions has proven challenging.

DISCLOSURE

Bernd Neumaier and Alexander E. Drzezga have applied for a patent on ^{18}F-JK-PSMA-7. No other potential conflict of interest relevant to this article was reported.

KEY POINTS

QUESTIONS: Does ^{89}Zr-PSMA-DFO exhibit a higher detection rate for subtle tumor lesions than existing PSMA tracers?

PERTINENT FINDINGS: ^{89}Zr-PSMA-DFO detected PSMA-positive lesions in 8 of 14 prostate cancer patients with a negative PET scan acquired previously with existing PSMA PET tracers. Most of the PSMA-positive patients had oligometastatic status or a local relapse.

IMPLICATIONS FOR PATIENT CARE: On the basis of the ^{89}Zr-PSMA-DFO PET scan, metastasis-directed radiotherapy was initiated in 5 of 8 patients. ^{89}Zr-PSMA-DFO may therefore offer a benefit to patients with weak PSMA positivity, in whom the localization of recurrent tumor lesions has proved challenging using existing PSMA tracers. Our data suggest that ^{89}Zr-PSMA-DFO might be used in combination with established PSMA tracers, but larger clinical cohorts will be required to characterize and confirm the clinical benefits of ^{89}Zr-PSMA-DFO.

REFERENCES

1. Perera M, Papa N, Roberts M, et al. Gallium-68 prostate-specific membrane antigen positron emission tomography in advanced prostate cancer: updated diagnostic utility, sensitivity, specificity, and distribution of prostate-specific membrane antigen-avid lesions—a systematic review and meta-analysis. *Eur Urol.* 2020;77:403–417.
2. Carlucci G, Ippisch R, Slavik R, et al. ^{68}Ga-PSMA-11 NDA approval: a novel and successful academic partnership. *J Nucl Med.* 2021;62:149–155.
3. Dietlein F, Kobe C, Neubauer S, et al. PSA-stratified performance of ^{18}F- and ^{68}Ga-PSMA PET in patients with biochemical recurrence of prostate cancer. *J Nucl Med.* 2017;58:947–952.
4. Bravaccini S, Puccetti M, Bocchini M, et al. PSMA expression: a potential ally for the pathologist in prostate cancer diagnosis. *Sci Rep.* 2018;8:4254.
5. Ferraro DA, Rüschoff JH, Muehlematter UJ, et al. Immunohistochemical PSMA expression pattern of primary prostate cancer tissue are associated with the detection rate of biochemical recurrence with ^{68}Ga-PSMA-11-PET. *Theranostics.* 2020;10:6082–6094.
6. Muñoz Vázquez S, Endepols H, Fischer T, et al. Translational development of a Zr-89-labeled inhibitor of prostate-specific membrane antigen for PET imaging in prostate cancer. *Mol Imaging Biol.* 2022;24:115–125.
7. Hohberg M, Kobe C, Täger P, et al. Combined early and late [^{68}Ga]PSMA-HBED-CC PET scans improve lesion detectability in biochemical recurrence of prostate cancer with low PSA levels. *Mol Imaging Biol.* 2019;21:558–566.
8. Hohberg M, Kobe C, Krapf P, et al. Biodistribution and radiation dosimetry of [^{18}F]-JK-PSMA-7 as a novel prostate-specific membrane antigen-specific ligand for PET/CT imaging of prostate cancer. *EJNMMI Res.* 2019;9:66.
9. Lee YS, Kim JS, Kim JY, et al. Spatial resolution and image qualities of Zr-89 on Siemens Biograph TruePoint PET/CT. *Cancer Biother Radiopharm.* 2015;30:27–32.
10. Kuhnert G, Boellaard R, Sterzer S, et al. Impact of PET/CT image reconstruction methods and liver uptake normalization strategies on quantitative image analysis. *Eur J Nucl Med Mol Imaging.* 2016;43:249–258.
11. Eiber M, Herrmann K, Calais J, et al. Prostate cancer molecular imaging standardized evaluation (PROMISE): Proposed miTNM classification for the interpretation of PSMA-ligand PET/CT. *J Nucl Med.* 2018;59:469–478.
12. Rowe SP, Pienta KJ, Pomper MG, Gorin MA. Proposal for a structured reporting system for prostate-specific membrane antigen-targeted PET imaging: PSMA-RADS Version 1.0. *J Nucl Med.* 2018;59:479–485.
13. The International Commission on Radiological Protection (ICRP). *ICRP Publication 60: 1990 Recommendations of the International Commission on Radiological Protection. Ann ICRP.* 1991;21(1–3).
14. Dietlein M, Kobe C, Kuhnert G, et al. Comparison of [^{18}F]DCFPyL and [^{68}Ga]Ga-PSMA-HBED-CC for PSMA-PET imaging in patients with relapsed prostate cancer. *Mol Imaging Biol.* 2015;17:575–584.
15. Dietlein F, Hohberg M, Kobe C, et al. An ^{18}F-labeled PSMA ligand for PET/CT of prostate cancer: first-in-humans observational study and clinical experience with ^{18}F-JK-PSMA-7 during the first year of application. *J Nucl Med.* 2020;61:202–209.
16. Dietlein F, Kobe C, Hohberg M, et al. Intraindividual comparison of ^{18}F-PSMA-1007 with renally excreted PSMA ligands for PSMA-PET imaging in patients with relapsed prostate cancer. *J Nucl Med.* 2020;61:729–734.
17. Connor MJ, Smith A, Miah S, et al. Targeting oligometastasis with stereotactic ablative radiation therapy or surgery in metastatic hormone-sensitive prostate cancer: a systematic review of prospective clinical trial. *Eur Urol Oncol.* 2020;3:582–593.
18. Cornford P, van den Bergh RCN, Briers E, et al. EAU-EANM-ESTRO-ESUR-SIOG guidelines on prostate cancer. Part II 2020 update: treatment of relapsing, metastatic, and castration-resistant prostate cancer. *Eur Urol.* 2021;79:263–282.
19. Phillips R, Yue Shi W, Deek M, et al. Outcomes of observation vs stereotactic ablative radiation for oligometastatic prostate cancer: the ORIOLE phase 2 randomized clinical trial. *JAMA Oncol.* 2020;6:650–659.
20. O'Donoghue JA, Danila DC, Pandit-Taskar N, et al. Pharmacokinetics and biodistribution of a [^{89}Zr]Zr-DFO-MSTP2109A anti-STEAP1 antibody in metastatic castration-resistant prostate cancer patients. *Mol Pharm.* 2019;16:3083–3090.
21. Zhang J, Maniawski P, Knopp MV. Performance evaluation of the next generation solid-state digital photon counting PET/CT system. *EJNMMI Res.* 2018;8:97.

First In Vivo and Phantom Imaging of Cyclotron-Produced ^{133}La as a Theranostic Radionuclide for ^{225}Ac and ^{135}La

Bryce J.B. Nelson[1], Simon Ferguson[1], Melinda Wuest[1,2], John Wilson[1], M. John M. Duke[1], Susan Richter[1,2], Hans Soenke-Jans[1,2], Jan D. Andersson[1,3], Freimut Juengling[1], and Frank Wuest[1,2]

[1]Department of Oncology, Cross Cancer Institute, University of Alberta, Edmonton, Alberta, Canada; [2]Cancer Research Institute of Northern Alberta, University of Alberta, Edmonton, Alberta, Canada; and [3]Edmonton Radiopharmaceutical Center, Cross Cancer Institute, Alberta Health Services, Edmonton, Alberta, Canada

Theranostic isotope pairs have gained recent clinical interest because they can be labeled to the same tracer and applied for diagnostic and therapeutic purposes. The goals of this study were to investigate cyclotron production of clinically relevant ^{133}La activities using natural and isotopically enriched barium target material, compare fundamental PET phantom imaging characteristics of ^{133}La with those of common PET radionuclides, and demonstrate in vivo preclinical PET tumor imaging using ^{133}La-PSMA-I&T. **Methods:** ^{133}La was produced on a 24-MeV cyclotron using an aluminum–indium sealed target with 150–200 mg of isotopically enriched $^{135}BaCO_3$, $^{nat}BaCO_3$, and ^{nat}Ba metal. A synthesis unit performed barium/lanthanum separation. DOTA, PSMA-I&T, and macropa were radiolabeled with ^{133}La. Derenzo and National Electrical Manufacturers Association phantom imaging was performed with ^{133}La, ^{132}La, and ^{89}Zr and compared with ^{18}F, ^{68}Ga, ^{44}Sc, and ^{64}Cu. In vivo preclinical imaging was performed with ^{133}La-PSMA-I&T on LNCaP tumor–bearing mice. **Results:** Proton irradiations for 100 μA·min at 23.3 MeV yielded 214 ± 7 MBq of ^{133}La and 28 ± 1 MBq of ^{135}La using $^{135}BaCO_3$, 59 ± 2 MBq of ^{133}La and 35 ± 1 MBq of ^{135}La using $^{nat}BaCO_3$, and 81 ± 3 MBq of ^{133}La and 48 ± 1 MBq of ^{135}La using ^{nat}Ba metal. At 11.9 MeV, ^{135}La yields were 81 ± 2 MBq, 6.8 ± 0.4 MBq, and 9.9 ± 0.5 MBq for $^{135}BaCO_3$, $^{nat}BaCO_3$, and ^{nat}Ba metal. $BaCO_3$ target material recovery was 95.4% ± 1.7%. National Electrical Manufacturers Association and Derenzo phantom imaging demonstrated that ^{133}La PET spatial resolution and scanner recovery coefficients were superior to those of ^{68}Ga and ^{132}La and comparable to those of ^{89}Zr. The apparent molar activity was 130 ± 15 GBq/μmol with DOTA, 73 ± 18 GBq/μmol with PSMA-I&T, and 206 ± 31 GBq/μmol with macropa. Preclinical PET imaging with ^{133}La-PSMA-I&T provided high-resolution tumor visualization with an SUV of 0.97 ± 0.17 at 60 min. **Conclusion:** With high-yield ^{133}La cyclotron production, recovery of $BaCO_3$ target material, and fundamental imaging characteristics superior to those of ^{68}Ga and ^{132}La, ^{133}La represents a promising radiometal candidate to provide high-resolution PET imaging as a PET/α-therapy theranostic pair with ^{225}Ac or as a PET/Auger electron therapy theranostic pair with ^{135}La.

Key Words: PET; radiolanthanum; ^{225}Ac; theranostics; cyclotron

J Nucl Med 2022; 63:584–590
DOI: 10.2967/jnumed.121.262459

Received Apr. 18, 2021; revision accepted Jul. 16, 2021.
For correspondence or reprints, contact Frank Wuest (wuest@ualberta.ca).
Published online Aug. 12, 2021.
Immediate Open Access: Creative Commons Attribution 4.0 International License (CC BY) allows users to share and adapt with attribution, excluding materials credited to previous publications. License: https://creativecommons.org/licenses/by/4.0/. Details: http://jnm.snmjournals.org/site/misc/permission.xhtml.
COPYRIGHT © 2022 by the Society of Nuclear Medicine and Molecular Imaging.

Theranostic pairs in nuclear medicine involve labeling molecular target vectors first with a diagnostic radionuclide, followed by a therapeutic particle–emitting radionuclide (*1*). Both radionuclides should have similar chemical properties, ideally being isotopes of the same element. Theranostics has strong potential in targeted radionuclide therapy, with a diagnostic positron or γ-emitting radionuclide used in PET or SPECT being paired with a therapeutic radionuclide emitting α-particles, β^--electrons, or Auger electrons (*2*). Recently introduced ^{133}La (half-life [$t_{1/2}$], 3.9 h), ^{132}La ($t_{1/2}$, 4.8 h), and ^{134}Ce ($t_{1/2}$, 3.2 d)/^{134}La ($t_{1/2}$, 6.5 min) PET radionuclides are uniquely suited as theranostic imaging partners for ^{225}Ac ($t_{1/2}$, 9.9 d) in targeted α-therapy or with ^{135}La ($t_{1/2}$, 19.5 h) in Auger electron therapy (AET) because of their chemical similarity to, and longer half-lives than, the ubiquitous PET radiometal ^{68}Ga ($t_{1/2}$, 68 min) (*2–7*). ^{225}Ac has shown considerable efficacy in clinical trials for treating metastatic cancers (*2*,*8*). ^{132}La has been proposed as a theranostic PET imaging surrogate for ^{225}Ac therapy and has displayed in vivo uptake characteristics similar to those of ^{225}Ac (*6*). However, there are fundamental imaging limitations inherent in ^{132}La because of its high maximum positron emission energy (E_{max}) and mean positron emission energy (E_{mean}) (E_{max}/E_{mean}, 3.67/1.29 MeV), which significantly reduces image spatial resolution and contrast compared with other PET radionuclides (e.g., ^{18}F E_{max}/E_{mean}, 0.634/0.250 MeV; ^{68}Ga E_{max}/E_{mean}, 1.90/0.829 MeV; ^{64}Cu E_{max}/E_{mean}, 0.653/0.278 MeV; ^{44}Sc E_{max}/E_{mean}, 1.47/0.632 MeV), and its high-energy and high-intensity γ-emissions, which are problematic from a dosimetric perspective (*3*,*9*). ^{133}La has a lower positron emission energy (E_{max}/E_{mean}, 1.02/0.461 MeV) than ^{132}La, ^{68}Ga, or ^{44}Sc; energy comparable to ^{89}Zr (E_{max}/E_{mean}, 0.902/0.396 MeV), and lower energy and lower-intensity γ-emissions than ^{89}Zr, ^{44}Sc, or ^{132}La (*3*). Here, as outlined in Figure 1, we describe a high-yield cyclotron production method for ^{133}La using natural and isotopically enriched $^{135}BaCO_3$; phantom measurements comparing fundamental imaging properties of ^{133}La with other PET radionuclides, including ^{18}F, ^{68}Ga, ^{64}Cu, ^{89}Zr, ^{44}Sc, and ^{132}La; and the first (to our knowledge) preclinical PET imaging with ^{133}La. We have chosen to radiolabel PSMA-I&T for imaging prostate cancers.

MATERIALS AND METHODS

Chemicals

Table 1 displays the isotopic compositions of $^{135}BaCO_3$, $^{nat}BaCO_3$, and ^{nat}Ba metal. Isotopically enriched $^{135}BaCO_3$ was obtained from Trace Sciences International. Barium carbonate (99.999% trace metals

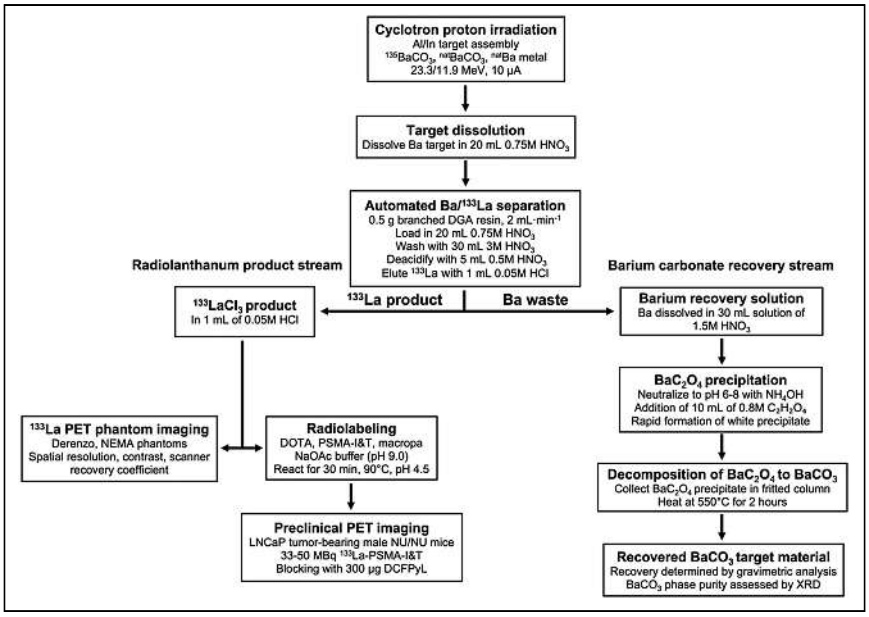

FIGURE 1. Experimental overview.

basis), barium metal (99.99% trace metals basis), American Chemical Society reagent–grade concentrated hydrochloric acid (37%), nitric acid (70%), ammonium hydroxide (28%), and periodic table mix inductively coupled plasma optical emission spectrometry (ICP-OES) elemental standards were obtained from Sigma-Aldrich. Oxalic acid dihydrate (99.5%) was purchased from Fisher Scientific. Aluminum disks were obtained from Michaels, and aluminum foil was purchased from Goodfellow Cambridge. Indium wire was purchased from AIM Specialty Materials. Branched diglycolamide resin was purchased from Eichrom. Eckert and Ziegler Isotopes National Institute of Standards and Technology–traceable γ-ray sources were used for high-purity germanium (HPGe) detector energy and efficiency calibration. Thin-layer chromatography silica gel sheets were purchased from Merck. Water (18 MΩ·cm) was obtained from a MilliporeSigma Direct-Q 3 ultraviolet system. ^{89}Zr was provided by the Washington University Cyclotron Facility. DOTA was purchased from Macrocyclics. Macropa was purchased from MedChemExpress. PSMA-I&T was obtained from ABX Advanced Biochemical Compounds. DCFPyL was synthesized in-house.

Instrumentation

Activity and radionuclidic purity were assessed using an Ortec GEM35P4-70-SMP HPGe detector running GammaVision software, with dead times below 25%. Elemental purity was assessed using an Agilent Technologies 720 Series ICP-OES. A NEPTIS Mosaic-LC synthesis unit (Optimized Radiochemical Applications) separated ^{133}La from the Ba target solution.

An Eckert and Ziegler AR-2000 radio-thin-layer chromatography imaging scanner quantified the fraction of chelator-bound ^{133}La after reaction. Solid targets were manufactured using a Carver model 6318 hydraulic press and an MTI Corp. 10-mm (internal diameter) EQ-Die-10D-B hardened steel die. A Carbolite 16/610-tube 3-zone furnace was used for $^{135}BaCO_3$ recovery. X-ray powder diffraction (XRD) patterns were acquired on starting and recovered $BaCO_3$ and intermediate BaC_2O_4 using a Rigaku Ultima IV x-ray diffractometer to confirm phase identity and purity.

Cyclotron Targeting and Irradiation

Figure 2 depicts nuclear reaction cross-sections for the ^{13x}Ba(p,xn)^{13x}La reactions of interest for $^{132/133/135}$La production from the TENDL 2019 library, weighted for ^{nat}Ba and isotopically enriched $^{135}BaCO_3$ target material (*10*). Cyclotron targets were prepared with 150–200 mg of ^{nat}Ba metal, $^{nat}BaCO_3$, or enriched $^{135}BaCO_3$, a roughened aluminum disk (24 mm in diameter, 1.35 mm thick), indium wire (1 mm in diameter), and aluminum foil (125 μm thick) in a manner similar to that previously described (*3*,*11*). Aluminum was shown to be an adequate substitute for silver, presenting a lower cost and activation. Target components are shown in Supplemental Figure 1 (supplemental materials are available at http://jnm.snmjournals.org). Targets were irradiated for 5–263 min at 11.9 and 23.3 MeV using an Advanced Cyclotron Systems Inc. TR-24 cyclotron, at proton beam currents of 10 μA incident on the target assembly. Higher energy runs (beam-extracted at 24 MeV, 23.3 MeV incident on target pellets, 20.2 MeV exiting Ba metal, and 19.4 MeV exiting $BaCO_3$) were performed with 200 mg of barium material with the aluminum target cover facing the beam, to maximize ^{133}La production based on TENDL 2019 cross-section simulation data (*10*). During higher-energy runs, a silver disk was placed behind the target to avoid ^{13}N production from the ^{16}O(p,α)^{13}N reaction. For lower-energy runs (18.2-MeV extraction, 11.9 MeV incident on target pellets, 7.8 MeV exiting Ba metal, and 6.4 MeV exiting $BaCO_3$), performed to maximize ^{135}La production, 150 mg of barium material were used, and the target was installed in reverse with the aluminum disk acting as a degrader to reduce beam energy from 18.2 to 11.9 MeV, as calculated using SRIM (*12*).

Automated ^{133}La Separation and Radiochemical Purity Analysis

^{133}La and $BaCO_3$ were separated using a process with aspects derived from previous studies (*3*,*4*). The target was opened by peeling back the aluminum cover and placed in a Teflon (DuPont) dissolution vessel. The vessel was filled with 10 mL of 18 MΩ·cm water and

TABLE 1
Isotopic Composition of Natural and Isotopically Enriched Barium Target Materials

Target material	^{138}Ba	^{137}Ba	^{136}Ba	^{135}Ba	^{134}Ba	^{132}Ba	^{130}Ba
$^{nat}BaCO_3$/^{nat}Ba metal	71.7	11.2	7.9	6.6	2.4	0.1	0.1
$^{135}BaCO_3$	2.6	0.8	3.6	92.7	0.3	<0.05	<0.05

Data are percentages.

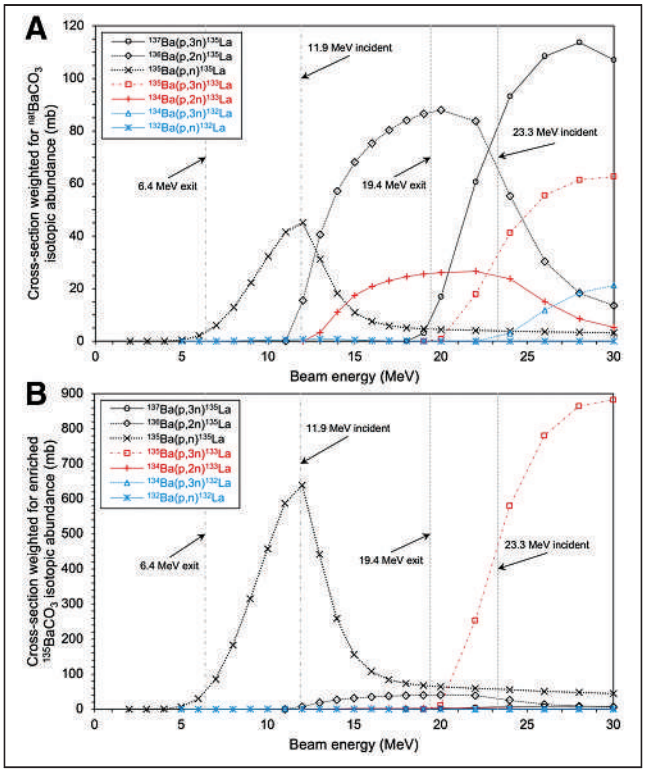

FIGURE 2. Nuclear reaction cross-section simulation data of proton-induced nuclear reactions on $^{132/134/135/136/137}$Ba for $^{132/133/135}$La production weighted for ^{nat}Ba isotopic abundance (A) and isotopically enriched $^{135}BaCO_3$ abundance (B) (*10*).

sonicated in an ultrasonic bath for 3 min to dislodge the $BaCO_3$ from the target backing. Target components were removed and rinsed with 5 mL of 18 MΩ·cm water into the vessel, and 5 mL of 3 M HNO_3 were added, resulting in a 0.75 M HNO_3 reaction mixture that dissolved the $BaCO_3$ in 5 min. This solution was passed through a solid-phase extraction cartridge containing 0.50 g of branched diglycolamide resin (conditioned with 10 mL of 3 M HNO_3) and washed with 50 mL of 3 M HNO_3 to remove residual barium and other metal impurities, followed by column deacidification with 5 mL of 0.5 M HNO_3. Flow rates were kept below 2 mL·min^{-1} to avoid ^{133}La loss from the resin. $^{133}LaCl_3$ was eluted using 1 mL of 0.05 M HCl. After passing through the resin, the first 30 mL of process solution were diverted to a collection vial for subsequent $BaCO_3$ recovery. After separation, target components were sonicated in 18 MΩ·cm water for reuse. Radionuclidic and elemental purity of $^{133}LaCl_3$ was determined by HPGe γ-ray spectroscopy and ICP-OES.

$BaCO_3$ Target Material Recovery

The 30 mL of barium recovery solution were neutralized to pH 6–8 with NH_4OH. Ten milliliters of 0.8 M $C_2H_2O_4$ were added to the recovery solution to precipitate BaC_2O_4. The solution was passed through a fritted column to trap BaC_2O_4 and washed with 50 mL of 18 MΩ·cm water. BaC_2O_4 was removed from the column and then heated to 550°C for 2 h in a sealed tube furnace with an airflow of 20 mL/min to decompose BaC_2O_4 to $BaCO_3$ while avoiding conversion to BaO (*13*). Waste gases from decomposition were vented to a fume hood. Recovery was quantified by gravimetric analysis of dried samples and tracked by HPGe γ-spectroscopy using γ-emissions from ^{135m}Ba (268 keV; $t_{1/2}$, 28.7 h). Samples of purchased $BaCO_3$, precipitated BaC_2O_4, and recovered $BaCO_3$ were analyzed by XRD to identify the product and evaluate its quality.

Phantom Imaging

Phantom imaging was performed using Derenzo and National Electrical Manufacturers Association (NEMA) image-quality phantoms on an Inveon PET/CT scanner (Siemens Preclinical Solutions), as described by Ferguson et al. (*14*). The Derenzo phantom, used to investigate image contrast and spatial resolution, consists of sections with rods of varying diameters (0.8, 1.0, 1.25, 1.5, 2.0, and 2.5 mm) that are filled with the radionuclide of interest diluted in 20–30 mL of water. The NEMA phantom, used to investigate image noise, spillover ratio, and recovery coefficient, consists of several fillable sections including two 7.5-mm-diameter cold-air and water cylindric volumes. NEMA and Derenzo phantom scans for ^{133}La, ^{132}La, and ^{89}Zr were acquired in list mode, binned into sinograms, and reconstructed with the default filtered backprojection, ordered-subset expectation maximization, and maximum a posteriori estimation algorithms. Acquisition, data processing, and evaluation followed the same procedure as used by Ferguson et al. (*14*) for ^{18}F, ^{64}Cu, ^{68}Ga, and ^{44}Sc to enable direct comparison of the different radionuclides' imaging performance.

Radiolabeling of DOTA, PSMA-I&T, and Macropa with ^{133}La

Similar to techniques in previous studies (*3*,*4*), the activity of a 500-μL $^{133}LaCl_3$ aliquot was measured, and the solution pH was adjusted to 4.5 with 50 μL of NaOAc buffer (pH 9.0). A 100-μL volume of this ^{133}La solution (5–150 MBq) was reacted with 0.1–20 μg of DOTA, PSMA-I&T, and macropa dissolved in 50 μL of 18 MΩ·cm water at 90°C for 30 min. Each solution was analyzed using radio–thin-layer chromatography on silica plates to determine radiochemical purity and incorporation with 0.1 M citric acid buffer as the mobile phase.

Preclinical PET Imaging

Animal studies using LNCaP tumor–bearing male nu/nu nude mice (Charles River Laboratories) were performed according to the guidelines of the Canadian Council on Animal Care and approved by the local Cross Cancer Institute Animal Care Committee. Static PET image scans (20-min duration) of ^{133}La-PSMA-I&T at 60 min after injection were performed on an Inveon PET/CT scanner (Siemens Preclinical Solutions). Blocking experiments were performed using the PSMA-targeting agent DCFPyL. Radiotracer (33–50 MBq of ^{133}La-PSMA-I&T in 80–120 μL of NaOAc/saline) and blocking compound (300 μg of DCFPyL, dosed 5 min beforehand) were injected into the tail vein of isoflurane-anesthetized mice (100% oxygen; gas flow, 1.5 L/min), the mice were placed in a prone position into the center of the field of view, and body temperature was kept constant at 37°C. A transmission scan for attenuation correction was not acquired. The frames were reconstructed using ordered-subset expectation maximization and maximum a posteriori algorithms. No correction for partial-volume effects was applied. The image files were processed using ROVER software (version 2.0.51; ABX GmbH).

Statistical Analysis

All data are given as mean ± SD ($n \geq 3$).

RESULTS

Cyclotron Targeting and Irradiation

Average end-of-bombardment activities ($n = 3$) of ^{133}La and coproduced ^{135}La for 100 μA·min runs (10 μA for 10 min) at 11.9- and 23.3-MeV beam energies with different barium target materials are summarized in Table 2. Irradiating enriched $^{135}BaCO_3$ at 23.3 MeV resulted in a significant increase in ^{133}La production compared with $^{nat}BaCO_3$ and ^{nat}Ba metal. Irradiating recovered $^{nat}BaCO_3$ at 23.3 MeV for 100 μA·min yielded 57 ± 1 MBq of ^{133}La and 36 ± 1 MBq of ^{135}La, similar to yields for fresh $^{nat}BaCO_3$.

TABLE 2
Average Experimental ($n = 3$) End-of-Bombardment Activities (MBq) and Saturated Yields (MBq/μA) of $^{133/135}$La for 100-μA·Min Runs at 11.9- and 23.3-MeV Incident Energies for Different Barium Target Materials

Beam energy (MeV)	$^{135}BaCO_3$ target yields		$^{nat}BaCO_3$ target yields		^{nat}Ba metal target yields	
	^{135}La	^{133}La	^{135}La	^{133}La	^{135}La	^{133}La
11.9	81 ± 2 (79); y = 1,377 ± 31	0	6.8 ± 0.4 (5.9); y = 115 ± 6	0	9.9 ± 0.5 (10); y = 167 ± 8	0
23.3	28 ± 1 (31); y = 475 ± 11	214 ± 7 (279); y = 736 ± 25	35 ± 1 (41); y = 598 ± 9	59 ± 2 (61); y = 204 ± 8	48 ± 1 (61); y = 809 ± 17	81 ± 3 (94); y = 277 ± 9

y = saturated yield in MBq/μA. Theoretic end-of-bombardment activities calculated with TENDL are in parentheses.

TABLE 3
ICP-OES Analysis ($n = 3$) of $^{133}LaCl_3$ Produced with Different Barium Target Materials

Metal	Elemental concentration (ppb)		
	Fresh $BaCO_3$	Recovered $BaCO_3$	Barium metal
Zinc	7.4 ± 1.7	5.5 ± 2.4	76 ± 55
Iron	3.2 ± 0.4	2.1 ± 0.8	16.8 ± 11.7
Aluminum	18 ± 2	16 ± 1	37 ± 19
Barium	240 ± 179	128 ± 108	1,150 ± 360
Indium	2.5 ± 1.2	3.9 ± 1.5	3.1 ± 0.9
Copper	5.5 ± 0.3	5.3 ± 0.1	5.3 ± 0.4

Data for barium metal are from Nelson et al. (*3*).

^{133}La Separation and Radiochemical Purity Analysis

Table 3 contains ICP-OES elemental purity results for the $^{133}LaCl_3$ product. After removal from the reactor after sonification, the aluminum target backing and cover contained no detectable ^{133}La activity. The entire separation took approximately 50 min. Over 92% of decay-corrected ^{133}La was recovered in 1 mL of 0.05 M HCl, and HPGe analysis of the $^{133}LaCl_3$ product produced with $^{nat}BaCO_3$ showed small activities of ^{131}La ($t_{1/2}$, 59 min) and ^{132}La ($t_{1/2}$, 4.8 h) with no other observed radionuclidic impurities, similar to previous findings (*3*). ^{131}La and ^{132}La were not observed in $^{133}LaCl_3$ produced with isotopically enriched $^{135}BaCO_3$. Elemental purity determined by ICP-OES of $^{133}LaCl_3$ produced with fresh and recovered $BaCO_3$ target material was superior to $^{133}LaCl_3$ previously produced with barium metal as described in a previous publication (*3*).

Enriched $^{135}BaCO_3$ Recovery

Figure 3 depicts the decay-corrected fraction of total ^{135m}Ba and ^{135}La activity as a function of process volume. The solution was collected in fractions (5 mL for 0–75 mL, 0.5 mL for 75–80 mL) after flowing through the resin, and each fraction was analyzed on the HPGe to quantify ^{135m}Ba and ^{135}La activity via their respective 268- and 481-keV γ-emissions. Over 99.7% of decay-corrected ^{135m}Ba activity was recovered in the first 6 fractions, with no detectable contributions from additional fractions; therefore, only the first 30 mL of process solution were collected for recovery.

BaC_2O_4 formed a white precipitate and was collected by the fritted column. After BaC_2O_4 thermal decomposition to $BaCO_3$ from heating at 550°C, gravimetric analysis indicated a recovery of 191.1 ± 3.2 mg, which for a 200.3 ± 0.3 mg initial target pellet mass corresponds to a $BaCO_3$ recovery of 95.4% ± 1.7% ($n = 3$).

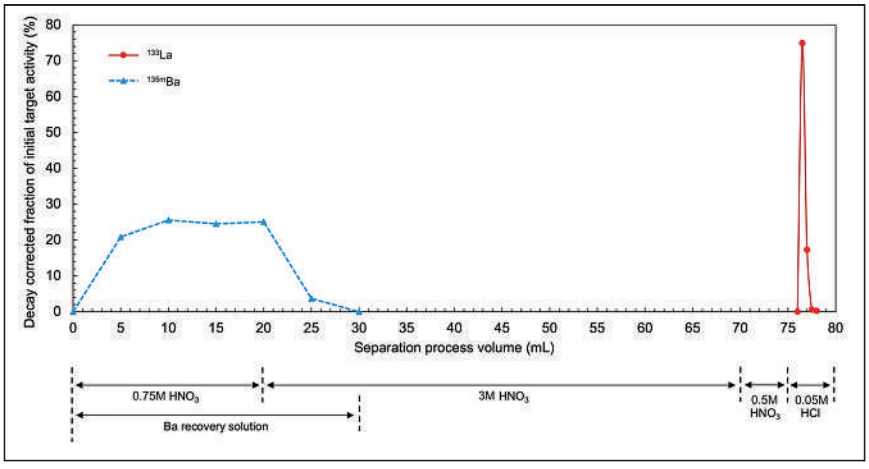

FIGURE 3. Decay-corrected fraction of initial ^{135m}Ba and ^{135}La target activity in solid-phase extraction cartridge eluate as function of process volume.

Figure 4 depicts the XRD diffractograms acquired for fresh $BaCO_3$, intermediate BaC_2O_4, and recovered $BaCO_3$ material. Complete XRD diffractogram data are in Supplemental Tables 1–3 and Supplemental Figures 2–4. The absence of unexplained reflections in all 3 patterns, compared with standard reference lines, confirmed the high phase purity of the compounds and the complete conversion of BaC_2O_4 to $BaCO_3$ (*15*).

Phantom Imaging

Figure 5 depicts Derenzo phantom scans with the mean and maximum positron energies of ^{133}La, ^{132}La, and other commonly used PET radionuclides. Derenzo phantom scans acquired with ^{18}F, ^{64}Cu, ^{89}Zr, ^{133}La, ^{44}Sc, ^{68}Ga, and ^{132}La clearly show that lower mean and maximum positron energies improve PET image spatial resolution and

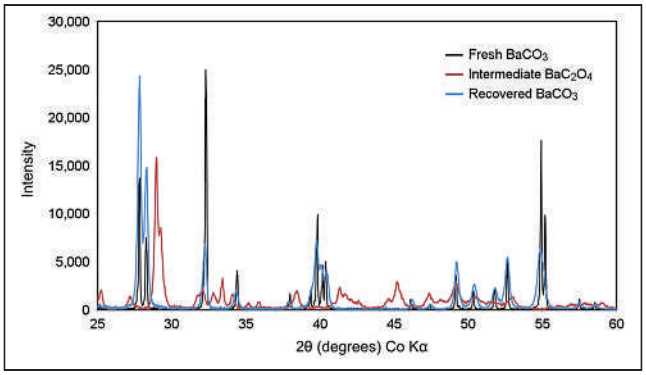

FIGURE 4. Background-stripped XRD diffractograms of fresh $BaCO_3$, intermediate BaC_2O_4, and recovered $BaCO_3$.

contrast. ^{133}La exhibits spatial resolution similar to that of ^{89}Zr, is an improvement over ^{44}Sc and ^{68}Ga, and is superior to ^{132}La.

Figure 6 plots the contrast between the rods and background for each of the 6 triangular segments in the Derenzo phantom and the recovery coefficients as a function of rod size in the NEMA image-quality phantom. Additional comparisons of imaging performance metrics between radionuclides for different reconstruction algorithms are included in Supplemental Figure 5. ^{133}La exhibits contrast similar to that of ^{89}Zr and is superior to ^{68}Ga and ^{44}Sc for larger rod diameters. ^{132}La was not included in the contrast comparison because of the low contrast for each rod diameter. The rods could not be distinguished below 1.25 mm in diameter for the higher-energy positron emitters ^{44}Sc and ^{68}Ga and 1 mm for the lower-energy positron emitters ^{18}F and ^{64}Cu. This blurring is due to the extrinsic scanner resolution, which is significantly impacted by the positron energy and therefore range. The recovery coefficient comparison demonstrates that ^{133}La exhibits favorable performance compared with ^{68}Ga and ^{132}La.

Radiolabeling

Radiolabeling was performed at 90°C for 30 min and analyzed with radio–thin-layer chromatography using 0.1 M citric acid buffer as the mobile phase. The ^{133}La-DOTA, ^{133}La-PSMA-I&T, and ^{133}La-macropa complexes remained close to the thin-layer chromatography baseline (R_f, 0.1–0.2), whereas unreacted ^{133}La migrated toward the solvent front (R_f, 0.9–1.0). Titration of $^{133}LaCl_3$ ($n = 3$) yielded an apparent molar activity of 130 ± 15 GBq/μmol with DOTA, 73 ± 18 GBq/μmol with PSMA-I&T, and 206 ± 31 GBq/μmol with macropa.

Preclinical PET Imaging

Figure 7 depicts static PET images of LNCaP tumor–bearing mice 60 min after injection of 33–50 MBq of ^{133}La-PSMA-I&T ($n = 4$). Tumor uptake was significant, reaching an SUV_{mean} of 0.97 ± 0.17 after 60 min. The SUV_{mean} for muscle was 0.05 ± 0.01, resulting in a tumor-to-muscle ratio of 22.4 ± 4.5. Mice predosed with 300 μg of DCFPyL 5 min before ^{133}La-PSMA-I&T injection exhibited significant tumor blocking, with a tumor SUV_{mean} of 0.11 ± 0.01 after 60 min. Most other radioactivity was excreted into the kidneys and urinary bladder.

DISCUSSION

This study presents cyclotron production of ^{133}La using natural and isotopically enriched barium target material, favorable fundamental PET phantom imaging characteristics of ^{133}La, and the first (to our knowledge) in vivo preclinical PET tumor imaging using ^{133}La-PSMA-I&T.

The new target assembly is well suited to the irradiation and processing of barium metal and $BaCO_3$ target material. Using aluminum instead of silver target backings as used in previous studies (*3*,*11*) avoids production of long-lived ^{107}Cd, ^{109}Cd, and ^{106m}Ag, thereby strongly reducing overall activation of the target, lowering operator exposure, and enabling rapid reuse. Using the target backing as an intrinsic degrader simplifies and enhances the available range of irradiation energies. The indium wire seal stayed 1–2 mm outside the target beam spot, avoiding activation and formation of radiotin isotopes. Sonicating used target disks in 18 MΩ·cm water allowed repeated reuse to make additional targets, with the same seal and target backing reused over 5 times.

Irradiating enriched $^{135}BaCO_3$ at 23.3 MeV produced far more ^{133}La than did other target materials, allowing production of clinically relevant ^{133}La activities with significantly shorter irradiation times than using ^{nat}Ba target material. Target separation gave a high $^{133}LaCl_3$ yield in a 1-mL product volume, ready for radiolabeling.

Recovery of $BaCO_3$ target material demonstrated feasibility for cost-effective recovery of expensive isotopically enriched $^{135}BaCO_3$. XRD analysis of recovered $BaCO_3$ showed complete conversion of the BaC_2O_4 intermediate and a pure recovered product, validating target material recovery and highlighting the potential for substantially improved economics with a simple and inexpensive recovery process. Radiolabeling DOTA, PSMA-I&T, and macropa with ^{133}La achieved high apparent molar activities for fresh and recovered $BaCO_3$ target material, similar to radiolanthanum chelation in previous studies (*3*–*5*,*16*).

Using isotopically enriched $^{135}BaCO_3$ target material permits selective production of ^{133}La and ^{135}La compared with ^{nat}Ba target material. Performing irradiations at energies of 23.3 MeV or higher

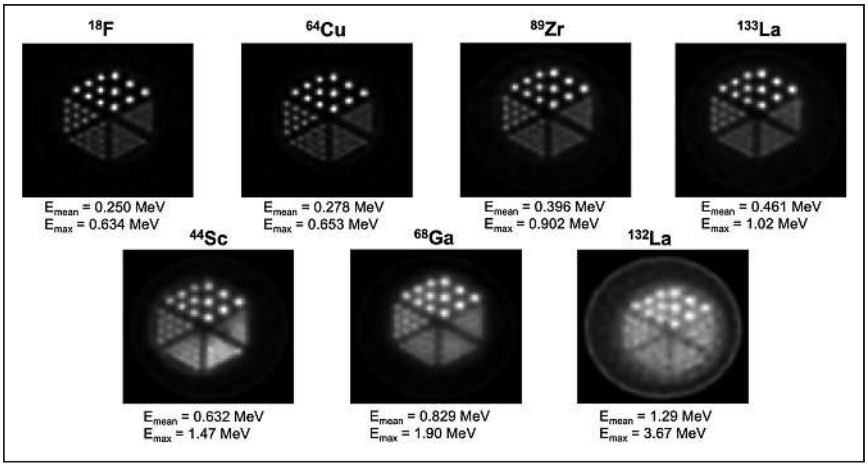

FIGURE 5. Derenzo phantom images reconstructed with maximum a posteriori estimation for different PET radionuclides, presented in order of increasing positron emission energy. ^{18}F, ^{64}Cu, ^{44}Sc, and ^{68}Ga data were taken from Ferguson et al. (*14*).

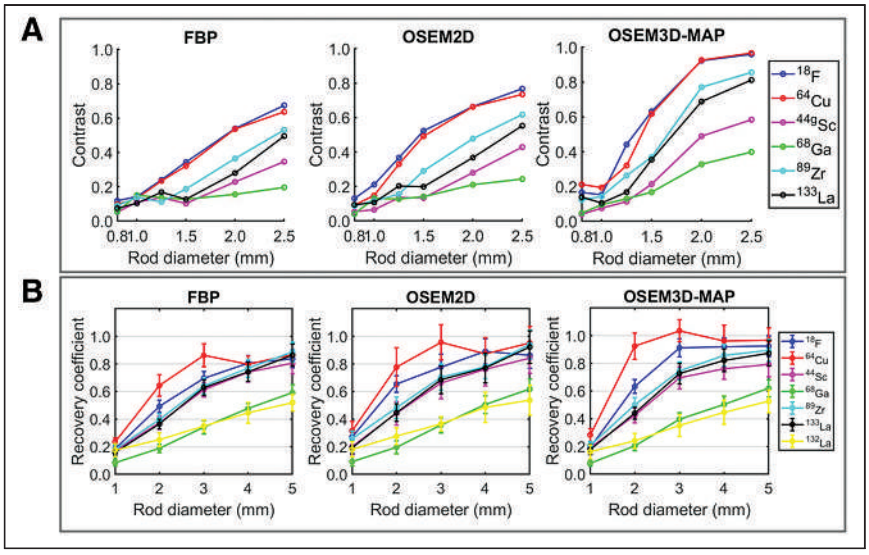

FIGURE 6. (A) Normalized contrast as function of rod size for different radionuclides in Derenzo phantom. (B) Impact of radionuclide and reconstruction method on measured recovery coefficients in NEMA image-quality phantom. ^{18}F, ^{64}Cu, ^{44}Sc, and ^{68}Ga data were taken from Ferguson et al. (*14*). 2D = 2-dimensional; 3D = 3-dimensional; FBP = filtered backprojection; MAP = maximum a posteriori; OSEM = ordered-subsets expectation maximization.

significantly increases ^{133}La production via the ^{135}Ba(p,3n)^{133}La reaction and reduces ^{135}La production from the ^{135}Ba(p,n)^{135}La reaction, which is ideal for PET imaging applications. Irradiating at 11.9 MeV with enriched $^{135}BaCO_3$ is ideal for producing large activities of pure ^{135}La for AET. Using these 2 distinct reactions permits production of a variety of $^{133/135}$La isotopic blends on a variable-energy cyclotron.

Another production route could use isotopically enriched $^{134}BaCO_3$ target material to produce ^{133}La via the ^{134}Ba(p,2n)^{133}La reaction. This would enable ^{133}La production on lower-energy cyclotrons because of the ^{134}Ba(p,2n)^{133}La cross-section threshold at 12 MeV as opposed to the 20 MeV threshold for the ^{135}Ba(p,3n)^{133}La reaction. The lower natural isotopic abundance of ^{134}Ba (2.4%) than of ^{135}Ba (6.6%) would result in a higher isotopic enrichment cost. However, this is a compelling option for PET centers with lower-energy cyclotrons because of the 95.4% recovery yield of $BaCO_3$ target material demonstrated in this study.

PET phantom imaging clearly showed that ^{133}La exhibits spatial resolution and contrast superior to those of ^{44}Sc, ^{68}Ga, ^{132}La but similar to those of ^{89}Zr. As expected, lower positron emission energy leads to improved spatial resolution (*17*) and results in superior image quality for ^{133}La versus ^{132}La, ^{68}Ga, and ^{44}Sc. This superiority is clearly translated to preclinical imaging, as evidenced by high spatial resolution. Even with the lower positron branching ratio of ^{133}La (7.2%) versus other PET radionuclides (96.7% ^{18}F, 88.9% ^{68}Ga, and 41.2% ^{132}La), the LNCaP tumor was clearly defined, reaching an SUV_{mean} of 0.97 ± 0.17 or 3.94 ± 0.68 %ID/g at 60 min after injection. For ^{68}Ga-PSMA-I&T, 4.95 ± 1.47 %ID/g uptake into LNCaP tumors was reported in an ex vivo biodistribution study (*18*). As discussed previously (*3*), in vivo studies involving retention and dosing of ^{133}La decay daughter ^{133}Ba would be useful to address this potential limitation; however, as shown by Newton et al. (*19*), most ^{133}Ba activity could be expected to be excreted within 10 d after injection.

Since lanthanum and actinium are group 3 elements with similar chemical properties, ^{133}La is highlighted as a strong candidate to become a clinical PET imaging surrogate for ^{225}Ac α-therapy, with PET imaging characteristics superior to those of ^{132}La. As established in this study and previously (*3*), compared with ^{132}La, ^{133}La has superior inherent cyclotron production characteristics, a lower positron energy that translates to a higher spatial resolution, and lower-energy and lower-abundance γ-emissions that would translate to a lower patient and operator dose. These characteristics suggest that ^{133}La represents an attractive candidate for diagnostic PET imaging and treatment monitoring of clinical ^{225}Ac targeted α-therapy and research involving ^{135}La AET.

CONCLUSION

This work demonstrates the strong potential of ^{133}La to serve as a theranostic PET imaging agent with ^{225}Ac targeted α-therapy or ^{135}La AET. The first preclinical in vivo PET imaging studies on LNCaP tumors resulted in high spatial resolution and contrast. Phantom imaging of ^{133}La demonstrated that fundamental PET imaging properties, including spatial resolution, contrast, and recovery coefficient, were superior to those of other PET radiometals such as ^{68}Ga, ^{44}Sc, and ^{132}La and similar to those of ^{89}Zr. With cyclotron production routes capable of generating clinically relevant ^{133}La activities, and with demonstrated feasibility for performing high-yield recovery of expensive isotopically enriched $^{135}BaCO_3$ target material, ^{133}La appears to be a promising radiometal candidate for high-resolution PET imaging as a PET/targeted α-therapy theranostic pair with ^{225}Ac or a PET/AET theranostic pair with ^{135}La.

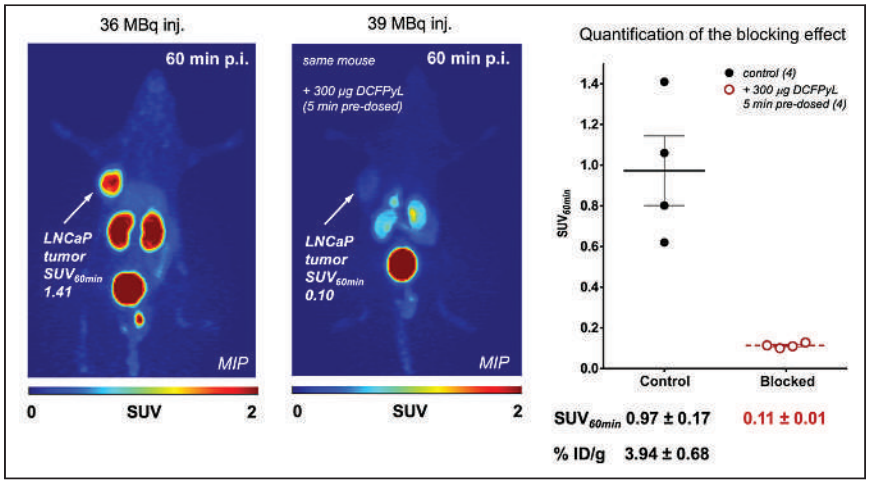

FIGURE 7. Representative PET maximum-intensity-projection images at 60 min of ^{133}La-PSMA-I&T with and without predose of DCFPyL in LNCaP tumor–bearing mice. ID = injected dose; MIP = maximum-intensity projection; p.i. = after injection.

DISCLOSURE

The Dianne and Irving Kipnes Foundation supported this work. Bryce Nelson received graduate scholarship funding from Alberta Advanced Education and the Natural Sciences and Engineering Research Council of Canada. No other potential conflict of interest relevant to this article was reported.

ACKNOWLEDGMENTS

We thank Jonathan Doupe (Alberta Health Services) for guidance throughout cyclotron production, Samantha Leier (Department of Oncology) for preparing ^{89}Zr for phantom imaging, and Rebecca Funk (Department of Earth and Atmospheric Sciences) for performing XRD data collection.

KEY POINTS

QUESTION: Is the positron emitter ^{133}La suitable for in vivo tumor imaging, and how do its production techniques and fundamental imaging characteristics compare with those of other PET radionuclides?

PERTINENT FINDINGS: Phantom imaging showed the PET spatial resolution of ^{133}La to be superior to that of ^{68}Ga, ^{44}Sc, and ^{132}La and comparable to that of ^{89}Zr. Preclinical imaging with ^{133}La-PSMA-I&T in tumor-bearing mice clearly delineated tumors with high spatial resolution. Robust, economical, high-yield cyclotron ^{133}La production was demonstrated using recoverable isotopically enriched $^{135}BaCO_3$ target material.

IMPLICATIONS FOR PATIENT CARE: This study showed that ^{133}La is a strong candidate to improve patient care by providing PET imaging of tumors as a theranostic pair with ^{225}Ac targeted α-therapy or potential ^{135}La AET.

REFERENCES

1. Velikyan I. Molecular imaging and radiotherapy: theranostics for personalized patient management. *Theranostics.* 2012;2:424–426.
2. Nelson BJB, Andersson JD, Wuest F. Targeted alpha therapy: progress in radionuclide production, radiochemistry, and applications. *Pharmaceutics.* 2020;13:49.
3. Nelson BJB, Wilson J, Andersson JD, Wuest F. High yield cyclotron production of a novel $^{133/135}$La theranostic pair for nuclear medicine. *Sci Rep.* 2020;10:22203.
4. Aluicio-Sarduy E, Hernandez R, Olson AP, et al. Production and in vivo PET/CT imaging of the theranostic pair $^{132/135}$La. *Sci Rep.* 2019;9:10658.
5. Aluicio-Sarduy E, Thiele NA, Martin KE, et al. Establishing radiolanthanum chemistry for targeted nuclear medicine applications. *Chemistry.* 2020;26:1238–1242.
6. Aluicio-Sarduy E, Barnhart TE, Weichert J, Hernandez R, Engle JW. Cyclotron-produced ^{132}La as a PET imaging surrogate for therapeutic ^{225}Ac. *J Nucl Med.* 2021;62:1012–1015.
7. Bailey TA, Mocko V, Shield KM, et al. Developing the ^{134}Ce and ^{134}La pair as companion positron emission tomography diagnostic isotopes for ^{225}Ac and ^{227}Th radiotherapeutics. *Nat Chem.* 2021;13:284–289.
8. Kratochwil C, Bruchertseifer F, Giesel FL, et al. ^{225}Ac-PSMA-617 for PSMA-targeted α-radiation therapy of metastatic castration-resistant prostate cancer. *J Nucl Med.* 2016;57:1941–1944.
9. NuDat 2.8: ground and isomeric state information for $^{133}_{57}$La. National Nuclear Data Center website. https://www.nndc.bnl.gov/nudat3/chartNuc.jsp. Accessed December 8, 2021.
10. Rochman D, Koning AJ, Sublet JC, et al. The TENDL library: hope, reality and future. In: *Proceedings of the International Conference on Nuclear Data for Science and Technology.* EPJ Web Conf.;2016:146.
11. Nelson BJB, Wilson J, Richter S, Duke MJM, Wuest M, Wuest F. Taking cyclotron ^{68}Ga production to the next level: expeditious solid target production of ^{68}Ga for preparation of radiotracers. *Nucl Med Biol.* 2020;80–81:24–31.
12. SRIM - the stopping and range of ions in matter. SRIM website. http://www.srim.org/. Accessed November 11, 2021.
13. Bhatti AS, Dollimore D, Armstrong B. The thermal decomposition of oxalates. Part 19. The thermal decomposition of barium oxalate hemihydrates. *Thermochim Acta.* 1984;79:217–230.
14. Ferguson S, Jans HS, Wuest M, Riauka T, Wuest F. Comparison of scandium-44 g with other PET radionuclides in pre-clinical PET phantom imaging. *EJNMMI Phys.* 2019;6:23.
15. Gates-Rector S, Blanton T. The powder diffraction file: a quality materials characterization database. *Powder Diffr.* 2019;34:352–360.
16. Fonslet J, Lee BQ, Tran TA, et al. ^{135}La as an Auger-electron emitter for targeted internal radiotherapy. *Phys Med Biol.* 2017;63:015026.
17. Levin CS, Hoffman EJ. Calculation of positron range and its effect on the fundamental limit of positron emission tomography system spatial resolution. *Phys Med Biol.* 1999;44:781.
18. Weineisen M, Schottelius M, Simecek J, et al. ^{68}Ga- and ^{177}Lu-labeled PSMA I&T: optimization of a PSMA-targeted theranostic concept and first proof-of-concept human studies. *J Nucl Med.* 2015;56:1169–1176.
19. Newton D, Ancill AK, Naylor KE, et al. Long-term retention of injected barium-133 in man. *Radiat Prot Dosimetry.* 2001;97:231–240.

Blind Image Restoration Enhances Digital Autoradiographic Imaging of Radiopharmaceutical Tissue Distribution

Peng Lu[1–3], Nadia Benabdallah[2,3], Wen Jiang[3,4], Brian W. Simons[5], Hanwen Zhang[2,3], Robert F. Hobbs[6], David Ulmert[7,8], Brian C. Baumann[9], Russell K. Pachynski[10], Abhinav K. Jha[1,2], and Daniel L.J. Thorek[1,2,3,11]

[1]Department of Biomedical Engineering, Washington University in St. Louis, St. Louis, Missouri; [2]Department of Radiology, Mallinckrodt Institute of Radiology, Washington University School of Medicine, St. Louis, Missouri; [3]Program in Quantitative Molecular Therapeutics, Washington University School of Medicine, St. Louis, Missouri; [4]Department of Biomedical Engineering, Johns Hopkins University, Baltimore, Maryland; [5]Center for Comparative Medicine, Baylor College of Medicine, Houston, Texas; [6]Radiation Oncology and Molecular Radiation Sciences, Johns Hopkins University School of Medicine, Baltimore, Maryland; [7]Department of Molecular and Medical Pharmacology, UCLA, Los Angeles, California; [8]Ahmanson Translational Imaging Division, David Geffen School of Medicine, UCLA, Los Angeles, California; [9]Department of Radiation Oncology, Washington University School of Medicine, St. Louis, Missouri; [10]Division of Oncology, Washington University School of Medicine, St. Louis, Missouri; and [11]Oncologic Imaging Program, Siteman Cancer Center, Washington University School of Medicine, St. Louis, Missouri

Digital autoradiography (DAR) is a powerful tool to quantitatively determine the distribution of a radiopharmaceutical within a tissue section and is widely used in drug discovery and development. However, the low image resolution and significant background noise can result in poor correlation, even errors, between radiotracer distribution, anatomic structure, and molecular expression profiles. Differing from conventional optical systems, the point-spread function in DAR is determined by properties of radioisotope decay, phosphor, and digitizer. Calibration of an experimental point-spread function a priori is difficult, prone to error, and impractical. We have developed a content-adaptive restoration algorithm to address these problems. **Methods:** We model the DAR imaging process using a mixed Poisson–gaussian model and blindly restore the image by a penalized maximum-likelihood expectation-maximization algorithm (PG-PEM). PG-PEM implements a patch-based estimation algorithm with density-based spatial clustering of applications with noise to estimate noise parameters and uses L2 and Hessian Frebonius norms as regularization functions to improve performance. **Results:** First, PG-PEM outperformed other restoration algorithms at the denoising task ($P < 0.01$). Next, we implemented PG-PEM on preclinical DAR images (^{18}F-FDG, treated mouse tumor and heart; ^{18}F-NaF, treated mouse femur) and clinical DAR images (bone biopsy sections from $^{223}RaCl_2$-treated castration-resistant prostate cancer patients). DAR images restored by PG-PEM of all samples achieved a significantly higher effective resolution and contrast-to-noise ratio and a lower SD of background ($P < 0.0001$). Additionally, by comparing the registration results between the clinical DAR images and the segmented bone masks from the corresponding histologic images, we found that the radiopharmaceutical distribution was significantly improved ($P < 0.0001$). **Conclusion:** PG-PEM is able to increase resolution and contrast while robustly accounting for DAR noise and demonstrates the capacity to be widely implemented to improve preclinical and clinical DAR imaging of radiopharmaceutical distribution.

Key Words: digital autoradiography; blind image restoration; Poisson–gaussian noise model; positron; α-particle emission

J Nucl Med 2022; 63:591–597
DOI: 10.2967/jnumed.121.262270

Autoradiography is a powerful, high-resolution, and quantitative molecular imaging technique used to study the tissue distribution of radioisotopes in biologic systems and for analytic assays (*1–4*). Originally, radioactivity distributions were acquired using photographic emulsions, which are of high resolution but require time-consuming, fickle, and variable processes. Currently, phosphor imaging plate–based digital autoradiography (DAR) has supplanted film because of its linear activity response, nondestructive approach, lack of a chemical-processing requirement, large dynamic range, and considerable sensitivity (*2*,*4*,*5*).

Generally, DAR is performed by placing tissue samples containing radioactivity apposed to the phosphor screen, which absorbs and stores the energy of the radioactive emissions, creating a latent image of activity distribution (Fig. 1A). Except for very low energy β-emitters (tritium), the phosphor layer and the specimens are typically separated by low-attenuation film to prevent contamination of the screen itself, and exposure lasts hours to days. The phosphor plate is raster-scanned with a small focal-spot red laser, and the photostimulated light is collected by a photomultiplier tube to form a digital image (Fig. 1B). The intensity of emitted light is proportional to the amount of radioactivity in the tissue sample.

Suboptimal image quality in DAR limits assessment of radioligand evaluation. Unlike optical microscopy systems, DAR does not use an aperture or collimator, and the solid angle subtended at the samples by the imaging plate is almost 2π. Therefore, the point-spread function (PSF) results from isotropic emission and is dependent on a combination of energy dispersion in the phosphor, plate properties (lattice and grain size), and readout laser, and physical properties also make the PSF isotope-dependent. Additionally, replicating relevant features of the signal for DAR acquisitions in a phantom is difficult. In aggregate, it is thus not practical to calibrate the PSF beforehand.

Received Mar. 9, 2021; revision accepted Jun. 29, 2021.
For correspondence or reprints, contact Daniel L.J. Thorek (thorekd@wustl.edu).
Guest Editor: David A. Mankoff, University of Pennsylvania
Published online Aug. 12, 2021.
Immediate Open Access: Creative Commons Attribution 4.0 International License (CC BY) allows users to share and adapt with attribution, excluding materials credited to previous publications. License: https://creativecommons.org/licenses/by/4.0/. Details: https://jnm.snmjournals.org/page/permissions.
COPYRIGHT © 2022 by the Society of Nuclear Medicine and Molecular Imaging.

Apart from blurring effects caused by PSF, background signal caused by environmental radiation is always present in the imaging process. DAR noise can be attributed to multiple sources: Poisson noise exists in the photon-counting imaging system; gaussian noise comes from the imaging reader readout process, phosphor sheet inhomogeneities, and grain (*6*). Few approaches have been tested to overcome noise and blur-related artifacts: a regularized iteration method after noise filtration (*7*) and the modeling of noise features (*8*). The results from these investigations are not ideal and have not been widely adopted, in part because several have used an emulsion film–based system (the predecessor to phosphor storage plate technology) and noise amplification effects. Common to these approaches are precalibration of PSF by a nonideal resolution phantom.

To model the noise in DAR systems of many isotopes, a blind estimation approach for restoration is preferred. Recently, a mixed-noise model has been used to denoise digital images, which can improve the quality of images contaminated by Poisson and gaussian noise sources (*9–12*). A key step in such a model is estimation of noise parameters. For single-image restoration, patch-based (*9*), segmentation-based (*11*), or Fourier-based (*12*) methods have been developed, and several blind and nonblind image restoration techniques for biomedical images have been advanced (*13–19*). For the specific task of blind restoration, the regularizations for PSF and specimen are considered in some of these methods, providing a path forward for blind DAR estimation.

Here, a blind image restoration algorithm based on a mixed Poisson–gaussian noise model and a penalized maximum-likelihood expectation maximization (MLEM) algorithm, PG-PEM, is presented. We first describe this model in the context of the DAR imaging process along with a patch-based noise parameter estimation method. We incorporate a penalized MLEM algorithm to jointly estimate the restored specimen image and corresponding PSF. L2 and Hessian Frebonius norms are implemented for PSF and specimen signal separately, to improve the quality of the restored image. PG-PEM improves resolution, improves contrast, and suppresses noise more effectively than contemporary restoration approaches, using both preclinical and clinical applied diagnostic and therapeutic radiopharmaceuticals.

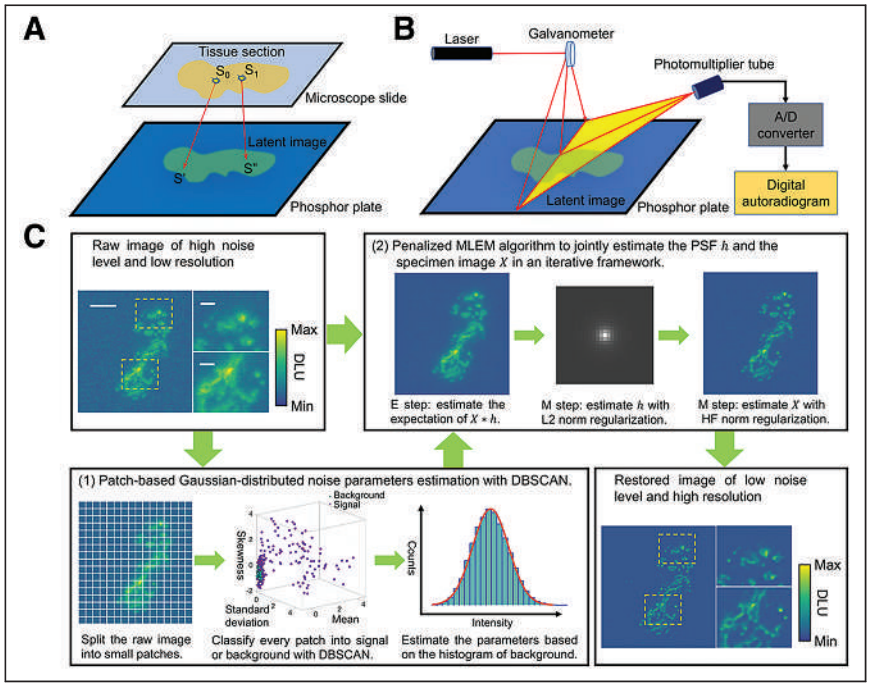

FIGURE 1. DAR imaging process and PG-PEM algorithmic framework. (A) Latent image generation, in which S_0 and S_1 are 2 point sources, detected at S' and S''. (B) DAR image generation. (C) PG-PEM framework: noise parameter estimation (1); PSF and specimen image estimation (2). Scale bars: large figure, 2.3 mm; small figures, 0.54 mm. A/D = analog/digital; DBSCAN = density-based spatial clustering of applications with noise; DLU = digital light unit; E = expectation; HF = hessian Frebonius; M = maximization.

MATERIALS AND METHODS

Mouse Tumor, Heart, and Femur Preparation

Experiments were performed in accordance with approved protocols (Institutional Animal Care and Use Committee protocol 2019006). Male C57BL/6 mice (6–10 wk old) from Jackson Laboratory were administered approximately 7.4 MBq (200 μCi) of either ^{18}F-FDG or ^{18}F-NaF, and harvested at 1 h. Tissues were embedded in optimal-cutting-temperature medium, frozen on dry ice, and sectioned at 8 μm by a cryostat (CM188; Leica). For all radiographic exposures, multisensitive phosphor plates were exposed at −20°C and read as digital light units using a Cyclone Plus (Perkin Elmer). We then used ImageJ (*20*) to crop regions of interest.

Human Bone Biopsy Preparation

Bone biopsies were obtained from 7 metastatic castration-resistant prostate cancer patients under fluoroscopic guidance after a bone scan, 24 h after injection of $^{223}RaCl_2$. The institutional review board approved this study (Human Research Protection Office protocol 201411135), and all subjects provided written informed consent. The biopsy sample was fixed in 4% paraformaldehyde for 24 h, transferred to 30% sucrose for 24 h, frozen, cut, and imaged.

Staining and Imaging

Sections were stained with hematoxylin and eosin and scanned at ×10 (Nikon Eclipse Ti2 for mouse tumor, heart, and femur slides; Zeiss Axio Scan Z1 for human bone biopsy slides).

Overview of Image Formation Model and Restoration Algorithm

According to the DAR imaging process, its physical model can be expressed as Equation 1:

$$R_p = \alpha Q_p + N_p,\ Q_p \sim \mathcal{P}\left[(X * h)_p + b_p\right],\quad N_p \sim \mathcal{N}\left(0, \sigma_G^2\right), \qquad \text{Eq. 1}$$

where p is the pixel index, R the raw image, α the scaling factor corresponding to the gain of the imaging system, X the clean radioactive signal, h the PSF, b the mean of background, $\mathcal{P}[x]$ the Poisson noise with mean x, and $\mathcal{N}(0,\sigma_G^2)$ the gaussian-distributed readout noise with mean of 0 and SD σ_G. Here, we assume b_p is invariant because of the homogeneous radiation around the tissue.

To estimate X, a careful modeling of gaussian noise $\mathcal{N}(0,\sigma_G^2)$ and Poisson noise $\alpha\mathcal{P}[b]$ from background b is necessary. We implement a noise model to jointly estimate parameters of the 2 components. This is

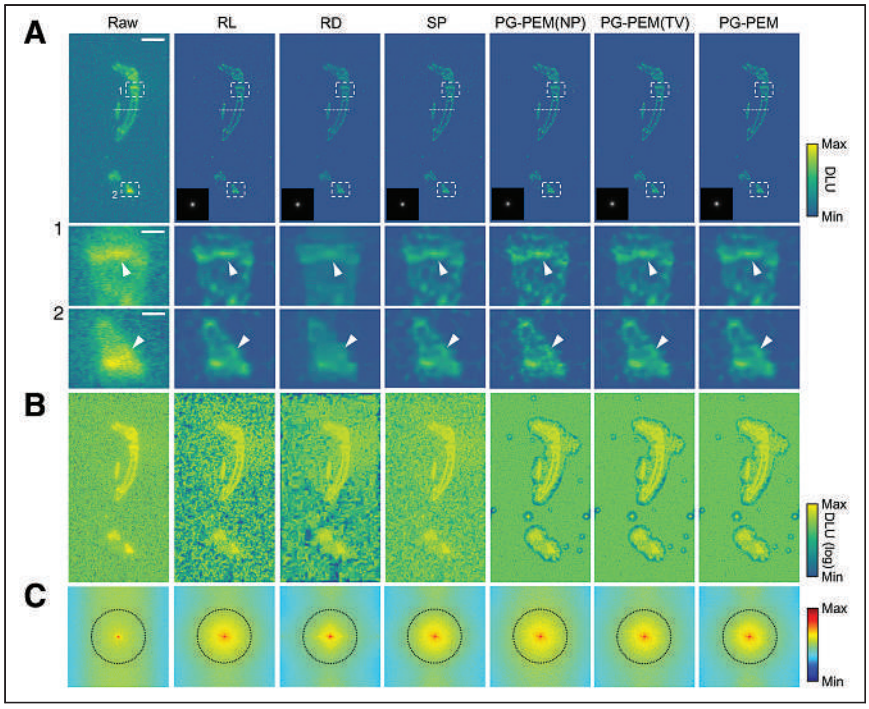

FIGURE 2. Blind restoration improves DAR. (A) Raw DAR image from mouse hindlimb after ^{18}F-NaF PET imaging and its restoration results using modified restoration algorithms. Estimated PSFs are inset in gray scale. (B) Log-scale transformed images from A for background appraisal. (C) Log-scale amplitude of Fourier transform of raw and restored images from A. Scale bars: 4.95 mm (A); 0.86 mm (A1 and A2). DLU = digital light unit.

based on the fact that Poisson distribution can be feasibly approximated by a gaussian distribution when b is greater than 3 (Supplemental Fig. 1; supplemental materials are available at http://jnm.snmjournals.org) (*21*). Notably, this condition is always satisfied for DAR imaging, and therefore, the 2 independent noise features are summed into a new single gaussian-distributed noise (Supplemental Note 1.1). Consequently, the raw image can be reorganized into a Poisson-distributed signal, $\alpha\mathcal{P}[X_p * h]$, and gaussian-distributed noise, $\mathcal{N}(\mu_N, \sigma_N^2)$, with mean of αb and variance of $\alpha^2 b + \sigma_G^2$. Obviously, $\mathcal{N}(\mu_N, \sigma_N^2)$ describes the statistical characterization of the background of DAR images.

Nontissue areas in DAR should have only background and noise and be highly similar to each other. From this assumption, we propose a patch-based estimation algorithm using density-based spatial clustering of applications with noise (Fig. 1C(1); Supplemental Note 1.2 (*22*); Supplemental Algorithm 1; Supplemental Fig. 2) (*23*) to robustly segment background and estimate μ_N and σ_N.

The PG-PEM algorithm uses these noise parameters and the raw image to blindly estimate X based on a penalized MLEM algorithm (Fig. 1C(2); Supplemental Notes 1.3 and 1.4 (*24, 25*)). The expectation step aims to eliminate the gaussian-distributed noise, $\mathcal{N}(\mu_N, \sigma_N^2)$, by calculating the expectation of $X * h$, whereas the maximization step deconvolutes the blurry image corrupted by Poisson-distributed data by jointly estimating h and X. In practice, the blind deconvolution problem is highly ill-posed. Through the iteration process, h tends to converge toward a δ-function because of high-frequency noise in the specimen image. To avoid the trivial solution and considering the smooth characteristics of h, it is regularized by L2 norm. L2 norm is linearly correlated to the power of h. Therefore, the smaller the L2 norm is, the smaller and thus smoother h is. During the same process, the noise of the estimated X may be amplified. Total variation is a popular approach (*16*,*19*) to suppressing such noise by restraining the summation of the derivative of an image, according to the empiric summary that signals are usually successive whereas noise arises randomly. However, total variation oversharpens boundaries between different regions, generating a staircase effect. To avoid this artifact, we implemented Hessian Frebonius norm regularization to enable smoother transitions between different regions and to suppress noise simultaneously (*15*,*17*,*18*). Compared with total-variation regularization, Hessian Frebonius is a second-order derivative norm and forces the second-order derivative to be sparse. The continuity between different pixels agrees more with the characteristics of biologic autoradiogram data. The regularization strengths for h and X are controlled by their regularization parameters λ_h and λ_X, respectively.

For our novel PG-PEM, initial estimates for h and X are needed. The raw image R is set as the initial guess of X divided by α. h can be initialized on the basis of the imaging model. Apart from even scattering, making h circularly symmetric, the finite focal point effect of the image reader and the modulation transfer function of the phosphor plate have minor effects on h. However, it is unnecessary to build a PSF model accounting for all effects in a blind restoration framework. Instead, initialization of h is based on the inverse square law (*26*) when only considering the scattering (Supplemental Note 1.5; Supplemental Fig. 3). Finally, the scaling factor α must be calibrated. Methods previously presented for optical imaging (*11*,*18*) are insufficiently robust for DAR images because it is difficult to find enough homogeneous regions to calibrate α. Empiric calibration is impractical and generally infeasible because of the stochastic decay process and short half-lives in DAR. Fortunately, the mixed Poisson–gaussian data can be approximated as a shifted-Poisson form (*18*), and further, in the deconvolution of Poisson-distributed images, results are not affected by this scaling parameter. Thus, PG-PEM yields a calibration-free algorithm when α is set in a proper range (Supplemental Note 1.6). The detailed algorithmic framework and runtime analysis are summarized (Supplemental Note 1.7; Supplemental Algorithm 2; Supplemental Table 1).

Quality Metrics

For experiments, the full width at half maximum, the SD of the background (STDB), and the contrast-to-noise ratio (CNR) are set as the accuracy metrics because of the lack of ground truth. Full width at half maximum and STDB can evaluate the resolution and noise level separately, whereas CNR assesses overall performance.

For DAR, it is difficult to measure full width at half maximum using microbeads. Alternatively, we use a recently published decorrelation-based method (Supplemental Fig. 4) (*27*). This method estimates not the theoretic resolution of the imaging system but the highest frequency with sufficiently high signal in relation to noise. We refer to the estimated full width at half maximum as effective resolution.

For simulations, accuracy metrics include root-mean-square error, signal-power–to–noise-power ratio (SNR), and structural similarity (*28*), with which the estimated images can be compared with the ground truth directly. These metrics, along with CNR, are defined in Supplemental Note 2.

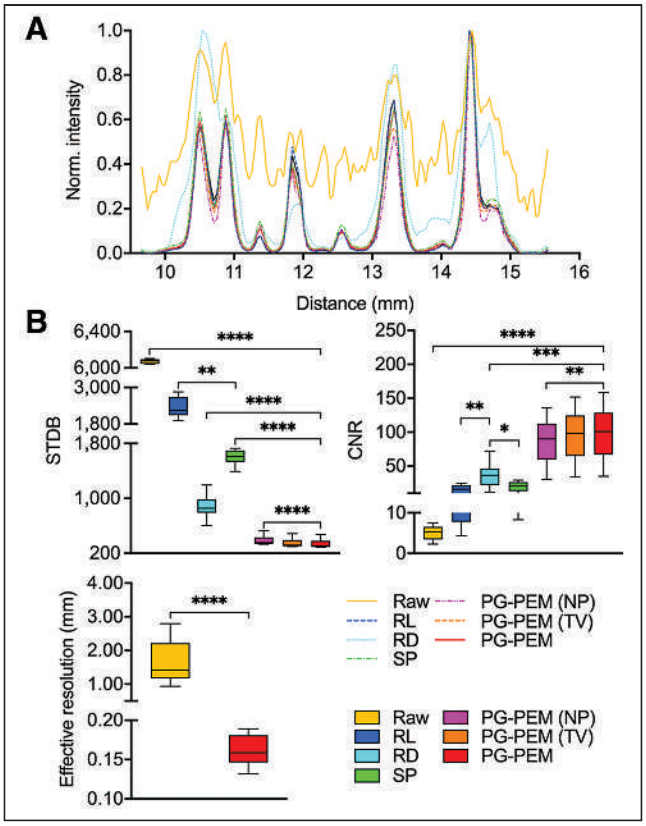

FIGURE 3. Quantitative assessment of different blind restoration approaches. (A) Profiles of dashed lines in Figure 2A. (B) STDB, CNR, and effective-resolution comparisons of approaches. *$P < 0.05$. **$P < 0.01$. ***$P < 0.001$. ****$P < 0.0001$.

Statistical Analysis

Quantitative data are presented as box-and-whisker plots (center line, median; limits, 75% and 25%; whiskers, maximum and minimum). We used paired 2-sided Student *t* testing to compare the data of raw and PG-PEM–restored DAR images, and we used the paired 1-way analysis of variation to compare all other data (Prism 8; GraphPad Software Inc.).

RESULTS

Assessment of Image Enhancement

We benchmarked the performance of several restoration frameworks: Richardson–Lucy (RL) (*13*), RL with wavelet-based residue denoising (RD) (*29*), Shift–Poisson (SP) (*18*), PG-PEM with no regularization for X (NP), and PG-PEM with total-variation regularization (TV). For comparison, we have applied our novel background reduction and blind restoration to all approaches and tuned h to be similar (Supplemental Notes 3.1–3.5). PG-PEM, together with the 5 modified reference algorithms, was implemented on both simulated images (Supplemental Note 4.1) and experimental images. Regularization parameters are tuned (Supplemental Note 4.2; Supplemental Figs. 5–6), and comparisons on simulated data are analyzed (Supplemental Note 4.3; Supplemental Figs. 7–11).

DAR images ($n = 10$) acquired from the mouse hindlimb after ^{18}F-NaF PET imaging were used as experimental data and to evaluate the performance of image restoration approaches. As is standard for short-lived diagnostic radioisotopes and required tissue-processing, sectioning, and exposure times, the SNRs of the raw images are low, providing a model setting for comparison. Visual assessment and analyses (Figs. 2 and 3; Supplemental Fig. 12) show that implementation of restoration algorithms improved resolution and suppressed noise to varying magnitudes. Log-scale images reveal that NP, TV, and PG-PEM have a more homogeneous background than other methods, a result of splitting the image components into Poisson-distributed signal and gaussian-distributed noise. The nonhomogeneous background in RL, RD, and SP correspond to noise and false-positive signal generated in their restoration process.

Next, we assessed the log-scale amplitude of the Fourier space. Because h is isotropic, the resolution of DAR images should be at least quasiisotropic. Curiously, we observed that high frequencies tended along the horizontal direction and were highly nonisotropic, which corresponds to the noise. By comparing the frequency maps of NP, TV, and PG-PEM, we found that the nonisotropic components of NP have the highest energy. TV produces a broader nonisotropic frequency portion than PG-PEM and a staircase effect. These, along with STDB and CNR, indicate that PG-PEM is the best denoiser. Meanwhile, RL, SP, NP, TV, and PG-PEM share similar quasiisotropic areas in the dotted black circles (the decorrelation boundaries defined in Fig. 2C), whereas that of RD has the lowest energy. The resolution of RD is the lowest because wavelet-denoising processes remove fine details. With an MLEM restoration framework (and the same regularization strategy for PSF h), RL, SP, NP, TV, and PG-PEM share similar resolutions. Notably, because of the lack of a regularization strategy for X, the resolution of NP may be slightly higher than those of the other methods, which can be neglected because of the impact of noise. The effective resolution improves at least 5-fold after restoration by PG-PEM ($P < 0.0001$). These data, along with the simulation results, demonstrate that PG-PEM is the best performer for blind restoration of DAR images.

PG-PEM Improves DAR of Diagnostic Radiopharmaceuticals

To determine whether PG-PEM could improve the quality of DAR images in diagnostic radiopharmaceuticals, we investigated the distribution of the widely used metabolic tracer ^{18}F-FDG, and the bone-seeking ^{18}F-NaF, in tissue samples from mouse tumor, heart, and femur ($n = 10$ per group). We used PG-PEM to restore these data, and we calculated STDB, CNR, and effective resolution for comparison to the raw images (Fig. 4). These results demonstrate the image quality improvement after restoration. Notably, a nonglycolytic (prostate) tumor section, which takes up little ^{18}F-FDG, has an extremely low SNR. Nevertheless, PG-PEM suppresses background noise and improves the resolution of regions of uptake (Supplemental Fig. 13). RL and SP algorithms were chosen as references to restore the same DAR images from tumors imaged with ^{18}F-FDG (Supplemental Fig. 14). Compared with PG-PEM, the results of RL and SP, especially their background components, have more apparent noise. The corresponding STDB and CNR reveal that PG-PEM is superior to restore DAR images under extremely low-SNR conditions, with a P value of less than 0.0001.

We next asked whether higher-SNR images, from ^{18}F-FDG in the heart and ^{18}F-NaF in the bone, could likewise be improved by PG-PEM. From the raw cardiac images, radioisotope signal is almost homogeneous. By contrast, the PG-PEM–restored data have a higher resolution and improved contrast, which may better reflect the spatial distribution of the tracer (Supplemental Figs. 13 and 15). We further compared the hematoxylin- and eosin-stained,

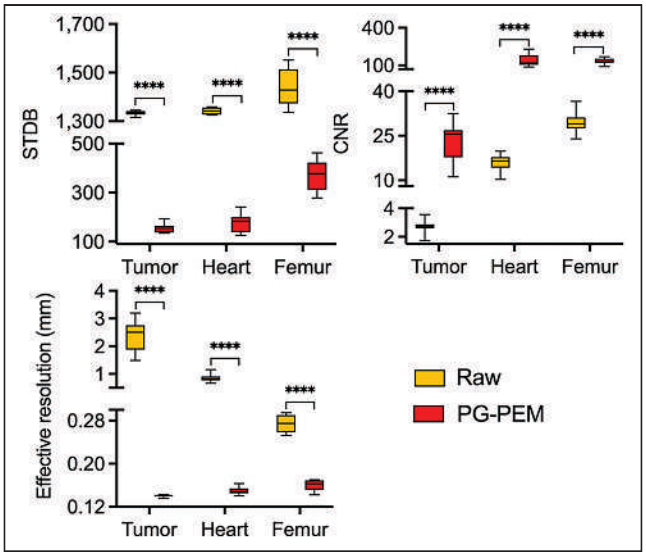

FIGURE 4. STDB, CNR, and effective resolution assessment of PG-PEM for preclinical DAR images. ****$P < 0.0001$.

raw, and restored DAR images of the murine femur (Fig. 5; Supplemental Fig. 16). After restoration, the endosteal and periosteal surfaces are clearly visualized, and the proximal head of the femur is resolved. Because the positron range of ^{18}F is considerable, its DAR is blurred compared with lower-energy β-emitters or high-linear-energy-transfer α-emitters, hindering assessment of radiopharmaceutical distribution. Our results indicate that PG-PEM can ameliorate this issue, underscoring preclinical utility.

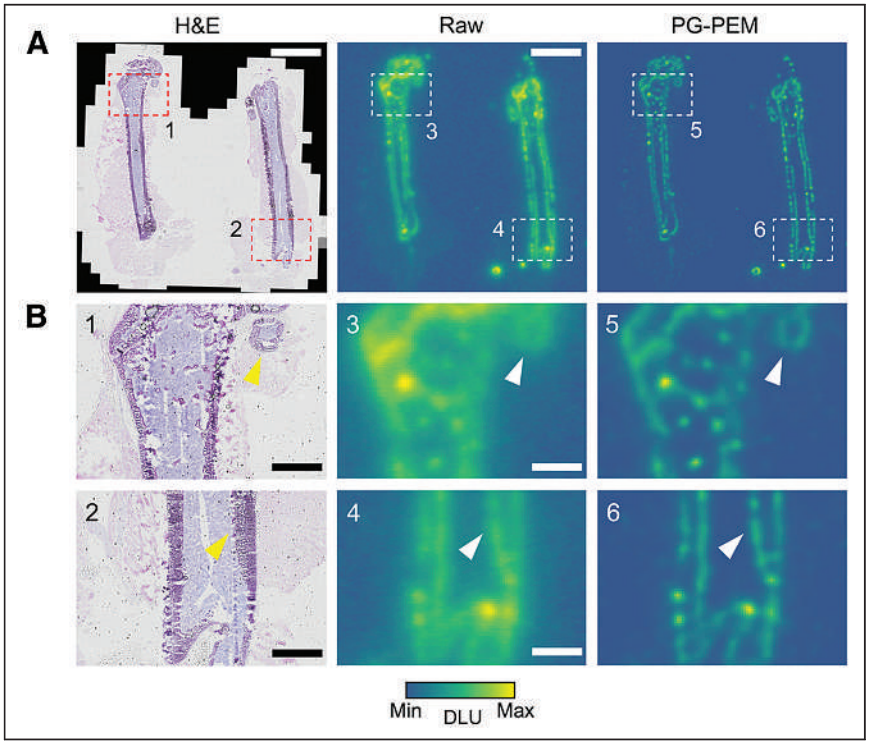

FIGURE 5. PG-PEM improves DAR images of ^{18}F-NaF treated femur sections. (A) Hematoxylin- and eosin-stained, raw, and PG-PEM–restored DAR images. (B) Zoomed-in regions of corresponding boxes in A. Scale bars: 5 mm (A); 1.2 mm (B). DLU = digital light unit.

Enhanced Targeted α-Particle Radiotherapy Evaluation by PG-PEM

Targeted delivery of α-particle–emitting radionuclides is an emerging application for metastatic cancer treatment (*30*,*31*). Analyzing the dose distribution for α-particle therapy near the cell scale plays a key role in predicting the treatment response and assessing the toxicity of this targeted paradigm, especially as the pathlength of α-particles is on the microscopic scale. Current small-scale dosimetry methods are based predominately on idealized computational anatomic models (*32*,*33*). Although useful, these provide limited real-world information in heterogeneous patient populations.

We investigate α-particle emitter activity distributions from a dataset of 10 bone biopsy slides from metastatic castration-resistant prostate cancer patients treated with $^{223}RaCl_2$ (Fig. 6; Supplemental Fig. 17). The raw DAR images suffer from blur and noise due to the imaging process, distorting the true radiotracer distribution. This can cause large errors in registration and degrades treatment response assessment and toxicity analysis. ^{223}Ra will adsorb on the bone surface (*34*), and the high-activity regions should be located here. On the basis of this knowledge, DAR and histopathology images can be registered, and restoration algorithms can be evaluated.

After registration (Supplemental Fig. 18), raw and restored DAR images were fused with an anatomic bone mask (Supplemental Fig. 19). PG-PEM not only can improve the resolution and remove noise in these DAR images but also results in more accurate correlation with underlying anatomy. Quantitatively, line profiles, STDB, and CNR improve, and the effective resolution increases by approximately 1.7-fold over raw data (Fig. 7). We then calculated the structural similarity between the high-activity regions of DAR images with their segmented bone masks and evaluated a fusion index, defined as the ratio of total activity at bone surfaces (Supplemental Fig. 20). Note that the higher the structural similarity and fusion index are, the better is the correlation between the modalities. The evaluation results show that PG-PEM is able to improve these two accuracy metrics significantly ($P < 0.0001$). Consequently, PG-PEM can be of great use in personalized targeted α-particle radiotherapy assessment.

DISCUSSION

Autoradiography is an important technique in drug development and evaluation of radiolabeled compounds for imaging and targeted therapy (*35*–*38*). In particular, there is considerable academic, pharmaceutical industry, and clinical interest in assessing targeted α- and β-particle emitters for endotherapy. Unlike external-beam radiation delivery, systemically administered radionuclides can irradiate all tissues in the body, and localized distribution is central to calculating absorbed doses and to predicting both treatment response and off-target toxicities. Conventional image

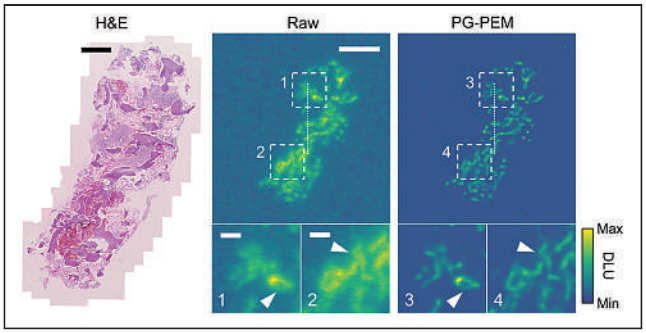

FIGURE 6. PG-PEM restoration in α-particle radiotherapy specimens. From left to right: hematoxylin- and eosin-stained histologic image of bone biopsy sample from patient with $^{223}RaCl_2$-treated metastatic castration-resistant prostate cancer, and corresponding raw and PG-PEM–restored DAR images. Scale bars: 1 mm (hematoxylin and eosin); 2.3 mm (raw); 0.5 mm (insets 1 and 2). DLU = digital light unit.

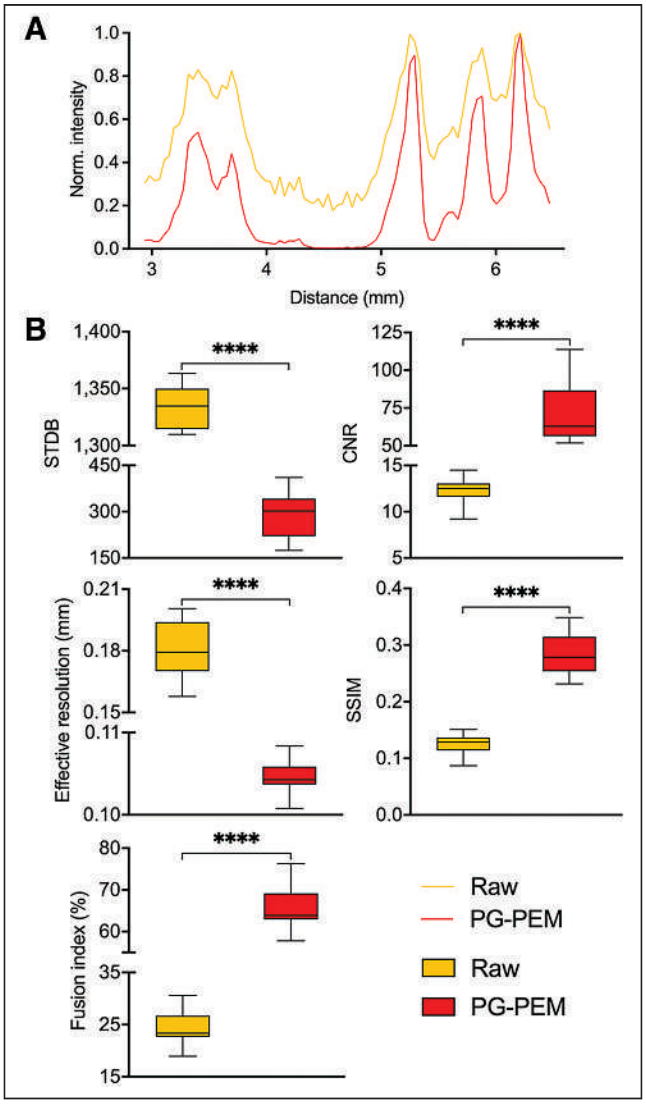

FIGURE 7. Quantitative assessment of PG-PEM for human bone biopsy DAR. (A) Profiles of dashed lines in Figure 6. (B) STDB, CNR, effective resolution, structural similarity, and fusion indices assessment for raw and restored DAR images. ****$P < 0.0001$.

formation methods using DAR suffer from noise and other image artifacts. In this work, we have defined and implemented a novel PG-PEM algorithm to restore blurred and noisy DAR data.

PG-PEM is based on the DAR imaging process and a mixed Poisson–gaussian noise model. The noise parameters are estimated with a patch-based algorithm after a Poisson–gaussian distribution conversion. A penalized MLEM approach is then used to jointly estimate the specimen image and its corresponding PSF, simultaneously. Specifically, we used the L2 norm to regularize the PSF in order to ensure its smoothness and avoid the trivial solution, and we used the Hessian Frebonius norm to regularize the estimated specimen image in order to ensure its continuity and suppress noise. Notably, this approach effectively eliminates the staircase effect caused by TV regularization. As a consequence, even low-SNR images are robustly restored. To the best of our knowledge, this is the first attempt to combine MLEM with Hessian norm–based regularization.

After analyzing the scaling factor α, we proved that it is free of precalibration in PG-PEM. Subsequently, the algorithm was quantitatively compared against alternative approaches across multiple datasets. Because of the blind restoration framework, PG-PEM is not a convex problem and we cannot guarantee that it can converge to a global solution. Nevertheless, simulation and experimental results show that PG-PEM is the lead performer, providing improved correlation between signal and tissue features.

Interestingly, even though both SP and PG-PEM are based on the mixed Poisson–gaussian noise model, PG-PEM has lower noise and reduced background false-positive signal. This difference comes from the iteration process: PG-PEM first filters gaussian-distributed noise in the expectation step and then filters Poisson-distributed noise in the maximization step. In addition, we have also compared the PSFs estimated from different isotopes ($^{223}RaCl_2$-treated human bone biopsy sample and ^{18}F-NaF–treated mouse hindlimb). Clearly, the kernel size of the PSF from the hindlimb is larger than that from the biopsy sample (Supplemental Fig. 21), consistent with the physics of α/positron travel, further validating the blind restoration approach.

Recently, convolutional neural networks have proved effective in biomedical image restoration (*39*,*40*). However, these networks may not be well suited for DAR restoration because of multiparametric factors influencing PSF, noise characteristics for each isotope and tissue, and the lack of clean label data.

CONCLUSION

We have developed the PG-PEM algorithm for improved DAR image quality. Predicated on a complete image formation model for DAR and implementation of a signal and background segmentation approach, this blind image restoration approach reduced background noise and image blur in simulated and primary image samples. For both high- and low-SNR datasets of diagnostic and therapeutic radionuclides, there were significant improvements in DAR resolution, contrast, and accuracy of localization. This method will be widely applicable to both preclinical- and clinical-sample autoradiograms to improve radiotracer and radiotherapy agent evaluation.

DISCLOSURE

This work was funded in part by the National Cancer Institute of the National Institutes of Health (R01CA229893, R01CA201035, and R01CA240711 [all to Daniel Thorek]) and by the

Society of Nuclear Medicine and Molecular Imaging Student Research Award (Peng Lu). No other potential conflict of interest relevant to this article was reported.

KEY POINTS

QUESTION: Can developments in computational imaging tools be leveraged to improve diagnostic tracer and therapeutic radionuclide distribution assessment on the tissue scale?

PERTINENT FINDINGS: A combination of noise reduction along with automated image restoration leads to significantly enhanced DAR images. Background noise can be efficiently reduced, with improved contrast and enhanced resolution. Particular benefits are found for low-SNR images as demonstrated on clinical bone biopsies from men treated with α-particle–emitting ^{223}Ra.

IMPLICATIONS FOR PATIENT CARE: Improved understanding of radioisotope distribution on the tissue scale is expected to benefit target engagement studies for drug development and to enable more accurate dose distribution.

REFERENCES

1. Solon EG. Autoradiography: high-resolution molecular imaging in pharmaceutical discovery and development. *Expert Opin Drug Discov.* 2007;2:503–514.
2. Johnström P, Bird JL, Davenport AP. Quantitative phosphor imaging autoradiography of radioligands for positron emission tomography. *Methods Mol Biol.* 2012; 897:205–220.
3. Bäck T, Jacobsson L. The α-camera: a quantitative digital autoradiography technique using a charge-coupled device for ex vivo high-resolution bioimaging of α-particles. *J Nucl Med.* 2010;51:1616–1623.
4. Griem-Krey N, Klein AB, Herth M, Wellendorph P. Autoradiography as a simple and powerful method for visualization and characterization of pharmacological targets. *J Vis Exp.* 2019;145:e58879.
5. Sonoda M, Takano M, Miyahara J, Kato H. Computed radiography utilizing scanning laser stimulated luminescence. *Radiology.* 1983;148:833–838.
6. Boncelet C. Image noise models. In: *The Essential Guide to Image Processing.* Academic Press; 2009:159–160.
7. Goyette J, Lapin G, Kang M, Katsaggelos AK. Regularized iterative image restoration algorithms applied to autoradiography. In: *Proceedings of the 15th Annual International Conference on IEEE Engineering in Medicine and Biology Society.* IEEE; 1993:490–491.
8. Zhang M, Chen Q, Li XF, et al. Image deconvolution in digital autoradiography: a preliminary study. *Med Phys.* 2008;35:522–530.
9. Jezierska A, Pesquet JC, Talbot H, Chaux C. Iterative Poisson-Gaussian noise parametric estimation for blind image denoising. In: *Proceedings: 2014 IEEE International Conference on Image Processing (ICIP).* IEEE; 2014:2819–2823.
10. Chouzenoux E, Jezierska A, Pesquet JC, Talbot H. A convex approach for image restoration with exact Poisson-Gaussian likelihood. *SIAM J Imaging Sci.* 2015;8: 2662–2682.
11. Foi A, Trimeche M, Katkovnik V, Egiazarian K. Practical Poissonian-Gaussian noise modeling and fitting for single-image raw-data. *IEEE Trans Image Process.* 2008;17:1737–1754.
12. Mandracchia B, Hua X, Guo C, Son J, Urner T, Jia S. Fast and accurate sCMOS noise correction for fluorescence microscopy. *Nat Commun.* 2020;11:94.
13. Fish D, Brinicombe A, Pike E, Walker J. Blind deconvolution by means of the Richardson-Lucy algorithm. *J Opt Soc Am A Opt Image Sci Vis.* 1995;12:58–65.
14. Kenig T, Kam Z, Feuer A. Blind image deconvolution using machine learning for three-dimensional microscopy. *IEEE Trans Pattern Anal Mach Intell.* 2010;32: 2191–2204.
15. Lefkimmiatis S, Bourquard A, Unser M. Hessian-based norm regularization for image restoration with biomedical applications. *IEEE Trans Image Process.* 2012; 21:983–995.
16. Keuper M, Schmidt T, Temerinac-Ott M, et al. Blind deconvolution of widefield fluorescence microscopic data by regularization of the optical transfer function (OTF). In: *Proceedings: 2013 IEEE Conference on Computer Vision and Pattern Recognition.* IEEE; 2013:2179–2186.
17. Huang X, Fan J, Li L, et al. Fast, long-term, super-resolution imaging with Hessian structured illumination microscopy. *Nat Biotechnol.* 2018;36:451–459.
18. Ikoma H, Broxton M, Kudo T, Wetzstein G. A convex 3D deconvolution algorithm for low photon count fluorescence imaging. *Sci Rep.* 2018;8:11489.
19. Koho S, Tortarolo G, Castello M, Deguchi T, Diaspro A, Vicidomini G. Fourier ring correlation simplifies image restoration in fluorescence microscopy. *Nat Commun.* 2019;10:3103.
20. Schindelin J, Arganda-Carreras I, Frise E, et al. Fiji: an open-source platform for biological image analysis. *Nat Methods.* 2012;9:676–682.
21. Janesick JR. Photon transfer noise sources. In: *Photon Transfer DN → λ.* SPIE Press; 2007:21–25.
22. Crain BR. Estimating the parameters of a truncated normal distribution. *Appl Math Comput.* 1979;5:149–156.
23. Ester M, Kriegel HP, Sander J, Xu X. A density-based algorithm for discovering clusters in large spatial databases with noise. In: *KDD.* AAAI; 1996:226–231.
24. Brune C, Sawatzky A, Burger M. Bregman-EM-TV methods with application to optical nanoscopy. In: *SSVM.* Elsevier; 2009:235–246.
25. Resmerita E, Anderssen RS. Joint additive Kullback-Leibler residual minimization and regularization for linear inverse problems. *Math Models Methods Appl Sci.* 2007;30:1527–1544.
26. Brownson JR. Laws of light. In: *Solar Energy Conversion Systems.* Academic Press; 2014:41–66.
27. Descloux A, Grussmayer KS, Radenovic A. Parameter-free image resolution estimation based on decorrelation analysis. *Nat Methods.* 2019;16:918–924.
28. Wang Z, Bovik AC, Sheikh HR, Simoncelli EP. Image quality assessment: from error visibility to structural similarity. *IEEE Trans Image Process.* 2004;13: 600–612.
29. Boussion N, Le Rest CC, Hatt M, Visvikis D. Incorporation of wavelet-based denoising in iterative deconvolution for partial volume correction in whole-body PET imaging. *Eur J Nucl Med Mol Imaging.* 2009;36:1064–1075.
30. Baidoo KE, Yong K, Brechbiel MW. Molecular pathways: targeted α-particle radiation therapy. *Clin Cancer Res.* 2013;19:530–537.
31. Abou D, Benabdallah N, Jiang W, et al. Prostate cancer theranostics: an overview. *Front Oncol.* 2020;10:884.
32. Sgouros G, Hobbs R, Song H. Modelling and dosimetry for alpha-particle therapy. *Curr Radiopharm.* 2011;4:261–265.
33. Hobbs RF, Song H, Watchman CJ, et al. A bone marrow toxicity model for ^{223}Ra alpha-emitter radiopharmaceutical therapy. *Phys Med Biol.* 2012;57:3207–3222.
34. Abou DS, Ulmert D, Doucet M, Hobbs RF, Riddle RC, Thorek DL. Whole-body and microenvironmental localization of radium-223 in naive and mouse models of prostate cancer metastasis. *J Natl Cancer Inst.* 2015;108:djv380.
35. Solon EG, Kraus L. Quantitative whole-body autoradiography in the pharmaceutical industry: survey results on study design, methods, and regulatory compliance. *J Pharmacol Toxicol Methods.* 2001;46:73–81.
36. Solon EG. Use of radioactive compounds and autoradiography to determine drug tissue distribution. *Chem Res Toxicol.* 2012;25:543–555.
37. McDevitt MR, Thorek DL, Hashimoto T, et al. Feed-forward alpha particle radiotherapy ablates androgen receptor-addicted prostate cancer. *Nat Commun.* 2018;9:1629.
38. Yang AC, Stevens MY, Chen MB, et al. Physiological blood–brain transport is impaired with age by a shift in transcytosis. *Nature.* 2020;583:425–430.
39. Weigert M, Schmidt U, Boothe T, et al. Content-aware image restoration: pushing the limits of fluorescence microscopy. *Nat Methods.* 2018;15:1090–1097.
40. Guo M, Li Y, Su Y, et al. Rapid image deconvolution and multiview fusion for optical microscopy. *Nat Biotechnol.* 2020;38:1337–1346.

Experience with a Perfusion-Only Screening Protocol for Evaluation of Pulmonary Embolism During the COVID-19 Pandemic Surge

Arun Kumar[1], Renée M. Moadel[1], Linda B. Haramati[2,3], Kenny Ye[4], Leonard M. Freeman[1], and Lionel S. Zuckier[1]

[1]Division of Nuclear Medicine, Montefiore Medical Center and Albert Einstein College of Medicine, Bronx, New York; [2]Division of Cardiothoracic Imaging, Montefiore Medical Center and Albert Einstein College of Medicine, Bronx, New York; [3]Departments of Radiology and Medicine, Montefiore Medical Center and Albert Einstein College of Medicine, Bronx, New York; and [4]Division of Biostatistics, Department of Epidemiology and Population Health, Albert Einstein College of Medicine, Bronx, New York

The purpose of this study was to evaluate a pulmonary embolism (PE) perfusion-only screening (POS) protocol introduced during the coronavirus disease 2019 (COVID-19) pandemic surge. Subjects without dense parenchymal lung opacities were studied; those with less than 1 segmental perfusion defect were considered to have no PE, whereas those exhibiting 1 or more defects were indeterminate, mandating additional examinations to determine the final diagnosis. **Methods:** We analyzed demographic information, clinical data, imaging findings, and follow-up data from the electronic records of COVID-19 patients who underwent lung scintigraphy during the 60-d study period. **Results:** In total, 53 studies were performed on 17 COVID-19–positive and 36 COVID-19–negative patients. The POS protocol efficiently excluded PE in 79% of cases; the remaining 21%, indeterminate for PE, were generally referred for alternative testing or were directly anticoagulated. In patients with negative POS results, there was a very low mortality before hospital discharge (1/42) and normal results on follow-up studies (6/6). **Conclusion:** The POS protocol, implemented during the COVID-19 surge, efficiently and safely excluded PE in 79% of patients.

Key Words: ventilation; pulmonary embolism; COVID-19; lung scintigraphy

J Nucl Med 2022; 63:598–601
DOI: 10.2967/jnumed.121.262580

The purpose of this study was to evaluate a screening protocol for pulmonary embolism (PE) that we introduced during the initial coronavirus disease 2019 (COVID-19) surge (*1*) and was modeled on an algorithm used at our institution for evaluation of PE in pregnant women (*2*). No ventilation scintigraphy was performed (*1*). Absence of PE was based on detecting less than 1 segmental planar perfusion defect; studies demonstrating 1 or more segmental defects are considered indeterminate for PE, mandating additional examinations to determine the final diagnosis. Patients with known dense parenchymal lung opacities, in whom corresponding perfusion defects are anticipated, are directly referred for alternate studies such as CT pulmonary angiography (CTPA). We hope our experience will help inform the global discussion of best practices during periods of elevated risk from infectious respiratory pathogens.

MATERIALS AND METHODS

Institutional review board approval was obtained with a waiver of the requirement for consent. We retrospectively retrieved demographic information, clinical data, imaging findings, and patient follow-up data from the electronic records of patients studied between March 21 and May 19, 2020, coincident with the initial surge of COVID-19 in our high-prevalence region. Continuous variables were summarized as mean ± SD, whereas highly skewed variables were described by median and interquartile ranges. The means of continuous variables were compared using the Welch *t* test unless otherwise indicated, and proportions were compared using the Fisher exact test. *P* values of less than 0.05 were considered statistically significant.

RESULTS

Demographic Findings

Fifty-three patients underwent lung scintigraphy during the 60-d period. Infection with severe acute respiratory syndrome coronavirus 2 virus was evaluated by polymerase chain reaction testing in 46 patients (13 of whom were positive and 33 negative), whereas 7 patients were categorized by clinical judgment (4 as infected and 3 as not). Demographic and laboratory values are listed in Table 1.

Prior Radiographic Findings

Chest radiographs or CT examinations were obtained for all patients within 0–5 d before the perfusion study (mean, 0.8 d). No dense parenchymal opacities were present; however, in 13 subjects there were 14 radiographic findings, consisting of ill-defined and nonsegmental opacities (7 patients), mild congestive heart failure (4 patients), and linear atelectatic changes (3 patients).

In the 17 COVID-19–positive (COV+) patients, 2 negative Doppler ultrasound studies of the legs were performed before scintigraphy. In the 36 COVID-19–negative (COV−) patients, there were 6 negative and 2 positive Doppler studies and 2 nondiagnostic CTPA examinations before scintigraphy.

Received May 14, 2022; revision accepted Jul. 15, 2022.
For correspondence or reprints, contact Lionel S. Zuckier (lzuckier@montefiore.org).
Published online Aug. 5, 2021.
Immediate Open Access: Creative Commons Attribution 4.0 International License (CC BY) allows users to share and adapt with attribution, excluding materials credited to previous publications. License: https://creativecommons.org/licenses/by/4.0/. Details: http://jnm.snmjournals.org/site/misc/permission.xhtml.
COPYRIGHT © 2022 by the Society of Nuclear Medicine and Molecular Imaging.

TABLE 1
Demographic and Clinical Findings

Parameter	All patients	COV+	COV−	*P*
COVID-19 status (*n*)				
Total	53	17	36	—
By polymerase chain reaction testing	46	13	33	—
By clinical assessment	7	4	3	—
Mean age ± SD (y)	49.0 ± 16.2	47.5 ± 17.2	49.8 ± 15.9	0.68
Females (*n*)	39 (74%)	10 (59)	29 (81)	0.11
Patients with serum creatinine ≥ 1.5 mg/dL (*n*)	19 (36%)	6 (35%)	13 (36%)	1
Patients with history of contrast allergy (*n*)	3 (6%)	1 (6%)	2 (6%)	1
Median D-dimer values (μg/mL)*	1.18 (IQR = 1.7)	1.34 (IQR = 2.3)	1.17 (IQR = 1.5)	0.66
Parenchymal findings on prior chest radiography (*n*)	13 (25%)	7 (41%)	6 (17%)	0.08
Patients with prior negative Doppler US (*n*)	8	2	6†	—
Patients with prior positive Doppler US (*n*)	2	0	2	—
Patients with prior nondiagnostic CTPA (*n*)	2	—	2†	—
Patients with ≥1 perfusion defects (*n*)	11 (21%)	3 (18%)	8 (22%)	1
Follow-up examinations on patients with ≥1 perfusion defects (*n*)	6/11 (55%)	0/3 (0%)	6/8 (75%)	0.06

*Reference value, ≤0.50 μg/mL. *P* values for D-dimer are based on Wilcoxon rank-sum testing.
†One patient had both negative Doppler findings and nondiagnostic CTPA.
IQR = interquartile range.
P values are for differences between COV+ and COV− subgroups.

Scintigraphic Studies

Planar perfusion scintigraphy was performed according to Society of Nuclear Medicine and Molecular Imaging guidelines (*3*). After injection of 148 MBq of ^{99m}Tc-macroaggregated albumin, planar images in 8 projections were acquired, at 180 s per view. Significant defects were wedge-shaped and pleura-based, with sizing conforming to Society of Nuclear Medicine and Molecular Imaging guidelines (*3*). Exceptions to the standard protocol occurred in 8 patients to whom reduced dosages of radiopharmaceutical were administered, 2 patients on whom low-dose ventilation was performed before scintigraphy, and 4 patients for whom SPECT/CT was additionally performed. Alterations in imaging confirmed but did not alter diagnoses based on planar perfusion imaging.

The frequency of segmental perfusion defects in the COV+ and COV− groups on planar perfusion scintigraphy was 18% and 22%, respectively (Figs. 1A and 1B); in 6 instances, single segmental defects were identified; in 4 patients, multiple segmental defects were identified; and in 1 patient there was a relative unilateral decrease in perfusion (Fig. 2).

Clinical Follow-up in Patients with Normal Perfusion Results

Of 14 patients with normal perfusion in the COV+ group, 12 were not studied further whereas 2 underwent Doppler ultrasound of the legs, with negative findings in both cases (Fig. 1A). Three patients were placed on anticoagulation treatment, one of whom had atrial fibrillation. One of the 11 nonanticoagulated patients died of respiratory failure during hemodialysis 2 d after scintigraphy; the remaining 13 COV+ patients with normal perfusion were successfully discharged home.

Of 28 patients with normal perfusion studied in the COV− group, 24 were not studied further whereas 2 underwent CTPA, 1 underwent Doppler ultrasound of the legs, and 1 underwent CTPA followed by Doppler ultrasound, all with negative results (Fig. 1B). Three patients with normal perfusion in this group were anticoagulated, 1 with prior positive findings on leg Doppler ultrasound, 1 with a history of PE 4 y earlier, and 1 in atrial fibrillation. All 28 patients with normal perfusion in the COV− group were discharged home.

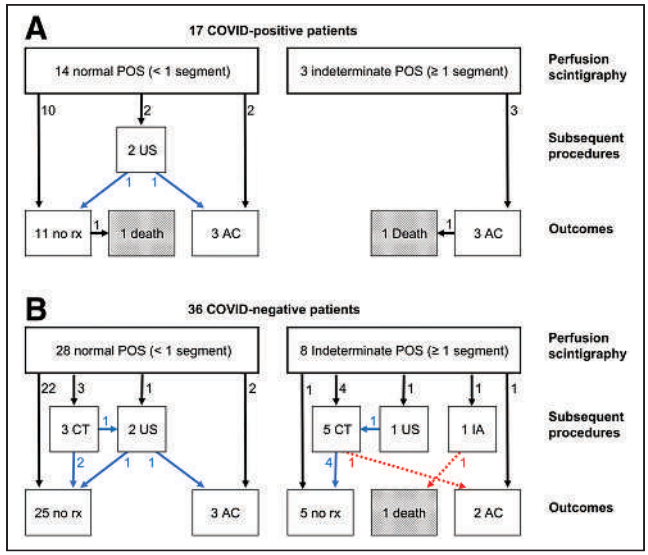

FIGURE 1. Diagnostic flowchart in 17 COV+ (A) and 36 COV− (B) patients. Arrows refer to flow of patients, whereas adjacent numbers indicate number of patients involved. Blue arrows indicate negative test result; red arrows signify positive test result. AC = anticoagulation; CT = CTPA; IA = interventional angiography; rx = therapy; US = leg Doppler ultrasound.

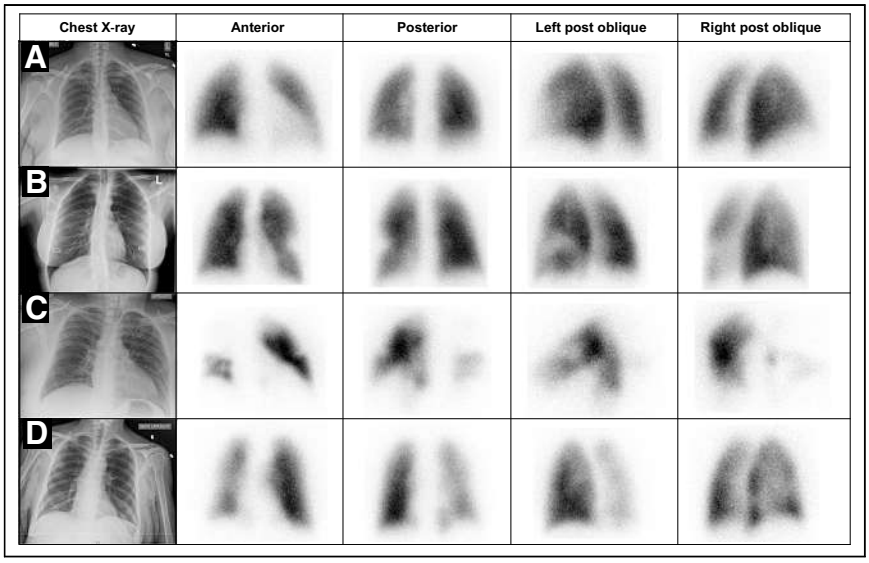

FIGURE 2. Key images of 4 representative patients. All chest radiographs demonstrate absence of significant opacities. (A) A 44-y-old woman, COV+ by polymerase chain reaction testing. No defects were noted on perfusion scintigraphy. Patient was not anticoagulated and was discharged without complication. (B) A 35-y-old woman, COV− by polymerase chain reaction testing. Well-defined segmental perfusion defect in superior lingula was indeterminate for PE. CTPA demonstrated normal pulmonary arterial perfusion; patient was discharged home without anticoagulation treatment. (C) A 43-y-old man, COV+ by polymerase chain reaction testing, with elevated D-dimer (19.7 μg/mL). Multiple bilateral segmental defects, especially involving right lung, were indeterminate for PE. Patient subsequently was discharged on anticoagulation treatment. (D) A 59-y-old woman, COV− by polymerase chain reaction testing. There is global decrease in perfusion of right lung, indeterminate for PE. CTPA demonstrated normal pulmonary arterial perfusion; patient was discharged home without anticoagulation treatment.

Clinical Follow-up in Patients with Indeterminate Perfusion Studies

None of the 3 COV+ patients with perfusion defects received any follow-up examinations, and all were directly anticoagulated (Fig. 1A), one of whom died of respiratory failure a day after scintigraphy. Six of 8 COV− patients with indeterminate findings were referred for further diagnostic imaging: a catheter angiogram with positive results in 1, Doppler ultrasound of the legs with negative results followed by CTPA with positive results in 1, and CTPA examinations with negative results in 4 (Fig. 1B). Another COV− patient with indeterminate findings had prior positive Doppler results and was directly anticoagulated without additional imaging or an adverse outcome. The final patient had a perfusion defect described as atypical and was discharged home without therapy. The patient who underwent catheter angiography had a contraindication to heparin; thrombolysis was performed, with placement of an inferior vena cava filter. However, she died of multisystem failure 11 d afterward. The patient with positive CTPA results was anticoagulated, whereas the 4 patients with negative CTPA results were not. Of all 11 patients with indeterminate perfusion studies, 9 patients were therefore ultimately discharged home (2 COV+ and 7 COV−).

DISCUSSION

A variety of approaches to performing lung scintigraphy were considered during the early COVID-19 period (*4*), designed to balance tension between potential spread of infection when ventilation scintigraphy is performed and suboptimal specificity of scintigraphy when ventilation is omitted. These considerations informed our approach, which used perfusion scintigraphy in a screening role, relying on the established sensitivity of perfusion scintigraphy to identify disease and not creating new criteria of interpretation.

The most salient observation regarding the perfusion-only screening (POS) protocol is that approximately 80% of patients had less than 1 segmental defect and required no further testing. By restricting the patients whom we studied to those with a relatively clear chest radiograph, we succeeded in obtaining a subgroup of subjects with a low prevalence of defects, thereby excluding PE efficiently and validating the anticipated benefit of the protocol. A subgroup of 13 patients was imaged despite the presence of mild parenchymal abnormalities, which did not interfere with performance of the examination.

The POS protocol was accurate and safe. Of 6 patients who underwent additional diagnostic examinations after negative results, no emboli or thrombi were confirmed. Among all 42 patients with negative POS results, there was only 1 fatality, a COV+ patient who died of respiratory failure. Of the 11 subjects with indeterminate perfusion scintigraphy, 6 underwent further testing, 2 of whom had PE substantiated on follow-up, demonstrating use of POS as a screening examination. One COV− patient with proven embolism and a contraindication to anticoagulation succumbed to multisystem failure, whereas a second COV+ patient, who was placed on anticoagulation treatment, died of respiratory failure 1 d after scintigraphy.

Limitations of our retrospective study include an inability to determine outcome by the optimal gold standard of 60 d of follow-up, because most patients were not enrolled within our health-care system after discharge. As well, we cannot easily reconstruct how many patients were referred away from scintigraphy because of radiographic abnormalities or other considerations and which alternative examinations they underwent. A final limitation relates to the generalizability of our findings. The prevalence of segmental defects in patients referred for testing is highly dependent on specific referral patterns and the regional incidence of disease. Nonetheless, the relatively robust results we obtained suggest that this protocol could be cautiously extrapolated to similar environments with ongoing monitoring of efficacy.

Although we imaged by planar scintigraphy, a similar screening protocol can be based on SPECT imaging, used in many regions (*5*). It is also possible that interim specificity can be improved by factoring in pretest probability (*6*) or by performing SPECT/CT, in which anatomic CT information can be used as a partial surrogate for ventilation (*6–8*).

An intriguing consideration deriving from our experience is whether performing a perfusion study first as a screening test should continue in noninfected patients with relatively clear chest radiographs in whom PE is being excluded (*9*). Only if segmental defects are noted on the perfusion study would a completion ventilation study or complementary imaging be performed.

CONCLUSION

We have reviewed our experience during 60 d of the initial COVID-19 surge using a POS protocol implemented in 53 patients

with minimal abnormalities on baseline chest radiography. This screening protocol efficiently and safely excluded PE in 79% of the patients studied.

DISCLOSURE

No potential conflict of interest relevant to this article was reported.

ACKNOWLEDGMENTS

We gratefully acknowledge the selfless contribution of our technologists and front-line staff, who faithfully provide compassionate and expert care.

KEY POINTS

QUESTION: Is the POS algorithm, introduced during the COVID-19 surge to assess for pulmonary embolus, an efficient and safe method of evaluation?

PERTINENT FINDINGS: We retrospectively analyzed chart data from 57 patients studied over the initial 60 d of the COVID-19 surge. POS was able to efficiently exclude PE in 79% of patients and was accurate and safe as determined by follow-up imaging and hospital discharge.

IMPLICATIONS FOR PATIENT CARE: POS protocols can safely be implemented when ventilation scintigraphy cannot be performed and serve to efficiently exclude PE in most patients.

REFERENCES

1. Zuckier LS, Moadel RM, Haramati LB, Freeman LM. Diagnostic evaluation of pulmonary embolism during the COVID-19 pandemic. *J Nucl Med.* 2020; 61: 630–631.
2. Sheen JJ, Haramati LB, Natenzon A, et al. Performance of low-dose perfusion scintigraphy and CT pulmonary angiography for pulmonary embolism in pregnancy. *Chest.* 2018;153:152–160.
3. Parker JA, Coleman RE, Grady E, et al. SNM practice guideline for lung scintigraphy 4.0. *J Nucl Med Technol.* 2012;40:57–65.
4. Zuckier LS. To everything there is a season: taxonomy of approaches to the performance of lung scintigraphy in the era of COVID-19. *Eur J Nucl Med Mol Imaging.* 2021;48:666–669.
5. Le Roux PY, Pelletier-Galarneau M, De Laroche R, et al. Pulmonary scintigraphy for the diagnosis of acute pulmonary embolism: a survey of current practices in Australia, Canada, and France. *J Nucl Med.* 2015;56:1212–1217.
6. Miniati M, Monti S, Bauleo C, et al. A diagnostic strategy for pulmonary embolism based on standardised pretest probability and perfusion lung scanning: a management study. *Eur J Nucl Med Mol Imaging.* 2003;30: 1450–1456.
7. Das JP, Yeh R, Schöder H. Clinical utility of perfusion (Q)-single-photon emission computed tomography (SPECT)/CT for diagnosing pulmonary embolus (PE) in COVID-19 patients with a moderate to high pre-test probability of PE. *Eur J Nucl Med Mol Imaging.* 2021;48:794–799.
8. Lu Y, Macapinlac HA. Perfusion SPECT/CT to diagnose pulmonary embolism during COVID-19 pandemic. *Eur J Nucl Med Mol Imaging.* 2020;47: 2064–2065.
9. Boone SL, Zuckier LS. Ventilation-perfusion scans after the COVID-19 pandemic: point-ventilation studies are dispensable. *AJR.* November 3, 2021 [Epub ahead of print].

^{18}F-FDG PET in Myocardial Viability Assessment: A Practical and Time-Efficient Protocol

Joyce Mhlanga[1], Paul Derenoncourt[1], Adeel Haq[1], Anita Bhandiwad[2], Richard Laforest[1], Barry A. Siegel[1], Farrokh Dehdashti[1], Robert J. Gropler[1,2], and Thomas H. Schindler[1,2]

[1]*Division of Nuclear Medicine, Mallinckrodt Institute of Radiology, Washington University School of Medicine, St. Louis, Missouri; and* [2]*Cardiovascular Division, John T. Milliken Department of Internal Medicine, Washington University School of Medicine, St. Louis, Missouri*

We assessed image quality using a practical and time-efficient protocol for intravenous glucose loading and insulin injection before administration of ^{18}F-FDG for PET myocardial viability evaluation in patients with ischemic cardiomyopathy (ICM), with and without type 2 diabetes mellitus. **Methods:** The metabolic preparation period (MPP) or optimal cardiac ^{18}F-FDG uptake was determined from the time of intravenous infusion of 12.5 or 25 g of 50% dextrose to the time of ^{18}F-FDG injection. Cardiac ^{18}F-FDG image quality was evaluated according to a 5-point scoring system (from 5, excellent, to 1, nondiagnostic) by 2 independent observers. In cases of disagreement, consensus was achieved in a joint reading. Fifteen patients with ICM who underwent oral glucose loading and intravenous insulin administration served as a reference for MPP comparisons. **Results:** Fifty-nine consecutive patients (age, 63 ± 10 y; 48 men and 11 women) underwent rest ^{99m}Tc-tetrofosmin SPECT/CT and ^{18}F-FDG PET/CT for the evaluation of myocardial viability. ^{18}F-FDG image quality was scored as excellent in 42%, very good in 36%, good in 17%, fair in 3%, and nondiagnostic in 2%. When diabetic and nondiabetic patients were compared, the quality scores were excellent in 29% versus 76%, very good in 41% versus 18%, good in 24% versus 6%, fair in 4% versus 0%, and nondiagnostic in 2% versus 0%. The mean (±SD) quality score was 4.12 ± 0.95, and overall it was better in nondiabetic than in diabetic patients (4.71 ± 0.59 vs. 3.88 ± 0.96; $P < 0.0001$). Notably, the average MPP was significantly less with intravenous glucose loading than with oral glucose loading (51 ± 15 min vs. 132 ± 29 min; $P < 0.0001$), paralleled by higher insulin doses (6.3 ± 2.2 U vs. 2.0 ± 1.69 U; $P < 0.001$). **Conclusion:** Using a practical and time-efficient protocol for intravenous glucose loading and insulin administration before ^{18}F-FDG injection reduces the MPP by 61% as compared with an oral glucose challenge and affords good-to-excellent image quality in 95% of ICM patients.

Key Words: coronary artery disease; ^{18}F-FDG; hibernation; myocardial perfusion; myocardial viability; SPECT; PET

J Nucl Med 2022; 63:602–608
DOI: 10.2967/jnumed.121.262432

Numerous clinical investigations (*1*) have documented that, in patients with ischemic cardiomyopathy (ICM), timely coronary revascularization to restore myocardial perfusion of ischemic, jeopardized viable myocardium improves heart failure symptoms and prognosis. ^{18}F-FDG PET and ^{99m}Tc SPECT afford high diagnostic accuracy for the detection and characterization of a perfusion–metabolism mismatch (*2,3*). Myocardium exhibiting this pattern in conjunction with segmental severe hypokinesis or akinesis is commonly referred to as hibernating myocardium and has a high probability of regaining myocardial contractility with timely revascularization (*1,3,4*). Accurate assessment of the extent and severity of the perfusion–metabolism mismatch is critical to define those ICM patients in whom early restoration of coronary blood flow will improve left ventricular function and cardiovascular outcome (*5,6*).

Although ^{18}F-FDG PET is the most sensitive imaging method for detecting viable, hibernating myocardium, the procedure commonly necessitates a tedious, time-consuming protocol of glucose loading and insulin administration to achieve the myocardial ^{18}F-FDG uptake that optimizes diagnostic accuracy (*7*). Particularly in diabetic patients, frequent blood glucose monitoring and supplemental insulin administration may lead to a significant delay in PET image acquisition and, thus, logistical problems in a busy clinical PET facility (*7*). Several protocols of glucose loading with insulin administration have been proposed for ^{18}F-FDG PET myocardial viability assessment in routine clinical practice (*7*). In this study, we evaluated a practical and time-efficient intravenous glucose loading and insulin administration protocol and assessed the quality of cardiac ^{18}F-FDG PET images for viability assessment in diabetic and nondiabetic patients with ICM.

MATERIALS AND METHODS

Study Population

The study population consisted of 59 patients with ICM who underwent ^{99m}Tc-tetrofosmin SPECT/CT followed by intravenous glucose loading and insulin injection before ^{18}F-FDG PET/CT (Table 1). The patients were referred for the evaluation of myocardial viability between September 2018 and July 2020. In addition, a group of 15 consecutive patients with ICM (56 ± 8 y old, 12 men and 3 women, 13 with diabetes and 2 without) underwent the same imaging protocol but with oral glucose loading and intravenous insulin administration (*7*), between March 2016 and September 2018. The Washington University institutional review board approved this retrospective study and waived the requirement for informed consent.

Cardiac SPECT/CT and PET/CT are described in detail in the supplemental materials (available at http://jnm.snmjournals.org).

Metabolic Preparation Protocol

Patients on oral antidiabetic medication or an insulin regimen were classified as patients with known and treated diabetes mellitus

Received Apr. 12, 2021; revision accepted Aug. 13, 2021.
For correspondence or reprints, contact Thomas Hellmut Schindler (thschindler@wustl.edu).
Published online Sep. 9, 2021.
COPYRIGHT © 2022 by the Society of Nuclear Medicine and Molecular Imaging.

TABLE 1
Patient and Study Characteristics

Characteristic	All	Diabetic	Nondiabetic
Patient characteristics			
n	59	42	17
Age (y)	62 ± 10	63 ± 11	62 ± 11
Sex			
Male	48	32	16
Female	11	10	1
Ejection fraction (%)	29 ± 10	30 ± 9	27 ± 9
Prior CABG	4	3	1
Prior PTCA	5	3	2
Prior myocardial infarction	43 (73%)	27 (64%)	16 (94%)
Hypertension	57 (96%)	25 (60%)	16 (94%)
Smoking	39 (66%)	28 (67%)	11 (65%)
Dyslipidemia	53 (90%)	38 (90%)	15 (88%)
Diabetes mellitus	42 (71%)	42 (100%)	0 (0%)
Study characteristics with intravenous glucose load			
Glucose at baseline (mg/dL)	121 ± 32 (70–214)	131 ± 33 (70–214)	97 ± 11* (83–122)
Glucose peak after challenge (mg/dL)	184 ± 31 (124–304)	188 ± 33 (126–304)	175 ± 24 (124–203)
Glucose before imaging (mg/dL)	101 ± 25 (62–166)	108 ± 24 (63–166)	87 ± 20* (62–146)
Insulin (U)	6.3 ± 2.2 (2–11)	6.8 ± 2.3 (2–11)	4.9 ± 1.3* (*3–8*)
MPP (min)	51 ± 15 (25–89)	51 ± 16 (25–85)	50 ± 14 (30–89)
^{18}F-FDG uptake period (min)	82 ± 19 (52–122)	86 ± 19 (52–122)	74 ± 17* (54–115)
Preparation period (min)	133 ± 26 (83/190)	137 ± 25 (83–190)	124 ± 25 (92–184)
Study characteristics with oral glucose load			
Glucose at baseline (mg/dL)	99 ± 9 (84–112)	105 ± 5 (101–112)	91 ± 7* (84–99)
Glucose peak after challenge (mg/dL)	158 ± 26 (123–187)	171 ± 11 (164–187)	146 ± 32* (116–185)
Glucose before imaging (mg/dL)	105 ± 23 (76–144)	101 ± 23 (76–129)	108 ± 28 (82–144)
Insulin U)	2.0 ± 1.69 (0–5)	3.0 ± 1.63 (1–5)	1.0 ± 1.16* (0–2)
MPP (min)	132 ± 29 (90–180)	141 ± 31 (110–180)	122 ± 28* (90–158)
^{18}F-FDG uptake period (min)	72 ± 15 (57–98)	64 ± 11 (57–80)	80 ± 17*(62–98)
Preparation period (min)	203 ± 25 (167–237)	205 ± 33 (167–237)	201 ± 19 (187–228)

*$P \leq 0.05$ vs. diabetic group.

CABG = coronary artery bypass surgery; PTCA = percutaneous transluminal coronary angioplasty; ^{18}F-FDG uptake period = time from ^{18}F-FDG injection to start of imaging; preparation period = time from start of MPP to start of imaging.

Qualitative data are number and percentage; continuous data are mean and range.

(n = 39). Patients without antidiabetic medication but with elevated fasting blood glucose levels (≥125 mg/dL) at the time of the PET study were also assigned to the diabetic group (n = 3) (Table 1). The metabolic preparation period (MPP) was defined as the period between intravenous infusion of 12.5 or 25 g of 50% dextrose in 50 mL of water and ^{18}F-FDG injection. All patients were studied after an overnight fast. The metabolic preparation protocol was performed by a highly skilled nurse in a dedicated preparation room, and patients were moved and positioned in the PET/CT scanner about 10 min before the scan was started. However, blood glucose levels were measured at baseline at the start of the MPP (Fig. 1). When baseline serum glucose levels were less than 125 mg/dL, 25 g of 50% dextrose in 50 mL of water were slowly infused intravenously, whereas when baseline serum glucose were 125–140 mg/dL, only 12.5 g of 50% dextrose in 50 mL of water were slowly infused intravenously. Postchallenge serum glucose levels were measured after a 20-min interval to capture the peak of the serum glucose increase for optimal dosing of insulin administration. If the serum glucose after the glucose challenge was between 140 and 180 mg/dL, insulin was administered intravenously according to the insulin protocol shown in Table 2, followed immediately by intravenous injection of approximately 370 MBq of ^{18}F-FDG. In this lower range of postchallenge serum glucose levels, insulin sensitivity can be assumed sufficient to lead to a marked decrease in serum glucose levels on insulin administration and to effectively drive the ^{18}F-FDG into the myocardium. In the rare case of a patient without an appropriate decline in serum glucose by at least 20 mg/dL, an additional 1–2 U of insulin were injected intravenously to stimulate an appropriate drop in serum glucose and, thus, cardiac ^{18}F-FDG uptake (Fig. 1).

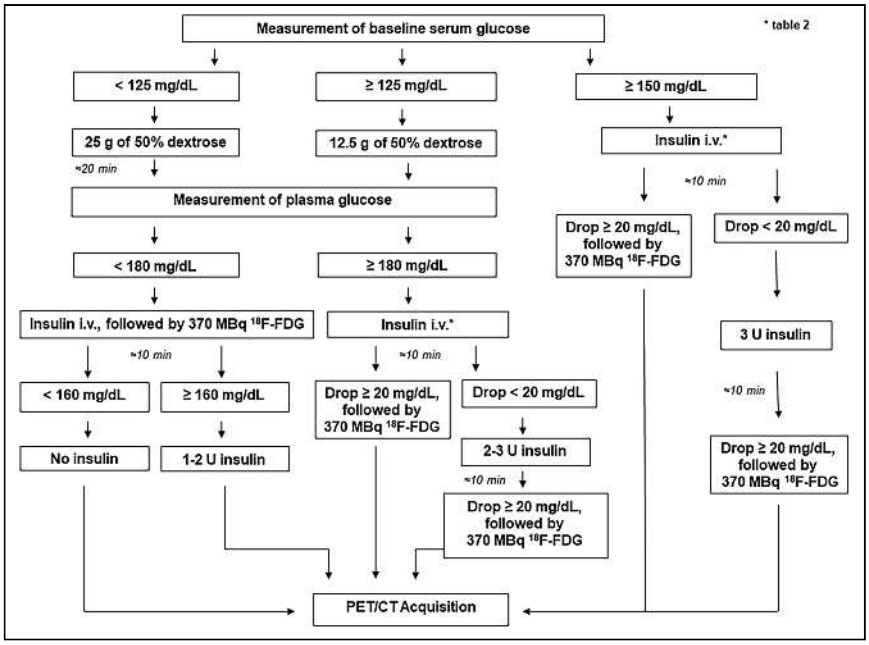

FIGURE 1. Schematic illustration of metabolic preparation protocol based on initial serum glucose levels. i.v. = intravenous.

If the serum glucose after the glucose challenge was at least 180 mg/dL (Fig. 1), insulin was administered intravenously according to the insulin protocol (Table 2) and serum glucose was remeasured 10 min later. The short 10-min interval was chosen because the aim was to verify that insulin had effectively initiated a reduction in postchallenge serum glucose levels and, thus, in effectiveness for driving the ^{18}F-FDG into the myocardium. If the serum glucose declined by at least 20 mg/dL, approximately 370 MBq of ^{18}F-FDG were injected immediately. If the decline in serum glucose was less than 20 mg/dL, another 2–3 U of insulin were administered and serum glucose was measured again after another 10 min. If serum glucose had then declined by at least 20 mg/dL, approximately 370 MBq of ^{18}F-FDG were injected. In diabetic patients arriving with a baseline serum glucose of 150 mg/dL or higher (Fig. 1), no glucose challenge was performed and intravenous insulin was administered according to the insulin protocol (Table 2). If, after 10 min, the serum glucose had then declined by at least 20 mg/dL, approximately 370 MBq of ^{18}F-FDG were injected. If the decline in serum glucose was less than 20 mg/dL, another 3 U of insulin were administered intravenously and serum glucose measured again after another 10 min. If serum glucose had then declined by at least 20 mg/dL, approximately 370 MBq of ^{18}F-FDG were injected. After ^{18}F-FDG injection, serum glucose was monitored every 15–20 min and before and after the 10-min PET/CT image acquisition. If a patient developed symptomatic or asymptomatic hypoglycemia (serum glucose <70 mg/dL) after receiving insulin, the protocol allowed for oral administration of 59–89 mL (2–3 oz) of orange juice to maintain normal blood glucose levels. However, if the orange juice was required within 30 min of the ^{18}F-FDG cardiac uptake period, the study was discontinued since the ^{18}F-FDG PET images were expected to be suboptimal. Patients on oral antidiabetic medication were instructed not to take it in the morning. Patients with insulin-dependent diabetes mellitus were asked to adhere to their regular diet and baseline insulin regimen the day before the study but to fast after midnight and to withhold insulin until the metabolic preparation of the ^{18}F-FDG PET study was begun. If a diabetic patient developed symptomatic or asymptomatic hypoglycemia, because of the fasting state, appropriate food or juice intake at the discretion of the patient was allowed; however, this intake was followed by a 6-h fasting period before the start of the metabolic preparation or glucose challenge for the ^{18}F-FDG PET examination.

TABLE 2
Insulin Dose in Response to Glucose Challenge After Intravenous Infusion of 25 g or 12.5 g of 50% Dextrose in 50 mL of Water in Nondiabetic and Diabetic Patients, Respectively

Serum glucose (mg/dL)	Intravenous insulin dose (regular insulin, U)	
	Nondiabetic	Diabetic
130–140	1	2
>140–150	2	3
>150–160	3	4
>160–170	4	5
>170–180	5	6
>180–200	6	7
>200	7	8

Evaluation of SPECT and PET Images

On the reoriented short- and long-axis myocardial images and the corresponding polar maps, the relative distributions of ^{99m}Tc-tetrofosmin and ^{18}F-FDG uptake were evaluated quantitatively using the standard American Heart Association–recommended 17-segment model and Corridor 4DM (Invia) software. As described previously, and consistent with the guidelines of the American Society of Nuclear Cardiology (*7*), myocardium with the highest ^{99m}Tc-tetrofosmin uptake on the rest perfusion images (5% of the sectors with the highest activity) was defined as 100% and served as a reference for normalization of regional ^{99m}Tc-tetrofosmin and ^{18}F-FDG activity concentrations. Regional ^{99m}Tc-tetrofosmin activity concentrations in the rest images of the patients were compared with a reference database (Corridor 4DM). Corresponding ^{99m}Tc-tetrofosmin and ^{18}F-FDG images were automatically scored quantitatively in all 17 segments by Corridor 4DM software. A 5-point scoring system was used to indicate segmental ^{99m}Tc-tetrofosmin and ^{18}F-FDG uptake (0, normal; 1, mildly reduced; 2, moderately reduced; 3, severely reduced; and 4, absent). Myocardium was defined as normal (and therefore viable) when the ^{99m}Tc-tetrofosmin uptake on SPECT images yielded a score of 0, regardless of the ^{18}F-FDG uptake on PET. A concordant reduction in ^{99m}Tc-tetrofosmin and ^{18}F-FDG activity scores was classified as a perfusion–metabolism match, indicating nonviable myocardium. A reduction in ^{99m}Tc-tetrofosmin uptake more severe than the reduction in ^{18}F-FDG uptake by at least 1 point was defined as a perfusion–metabolism mismatch, indicating viable myocardium. The total myocardial extent of match or mismatch patterns was determined as n/17, where n was the number of segments exhibiting match or mismatch (*2*).

Cardiac ^{18}F-FDG PET Image Quality Analysis

The quality of ^{18}F-FDG PET images was assessed visually by 2 independent experienced nuclear medicine physicians. Nine instances of minor disagreement were settled by a joint consensus reading. Cardiac ^{18}F-FDG image quality was evaluated according to a 5-point

scoring system (5, excellent; 4, very good; 3, good; 2, fair; and 1, nondiagnostic) (Fig. 2).

As resting ischemia may cause a disproportionate increase in ^{18}F-FDG uptake in jeopardized but viable myocardium, likely related to an increase in glucose transporter receptor 4 and other yet unknown factors, the ^{18}F-FDG uptake in the ischemic region may exceed that in the remote and normally perfused myocardium. In addition, this ischemic region with high ^{18}F-FDG uptake then defines the 100% uptake that again leads to a relative downscaling of ^{18}F-FDG signal in the remote nonischemic myocardium. Apart from the intensity of the homogeneous or heterogeneous myocardial ^{18}F-FDG uptake, the residual ^{18}F-FDG blood activity served as a second evaluation criterion. Accordingly, excellent image quality (score 5) was defined as homogeneous or heterogeneous ^{18}F-FDG signal and no blood-pool activity; very good image quality (score 4), as homogeneous or heterogeneous ^{18}F-FDG signal and mild blood-pool activity; good image quality (score 3), as homogeneous or heterogeneous ^{18}F-FDG signal and moderate blood-pool activity; fair image quality (score 2), as homogeneous or heterogeneous ^{18}F-FDG signal and high blood-pool activity; and nondiagnostic image quality (score 1), as low or no homogenous or heterogenous ^{18}F-FDG signal and high blood-pool activity. In addition, the absolute counts of the left ventricular ^{18}F-FDG uptake were automatically displayed for the left anterior descending, left circumflex, and right coronary artery distributions on the polar map analysis, and the averaged value of the left ventricle was calculated.

Statistical Analysis

Data are presented as mean ± SD for quantitative variables and as absolute frequencies for qualitative variables. The appropriate Wilcoxon rank test for independent or paired samples was used. The different groups were compared by 1-way ANOVA, followed by Scheffé multiple-comparison tests. Statistical significance was assumed if a null hypothesis could be rejected at a P value of less than 0.05. All statistical analyses were performed with SPSS 22.0 (IBM) for Microsoft Windows.

RESULTS

Clinical and Study Characteristics

The characteristics of the study population are given in Table 1. Coronary angiography revealed coronary lesions in all patients, defined as at least a 50% narrowing of an epicardial artery (1 vessel in 9 patients [15%], 2 in 15 [25%], and 3 in 43 [73%]). Serum glucose levels at baseline and the dose of insulin were significantly higher in diabetic than in nondiabetic patients, whereas serum glucose levels after the intravenous glucose challenge did not differ significantly between groups (Table 1). Interestingly, when compared with the group with oral glucose loading, both the groups and the subgroups of diabetic and nondiabetic patients with intravenous glucose loading showed no significant difference in baseline serum glucose levels ($P = 0.06$), whereas peak serum glucose levels after the glucose challenge were significantly less with oral than with intravenous glucose loading both in the groups and in the subgroups ($P \leq 0.05$) (Table 1). Accordingly, the dose of intravenous insulin was also significantly less in the group with oral glucose loading than in the group with intravenous glucose loading ($P < 0.0001$) (Table 1). For the whole study group with intravenous glucose loading, the MPP averaged 51 ± 15 min and did not differ between diabetic and nondiabetic patients (51 ± 16 and 50 ± 14 min, respectively) (Table 1). However, in the group with oral glucose loading, the mean MMP was significantly longer than in the intravenous glucose loading group (132 ± 29 vs. 51 ± 15 min, $P < 0.0001$) and in the subgroups of diabetic and nondiabetic patients (141 ± 31 vs. 51 ± 16 min and 122 ± 28 vs. 50 ± 14 min, respectively; $P < 0.0001$).

With the intravenous glucose protocol, administration of a small amount of orange juice was necessary in 11 patients (19%) whose serum glucose levels decreased below 70 mg/dL (Table 3), whereas this was not necessary for the group receiving oral glucose loading. Nine of the patients in the intravenous glucose cohort developed hypoglycemia that did not become symptomatic, likely because of timely administration of orange juice to restore normal blood glucose levels. Two patients had hypoglycemia with minor symptoms—such as dizziness, headache, or sweating—that were resolved immediately by administration of orange juice (Table 3).

Imaging Results and Quality Assessment

Combined ^{99m}Tc-SPECT and ^{18}F-FDG PET demonstrated ischemic, compromised, but predominantly viable myocardium in most patients (75%; $n = 44$) with ICM (Figs. 3 and 4; Supplemental Figs. 1 and 2 with quantitative polar map display). Of the 59 patients who were studied, standard quantitative polar map analysis showed perfusion– metabolic mismatches (viable myocardium) in 44 (75%), and 15 (25%) had perfusion–metabolic matches (nonviable myocardium). Both mismatches and matches coexisted in 26 patients (44%). For the whole study population, the total mismatch score in viable myocardium was 17 ± 9. When evaluated in relation to arterial territory, the regional mismatch score was 8 ± 5 for the left anterior descending coronary artery distribution, 5 ± 4 for the left circumflex coronary artery distribution, and 4 ± 3 for the right coronary artery distribution. Regarding myocardial ^{18}F-FDG image quality assessment, the mean quality score in the study population was 4.12 ± 0.95, and overall it was better in nondiabetic than in diabetic patients (4.71 ± 0.59 vs. 3.88 ± 0.96; $P \leq 0.0001$). For the total study population, myocardial ^{18}F-FDG PET images were scored as excellent in 42% ($n = 25$), very

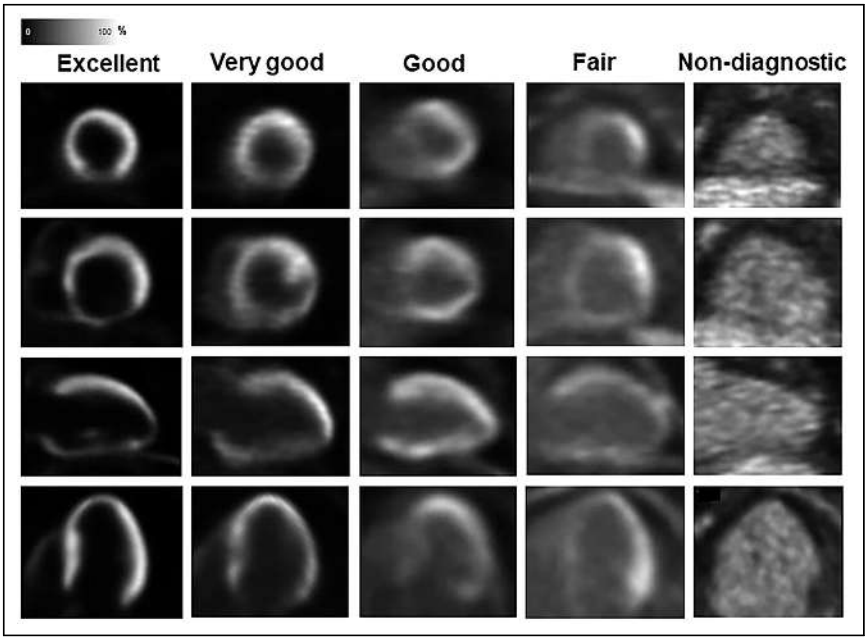

FIGURE 2. Myocardial ^{18}F-FDG image quality was evaluated according to 5-point score system.

TABLE 3
Hypoglycemia and Adverse Side Effects of Intravenous Insulin Administration in Response to Intravenous Glucose Challenge in Nondiabetic and Diabetic Patients, Respectively

Side effect	Nondiabetic	Diabetic
Hypoglycemia without symptoms	4	5
Hypoglycemia with symptoms	1	1
Dizziness or light-headedness	1	0
Headache	0	1
Shakiness	0	1
Irritability	0	0
Sweating	1	0
Blurred vision	0	0
Fast heart rate	0	0
Mood change	0	0
Confusion	0	0
Slurred speech	0	0
Anxiety	0	0
Hunger	0	0
Allergic reactions	0	0
Rash	0	0

Hypoglycemia is defined as serum glucose < 70 mg/dL.

good in 36% (n = 21), good in 17% (n = 10), fair in 3% (n = 2), and nondiagnostic in 2% (n = 1) (Fig. 5). Comparing diabetic and nondiabetic patients, the quality scores were excellent in 29% (n = 12) versus 76% (n = 13), very good in 41% (n = 17) versus 18% (n = 3), good in 24% (n = 10) versus 6% (n = 1), fair in 4% (n = 2) versus 0% (n = 0), and nondiagnostic in 2% (n = 1) versus 0% (n = 0) (Fig. 4B). Thus, the most diagnostic ^{18}F-FDG image quality in diabetic patients was very good, at 41%, and in nondiabetic patients it was predominantly excellent, at 76%. Notably, there was a significant and progressive decrease in the left ventricular absolute count statistics of ^{18}F-FDG uptake on polar map analysis from excellent ^{18}F-FDG uptake scores to very good, good, fair, and nondiagnostic (score 5, 21,671 ± 7,802; score 4, 13,652 ± 7,430; score 3, 7,281 ± 2,734; score 2, 3,847 ± 56; and score 1, 2,121 counts [$P < 0.0001$ by ANOVA]).

DISCUSSION

The current study is unique in demonstrating a practical and time-efficient protocol for intravenous glucose loading and insulin injection before intravenous ^{18}F-FDG injection that affords good-to-excellent image quality in 95% of patients with ICM. Notably, the ^{18}F-FDG image quality with our protocol is in keeping with the findings of previous studies (*2,5,6,8,9*) and is maintained despite our shortened metabolic preparation protocol, even in diabetic patients, as compared with oral glucose loading.

Although myocardial ^{18}F-FDG PET may be considered the reference standard among cardiac imaging modalities for the detection of viability in dysfunctional myocardium (*3,4,10*), the metabolic preparation protocol for this test needed to achieve optimal myocardial ^{18}F-FDG uptake, and thus, image quality is commonly quite complex and time-consuming (*7*). It is well known that, in fasting nondiabetic subjects, 40%–60% of myocardial ^{18}F-FDG PET scans may be uninterpretable because of low radiotracer uptake and significant regional heterogeneity, reflecting predominant reliance of the heart on free fatty acids as a source of energy (*7,11*). In this respect, oral or intravenous glucose loading has been used to stimulate endogenous insulin release to enhance the myocardial uptake of glucose and, thus, of ^{18}F-FDG. Standard protocols have typically involved oral administration of 50–100 g of dextrose solution to fasting patients followed by intravenous injection of ^{18}F-FDG intravenously 60–90 min later (*7*). However, oral glucose administration without insulin injection yielded poor cardiac image quality in 2%–33% of patients, including nondiabetic patients (*12,13*). With intravenous administration of insulin for elevated serum glucose levels after oral glucose loading, the rate of poor image quality could be substantially reduced to 8%–15% (*14,15*). One important limitation of oral glucose loading is the long MPP because of a large proportion of patients with undiagnosed impaired glucose tolerance or insulin resistance, as well as a variability in the rate of intestinal glucose absorption (*7,15*). The MPP of oral glucose loading with insulin administration may

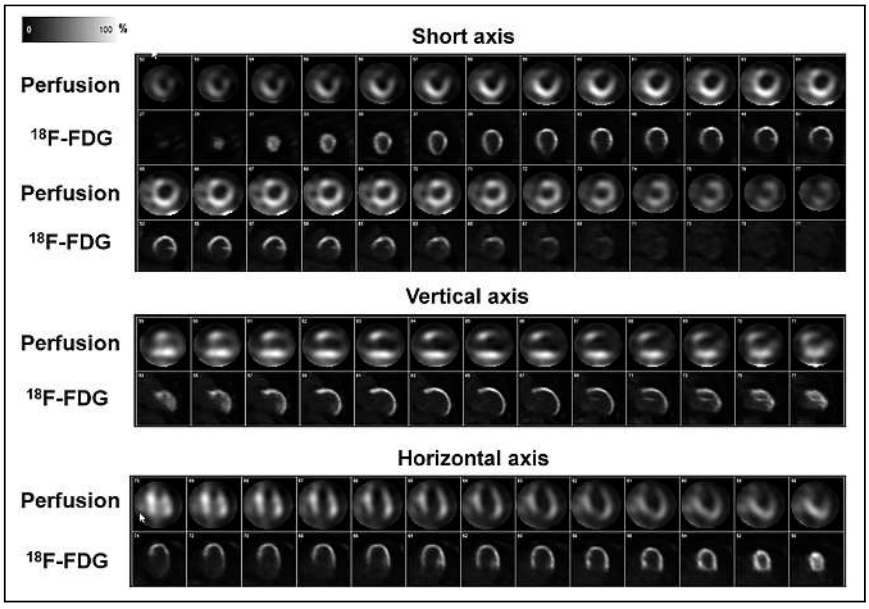

FIGURE 3. Rest myocardial perfusion ^{99m}Tc-tetrofosmin SPECT/CT images demonstrating mismatch with ^{18}F-FDG PET/CT images in patient with dilated ICM. SPECT/CT shows severe perfusion defect in predominantly akinetic anteroseptoapical, apical, and anterolateral walls, whereas PET shows normal or upregulated ^{18}F-FDG uptake, consistent with hibernating myocardium. Given the disproportionately high ^{18}F-FDG uptake in mismatch regions (reflecting 100% reference for signal normalization), some remaining myocardium demonstrates mildly lower or no ^{18}F-FDG signal (e.g., inferoseptal and inferior wall segments, respectively) associated with normal rest perfusion (reverse mismatch), indicating viability in these segments.

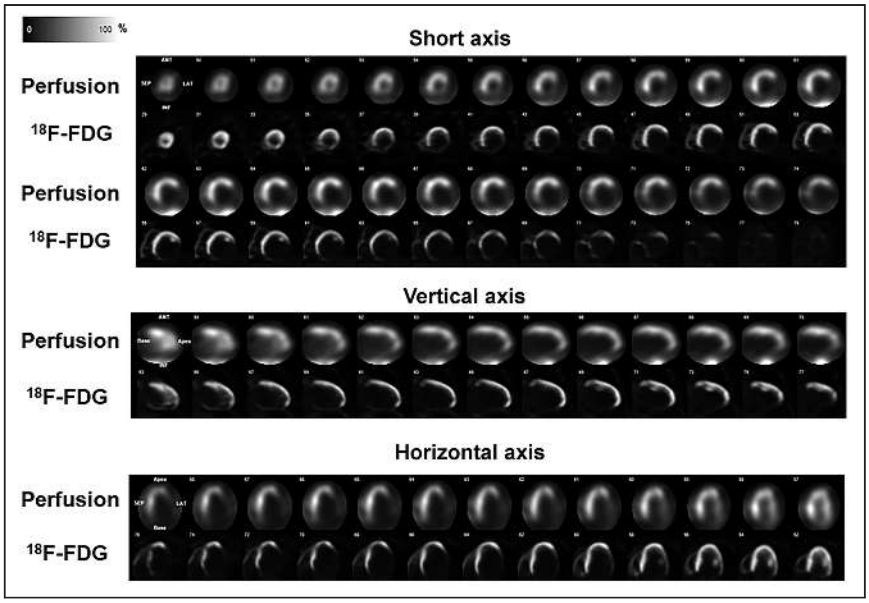

FIGURE 4. Rest myocardial perfusion ^{99m}Tc-tetrofosmin SPECT/CT images demonstrating match with ^{18}F-FDG PET/CT images in patient with ICM. ^{99m}Tc-SPECT/CT shows severe perfusion defect in inferior and inferolateral walls, with mild extension inferoseptally and laterally, and PET shows predominant absence of ^{18}F-FDG uptake. Thus, findings match, with concordant absence of perfusion and viability to signify predominantly transmural necrosis in left circumflex and right coronary artery distribution.

therefore be 120–160 min. The current approach with intravenous glucose loading and insulin administration had an average MPP of approximately only 51 min as compared with approximately 132 min when we used oral glucose loading with subsequent insulin administration. The substantially shorter MPP with intravenous glucose loading likely is related to a markedly higher serum glucose peak with subsequently higher insulin dose administration, as compared with oral glucose loading, which is commonly associated with delayed and variable intestinal glucose absorption and a substantially lower glucose peak necessitating lower insulin doses. Higher peak glucose levels with intravenous glucose loading not only necessitate a substantially higher dose of insulin but also stimulate greater endogenous release of insulin from pancreatic β-cells. Thus, the blood insulin levels can be assumed to be much higher than those achieved with oral glucose loading; this, in turn, will lead to greater myocardial ^{18}F-FDG uptake, resulting in good-to-excellent image quality in most patients. Further, the metabolic preparation time did not differ between diabetic and nondiabetic patients with intravenous glucose loading, likely related to the significantly higher insulin doses applied in diabetic patients after a glucose challenge.

This practical and time-efficient MPP offers the advantage that the injection and myocardial uptake of ^{18}F-FDG are occurring when the effect of insulin likely is maximal. Similar protocols have recommended delaying ^{18}F-FDG injection until the serum glucose level decreases below 125–140 mg/dL after insulin injection (*7*). This, however, necessitates repeat assessments of serum glucose and carries the risk of missing the maximal insulin effect required to drive the ^{18}F-FDG into the myocardium, resulting in suboptimal image quality. When compared with protocols using oral glucose loading, the advantage of the proposed protocol with an average MPP of 51 min is the ability to better plan the timing of the PET scan while maintaining diagnostic image quality even in diabetic patients. After ^{18}F-FDG injection, we typically aimed for 60- and 90-min cardiac uptake periods in nondiabetic and diabetic patients, respectively. The average ^{18}F-FDG uptake period in the whole study population was 82 min (86 min in diabetic patients and 74 min in nondiabetic patients). The difference from our planned goals reflects the scanner availability in routine clinical practice.

Our protocol allowed administering orange juice orally after an ^{18}F-FDG uptake period of at least 30 min if serum glucose levels decreased below 70 mg/dL after insulin administration. This was necessary in 11 (19%) of our patients, and 2 of these had symptoms, which were mild and resolved immediately after ingestion of orange juice. The fact that none of the patients had severe side effects emphasizes the safety profile of the proposed protocol despite administration of higher insulin doses than with an oral glucose challenge.

CONCLUSION

A clinically practical and time-efficient protocol for intravenous glucose loading and insulin injection before ^{18}F-FDG injection reduces the MPP by 61% as compared with an oral glucose challenge. The intravenous protocol is safe and affords good-to-excellent diagnostic image quality in 95% of patients with ICM. This protocol holds promise to improve the application and efficacy of ^{18}F-FDG PET–determined myocardial viability in routine clinical practice.

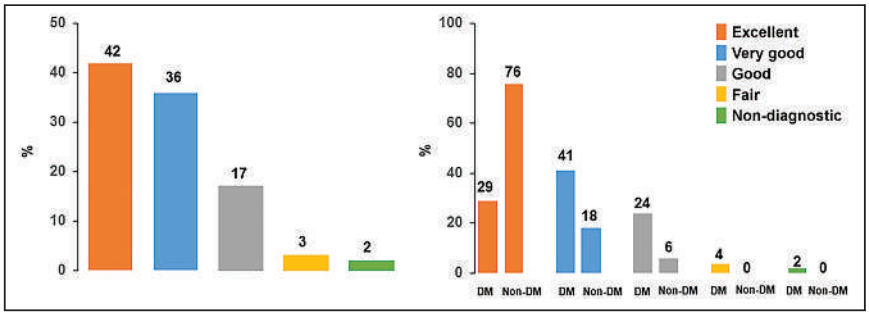

FIGURE 5. Distribution of myocardial ^{18}F-FDG image quality scores in whole study population (left) and when subgrouped and compared between those with diabetes mellitus (DM) and those without (right).

DISCLOSURE

This work was supported by a departmental fund from Washington University. No other potential conflict of interest relevant to this article was reported.

ACKNOWLEDGMENTS

We are indebted to Lisa Konrad, Martin Schmitt, and the technical staff of the

Division of Nuclear Medicine for their technical assistance and support.

KEY POINTS

QUESTION: Is it feasible to apply a practical and time-efficient protocol for intravenous glucose loading and insulin injection before ^{18}F-FDG injection, while maintaining safety and the diagnostic quality of myocardial ^{18}F-FDG PET images?

PERTINENT FINDINGS: The shortened metabolic preparation protocol with intravenous glucose loading, insulin injection, and ^{18}F-FDG injection consistently yielded good-to-excellent diagnostic image quality even in diabetic patients with ICM.

IMPLICATIONS FOR PATIENT CARE: The suggested protocol is safe, practical, and should enhance the clinical application and cost-effectiveness of ^{18}F-FDG PET for the detection and characterization of viable myocardium.

REFERENCES

1. Allman KC, Shaw LJ, Hachamovitch R, Udelson JE. Myocardial viability testing and impact of revascularization on prognosis in patients with coronary artery disease and left ventricular dysfunction: a meta-analysis. *J Am Coll Cardiol.* 2002;39:1151–1158.
2. Auerbach MA, Schoder H, Hoh C, et al. Prevalence of myocardial viability as detected by positron emission tomography in patients with ischemic cardiomyopathy. *Circulation.* 1999;99:2921–2926.
3. Valenta I, Quercioli A, Ruddy T, Schindler TH. Assessment of myocardial viability after the STICH trial: still viable? *Cardiovasc Med.* 2013;16:289–298.
4. Schinkel AF, Bax JJ, Poldermans D, Elhendy A, Ferrari R, Rahimtoola SH. Hibernating myocardium: diagnosis and patient outcomes. *Curr Probl Cardiol.* 2007;32:375–410.
5. Di Carli MF, Asgarzadie F, Schelbert HR, et al. Quantitative relation between myocardial viability and improvement in heart failure symptoms after revascularization in patients with ischemic cardiomyopathy. *Circulation.* 1995;92:3436–3444.
6. Tillisch J, Brunken R, Marshall R, et al. Reversibility of cardiac wall-motion abnormalities predicted by positron tomography. *N Engl J Med.* 1986;314:884–888.
7. Dilsizian V, Bacharach SL, Beanlands RS, et al. PET myocardial perfusion and metabolism clinical imaging. *J Nucl Cardiol.* 2009;16:651.
8. Sun XX, Li S, Fang W, et al. Preserved myocardial viability in patients with-chronic total occlusion of a single coronary artery. *J Nucl Cardiol.* 2021;28:2812–2822.
9. Kiko T, Yokokawa T, Misaka T, et al. Myocardial viability with chronic total occlusion assessed by hybrid positron emission tomography/magnetic resonance imaging. *J Nucl Cardiol.* 2021;28:2335–2342.
10. Wu YW, Tadamura E, Yamamuro M, et al. Comparison of contrast-enhanced MRI with ^{18}F-FDG PET/^{201}Tl SPECT in dysfunctional myocardium: relation to early functional outcome after surgical revascularization in chronic ischemic heart disease. *J Nucl Med.* 2007;48:1096–1103.
11. Gropler RJ, Siegel BA, Lee KJ, et al. Nonuniformity in myocardial accumulation of fluorine-18-fluorodeoxyglucose in normal fasted humans. *J Nucl Med.* 1990;31:1749–1756.
12. Eitzman D, al-Aouar Z, Kanter HL, et al. Clinical outcome of patients with advanced coronary artery disease after viability studies with positron emission tomography. *J Am Coll Cardiol.* 1992;20:559–565.
13. Berry JJ, Baker JA, Pieper KS, Hanson MW, Hoffman JM, Coleman RE. The effect of metabolic milieu on cardiac PET imaging using fluorine-18-deoxyglucose and nitrogen-13-ammonia in normal volunteers. *J Nucl Med.* 1991;32:1518–1525.
14. Hicks RJ, Herman WH, Kalff V, et al. Quantitative evaluation of regional substrate metabolism in the human heart by positron emission tomography. *J Am Coll Cardiol.* 1991;18:101–111.
15. Schelbert HR. Euglycemic hyperinsulinemic clamp and oral glucose load in stimulating myocardial glucose utilization during positron emission tomography. *J Nucl Med.* 1992;33:1263–1266.

Imaging Pituitary Vasopressin 1B Receptor in Humans with the PET Radiotracer ^{11}C-TASP699

Mika Naganawa[1], Nabeel B. Nabulsi[1], David Matuskey[1], Shannan Henry[1], Jim Ropchan[1], Shu-Fei Lin[1], Hong Gao[1], Richard Pracitto[1], David Labaree[1], Ming-Rong Zhang[2], Tetsuya Suhara[2], Izumi Nishino[3], Helene Sabia[4], Satoshi Ozaki[4], Yiyun Huang[1], and Richard E. Carson[1]

[1]*Yale PET Center, Department of Radiology and Biomedical Imaging, Yale University, New Haven, Connecticut;* [2]*National Institutes for Quantum and Radiological Science and Technology, Chiba, Japan;* [3]*Taisho Pharmaceutical Co., Ltd., Tokyo, Japan; and* [4]*Taisho Pharmaceutical R&D Inc., Morristown, New Jersey*

Arginine vasopressin is a hormone that is synthesized mainly in the hypothalamus and stored in the posterior pituitary. Receptors for vasopressin are categorized into at least 3 subtypes (V_{1A}, V_{1B}, and V_2). Among these subtypes, the V_{1B} receptor (V_{1B}R), highly expressed in the pituitary, is a primary regulator of hypothalamic-pituitary-adrenal axis activity and thus a potential target for treatment of neuropsychiatric disorders such as depression and anxiety. *N-tert*-butyl-2-[2-(6-methoxypyridine-2-yl)-6-[3-(morpholin-4-yl)propoxy]-4-oxopyrido[2,3-d]-pyrimidin-3(4*H*)-yl]acetamide (TASP699) is a novel PET radiotracer with high affinity and selectivity for V_{1B}R. The purpose of this study was to characterize the pharmacokinetic and binding profiles of ^{11}C-TASP699 in humans and determine its utility in an occupancy study of a novel V_{1B}R antagonist, TS-121. **Methods:** Six healthy subjects were scanned twice with ^{11}C-TASP699 to determine the most appropriate kinetic model for analysis of imaging data and test–retest reproducibility of outcome measures. Nine healthy subjects were scanned before and after administration of TS-121 (active component: THY1773) to assess V_{1B}R occupancy. Metabolite-corrected arterial input functions were obtained. Pituitary time–activity curves were analyzed with 1- and 2-tissue-compartment (1TC and 2TC, respectively) models and multilinear analysis 1 (MA1) to calculate distribution volume (V_T). Relative test–retest variability (TRV) and absolute TRV were calculated. Since no brain region could be used as a reference region, percentage change in V_T after TS-121 administration was computed to assess its receptor occupancy and correlate with plasma concentrations of the drug. **Results:** ^{11}C-TASP699 showed high uptake in the pituitary and no uptake in any brain region. The 2TC model provided better fits than the 1TC model. Because the MA1 V_T estimates were similar to the 2TC V_T estimates, MA1 was the model of choice. The TRV of V_T was good (TRV, $-2\% \pm 14\%$; absolute TRV, 11%). THY1773 reduced V_T in a dose-dependent fashion, with a half-maximal inhibitory concentration of 177 $\pm$ 52 ng/mL in plasma concentration. There were no adverse events resulting in discontinuation from the study. **Conclusion:** ^{11}C-TASP699 was shown to display appropriate kinetics in humans, with substantial specific binding and good reproducibility of V_T. Therefore, this tracer is suitable for measurement of V_{1B}R in the human pituitary and the V_{1B}R occupancy of TS-121, a novel V_{1B}R antagonist.

Key Words: PET; kinetic modeling; receptor imaging; pituitary; vasopressin V_{1B} receptor

J Nucl Med 2022; 63:609–614
DOI: 10.2967/jnumed.121.262430

Arginine vasopressin (AVP) is a key regulator of the hypothalamic-pituitary-adrenal axis. In response to stress exposure, AVP potentiates the effects of corticotropin-releasing factor on adrenocorticotropin release from pituitary corticotrophs (*1*). Among the 3 vasopressin receptor subtypes (V_{1A}, V_{1B}, and V_2), the V_{1B} receptor (V_{1B}R), which is expressed abundantly in the anterior pituitary (*2*), mediates the pituitary actions of AVP and regulates hypothalamic-pituitary-adrenal axis activity (*3*).

Several clinical studies have reported on the role of AVP in stress-related disorders. For example, AVP plasma levels were elevated in patients with major depressive disorder in comparison with healthy controls (*4*) and in depression with anxiety and slowed psychomotor activity (*5*). Cerebrospinal fluid AVP levels significantly decreased in patients who have major depressive disorder treated with the antidepressant fluoxetine, which is accompanied by a decrease in depression scores (*6*). In general, hyperactivity of the hypothalamic-pituitary-adrenal axis is a common finding in depression (*7,8*) and is thus a target of antidepressant treatment. These findings suggest that V_{1B}R antagonists may be indicated in the treatment of major depressive disorder via reducing hypothalamic-pituitary-adrenal axis activity (*9,10*).

Development of V_{1B}R imaging agents for PET will permit the in vivo characterization of this receptor subtype in humans, as well as accurate quantification of target engagement by drug candidates. To date, such development has been hampered by a lack of selective V_{1B}R ligands. A nonpeptide V_{1B}R antagonist, ^{11}C-SSR149415, was evaluated in nonhuman primates and shown to have minimal uptake in the brain and high uptake in the pituitary (*11*). However, human imaging of ^{11}C-SSR149415 has not been reported. More recently, a novel pyridopyrimidin-4-one analog, *N-tert*-butyl-2-[2-(6-methoxypyridine-2-yl)-6-[3-(morpholin-4-yl)propoxy]-4-oxopyrido[2,3-d]pyrimidin-3(4*H*)-yl]acetamide (TASP699), was identified as a V_{1B}R antagonist with high affinity and selectivity for V_{1B}R (V_{1B}, 0.16 nM; 87 other off-target molecules including V_{1A}, V_2, and oxytocin receptors, >1 μM) (*12*). The ^{11}C-labeled ligand ^{11}C-TASP699 was then developed as a PET radiotracer and shown to have high uptake in the monkey pituitary. Further, the pituitary uptake was dose-dependently inhibited by pretreatment with TASP0390325 (*12*), a selective V_{1B}R antagonist that has been well characterized in

Received Apr. 19, 2021; revision accepted Jul. 15, 2021.
For correspondence, contact Mika Naganawa (mika.naganawa@ yale.edu).
Published online Aug. 12, 2021.
COPYRIGHT © 2022 by the Society of Nuclear Medicine and Molecular Imaging.

pharmacologic studies (*13*), thus demonstrating the $V_{1B}R$ binding specificity of ^{11}C-TASP699.

The aim of this first-in-humans PET study was to evaluate the tracer ^{11}C-TASP699 for measurement of $V_{1B}R$ availability, in order to assess the reproducibility of binding parameters. An open-label, single-dose study was also done to determine the target occupancy of a novel $V_{1B}R$ antagonist TS-121 (*14*) in the pituitary and to evaluate the relationship between plasma exposure of THY1773 (active component of TS-121) and receptor occupancy.

MATERIALS AND METHODS

Human Subjects

This was a 2-part study: test–retest and receptor occupancy. Fifteen healthy men were enrolled (test–retest: $n = 6$, 37–50 y old, body weight of 88 ± 11 kg; occupancy: $n = 9$, 32–52 y old, body weight of 80 ± 10 kg). Individuals were excluded if they had a diagnosis of a current or lifetime psychiatric disorder, a diagnosis of a current or past serious medical or neurologic illness, metal in the body that would result in an MRI contraindication, or a history of substance abuse or dependence. PET imaging experiments were conducted under a protocol approved by the Yale University School of Medicine Human Investigation Committee and the Yale–New Haven Hospital Radiation Safety Committee and were in accordance with U.S. federal guidelines and regulations for the protection of human research subjects (title 45, part 46, of the *Code of Federal Regulations*). Written informed consent was obtained from all subjects. MR images were acquired on all subjects to verify the absence of brain structural abnormalities. MRI was performed on a 3-T whole-body scanner (Trio; Siemens Medical Systems). The dimensions and pixel size of MR images were 256 × 256 × 176 voxels and 0.98 × 0.98 × 1.0 mm^3, respectively.

Safety assessments included monitoring of adverse events and serious adverse events, routine hematology, biochemistry and urinalysis testing, physical and neurologic examinations, vital signs and electrocardiograms, concomitant medications, and extent of exposure (^{11}C-TASP699 exposure in terms of radioactivity [MBq] per kilogram of body weight and total radioactivity, and, for part 2, extent of exposure to TS-121 in terms of milligrams of drug per kilogram of body weight at admission).

Radiotracer Synthesis

^{11}C-TASP699 (Fig. 1) was radiolabeled with ^{11}C-CH_3I as reported previously (*12*). The PET drug was purified by high-performance liquid chromatography (Luna C18(2) [Phenomenex], 10 μm, 10 × 250 mm, 25% acetonitrile/75% 0.1 M ammonium formate with 0.5% acetic acid, pH 4.2, at 5 mL/min and 254 nm), isolated by solid-phase extraction, and formulated in 10 mL of saline containing 1 mL of ethanol. The detailed radiosynthesis procedure is described in the supplemental materials (available at http://jnm.snmjournals.org).

PET Imaging Experiments

Six subjects underwent two 2-h ^{11}C-TASP699 PET scans on a single day to measure the reproducibility of the binding parameters in part 1 of the study. The start of the 2 scans were separated by 5.3 ± 0.7 h. In part 2 of the study, 9 subjects completed three 90-min PET scans (baseline, postdose 1, and postdose 2) to assess $V_{1B}R$ occupancy in the pituitary after a single oral administration of TS-121. The TS-121 dose was adaptively determined (3 mg, $n = 1$; 10 mg, $n = 3$; 30 mg, $n = 2$; 50 mg, $n = 3$). Postdose 1 scans were acquired 2.3 h after the dose of TS-121, and postdose 2 scans were acquired 1 or 2 d after the dose of TS-121 (3 mg, 2 d; 10 mg, 1 d; 30 mg, 2 d; 50 mg, 1 d [$n = 2$] and 2 d [$n = 1$]). The concentrations of THY1773 in plasma at pre-, mid-, and postscanning were determined by liquid chromatography and tandem mass spectrometry at CMIC, Inc., on behalf of Taisho Pharmaceutical Co., Ltd. The measured concentrations were averaged and used as the mean plasma exposure for each postdose scan.

All PET scans were conducted on a High Resolution Research Tomograph (Siemens Medical Solutions), which acquires 207 slices (1.2-mm slice separation) with a reconstructed image resolution of about 3 mm in full width at half maximum. After a 6-min transmission scan for attenuation correction, PET scans were acquired in list mode after intravenous administration of ^{11}C-TASP699 over 1 min by an automatic pump (Harvard PHD 22/2000; Harvard Apparatus). Dynamic scan data were reconstructed in 33 (test–retest) or 27 (occupancy) frames (6 × 0.5 min, 3 × 1 min, 2 × 2 min, 22 or 16 × 5 min) with corrections for attenuation, normalization, scatter, randoms, and dead time using the MOLAR algorithm (*15*). Event-by-event motion correction (*16*) was included in the reconstruction on the basis of measurements with the Polaris Vicra sensor (NDI Systems) with reflectors mounted on a swim cap worn by the subject.

In 4 scans, the Vicra motion-tracking signal was unstable or lost because of slippage of the cap. In these cases, head motion was estimated by registration of the emission images reconstructed without attenuation or scatter corrections, and then dynamic PET images were reconstructed using the estimated motion. For 4 other scans, slight residual motion was visible; each image frame was therefore aligned to the early average image from 0 to 10 min after injection.

Input Function Measurement

Arterial input functions were generated for all scans. Discrete blood samples were manually drawn every 10 s from 10 to 90 s, every 15 s from 90 s to 3 min, and then at 3.5, 5, 6.5, 8, 12, 15, 20, 25, 30, 45, 60, 75, 90, 105, and 120 min. In addition to samples for the whole-blood and plasma radioactivity curves, arterial blood samples were drawn to determine the unmetabolized fraction of tracer at 3, 8, 15, 30, 60, and 90 min for test–retest scans and at 5, 15, 30, 60, and 90 min for occupancy scans. Radiometabolite analysis was performed using the column-switching high-performance liquid chromatography method (*17*). Briefly, plasma was separated from the whole blood by centrifugation. Up to 5 mL of filtered plasma samples treated with urea (8 M) were injected into the automatic column-switching system equipped with a capture column (19 × 4.6 mm) packed with Phenomenex SPE Strata-X sorbent and a Luna C18(2) analytic column (5 μm, 4.6 × 250 mm) eluting with 1% acetonitrile in water at a flow rate of 2 mL/min for the first 4 min and then with a mobile phase of 31% acetonitrile and 69% 0.1 M ammonium formate (v/v) at 1.85 mL/min. The unmetabolized parent fraction was determined as the ratio of the sum of radioactivity in fractions containing the parent compound (retention time of ~10.5 min) to the total radioactivity collected and was fitted with an inverted γ-function.

For 1 baseline scan, reliable metabolite data were not available; the parent fraction curve at the postdose 2 study was therefore used to calculate a metabolite-corrected input function. For 1 postdose 2 scan, arterial blood samples were not available; the input function from the

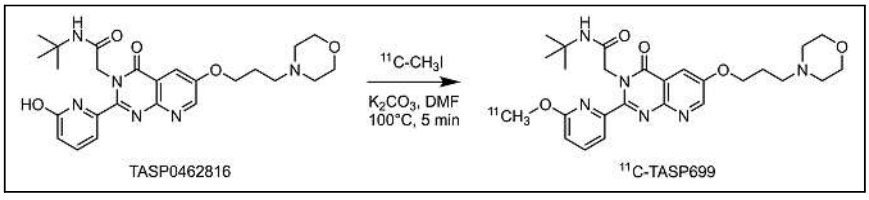

FIGURE 1. Synthesis of ^{11}C-TASP699. DMF = dimethylformamide.

baseline scan was therefore scaled using the ratio of the injected doses between the 2 scans.

An ultrafiltration-based method was used to measure the unbound portion (free fraction) of ^{11}C-TASP699 in plasma (*18*).

Quantitative Analysis

Analysis was performed directly on the PET images. A pituitary region of interest (ROI) was determined as the 400 voxels (730 mm^3) with the highest values on the SUV image (test–retest scans, 10–120 min; occupancy scans, 10–90 min), and a pituitary time–activity curve was generated. The ROI was chosen to be larger than the pituitary size to reduce variability across frames. The regional distribution volume (V_T) was computed using 1-tissue- and 2-tissue-compartment (1TC and 2TC, respectively) models and the multilinear analysis 1 (MA1) method. The effect of inclusion of a blood volume term was also assessed. The *F* test was used to compare model fits. Data points were weighted on the basis of noise-equivalent counts in each frame. Percentage SE was estimated from the theoretic parameter covariance matrix.

The mean and SD of the test–retest variability (TRV) was calculated as follows:

$$\mathrm{TRV} = 100 \times \frac{V_T^{\mathrm{retest}} - V_T^{\mathrm{test}}}{\left(V_T^{\mathrm{retest}} + V_T^{\mathrm{test}}\right)/2}. \qquad \text{Eq. 1}$$

Mean TRV is an index of trend in V_T values between test and retest scans, and the SD of TRV is an index of the variability of the percentage difference between the 2 measurements. The absolute value of TRV, which combines these 2 effects into a single value, was also computed.

The time stability of pituitary V_T values was assessed by comparing V_T values from scans shortened from 110 to 50 min with V_T values from 120-min scans in the test–retest dataset. Two criteria were used to determine a minimum scan duration (*19*): the average of the ratio was between 0.95 and 1.05, and the interindividual SD of the ratio was less than 0.1.

For the occupancy study, the fractional difference, that is, apparent receptor occupancy (*aRO*), between baseline and postdose V_T values was computed using the following formula, which also shows the physiologic interpretation of *aRO*:

$$aRO = 1 - \frac{V_T^{\text{post-dose}}}{V_T^{\text{baseline}}} = 1 - \frac{V_{ND}(1 + BP_{ND}(1-RO))}{V_{ND}(1 + BP_{ND})} = RO\frac{BP_{ND}}{1 + BP_{ND}}. \qquad \text{Eq. 2}$$

V_{ND} is the nondisplaceable volume of distribution, BP_{ND} is the pituitary binding potential with respect to the nondisplaceable pool, and *RO* is the true receptor occupancy. Since *aRO* is proportional to *RO,* the half-maximal inhibitory concentration (IC_{50}) of THY1773 can be estimated with the following formula using the plasma concentration and *aRO*:

$$aRO = aRO_{max}\frac{C}{IC_{50} + C}. \qquad \text{Eq. 3}$$

where aRO_{max} is the maximum possible value of *aRO* [$BP_{ND}/(1 + BP_{ND})$] and *C* is the THY1773 plasma concentration during each scan.

All modeling was performed with in-house programs using IDL 8.0 (ITT Visual Information Solutions).

RESULTS

Radiochemistry

^{11}C-TASP699 was prepared in 24% ± 6% radiochemical yield based on trapped ^{11}C-CH_3I (range, 7.3%–44.1% for n = 41, decay-corrected to the end of bombardment). At the end of synthesis, the radiochemical and chemical purities were 97% ± 2% and 99% ± 7%, respectively, and the molar activity was 1,017.1 ± 465.0 GBq/μmol (173.5–1910 GBq/μmol). The average synthesis time was 46 ± 2 min.

Injection Parameters and Plasma Analysis

Table 1 lists the injected radioactivity dose, molar activity at time of injection, injected mass, and plasma free fractions. There were no significant differences between test and retest scans or between baseline and postdose scans. The administered activity of ^{11}C-TASP699 was 569 ± 169 MBq (range, 301–756 MBq) for the test–retest study and 533 ± 118 MBq (range, 312–707 MBq) for the occupancy study. There were no adverse or clinically detectable pharmacologic effects by the administered radiotracer in any subject. No significant changes in vital signs or the results of laboratory studies were observed.

Figure 2 shows the mean (±SD) of parent fractions and metabolite-corrected plasma curves. In part 1, the mean parent fractions at 30 min were 71% ± 7% for the test scans (n = 6) and 69% ± 6% for the retest scans (n = 6), and in part 2, the mean parent fractions at 30 min were 70% ± 3% for the baseline scans, 69% ± 3% for postdose scan 1, and 69% ± 6% for postdose scan 2. The free fraction of ^{11}C-TASP699 in plasma was 48% ± 6% (n = 12) for the test–retest scans, 50% ± 7% (n = 9) for the baseline scans, 51% ± 5% (n = 9) for postdose scan 1, and 52% ± 6% (n = 9) for postdose scan 2. The free fraction displayed no difference between test and retest scans or between baseline and postdose scans.

Modeling Results

High uptake of ^{11}C-TASP699 was reliably seen in the pituitary, with no substantial uptake in brain regions such as the choroid plexus and pineal gland (Fig. 3B). Pituitary regional time–activity curves for ^{11}C-TASP699 (Fig. 4) showed peak uptake at approximately 10–30 min after injection followed by gradual clearance. Typical examples of fits are shown in Figure 4A. The pituitary time–activity curve was fitted well with the 2TC and MA1 models, and the *F* test showed that 2TC fitting was better than the 1TC model ($P < 0.05$ in 11 of 12 fits). However, the 2TC model provided unstable V_T estimation (relative SE > 10%) and physiologically implausible microparameters (relative SE of K_1 and k_2 > 100%). The mean pituitary K_1 from 1TC was 0.10 ± 0.02 mL/cm^3/min. 1TC V_T was somewhat underestimated compared with the reliable 2TC values but correlated well with 2TC V_T estimates ($V_{T,1TC} = 0.91 \times V_{T,2TC} + 0.11$, $R^2 = 0.99$). MA1 V_T estimates were similar to those from 2TC with a good correlation ($V_{T,MA1,t^* = 10\ \mathrm{min}} = 0.97 \times V_{T,2TC} + 0.21$, $R^2 = 1.00$). Since the MA1 method provided reliable V_T estimates (relative SE < 10%) similar to those from 2TC, the MA1 V_T values were used in the following analysis.

MA1 V_T values showed large intersubject variability, ranging from 3.6 to 9.7 mL/cm^3 (n = 19; test, retest, and baseline scans), and approximately 15 mL/cm^3 for 1 subject, which may have been caused in part by the ROI definition. Note, however, that the TRV and absolute TRV were reasonably good (TRV, −2% ± 14%; absolute TRV, 11%; intraclass correlation coefficient, 0.94) (Fig. 5A), indicating good reliability of the measurements from repeated scans. The V_T estimates for all models did not change with the inclusion of 2 additional parameters: a blood volume term and the time delay between the blood sampling site and pituitary. The percentage differences were 3% ± 3% for 1TC, 4% ± 3% for 2TC, and 0% ± 2% for MA1. Many 2TC V_T values were unstable with the addition of

TABLE 1
PET Scan Parameters

Parameter	Test–retest (n = 6)		Occupancy (n = 9)		
	Test	Retest	Baseline	Postdose 1	Postdose 2
Injected dose (MBq)	618 ± 134	519 ± 196	528 ± 126	540 ± 132	532 ± 109
Injected mass (μg)	0.90 ± 0.57	0.75 ± 0.59	1.16 ± 1.13	1.19 ± 1.19	0.93 ± 0.48
Plasma free fraction	47% ± 5%	50% ± 7%	50% ± 7%	51% ± 5%	52% ± 6%

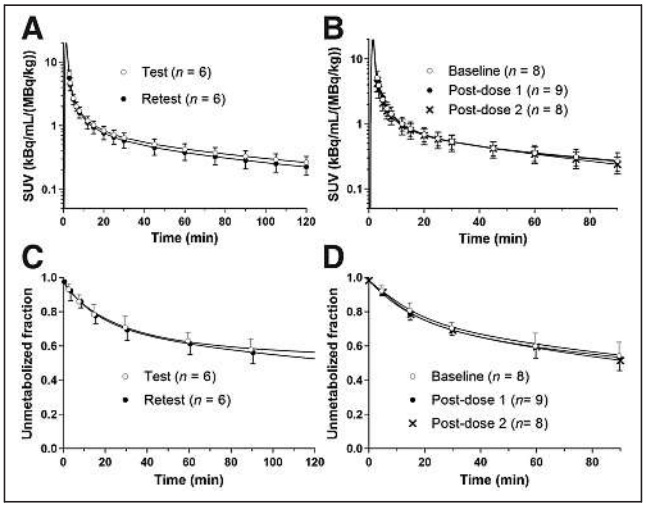

FIGURE 2. Mean ± SD of total plasma activity and parent fraction in plasma in test and retest scans (A and C) and in baseline, postdose 1, and postdose 2 scans (B and D).

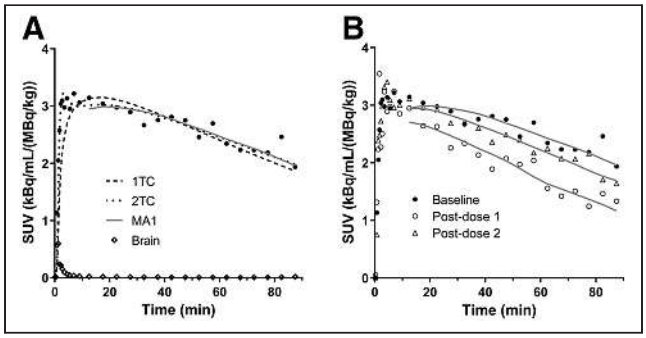

FIGURE 4. (A) Representative pituitary time–activity curve in baseline scan with 1TC (dashed), 2TC (dotted), and MA1 (t^* = 10 min, solid) fits with brain time–activity curve. (B) Pituitary time–activity curves in baseline, postdose 1, and postdose 2 conditions with MA1 fits.

delay and blood volume parameters (8/20 fits), and these values were excluded from this comparison. Pituitary blood volume was estimated to be about 20%. The minimum scan time for stable MA1 V_T estimates was 90 min. The percentage difference in V_T with respect to 120-min estimate was −6% ± 13%, −2% ± 16%, 1% ± 14%, 1% ± 9%, 0% ± 6%, and 0% ± 3% for the 60-, 70-, 80-, 90-, 100-, and 110-min scans.

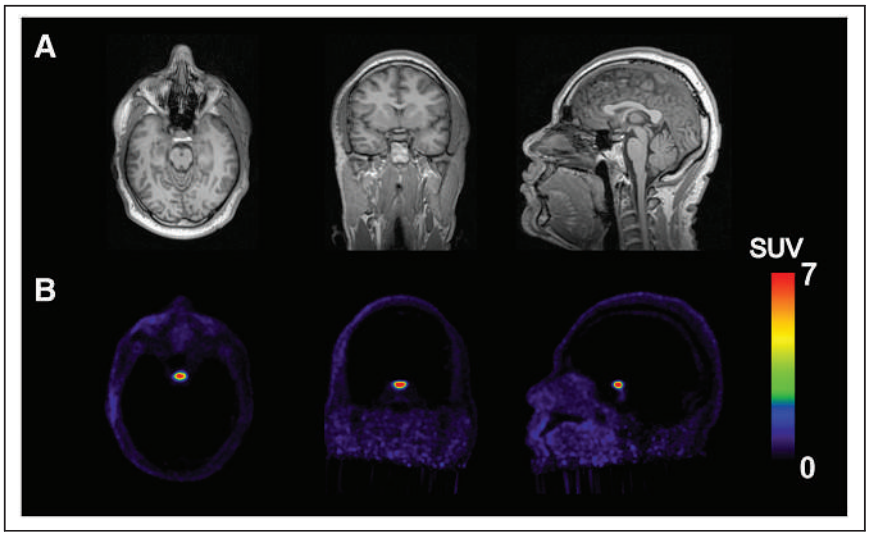

FIGURE 3. Typical MR (A) and coregistered PET images summed from 30 to 120 min after injection of ^{11}C-TASP699. Coregistration (rigid transform) was applied using extracranial uptake (blue or purple area).

Occupancy Results

Figure 4B shows a set of pituitary time–activity curves from the baseline and postdose scans after a 10-mg dose of TS-121. A moderate blocking effect was observed in the pituitary region. Figure 5B summarizes the percentage reductions in V_T in the pituitary using MA1, whereas Figure 6 shows a plot of the percentage change in V_T with THY1773 concentration in the plasma. The THY1773 plasma concentration over time is shown in Supplemental Figure 1. Using Equation 3, the IC_{50} (mean ± SE) was estimated at 177 ± 52 ng/mL, with an aRO_{max} of 62% ± 7%. Using the estimated aRO_{max} and Equation 2, the pituitary binding potential (BP_{ND}), representing the equilibrium ratio of specific to nondisplaceable binding, was calculated to be 1.6. Using the estimated aRO_{max}, percentage change in V_T was converted to RO, shown as the y-axis on the right of Figure 6.

In fitting PET-measured occupancy values, it is typically assumed that the plasma drug levels are an accurate reflection of the drug levels in the tissue. This assumption may not be met at early times, depending on how rapidly the drug enters the tissue (*20*). We thus assessed whether the occupancy values at all times were consistent by using the F test to compare regression

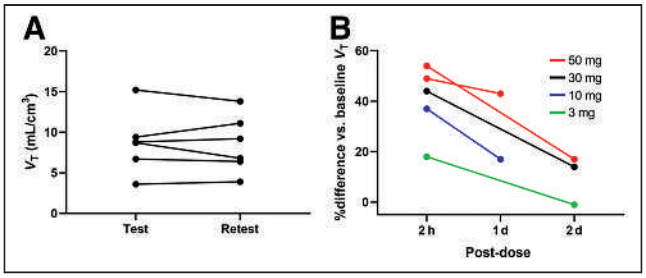

FIGURE 5. (A) Pituitary V_T values in test and retest conditions. Each symbol corresponds to a subject. (B) Mean percentage difference in V_T in comparison with baseline V_T values (*aRO*) at 2 h, 1 d, and 2 d after administration of TS-121.

curve fits of Equation 3. The null hypothesis was that 1 set of model parameters was appropriate for all postdose scans. The alternative hypothesis was that a different curve was needed for the postdose scan 1 data versus the postdose scan 2 data, because of potential hysteresis. The null hypothesis was not rejected ($P = 0.29$). Therefore, hysteresis was not considered in the estimation. However, the ability to detect hysteresis may be limited since the data points for postdose 1 and postdose 2 scans were centered on different concentrations of the curve.

Safety

Overall, no safety issues were identified that would prevent further development and testing of either the investigational radiotracer ^{11}C-TASP699 or the investigational drug TS-121.

No adverse events or serious adverse events resulting in discontinuation from the study (pain or burning at or arterial line or injection site was the most common adverse event, occurring in 3 subjects). No apparent safety trends in clinical laboratory results, vital sign measurements, electrocardiogram results, or physical and neurologic examinations were observed.

DISCUSSION

This first-in-humans PET study was conducted to assess the ability of a novel V_{1B}R antagonist PET radiotracer, ^{11}C-TASP699, to image V_{1B}R in the human pituitary. Modeling methods were evaluated on the basis of time–activity curves and metabolite-corrected input functions. The volume of distribution was determined and used to estimate receptor occupancy by the V_{1B}R antagonist, TS-121. A clear relationship between plasma concentration of the drug and receptor occupancy was found.

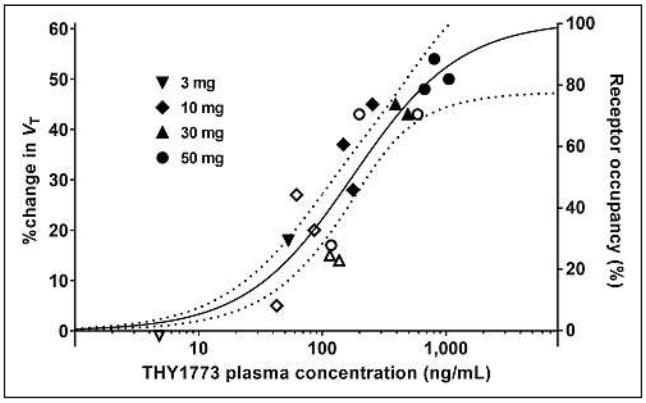

FIGURE 6. Relationship between THY1773 plasma concentrations and percentage change in V_T (left *y*-axis) and receptor occupancy (right *y*-axis). Estimated IC_{50} and aRO_{max} are 177 ± 52 ng/mL and 62% ± 7%, respectively. Solid symbols and open symbols denote postdose 1 and postdose 2, respectively.

Modeling analysis assumes that only parent compound enters tissue and binds to the receptor. However, radiolabeled metabolites are likely to access the pituitary, since it has no blood–brain barrier. If the magnitude of the metabolite effect is large, it may bias the results. This does not seem to have been the case in the current study, since, first, V_T did not show a continuous increase with scan time, as would be expected from tissue uptake of metabolites, and second, the metabolite fraction in plasma was moderate. In addition, since the fraction of metabolites was similar in the baseline and postdose scans, even if radiolabeled metabolites were present and were incorrectly increasing the estimated V_T values, the IC_{50} estimates would likely not be affected although the aRO_{max} could be biased.

Large intersubject variability was seen in V_T (4–10 mL/cm^3), although the test–retest reproducibility was good (absolute TRV, 11%). We evaluated whether there was a relationship between V_T estimates at baseline scans and subject age, weight, body mass index, scan starting time, and injected mass, but we found no significant effects. V_T might be affected by the pituitary volume itself, since it varies by age, sex, season, and subject conditions (*21–23*). However, we were not able to accurately define pituitary volumes from MR images since separation of the pituitary from neighboring tissues was challenging in many cases. Thus, we used a standard ROI size. Mean pituitary volume in healthy men is 500 ± 79 mm^3 (*22*), and a larger ROI (730 mm^3) was used to ensure that all uptake was included. To further consider this factor, the effect of ROI size on V_T values was evaluated. As expected, V_T values increased with smaller ROI sizes because of a reduced partial-volume effect. A near-identical TRV was found for ROIs above 500 mm^3 (TRV, −3% ± 15% with 550 mm^3 and −2% ± 13% with 910 mm^3). Thus, the large intersubject variability in V_{1B}R could have some biologic meaning. There have been several studies using immunohistochemistry, reverse-transcription polymerase chain reaction, and in situ hybridization histochemistry to investigate V_{1B}R distribution in rodents. However, to the best of our knowledge, there are no quantitative postmortem studies in humans or nonhuman primates.

For the 2 subjects for whom plasma or metabolite data were not available from one scan, the data from another scan were used to generate the input function. We evaluated the effect of using these data from other scans in the subjects for whom all data were available. Percentage differences in V_T were 1% ± 8% (plasma) and 0% ± 4% (metabolites).

Using ^{11}C-TASP699, we evaluated the V_{1B}R occupancy of TS-121, a drug candidate targeted for major depressive disorder. On the basis of animal model experience with THY1773, attenuated hyperactivity of the hypothalamic-pituitary-adrenal axis and antidepressantlike effects were found with more than 50% pituitary V_{1B}R occupancy. This study showed that 10–50 mg of TS-121 achieved more than 50% occupancy at 2 h after a single oral administration in healthy men (Fig. 6). A phase 2 clinical trial using TS-121 (*14*) in patients with major depressive disorder showed reductions in the Montgomery-Asberg Depression Rating Scale score for subjects who had a daily oral TS-121 dose of 10 or 50 mg at week 6, though these reductions did not achieve statistical significance. If the plasma concentration was similar in both groups (patients with major depressive disorder with daily dosing, and our healthy subjects with a single administration), the dose of 10–50 mg should have been sufficient. However, plasma concentration may differ between

patients and healthy subjects, as was seen in a glycine transporter-1 inhibitor study (*24*) in which the IC_{50} was similar between healthy controls and schizophrenic patients but the ID_{50} values were significantly different.

CONCLUSION

The novel V_{1B}R antagonist tracer ^{11}C-TASP699 showed high uptake in the pituitary but did not enter the brain. Its tracer kinetics could be modeled using MA1 to quantify V_T values. V_T values were variable between subjects but showed good test–retest reproducibility. ^{11}C-TASP699 was successfully used in an occupancy study, which showed a consistent relationship between THY1773 (active component of TS-121) plasma concentration and V_{1B}R occupancy. Single oral doses of TS-121 (3, 10, 30, and 50 mg) were found to be safe and well tolerated.

DISCLOSURE

This study was funded by Taisho Pharmaceutical R&D Inc. Izumi Nishino is a full-time employee of Taisho Pharmaceutical Co., Ltd. Satoshi Ozaki and Helene Sabia are a full-time employees of Taisho Pharmaceutical R&D Inc. Ming-Rong Zhang and Tetsuya Suhara hold a patent for ^{11}C-TASP699 (Japan patent JP2015-1206 44A). No other potential conflict of interest relevant to this article was reported.

ACKNOWLEDGMENTS

The clinical trial registration identifier of this study is NCT0244-8212. We appreciate the excellent technical assistance of the staff at the Yale University PET Center. We thank Dr. Shigeyuki Chaki for reviewing this manuscript.

KEY POINTS

QUESTION: Does ^{11}C-TASP699 show suitable kinetic properties to quantify pituitary V_{1B}R in humans?

PERTINENT FINDINGS: The novel V_{1B}R antagonist tracer ^{11}C-TASP699 showed a good test–retest reproducibility. The tracer showed high uptake in the pituitary but did not enter the brain. The occupancy of TS-121 increased in a dose-dependent fashion (IC_{50} was 177 ng/mL as THY1773).

IMPLICATIONS FOR PATIENT CARE: ^{11}C-TASP699 provides excellent measurements of V_{1B}R binding in the human pituitary.

REFERENCES

1. Aguilera G, Rabadan-Diehl C. Vasopressinergic regulation of the hypothalamic-pituitary-adrenal axis: implications for stress adaptation. *Regul Pept.* 2000;96:23–29.
2. Serradeil-Le Gal C, Raufaste D, Derick S, et al. Biological characterization of rodent and human vasopressin V1b receptors using SSR-149415, a nonpeptide V1b receptor ligand. *Am J Physiol Regul Integr Comp Physiol.* 2007;293:R938–R949.
3. Tanoue A, Ito S, Honda K, et al. The vasopressin V1b receptor critically regulates hypothalamic-pituitary-adrenal axis activity under both stress and resting conditions. *J Clin Invest.* 2004;113:302–309.
4. van Londen L, Goekoop JG, van Kempen GM, et al. Plasma levels of arginine vasopressin elevated in patients with major depression. *Neuropsychopharmacology.* 1997;17:284–292.
5. de Winter RF, van Hemert AM, DeRijk RH, et al. Anxious-retarded depression: relation with plasma vasopressin and cortisol. *Neuropsychopharmacology.* 2003; 28:140–147.
6. De Bellis MD, Gold PW, Geracioti TD Jr, Listwak SJ, Kling MA. Association of fluoxetine treatment with reductions in CSF concentrations of corticotropin-releasing hormone and arginine vasopressin in patients with major depression. *Am J Psychiatry.* 1993;150:656–657.
7. Scott LV, Dinan TG. Vasopressin and the regulation of hypothalamic-pituitary-adrenal axis function: implications for the pathophysiology of depression. *Life Sci.* 1998;62:1985–1998.
8. Inder WJ, Donald RA, Prickett TC, et al. Arginine vasopressin is associated with hypercortisolemia and suicide attempts in depression. *Biol Psychiatry.* 1997;42:744–747.
9. Griebel G, Stemmelin J, Gal CS, Soubrie P. Non-peptide vasopressin V1b receptor antagonists as potential drugs for the treatment of stress-related disorders. *Curr Pharm Des.* 2005;11:1549–1559.
10. Roper J, O'Carroll AM, Young W III, Lolait S. The vasopressin Avpr1b receptor: molecular and pharmacological studies. *Stress.* 2011;14:98–115.
11. Schönberger M, Leggett C, Kim SW, Hooker JM. Synthesis of [^{11}C]SSR149415 and preliminary imaging studies using positron emission tomography. *Bioorg Med Chem Lett.* 2010;20:3103–3106.
12. Koga K, Nagai Y, Hanyu M, et al. High-contrast PET imaging of vasopressin V1B receptors with a novel radioligand, ^{11}C-TASP699. *J Nucl Med.* 2017;58:1652–1658.
13. Iijima M, Yoshimizu T, Shimazaki T, et al. Antidepressant and anxiolytic profiles of newly synthesized arginine vasopressin V1B receptor antagonists: TASP0233278 and TASP0390325. *Br J Pharmacol.* 2014;171:3511–3525.
14. Kamiya M, Sabia HD, Marella J, et al. Efficacy and safety of TS-121, a novel vasopressin V1B receptor antagonist, as adjunctive treatment for patients with major depressive disorder: a randomized, double-blind, placebo-controlled study. *J Psychiatr Res.* 2020;128:43–51.
15. Carson RE, Barker WC, Liow JS, Johnson CA. Design of a motion-compensation OSEM list-mode algorithm for resolution-recovery reconstruction for the HRRT. *IEEE 2003 Nucl Sci Symp Conf Rec.* 2003;5:3281–3285.
16. Jin X, Chan C, Mulnix T, et al. List-mode reconstruction for the Biograph mCT with physics modeling and event-by-event motion correction. *Phys Med Biol.* 2013;58:5567–5591.
17. Hilton J, Yokoi F, Dannals RF, Ravert HT, Szabo Z, Wong DF. Column-switching HPLC for the analysis of plasma in PET imaging studies. *Nucl Med Biol.* 2000;27: 627–630.
18. Li S, Cai Z, Zheng MQ, et al. Novel ^{18}F-labeled κ-opioid receptor antagonist as PET radiotracer: synthesis and in vivo evaluation of ^{18}F-LY2459989 in nonhuman primates. *J Nucl Med.* 2018;59:140–146.
19. Frankle WG, Huang Y, Hwang DR, et al. Comparative evaluation of serotonin transporter radioligands ^{11}C-DASB and ^{11}C-McN 5652 in healthy humans. *J Nucl Med.* 2004;45:682–694.
20. Naganawa M, Gallezot JD, Rossano S, Carson RE. Quantitative PET imaging in drug development: estimation of target occupancy. *Bull Math Biol.* 2019;81:3508–3541.
21. Lurie SN, Doraiswamy PM, Husain MM, et al. In vivo assessment of pituitary gland volume with magnetic resonance imaging: the effect of age. *J Clin Endocrinol Metab.* 1990;71:505–508.
22. Schwartz PJ, Loe JA, Bash CN, et al. Seasonality and pituitary volume. *Psychiatry Res.* 1997;74:151–157.
23. Büschlen J, Berger GE, Borgwardt SJ, et al. Pituitary volume increase during emerging psychosis. *Schizophr Res.* 2011;125:41–48.
24. D'Souza DC, Carson RE, Driesen N, et al. Dose-related target occupancy and effects on circuitry, behavior, and neuroplasticity of the glycine transporter-1 inhibitor PF-03463275 in healthy and schizophrenia subjects. *Biol Psychiatry.* 2018;84: 413–421.

A Path to Qualification of PET/MRI Scanners for Multicenter Brain Imaging Studies: Evaluation of MRI-Based Attenuation Correction Methods Using a Patient Phantom

Ciprian Catana*[1], Richard Laforest*[2], Hongyu An[2], Fernando Boada[3], Tuoyu Cao[4], David Faul[5], Bjoern Jakoby[6], Floris P. Jansen[7], Bradley J. Kemp[8], Paul E. Kinahan[9], Peder Larson[10], Michael A. Levine[1], Piotr Maniawski[11], Osama Mawlawi[12], Jonathan E. McConathy[13], Alan B. McMillan[14], Julie C. Price[1], Abhejit Rajagopal[10], John Sunderland[15], Patrick Veit-Haibach[16], Kristen A. Wangerin[17], Chunwei Ying[18], and Thomas A. Hope[10]

[1]Athinoula A. Martinos Center for Biomedical Imaging, Department of Radiology, Massachusetts General Hospital and Harvard Medical School, Charlestown, Massachusetts; [2]Mallinckrodt Institute of Radiology, Washington University School of Medicine, St Louis, Missouri; [3]Center for Advanced Imaging Innovation and Research, Department of Radiology, New York University Langone Medical Center, New York, New York; [4]Shanghai United Imaging Healthcare Co., Ltd., Shanghai, China; [5]Siemens Medical Solutions USA, Inc., Malvern, Pennsylvania; [6]Siemens MR, Siemens Healthcare GmbH, Erlangen, Germany; [7]PET/MR Engineering, GE Healthcare, Chicago, Illinois; [8]Division of Nuclear Medicine, Mayo Clinic, Rochester, Minnesota; [9]Imaging Research Laboratory, University of Washington, Seattle, Washington; [10]Department of Radiology and Biomedical Imaging, University of California, San Francisco, California; [11]Advanced Molecular Imaging, Philips Healthcare, Cleveland, Ohio; [12]Department of Imaging Physics, University of Texas M.D. Anderson Cancer Center, Houston, Texas; [13]Department of Radiology, University of Alabama at Birmingham, Birmingham, Alabama; [14]Department of Radiology, University of Wisconsin School of Medicine and Public Health, Madison, Wisconsin; [15]Division of Nuclear Medicine, Department of Radiology, University of Iowa, Iowa City, Iowa; [16]Toronto Joint Department of Medical Imaging, University Health Network, Sinai Health System, and Women's College Hospital, Department of Medical Imaging, University of Toronto, Toronto, Canada; [17]GE Healthcare, Chicago, Illinois; and [18]Department of Biomedical Engineering, Washington University in St. Louis, St. Louis, Missouri

PET/MRI scanners cannot be qualified in the manner adopted for hybrid PET/CT devices. The main hurdle with qualification in PET/MRI is that attenuation correction (AC) cannot be adequately measured in conventional PET phantoms because of the difficulty in converting the MR images of the physical structures (e.g., plastic) into electron density maps. Over the last decade, a plethora of novel MRI-based algorithms has been developed to more accurately derive the attenuation properties of the human head, including the skull. Although promising, none of these techniques has yet emerged as an optimal and universally adopted strategy for AC in PET/MRI. In this work, we propose a path for PET/MRI qualification for multicenter brain imaging studies. Specifically, our solution is to separate the head AC from the other factors that affect PET data quantification and use a patient as a phantom to assess the former. The emission data collected on the integrated PET/MRI scanner to be qualified should be reconstructed using both MRI- and CT-based AC methods, and whole-brain qualitative and quantitative (both voxelwise and regional) analyses should be performed. The MRI-based approach will be considered satisfactory if the PET quantification bias is within the acceptance criteria specified here. We have implemented this approach successfully across 2 PET/MRI scanner manufacturers at 2 sites.

Key Words: PET/MRI; attenuation correction; multicenter trials; qualification

J Nucl Med 2022; 63:615–621
DOI: 10.2967/jnumed.120.261881

Received Jan. 4, 2021; revision accepted Jun. 6, 2021.
For correspondence or reprints, contact Ciprian Catana (ccatana@mgh.harvard.edu).
*Contributed equally to this work.
Published online Jul. 22, 2021.
COPYRIGHT © 2022 by the Society of Nuclear Medicine and Molecular Imaging.

Simultaneous PET/MRI scanners were introduced commercially for human imaging in 2010 and have since made their way into research laboratories and clinics following in the footsteps of hybrid PET/CT, which saw its introduction in early 2000. In contrast to PET/CT, which experienced rapid clinical acceptance by adding much needed high-resolution anatomic information and faster attenuation correction (AC) to functional and molecular imaging, combined PET/MRI has seen a much slower acceptance. In addition to the higher cost of the modality, one of the reasons for this slower adoption has been the fact that AC is more challenging (*1*) because bone tissue cannot easily be imaged by MRI and may be misclassified, resulting in quantitative uncertainties that have helped to perpetuate the viewpoint that PET/MRI remains investigational. Over the last decade, several MRI-based algorithms have been developed to more accurately derive the PET (511 keV) attenuation properties of the human head, including the bone tissue. Algorithms such as ultrashort time of echo, zero time of echo (ZTE; GE Healthcare), atlas-based, or, most recently, machine learning approaches have been proposed to replace or complement the vendor-provided 2-point Dixon (or LAVA Flex; GE Healthcare) sequence that is routinely used in clinical settings (*1*,*2*). These MRI-based AC (MRAC) algorithms have been evaluated by imaging patients sequentially on PET/CT and PET/MRI scanners and using the CT-based AC as the gold standard. Considering these developments and the need for scanner validation, a clear path to the qualification of this modality is both timely and necessary. Although methods to perform a transmission scan inside the PET/MRI scanner have also been proposed (*3*–*5*) and could also be used for validating MRAC approaches, they require additional hardware and expertise.

A related limitation to clinical acceptance and inclusion in clinical trials has been that PET/MRI scanners cannot be qualified in the manner adopted for PET/CT. PET/CT qualification or scanner validation, for purposes ranging from clinical use to participation in a clinical trial with PET quantitative endpoints, typically proceeds with scanning of standardized phantoms (filled with a radiotracer mixed with water) of predefined geometry such as the American College of Radiology (ACR), Clinical Trials Network, or National Electrical Manufacturers Association International Electrotechnical Commission phantoms. For PET/CT scanners, this works well because the linear attenuation coefficient of water is close to that of soft tissue for both PET and CT. Additionally, CT provides sufficient information to infer the linear attenuation coefficients of other materials (*6*). These traditional phantoms, however, cannot be imaged accurately by MRI because proton properties in magnetic fields do not readily translate to electron density, atomic structure, and 511-keV photon attenuation. Specifically, the transverse relaxation time (T2) of protons in phantom materials such as plastic is too short to be captured conventionally, leading to little measurable signal from nearly all types of MRI pulse sequences. Although substantial progress has been made in manufacturing phantoms capable of mimicking both electron density and MRI contrast characteristics of human tissues (*7*–*9*), no such phantom that could be used to assess the performance of multiple MRAC techniques is yet widely available. Additionally, water-filled phantoms, a mainstay in the accreditation of PET scanners (*10*), produce resonance artifacts in MR images (*11*). In other words, although the standard phantoms accurately replicate the imaging physics of PET and CT for patients, the same is not true for MRI.

In this work, we propose a path for PET/MRI qualification for brain imaging studies using a patient as a phantom. We explain the differences between accreditation and qualification, outline the need for both, review the accreditation and qualification process in the context of PET/CT, and describe the proposed solution in terms of data acquisition and analysis and the definition of qualification criteria.

ACCREDITATION AND QUALIFICATION

The term *accreditation* is used primarily in the clinical setting. For example, all centers in the United States that bill for nuclear medicine procedures are required to be accredited to receive all the reimbursement from Medicare. The term *qualification* describes the process of determining whether a specific scanner can be used in the setting of a specific clinical trial. Frequently, contract research organizations will require specific phantom imaging tests to qualify scanners before allowing sites to enroll in imaging trials. In many settings, approaches to accreditation are used as part of a qualification process. There are many organizations that provide qualification services in the setting of multicenter clinical trials (*12*,*13*). Though the terms *accreditation* and *qualification* are often used interchangeably, it is important to understand the distinctions between them. The goal of this article is to propose an approach to PET/MRI qualification for brain studies, such that these devices can be used for multicenter clinical trials.

APPROACHES USED IN PET/CT

One of the most commonly used means of accreditation in PET/CT is the ACR accreditation program (*10*,*14*). The ACR accreditation program defines the requirements for the personnel performing and interpreting the study, quality control, and peer review. Additionally, each site must provide images of a specific PET phantom and clinical images that are reviewed centrally. The phantom and clinical images are evaluated qualitatively before accreditation. The phantom images have specific quantitative acceptance criteria. For example, ACR requires ±15% error in the SUV of the background (as well as other requirements for contrast recovery). Accreditation does not define the performance of the procedure (e.g., uptake time and injected activity) but rather focuses on the facility, personnel, device, and resultant images. Other organizations also provide accreditation services, such as the Intersocietal Accreditation Commission, RadSite, and the Joint Commission (*15*,*16*).

For qualification, many clinical trials will accept ACR accreditation, but those focused on novel radiotracers or quantitative PET measures frequently require more stringent approaches, which can overlap with harmonization. *Harmonization* is a term that describes setting up the image acquisition and reconstruction parameters so that approximately the same quantitative outcomes are obtained independently of scanners; this approach is sometimes used in trials with quantitative primary or secondary endpoints. Two main approaches for harmonization are those put forth by the Clinical Trials Network and the European Association of Nuclear Medicine Research Ltd. (*13*,*17*). These approaches use phantoms with spheres of varying sizes, filled following exact phantom preparation procedures, to determine harmonized reconstruction parameters capable of producing quantitative results that yield measured SUVs within a predetermined range. Using these approaches, one can minimize variability in PET quantification across imaging devices.

All accreditation, qualification, and harmonization procedures in PET/CT require the imaging of a phantom filled with a known quantity of radiotracer in a water solution.

PROPOSED SOLUTION FOR PET/MRI SCANNERS: QUALIFICATION USING HUMAN PHANTOMS

Given the above-mentioned challenges in imaging standard phantoms, a more manageable approach to PET/MRI qualification is to evaluate the PET reconstruction pipeline's constituent parts independently. Specifically, the challenge in the generation of the attenuation map can be isolated from the other effects that influence the PET quantification (i.e., such corrections as those for randoms, dead time, and decay and those related to the image reconstruction). To address the former challenge, we propose to use patients scanned sequentially on both CT or PET/CT and PET/MRI as phantoms and evaluate the difference in the resultant attenuation maps and impact on PET data quantification. This approach builds on the methodology typically used for validating MRAC using CT-based AC as the standard. We propose the below procedures to standardize this approach so it can be used to qualify a particular PET/MRI scanner. The guideline recommended here is specific to the head but could in principle be adapted to other more complex regions, although additional challenges would obviously need to be considered for whole-body applications (*1*). Other

factors relevant for the qualification of the PET component of the integrated PET/MRI scanner in a multicenter trial will be assessed using separate imaging phantoms and procedures already in place for PET/CT.

Data Acquisition

CT Data Acquisition. A noncontrast CT study should be performed using parameters typically used for AC in PET scans or diagnostic examinations according to the clinical protocols, and the images should be reconstructed using standard algorithms (e.g., analytic filtered backprojection and iterative techniques). The subject should be positioned on the CT scanner with the arms outside the field of view (i.e., arms down, as is typically done for head PET/CT and PET/MRI examinations), and the entire head should be scanned (i.e., from the top of the head to the lower neck). Patients with metallic implants should not be used as they could bias both the CT-based and the MRI-based attenuation maps. Additionally, subjects should be excluded if significant artifacts (e.g., streaks, motion, or scanner malfunction) are seen in the CT images.

MRI Data Acquisition. MRI data should be acquired using the radiofrequency coil that will be used in the clinical study or clinical trial. The site-specific MRI sequence used for generating the attenuation map (e.g., Dixon–volumetric interpolated breath-hold examination, magnetization-prepared rapid acquisition with gradient echo, ZTE, or ultrashort time of echo) should also be acquired with the same parameters as those used in the clinical trial. The whole head (including nose and ears) and the part of the neck present in the physical PET field of view should be covered. If the site-specific MRAC method is different from the vendor-specific one, the vendor-specific MRAC sequences should also be acquired. Additionally, a vendor-specific sequence for obtaining high-resolution morphologic MRI data (e.g., magnetization-prepared rapid acquisition with gradient echo or BRAVO [GE Healthcare] sequences with approximately 1 mm^3 resolution and maximum 1.5-mm slice thickness) should be acquired for the purposes of image registration to the CT scan and region-of-interest (ROI) definition. Any MR images with artifacts that are known to bias the PET data quantification (e.g., susceptibility, water–fat inversion, ghosting, or motion) should be excluded from the evaluation. Dental fillings, which might be present in many subjects, do not usually lead to significant artifacts and would not be excluded. The MRI-based attenuation map should be generated using the site-specific algorithm to be used in the clinical trial (either developed in-house or provided by the manufacturer).

PET Data Acquisition. The radiotracer used for evaluation will depend on the specific study. The emission data should be acquired using the integrated PET/MRI in one of the following 2 ways: PET/CT followed by same-day PET/MRI or CT-only followed by same-week PET/MRI. In the first scenario, the subject should undergo the additional PET/MRI examination within a reasonable time specific to the radiotracer to provide adequate counts in the PET data acquired on the PET/MRI device (e.g., within 3 h from the time of ^{18}F-FDG administration). The emission data acquired as part of the PET/CT examination are not used in the analysis, as the focus is on analyzing the impact on the PET data quantification acquired on the PET/MRI scanner. In the second scenario, the PET/MRI examination should be scheduled within 1 wk of the clinical CT scan. As significant changes could occur within a week even without surgical interventions (e.g., differences in the filling of the sinuses could introduce bias in adjacent gray matter structures), subjects with a recent onset of upper respiratory infections, acute sinusitis, and other such conditions should be excluded. The acquisition duration on the PET/MRI device should be at least 10 min in both scenarios, and the emission data should be saved in a manner that permits retrospective reconstruction (i.e., list mode or sinograms, plus associated data for corrections).

In both cases, the patients should be scanned with arms down and the head positioned in the MRI scanner as similarly as possible to the CT scan. Specifically, the technologist should review the CT images and try to position the head in a similar orientation with respect to the neck (e.g., no head lateral rotation and a similar degree of flexion) to minimize the need for nonrigid body registration. Additionally, the head should be centered in the PET axial field of view to ensure full coverage in a single acquisition.

Centralized Data Processing and Analysis

We recommend the creation of a PET/MRI scanner accreditation group or organization to perform the steps described below. This group should have the capability to process and analyze the data collected on any of the PET/MRI scanners and reproduce all the steps described below using the following data: site-specific MRI-based attenuation maps, morphologic MR images, CT images (or CT-based attenuation map), and raw emission data in sinogram or list-mode format and the additional files required for image reconstruction (e.g., normalization file and hardware attenuation maps).

To minimize the contribution of factors not related to the MRI-based attenuation map generation procedure, the accreditation group will use software provided by the manufacturers or freely available packages to standardize the following steps.

Data Processing

CT Data Processing. First, the patient bed and head holder will be removed from the CT images using vendor-provided software. Second, the CT volume will be coregistered to the morphologic high-resolution MRI volume using rigid body registration with normalized mutual information as the objective function (e.g., using Elastix (*18*,*19*), Statistical Parametric Mapping (*20*), Insight Toolkit (*21*,*22*), or similar software). The accuracy of the coregistration will be assessed visually by an experienced reader. Third, the Hounsfield units will be converted to linear attenuation coefficients at 511 keV using the vendor-specific procedure. Fourth, the resulting CT-based attenuation maps will be smoothed using a gaussian filter (with a kernel size that ensures the resulting attenuation maps match the PET scanner spatial resolution) and resampled into the PET space of the specific PET/MRI device. If the CT-based attenuation map is incomplete (because of the shorter axial coverage in the neck region or different positioning between the 2 examinations), the missing data will be copied from the MRI-based attenuation map. Finally, the attenuation map will be exported in a format that allows its use for AC using the standard PET image reconstruction pipeline.

PET Data Processing. The PET images will be reconstructed with the reconstruction algorithm used in the clinical trial, applying both the CT-based AC and the MRAC maps created above. Typically, the scatter correction provided by the manufacturer will be used in both cases (although the attenuation map is usually used for scatter estimation, only the joint impact of both attenuation and scatter corrections on PET data quantification is of

interest here). Postreconstruction smoothing will be applied according to the study protocol.

Data Analysis

ROI Definition. Subject-specific ROIs will be defined from the morphologic MRI data using FreeSurfer (*23*). A representative subset of study-specific ROIs will be selected for regional data analysis. Additionally, a brain mask (i.e., all the voxels corresponding to gray and white matter) will be obtained from the MRI data.

Quantitative Evaluation of the Attenuation-Corrected PET Data. The bias present in the PET images reconstructed with MRAC relative to those reconstructed with CT-based AC will be assessed by computing the voxelwise percentage differences throughout the whole brain mask (i.e., all the voxels corresponding to brain tissue). Additionally, a regional analysis will be performed using the FreeSurfer-defined ROIs. Average percentage differences, as well as average absolute percentage differences, will be computed for all selected ROIs.

Qualification Criteria (QC)

QC 1. The MRI-based attenuation maps and corresponding PET images should be free of artifacts (e.g., fat–water inversion, susceptibility artifacts in the MRI-based map or streak artifacts in the CT-based map, and incomplete head coverage), and no obvious misregistration should be noted in the overlaid images.

QC 2. The voxelwise relative differences between the PET images attenuation corrected using the MRAC and CT-based approaches should be below 10% in at least 90% of the voxels included in the brain mask.

QC 3. The average absolute percentage differences between the PET images attenuation corrected using the MRAC and CT-based approaches should be below 10% in all study-specific ROIs.

QC 4. For studies involving reference tissue analysis (e.g., SUV ratios for amyloid PET imaging in neurodegeneration), a more stringent threshold could be set for the reference ROI (e.g., less than 5% bias in the cerebellum in the case of amyloid PET imaging).

EXAMPLE APPLICATION

Methods

The procedures described above were followed for acquiring, processing, and analyzing the data to qualify 2 different PET/MRI scanners for a hypothetical study aimed at assessing β-amyloid accumulation in Alzheimer disease subjects. A total of 10 datasets were assessed, obtained from 5 subjects scanned on the Biograph mMR and 5 on the Signa PET/MRI scanners. The results from representative cases are discussed below.

At 1 institution (UCSF), subjects underwent ^{18}F-AV-45 (florbetapir) imaging using the Signa PET/MRI and Discovery STE PET/CT scanners (GE Healthcare). The MRI-based attenuation maps were generated using atlas- (*24*,*25*) and ZTE-based (*26*,*27*) approaches. At the other institution (Washington University in St. Louis), subjects underwent ^{18}F-AV-45 imaging using the Biograph mMR and Biograph Vision PET/CT scanners (Siemens Healthineers). The MRI-based attenuation maps were generated using the Dixon- (*28*) and skull model-based (*29*) approaches. The FreeSurfer-derived cortical ROIs were combined into 4 study-specific large bilateral regions (frontal, cingulate, parietal, and lateral temporal) previously proposed for assessing β-amyloid deposition in this patient population (*30*,*31*). Additionally, bilateral regions corresponding to white matter and whole cerebellum were defined.

Results

The attenuation maps and the corresponding PET images for 2 representative subjects free of artifacts and properly registered are presented in Figure 1 and Supplemental Figures 1 and 2 (supplemental materials are available at http://jnm.snmjournals.org) (QC 1).

Figure 2 shows the cumulative pixelwise absolute difference histogram (blue) and pixelwise absolute percentage difference histogram (green) for Dixon- and skull model-based AC on the Biograph mMR, and atlas- and ZTE-based AC on the Signa PET/MRI scanners. The relative differences between the PET images obtained using the Siemens skull model- and ZTE-based methods with respect to the CT-based approach were below 10% in 94.67% and 96.59% of the voxels included in the brain mask, respectively (QC 2). On the other hand, the Siemens Dixon- and GE atlas-based approaches did not meet this acceptance criterion.

The regional absolute relative differences were below 10% for all the study-specific ROIs described above for the Siemens skull model- and ZTE-based approaches as depicted in the Bland–Altman plots shown in Figure 3 (QC 3). The Siemens Dixon- and GE atlas-based approaches did not meet this acceptance criterion.

Plots of cumulative histograms of absolute pixelwise differences and a summary report for all 10 subjects included in the analysis are given in Figure 4 and Supplemental Table 1. The relative differences between the PET images obtained using the Siemens skull model- and ZTE-based methods with respect to the CT-based approach were below 10% in more than 90% of the voxels included in the brain mask for all subjects (QC 2). On the other hand, the Siemens Dixon- and GE atlas-based approaches did not meet this acceptance criterion for 5 and 3 of the subjects, respectively.

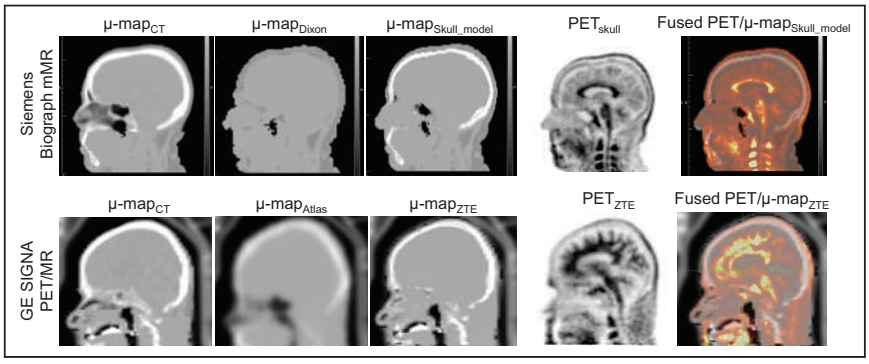

FIGURE 1. Attenuation maps and corresponding ^{18}F-AV-45 PET images for 2 representative subjects. No artifacts or obvious misregistration can be observed (QC 1).

DISCUSSION

We have proposed to use the patient as a phantom to qualify PET/MRI scanners for brain imaging multicenter trials. Because of the absence of suitable phantoms to evaluate MRAC methods, patient phantoms provide the fastest path forward to evaluating quantitative errors associated with AC. The main advantage to this approach is that it will remain robust independently of the

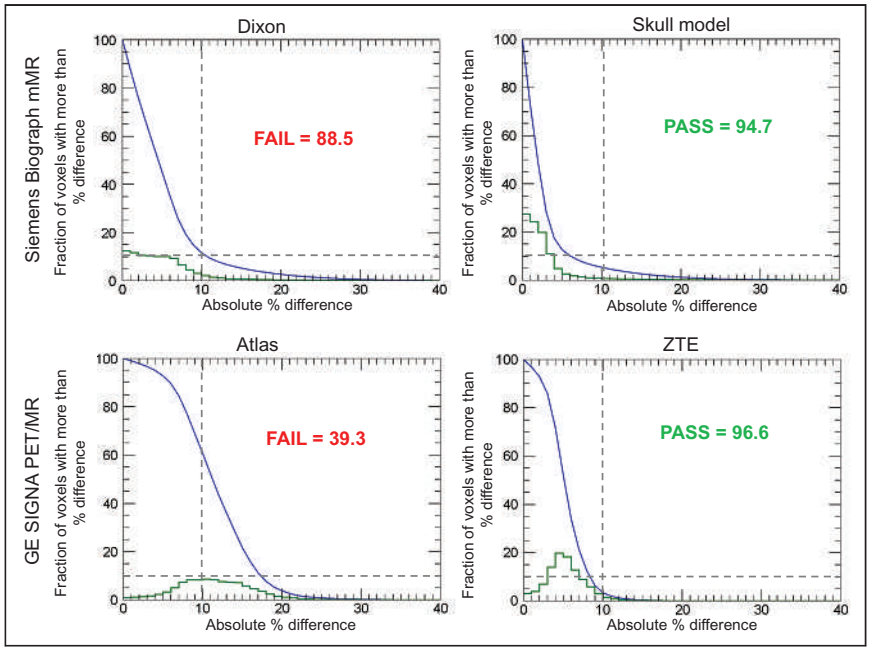

FIGURE 2. Cumulative voxelwise relative differences between PET images obtained using 4 attenuation map generation methods and those generated using reference CT-based approach for 2 representative subjects (blue). Voxelwise relative differences are below 10% in at least 90% of voxels included in brain masks for Siemens skull model-based and GE ZTE-based approaches (QC 2). Percentage of voxels with absolute relative difference smaller than 10% is indicated in each case. Green line represents histogram of pixelwise percentage difference.

MRAC methodology over time. It is important to note that site qualification for evaluating reconstruction methods is still required; this can be done using standard PET/CT phantoms.

Although a study-specific radiotracer is preferred, ^{18}F-FDG may also suffice in many indications because of its global uptake pattern, making the assessment of bias from the MRAC generalizable to most other radiotracers relevant to neurologic applications. Although the evaluation methods and qualification criteria were defined to ensure that the assessment is applicable across radiotracers, additional radiotracer- or patient population–specific assessments could be defined and performed if needed. Finally, the proposed methods are also applicable to AC methods that use the emission data to estimate the attenuation map (*32*), as well as the latest generation of machine learning approaches (*33*), including those methods that generate attenuation- and scatter-corrected images directly from the noncorrected images without needing to generate an attenuation map (*34*).

Given the complexity of this method compared with the one applied for qualifying PET/CT scanners using innate phantoms, we have recommended that the data processing be performed by the accreditation group or organization. Although each site would have to submit images and raw data, this task does not require advanced software or training. The centralized processing would ensure that all the steps are performed consistently. The differences between the offline and online data-processing tools could be minimized by obtaining from the equipment manufacturers the tools corresponding to the software version installed on the scanner to be qualified. Furthermore, the PET images attenuation-corrected using the CT- and MRI-based attenuation maps would be reconstructed using the same input parameters. For these reasons, the remaining differences between the offline and online reconstructions would not affect the quantitative evaluation of the AC procedure, which is our only goal here. Other effects relevant for PET data quantification would be assessed using images of standard phantoms (e.g., National Electrical Manufacturers Association or SNMMI Clinical Trials Network phantom) reconstructed using the online tools to ensure that the images meet study-specific criteria such as those related to image uniformity, spatial resolution, and image quality.

One limitation of the proposed approach is that it requires CT data to be acquired either onsite or at a different facility. Furthermore, the need to perform 2 examinations places additional burden on the participants, staff and increases the costs compared with scanning an innate phantom. The radiation exposure is also increased in the CT-only followed by PET/MRI examination scenario.

Another drawback to the proposed approach is that each imaging center is required to transfer raw data (i.e., list-mode

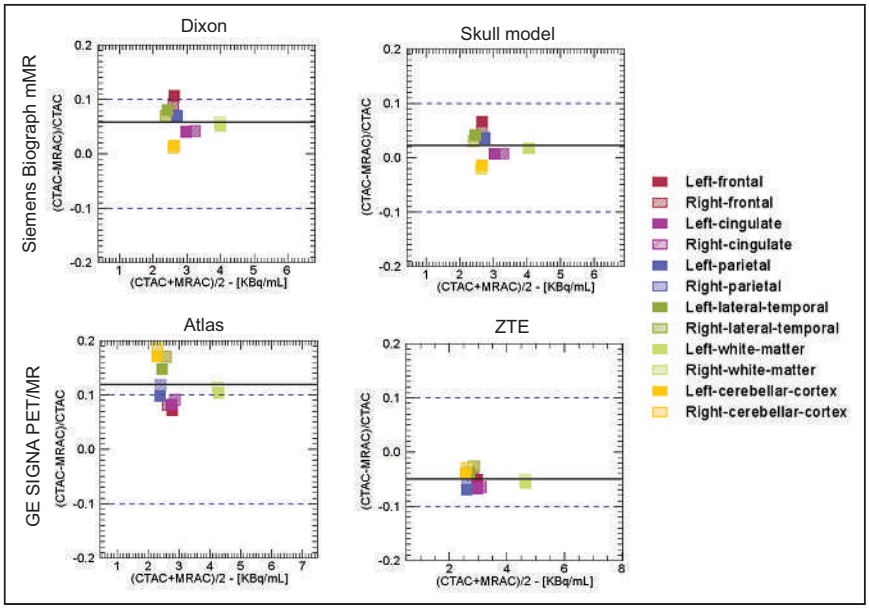

FIGURE 3. Bland–Altman plots of absolute relative differences between PET images obtained using 4 attenuation map generation methods and those generated using reference CT-based approach for study-specific FreeSurfer-based ROIs for 2 representative subjects. Average absolute percentage differences are below 10% in all study-specific ROIs for Siemens skull model-based and GE ZTE-based approaches (QC 3). CTAC = CT-based AC.

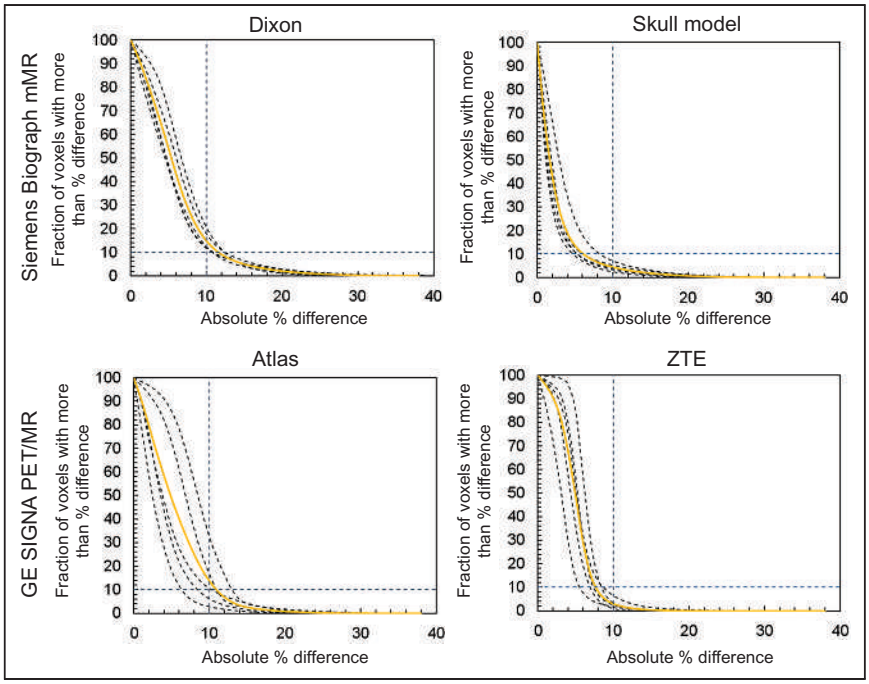

FIGURE 4. Cumulative voxelwise relative differences between PET images obtained using MRI-based methods with respect to CT-based approach for all 10 subjects analyzed. Solid curve represents mean across 5 subjects for each method. Voxelwise relative differences are below 10% in at least 90% of voxels included in brain masks for all subjects when using Siemens skull model-based and GE ZTE-based approaches.

CONCLUSION

We have proposed a solution for qualifying PET/MRI scanners for brain imaging clinical trials. The most significant challenge is to develop PET/MRI-specific phantoms that are applicable across different MRAC approaches. To address this issue, we have proposed using the patient as a phantom, whereby the scaled CT attenuation map is used to validate the MRI-based map generated for the same patient. The approach was successfully implemented across 2 PET/MRI scanner manufacturers at 2 sites.

DISCLOSURE

This work was partially supported by the National Institutes of Health (grants 5R01 CA212148 and 1U01EB029826). Tuoyu Cao is employed by United Imaging Health Care, David Faul and Bjoern Jakobi are employed by Siemens Healthineers, Floris Jansen and Kristen Wangerin are employed by GE Healthcare, and Piotr Maniawski is employed by Philips Healthcare. No other potential conflict of interest relevant to this article was reported.

or sinogram PET data) to a central processing site to have the dataset reconstructed using both CT- and MRI-based attenuation maps. Sites may not be immediately familiar with how to access and export these large datasets. There is also potential variability associated with CT-to-MRI registration. Nonetheless, in our initial evaluation of the proposed approach we were able to successfully implement the process across 2 centers using 2 different PET/MRI manufacturers, with comparable results. Further work needs to be performed to automate the analysis and to minimize the burden on the central site.

The proposed solution was here applied to the brain, but future work will focus on extending the patient phantom to other parts of the body as accurate MRAC approaches become available. Regional analysis and the impact of MRAC on focal lesion uptake would have to be defined outside the brain (as well as for assessing the impact of AC in the presence of bone lesions in the head). This translation to other body regions will also be facilitated by using a patient phantom, as new phantom geometries do not need to be developed.

Lastly, this approach uses a best-case-scenario patient selected by the individual site, as is done with other qualification approaches, but it does not evaluate the variability across patients. The goal of this qualification approach is to demonstrate that the MRAC methods used on the site-specific scanner are functioning as expected on the basis of manufacturer recommendations. As with all qualification approaches, this approach does not prevent errors in PET quantitation due to large patient-level abnormalities. It was also not our goal to propose a guideline for harmonization of AC methods. However, the proposed method could be adapted for this purpose although that would require different data acquisition and processing protocols (e.g., scanning the same subject on different PET/MRI scanners).

KEY POINTS

QUESTION: Can patient phantoms be used to test the head MRAC methods to qualify PET/MRI scanners for multicenter trials?

PERTINENT FINDINGS: In this consensus paper, we proposed to use a patient as a phantom to assess the accuracy of MRAC using CT as the reference standard. Following the proposed guidelines for data acquisition, image reconstruction, and data analysis, we have tested the proposed approach successfully across 2 PET/MRI scanner manufacturers at 2 sites.

IMPLICATIONS FOR PATIENT CARE: Integrated PET/MRI scanners can be qualified for multicenter trials focused on neurologic applications.

REFERENCES

1. Catana C. Attenuation correction for human PET/MRI studies. *Phys Med Biol.* 2020;65:23TR02.
2. Chen Y, An H. Attenuation correction of PET/MR imaging. *Magn Reson Imaging Clin N Am.* 2017;25:245–255.
3. Bowen SL, Fuin N, Levine MA, Catana C. Transmission imaging for integrated PET-MR systems. *Phys Med Biol.* 2016;61:5547–5568.
4. Farag A, Thompson RT, Thiessen JD, Prato FS, Théberge J. Improved PET/MRI accuracy by use of static transmission source in empirically derived hardware attenuation correction. *EJNMMI Phys.* 2021;8:24.
5. Mollet P, Keereman V, Bini J, Izquierdo-Garcia D, Fayad ZA, Vandenberghe S. Improvement of attenuation correction in time-of-flight PET/MR imaging with a positron-emitting source. *J Nucl Med.* 2014;55:329–336.
6. Kinahan PE, Hasegawa BH, Beyer T. X-ray-based attenuation correction for positron emission tomography/computed tomography scanners. *Semin Nucl Med.* 2003;33:166–179.

7. Harries J, Jochimsen TH, Scholz T, et al. A realistic phantom of the human head for PET-MRI. *EJNMMI Phys.* 2020;7:52.
8. Mitsouras D, Lee TC, Liacouras P, et al. Three-dimensional printing of MRI-visible phantoms and MR image-guided therapy simulation. *Magn Reson Med.* 2017;77:613–622.
9. Rausch I, Valladares A, Sundar LKS, et al. Standard MRI-based attenuation correction for PET/MRI phantoms: a novel concept using MRI-visible polymer. *EJNMMI Phys.* 2021;8:18.
10. MacFarlane CR. ACR accreditation of nuclear medicine and PET imaging departments. *J Nucl Med Technol.* 2006;34:18–24.
11. Ziegler S, Braun H, Ritt P, Hocke C, Kuwert T, Quick HH. Systematic evaluation of phantom fluids for simultaneous PET/MR hybrid imaging. *J Nucl Med.* 2013; 54:1464–1471.
12. Scheuermann JS, Saffer JR, Karp JS, Levering AM, Siegel BA. Qualification of PET scanners for use in multicenter cancer clinical trials: the American College of Radiology Imaging Network experience. *J Nucl Med.* 2009;50:1187–1193.
13. Aide N, Lasnon C, Veit-Haibach P, Sera T, Sattler B, Boellaard R. EANM/EARL harmonization strategies in PET quantification: from daily practice to multicentre oncological studies. *Eur J Nucl Med Mol Imaging.* 2017;44:17–31.
14. Complete accreditation information. nuclear medicine and PET (revised 12-12-19). Accreditation Support website. https://accreditationsupport.acr.org/support/solutions/articles/11000063279-complete-accreditation-information-nuclear-medicine-and-pet. Modified April 5, 2021. Accessed November 23, 2021.
15. *The IAC Standards and Guidelines for Nuclear/PET Accreditation*. Intersocietal Accreditation Commission. 2021:36–37.
16. *Accreditation Handbook for Diagnostic Imaging Centers: What You Need to Know About Obtaining Accreditation*. The Joint Commission; 2011:8–15.
17. Sunderland JJ, Christian PE. Quantitative PET/CT scanner performance characterization based upon the Society of Nuclear Medicine and Molecular Imaging clinical trials network oncology clinical simulator phantom. *J Nucl Med.* 2015;56:145–152.
18. Klein S, Staring M, Murphy K, Viergever MA, Pluim JPW. elastix: a toolbox for intensity-based medical image registration. *IEEE Trans Med Imaging.* 2010;29: 196–205.
19. Shamonin DP, Bron E, Lelieveldt B, Smits M, Klein S, Staring M. Fast parallel image registration on CPU and GPU for diagnostic classification of Alzheimer's disease. *Front Neuroinform.* 2014;7:50.
20. Penny WD, Friston KJ, Ashburner JT, Kiebel SJ, Nichols TE. *Statistical Parametric Mapping: The Analysis of Functional Brain Images*. Elsevier; 2011:49–62.
21. Yoo TS, Ackerman MJ, Lorensen WE, et al. Engineering and algorithm design for an image processing Api: a technical report on ITK—the Insight Toolkit. *Stud Health Technol Inform.* 2002;85:586–592.
22. McCormick M, Liu X, Ibanez L, Jomier J, Marion C. ITK: enabling reproducible research and open science. *Front Neuroinform.* 2014;8:13.
23. Fischl B. FreeSurfer. *Neuroimage.* 2012;62:774–781.
24. Wollenweber SD, Ambwani S, Delso G, et al. Evaluation of an atlas-based PET head attenuation correction using PET/CT & MR patient data. *IEEE Trans Nucl Sci.* 2013;60:3383–3390.
25. Sekine T, Buck A, Delso G, et al. Evaluation of atlas-based attenuation correction for integrated PET/MR in human brain: application of a head atlas and comparison to true CT-based attenuation correction. *J Nucl Med.* 2016;57:215–220.
26. Wiesinger F, Sacolick LI, Menini A, et al. Zero TE MR bone imaging in the head. *Magn Reson Med.* 2016;75:107–114.
27. Sekine T, Ter Voert EEGW, Warnock G, et al. Clinical evaluation of zero-echo-time attenuation correction for brain ^{18}F-FDG PET/MRI: comparison with atlas attenuation correction. *J Nucl Med.* 2016;57:1927–1932.
28. Delso G, Martinez-Moller A, Bundschuh RA, Nekolla SG, Ziegler SI. The effect of limited MR field of view in MR/PET attenuation correction. *Med Phys.* 2010; 37:2804–2812.
29. Paulus DH, Quick HH, Geppert C, et al. Whole-body PET/MR imaging: quantitative evaluation of a novel model-based MR attenuation correction method including bone. *J Nucl Med.* 2015;56:1061–1066.
30. Mormino EC, Betensky RA, Hedden T, et al. Amyloid and APOE ε4 interact to influence short-term decline in preclinical Alzheimer disease. *Neurology.* 2014;82: 1760–1767.
31. Buckley RF, Mormino EC, Rabin JS, et al. Sex differences in the association of global amyloid and regional tau deposition measured by positron emission tomography in clinically normal older adults. *JAMA Neurol.* 2019;76:542–551.
32. Rezaei A, Defrise M, Bal G, et al. Simultaneous reconstruction of activity and attenuation in time-of-flight PET. *IEEE Trans Med Imaging.* 2012;31: 2224–2233.
33. Liu F, Jang H, Kijowski R, Bradshaw T, McMillan AB. Deep learning MR imaging-based attenuation correction for PET/MR imaging. *Radiology.* 2018;286: 676–684.
34. Yang J, Park D, Sohn JH, Wang ZJ, Gullberg GT, Seo Y. Joint correction of attenuation and scatter using deep convolutional neural networks (DCNN) for time-of-flight PET. *Phys Med Biol.* 2019;64:16–19.

Whole-Body Parametric Imaging of ^{18}F-FDG PET Using uEXPLORER with Reduced Scanning Time

Yaping Wu*[1], Tao Feng*[2], Yizhang Zhao[3], Tianyi Xu[3], Fangfang Fu[1], Zhun Huang[1], Nan Meng[1], Hongdi Li[2], Fengmin Shao[1], and Meiyun Wang[1]

[1]*Department of Medical Imaging, Henan Provincial People's Hospital, Henan, China;* [2]*UIH America Inc., Houston, Texas; and* [3]*United Imaging Healthcare, Shanghai, China*

Parametric imaging of the net influx rate (K_i) in ^{18}F-FDG PET has been shown to provide improved quantification and specificity for cancer detection compared with SUV imaging. Current methods of generating parametric images usually require a long dynamic scanning time. With the recently developed uEXPLORER scanner, a dramatic increase in sensitivity has reduced the noise in dynamic imaging, making it more robust to use a nonlinear estimation method and flexible protocols. In this work, we explored 2 new possible protocols besides the standard 60-min one for the possibility of reducing scanning time for K_i imaging. **Methods:** The gold standard protocol (protocol 1) was conventional dynamic scanning with a 60-min scanning time. The first proposed protocol (protocol 2) included 2 scanning periods: 0–4 min and 54–60 min after injection. The second proposed protocol (protocol 3) consisted of a single scanning period from 50 to 60 min after injection, with a second injection applied at 56 min. The 2 new protocols were simulated from the 60-min standard scans. A hybrid input function combining the population-based input function and the image-derived input function (IDIF) was used. The results were also compared with the IDIF acquired from protocol 1. A previously developed maximum-likelihood approach was used to estimate the K_i images. In total, 7 cancer patients imaged using the uEXPLORER scanner were enrolled in this study. Lesions were identified from the patient data, and the lesion K_i values were compared among the different protocols. **Results:** The acquired hybrid input function was comparable in shape to the IDIF for each patient. The average difference in area under the curve was about 3%, suggesting good quantitative accuracy. The visual difference between the K_i images generated using IDIF and those generated using the hybrid input function was also minimal. The acquired K_i images using different protocols were visually comparable. The average K_i difference in the lesions was 2.8% ± 2.1% for protocol 2 and 1% ± 2.2% for protocol 3. **Conclusion:** The results suggest that it is possible to acquire K_i images using the nonlinear estimation approach with a much-reduced scanning time. Between the 2 new protocols, the protocol with dual injection shows the greatest promise in terms of practicality.

Key Words: image reconstruction; radiotracer tissue kinetics; dual injections; PET parametric imaging; reduced scanning time; total-body PET

J Nucl Med 2022; 63:622–628
DOI: 10.2967/jnumed.120.261651

PET with SUVs (*1*,*2*) is widely used in clinical oncology for tumor imaging. However, the use of SUVs suffers from several drawbacks (*3*). For instance, the kinetics of uptake time for ^{18}F-FDG may vary significantly in different tissues (*4*). In addition, the use of SUV measurements to differentiate malignant tumors from processes such as inflammation is challenging (*5*–*7*).

Parametric imaging provides an alternative to SUV imaging and has the potential to provide added information. For ^{18}F-FDG studies, a few parameters are commonly derived, such as the net influx rate (K_i), the delivery rate constant (K_1), and blood fractions in tissue. K_i is more commonly used and often acquired using graphical methods because of its simplicity (*8*). The acquired K_i has been found to yield improved specificity at a similar sensitivity for cancer detection (*9*). K_i images have also been found to yield better results for tumor volume delineation than SUV images (*10*). ^{18}F-FDG K_1 alone or combined with K_i was found to be an indicator of tumor subgroup (*11*) and a way to evaluate chemotherapy response (*12*). The combined ^{18}F-FDG parameters were found to be helpful for assessing metabolic tumors (*13*) as well.

Compared with SUV imaging, parametric imaging also has its challenges. One is the need for an accurate input function. The conventional approach requires invasive sampling of arterial blood. In recent years, more studies have been suggesting that the image-derived input function (IDIF) (*14*,*15*), population-based input function (*16*), or hybrid input function with both image data and population samples (*17*) can be used as a noninvasive replacement. Another practical issue is the much-increased scanning time. In estimating K_i using the conventional Patlak method, a much longer scan is unavoidable. This is because the K_i image is the slope image in the Patlak model; with slow-changing dynamics, it requires a long scanning time to accurately estimate the change in activity. As a result, a minimal scanning time of 30 min is often used to estimate K_i with the Patlak model. Compared with state-of-art whole-body SUV scans, which last less than 10 min, the much-increased scanning time has limited the daily application of parametric imaging. The much-increased scanning time also increases the likelihood of patient motion during scans, which may further degrade image quality.

Although a single-bed-position acquisition is usually conventional for parametric imaging, whole-body Patlak analysis using regular scanners (*18*) or the total-body uEXPLORER scanner (*19*) has recently been proposed and validated. Whole-body parametric imaging provides a unique opportunity for the inspection of disseminated disease—also a major application of PET imaging.

Compared with the graphical method, K_i can also be estimated using a nonlinear approach with an 2-tissue-compartment irreversible

Received Dec. 9, 2020; revision accepted Jun. 14, 2021.
For correspondence or reprints, contact Meiyun Wang (mywang@ha.edu.cn).
*Contributed equally to this work.
Published online Aug. 12, 2021.
COPYRIGHT © 2022 by the Society of Nuclear Medicine and Molecular Imaging.

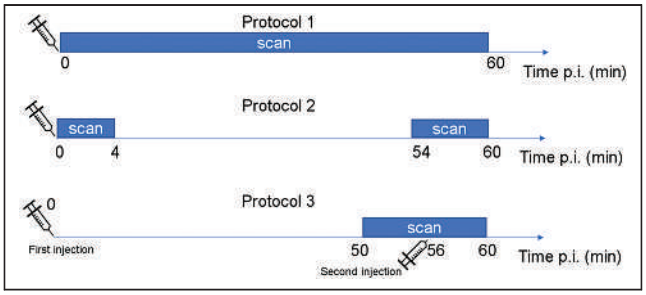

FIGURE 1. Illustration of the 3 protocols proposed in this study. p.i. = after injection.

model. An entire time–activity curve consisting of a 60-min scan or an even longer scanning time is usually used for this purpose. With the uEXPLORER (*20*), the much-increased sensitivity of the whole-body scan has dramatically reduced noise in the reconstructed dynamic images. This reduction has made nonlinear estimation more robust. An advantage of nonlinear estimation is that it can better use dynamic data than models (Patlak model) that require data after equilibrium for estimation (*21*), therefore providing more freedom in protocol design. In previous studies, we demonstrated the possibility of reducing scanning time for estimating parameters such as K_1 and the blood fraction (*22*). In this work, we further explored the possibility of accurately estimating K_i using a much shorter dynamic scanning sequence with a total scanning time of 10 min for whole-body imaging. Two alternatives were investigated. One used a combination of early-time-point and late-time-point scanning (dual-time-point scanning), and the other used a dual-injection protocol to combine both early dynamic information and late dynamic information within a single scan.

MATERIALS AND METHODS

Scanning Protocols

Three protocols were studied in this work. Protocol 1 was a conventional 0 min to 60 min dynamic scan. It was used as the gold standard to evaluate the performance of the 2 proposed protocols.

The first proposed protocol (protocol 2) consisted of a combination of 2 time points, that is, an early time point at 0–4 min after injection and a late time point at 54–60 min after injection. To minimize use of scanner time, the patients were scanned twice, with registration taking place between the scans. As a proof of concept, this protocol was simulated by excluding the 4 min to 54 min post-injection interval of an entire 0 min to 60 min dynamic scan. The main goal of this protocol was to examine the accuracy of the estimation by using information from only the early and late phases.

The second proposed protocol (protocol 3) used a single scanning period of 50–60 min after injection, with the help of a dual-injection scheme. The first injection occurred at t = 0 (protocol began with the first injection), and the second injection occurred 56 min later. In this case, the last 4 min provided the early dynamic data, and the first 6 min provided information similar to that of the second scanning period in protocol 2. This scanning protocol was simulated by combining the dynamic images from 0 to 4 min after injection with those from 56 to 60 min after injection. Figure 1 illustrates the 3 protocols, and Table 1 shows their dynamic time frames.

Input Functions

For protocol 1, the IDIF was used. The ascending aorta was used to extract the IDIF, as it is less affected by respiratory motion. For the other 2 protocols, with the limited scanning time, the IDIF was not available for the entire dynamic range. In this work, we acquired the input function using a hybrid approach by combining the population-based input function, the model-based input function, and the IDIF. The input function for protocol 2 is proposed as

$$C_p(t) \triangleq \begin{cases} C_{\text{image }1}(t) & t \le t_1 \\ \mu e^{-\gamma(t-t_1)} C_{p0}(t) & t \le t_1 \text{ and } t \le t_2 \\ C_{\text{image }2}(t) & t \le t_2 \end{cases} \quad \text{Eq. 1}$$

where $C_{\text{image }1}(t)$ is the IDIF of the first 4 min and $C_{\text{image }2}(t)$ is the IDIF of the last 6 min. $C_{p0}(t)$ is the population-based input function, γ and μ are the scaling constants that satisfy $\mu C_{p0}(t_1) = C_{\text{image }1}(t_1)$, and $\mu e^{-\gamma(t_2-t_1)} C_{p0}(t_2) = C_{\text{image }2}(t_2)$.

For protocol 3, the input function was based on 2 assumptions: the first is that the later phase of the input function can be approximated as a single exponential function, and the second is that the shape of the input function from the second injection has the same shape as the input function from the first injection. In literature studies with multiple injections in 1 patient, the similarity of the produced input function (*23*) supports the second assumption.

The IDIF was first separated into 2 regions: before the second injection ($C_B(t)$) and after the second injection ($C_A(t)$), where t_0 represents the second injection time. An exponential curve ($C_{B0}e^{-bt}$) was used to fit $C_B(t)$, and the contribution of the second injection was estimated by subtracting the exponential curve from the IDIF $C_A(t)$, that is, $C_A(t) - C_{B0}e^{-bt}$. The contribution from the second injection was treated as the early-phase input function ($C_{\text{image }1}(t)$), like that in protocol 2, and $C_B(t)$ was treated as the late phase input function ($C_{\text{image }2}(t)$), like that in protocol 2. The missing part was approximated using the same approach as shown in Equation 1.

For both protocol 2 and protocol 3, the original IDIF acquired using the whole dynamic process was used as the gold standard.

Maximum-Likelihood Estimation

The dynamic changes in ^{18}F-FDG within the human body can be approximated using the 2-tissue-compartment model, where

TABLE 1
Dynamic Frames for Different Protocols

Parameter	Protocol 1	Protocol 2	Protocol 3
Start time (min)	0	0	50
Dynamic frames	5 (s) × 30	5 (s) × 30	120 (s) × 3
	30 (s) × 15	30 (s) × 3	5 (s) × 30
	120 (s) × 25	50 (min) × 1 (no scan); 120 (s) × 3	30 (s) × 3

TABLE 2
Patient Data Used in This Study

Patient no.	Sex	Weight (kg)	Injected dose (MBq)	Preliminary diagnosis
1	M	75	224.7	Prostate cancer
2	F	60	223.5	None
3	F	50	246.4	Pulmonary nodule
4	M	60	317.1	Space-occupying lesion (brain)
5	M	83	306.0	Gastric cancer
6	F	55	219.6	Leiomyoma
7	M	81	375.7	Pulmonary nodule

the first compartment (C_1) describes perfusion of ^{18}F-FDG to the tissue and the second compartment (C_2) models the phosphorylation process within the cells. The 2 compartments can be modeled mathematically using the rate constants

$$\begin{cases} \dfrac{dC_1}{dt} = K_1 C_p + k_4 C_2 - k_2 C_1 - k_3 C_1 \\ \dfrac{dC_2}{dt} = k_3 C_1 - k_4 C_2 \end{cases} \quad \text{Eq. 2}$$

where K_1 and k_2 describe the forward and backward perfusion process of ^{18}F-FDG in the tissue, and k_3 and k_4 describe the phosphorylation and dephosphorylation process. In many cancer cells, FDG-6-phosphate is only minimally dephosphorylated and is trapped within the cell (*24*). This process allows us to simplify the model by assigning a value of 0 to k_4. The acquired dynamic PET image, $X(t)$, can be represented using the equation below when k_4 is 0.

$$X = v_b C_p + C_1 + C_2 = v_b C_p + \frac{k_2 K_1}{k_2 + k_3} \exp(-(k_2 + k_3)t) \otimes C_p(t) + \frac{k_3 K_1}{k_2 + k_3} \int C_p dt \quad \text{Eq. 3}$$

where $K_1' = K_1 \frac{k_2 K_1}{k_2 + k_3}$, $k_2' = k_2 + k_3$, $K_i = \frac{k_3 K_1}{k_2 + k_3}$, and $C_i(t) = \int C_p dt$. With these definitions, the above equation can be written as

$$X = v_b C_p + C_1 + C_2 = v_b C_p(t) + K_1' \exp\left(-k_2' t\right) \otimes C_p(t) + K_i C_i(t) \quad \text{Eq. 4}$$

The above equation is similar to the Patlak model, where the K_i has the same definition as that in the Patlak model, and the combined effect of $v_b + K_1' \exp\left(-k_2' t\right) \otimes / C_b(t)$ was treated as a constant after equilibrium in the Patlak model.

With the assumption that the voxel values in the dynamic image approximately follow a scaled Poisson distribution (*25*), the maximum-likelihood estimation approach was used for estimating K_i. The update equation for K_i can be derived as

$$K_i^{p+1} = \frac{K_i^p}{\sum_t C_i(t)} \sum_t \frac{C_i(t) \boldsymbol{X}(t)}{\hat{C}^p(t)} \quad \text{Eq. 5}$$

where $\hat{C}^p(t) = v_b^p C_b + K_1' p e^{-k_2' pt} \otimes C_p(t) + K_i' p C_i(t)$ is the estimated dynamic image at time t given the estimated parametric images and p is the iteration number. The effects of different frame lengths were included in C_p and C_i in the above equations. The derivation is similar to our previous proposed update equation for v_b and K_1 (*22*). For whole-body imaging, the input function C_p may also be subject to the delay and dispersion effects. The delay effect is modeled and estimated using the same approach as one previously proposed (*22*). In total, 5 parameters, including K_1', k_2', v_b, K_i, and the time delay, were estimated jointly. The estimated K_i was analyzed subsequently because it is the target of interest in this study.

Patient Data and Image Reconstruction

In our study, 7 potential cancer patients (Table 2) referred to the Henan Hospital were imaged using the uEXPLORER scanner (Shanghai United Imaging Healthcare) with the dynamic scanning protocol. The patient group was preselected to exclude those with significant motion artifacts and those with nonbolus input functions. Visual examinations were used to determine the motion artifacts, and the exclusion criteria were examinations with visible motion greater than 5 voxels or 15 mm. The dynamic study was approved by the Institutional Review Board of the hospital, and written informed consent was obtained from each patient. The patients included 4 men and 3 women, with a weight of 66±13 kg and an injected dose of 273±60 MBq (mean ± SD). The leg was chosen as the injection site because it is closer to the end of the gantry.

Dynamic images were reconstructed using the vendor-recommended settings with random, scatter, attenuation, normalization, and dead-time corrections; the reconstructed images had a 2.89-mm slice thickness and a 3.125-mm voxel size in the transaxial plane. The number of voxels in the reconstructed image was 192 by 192 by 672. Time-of-flight reconstructions were applied using manufacturer-supplied reconstruction software (ordered-subsets expectation maximization with 3 iterations and 24 subsets) with the point-spread-function model.

An alternate update approach was applied for the joint estimation process. Twenty-seven main iterations were used. In each iteration, 6 subiterations were used for K_i, K_1', and the blood fraction (with a total iteration number of 162); 2 subiterations were used

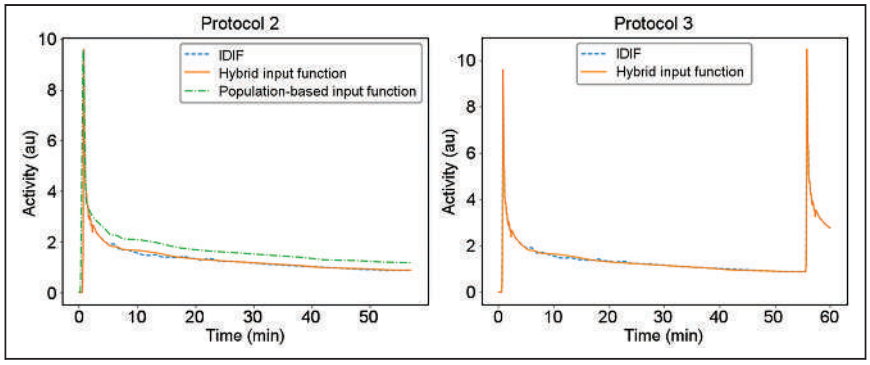

FIGURE 2. Comparison of IDIF and hybrid input function for protocols 2 and 3. Original population-based input function is also displayed for comparison. au = arbitrary units.

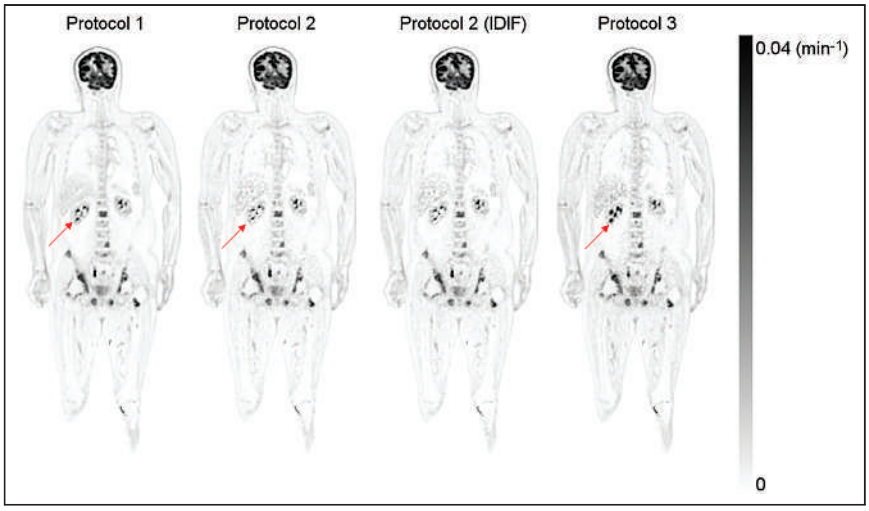

FIGURE 3. Estimated K_i image of patient with prostate cancer. Arrows show regions with large K_i differences using different protocols.

for the time delay; and 1 subiteration was used for k_2'. The K_i estimated using protocol 1 with the IDIF was selected as the gold standard. K_i was also estimated using the conventional Patlak model for comparison. In the Patlak method, data from 20 min after injection to 60 min after injection with IDIF were used. The framing sequence was the same as for protocol 1. No postsmoothing filter was applied. The noise of the estimated images was calculated using VOIs in the thigh muscle region. The coefficient of variation was used as the surrogate for noise. A region-growing approach with a threshold of 90% of the maximum value in the K_i image (protocol 1) was used for lesion acquisition. The average K_i value of the lesions from images acquired using different methods was also measured to study quantitative accuracy.

RESULTS

Figure 2 shows the input functions acquired from a patient using the IDIF approach and the proposed hybrid approach. The original population-based input function (*17*) is also displayed with normalized peak value. A significant difference existed between the population-based input function and the IDIF when normalized to the same peak value, but good agreement could be achieved with the hybrid method. For all patient data, the average area-under-the-curve ratio between the hybrid input function and the IDIF was 1.03 ± 0.04, suggesting it is possible to use the hybrid input function for K_i estimation when the whole dynamic data are unavailable.

Figure 3 shows the reconstructed K_i images of patient 1 using the 3 protocols (K_1' and k_2' images are included in Supplemental Figs. 1 and 2; supplemental materials are available at http://jnm.snmjournals.org). The same color scale was used for all images. The IDIF was used in protocol 1, and both the IDIF and the hybrid input function were used in the other protocols. The K_i images acquired using protocols 2 and 3 were visually comparable to that using protocol 1 but noisier. Figure 4 shows the difference images of K_i generated using different protocols (Supplemental Fig. 3 shows the corresponding percentage images). Minimal difference was observed between IDIF-based and hybrid input function–generated K_i images. Figure 5 shows the maximum-intensity projections of the reconstructed K_i images, as well as the SUV image for patient 5. The same scale was used for all K_i images, and the SUV image was scaled for comparable muscle uptake.

Image noise using the 3 estimations was also calculated. The average coefficient of variation was 0.12 ± 0.04 for K_i images estimated using protocol 1 in the thigh muscle region, 0.22 ± 0.05 for K_i images estimated using protocol 2, and 0.20 ± 0.04 with protocol 3. The much-reduced noise level in protocol 1 was likely caused by the long scanning time. Protocol 3 also showed a reduced noise level when compared with protocol 2; this reduction was likely caused by the use of summed data, as it is effectively 2 times the dose compared with protocol 2.

Using protocol 1, K_i was calculated with the proposed nonlinear approach and the conventional Patlak approach (Fig. 6). The images generally agree with each other, with some minor differences. The noise level in the nonlinear estimation was visually lower than that in the linear estimation, as agrees with literature findings (*26*). A higher muscle-background K_i value was detected in the nonlinear approach.

In total, 26 lesions were identified and segmented from the patients. The same region of interest was used for different K_i images generated in different protocols for consistency. The average diameter of the segmented lesions was 13.8 mm. The K_i values inside the region of interest measured by the gold standard and the protocols with the reduced scanning time are plotted in Figure 7. An example of the fitted time–activity curve is included in Supplemental Figure 4. The mean difference between protocol 2 and protocol 1 was 2.8% ± 2.1%. The mean difference between protocol 3 and protocol 1 was 1% ± 2.2%. This result suggests that with a total scanning time of 10 min, the new protocols were able to maintain quantitative accuracy for the lesions despite the much-reduced scanning time.

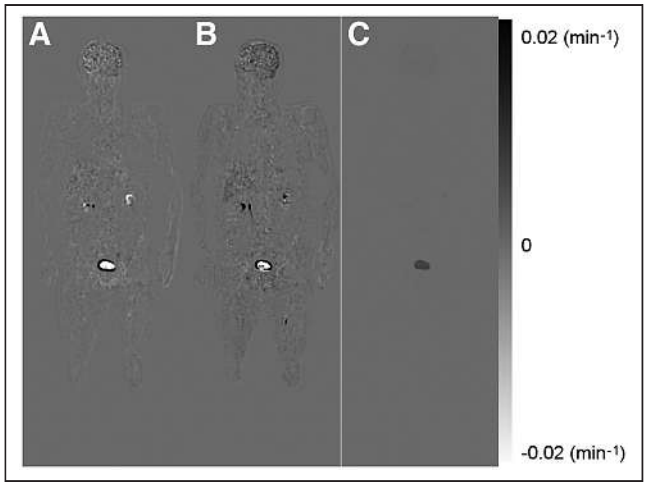

FIGURE 4. (A) Difference image of K_i between protocols 2 and 1. (B) Difference image of K_i between protocols 3 and 1. (C) Difference image of K_i estimated using IDIF and hybrid input function with protocol 2.

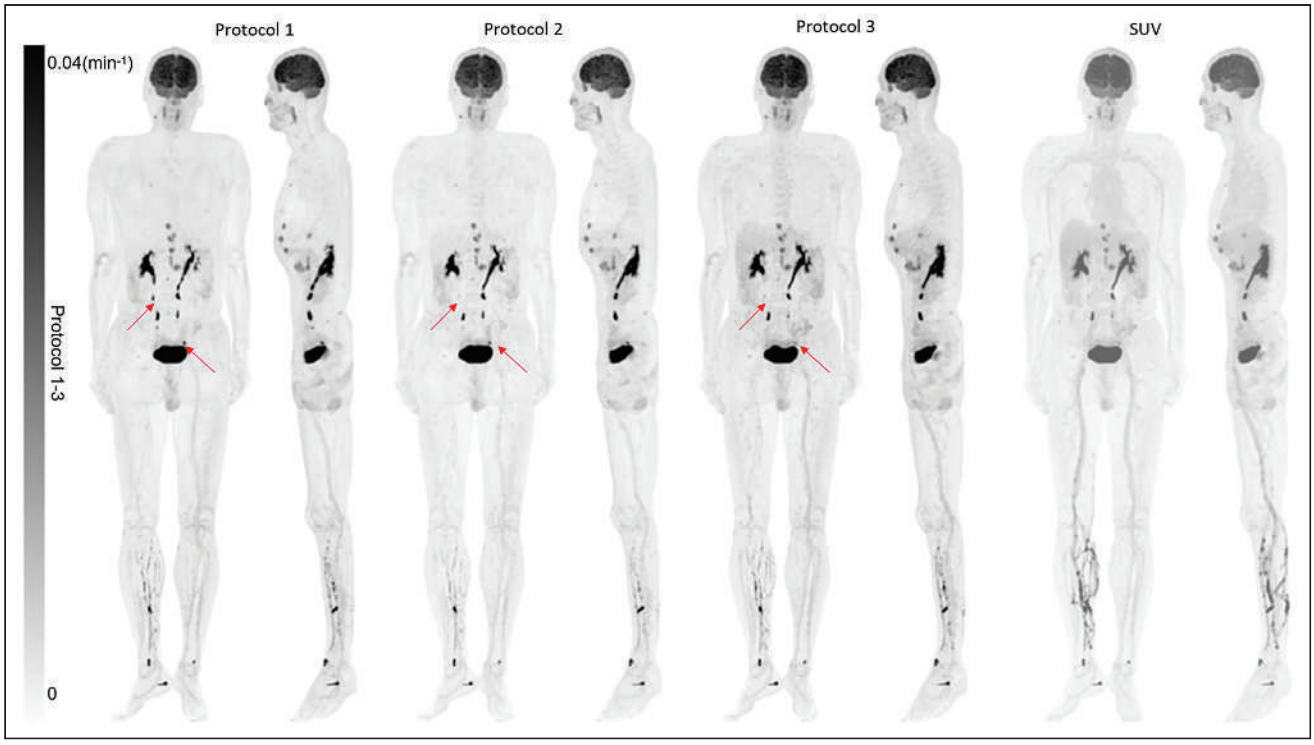

FIGURE 5. Maximum-intensity-projection PET image of K_i from protocols 1–3 and SUV image acquired at 60 min. Arrows show regions with large K_i differences using different protocols.

DISCUSSION

The K_i difference between images (Fig. 4C) estimated using IDIF and the hybrid input function was negligible in most cases, suggesting that the hybrid input function can be a reliable approach for estimating K_i images. However, with the hybrid input function, quantitative errors can still be present because of patient variations. The hybrid input function was also noninvasive and does not rely on data outside the acquisition period, making it easier to be incorporated into clinical studies.

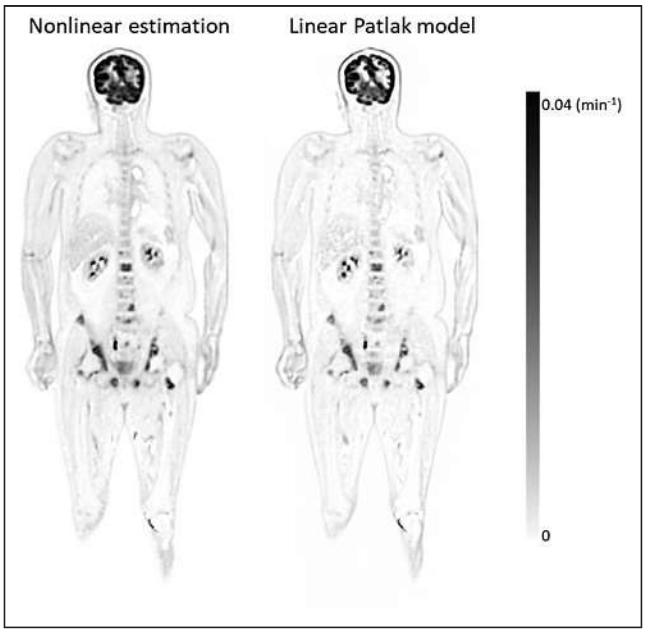

FIGURE 6. Estimated K_i image using nonlinear model (protocol 1) and linear Patlak model.

Because of the residual activity around the injection site, some differences were present in the veins on the left leg among the different protocols. A large difference in K_i was observed in the kidney region among the different protocols. The difference might be explained by the fact that the 2-tissue-compartment irreversible model cannot accurately model the renal excretion process, and therefore a large difference can be expected with different protocols. In general, K_i images show much-improved lesion contrast when compared with SUV images, suggesting improved clinical value with K_i imaging.

Although good quantitative accuracy was observed in the lesions, a slight overestimation was observed in the muscle and liver region with the nonlinear approach and protocol 3. One reason could be the reduction in estimation accuracy due to combined early-phase and late-phase information in the dynamic data. As shown in the supplemental figures, the accuracy of estimated K_1' and k_2' in protocol 3 was also not as good as that in protocol 2. Another reason could be the model mismatch effect. Because it was shown that the 2-tissue-compartment irreversible model may not be true in some tissues, as a nonzero k_4 can be expected in some normal cells (*24*), different estimated results can be expected with different estimation methods or protocols.

A limitation of our approaches is that they require 2 scanning sessions (protocol 2) or 2 ^{18}F-FDG administrations (protocol 3). This requirement makes the methods less practical but reduces the

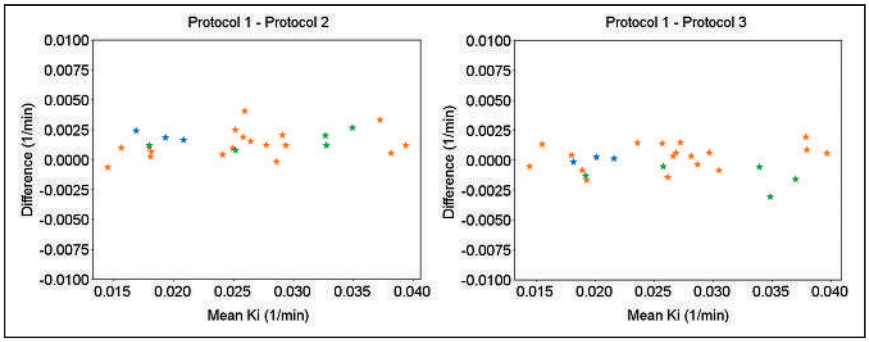

FIGURE 7. Bland–Altman plot for estimated K_i in different lesions using different protocols. *x*-axis shows mean K_i, and *y*-axis shows K_i difference. Lesions from different patients are encoded using different colors.

overall time spent on the PET/CT system. Protocol 2 requires additional image registration, which was not modeled in this study. The additional image registration may also introduce image artifacts that were not studied here. A second CT scan or a low-dose CT scan may also be required in the second scan for accurate image registration and attenuation correction. These challenges make protocol 2 less practical. On the other hand, the estimation method in protocol 2 provides a foundation for protocol 3 to work, as it shows that K_i can be estimated by combining the early-phase and late-phase dynamic data. Protocol 3 provides a much better alternative for practical application of fast K_i imaging with dual injections, as the data were acquired in a single scan frame without the need for registration or another CT scan. The absence of a second scan also makes patient management much easier and—because of the much shorter scanning time—reduces the likelihood of voluntary patient motion. However, patient motion may still impact the method, and therefore, motion compensation is still required for an improved quantitative result. There are potential challenges in protocol 3 as well. One is the assumption that the early-phase input function is the same as the second bolus injection. Future studies are required to study the impact of this effect. The direct addition of the images for simulating protocol 3 also doubles the effective injected dose, making the estimated noise in protocol 3 smaller than that in protocol 2. When the injected dose is kept the same, image noise is expected to be higher when using protocol 3.

van Sluis et al. also showed the possibility of reducing the scanning duration using the conventional Patlak model with the help of the population-based input function (*27*). The advantage of using the Patlak model is that it requires only a single injection. With the dual-injection protocols proposed in this study, we can achieve an even shorter scanning time and the potential for multiparametric imaging. Both approaches could be useful in clinical situations to promote the practical use of parametric imaging protocols.

CONCLUSION

In this study, we have shown that with the modified protocols, it is possible to dramatically reduce the required scanning time for whole-body K_i imaging to 10 min. The estimation of K_i is possible because of the presence of both early-phase and late-phase information in the new protocols. The reduction in scanning time makes it easier to incorporate K_i imaging into clinical routine.

DISCLOSURE

This work was partially supported by the National Key R&D Program of China (2017YFE0103600), the National Science Foundation of China (81720108021), the Zhongyuan Thousand Talents Plan Project (ZYQ201810117), and the Zhengzhou Collaborative Innovation Major Project (20XTZX05015). Tao Feng and Hongdi Li are employed by UIH America, Inc., and Yizhang Zhao and Tianyi Xu are employed by United Imaging Healthcare. No other potential conflict of interest relevant to this article was reported.

KEY POINTS

QUESTION: Can whole-body K_i imaging be achieved using a much-reduced scanning time (10 min)?

PERTINENT FINDINGS: We have demonstrated with the new protocols (dual scanning points or dual injections) that it is possible to generate whole-body K_i images with a total scanning time of 10 min.

IMPLICATIONS FOR PATIENT CARE: A much-reduced scanning time for K_i imaging improves the practicality for parametric imaging. A wider application of parametric imaging could be helpful for better diagnosis and treatment.

REFERENCES

1. Delbeke D, Coleman RE, Guiberteau MJ, et al. Procedure guideline for tumor imaging with ^{18}F-FDG PET/CT 1.0. *J Nucl Med.* 2006;47:885–895.
2. Lindholm P, Minn H, Leskinen-Kallio S, Bergman J, Ruotsalainen U, Joensuu H. Influence of the blood glucose concentration on FDG uptake in cancer: a PET study. *J Nucl Med.* 1993;34:1–6.
3. Adams MC, Turkington TG, Wilson JM, Wong TZ. A systematic review of the factors affecting accuracy of SUV measurements. *AJR.* 2010;195:310–320.
4. Shankar LK, Hoffman JM, Bacharach S, et al. Consensus recommendations for the use of ^{18}F-FDG PET as an indicator of therapeutic response in patients in National Cancer Institute Trials. *J Nucl Med.* 2006;47:1059–1066.
5. Metser U, Even-Sapir E. Increased 18F-fluoro- deoxyglucose uptake in benign, nonphysiologic lesions found on whole-body positron emission tomography/computed tomography (PET/CT): accumulated data from four years of experience with PET/CT. In: *Seminars in Nuclear Medicine.* Vol 37. Elsevier; 2007:206–222.
6. Shreve PD, Anzai Y, Wahl RL. Pitfalls in oncologic diagnosis with FDG PET imaging: physiologic and benign variants. *Radiographics.* 1999;19:61–77.
7. Strauss LG. Fluorine-18 deoxyglucose and false-positive results: a major problem in the diagnostics of oncological patients. *Eur J Nucl Med.* 1996;23:1409–1415.
8. Patlak CS, Blasberg RG. Graphical evaluation of blood-to-brain transfer constants from multiple-time uptake data: generalizations. *J Cereb Blood Flow Metab.* 1985; 5:584–590.
9. Magri A, Krol A, Lee W, Lipson E, McGraw W, Feiglin D. A new method to determine probability of malignancy using dynamic breast F-18-FDG PET studies [abstract]. *J Nucl Med.* 2009;50(suppl 2):1445.
10. Visser EP, Philippens MEP, Kienhorst L, et al. Comparison of tumor volumes derived from glucose metabolic rate maps and SUV maps in dynamic ^{18}F-FDG PET. *J Nucl Med.* 2008;49:892–898.
11. Sugawara Y, Zasadny KR, Grossman HB, Francis IR, Clarke MF, Wahl RL. Germ cell tumor: differentiation of viable tumor, mature teratoma, and necrotic tissue with FDG PET and kinetic modeling. *Radiology.* 1999;211:249–256.

12. Song SL, Deng C, Wen L, et al. ^{18}F-FDG PET/CT-related metabolic parameters and their value in early prediction of chemotherapy response in a VX2 tumor model. *Nucl Med Biol.* 2010;37:327–333.
13. Wang G, Parikh M, Nardo L, et al. Total-body dynamic PET of metastatic cancer: first patient results [abstract]. *J Nucl Med.* 2020;61(suppl 1):208.
14. Chen K, Bandy D, Reiman E, et al. Noninvasive quantification of the cerebral metabolic rate for glucose using positron emission tomography, ^{18}F-fluoro-2-deoxyglucose, the Patlak method, and an image-derived input function. *J Cereb Blood Flow Metab.* 1998;18:716–723.
15. Feng T, Tsui BMW, Li X, et al. Image-derived and arterial blood sampled input functions for quantitative PET imaging of the angiotensin II subtype 1 receptor in the kidney. *Med Phys.* 2015;42:6736–6744.
16. Rissanen E, Tuisku J, Luoto P, et al. Automated reference region extraction and population-based input function for brain [^{11}C] TMSX PET image analyses. *J Cereb Blood Flow Metab.* 2015;35:157–165.
17. Yao S, Feng T, Zhao Y, et al. Simplified protocol for whole body Patlak parametric imaging with ^{18}F-FDG PET/CT: feasibility and error analysis. *Med Phys.* 2021;48:2160–2169.
18. Karakatsanis NA, Lodge MA, Tahari AK, Zhou Y, Wahl RL, Rahmim A. Dynamic whole-body PET parametric imaging: I. Concept, acquisition protocol optimization and clinical application. *Phys Med Biol.* 2013;58:7391–7418.
19. Zhang X, Xie Z, Berg E, et al. Total-body dynamic reconstruction and parametric imaging on the uEXPLORER. *J Nucl Med.* 2020;61:285–291.
20. Badawi RD, Shi H, Hu P, et al. First human imaging studies with the EXPLORER total-body PET scanner. *J Nucl Med.* 2019;60:299–303.
21. Yu D-C, Huang S-C, Barrio JR, Phelps ME. The assessment of the non-equilibrium effect in the 'Patlak analysis' of Fdopa PET studies. *Phys Med Biol.* 1995;40:1243–1254.
22. Feng T, Zhao Y, Shi H, et al. Total-body quantitative parametric imaging of early kinetics of ^{18}F-FDG. *J Nucl Med.* 2021;62:738–744.
23. Lodge MA, Jacene HA, Pili R, Wahl RL. Reproducibility of tumor blood flow quantification with ^{15}O-water PET. *J Nucl Med.* 2008;49:1620–1627.
24. Tsurusaki M, Okada M, Kuroda H, Matsuki M, Ishii K, Murakami T. Clinical application of ^{18}F-fluorodeoxyglucose positron emission tomography for assessment and evaluation after therapy for malignant hepatic tumor. *J Gastroenterol.* 2014;49:46–56.
25. Wilson DW, Tsui BMW, Barrett HH. Noise properties of the EM algorithm. II. Monte Carlo simulations. *Phys Med Biol.* 1994;39:847–871.
26. Zhang X, Xie Z, Wang G, et al. Comparison of linear and non-linear total-body PET parametric imaging [abstract]. *J Nucl Med.* 2020;61(suppl 1):206.
27. van Sluis J, Yaqub M, Brouwers AH, Dierckx RAJO, Noordzij W, Boellaard R. Use of population input functions for reduced scan duration whole-body Patlak ^{18}F-FDG PET imaging. *EJNMMI Phys.* 2021;8:11.

Influence of Fc Modifications and IgG Subclass on Biodistribution of Humanized Antibodies Targeting L1CAM

Sai Kiran Sharma[1], Maya Suzuki[2,3], Hong Xu[2,4], Joshua A. Korsen[1,5], Zachary Samuels[1], Hongfen Guo[2,4], Brandon Nemieboka[1,6], Alessandra Piersigilli[7], Kimberly J. Edwards[1], Nai-Kong V. Cheung[2,5,6], and Jason S. Lewis[1,4,6,8,9]

[1]Department of Radiology, Memorial Sloan Kettering Cancer Center, New York, New York; [2]Department of Pediatrics, Memorial Sloan Kettering Cancer Center, New York, New York; [3]Center for Clinical and Translational Research, Kyushu University Hospital, Fukuoka, Japan; [4]Molecular Pharmacology Program, Memorial Sloan Kettering Cancer Center, New York, New York; [5]Department of Pharmacology, Weill Cornell Medical College, New York, New York; [6]Gerstner Sloan Kettering Graduate School of Biomedical Sciences, Memorial Sloan Kettering Cancer Center, New York, New York; [7]Tri-Institutional Laboratory of Comparative Pathology, Memorial Sloan Kettering Cancer Center, Weill Cornell Medical College, and Rockefeller University, New York, New York; [8]Department of Radiology, Weill Cornell Medical College, New York, New York; and [9]Radiochemistry and Molecular Imaging Probes Core, Memorial Sloan Kettering Cancer Center, New York, New York

Immuno-PET is a powerful tool to noninvasively characterize the in vivo biodistribution of engineered antibodies. **Methods:** L1 cell adhesion molecule–targeting humanized (HuE71) IgG_1 and IgG_4 antibodies bearing identical variable heavy- and light-chain sequences but different fragment crystallizable (Fc) portions were radiolabeled with ^{89}Zr, and the in vivo biodistribution was studied in SKOV3 ovarian cancer xenografted nude mice. **Results:** In addition to showing uptake in L1 cell adhesion molecule–expressing SKOV3 tumors, as does its parental counterpart HuE71 IgG_1, the afucosylated variant having enhanced Fc-receptor affinity showed high nonspecific uptake in lymph nodes. On the other hand, aglycosylated HuE71 IgG_1 with abrogated Fc-receptor binding did not show lymphoid uptake. The use of the IgG_4 subclass showed high nonspecific uptake in the kidneys, which was prevented by mutating serine at position 228 to proline in the hinge region of the IgG_4 antibody to mitigate in vivo fragment antigen-binding arm exchange. **Conclusion:** Our findings highlight the influence of Fc modifications and the choice of IgG subclass on the in vivo biodistribution of antibodies and the potential outcomes thereof.

Key Words: immuno-PET; aglycosylated antibody; afucosylated antibody; Fab arm exchange

J Nucl Med 2022; 63:629–636
DOI: 10.2967/jnumed.121.262383

Monoclonal antibodies rank among the most sought-after class of pharmaceuticals being developed for the treatment of several diseases in humans (*1*). Their increasing utility has bolstered antibody-engineering efforts to improve efficacy and mitigate toxicities (*2*,*3*). Altering the glycosylation status, introducing point mutations in the fragment crystallizable (Fc) region, and changing the immunoglobulin G (IgG) subclass are common strategies whereby the binding of an IgG to Fc γ-receptors (FcγR) on immune effector cells can be modulated (*4*–*7*). However, the impact of these modifications on antibody biodistribution has not been adequately examined. Arguably, most therapeutic antibodies are unnaturally engineered biomolecules synthesized using recombinant technologies; hence, their in vivo biodistribution cannot be taken for granted. Intriguingly, of all the Food and Drug Administration (FDA)–approved antibodies, only a few have dynamic time-dependent in vivo biodistribution and pharmacokinetics data profiled in patients (*8*). Furthermore, only a handful of these antibodies have had preclinical biodistribution analysis before or after FDA approval (*9*). Longitudinal imaging by immuno-PET can fill this existing knowledge gap by enabling quantitation of the in vivo pharmacokinetics and biodistribution of antibodies while delineating their on-target binding and off-target disposition. Critically, immuno-PET and biodistribution studies performed in relevant preclinical animal models early in antibody drug development campaigns can serve as a harbinger for clinical translation and success of antibody therapeutics in human patients (*10*,*11*).

Most FDA-approved antibody therapeutics belong to the fully human or humanized IgG_1 subclass. In addition to target-specific binding at the fragment antigen-binding end of the IgG molecule, human or humanized IgG_1 antibodies bind strongly to activating FcγRs such as FcγRIIIa, which is expressed on immune effector cells such as natural killer cells to mediate antibody-dependent cellular cytotoxicity (ADCC), a key mechanism of action of several therapeutic antibodies. Furthermore, afucosylated IgG_1 antibodies lacking a core fucose in the N-linked biantennary oligosaccharide units of the Fc region have stronger Fc–FcγRIIIa binding, leading to enhanced ADCC activity (Fig. 1) (*12*). On the other hand, aglycosylated IgG_1 antibodies lacking the N-linked biantennary oligosaccharide unit in the Fc region have abrogated Fc–FcγR interactions (Fig. 1) (*13*). Of late, IgG_4—the least abundant IgG in human serum—has emerged as a subclass of choice for the development of therapeutic antibodies, including those used for immunotherapy (*14*). The low affinity of IgG_4 antibodies for activating FcγRs but high affinity for the inhibitory FcγRIIB renders them relatively benign for ADCC. In fact, IgG_4s are considered antiinflammatory antibodies because of their ability to dampen immune responses against repetitive allergen exposure (*15*). These

Received Mar. 31, 2021; revision accepted Jul. 15, 2021.
For correspondence or reprints, contact Jason S. Lewis (lewisj2@mskcc.org) or Nai-Kong V. Cheung (cheungn@mskcc.org).
Published online Aug. 5, 2021.
COPYRIGHT © 2022 by the Society of Nuclear Medicine and Molecular Imaging.

properties make IgG_4 a subclass of choice for the design of immunotherapeutics such as nivolumab and pembrolizumab, which bind to programmed cell death protein 1 on effector T cells in the tumor microenvironment and render efficacy without eliciting secondary immune mechanisms such as ADCC (*5*,*7*,*16*). Collectively, all the aforementioned features highlight the importance of in vivo biomolecular interactions along the Fc–Fc receptor axis that are worth considering during the design and development of therapeutic antibodies (*17*).

In the work at hand, we asked 3 questions fundamental to the molecular composition of humanized IgGs targeting the cell surface glycoprotein L1 cell adhesion molecule (L1CAM), without interfering with the antibody's ability to bind its cognate antigen or interact with the neonatal Fc receptor. Foremost, we asked how enhancement of Fc–FcγR affinity by afucosylation impacts the in vivo distribution of humanized IgG_1. Next, we were curious to know how Fc silencing via antibody aglycosylation, which abrogates Fc–FcγR interaction, influences the in vivo distribution of humanized IgG_1. Lastly, we wanted to know how the choice of IgG subclass—switching from IgG_1 to IgG_4 with and without fab arm exchange (FAE), and loss of most Fc functions—affects antibody distribution in vivo. To that end, we developed a panel of humanized antibodies (Fig. 1; Table 1) targeting human L1CAM, which is overexpressed in several malignancies (*18*,*19*). To noninvasively visualize the antibodies in vivo, we radiolabeled them with ^{89}Zr and used immuno-PET in athymic nude mice bearing subcutaneously implanted L1CAM-expressing SKOV3 tumors.

MATERIALS AND METHODS

Animal Model

All animals were treated as per guidelines approved by the Research Animal Resource Center and Institutional Animal Care and Use Committee at Memorial Sloan Kettering Cancer Center. Female athymic nude (Nu/Nu) mice 8–10 wk old were purchased from Charles River Laboratories. Animals were housed in ventilated cages, given food and water ad libitum, and allowed to acclimatize for 1 wk before inoculation of tumor cells. SKOV3 tumors were induced on the right shoulder via subcutaneous injection of 5 million cells in a 150-μL cell suspension of a 1:1 (v/v) mixture of fresh medium and Matrigel (BD Biosciences). The xenografted mice were used for in vivo studies when the tumor volumes reached approximately 300 mm^3.

PET Imaging

PET imaging was conducted using a mouse hotel on an Inveon PET/CT scanner (Siemens Healthcare) (*20*). SKOV3-xenografted mice were intravenously administered ^{89}Zr-labeled antibodies (8 MBq; 45 μg suspended in 150 μL of phosphate-buffered saline per mouse; $n = 2$ mice per antibody variant). Animals were scanned under the influence of anesthesia by inhalation of 2% isoflurane (Baxter Healthcare) and medical air. PET data for each mouse were recorded via static scans at 48, 96, and 144 h after injection. The PET/CT images were calibrated and cropped before analysis and scaled using AMIDE software (Stanford University). The images were rendered using VivoQuant (Invicro).

Biodistribution

Ex vivo biodistribution analysis was performed on a separate cohort of SKOV3-xenografted mice that were intravenously administered 1.15 MBq (6.4 μg of each ^{89}Zr-labeled antibody variant suspended in 150 μL of phosphate-buffered saline per mouse). Six animals were used per antibody variant, wherein 3 animals were injected with ^{89}Zr-labeled antibody alone and 3 animals were injected with a mixture of ^{89}Zr-labeled antibody and a 38-fold excess (mass) of the unlabeled antibody variant. Animals were euthanized by CO_2 asphyxiation at 144 h after injection. After euthanasia, tissues of interest were harvested via necropsy, weighed, and assayed for radioactivity on a γ-counter calibrated for ^{89}Zr. Counts were converted into activity using a calibration curve generated from known standards. Count data were background- and decay-corrected to the time of injection, and the percentage injected dose (%ID) per gram for each tissue sample was calculated by normalization to the total activity injected.

Statistics

All data are expressed as mean ± SD. Statistical analysis was performed using GraphPad Prism, version 9.1.0. Statistical comparisons of radioactivity concentrations in each organ across the various groups in the ex vivo biodistribution studies were done using nonparametric multiple Mann–Whitney tests to compare ranks. The Holm–Šídák multiple-comparison test was applied, and the threshold for P value comparison was set to 0.05.

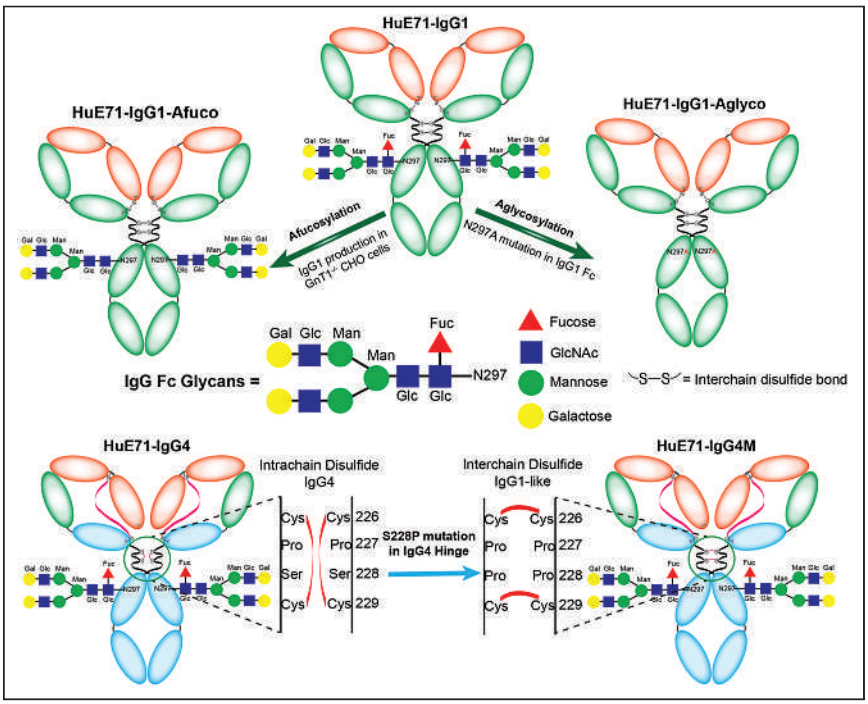

FIGURE 1. Schematic describing the generation of Fc variants of humanized IgG_1 and hinge-mutated IgG_4 L1CAM-targeted antibodies. Fc-glycosylated variants of L1CAM-targeted humanized IgG_1 antibody, HuE71-IgG_1 (top center), were obtained by producing IgG_1 antibody in $GnT1^{-/-}$ CHO cells that are defective for fucosylation and thus yield HuE71-IgG_1-Afuco (top left) (25), whereas substituting asparagine at position 297 in Fc region to alanine (N297A) yielded aglycosylated variant, HuE71-IgG_1-Aglyco (top right). Engrafting anti-L1CAM binding variable heavy- and variable light-chain sequences onto IgG_4 framework yielded HuE71-IgG_4 (bottom left). S228P in hinge region of HuE71-IgG_4 yielded HuE71-IgG_4M. Fuc = fucose; Glc = *N*-acetylglucosamine; Man = mannose; Gal = *N*-acetylgalactosamine.

TABLE 1
Antibodies Used in This Study and Their Biochemical and Functional Characteristics

Antibody	HuE71-IgG_1	HuE71-IgG_1 Afucosylated	HuE71-IgG_1 Aglycosylated	HuE71-IgG_4	HuE71-IgG_4M	Hu3F8-IgG_4
Target	L1CAM	L1CAM	L1CAM	L1CAM	L1CAM	GD2
Immunoreactive fraction (%)	93.1 ± 2.2	89.5 ± 1.5	85.8 ± 2.9	86.7 ± 0.2	88.6 ± 0.3	NA
Subclass	IgG_1	IgG_1	IgG_1	IgG_4	IgG_4	IgG_4
Antibody modification	Wild-type IgG_1	Afucosylated IgG_1	Aglycosylated IgG_1	Wild-type IgG_4	S228P Mut IgG_4	Wild-type IgG_4
FcγR binding	++	+++	−	+	+	+
Fragment antigen-binding arm exchange	−	−	−	+	−	+

RESULTS

A panel of IgG_1 and IgG_4 antibodies having identical variable heavy- and light-chain sequences targeting human L1CAM but modified Fc regions was generated (Table 1) to gain insights into the influence of Fc modifications and subclass on the in vivo biodistribution of IgG_1 and IgG_4 antibodies, respectively.

After purification of the various ^{89}Zr-labeled antibodies, we obtained radioimmunoconjugates having an average molar activity of 26.6 MBq/nmol. A cell-based immunoreactivity assay confirmed the ability of the various radioimmunoconjugates to bind L1CAM-expressing SKOV3 cells (Table 1; Supplemental Fig. 1; supplemental materials are available at http://jnm.snmjournals.org) (*21*). Incubation of the radioimmunoconjugates in serum and evaluation by radio–instant thin-layer chromatography demonstrated less than 4% demetallation up to 7 d after radiosynthesis, suggesting high stability of the radioimmunoconjugates in a biologically relevant medium (Supplemental Fig. 2). Size-exclusion high-performance liquid chromatography of the ^{89}Zr-labeled antibodies incubated without a radioprotectant in chelexed phosphate-buffered saline at 37°C showed more than 80% of the radioimmunoconjugates being stable and existing as monomers up to 6 d after radiosynthesis (Supplemental Figs. 3 and 4).

Athymic nude mice were used in our studies because of their ability to grow tumors from implanted human cancer cell lines and the presence of functional innate immune cells such as macrophages, dendritic cells, and natural killer cells in this strain. Macrophages and natural killer cells comprise 2 main Fc-dependent effector cells responsible for eliciting antibody-dependent cellular phagocytosis and ADCC, respectively (*22*). Furthermore, despite only 60%–70% homology between mouse and human FcγRs, human IgGs are reported to bind orthologous mouse FcγRs with similar strength, suggestive of potentially similar downstream biologic activities mediated by human Fc–murine FcγR interactions in mice (*23*). Immuno-PET imaging of the three ^{89}Zr-labeled IgG_1 variants—humanized (HuE71)-IgG_1, HuE71-IgG_1-Afuco, and HuE71-IgG_1-Aglyco—demonstrated uptake of radioactivity in SKOV3 tumors (Figs. 2A–2C). However, the three IgG_1 variants yielded distinct vivo distribution patterns of radioactivity. SKOV3-xenografted mice injected with ^{89}Zr-HuE71-IgG_1 showed persistence of radioactivity in blood up to 96 h after injection, suggesting slow in vivo clearance of L1CAM-targeted antibodies in this model (Fig. 2A). Besides target-specific tumoral uptake of radioactivity, nonspecific uptake was found in the liver and joints of the long bones of mice. Similarly, ^{89}Zr-HuE71-IgG_1-Afuco yielded uptake of radioactivity in the tumor, liver, and joints of the long bones. However, this variant revealed high-intensity bilateral hot spots corresponding to the axillary and cervical lymph nodes (Fig. 2B) and demonstrated increased clearance from circulation relative to ^{89}Zr-HuE71-IgG_1. Additionally, ^{89}Zr-HuE71-IgG_1-Afuco outlined the spleen and showed a higher radioactivity concentration in long bone joints and the vertebral column. The faster clearance and elevated nonspecific tissue uptake patterns observed for ^{89}Zr-HuE71-IgG_1-Afuco may be attributed to enhanced binding of the afucosylated Fc with mouse FcγRIV-expressing immune cells in the lymph nodes and reticuloendothelial system. The latter is exemplified by results from the analysis of Fc–FcγR binding by surface plasmon resonance (Table 2). Notably, conjugation of desferrioxamine to lysine residues distributed randomly in the Fc region of IgG_1 molecules did not impact binding to murine FcγRIV and human FcγRIIIa-158V.

Previous studies found significant increases in the binding affinity of afucosylated IgG_1 antibody to human FcγRIIIa but no change in the binding affinity to human FcγRI and human neonatal Fc receptor (*12*,*24*,*25*). So, we focused our surface plasmon resonance (SPR) analysis of the differentially glycosylated IgG_1 Fc variants to human FcγRIIIa. Murine FcγRIV was included in the surface plasmon resonance assay since it is a functional ortholog of human FcγRIIIa, and binding to murine FcγRIV may contextualize findings from in vivo studies performed in mice (*26*). Notably, ADCC in humans is mediated via interaction of the Fc of target antigen-bound $hIgG_1$ and human FcγRIIIa expressed on immune effector cells. Furthermore, afucosylated human or humanized IgG_1 antibodies have been shown to target murine FcγRIV for enhanced tumor therapy by ADCC in mice (*27*). SPR analysis of the anti-L1CAM IgG_1 variants used in our study demonstrated 3-fold higher affinity of the HuE71-IgG_1-Afuco for murine FcγRIV than of the HuE71-IgG_1. Interestingly, HuE71-IgG_1-Afuco also showed a similar 3-fold higher binding to the 158V isoform of human FcγRIIIa. On the other hand, and as expected, HuE71-IgG_1-Aglyco showed no binding to either mouse or human FcγRs. Lastly, immuno-PET of ^{89}Zr-HuE71-IgG_1-Aglyco in SKOV3-xenografted mice displayed tumoral uptake of radioactivity with a relatively lower concentration in the liver and bone joints and no detectable uptake in lymph nodes (Fig. 2C).

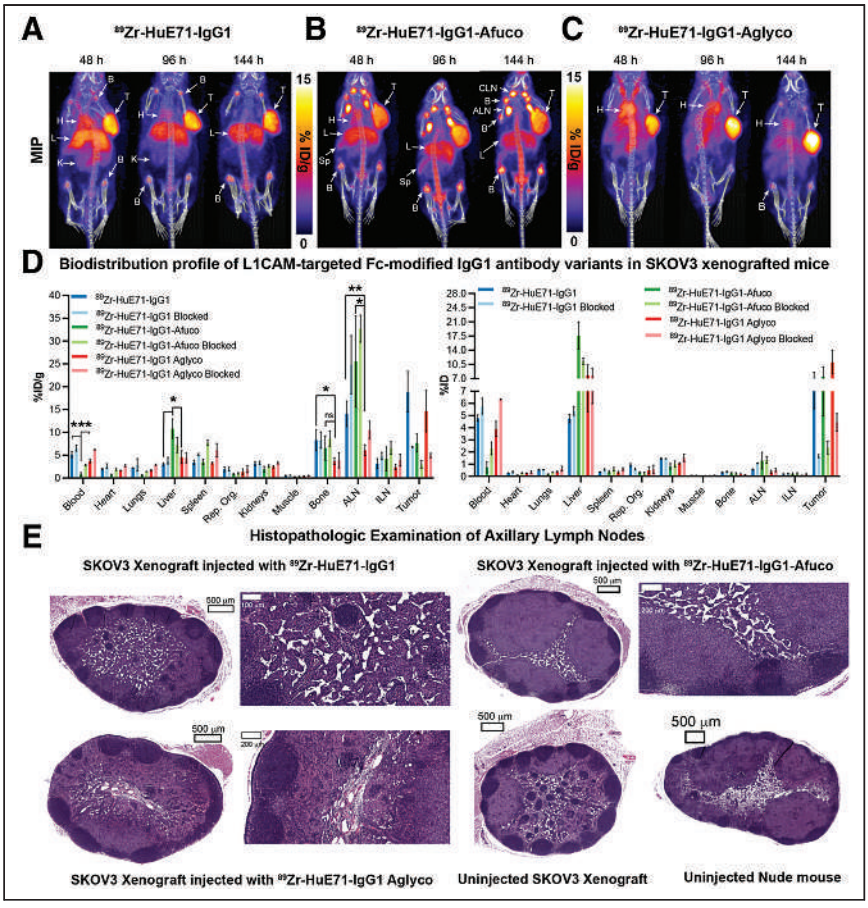

FIGURE 2. Delineation of differential in vivo profiles of Fc-modified L1CAM-targeted IgG_1 variants in SKOV3-xenografted mice through immuno-PET imaging, ex vivo biodistribution analysis, and histopathology. (A–C) Longitudinal PET/CT images acquired at 48, 96, and 144 h after injection of 1.8 mg/kg (7.95 MBq, 45 μg) of ^{89}Zr-HuE71-IgG_1 (A), ^{89}Zr-HuE71-IgG_1-Afuco (B), and ^{89}Zr-HuE71-IgG_1-Aglyco (C) show distribution of radioactivity in blood (indicated by heart (H), tumor (T), liver (L), long bone joints, axillary lymph nodes (ALN), cervical lymph nodes (CLN), and spleen (Sp). Maximum-intensity projections (MIPs) were calibrated and scaled 0–15 %ID/g. (D) Ex vivo biodistribution profile (%ID/g vs. %ID) at 144 h after injection of 0.25 mg/kg (1.15 MBq, 6.4 μg) of 3 ^{89}Zr-labeled L1CAM-targeted Fc-modified IgG_1 variants and their corresponding low-specific-activity blocking dose groups in SKOV3-xenografted mice. Detailed % ID/g and %ID values can be found in Supplemental Tables 1 and 2. (E) Panel of representative low- and high-magnification hematoxylin- and eosin-stained images from histopathologic examination of axillary lymph nodes harvested from SKOV3-xenografted mice injected with the three ^{89}Zr-labeled L1CAM-targeted IgG_1 Fc variants compared with low-magnification images of axillary lymph nodes harvested from uninjected SKOV3-xenografted mouse and healthy tumor-naïve nude mouse. Scale bars on low-magnification images represent 500 μm, whereas those on high-magnification images represent 200 μm. ILN = inguinal lymph node; $^{*}P \leq 0.03$. $^{**}P \leq 0.01$. $^{***}P \leq 0.0005$.

^{89}Zr-HuE71-IgG_1-Aglyco demonstrated the longest persistence of radioactivity in systemic circulation, suggesting an enhanced in vivo half-life plausibly due to the lack of human Fc–murine FcγRIV interactions with resident immune effector cells in the lymph nodes and reticuloendothelial system.

Quantification of the in vivo biodistribution of the three L1CAM-targeted IgG_1 variants was done in a separate cohort of SKOV3 xenografted mice injected with the ^{89}Zr-labeled anti-L1CAM-targeted Fc-modified antibodies. Foremost, the three IgG_1 variants displayed differential radioactivity concentrations in the blood. ^{89}Zr-HuE71-IgG_1-Afuco showed less than 1 %ID/g remaining in circulation at 144 h after injection, whereas the other two variants showed up to 6 %ID/g at this time point. Next, ^{89}Zr-HuE71-IgG_1-Afuco demonstrated high liver uptake (10.8 ± 2.1 %ID/g) compared with the other two variants, which showed less than 6 %ID/g in this tissue. Most other nontarget tissues showed unremarkable differences in uptake of radioactivity between the three Fc-modified IgG_1 variants. However, axillary lymph nodes isolated from SKOV3-xenografted mice injected with ^{89}Zr-HuE71-IgG_1-Aglyco yielded a significantly lower radioactivity concentration in this tissue. Unlike PET images, only mice injected with ^{89}Zr-HuE71-IgG_1 demonstrated a significantly higher radioactivity concentration in the bone (femur) than did xenografts injected with ^{89}Zr-HuE71-IgG_1-Aglyco. Indeed, SKOV3 tumors showed high and specific uptake of radioactivity for all three ^{89}Zr-labeled L1CAM-targeted IgG_1 variants. However, the tumoral uptake values (%ID/g) in mice dosed with the unblocked L1CAM-targeted ^{89}Zr-radioimmunoconjugates demonstrated significantly decreased uptake of ^{89}Zr-HuE71-IgG_1-Afuco compared with radioimmunoconjugates of the other two IgG_1 variants. The relatively low tumoral uptake (7.7 ± 2 %ID/g) of ^{89}Zr-HuE71-IgG_1-Afuco may be attributed to concentration of a significant proportion of the radioactivity or antibody in the liver and lymph nodes of SKOV3-xenografted mice. Determining the %ID taken up in the various tissues revealed that despite having the highest radioactivity concentration (%ID/g) for ^{89}Zr-HuE71-IgG_1-Afuco, the axillary lymph nodes had less than 2% of the total injected radioactivity at 144 h after injection. Instead, the liver accumulated more radioactivity (17.6 ± 3.4 %ID) and turned out to be a major sink for the afucosylated IgG_1 variant.

Importantly, the histopathologic examination of lymph nodes harvested from SKOV3-xenografted mice injected with ^{89}Zr-HuE71-IgG_1-Afuco showed no morphologic evidence of infiltrating neoplastic cells. Instead, these nodes demonstrated reactive hyperplasia characterized by marked paracortical and medullary histio- and plasmacytosis (Fig. 2E). The latter was a unique feature relative to lymph nodes harvested from SKOV3-xenografted mice and tumor-naïve mice that never received ^{89}Zr-HuE71-IgG_1-Afuco. Along those lines, axillary lymph nodes harvested from SKOV3-xenografted mice injected with ^{89}Zr-HuE71-IgG_1 and ^{89}Zr-HuE71-IgG_1-Aglyco showed minor sinus histiocytosis but displayed normal lymphoid tissue architecture (Fig. 2E).

Next, we studied the influence of IgG subclass on the in vivo biodistribution of antibody drugs. To delineate the in vivo biodistribution of IgG_4 antibodies, we generated a humanized IgG_4 variant of the L1CAM-targeting antibody and conducted serial PET

TABLE 2
Analysis of Fc–Fc Receptor Binding by Surface Plasmon Resonance (Biacore T200)

Antibody	KD (M) murine FcγRIV	Relative murine FcγRIV binding	KD (M) human FcγRIIIa-158V	Relative human FcγRIIIa-158V binding
HuE71-IgG_1	7.24E−07	1.00	8.73E−07	1.00
Desferrioxamine-HuE71-IgG_1	5.39E−07	1.34	6.64E−07	1.31
HuE71-IgG_1-Afuco	2.27E−07	3.19	2.86E−07	3.05
Desferrioxamine-HuE71-IgG_1-Afuco	2.19E−07	3.31	2.94E−07	2.96
HuE71-IgG_1-Aglyco	NB	—	NB	—
Desferrioxamine-HuE71-IgG_1-Aglyco	NB	—	NB	—

KD (M) = equilibrium dissociation constant; NB = no binding.

imaging studies in SKOV3-xenografted mice. Serial PET imaging of ^{89}Zr-HuE71-IgG_4 revealed slow in vivo clearance of the antibody from blood and a high radioactivity concentration in the liver (Fig. 3A). In addition to tumoral uptake of radioactivity, ^{89}Zr-HuE71-IgG_4 showed a radioactivity concentration in the kidneys and axillary lymph nodes of SKOV3 xenografts. We hypothesized that uptake of radioactivity in the kidneys may be attributed to FAE, leading to instability of the antibody in vivo. FAE is an intrinsic property of the IgG_4 subclass whereby two half-molecules (heavy-chain–light-chain pair) of the antibodies dissociate from one another at the hinge and recombine spontaneously with other IgG_4 half-molecules in serum to form monovalent bispecific antibodies in vitro and in vivo (*28*). Introducing a point mutation from serine to proline at position 228 (S228P) in the hinge region of IgG_4 antibodies has been shown to mitigate the propensity of FAE (*6*). To validate our hypothesis, an S228P hinge-mutated IgG_4 variant—^{89}Zr-HuE71-IgG_4M—was synthesized and evaluated in vivo. ^{89}Zr-HuE71-IgG_4M demonstrated gradual accretion of radioactivity in the SKOV3 tumor while showing little to no radioactivity in the kidneys (Fig. 3B). Of note, ^{89}Zr-HuE71-IgG_4M faintly highlighted the liver, axillary lymph nodes, and bone joints in this model.

The use of an IgG_4 variant of the anti-GD2 antibody, Hu3F8, as an isotype control and the similarity in radioactivity uptake in the kidneys of SKOV3-xenografted mice injected with ^{89}Zr-Hu3F8-IgG_4 and ^{89}Zr-HuE71-IgG_4 further validated that the abnormal kidney uptake is attributed to FAE intrinsic to IgG_4 antibodies (Fig. 3C). Further, results from an ex vivo biodistribution analysis performed on SKOV3-xenografted mice injected with the three ^{89}Zr-labeled IgG_4 antibodies corroborated findings from immuno-PET studies (Fig. 3D). Importantly, ^{89}Zr-HuE71-IgG_4M yielded a significantly lower radioactivity concentration (2.5 ± 0.56 %ID/g) in the kidneys than did ^{89}Zr-HuE71-IgG_4 (7.4 ± 2.32 %ID/g; P = 0.02). Furthermore, blockade of tumoral uptake of radioactivity by coinjection of a 0.25 mg/kg dose of ^{89}Zr-labeled IgG_4 antibody with a 38-fold excess (mass) of unmodified L1CAM-targeted IgG_4 antibodies in ex vivo biodistribution studies confirmed target-mediated uptake in SKOV3 tumors (Fig. 3D). Notably, ^{89}Zr-HuE71-IgG_4M demonstrated increased tumoral uptake of radioactivity (16.1 ± 4.26 %ID/g) compared with ^{89}Zr-HuE71-IgG_4 (5.5 ± 2.4 %ID/g; P = 0.03) and ^{89}Zr-Hu3F8-IgG_4 (3.6 ± 1.76 %ID/g; P = 0.02). Concordant with PET data, ^{89}Zr-Hu3F8-IgG_4 yielded a high radioactivity concentration in the kidneys (15.2 ± 5.14 %ID/g) and showed between 1 and 8 %ID/g in most healthy tissues. Tumoral uptake (4.9 ± 0.46 %ID/g) of the isotype antibody may be attributed to enhanced permeability and retention in this compartment. Lastly, the high radioactivity concentration in multiple tissues harvested from mice injected with the ^{89}Zr-HuE71-IgG_4M-blocking dose arm is most likely a result of persistence of ^{89}Zr-HuE71-IgG_4M in the blood at 144 h after injection.

DISCUSSION

Recent insights into pharmacologic modulation at the Fc–FcγR axis have made this molecular interaction an important consideration in the development of antibody-based drugs for cancer immunotherapy (*16*,*17*,*29*). Furthermore, single-nucleotide polymorphisms in FcγR-encoding genes have been implicated in disease etiology and clinical responses (*30*). Specifically, patients carrying the 158V/V genotype showed improved outcomes from rituximab therapy due, in part, to improved ADCC activity in vivo (*31*). Additionally, we have previously shown that stronger in vitro Fc–FcγR binding for an afucosylated variant of the humanized anti-GD2 IgG_1 antibody yielded improved preclinical efficacy because of enhanced ADCC in vivo (*25*).

Our current findings with the afucosylated anti-L1CAM IgG_1 variant concur broadly with two ^{89}Zr-immuno-PET studies done using HER3-targeted humanized IgG_1 antibodies—GSK2849330 and RG7116—which were Fc-glycoengineered for enhanced ADCC activity (*32*,*33*). The high uptake of radioactivity in the liver and spleen of xenograft models developed in immunodeficient SCID mice used in those studies was attributed to enhanced binding of the antibodies with FcγRs expressed on tissue-resident auxiliary immune cells in the reticuloendothelial system (*32*,*33*). However, neither of those antibodies showed elevated radioactivity concentrations in lymph nodes. The latter may be due, in part, to the higher immunodeficient status of SCID mice used in those studies and the presence of functional natural killer cells in athymic

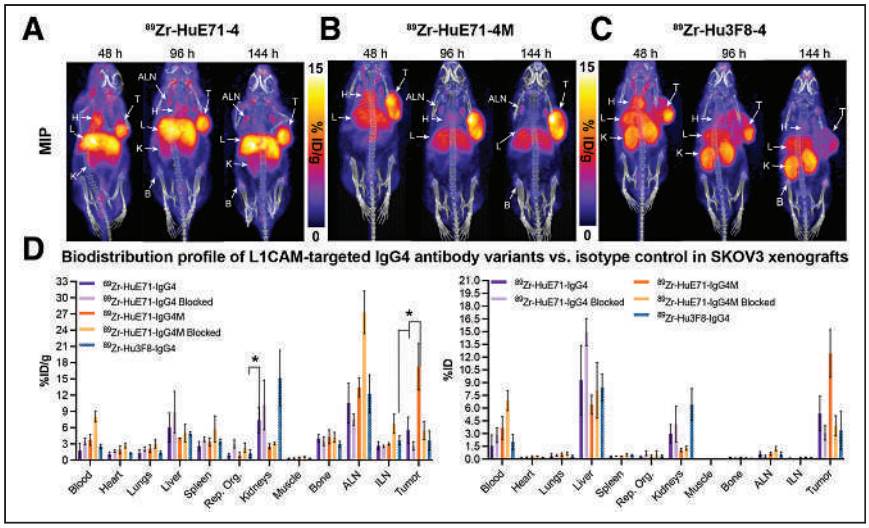

FIGURE 3. Delineation of differential in vivo profiles of L1CAM-targeted IgG_4 variants in SKOV3-xenografted mice through immuno-PET imaging and ex vivo biodistribution analysis. (A–C) Longitudinal PET/CT images acquired at 48, 96, and 144 h after injection of 1.8 mg/kg (7.95 MBq, 45 μg) of ^{89}Zr-HuE71-IgG_4 (A), ^{89}Zr-HuE71-IgG_4M (B), and ^{89}Zr-Hu3F8-IgG_4 (C) show distribution of radioactivity in blood (indicated by heart [H]), tumor (T), liver (L), kidneys (K), axillary lymph nodes (ALN), and long bone joints (B). Maximum intensity projections (MIPs) were calibrated and scaled 0%–15 %ID/g. (D) Ex vivo biodistribution profile (%ID/g vs. %ID) at 144 h after injection of 0.25 mg/kg (1.15 MBq, 6.4 μg) of 2 ^{89}Zr-labeled L1CAM-targeted IgG_4 variants and isotype control IgG_4 antibody in SKOV3-xenografted mice. ILN = inguinal lymph node. *$P \leq 0.05$. Detailed % ID/g and %ID values can be found in Supplemental Tables 3 and 4.

nude mice used in our study. Although suggestive of an Fc-mediated phenomenon, the pronounced lymph node uptake of radioactivity in mice injected with the afucosylated variant warrants further validation in immunocompetent syngeneic tumor models or xenograft models developed in mice reconstituted with a functional human immune system. Admittedly, immunodeficient mice impact the in vivo biodistribution of exogenously injected human or humanized IgG_1 because of relatively low titers of endogenous IgG and the availability of unoccupied high-affinity FcγRs on tissue-resident immune cells in the liver, spleen, and bone marrow (*34*). This phenomenon is exacerbated in highly immunodeficient mouse strains developed on the NOD-SCID background (*35*). However, low levels of serum IgG_{2a} in athymic nude mice have also been implicated in the rapid clearance of exogenously injected human IgG_1 and mouse IgG_{2a} (*36*).

Along those lines, a comparison of the afucosylated versus parental L1CAM-targeting IgG_1 in tumor-naïve athymic nude mice revealed a lower radioactivity concentration of ^{89}Zr-HuE71-IgG_1-Afuco in the blood at 120 h after injection, suggesting faster in vivo pharmacokinetics (Supplemental Fig. 5), which is consistent with our findings for this variant in SKOV3-xenografted mice. Furthermore, the relatively high radioactivity concentration in the long bone joints of mice injected with ^{89}Zr-HuE71-IgG_1-Afuco is also indicative of faster in vivo catabolism of the radioimmunoconjugate, leading to the release of ^{89}Zr for in vivo uptake and complexation with hydroxyapatite in the bone joints. When target expression is absent in the bones, radioactivity uptake in this tissue is commonly attributed to the in vivo catabolism of desferrioxamine-conjugated ^{89}Zr-labeled antibodies in mice and the osteophilic nature of ^{89}Zr (*37*). Intriguingly, there was no significant difference between radioactivity concentrations in the liver and those in the axillary lymph nodes harvested from tumor-naïve mice injected with either ^{89}Zr-labeled L1CAM-targeted IgG_1 variant. That finding points to a potential contribution of the tumor—a target sink, which may account for a pronounced difference noted between ^{89}Zr-HuE71-IgG_1 and ^{89}Zr-HuE71-IgG_1-Afuco in SKOV3-xenografted animals. Taken together, our findings suggest that afucosylated IgG_1 antibodies having improved Fc–FcγR binding and enhanced ADCC capability are likely to have significantly faster in vivo pharmacokinetics due to sequestration in the reticuloendothelial system and resident immune cells in lymph nodes. On the other hand, IgG_1 aglycosylation yielded an Fc-silenced antibody, which showed no lymph node uptake when tested in the same animal model as its Fc-active counterparts.

In light of our findings with the L1CAM-targeting IgG_4 variants, it is no surprise that several FDA-approved IgG_4 antibody therapeutics harbor the S228P mutation to impart in vivo stability while minimizing therapeutic variability due to in vivo FAE (*14*). Of interest, lower uptake of radioactivity was found in the bone joints of SKOV3-xenografted mice injected with L1CAM-targeted ^{89}Zr-labeled IgG_4 antibodies than with their Fc-active IgG_1 counterparts. Case in point, femurs harvested from SKOV3-xenografted mice injected with ^{89}Zr-HuE71-IgG_4 and ^{89}Zr-HuE71-IgG_4M showed 4.0 ± 0.74 %ID/g ($P = 0.03$) and 4.4 ± 1.58 %ID/g ($P = 0.047$), respectively, compared with ^{89}Zr-HuE71-IgG_1, which yielded 8.3 ± 2.35 %ID/g in this tissue. Furthermore, radioactivity concentrations of ^{89}Zr-labeled L1CAM-targeted IgG_4 variants were comparable to that yielded by the Fc-silent IgG_1 variant—^{89}Zr-HuE71-IgG_1-Aglyco (3.7 ± 0.75 %ID/g)—in this tissue. The latter is suggestive of slow in vivo catabolism and low nonspecific uptake in healthy nontarget tissue. Lastly, the nonspecific hepatic uptake of radioactivity highlights a plausible contribution of Fc–FcγR interactions between Fc-active radiolabeled IgG_1s and parenchymal and nonparenchymal cells in the liver (*38*). It is known that the liver is involved in the vivo catabolism of radiometal-labeled antibodies, leading to initial accumulation of ^{89}Zr-radiometabolites and subsequent complexation of free ^{89}Zr in the long bone joints of mice (*37*,*39*,*40*).

Highlights aside, a limitation of the current work is that it uses antibody variants developed for a single tumor-associated antigen in a singular xenograft model developed on an immunodeficient background. Additionally, identification of cells having elevated expression of murine FcγRIV in lymph nodes leading to the manifestation of reactive hyperplasia, and pinpointing cells in the liver that bind ADCC-enhanced IgG_1 antibodies to impact in vivo pharmacokinetics, are outstanding questions that warrant further investigation.

CONCLUSION

Collectively, our findings highlight the influence of Fc-glycosylation status and choice of IgG subclass on the in vivo

biodistribution of the most widely used human or humanized antibody subclasses (IgG_1 and IgG_4) approved as therapeutics for human use. Our results demonstrate that deglycosylated IgG_1 antibodies yield low nonspecific off-target uptake in healthy tissues, whereas S228P hinge-mutated IgG_4 antibody eliminates FAE-mediated renal uptake of radioactivity. Importantly, this work illustrates the value of immuno-PET in delineating the in vivo biodistribution of ADCC-enhanced IgG_1 antibodies and in macroscopically highlighting potential nontumor tissue depots. Doing so can inform antibody drug development efforts to uncover mechanisms leading to in vivo therapeutic benefit or toxicity. From a theranostic perspective, our results suggest that developing immuno-PET agents using ADCC-enhanced tumor-targeting IgG_1 antibodies may yield false-positive results in lymph nodes because of Fc–FcγR interactions in vivo. Similarly, immuno-PET agents developed using tumor-targeting wild-type IgG_4 antibodies may yield false-positive results from nonspecific uptake of radioactivity in the kidneys while grossly underestimating tumor burden because of loss of the radiotracer to in vivo FAE. In sum, we hope that the results described herein further motivate the use of molecular imaging to inform the preclinical development of novel antibody-based theranostic agents.

DISCLOSURE

This work was supported by the MSKCC Small Animal Imaging Core, funded in part by NIH Small-Animal Imaging Research Program (SAIRP) grant R24 CA83084 and NIH center grant P30 CA08748 and by the Tri-Institutional Laboratory of Comparative Pathology, which was funded in part by NIH grant P30 CA08748. The work was also supported by an R01 CA176671 awarded to Jason Lewis and a diversity supplement R01 CA176671 awarded to Brandon Nemieboka. Brandon Nemieboka was supported by a Medical Scientist Training Program grant from the National Institute of General Medical Sciences of the National Institutes of Health under award number T32GM007739 to the Weill Cornell/Rockefeller/Sloan Kettering Tri-Institutional MD-PhD Program. Jason Lewis was supported by R01 CA204167 and R35CA2 32130. Jason Lewis acknowledges funding support from the Mr. William H. Goodwin and Mrs. Alice Goodwin and the Commonwealth Foundation for Cancer Research and the Center for Experimental Therapeutics at Memorial Sloan Kettering Cancer Center. Sai Kiran Sharma acknowledges the Tow Foundation for a Postdoctoral Fellowship Award. Nai-Kong Cheung, Maya Suzuki, Brandon Nemieboka, Hong Xu, and Jason Lewis were named as inventors on the L1CAM patent (WO2018232188A1) filed by Memorial Sloan Kettering. Both Memorial Sloan Kettering and Nai-Kong Cheung have financial interest in Y-mAbs Therapeutics Inc., Abpro-Labs, and Eureka Therapeutics. Nai-Kong Cheung reports receiving commercial research grants from Y-mAbs Therapeutics Inc. and Abpro-Labs Inc. Nai-Kong Cheung was named as inventor on multiple patents filed by Memorial Sloan Kettering, including those licensed to Y-mAbs Therapeutics Inc., Biotec Pharmacon, and Abpro-labs. Nai-Kong Cheung is a Scientific Advisory Board member for Abpro-Labs and Eureka Therapeutics. Jason Lewis is an associate editor of *The Journal of Nuclear Medicine* but had no involvement or access to information regarding the peer review of this article. Sai Kiran Sharma is a member of the editorial board of *The Journal of Nuclear Medicine.* No other potential conflict of interest relevant to this article was reported.

KEY POINTS

QUESTION: What is the impact of Fc modification and choice of IgG subclass on the in vivo pharmacologic profile of humanized antitumor antibodies?

PERTINENT FINDINGS: Humanized IgG_1 antibodies yield differential in vivo pharmacokinetics and biodistribution based on the glycosylation status of the Fc. Afucosylated IgG_1 antibodies with enhanced Fc–FcγR binding and ADCC activity yield faster in vivo pharmacokinetics and show nonspecific Fc-mediated sequestration in lymph nodes and the reticuloendothelial system. Aglycosylated IgG_1 antibodies with abrogated Fc–FcγR binding yield lesser nonspecific uptake of the antibody and related radiocatabolites in vivo, yielding stealth targeting vectors. S228P hinge-mutated IgG_4 antibodies overcome in vivo FAE to yield a better radiopharmacologic profile by eliminating uptake of antibody and associated radioactivity in the kidneys.

IMPLICATIONS FOR PATIENT CARE: Using immuno-PET to characterize the in vivo pharmacokinetics and biodistribution to uncover potential mechanism of action or toxicity of engineered antibodies can yield better and safe antibody-based drugs to improve patient care.

REFERENCES

1. Carter PJ, Lazar GA. Next generation antibody drugs: pursuit of the 'high-hanging fruit.' *Nat Rev Drug Discov.* 2018;17:197–223.
2. Weiner GJ. Building better monoclonal antibody-based therapeutics. *Nat Rev Cancer.* 2015;15:361–370.
3. Wang X, Mathieu M, Brezski RJ. IgG Fc engineering to modulate antibody effector functions. *Protein Cell.* 2018;9:63–73.
4. Arnold JN, Wormald MR, Sim RB, Rudd PM, Dwek RA. The impact of glycosylation on the biological function and structure of human immunoglobulins. *Annu Rev Immunol.* 2007;25:21–50.
5. Bruhns P, Iannascoli B, England P, et al. Specificity and affinity of human Fcgamma receptors and their polymorphic variants for human IgG subclasses. *Blood.* 2009;113:3716–3725.
6. Silva JP, Vetterlein O, Jose J, Peters S, Kirby H. The S228P mutation prevents in vivo and in vitro IgG4 Fab-arm exchange as demonstrated using a combination of novel quantitative immunoassays and physiological matrix preparation. *J Biol Chem.* 2015;290:5462–5469.
7. Vidarsson G, Dekkers G, Rispens T. IgG subclasses and allotypes: from structure to effector functions. *Front Immunol.* 2014;5:520.
8. O'Donoghue JA, Lewis JS, Pandit-Taskar N, et al. Pharmacokinetics, biodistribution, and radiation dosimetry for ^{89}Zr-trastuzumab in patients with esophagogastric cancer. *J Nucl Med.* 2018;59:161–166.
9. Ulaner GA, Sobol NB, O'Donoghue JA, et al. CD38-targeted immuno-PET of multiple myeloma: from xenograft models to first-in-human imaging. *Radiology.* 2020;295:606–615.
10. Crawford A, Haber L, Kelly MP, et al. A mucin 16 bispecific T cell-engaging antibody for the treatment of ovarian cancer. *Sci Transl Med.* 2019;11:497:eaau7534.
11. Kelly MP, Makonnen S, Hickey C, et al. Preclinical PET imaging with the novel human antibody ^{89}Zr-DFO-REGN3504 sensitively detects PD-L1 expression in tumors and normal tissues. *J Immunother Cancer.* 2021;9:1:e002025.
12. Shields RL, Lai J, Keck R, et al. Lack of fucose on human IgG1 N-linked oligosaccharide improves binding to human Fcgamma RIII and antibody-dependent cellular toxicity. *J Biol Chem.* 2002;277:26733–26740.
13. Radaev S, Sun PD. Recognition of IgG by Fcgamma receptor: the role of Fc glycosylation and the binding of peptide inhibitors. *J Biol Chem.* 2001;276:16478–16483.
14. Chen X, Song X, Li K, Zhang T. FcgammaR-binding is an important functional attribute for immune checkpoint antibodies in cancer immunotherapy. *Front Immunol.* 2019;10:292.

15. Davies AM, Sutton BJ. Human IgG4: a structural perspective. *Immunol Rev.* 2015; 268:139–159.
16. Dahan R, Sega E, Engelhardt J, Selby M, Korman AJ, Ravetch JV. FcgammaRs modulate the anti-tumor activity of antibodies targeting the PD-1/PD-L1 axis. *Cancer Cell.* 2015;28:285–295.
17. DiLillo DJ, Ravetch JV. Fc-receptor interactions regulate both cytotoxic and immunomodulatory therapeutic antibody effector functions. *Cancer Immunol Res.* 2015;3:704–713.
18. Schäfer MK, Altevogt P. L1CAM malfunction in the nervous system and human carcinomas. *Cell Mol Life Sci.* 2010;67:2425–2437.
19. Ganesh K, Basnet H, Kaygusuz Y, et al. L1CAM defines the regenerative origin of metastasis-initiating cells in colorectal cancer. *Nat Cancer.* 2020;1:28–45.
20. Carter LM, Henry KE, Platzman A, Lewis JS. 3D-printable platform for high-throughput small-animal imaging. *J Nucl Med.* 2020;61:1691–1692.
21. Lindmo T, Boven E, Cuttitta F, Fedorko J, Bunn PA Jr. Determination of the immunoreactive fraction of radiolabeled monoclonal antibodies by linear extrapolation to binding at infinite antigen excess. *J Immunol Methods.* 1984;72:77–89.
22. Budzynski W, Radzikowski C. Cytotoxic cells in immunodeficient athymic mice. *Immunopharmacol Immunotoxicol.* 1994;16:319–346.
23. Overdijk MB, Verploegen S, Ortiz Buijsse A, et al. Crosstalk between human IgG isotypes and murine effector cells. *J Immunol.* 2012;189:3430–3438.
24. Junttila TT, Parsons K, Olsson C, et al. Superior in vivo efficacy of afucosylated trastuzumab in the treatment of HER2-amplified breast cancer. *Cancer Res.* 2010; 70:4481–4489.
25. Xu H, Guo H, Cheung IY, Cheung NK. Antitumor efficacy of anti-GD2 IgG1 is enhanced by Fc glyco-engineering. *Cancer Immunol Res.* 2016;4:631–638.
26. Bruhns P. Properties of mouse and human IgG receptors and their contribution to disease models. *Blood.* 2012;119:5640–5649.
27. Braster R, Bogels M, Benonisson H, et al. Afucosylated IgG targets FcgammaRIV for enhanced tumor therapy in mice. *Cancers (Basel).* 2021;13:2372.
28. Rispens T, Ooijevaar-de Heer P, Bende O, Aalberse RC. Mechanism of immunoglobulin G4 Fab-arm exchange. *J Am Chem Soc.* 2011;133:10302–10311.
29. Arlauckas SP, Garris CS, Kohler RH, et al. In vivo imaging reveals a tumor-associated macrophage-mediated resistance pathway in anti-PD-1 therapy. *Sci Transl Med.* 2017;9:389:eaal3604.
30. Paul P, Pedini P, Lyonnet L, et al. FCGR3A and FCGR2A genotypes differentially impact allograft rejection and patients' survival after lung transplant. *Front Immunol.* 2019;10:1208.
31. Mellor JD, Brown MP, Irving HR, Zalcberg JR, Dobrovic A. A critical review of the role of Fc gamma receptor polymorphisms in the response to monoclonal antibodies in cancer. *J Hematol Oncol.* 2013;6:1.
32. Alsaid H, Skedzielewski T, Rambo MV, et al. Non invasive imaging assessment of the biodistribution of GSK2849330, an ADCC and CDC optimized anti HER3 mAb, and its role in tumor macrophage recruitment in human tumor-bearing mice. *PLoS One.* 2017;12:e0176075.
33. Terwisscha van Scheltinga AG, Lub-de Hooge MN, Abiraj K, et al. ImmunoPET and biodistribution with human epidermal growth factor receptor 3 targeting antibody ^{89}Zr-RG7116. *MAbs.* 2014;6:1051–1058.
34. Sharma SK, Chow A, Monette S, et al. Fc-mediated anomalous biodistribution of therapeutic antibodies in immunodeficient mouse models. *Cancer Res.* 2018;78: 1820–1832.
35. Li F, Ulrich ML, Shih VF, et al. Mouse strains influence clearance and efficacy of antibody and antibody-drug conjugate via Fc-FcgammaR interaction. *Mol Cancer Ther.* 2019;18:780–787.
36. Reddy N, Ong GL, Behr TM, Sharkey RM, Goldenberg DM, Mattes MJ. Rapid blood clearance of mouse IgG2a and human IgG1 in many nude and nu/+ mouse strains is due to low IgG2a serum concentrations. *Cancer Immunol Immunother.* 1998;46:25–33.
37. Chomet M, Schreurs M, Bolijn MJ, et al. Head-to-head comparison of DFO* and DFO chelators: selection of the best candidate for clinical ^{89}Zr-immuno-PET. *Eur J Nucl Med Mol Imaging.* 2021;48:694–707.
38. Jones PL, Brown BA, Sands H. Uptake and metabolism of ^{111}In-labeled monoclonal antibody B6.2 by the rat liver. *Cancer Res.* 1990; 50(suppl):852s–856s.
39. Meijs WE, Haisma HJ, Klok RP, et al. Zirconium-labeled monoclonal antibodies and their distribution in tumor-bearing nude mice. *J Nucl Med.* 1997;38: 112–118.
40. Motta-Hennessy C, Sharkey RM, Goldenberg DM. Metabolism of indium-111-labeled murine monoclonal antibody in tumor and normal tissue of the athymic mouse. *J Nucl Med.* 1990;31:1510–1519.

Be Recognized as an **SNMMI Designated Radiopharmaceutical Therapy Center of Excellence**

SNMMI designated Centers of Excellence in Radiopharmaceutical Therapy are:

- Well-integrated into a patient's care pathway
- Led by physicians appropriately trained in nuclear medicine
- Staffed by highly qualified therapy teams
- Designed to meet strict regulatory, training, qualification, experience, and performance criteria

Learn more about how your site can become an **SNMMI Designated Radiopharmaceutical Therapy Center of Excellence.**

www.snmmi.org/RPTCoE

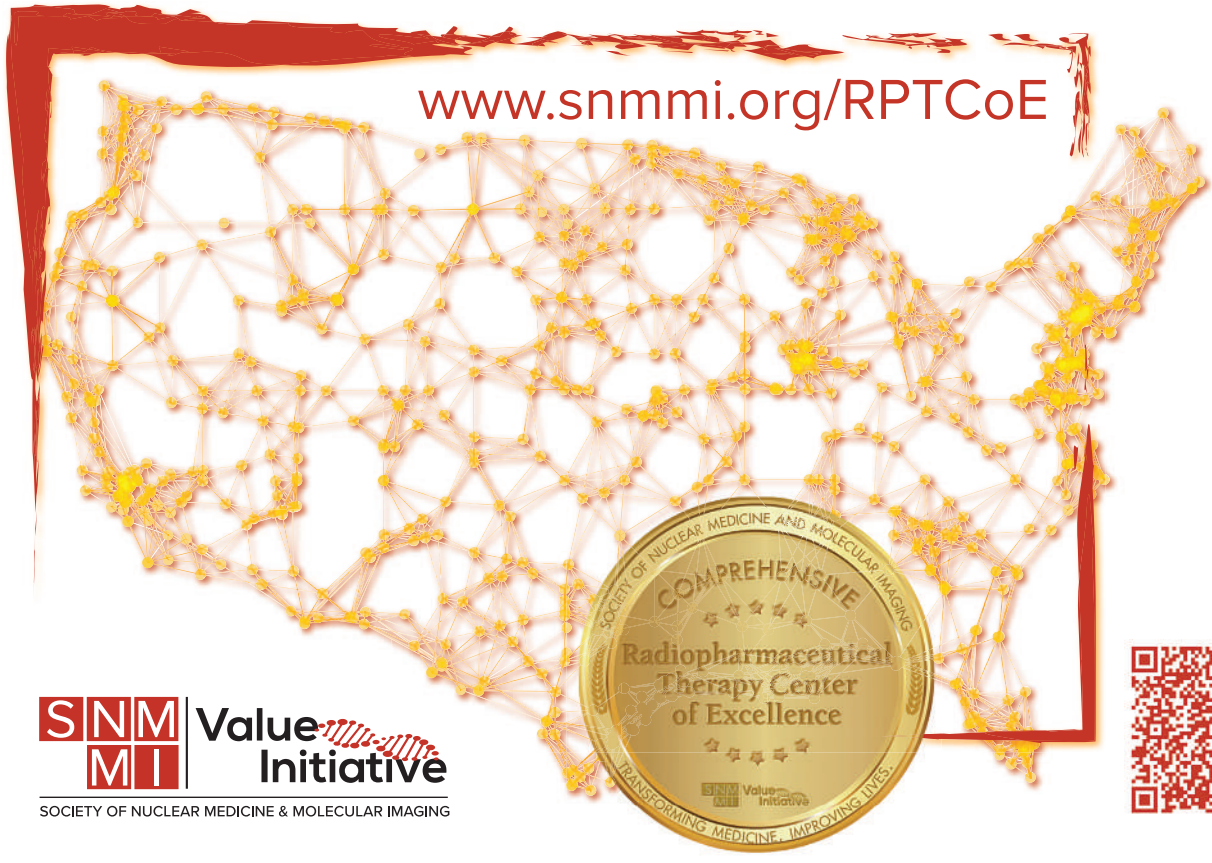

SNMMI Value Initiative

SOCIETY OF NUCLEAR MEDICINE & MOLECULAR IMAGING

SNMMI 2022 Annual Meeting

2022 HOT TROT 5K

VIRTUAL

Recognizing the hybrid approach to this year's meeting, we have made the decision to keep the **Hot Trot 5K Run/Walk** as a virtual event in 2022, allowing ALL attendees to participate. Local running recommendations will be available onsite for in-person attendees. In-person participants who register by **April 14, 2022** can pick up their race t-shirt and medal in Vancouver. All other race materials will be mailed to participants following the Annual Meeting.

Add the Hot Trot when you register for the meeting, register at:

www.snmmi.org/HotTrot5K

Professional Development and Education Fund PDEF Give. Learn. Lead.

SNMMI Technologist Section
SOCIETY OF NUCLEAR MEDICINE & MOLECULAR IMAGING

THE UNIVERSITY OF TEXAS
MD Anderson Cancer Center
Making Cancer History®

OPEN RANK, CLINICAL FACULTY APPOINTMENT
DEPARTMENT OF NUCLEAR MEDICINE

The faculty member is expected to hold a Clinical Faculty Appointment (CFA) position at The University of Texas MD Anderson Cancer Center in the Department of Nuclear Medicine within the Division of Diagnostic Imaging. The faculty member is a clinician qualified to work in the field of Nuclear Medicine at either an Assistant, Associate or Professor level. The primary academic appointment will be in the Department of Nuclear Medicine.

Functional Responsibilities: The Sections of Positron Emission Tomography (PET) and Clinical Nuclear Medicine (CNM) are administrative units that provide comprehensive, diagnostic and therapeutic services within the Department of Nuclear Medicine. Faculty within these Sections provide (1) excellent, comprehensive and compassionate care for an oncologic patient population; (2) nuclear imaging and therapeutic procedures in a cost effective environment; (3) programs and projects conducted to advance fundamental or clinical understanding of oncology and nuclear medicine; (4) education for medical students, residents, fellows, graduate students and technologists; and (5) multidisciplinary and collaborative approaches to patient-centered imaging, transformative research, prevention and exceptional education.

The faculty will actively engage in clinical research and scholarly activity that promotes responsible conduct of research within the Department and Institution. The candidate is expected to assess and seek appropriate funding mechanisms to support clinical research focused on theranostics. Requires completion of grant applications and contracts, budget development and resource analysis.

The members of the Department are appointed upon the recommendation of the Chair of the Department of Nuclear Medicine with concurrence of the Division Head of Diagnostic Imaging, and approval by the President of the Institution. This position is supervised by the Section Chief(s) for day-to-day clinical operations. The primary evaluator on an Annual Faculty Performance Appraisal is the Department Chair, reflecting faculty member's education, research, patient care and administrative activities. These functional responsibilities require the mental ability to reason deductively; act decisively; communicate and execute the Institution's acceptable standards of conduct; interact with highly sophisticated technology; and understand complicated, comprehensive concepts and technologies.

Qualifications: Medical degree, board certification by the American Board of Nuclear Medicine, licensure by the Texas State Board of Medical Examiners and ACLS certification upon 90 days of employment.

Additional Preferred Qualifications:
- Board certification by the American Board of Radiology
- Record of high-quality, peer-reviewed publications
- ACLS certification preferred

Interested qualified candidates should submit their curriculum vitae and names and addresses of at least three references to:

Homer A. Macapinlac, M.D., Chair
Department of Nuclear Medicine
The University of Texas MD Anderson Cancer Center
1515 Holcombe Blvd, Unit 1485
Houston, TX 77030
Email: hmacapinlac@mdanderson.org
Req #: 00091343- 220131

MD Anderson Cancer Center is an equal opportunity employer and does not discriminate on the basis of race, color, religion, age, national origin, sex, sexual orientation, gender identity/expression, disability, veteran status, genetic information, or any other basis protected by federal, state, or local laws, unless such distinction is required by law. All positions at The University of Texas MD Anderson Cancer Center are security sensitive and subject to examination of criminal history record information. Smoke-free and drug-free environment.

THE UNIVERSITY OF TEXAS
MD Anderson Cancer Center
Making Cancer History®

OPEN RANK, TERM TENURE-TRACK
DEPARTMENT OF NUCLEAR MEDICINE

The faculty member is expected to hold a term tenure-track position at The University of Texas MD Anderson Cancer Center in the Department of Nuclear Medicine within the Division of Diagnostic Imaging. The faculty member is a clinician qualified to work in the field of Nuclear Medicine at an Assistant Professor level or higher. The primary academic appointment will be in the Department of Nuclear Medicine.

Functional Responsibilities: The Sections of Positron Emission Tomography (PET) and Clinical Nuclear Medicine (CNM) are administrative units that provide comprehensive, diagnostic and therapeutic services within the Department of Nuclear Medicine. Faculty within these Sections provide (1) excellent, comprehensive and compassionate care for an oncologic patient population; (2) nuclear imaging and therapeutic procedures in a cost effective environment; (3) programs and projects conducted to advance fundamental or clinical understanding of oncology and nuclear medicine; (4) education for medical students, residents, fellows, graduate students and technologists; and (5) multidisciplinary and collaborative approaches to patient-centered imaging, transformative research, prevention and exceptional education.

The faculty member will practice clinical diagnostic and therapeutic nuclear medicine in an exemplary manner to standards set forth by the Texas State Board of Medical Examiners and the American Boards of Nuclear Medicine, or its equivalent, for oncology, cardiac imaging and neurologic imaging. Perform the procedures that fall within the scope of their privileges and credentials for diagnostic nuclear medicine and therapy as granted by the University of Texas Board of Regents on the recommendation of the Credentials Committee and the Executive Committee of the Medical Staff.

The faculty will actively engage in clinical research and scholarly activity that promotes responsible conduct of research within the Department and Institution. The candidate is expected to assess and seek appropriate funding mechanisms to support clinical research. Requires completion of grant applications and contracts, budget development and resource analysis. Requires the ability to identify research opportunities as well as to develop and coordinate research programs. The applicant is expected to identify, apply for and obtain independent extramural peer reviewed funding from federal agencies; and to develop meaningful relationships with industry partners and private organizations.

The members of the PET and CNM Sections are appointed upon the recommendation of the Chair of the Department of Nuclear Medicine with concurrence of the Division Head of Diagnostic Imaging, and approval by the President of the Institution. This position is supervised by the Department Chair for day-to-day clinical operations. The primary evaluator on an Annual Faculty Performance Appraisal is the Department Chair, reflecting faculty member's education, research, patient care and administrative activities. These functional responsibilities require the mental ability to reason deductively; act decisively; communicate and execute the Institution's acceptable standards of conduct; interact with highly sophisticated technology; and understand complicated, comprehensive concepts and technologies.

Qualifications: Medical degree, board certification by the American Board of Nuclear Medicine, licensure by the Texas State Board of Medical Examiners and ACLS certification upon 90 days of employment.

Additional Preferred Qualifications:
- Board certification by the American Board of Radiology
- Record of high-quality, peer-reviewed publications
- ACLS certification preferred

Interested qualified candidates should submit their curriculum vitae and names and addresses of at least three references to:

Homer A. Macapinlac, M.D., Chair
Department of Nuclear Medicine
The University of Texas MD Anderson Cancer Center
1515 Holcombe Blvd, Unit 1485
Houston, TX 77030
Email: hmacapinlac@mdanderson.org
Req #: 00010315 - 220131

MD Anderson Cancer Center is an equal opportunity employer and does not discriminate on the basis of race, color, religion, age, national origin, sex, sexual orientation, gender identity/expression, disability, veteran status, genetic information, or any other basis protected by federal, state, or local laws, unless such distinction is required by law. All positions at The University of Texas MD Anderson Cancer Center are security sensitive and subject to examination of criminal history record information. Smoke-free and drug-free environment.

A STREAMLINED CLINICAL CARE PATH ENABLED BY DIGITAL 360° SPECT/CT IMAGING

VERITON-CT®

DIGITAL SPECT/CT

Optimization of every step

For optimal patient outcomes, clinicians require access to imaging that ensures the most accurate diagnosis and appropriate treatment management decisions.

Spectrum Dynamics has integrated its ground-breaking Broadview Technology design into the VERITON-CT system, providing a digital platform that handles routine 3D workflow in one place. The result is optimization of every step, from image acquisition to interpretation.

VERITON-CT digital SPECT/CT combines the best-in-class CZT detectors, novel system design, high resolution CT, and advanced software technology to elevate the performance of CZT digital SPECT.

Digital Technology
360° design for high sensitivity and coverage

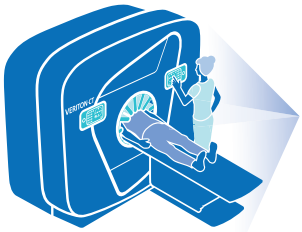

Workflow is reproducible and optimized for patient needs

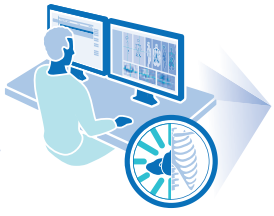

Image quality tools in TruView Console for advanced reconstruction and artifact reduction for both NM and CT data

Quantitative analysis
accessible in TruView Console integration with MIM-SD platform

Comprehensive results
from transformative technology that provides a greater volume of high quality data for informed decision-making

spectrum-dynamics.com

SPECTRUM
DYNAMICS MEDICAL

4/22

The Journal of Nuclear Medicine

April 2022 ▪ **Vol. 63** ▪ **Pages** 497–636